IMPACT AND QUASI-STATIC RESPONSE OF CYLINDRICAL COMPOSITE SHELLS

by

Brian L. Wardle

B. S., The Pennsylvania State University
(1992)

Submitted to the Department of Aeronautics and Astronautics
in partial fulfillment of
the requirements for the degree of

Master of Science
in Aeronautics and Astronautics

at the
Massachusetts Institute of Technology

May 1995

Signature of Author _____
Department of Aeronautics and Astronautics
May 4, 1995

Certified by _____
Professor Paul A. Lagace
MacVicar Faculty Fellow, Professor of Aeronautics and Astronautics
Thesis Supervisor

Accepted by _____
Professor Harold Y. Wachman
Chairman, Departmental Graduate Committee

IMPACT AND QUASI-STATIC RESPONSE OF CYLINDRICAL COMPOSITE SHELLS

by
Brian L. Wardle

Submitted to the Department of Aeronautics and Astronautics on Mary 4, 1995 in partial fulfillment of the requirements for the Degree of Master of Science in Aeronautics and Astronautics

ABSTRACT

Work was conducted to explore and begin to understand the impact response of composite shells over a range of impact events considered in the large-mass, low-velocity regime. Both impact and quasi-static experiments were conducted on various structural configurations including convex shells, concave shells, plates, and cylinders with boundary conditions of pinned/no in-plane sliding on the axial edges and free on the circumferential edges. Specimens with a planar aspect ratio of 1 were constructed in $[\pm 45_n/0_n]_s$ (n = 1, 2, 3) layups from Hercules AS4/3501-6 graphite epoxy prepreg. Basic structural parameters (radius, span, and thickness) were varied via scaling to determine the effects of these parameters and ratios of these parameters on the response. Damage states were characterized visually and with the dye-penetrant x-ray photography method and compared by defining damage metrics such as the average damage extent and damage extent ratio. An instability phenomenon was noted in the response of many convex shells which has a strong influence on the response. The Hertzian type contact relation does not capture the local response of indented shells and initial stiffness does not characterize the overall shell response. Relative contributions of membrane stiffness and bending stiffness are noted to be key in the overall convex shell response. Boundary conditions were also noted to have a strong influence on the response. Quasi-static and impact response are found to be nearly identical in all respects, including compelling evidence from the damage state comparisons. Two noted differences are that backface spalling was observed for a small number of specimens in impact tests only and that some showed a low frequency, high amplitude response in impact tests which was not observed in quasi-static tests. All structural parameters were shown to affect the response, including the shell height, although thickness was of particular importance. Nondimensional ratios were not found that capture the behavior of convex shells over the entire range of data but the data indicates regimes where different ratios are important, especially the height-to-thickness ratio. Peak force is found to be an excellent damage resistance metric. Impact energy consumption of convex shells through structural deformation, resulting in lower peak forces, is observed to give convex shells improved damage resistance over plate specimens. However, at the barely visible impact damage (BVID) level, convex shells that do not undergo an instability can incur more nonvisible damage than plates at a given force. This damage behavior, which includes different damage distributions, is attributed to differences caused by compressive versus tensile membrane stresses. The general response and resulting local stress and damage state, with relative contributions from both membrane and bending effects, needs to be determined through careful analysis to better determine the important parameters in the response. The damage distribution through the thickness needs to be characterized through experimentation, and then related to the stress state through analysis.

Thesis Supervisor: Paul A. Lagace
Title: MacVicar Faculty Fellow, Professor of Aeronautics and Astronautics, Massachusetts Institute of Technology

Acknowledgments

Many people made this thesis possible - Paul Lagace heads the list and, whether he likes it or not, is partly responsible for this work. Much thanks to the other Profs. in TELAC for advice whenever needed: Professor Dugundji, Hugh, and Michael. The real power lies with Ping and Debbie - without them nothing gets done, thanks. Thanks also to Al, Don, and Earle for their help in getting all my experimental work completed.....along those lines I gotta acknowledge Eric and Howard for a semester of late night company. All the grad-students in TELAC are simply excellent; special thanks to Bhatman, Wilson, Hary, Steve, and Aaron. Of course my coohl UROPs did all of the real work: Willy, Corinne, Janeen, Sevgi, Dylan, and Nate. Thanks to Lyn for the beginning and all my friends for keeping me (sane?). Cecelia has been so great with support, understanding, and humor; later alli-! Special thanks to my family and Gram for my original education and support over the years.

> ...and I stared out the window again. As I looked down, it dawned on me that the airplane on which we were riding contained within its technology nearly four centuries of progress. We had learned much about manipulating the resources we had found on the Earth. How many people, I mused, how many generations did it take to create the products and the understanding that enabled this airplane to come into being? And how many spent their whole lives focused on one tiny aspect, one small step, without ever lifting their heads from that preoccupation?
>
> -*James Redfield*, The Celestine Prophecy

> ...*The test of all knowledge is experiment*. Experiment is the *sole judge* of scientific "truth".
>
> -*Richard P. Feynman*, The Feynman Lectures on Physics

Foreword

This work was performed in the Technology Laboratory for Advanced Composites (TELAC) in the Department of Aeronautics and Astronautics at the Massachusetts Institute of Technology. This work was sponsored by the Federal Aviation Administration under Research Grant 94-G-037 and the NASA Langley Research Center under NASA Grant NAG-1-991.

Table of Contents

List of Figures

List of Tables

Nomenclature

$a(t)$	specimen acceleration at time t
F	contact force
F_{tot}	contact force experienced by the impactor
F_{ft}	force experienced by the force transducer
h	shell height
K	contact stiffness
m	exponent in nonlinear contact law
M_{ft}	mass of the force transducer (25 g)
M_{rod}	mass of the impacting rod (1450 g)
M_{tup}	mass of the tup (125 g)
n	structural scaling parameter
R	shell radius
Rn	scaled specimen radius
RP	radius identifying plate specimens
S	shell span
SC	span identifying full cylinder
Sn	scaled specimen span
t	time
t_{ply}	ply thickness
T	shell thickness
Tn	scaled specimen thickness
v_o	initial specimen velocity
$w(t)$	specimen deflection at time t
x_o	initial specimen deflection

X1	base for generic scaled structural variable
Xn	generic scaled structural variable
α	indentation
β	spanwise twist
Φ	shell included angle
γ	axial twist
θ	ply angle

CHAPTER 1

INTRODUCTION

Laminated composite materials have gained increasing use in structural applications in recent years. Performance advantages over traditional metallic structures abound. High specific stiffness and strength, mechanical tailoring capabilities, and excellent fatigue characteristics are some of the attributes that make structures built from laminated composites attractive to designers. This is especially true in the aerospace community where composites are seen to provide increased performance for both military and commercial structures.

Design with composite laminates is not without drawbacks, however. Damage mechanisms of laminated composites not only differ, but are more complex than in metallic structures. Modes of damage not seen in metals are found in composite laminates: delaminations are an example. Additionally, composites with impact damage can have substantial strength reductions with little or no indication of damage on the surface. The lack of both a qualitative and quantitative understanding of these damage mechanisms has necessitated conservative designs with advanced composites - somewhat mitigating the advantages of composites over metals. Oftentimes damage becomes the limiting design consideration for structures made out of advanced composites.

In the aircraft industry, composites initially replaced secondary structures that were typically made from aluminum, e.g. [1, 2]. Damage

considerations in secondary structures are typically not critical. However, composites have seen increased application in design of primary structures, especially in military aircraft such as the V-22 Osprey but also in large transport commercial designs. The Beechcraft Starship was the first all-composite aircraft certified by the FAA and even more recently, composites have seen application as primary structures in the empennage of the Boeing 777. The use of composites in primary structures necessitates a detailed understanding of damage and failure mechanisms of these materials [3].

The need to understand damage and failure of aircraft structures is formalized in safety regulations written and enforced by aircraft governing agencies [4, 5]. Safety and reliability of the structural design must be demonstrated. A key philosophy exists that provides for a clear understanding of safety and reliability in design. The philosophy is one of damage tolerance. Damage tolerance is a measure of the ability of a material/structure to "perform" (given particular requirements) with damage present. Safety regulations are written with this philosophy in mind.

In order to design damage tolerant structures, engineers must first understand and characterize the damage types likely to occur. Given a structure and a damaging event, the damage state must be determined. Damage states are characterized in a damage resistance study, a counterpart to damage tolerance. Damage resistance is the measure of the damage incurred by a material/structure due to a particular event. Only after damage has been defined, such as in a damage resistance study, can a determination of damage tolerance be made. Utilizing the concepts of damage resistance and tolerance, a consistent approach to impact can be defined for laminated composite structures [6].

In aircraft design with composites, the issue of impact damage becomes paramount. The low through-thickness strength of composites, along with the complicated nature of the impact damage state, make impact one of the most detrimental damage types. This has naturally hampered efforts to determine damage resistance of composite structures. This has limited design with composites because of unresolved damage tolerance issues. However, the performance advantages of composites have continued to propel much research into the issue of impact damage resistance over the past 20 years. Preliminary experimental work has been completed on plate composite structures, forming a large collection of results and conclusions. However, aircraft components are not flat and have some degree of curvature. This is where experience and research into composite impact resistance falls short. There is a substantial need to characterize resistance in composite shells, especially in comparison to plates.

The aim of the present experimental work is to explore the impact resistance of cylindrical composite shells. This is done through a static indentation program and a larger series of impact tests. Primary structural and impact parameters are varied to determine basic trends in the damage resistance of composite shells. The objective is to compare/contrast shell response with that of plates as well as to form a basis for understanding the important issues involved in the impact resistance of composite shells.

The work is organized as follows. Relevant work relating to impact resistance is reviewed in chapter 2. This is followed by the problem definition and approach taken in this work in chapter 3. Experimental procedures are outlined in chapter 4. Contained in chapter 5 are the results of the experimental program followed by a discussion of these results in chapter 6.

Finally, in chapter 7, conclusions are drawn based on the results of the investigation and recommendations are made for future research.

CHAPTER 2

BACKGROUND

There is one consistent comment in the literature with regard to impact and composite shell structures - not much has been done. This is in contrast to composite plates where much work has been done, both experimentally and analytically, e.g. [7-9]. So much work, in fact, that comprehensive reviews on the subject have recently appeared in various journals [10, 11]. In the most logical chronological progression, plates are studied extensively as a prelude to more complicated geometries such as shells. Shells are one step closer than plates to actual aerospace structures, such as fuselage components and wing cover panels, due to curvature. Shells under transverse loads immediately experience membrane forces due to geometric coupling. Plates, however, experience this membrane effect only after relatively large displacements are reached. The importance of membrane effects on the dynamic response of composite plates has already been demonstrated [12].

Impact in composite materials can be viewed as two related but different concepts: damage resistance and damage tolerance. The two concepts are defined as follows: damage resistance is the measure of the damage incurred by a material/structure due to a particular event whereas damage tolerance is a measure of the ability of a material/structure to "perform" (given particular requirements) with damage present. Utilizing

these concepts, a consistent approach to impact can be defined for composite structures. A consistent approach, along with an example, is presented in [6].

The distinction between resistance and tolerance is very muddied in the literature. The distinction is either implied without qualification or is simply ignored. The paper on damage tolerance by Munjal et. al. [13], which is actually about impact damage resistance *and* tolerance, is an example where no distinction is made. Generally, this lack of distinction mitigates the effectiveness of a paper. Previous research is reviewed in this chapter with the difference between damage resistance and tolerance clearly delineated.

In this chapter, research into impact damage resistance and tolerance of monolithic composite shell structures, including cylinders and plates, is reviewed. The two major issues in damage to composite materials, damage resistance and damage tolerance, provide a format for evaluating previous work and a language by which to address it. A review of composite plate research pertaining to impact damage resistance is presented in a section separate from shell work, even though plates are simply shells of infinite radius. This is done because the bulk of impact research with composites has been concerned with plates. Damage tolerance studies of composite shells are included in this chapter as motivation for understanding damage resistance, and also because much of the work mixes tolerance and resistance. Designing safe and reliable structures necessitates an evaluation of the damage (damage resistance) before any tolerance predictions can be made.

2.1 Composite Plates

Research into impact damage in composite aircraft/spacecraft structures began with basic issues to gain direction and insight. This insight

would then be taken and utilized to help understand more complicated problems. This logical progression began with monolithic composite plates and moved onto more complicated structures such as sandwich panels and shells. Impact damage research on composite plates is extensive, as stated in the introduction. General results relating to impact of composites have been obtained through investigations into plates. These results, and approaches to the problem of impact damage in composites, are summarized in this section to form a basis for discussion of impact damage in composite shells.

Through observations of impact damage to composite plates, researchers have identified the concept of barely visible impact damage (BVID). BVID refers to an impact damage level in composite structures that has little visual indication of damage to the naked eye. However, a composite structure can be severely damaged internally by an impact event and have little or no signs of visible damage. Since impact damage to composite structures cannot be reliably characterized visually, there exists the possibility that substantial damage can be missed during inspection. This possibility has to be understood and taken into consideration when designing damage tolerant composite structures.

For a given impact event, the response of composite plates has been shown to be a function of material, stacking sequence, specimen geometry, boundary conditions, structural stiffness, as well as impactor mass, geometry, and velocity [11]. These parameters affect the structural response as well as the extent and modes of damage which occur (damage resistance). Along with this observation, important conclusions about impact damage resistance of composite plates have been reached concerning threshold energies [14, 15]. With plates, an energy (for a given impactor mass) is usually found below which no damage occurs and another higher energy above which no further

damage occurs. The higher energy typically corresponds to the penetration energy where the impactor passes completely through the composite.

Previously, it was thought that impact energy (energy of the impactor) was the most important metric in the impact of composites. It was believed that keeping the energy constant would provide for a basis of comparison between impacts, e.g. [16]. It was later found, and supported both experimentally and analytically, that peak impact force was a much better metric [17-20]. Large-mass, low-velocity impacts having the same energy as low-mass, high-velocity tests, were shown to have different dynamic responses and damage states. However, peak impact force was shown to correlate very well with the amount and type of damage. Additionally, while maintaining a consistent peak force, excellent agreement is obtained when damage from low-velocity impact and static indentation tests are compared [19, 21, 22]. Impact events are considered in the low-velocity regime when dynamic effects are unimportant. Qualitatively this can be assessed by considering the mass ratio of the impactor to the structure and the bending to contact stiffness ratio: the higher these ratios, the less important dynamic effects become. Comparative investigations are motivated by the simple observation that quasi-static testing is much easier and less expensive than impact tests.

Impact damage, and thus composite damage resistance, is a combination of both local and global (structural) effects [23]. Ignoring boundary difficulties, impact damage to composites begins local to the indentor and grows outward. Composites have many damage modes including fiber breaks, fiber splits, delamination, and matrix cracks. The type and amount of damage which occurs in an impact event is related to the peak force which occurs. The peak force is a function of both the structure

and impactor. Thus, both the local contact problem and the structural response (bending and membrane loading) must be considered if the damage resistance of a structure is to be evaluated.

The most common approach to the local problem for plates is to model the area immediate to the indentor/impactor with a Hertzian type nonlinear contact law [21] of the form:

$$F = K\alpha^m \tag{2.1}$$

where F is the contact force, K is the contact stiffness, α is the indentation, and m is a fitting parameter (usually taken as 1.5 as described subsequently). The indentation is the reduction in laminate thickness directly under the indentor/impactor. The contact law is elastic and static in the nature of its derivation but has been widely applied to impact events as well as to structures that are not isotropic [21, 24, 25]. An example is the exponent m in equation 2.1. The value of 1.5 is strictly valid only for an isotropic elastic half-space but it has been used to fit experimental data for composite plates (K becomes the empirical fitting parameter).

The local stress field is analyzed using the contact law and other assumptions that vary between investigations. The plate response is then evaluated in bending under a transverse load. The local and bending solutions are matched and combined in some manner to determine the overall response of the plate. Recent work by Wu et. al. [26, 27] has shown that the local and bending solutions may not superpose as previously thought. That work has also shown that global bending of the composite plate can significantly change the area of contact with the indentor/impactor; enough to redistribute pressure in the region of contact and alter the resulting

contact relation, equation 2.1. This effect has not been accounted for in most of the previous investigations of the impact/contact problem.

It is important to note that the uncertain understanding of damage modes and adequate failure criteria for composites limit even the most accurate analysis in terms of determining a damage state. Accurate description of the stress/strain state during impact must be coupled with equally accurate failure criteria to be able to define the damage state of the composite. Accurate failure criteria have not been defined up to this point; engineering approximations/correlations have been made. This lack of adequate failure criteria is exemplified by the large number of different (but similar) criteria that are available in the open literature for analyzing composites [28, 29].

2.2 Composite Shells

Research into impact damage of composite shells is very limited. This is partially a result of the fact that shells are difficult to constrain and test. Additionally, resistance and tolerance issues have not been delineated in previous work with composite shells. Although damage tolerance is not addressed in this research, it is the motivation for exploring damage resistance, and is summarized in section 2.2.2. To design safe and reliable structures using a damage tolerance philosophy, the amount and type of damage must first be determined. Thus, knowing the damage resistance of the structure is key.

Comparative studies of damage resistance and tolerance of composite plate and shell structures is a natural progression [30-34]. This comparative type approach has met with some success but results are preliminary and

mixed. As a general comment, it seems that most investigators have found that composite shells act like plates with regard to damage resistance. If this is true, it would be convenient for design engineers because plate results and analyses could be directly applied to shell geometries and the matter quickly settled. However, recent limited work indicates that damage resistance of composite shells and plates does differ in both mode and extent [35].

The fundamental difference between plates and shells is the radius of curvature with plates having infinite radius as the limiting case. The effect of curvature and the resultant membrane stiffening on the response of composite structures, including plates, is discussed here as a prelude to damage resistance in section 2.2.1. The response of a structure to any loading obviously plays a large role in the damage resistance of the structure.

As with composite plates, many analytic methods to determine the stress-strain state and dynamic response in composite shells have been established. Even the more difficult problem of static and dynamic snap-through of composite shells has been modeled with excellent agreement to experimental results [31, 36-40]. The problem still remains, however, to characterize the specifics of the damage state. Most investigations to date model the response of composite shell structures to concentrated static or impact loads while avoiding predictions of the resulting damage. Two investigations are summarized here to illustrate typical results and highlight differences between plate and shell response [31, 36].

The membrane stiffening effect of shells has been investigated analytically and compared with plates [31]. Analytic results compared favorably with experimental work done with composite plates only. A radius of curvature to laminate thickness ratio of less than 100 is suggested by the authors for curvature effects to be important in the response of the composite

structures. The authors reached this conclusion by plotting mid-point deflection versus the radius-to-thickness ratio and subjectively noting the approximate region where the response deviated, presumably due to curvature effects. This is typical in that many other papers cite the radius-to-thickness ratio as a primary metric for defining the response of shells. Snap-through buckling, which can be important for shallow shells, was not considered. However, other work not only shows the importance of snap-through buckling in the response of shells, but also concludes that dynamic snap-through may have a different response than in the static case [36].

Snap-through buckling of a shallow shell is an instantaneous instability resulting from compressive membrane forces in the shell which arise during transverse loading. This occurs because of geometric coupling in the shell due to curvature. The instability manifests itself as a highly nonlinear load-deflection curve in the static case. Analysis has shown that in the case of snap-through due to a dynamic load, two phenomena are possible [36]. When the applied dynamic load peaks below the critical (static) snapping level, the dynamic response oscillates harmonically around the static solution (before snap-through). For an applied dynamic load greater than the critical (static) snapping load, the response shows snap-through and then non-periodic large oscillations around the solution for the static snap-through displacement. The conclusion from this numerical analysis is that oscillations in the dynamic load case are drastically different if the shell snaps through. It was shown, however, that stability characteristics and the critical snapping load can be predicted using a static solution, even though the behavior around the instability is itself a dynamic phenomenon.

Experimental work on the impact response of composite shells has yielded some preliminary conclusions. Work on composite cylinders has

shown that static force versus deflection curves are highly nonlinear [41] and show similar trends when compared to impact curves [42]. Constant contact times over a range of impact velocities have been reported [43, 44]. A very limited experimental study has shown that peak force increases while contact time and maximum center deflection decrease, with increasing curvature [35]. This experimental work has indicated that curvature plays a significant role in determining the impact response of composite shells because of snap-through buckling and membrane stiffening. It should be noted that experimental response characteristics, i.e. force and deflection histories, for composite shells are not available in the open literature at the current time.

2.2.1 Damage Resistance

As noted previously, damage resistance in composite shells has primarily been addressed from a comparative perspective (i.e. as compared to plates). This approach was undoubtedly taken to build upon existing knowledge of composite plate damage resistance. This comparative approach has met with some success but results within the open literature are somewhat contradictory and must be considered preliminary. The underlying effect of membrane stiffening on the response/damage of shells is usually not directly addressed. Typically, results are stated and the relatively larger 'shell' stiffness due to membrane stiffening, as compared to the plate, is cited as the reason for any noted differences, e.g. [33].

Comparative damage resistance studies have mixed and seemingly contradictory findings regarding composite shells and plates. For example, in one investigation the damage modes were found to be the same for composite plates and cylinders, but the damage to the cylinders was contained inside a smaller region around the impact site [32]. However, in another study, the

modes and extent of damage are clearly different between shells and plates [45]. Graphite/epoxy fabric was used in [32] while tape was used in [45]. This may account for the different conclusions about the damage state. The former study also found that both plates and cylinders exhibit an impact energy threshold below which no damage occurs [32].

The latter study [45] included a more comprehensive damage evaluation procedure than the first [32]. Sectioning with dye-penetrant enhanced optical microscopy was used in [45] versus dye-penetrant enhanced x-ray in [32]. Two stacking sequences were considered, $[0_5/90_5/0_5]$ and $[90_5/0_5/90_5]$, with one shell and one plate geometry for a total of only four specimen types [45]. It was shown that the damage extent and even type in laminated plates and shells can be different due to the different impact-induced stresses. Matrix cracks on the face opposite impact as well as delamination between lower plies were observed with plates and attributed to high tensile bending strains. Fiber breaks in the top-layer (convex, impact side), fiber splits in the middle layers, and delaminations between both lower and upper plies were observed in the composite shells at the same impact velocity. Peak force was not discussed so it is not known whether the increased force due to the shells being structurally stiffer was the actual cause for the differing damage states. It was further shown experimentally that the constant K in the Hertzian contact relation, equation 2.1, is smaller for the cylindrical shells than for the plates. This was attributed to the decreased contact area due to the curvature of the shells [34].

As with plates, peak impact force has shown good correlation for cylinders as the primary damage metric [42, 46-48]. As an example, filament-wound composite cylinders were transversely impacted and statically indented to the same force levels [46]. The authors concluded from visual

inspection and sectioning that damage from a static test was equivalent to the damage state from an impact test at the same force level for various tape-winding angles. Hysteresis was observed in the load-unload curves of force versus deflection indicating permanent deformation and damage. No new damage was observed with reload (static) to the same load level but re-impact studies were not undertaken. The authors concluded that damage incipience may be indicated by a sudden drop in the experimental load versus deflection curves.

The effects of basic structural variables on damage resistance of composite shells have been investigated for a few specific cases. Structural configuration [42], layup (stacking sequence) [43, 44, 49], thickness [43, 44, 49], and material [49] were shown to influence damage modes and extent. Curvature, the most basic structural parameter, has been investigated in only one study and not compared with plates [35].

Structural configuration, in the form of internal reinforcement, was investigated with transverse impact and quasi-static tests of filament-wound graphite/epoxy cylinders [42]. Composite cylinders were internally reinforced with concentric cylinders of aluminum or rubber and compared with composite cylinders with no reinforcement. The authors report that for the load and energy levels tested, the reinforcement type governed the damage resistance results. With no reinforcement, bending caused a larger damage extent (area) in the form of delaminations and matrix cracking than in the reinforced cases. In the case of aluminum reinforcement (the stiffest configuration), the damage was more local to the impact site and was manifested as fiber breakage and matrix crushing with no delaminations. In the rubber core tests (intermediate stiffness configuration), all modes of

damage seen in the other cases (delaminations, matrix cracking, and fiber breaks) were present.

Layup, material, and thickness were investigated by two similar impact investigations at the Air Force Institute of Technology (AFIT) [43, 44, 49]. All the shells in these investigations have the same curvature, 305 mm (12") radius, chord, and length . The impact velocities considered fall into the low-velocity regime where quasi-static assumptions are typically applied. C-scan, sectioning, and optical microscopy were used to determine the damage state. All four fully clamped shell edges left a 127 mm x 127 mm (5" x 5") exposed panel area impacted by a 12.7 mm (0.5") diameter hemispherical indentor.

The layup changed the load and/or displacement for damage incipience [35, 36]. C-scans showed that the damage shapes varied widely with layup (rectangular, elliptical, and circular shapes were noted). Sectioning revealed that delaminations occurred at ply angle mismatch interfaces and that transverse cracking occurred within many of the layers. It was also found that the minimum sustainable impact energy before incipience (including sub-visual) is a function of layup [49]. The damage state, in general, was found to be elongated in the circumferential direction of the shells.

Thickness (effective ply thickness) was also found to affect the damage extent [43, 44] and incipience [49]. Globally stiffer shells (thicker) showed that damage was kept closer to the impact site [43, 44] and showed the highest threshold energy before damage was detected [49]. No conclusions were reached with respect to damage location or mode changing with effective ply thickness. Material effects were investigated in the second study [49]. Graphite/epoxy showed larger force and shorter contact times than kevlar/epoxy for the same impact event and layup. This was attributed to the

higher stiffness of the graphite/epoxy material system. Generally, the same trends typically found with composite plates were reported in these shell investigations. Finally, the effect of curvature was investigated in an extremely limited experimental investigation [35]. Two radii were considered but no conclusions were reached about the effect of the curvature on the damage state. However, it can be inferred from graphical data in the paper that damage extent may increase with increasing curvature for a constant impact event. This may occur because the peak force (shell response) changes due to different curvatures.

Impact velocity was varied in a cylinder study [41] showing a range where no damage was observed and a possible velocity beyond which damage would not increase (a threshold). As the velocity increased, a flattening of the damage area versus velocity curve was noted. Some interesting effects concerning impact and quasi-static testing were reported concerning thick kevlar/epoxy filament-wound rocket motor cases [47]. In the statically loaded cases, more of the loading energy was absorbed through permanent deformation than in the impact case. This indicates a strain-rate dependence on the damage resistance of this structure. In general, the fibers local to the indentor were pushed aside during loading instead of breaking as in the dynamic case. The fiber/matrix damage area (core damage) was noted to be elliptical with the ellipse major axis perpendicular to the composite fiber direction. The tube was noted to be hot to the touch after impact, but not after quasi-static testing.

Lastly, a full-scale impact resistance study was performed on a complete XFV-12A composite wing [50]. Visual and sub-visual damage states were created with an impactor at various locations on the 18-ply, curved, graphite/epoxy (fiberglass core) wing skin. The damage was inspected by

'field-methods' - visual and pulse-echo. The research reported that the damage areas were approximately circular in nature and specifically that the sub-visually damaged regions (delaminations) were also nearly circular. This was a case-specific study of a real aircraft component, the curvature of the wing was not given, and effects of curvature on the resistance were not discussed. However, it was noted that damage states of the full-scale component were typical of those found in investigations using small specimens. This indicates that resistance studies of small specimens may be appropriate for use with larger laminated composite shell structures.

2.2.2 Damage Tolerance

Damage tolerance of composite tubes and pressure vessels (shells) is of great importance to the aerospace community. For example, a fuselage can be thought of as a complicated pressure vessel. Early work considering shell geometries was primarily concerned with transverse impact to full cylinder and pressure vessel configurations. Cylinders and pressure vessels model such things as pipelines, fuselage sections, and submarine hulls. This early work was usually not compared to composite plate results because the goemetries were so different and the research was usually for specific applications.

Various studies have looked at damage tolerance of composite pressure vessels and cylinders after impact [20, 30, 32, 41, 42, 51-62]. Some of the problems with these investigations include proper modeling of 'impact damage', lack of any type of experimental correlation, and the general problem of identifying and using proper failure criteria. Progressive damage finite element models have been developed by several researchers [51, 52, 62] but not verified experimentally. The model given by Minnetyan [52] predicts

the failure pressure of composite cylinders to decrease by up to 85% with damage on the inner and outer surfaces. Obtaining confidence in the damage types/extent used in tolerance models that predict such large strength reductions provides excellent motivation for studying impact damage resistance of composite shells.

Some of the resistance studies from section 2.2.1 were actually mixed damage resistance and tolerance investigations [32, 42, 49, 63-68]. The investigation that considered boundary conditions in the form of internal supports [42], also experimentally investigated damage tolerance of these impacted specimens. The tubes with the most damage (least resistance), corresponding to the intermediate stiffness internal support (rubber) during impact testing, were found to have the lowest burst pressures. Another investigation found that the failure pressure of composite cylinders decreased with increasing visible damage [32]. An amount of damage corresponding to a threshold in failure pressure reduction was also reported.

Previous investigators have proposed that one of the reasons for the highly nonlinear load-deflection curves of composite shells is damage from delaminations [41]. The effect of delaminations on the damage tolerance of AS4/3501-6 graphite/epoxy shells has been investigated in studies at AFIT [63-68]. The boundary conditions in these compression tolerance tests are clamped-clamped perpendicular to the cylindrical shell axis (direction of load application) and simply-supported along the other two (straight) edges with a knife-edge support. All the panels have the same curvature, 305 mm (12") radius, chord, and length.

Impact damage was mimicked by artificially creating circular delaminations in shells with teflon inserts [66-68]. The inserts were placed at the geometric center of the shells but at varying positions through the

thickness. This was meant to simulate delamination impact damage, although shells were not impacted to verify this assumption. The insert thickness was on the same order as a ply thickness and some dimpling and cracking occurred on the outer surface of the manufactured shells (8-ply laminates). This, therefore, puts the results of this investigation somewhat in question. Nevertheless, knockdown factors of 20 to 30% with regard to failure (buckling was considered failure in these tests) were reported. Another investigator also had manufacturing difficulties, but reported that the delamination sizes tested did not decrease the buckling (failure) load above error in the data [63-65]. This is contrary to the previous study.

Material and stacking sequence effects were investigated in a combined impact damage resistance/tolerance study [49]. Damage resistance results from this study were discussed in section 2.2.1 and the tolerance study used the same loading configuration (AFIT) as in [63-68]. The study found that the impact damage from these tests had no effect on damage tolerance during compressive testing (buckling failure) [49]. Delamination growth during compression loading was noted in both materials (graphite and kevlar/epoxy), contrary to observations made in [64, 67]. This places some doubt on whether the teflon implants accurately modeled delaminations from an impact event.

The problems encountered in these tolerance studies of composite shells emphasize the difficulties involved in undertaking such investigations. However, the importance of such studies in understanding tolerance issues is unquestionable. The large knockdown factors with regard to burst pressure predicted by analyses such as [52] provide the impetus for studying damage resistance and damage tolerance of composite shells.

2.3 Summary

This review of the current literature on impact damage resistance and tolerance of composite shells identifies many issues in the area that still need to be addressed. There are contradictory findings within the literature which seem to be a result of the difficulties associated with testing shell structures. Generally, curvature effects still need to be investigated, but most importantly, differences between composite plate and shell structures must be addressed from a damage resistance perspective. Preliminary and limited work has identified differences in modes/extent of damage [45] between composite shells and plates, but this work needs to be built upon substantially. Specifically, impact response and damage mechanisms need to be characterized for composite shells with respect to basic structural and impact parameters. Additionally, an investigation using the more consistent peak force damage metric has yet to be undertaken for composite shells.

The understanding impact damage resistance of composite shells is a nascent one at best. The sparse amount of experimental information on impact damage response of composite shells is apparent from this review of the current literature. Essentially, very limited work has been done in this area and conclusions up to this point have been ambiguous. There is a clear need to identify the key issues and mechanisms relating to the characterization of damage states and structural response of impacted composite shells. Damage resistance will help provide the description of the damage state needed as the starting point for understanding damage tolerance. This will help engineers to adequately fulfill damage tolerance requirements from a design standpoint.

CHAPTER 3

APPROACH

The objective of the present work is to experimentally investigate the impact response of composite shells with emphasis on characterizing damage resistance. This is a bold statement if taken generally. More specifically, in this research, the effects of basic structural and impact parameters on the impact response of cylindrical composite shells were investigated. The four basic parameters are radius of curvature, span, thickness, and impact velocity. Various structural configurations are considered, including composite cylinders and plates. Experimental response data was taken and impact damage characterized for all specimens. Since this is preliminary work in a new area, one major aim of this research is to establish basic trends to guide future work in the area of impact-damaged composite shells.

The general approach taken in this research is explained in section 3.1. In section 3.2, the reasoning behind the chosen test matrix and specifics of the final test matrix including a physical description of the specimen geometries is given. The experimental boundary conditions for this research are described separately in section 3.3.

3.1 General Overview

It is desired in this work to experimentally characterize the impact response of composite shells with particular attention to the resulting

damage state. Composite 'shells' in this research include plates, cylinders, and cylindrical shell sections. Plates are the limiting case of shells, having an infinite radius. Cylinders also form a limiting case in that they are full shell sections. The geometry of the composite shells, specifically the way by which the structural parameters are varied, is discussed in detail in section 3.2. The methods chosen to characterize the response and damage state are described in this section.

Shell impact response is evaluated by measuring force-time histories during the impact event. Quasi-static testing as well as impact testing is undertaken to draw comparisons between the response and damage states for the two loading types. Quasi-static tests are readily comparable to low-velocity impact from a damage resistance perspective in a number of cases. They are cheaper and more repeatable than impact testing and thus it is desirable to experimentally investigate how well the two loading conditions correlate for shell configurations. Response of composite shells to quasi-static loading is compared to impact results based on amount and type of damage as well as response parameters such as force-deflection curves.

Impact testing is undertaken before static-indentation tests. The peak force measured during the impact event for a specific shell is used as the upper limit load in a quasi-static test of the same shell configuration. In this way, the damage states can be directly compared using peak force as the damage resistance metric. As mentioned in chapter 2, peak force has been shown to be an excellent metric by which to make damage resistance comparisons for plates [17]. Force-indentation data, taken during quasi-static testing, can later be used to model the impact event on a local level. The damage state of impacted composites is characterized in this study in two ways - visual and x-ray evaluation. X-ray damage characterization is a two-

dimensional method that provides an integrated view of the damage state through the thickness of the specimen.

3.2 Test Matrix and Specimen Description

A description of the test specimens is presented in this section along with the finalized test matrix and the philosophy behind its design. Four basic parameters were chosen to be varied in this investigation: radius of curvature, span, thickness, and velocity. Many other parameters associated with the impact damage resistance of composite shells were identified at the outset of this research. These parameters fall into three primary categories: structural, impactor/indentor, and impact event. These parameters are all potential experimental variables. Reasons for the choice of the four variables given above complement a discussion of the potential variables that have been identified.

Potential experimental variables associated with the impact response of composite shells include, but are not limited to, the following list: structural parameters such as material (e.g. fiber, matrix, sandwich core), layup, radius of curvature, number of curvatures (e.g. twist), curvature type (e.g. circular, elliptic, airfoil), span, thickness, planar aspect ratio, boundary conditions, internal support, pre-existing damage (e.g. multiple impacts), pre-stressed structure, and structural anomalies (e.g. ply-drops, cutouts, stiffeners); impactor/indentor parameters such as shape (e.g. hemispherical, conical), size, material, and mass; and impact event parameters such as type of loading (quasi-static or dynamic), velocity, transverse or glancing impact, eccentric impact, side impacted (concave or convex), and testing environment.

This is a daunting list of experimental variables that must be reduced to produce a tractable experimental investigation.

The review of the current literature given in chapter 2 shows that research into impacted composite shells is very much at a preliminary stage. Thus, potential variables cannot be eliminated by previous work. However, this also allows the most basic, and likely the most important, parameters to be considered as variables in this research. Other parameters are chosen (fixed) based on previous experience, industry standards, and experimental limitations.

Radius of curvature, span, and thickness are obviously basic structural parameters and they are also feasible experimental variables. Radius of curvature was chosen as it is the key parameter in considering the difference between shells and plates. Analyses of the impact response of shells (e.g. [31]) have shown that the radius-to-thickness ratio is an important parameter in the response of transversely loaded shells. Therefore, thickness also becomes an experimental variable. Span, along with curvature, defines whether or not a shell is shallow. Numerous investigations have also shown that deep and shallow shells have different response characteristics, so this effect is considered important. Velocity becomes the fourth basic variable because it can be used as a metric to define the severity of the impact event and give different shell responses ranging from elastic (no damage) to penetration (severe damage) depending on the magnitude of the velocity, and thus the resultant peak force.

Many of the potential experimental variables can be ignored based on experimental and time limitations, e.g. structural anomalies. Others, such as material, must be fixed based on other considerations in order to limit the extent of the test matrix. Material and layup are taken as Hercules

AS4/3501-6 graphite epoxy in a $[\pm 45_n/0_n]_s$ configuration because a database for this laminate already exists in the Technology Laboratory for Advanced Composites (TELAC) at the Massachusetts Institute of Technology (MIT) where this research was conducted. Cylindrical shell sections are used to minimize manufacturing complexity. A planar aspect ratio of one is maintained for a consistent comparison of the dynamic response of shells with different spans. A 1.60 kg (3.53 lb), rigid (steel), 12.7 mm (0.5") diameter hemispherical impactor/indentor is used for this research. This is done because a database comprised of previous composite plate investigations in TELAC and the aerospace industry exists for this type of impactor configuration, e.g. [7, 22]. Transverse, centered loading is utilized because of the preliminary nature of this investigation and because it is the typical condition used in both the research and industrial communities [10]. Boundary conditions are discussed in section 3.3.

The three structural parameters (radius, span, and thickness) are varied based on scaling considerations. To obtain trends from the experimental data, a minimum of three scalings must be considered. Manufacturing and time limitations allow only three scalings of the structural parameters. Effective ply thickness is used as the basis for scaling the structural parameters. Effective ply thickness is simply the total thickness of adjacent plies with the same fiber orientation in a laminate. Several authors have indicated that suppressing the number of ply interfaces by using effective plies causes the laminate to damage in different modes, such as fiber breaks and matrix cracks, and that the extent of the damage is a function of the effective ply thickness [7, 69]. Laminate thickness is therefore increased in this investigation using effective plies. This also keeps the number of ply interfaces, where delamination is most likely to occur,

constant. Thus, a thicker specimen does not have more ply interfaces where delamination is likely to occur.

Therefore, if t_{ply} is the basic ply thickness, then the effective ply thickness is varied by laying up plies of the same orientation in sequence such that:

$$\left(t_{ply}\right)_{effective} = n\left(t_{ply}\right) \tag{3.1}$$

where n is the number of repeated plies. This results in a natural parameter by which to scale the structural variables in various combinations. The basic scaling relation for any of the three structural variables is given by:

$$(Xn) = n(X1) \tag{3.2}$$

with n taking on the values 1, 2, and 3. The variable X represents any of the three structural parameters (R for radius, S for span, and T for thickness), while X1 represents the base value for the structural parameter X. Nominal values for the structural parameters are given in Table 3.1. The base radius was chosen as 152 mm (6") for comparison to 305 mm (12") diameter cylinders used in damage tolerance work in TELAC [70, 71]. The base value for span, 102 mm (4"), was chosen with scaling in mind so that the largest span would coincide with the 305 mm (12") diameter cylinders. The base thickness, 0.804 mm, was chosen because it is the thinnest laminate with the desired layup and also because it has been used in previous work, e.g. [14, 15, 71-73]. These choices for thickness and span help to reduce the amount of material and manufacturing required for this research. Specimens can be completely described by the three structural variables, i.e. RnSnTn. As an example, R1S2T3 is a shell with a 152 mm (6") radius, a 203 mm (8") span, and a 2.412 mm thickness (18 plies).

Table 3.1 Nominal Structural Parameters

n	Rn = Radius	Sn = Span	Tn = Thickness
1[a]	152 mm	102 mm	0.804 mm
2	305 mm	203 mm	1.608 mm
3	457 mm	305 mm	2.412 mm

[a] Base values have n equal to 1.

An illustration of a generic specimen is shown in Figure 3.1. Ply angles are measured from the circumferential axis of the shell (taken as 0°) with positive ply angles taken as counter-clockwise looking down at the convex side of the shell. Span is taken as the straight-line distance between the straight (axial) edges of the shell.

Scaling the structural parameters in different combinations provides for various constant structural ratios. For example, the radius and effective ply thickness can be varied while still maintaining a constant radius-to-thickness ratio, e.g. R1/T1 = R3/T3. In contrast, scaled structural ratios can also be compared by varying only one structural parameter, e.g. R3/T1 = 3(R1/T1). Varying the structural parameters in this fashion provides for shell comparisons based on convenient nondimensional ratios. The key ratios explored in this research are radius to thickness (R/T), span to thickness (S/T). and radius to span (R/S).

Impact velocities were determined by undertaking preliminary impact tests. A number of shells, with various structural stiffnesses (least stiff, intermediate stiffness, and stiffest in the test matrix), were impacted at different velocities prior to actual testing for this research. These tests were performed to identify velocities that would provide responses ranging from purely elastic (no damage) to severe damage (near penetration). The preliminary impacts indicated that velocities of 1 to 4 m/s provided a desirable range of damage states (response). The four velocities of 1, 2, 3, and 4 m/s were thus chosen to obtain a range of damage states and responses. With the impactor mass of 1.60 kg, the energies associated with these velocities are, respectively: 0.8 Joules (0.6 ft-lb), 3.2 Joules (2.4 ft-lb), 7.2 Joules (5.3 ft-lb), and 13 Joules (9.4 ft-lb).

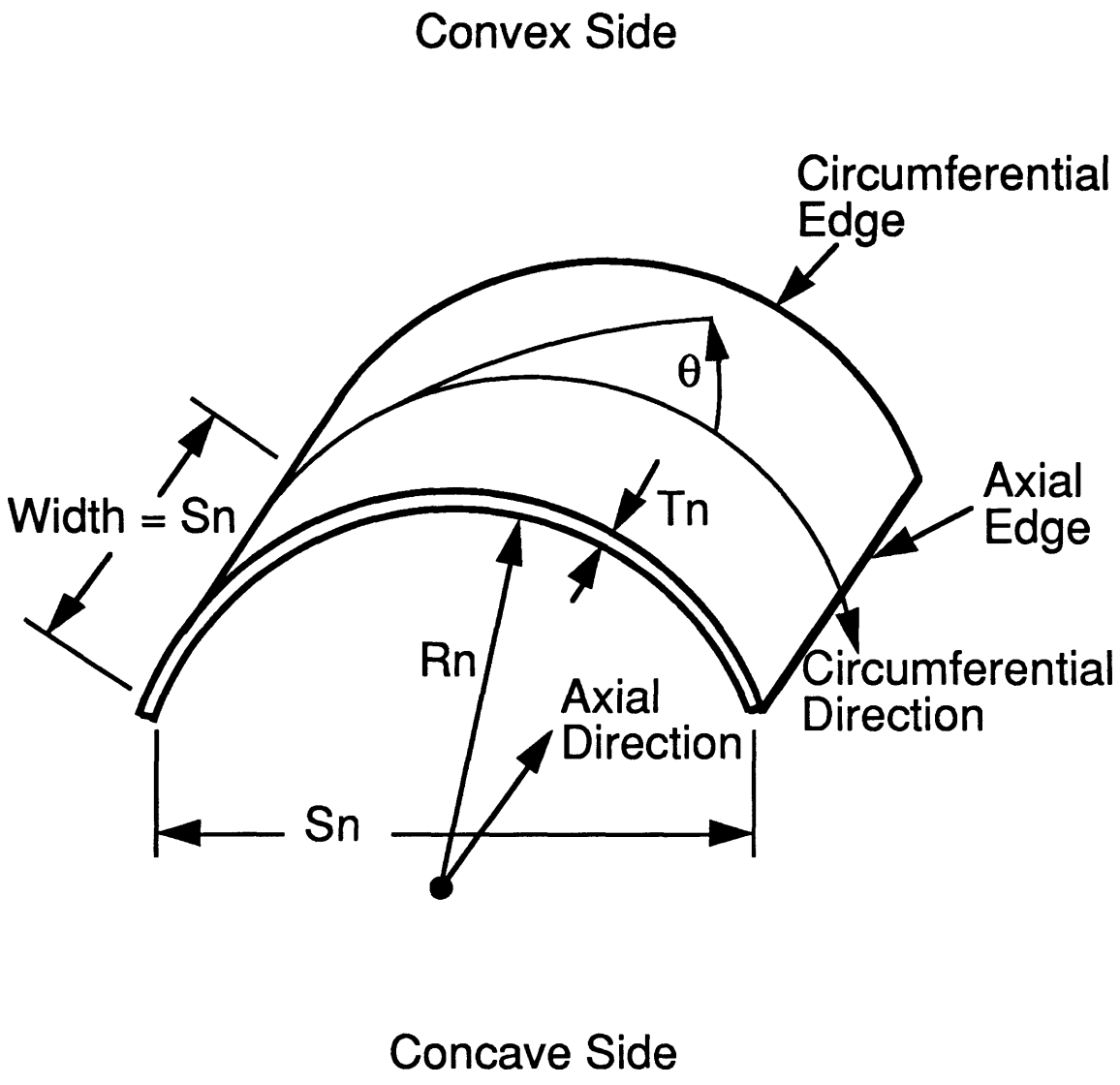

Figure 3.1 Illustration of generic test specimen showing radius, span, thickness, and ply angle.

In order to consistently compare response and damage between quasi-static and impact tests for all cases, it was desired to choose an impact velocity that would cause damage in most specimens. The impact velocity used for comparison to quasi-static loading was determined from the same preliminary impact testing used to determine the range of impact velocities. An impact velocity of 3 m/s was chosen because it caused damage, but not penetration, in most specimens. Damage from penetration is difficult to quantify which makes comparisons difficult. Thus, the peak force measured during impact tests at 3 m/s is used as the maximum load for quasi-static tests.

Cylinders and plates are included in this research, as well as cylindrical shell sections. Plates represent the limiting case of shells with infinite radius, and are considered for direct comparison with the shell results and for comparison to previous plate research. Force-time histories, peak force measurements, and damage states are compared between full cylinders and equivalent shells (half-cylinders) mounted in the test fixture to gain insight into the appropriateness of the designed boundary conditions. Cylinders deform in a mode which tends to make the cross-section oval instead of round. Therefore, these comparative test cases are useful in determining appropriate boundary conditions for a shell investigation if the response of a full cylinder is desired.

Concave loading of cylindrical shells is also considered in this work. Concave shells are geometrically equivalent to convex cylindrical shells but are impacted on the opposite face. A standard impact (convex) would occur from the top of the page in Figure 3.1 and a concave impact from the bottom. Concave impacts are considered for two reasons. First, these shells immediately develop tensile membrane stresses on the face opposite impact.

Plates experience this same effect only when large transverse displacements are reached. This allows the membrane stiffening effect to be investigated in a qualitative sense for its influence on damage resistance. This stiffening effect has been shown to be important in the damage resistance of composite plates [12]. Secondly, concave impacts are investigated because of interest in possible accidental damage incurred by aerospace structural components during manufacturing or servicing.

In summary, this research considers four basic parameters as variables: radius, span, thickness, and impact velocity. Additionally, plate and cylinder structural configurations are included, as well as concave loading of cylindrical shell sections. Finally, quasi-static testing is included to compare shell response with impact loading and to determine the nonlinear Hertzian contact stiffness relation. These considerations yield a four-dimensional test matrix which can be represented as in Table 3.2. A plate geometry (infinite radius) is indicated by the notation "RP" and cylinders by the notation "SC". The test matrix can be visualized as a cube with each side representing a structural variable and each entry indicating the type of test (number of impact velocities). Note that all impact tests at 3 m/s have a concomitant quasi-static test indicating the importance of this comparison.

A fully populated test matrix would provide information about every combination of structural and impact variables in this investigation. Due to experimental limitations, the test matrix is not fully populated. However, it does contain a total of 89 shell/plate specimens and 5 cylinders. Nevertheless, such a sparse, but well-devised, test matrix is thought to provide the same types of information as a fully populated test matrix, although not as detailed. Therefore, the sparse portions of the test matrix are

Table 3.2 Test Matrix

	T1				T2				T3			
Span	R1	R2	R3	RP[a]	R1	R2	R3	RP	R1	R2	R3	RP
S1	4[c]	4	4	4	1	4	1	1	1	1	4	1
S2	4	1	1			1				1	1	
S3	4	1	1			1	1				1	
S1 concave	4	1	1		1	1			1		1	
SC[b]	4											

[a] "RP" indicates plate configuration (radius equal to ∞).

[b] "SC" indicates cylinder configuration.

[c] Indicates one quasi-static test and number of impact tests at different velocities.

deliberate. Border rows and columns are populated so that information from these tests can establish trends that relate to untested entries in the interior of the matrix. It is expected that trends can be established so that the response of specimens not tested can be inferred from the specimens that are tested. Description of the sparse test matrix serves to illustrate the reasoning behind the populated entries.

As mentioned previously, the four-dimensional test matrix can be viewed as a cube with the three sides of the cube being the radius, span, and thickness. Entries in the cube represent the number of impact tests (velocities). Rows and columns in the three-dimensional (cube) test matrix represent the three structural parameters which are used as the basis for shell comparison in this research. Each structural parameter can be varied independently in the three-dimensional test matrix. Rows in Table 3.2 represent varying the radius while columns represent varying the span. The third dimension of the test matrix represents varying the thickness. Thus, the three-by-three thickness submatrices in Table 3.2 represent the depth of the cube. Although each structural parameter can be varied independently, it is more convenient to compare shell response based on nondimensional ratios of these parameters because the parameters were scaled.

Radius-to-thickness (R/T), span-to-thickness (S/T), and radius-to-span (R/S) ratios are used to compare shell response. Constant and scaled structural ratios are key in the design of the test matrix. A thickness submatrix in Table 3.2 is simply one plane of the cube. Specifically, it is the radius-span plane. Rows in a particular thickness submatrix represent linear scaling of the radius-to-thickness ratio (nR/T) for a constant span while columns represent a constant radius-to-thickness ratio (R/T) with the span varying. The diagonal in this submatrix (radius-span plane) represents a

constant radius-to-span ratio (R/S). This constant ratio is maintained because both the radius and span increase with n due to the scaling used in the design of the test matrix. Thus, along the diagonal of a thickness submatrix, structurally different shells with the same thickness and radius-to-span ratio can be compared.

The two other planes of the three-dimensional test matrix have the same types of trends found in the radius-span plane (thickness submatrix). These two planes of the cube are the radius-thickness and span-thickness planes. Another aspect of any of the planes is that the structural ratio in a particular plane takes on a large range of values. As an example, consider the radius-thickness plane. The radius-to-thickness ratio was shown to be very important in the response of shells in chapter 2. The radius-to-thickness ratio varies from 63 to 570 (R1/T3 to R3/T1) in the test matrix.

To understand the sparse design of the test matrix, first consider the upper three rows in the test matrix, specifically the T1 section in Table 3.2. This part of the test matrix is the most densely populated. This is done so that trends found in this portion of the test matrix can be extrapolated to the other two three-by-three thickness submatrices. More specifically, the border row and column is fully populated with all five testing conditions (four impact velocities and a quasi-static test for each specimen type). Thus, the response is fully defined along the borders of the first thickness submatrix for this investigation. Along with this information, additional information is obtained on the interior of the submatrix by extrapolating the border information to the interior specimens using the 3 m/s impact and quasi-static tests as the basis for the extrapolation. Thus, the response in the T1-submatrix is well defined and this information can be used as the basis for establishing trends in the other two thickness submatrices.

The basis for extrapolating information from the T1-submatrix to the T2- and T3-submatrices is the populated upper row and Rn/Tn column of all the thickness submatrices. The radius-to-thickness ratio, as indicated in chapter 2, is considered the most important parameter in defining the response of shells. Therefore, the columns corresponding to the constant radius-to-thickness ratio (R1/T1 = R2/T2 = R3/T3), and the upper row, are populated for each thickness submatrix. The T1-submatrix has this row and column fully populated with all four velocities because these form the basis for establishing trends that will be used in assessing the response of shells not tested in the T2- and T3-submatrices. Additionally, to obtain information on large variations in the radius-to-thickness ratio, diagonals in all of the thickness submatrices are populated. This test matrix design allows for qualitative information to be assessed for specimens that are not tested through extrapolation and interpolation of data from specimens that are tested.

In addition to convex shell specimens, there are plates, cylinders, and concave shells in the test matrix. The plate specimens provide a basis for comparison with shells and previous work, so only one span is considered. Likewise, cylinders are included only for comparison to half-cylinder shells. Therefore, only one structural configuration is required although a full range of dynamic tests are performed. Lastly, concave shells, as discussed previously, are included in the test matrix to determine how differences in shell orientation affect the response. Concave shells experience tensile membrane stiffening much like plates whereas convex shells have compressive membrane forces during transverse loading. The same test matrix design scheme is applied to concave shells except that only one span

(S1) is considered simply to determine if the response changes due to the orientation change.

3.3 Boundary Conditions

One of the keys to this experimental work is the experimental boundary conditions. Boundary conditions for this investigation were chosen to be pinned/no in-plane sliding on the axial edges and free on the circumferential edges. Idealized boundary conditions are illustrated in Figure 3.2. No in-plane sliding was chosen in the circumferential direction of the shells to investigate the membrane stiffening effect that plates experience under large transverse displacements. This in-plane restriction is also much like having a composite skin with frames or longerons in a fuselage.

Membrane stiffening in the circumferential direction is seen as the primary difference between plate and shell structures and therefore it is desirable to investigate this effect on the response of the shells. Fixing the boundary in this direction (in-plane sliding) provides greater membrane stiffening than allowing in-plane sliding. More importantly, the fixed in-plane boundary condition is better defined than if the shell were allowed to slide. It is known that there is no in-plane displacement for the fixed in-plane condition whereas sliding involves an unknown amount of friction. Thus, the in-plane boundary condition is known. For the out-of-plane restriction, pinned was chosen over clamped because of manufacturing difficulties associated with clamps for different radii shells. These needs for the experimental boundary conditions were met by design of a special test fixture to simulate the idealized boundary conditions. Details of the test fixture can be found in chapter 4.

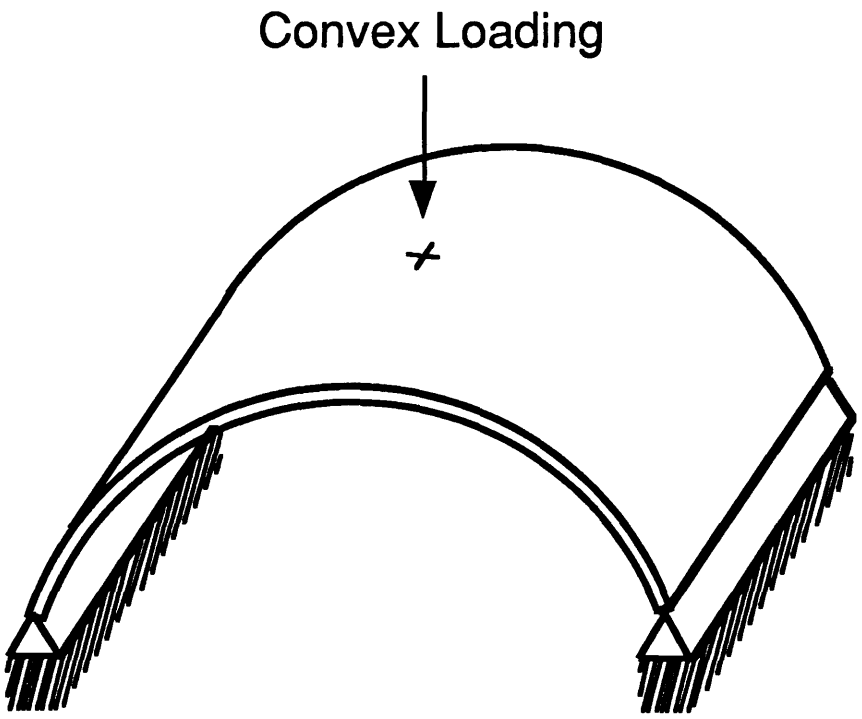

Figure 3.2 Idealized boundary conditions for test specimens.

CHAPTER 4

EXPERIMENTAL PROCEDURES

Experimental procedures followed in this research are presented in this chapter. Also included in this chapter are descriptions of the specimen manufacturing process, test fixture, and methods for damage characterization. Results from specimen surveys used to evaluate manufacturing procedures are also presented.

4.1 Manufacturing Procedures

The manufacturing procedures for the composite shells, plates, and cylinders are outlined in this section. An assessment of the quality of the manufacturing process is given in section 4.2. Manufacturing of shells consists of layup, placement on molds, curing, postcuring, and final specimen preparation. Flat specimens and shells are manufactured in the same fashion, but cylinders require a slightly different procedure. Cylinder manufacture is described in detail in [71] and this procedure is followed exactly except for one item. Typically, one 762 mm (30") long (axial direction) cylinder is manufactured on the mandrel for each autoclave cycle. This research required 305 mm (12") long cylinders, so two 305 mm long cylinders are manufactured on the mandrel for each autoclave run. This is accomplished by placing a cork dam border along the circumference of the mandrel to divide it into two halves.

4.1.1 Graphite/Epoxy Prepreg Layup

The AS4/3501-6 material is received in pre-impregnated (prepreg) form on 305 mm (12") wide rolls. The AS4/3501-6 utilized is a bleed-type material system with an uncured areal weight of 149 g/m^2 and 42% resin content. Nominal cured ply thickness is 0.134 mm. To begin laminate manufacture, the prepreg tape material is removed from freezer storage and allowed to warm up in the sealed storage bag for a minimum of 45 minutes. This prevents moisture in the ambient air from condensing on the cold prepreg.

Plies are cut with a utility-knife utilizing teflon-covered templates manufactured previously for use in TELAC. The templates form plies with matrix joints only, fiber joints (discontinuous fibers) are not used except in the unavoidable case of the zero degree ply of a full cylinder. To minimize waste prepreg, plies are either cut exactly to the size of the desired specimen or a larger, 349 mm by 305 mm (13.75" by 12"), ply size is cut. Individual plies are then put together to form a flat laminate. In the latter case, once completed, the large uncured laminate is cut to desired specimen size using the utility knife and a straight-edge. To complete the layup process, the laminates are sandwiched between two layers of peel-ply release cloth.

4.1.2 Cylindrical Molds

Manufacture of composite shells, aside from the full cylinders, did not have a standardized manufacturing procedure in TELAC. Additionally, molds were not available for use in curing. Various mold options were considered before deciding on the method used in this research. The molds are based upon a previous design used in TELAC [74]. The molds are manufactured from 6061 aluminum and consist of bulkheads, a baseplate, top-sheet, and clamping bars. Five 9.53 mm (3/8") thick bulkheads were

manufactured for each of the molds having radii of 152, 305, and 457 mm (6", 12", and 18"). The baseplate is 737 mm long, 838 mm wide, and 9.53 mm thick (33" x 29" x 3/8").

The bulkheads are bolted into slotted grooves in the baseplates. The 6061 aluminum sheets, 0.794 mm (1/32") thick, are placed over the bulkheads and clamped against the baseplates using two clamping bars. The clamping bars are 711 mm long, 102 mm wide, and 9.53 mm thick (28" x 4" x 3/8"). Five bolts aligned with the bulkheads are used to tighten down the clamping bars until the top-sheet conforms to the bulkheads, thus forming a section of a cylindrical mold. Prior to assembling the molds, it was found helpful to bend the aluminum sheets, using a sheet metal forming tool, at the sharp juncture where the bulkheads and baseplate meet. The entire mold assembly is depicted in Figure 4.1 and photographs of two molds, one with exposed bulkheads, appear in Figure 4.2. The bulkheads have center cutouts which allow equal pressure on both sides of the mold (aluminum top-sheet) during autoclave pressurization. This prevents collapse of the molds during curing.

The next step in the manufacturing process is to place the laminates onto the cylindrical molds. It should be noted that an investigation into the effect of laying-up flat laminates and then conforming them to the cylindrical geometry of the molds was undertaken before final specimen manufacturing began. Layup of laminates on flat (standard TELAC procedure) and cylindrical surfaces were compared based on specimen quality. No special precautions were taken when the flat-layup laminates were conformed (by hand) to the molds prior to curing. The laminates were cured together and thickness/radius differences noted. There was no noted difference in surface quality, thickness variation, or radius of curvature between the flat and

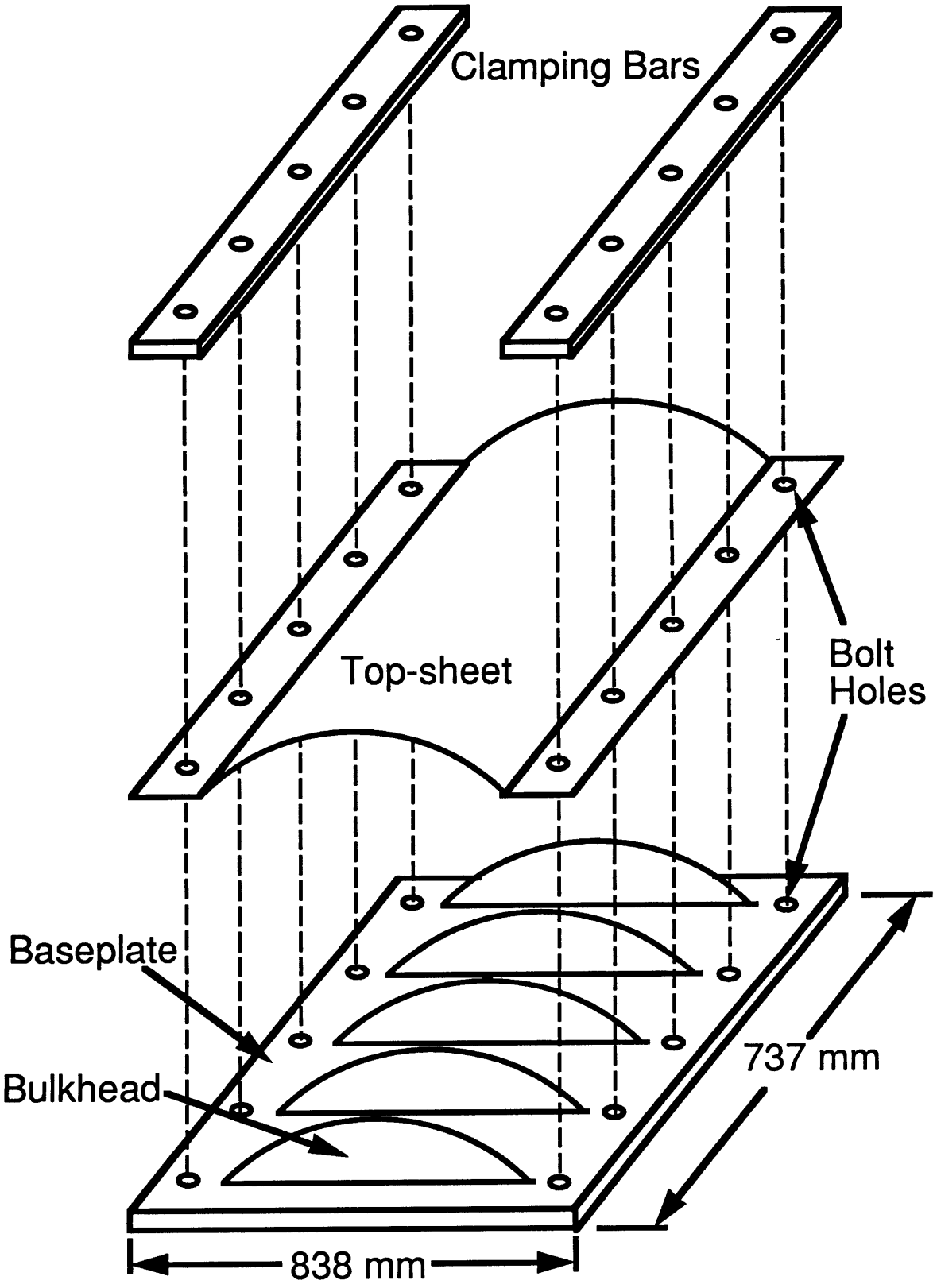

Figure 4.1 Illustration of cylindrical mold assembly.

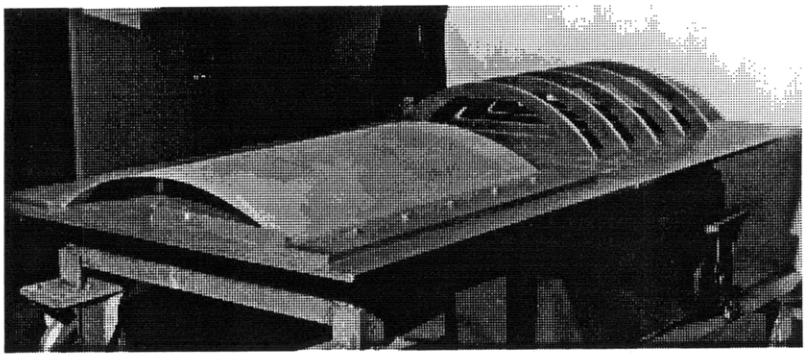

300 mm

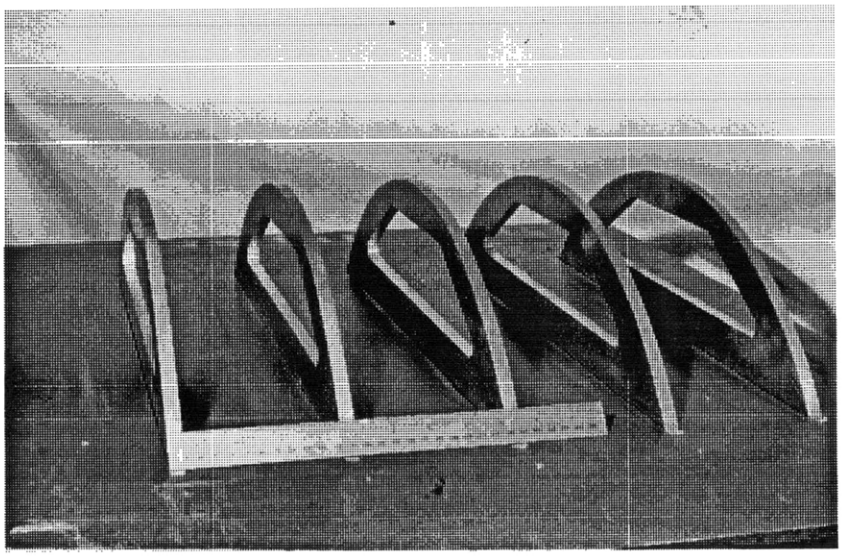

100 mm

Figure 4.2 Photographs of: (*top*) a finished manufacturing mold alongside a mold with exposed bulkheads, and (*bottom*) a close-up of the exposed bulkheads.

curved layup geometries. It was decided, for ease of manufacturing, to continue with the standard TELAC layup procedure. Thus, in this research, flat layup of specimens was used and then the laminates were conformed to the cylindrical molds by hand prior to curing.

Small modifications to the standard TELAC cure procedure for the AS4/3501-6 material system were necessitated by the curved geometry of the molds. The cure procedure is thus discussed in detail and the modifications noted. Details of standard TELAC procedures for this material system can be found in [75] and supplement the description found in this section.

The mold surface (aluminum sheet) is carefully cleaned and then sprayed with mold release Mold Wiz® prior to placement of cure materials. The mold release is manufactured by Axel and facilitates cleaning of the aluminum top-sheets after curing. Guaranteed nonporous teflon (GNPT) is flash-taped to the aluminum top-sheet. The GNPT covers the cylindrical section of the mold leaving about 25.4 mm (1") of aluminum top-sheet uncovered on all four edges. The uncovered portion of the top-sheet is later used to attach the vacuum bag. Dams made from 25.4 mm (1") wide cork tape are used to create an enclosure on the curved top-sheet in which the laminates are placed. This is pictured in Figure 4.3. Aluminum T-dams and cork tape are typically used in TELAC for the enclosure in the cure of flat specimens.

The remainder of the cure assembly is standard in TELAC [75] for this material system except for the top plates and vacuum ports. The cure assembly is illustrated in Figure 4.4. The peel-ply covered laminates are conformed to the mold by hand on top of the GNPT and between the cork dam enclosures. The laminates are then covered with porous teflon and bleeder paper. Top-plates are then placed over the laminates.

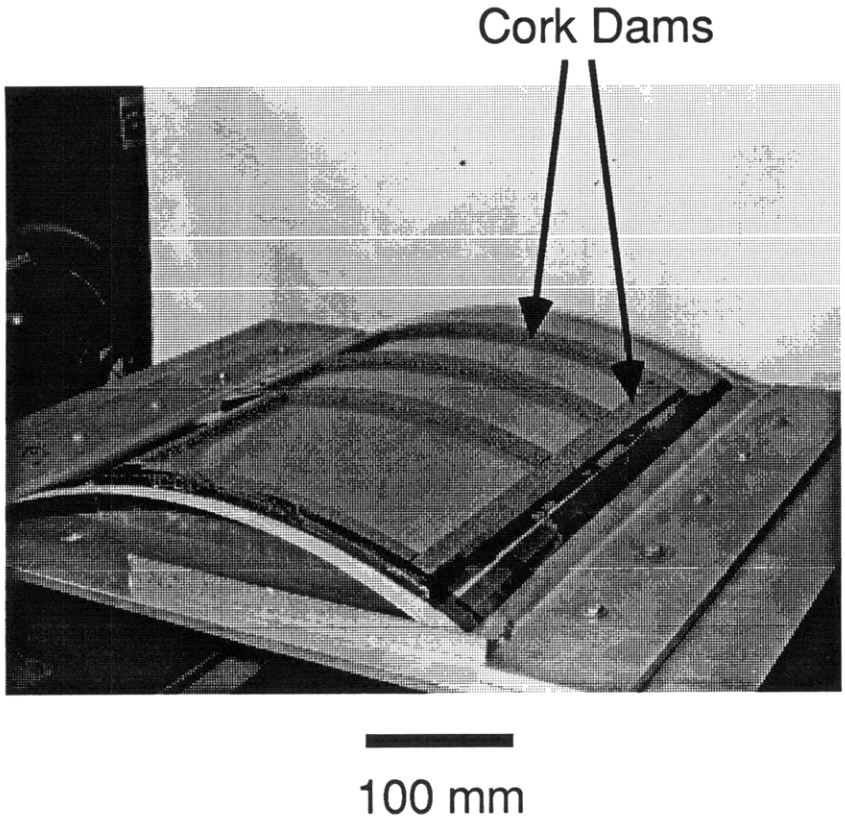

Figure 4.3 Photograph of a cylindrical mold showing cork dams.

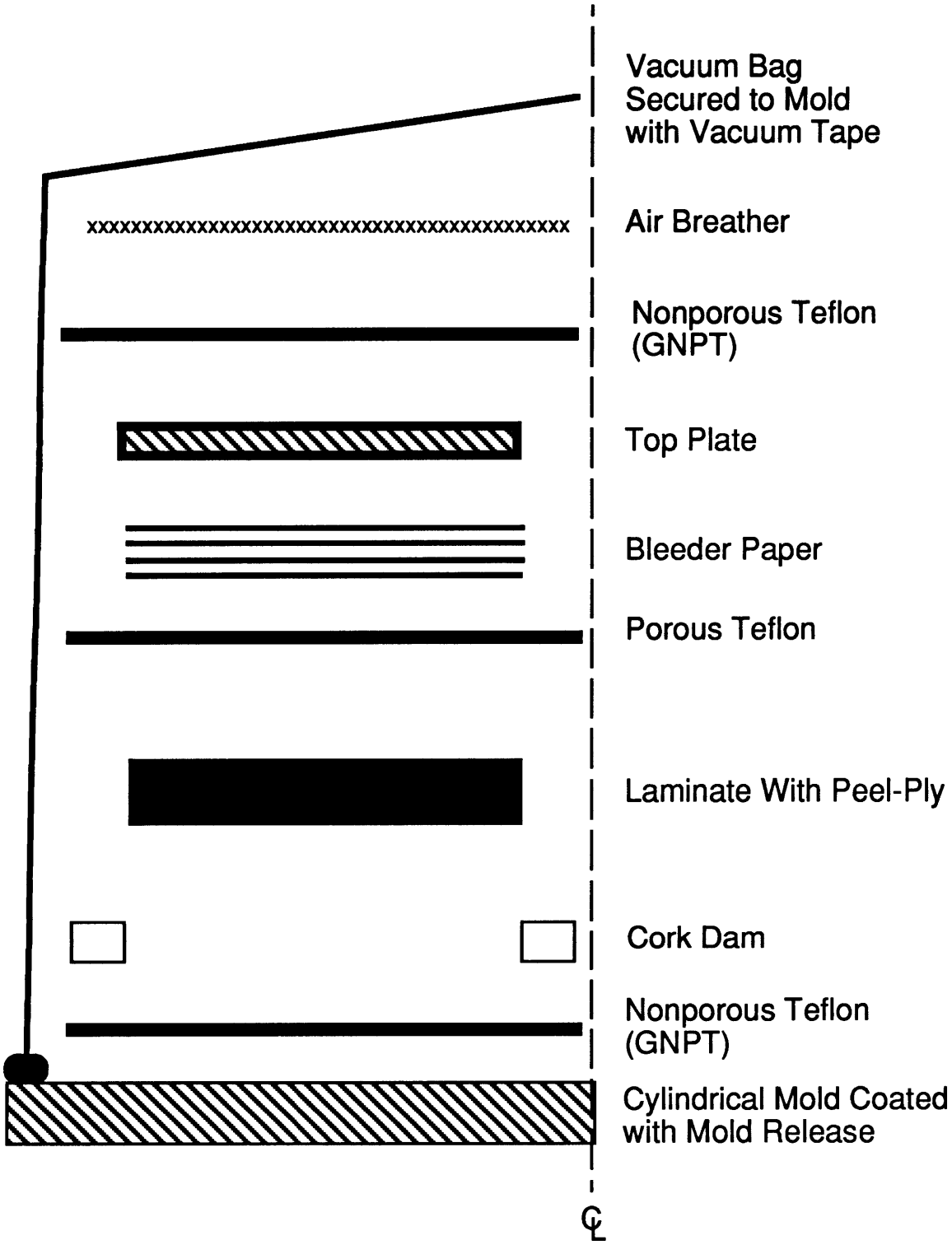

Figure 4.4 Illustration of cure assembly.

Top-plates used in flat specimen curing are normally 9.53 mm (3/8") thick aluminum plates. For the curved molds, a different approach was needed. It was found that 0.635 mm (0.025") thick 6061 aluminum sheeting gave the best results as top-plates. This was due to a number of considerations. It was found that thicker sheets were too stiff to conform to the cylindrical molds over the laminates. Thinner sheets were found to plastically deform in local regions when placed over the laminates and these local deformations were impressed into the cured laminates. The intermediate gage aluminum that was used was found to easily elastically deform when placed over the laminates. The top-plates are placed over the laminates and flash-taped in the circumferential direction to remain fixed until vacuum is pulled.

A layer of GNPT is placed over the entire cure assembly so that excess resin bled during cure does not flow into the next layer of cure material, the air breather. After all cure materials are on the mold, vacuum bag material is vacuum-taped over the entire cure assembly and a vacuum port installed in a slit cut in the bag. The vacuum is usually pulled through a port cut in the cure plate (mold) when flat specimens are manufactured. This completes the cure assembly for the cylindrical shells. Two molds were cured in each autoclave run which necessitated linking the molds in series to pull vacuum.

The cure and postcure cycles are standard for this material system and details can again be found in [75]. A vacuum is maintained around the cure assembly of 737 to 762 mm (29" to 30") of mercury throughout the cure process. The nominal temperature, pressure, and vacuum profiles for the cure are given in Figure 4.5. Cured laminates are removed from the molds and all cure materials taken off. The laminates are later postcured for 8 hours at 177° C (350° F).

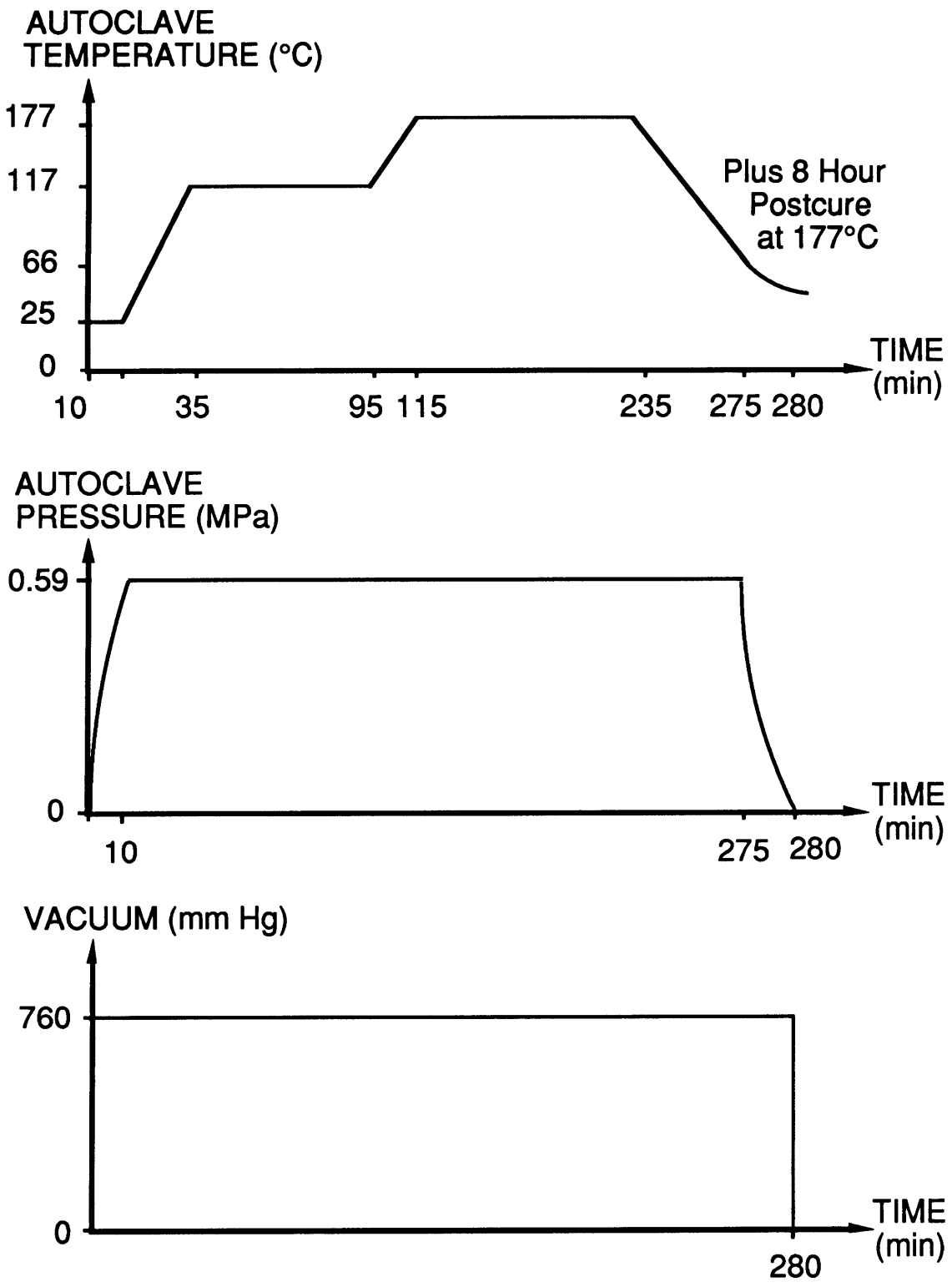

Figure 4.5 Nominal temperature, pressure, and vacuum profiles for cure cycle.

4.1.3 Final Specimen Preparation

Typically, flat specimens are trimmed on all edges to remove 'ridges' from epoxy and any small amount of fiber washout during cure. This is done using a diamond grit cutting blade mounted on a milling machine equipped with water cooling. Specimens are also cut to the correct size for testing using this method. This option was available only along the axial edges of the shells because the shell height interfered with the blade. Shells were trimmed in this manner either to remove 'ridges' or to trim the shells to the appropriate size for testing. This trimming was aided by a special cutting jig designed and built for this research and depicted in Figure 4.6. The jig simply allows the shells to be supported perpendicular to the cutting blade during cutting/trimming. The bracing wall of the jig is perpendicular to the path of the cutting blade. The travel of the milling machine table is in and out of the page in Figure 4.6. The cutting jig provides support at three points along the circumferential direction of the shell. It was found that only two points were needed to adequately support the shells.

Small 'ridges', approximately one laminate thickness high and wide, still remain on the specimens along the circumferential edges. These slight edge irregularities are assumed to have negligible effect on the response of the shells because they are small and away from the point of impact. However, they do interfere with the boundary conditions along the axial direction (no in-plane sliding/pinned condition). Therefore, in the area immediate to the boundary condition, these ridges were removed with the use of a Dremel® Moto-Tool® cutting/grinding tool equipped with a 25.4 mm diameter grinding wheel. Cylinders require no final preparation. However, R1S3T1 (half-cylinder) shells are obtained by cutting full cylinders in half using the Dremel® Moto-Tool® cutting/grinding tool with a 25.4 mm

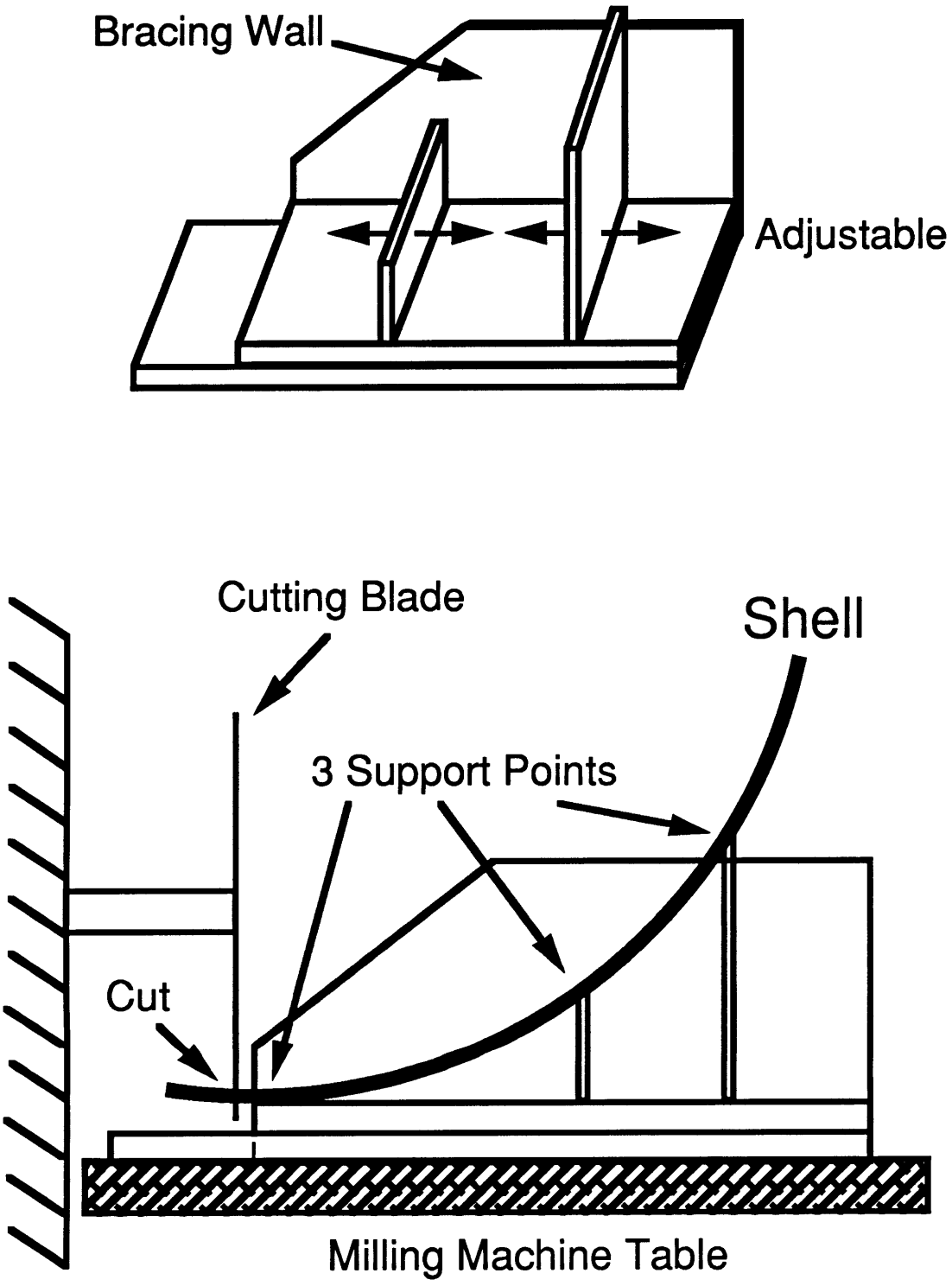

Figure 4.6 Illustration of specimen cutting jig: (*top*) a view of the cutting jig that shows the adjustable supports, and (*bottom*) a shell held in the jig ready for cutting.

diameter cutting wheel. Straight cuts are obtained using the Dremel® Moto-Tool® by mounting it on the same milling machine used to trim the composite shells.

4.2 Curvature and Thickness Mapping

To evaluate the manufacturing process, mapping schemes were utilized to determine the radius, twist, and thickness of each shell. Nine points on each shell were used to determine thickness for each shell. Thickness was measured using a deep throat micrometer with a resolution of 0.001 mm. The locations (approximate) of the nine points used in the thickness mapping for the three shell spans are shown in Figure 4.7. This figure can be considered a template which is placed over the shell to determine the locations to take thickness measurements. The shell curves in the circumferential direction of the page so the distances in Figure 4.7 are not planar in this direction. A special jig was designed to constrain the shells during curvature mapping and a heuristic developed to calculate the curvature at three locations along the axis of the shell. These measurements also allow twist along the axial and circumferential directions to be estimated.

The jig for mapping curvature constrains three of the shell corners in a plane with the fourth edge being adjustable. The constraining jig is mounted on a milling machine table with a traverse. The traverse has a digital display for measuring the displacement of the milling machine table. A dial gage, mounted in the milling machine head is used to measure the third dimension (z) of the specimens. Using simple geometric considerations, the curvature at a station (y-location) of a shell can be calculated by measuring the x- and z-

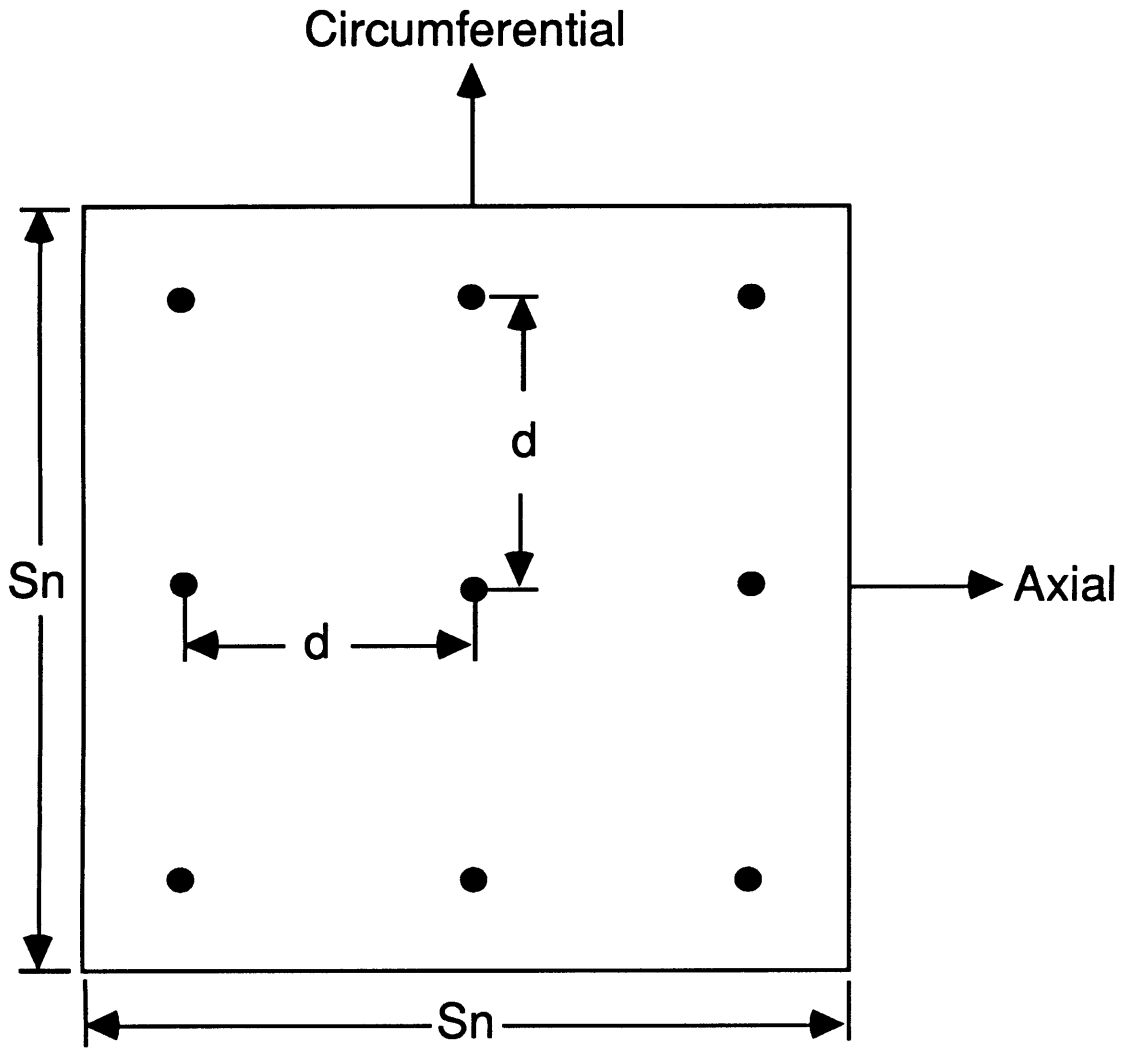

S1 d = 25.4 mm (1")

S2 d = 50.8 mm (2")

S3 d = 76.2 mm (3")

Figure 4.7 Approximate locations used for mapping shell thickness.

location of three points. This is shown generally in Figure 4.8: by measuring a and b, the radius (R) can be calculated. To calculate the radius, the length (2a in Figure 4.8) of a straight line must be determined across the shell as well as the height in the middle of the line (b in Figure 4.8).

Specifically, the measurements used to calculate the radii and twist are shown in Figure 4.9. Using Figure 4.9, radii are calculated with equation 4.1:

$$R_i = \frac{\left(\frac{x_i}{2}\right)^2 + (z_{ic} - z_i)^2}{2(z_{ic} - z_i)}; \quad i = 1,2,3 \tag{4.1}$$

where the R_i are the radii at y-location i. The distance x_i changes at each y-location either because the shell is twisting or because the radius changes between each y-station. The origin for all measurements is indicated in the upper right of Figure 4.9. The origin is taken as one of the corner points in Figure 4.7 for each shell. There are three y-locations (y_1, y_2, and y_3 in Figure 4.9) where measurements are taken for each shell. The distance d in Figure 4.7 separates the y-locations in Figure 4.9. The measurements at each y-station consist of x-, y-, and z-coordinates for three points on the shell taken along the x-direction in Figure 4.9.

The three points at each y-location are measured in the following way, using y_1 as an example: the origin is defined as above and the distance (x_1) across the shell to an equivalent depth (z-direction) is measured. This determines a straight line across the shell that is level with the milling machine table and traverse. The height (z_{1c}) at the center of the line ($x_1/2$) is measured next. The length 2a in Figure 4.8 corresponds to x_i and b corresponds to z_{ic} in equation 4.1. Therefore, the radius at y_1 can be calculated. The same procedure is followed at stations y_2 and y_3 where the x-

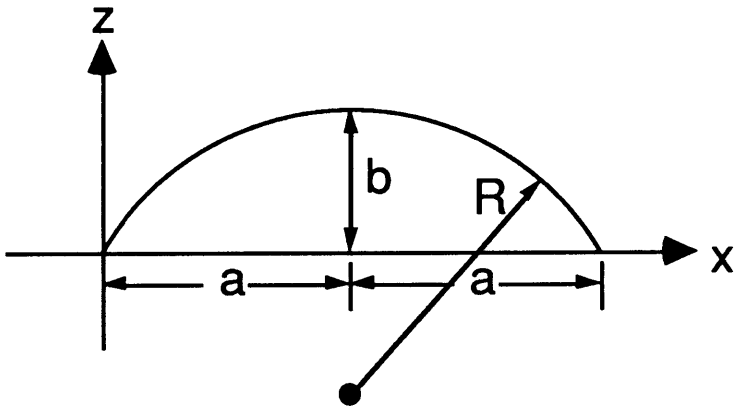

$$R = \frac{a^2 + b^2}{2b}$$

Figure 4.8 Illustration of geometric relation used to calculate curvature (R) by measuring a and b.

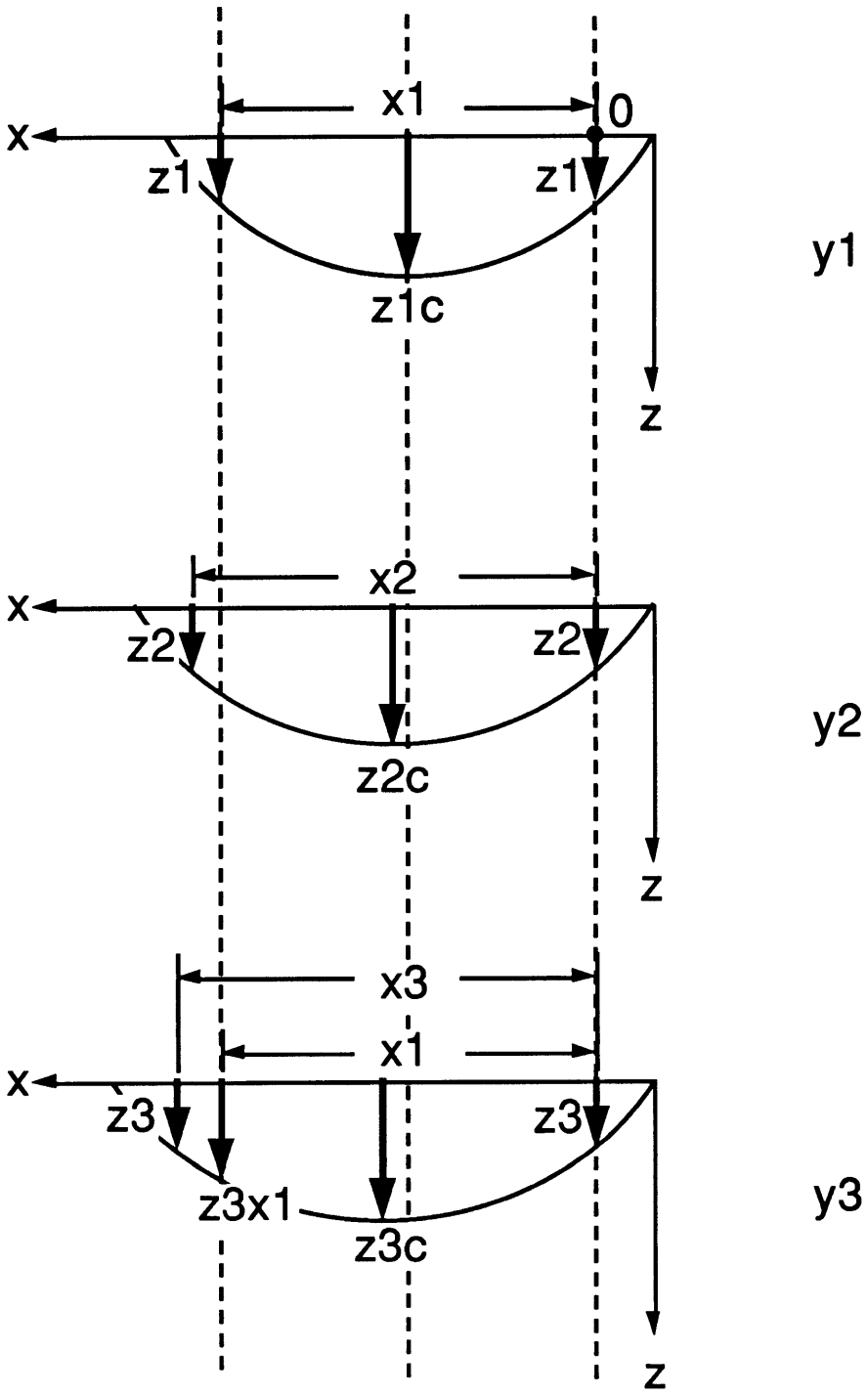

Figure 4.9 Illustration of measurements for radii and twist calculation with the radius shown increasing downward.

location of the starting point is kept constant (equal to 0). The distance between y-stations is equal to the distance d in Figure 4.7. The radius increases at each y-location in Figure 4.9 to illustrate how the radius can vary. Radii of full cylinders were estimated by measuring the cylinder circumference at the appropriate stations (y-location) with a tape measure.

Twist of each shell can also be calculated about the x- and y-axes in Figure 4.9. The straight line defined at y_1 is useful for calculating the twist. At the third y-location, y_3, the change in height (z_{3x1} - z_3) of the same line can be used to calculate the twist of the shell along the y-axis. This change in height indicates the rotation of the straight line about the y-axis. A similar change in height can be defined to calculate twist about the x-axis. Therefore, axial and spanwise twist are given by equations 4.2 and 4.3, respectively:

$$\gamma = tan^{-1}\left(\frac{z_{3x1} - z_1}{x_1}\right) \tag{4.2}$$

and

$$\beta = tan^{-1}\left(\frac{z_{3x1} - z_3}{y_3 - y_1}\right) \tag{4.3}$$

where γ is the axial twist and β is the spanwise twist, in radians. The height at x_1 at the third y-location, designated as z_{3x1}, is used to calculate both twists. Twist was not calculated for the full cylinders.

For each nominal value of radius and thickness, the average and coefficient of variation over all test specimens was calculated and is given in Table 4.1. Only 92 of the total 94 specimens in the test matrix are reported in Table 4.1. Although manufactured, two specimens (RPS1T1 and R1S1T1 concave) were not tested because tests at 3 m/s impact velocity showed

Table 4.1 Results of Curvature and Thickness Mapping[a]

Metric	Average	C. V.[b]	Nominal	Difference
T1	0.821 mm	2.2 %	0.804 mm	+2.1 %
T2	1.583 mm	1.9 %	1.608 mm	-1.6 %
T3	2.318 mm	2.9 %	2.412 mm	-3.9 %
R1	146 mm	4.6 %	152 mm	-3.9 %
R2	294 mm	2.9 %	305 mm	-3.5 %
R3	452 mm	4.7 %	457 mm	-1.2 %

[a] 92 of 94 specimens from test matrix are reported.

[b] Coefficient of Variation.

penetration. Thus, 4 m/s tests were not performed and manufacturing data for these two specimens is not reported. The nominal values for radius and thickness, as well as the percent difference of the average radius and thickness from the nominal values, are also given in Table 4.1. All twist angles are below 1° and are considered negligible. The average twists, alpha and beta, are 0.2° and 0.3° respectively. Detailed information on the radius and thickness measurements for each specimen is given in Appendix A.

The manufacturing data in Table 4.1 indicates that the manufacturing process utilized in this research is very good. Average thickness values are all within 4% of nominal values with acceptable coefficients of variation (less than 3%). The average radius of curvature values are also all within 4% of nominal (desired) values with slightly higher, but still acceptable, coefficients of variation. The average experimental values for the radius of curvature are all less than the nominal values. Radius of curvature values lower than nominal are expected due to the 'spring-in' phenomenon which occurs in the manufacture of curved composite structures. This phenomenon is well-documented, e.g. [76]. Spring-in is a physical manifestation of residual thermal strains encountered in manufacturing composite materials.

4.3 Design and Manufacture of Test Fixture

Various structural configurations must be constrained for testing in the same fashion (same boundary conditions). The boundary conditions for testing, as described in chapter 3, are pinned/no in-plane sliding on the axial edges and free on the circumferential edges. In order to achieve the chosen boundary conditions, plates and cylindrical shell sections in the concave and convex loading orientation must be restrained in- and out-of-plane, while still

being allowed to rotate. Experimental boundary conditions are never mathematically ideal. Consistency in the experimental boundary conditions for all structural configurations was considered most important in the design of the test fixture.

Many non-trivial issues had to be addressed in the test fixture design. The fixture had to support shells with various combinations of radius, span, thickness, and width during both impact and quasi-static testing. Composite plates and concave specimens also had to be supported. Stiffness of the test fixture had to be appropriately large so as not to appreciably affect displacement measurements. Lastly, allowance had to be made for the insertion of a (Linearly Variable) Displacement Transducer (LVDT) beneath the shell during quasi-static testing which is used to measure indentation.

Each of the design issues, except stiffness, are addressed in the following description of the test fixture. The issue of stiffness is discussed in chapter 6. Stiffness was accounted for in design by using many conservative approximations keeping in mind that the fixture may subsequently be used by other researchers with slightly different requirements. The test fixture was conservatively designed for stiffness based on previous work with static indentation of composite plates [73]. Results from testing, presented in chapter 6, show that the test fixture met stiffness requirements.

First, basic construction of the test fixture is discussed for general convex shell orientations. Restraints for concave and plate specimens utilize the same test fixture but require additional attachments. These additional attachments are discussed after the basics of the test fixture have been illustrated. The test fixture consists of three primary components for constraining specimens along the axial edges (pinned/no in-plane sliding condition): a stand which provides a rigid foundation, adjustable rods which

comprise the actual boundary condition, and cushions with clamps for the rods to rest in. These three components are manufactured from 6061 aluminum and are illustrated in Figure 4.10 for one side of the test fixture.

A side-view representation of the entire test fixture is shown in Figure 4.11 for convex loading of a shell. The upper plate of the rigid stand has adjustments for the three shell spans considered in this work, as illustrated in Figure 4.12. The adjustable rod/cushion shown in Figure 4.11 can be bolted onto the upper plate at three different spanwise locations. Additionally, each span adjustment is slightly adjustable to account for small deviations in shell length. This is accomplished by elongating the holes in the upper plate where the cushions and clamps mount onto the stand. However, due to geometric coupling in transversely loaded shells, load is also transferred to the cushion/rod supports perpendicular to the applied loading. This tends to separate the cushion/rod supports in the spanwise direction which would violate the no in-plane sliding condition. Therefore, to account for the elongated holes, a fixed brace was installed with adjustable steel rods to reinforce the no in-plane sliding condition. The fixed brace is also shown in Figure 4.11.

The upper plate of the rigid stand has a 318 mm x 254 mm (12.5" x 10") cutout in its center to allow for shell snap-through as well as indentation measurements. Indentation is measured with an LVDT protruding through the cutout in the upper plate from underneath the shell during quasi-static testing. The LVDT is represented in Figure 4.11 and the cutout in the upper plate is illustrated in Figure 4.12. The elongated holes used with the spanwise adjustments of the adjustable rod/cushion are also represented in Figure 4.12 along with the holes (round) for bolting down the fixed brace and rod/cushion.

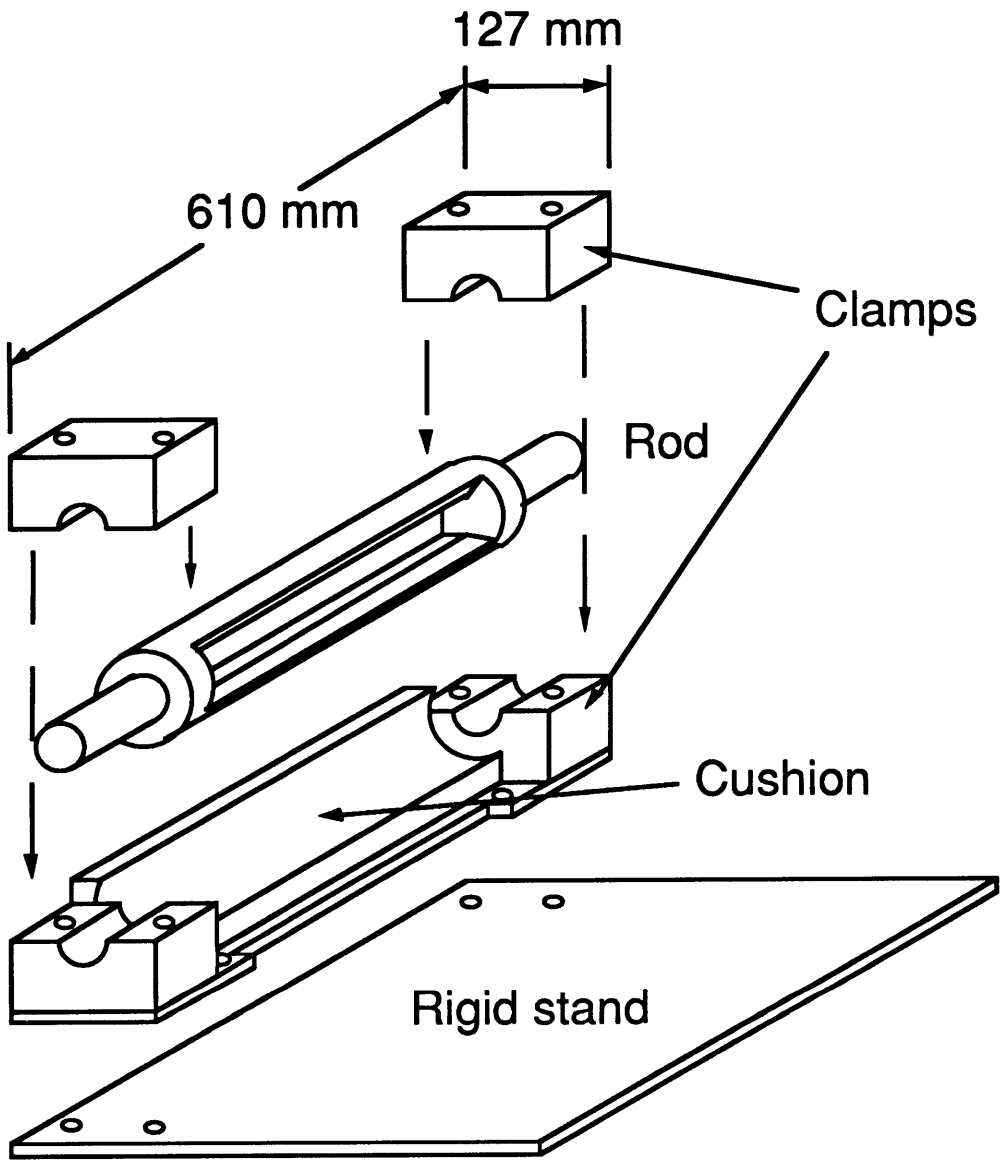

Figure 4.10 Illustration of the primary components of the test fixture.

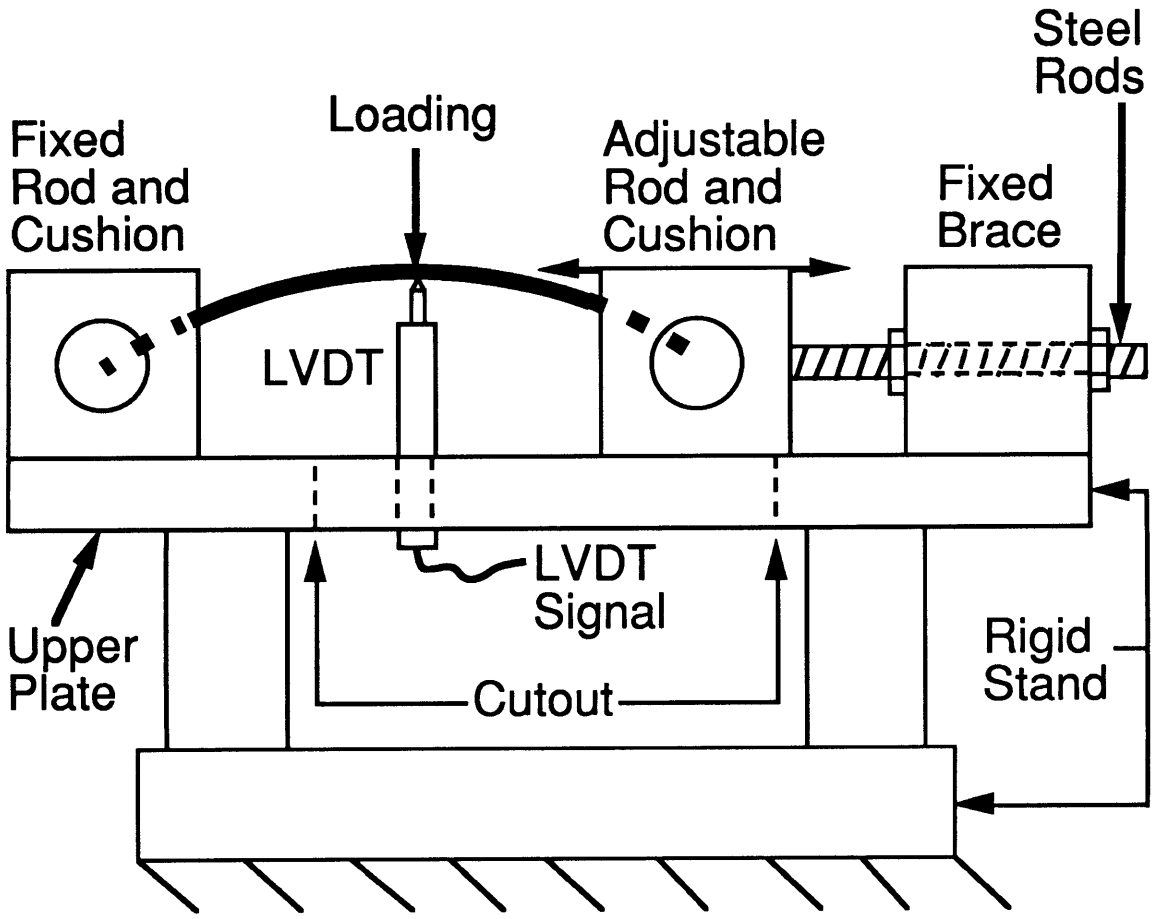

Figure 4.11 Side-view illustration of entire test fixture with shell shown mounted for loading in the convex configuration.

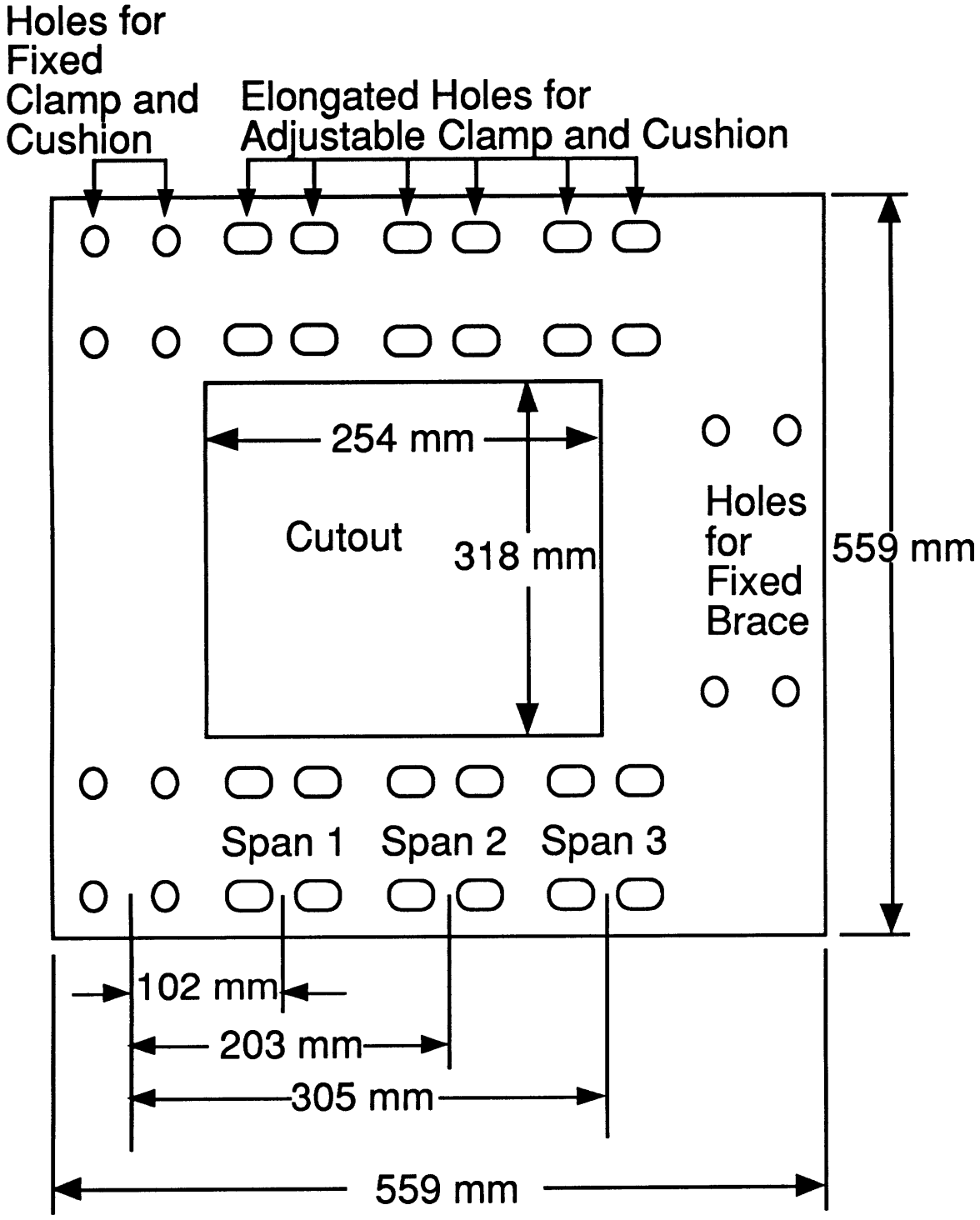

Figure 4.12 Top-view illustration of upper plate with spanwise adjustments (elongated holes), center cutout, holes for fixed brace, and holes for fixed clamp and cushion.

Schematics used for the manufacture of the cushions and rods are shown in Figures 4.13 through 4.15. Cross-section A-A in Figure 4.13 refers to the view in Figure 4.14. The desired boundary condition of no in-plane sliding requires that the edge of the shell be restrained in the spanwise direction. The cushions mount to the rigid test stand and simply provide a continuous support for the rods. The rods are the key to the boundary condition because they provide rotational adjustment prior to testing to allow for shells with different radii and span.

Prior to testing, the cushions provide a means by which the rods can be rotated in cross-section for adjustment. Once adjusted, the rods are kept from rotating by tightening the clamps shown in Figure 4.10 down on the 50.8 mm (2") diameter ends pictured in Figures 4.10 and 4.13. This rod adjustment is necessary so that each different shell can be made to impinge perpendicular to the flat, inner surface of the rod. This impingement provides the no in-plane sliding condition. The shells are held between two 'knife' edges in each rod. The 'knife' edges are illustrated in Figure 4.16. The 'knife' edges are made of steel and actually have rounded tips of radius 1.59 mm (1/16") instead of sharp knife edges. These knife edges are supported by 6.35 mm (0.25") steel rods every 50.8 mm (2") along the edge of the shell and are adjustable to accommodate the three specimen thicknesses used in this research. Figure 4.17 contains a photograph of a close-up of one of the rods mounted in the test fixture and Figure 4.18 has a photograph of a shell mounted in the test fixture in the convex (standard) testing configuration. Figure 4.19 is a representation of the cross-section of the upper plate and rod/cushions of the test fixture showing a shell mounted for convex loading.

Plates and concave shells require additional attachments to maintain the pinned/no in-plane sliding support. Such specimens would tend to slip

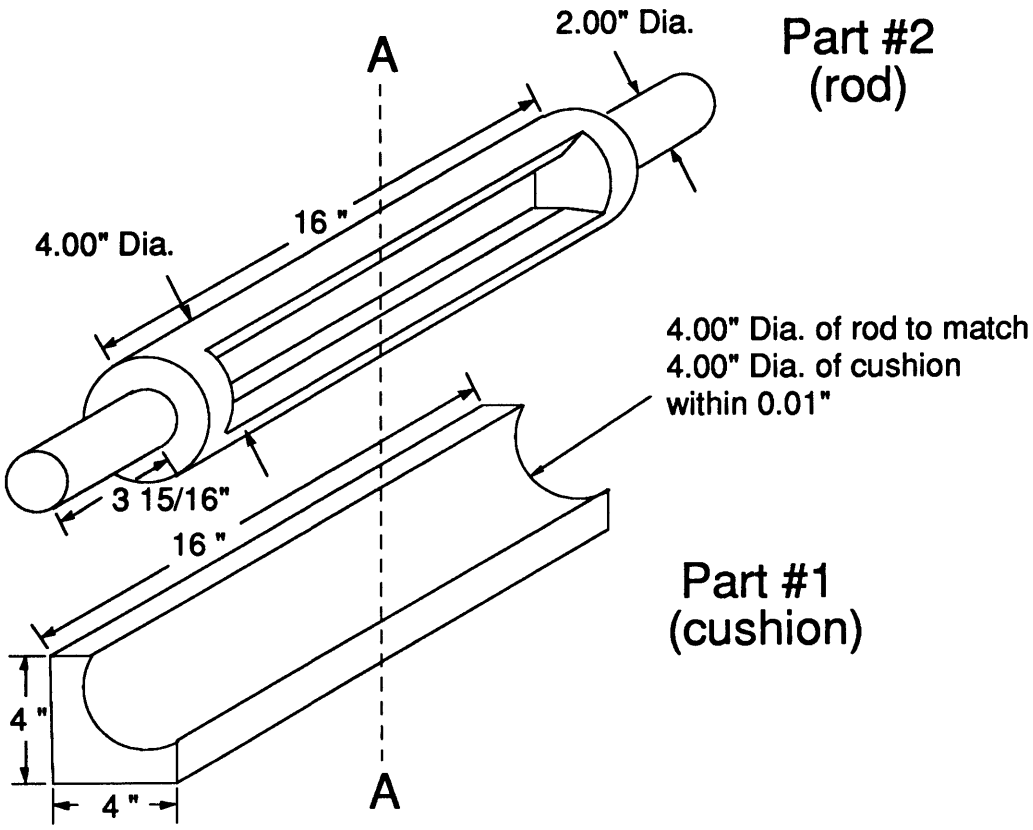

Tolerances: (unless otherwise noted)
x" = x ± 1/64"
x.xx" = x.xx ± 0.01"
x.xxx" = x.xxx ± 0.005"

Figure 4.13 Schematic of rod and cushion.

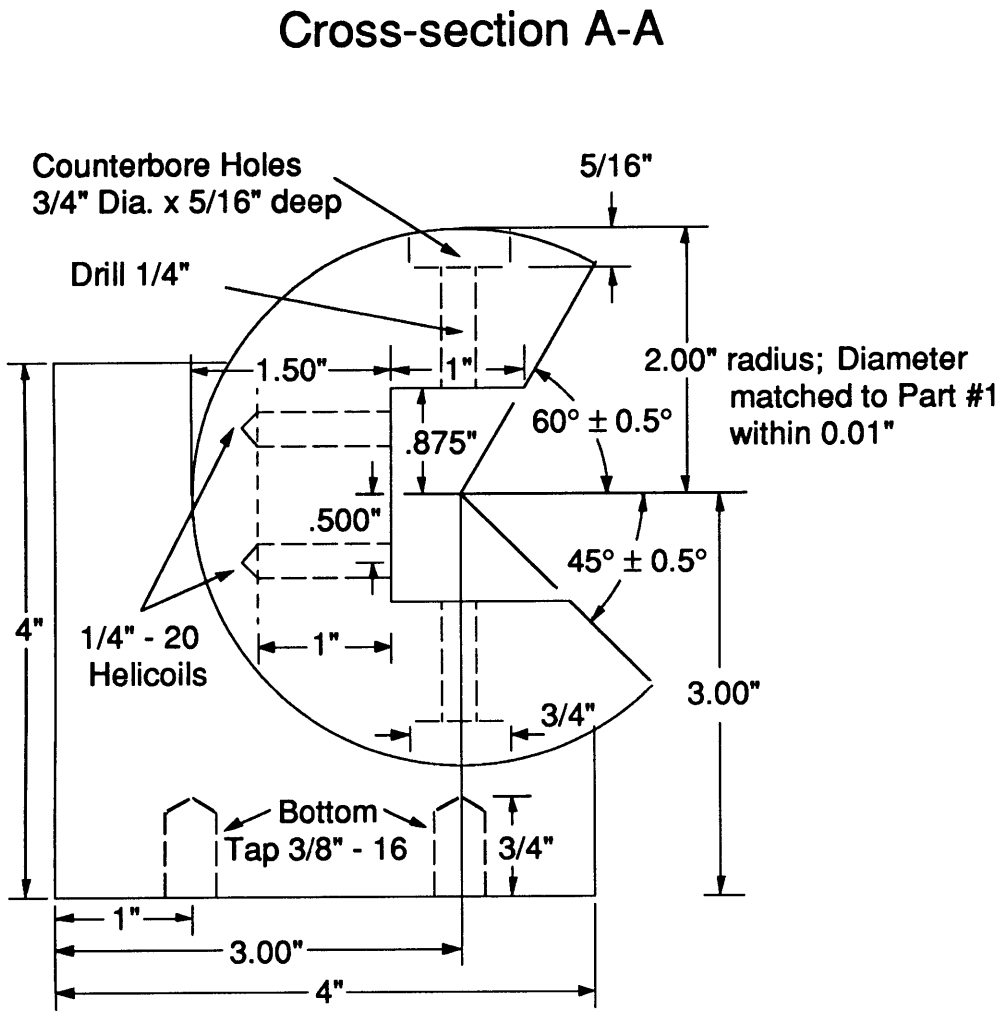

Tolerances: (unless otherwise noted)

x" = x ± 1/64"

x.xx" = x.xx ± 0.01"

x.xxx" = x.xxx ± 0.005"

Figure 4.14 Schematic of rod and cushion cross-section.

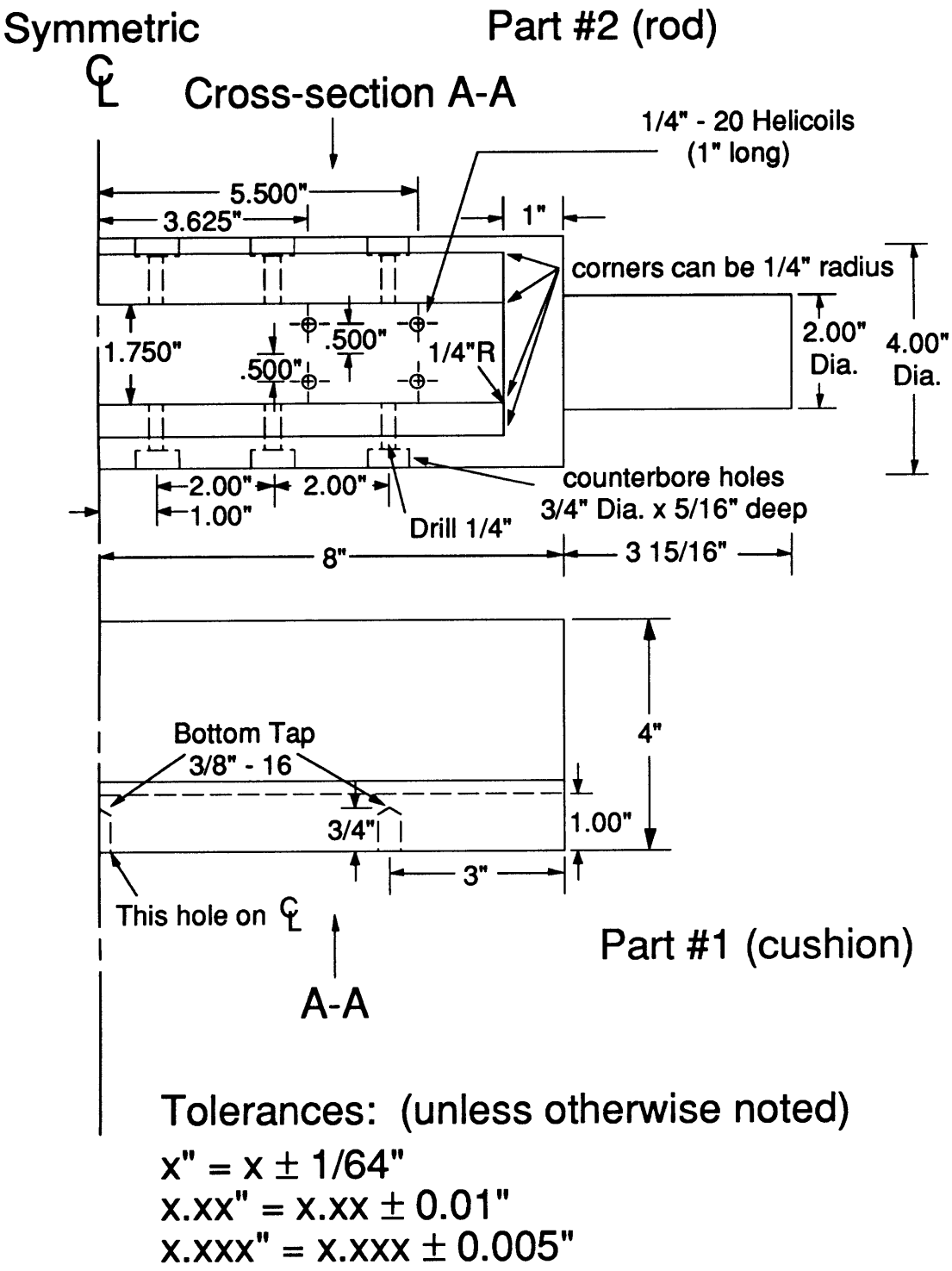

Figure 4.15 Schematic of front-view of rod and cushion.

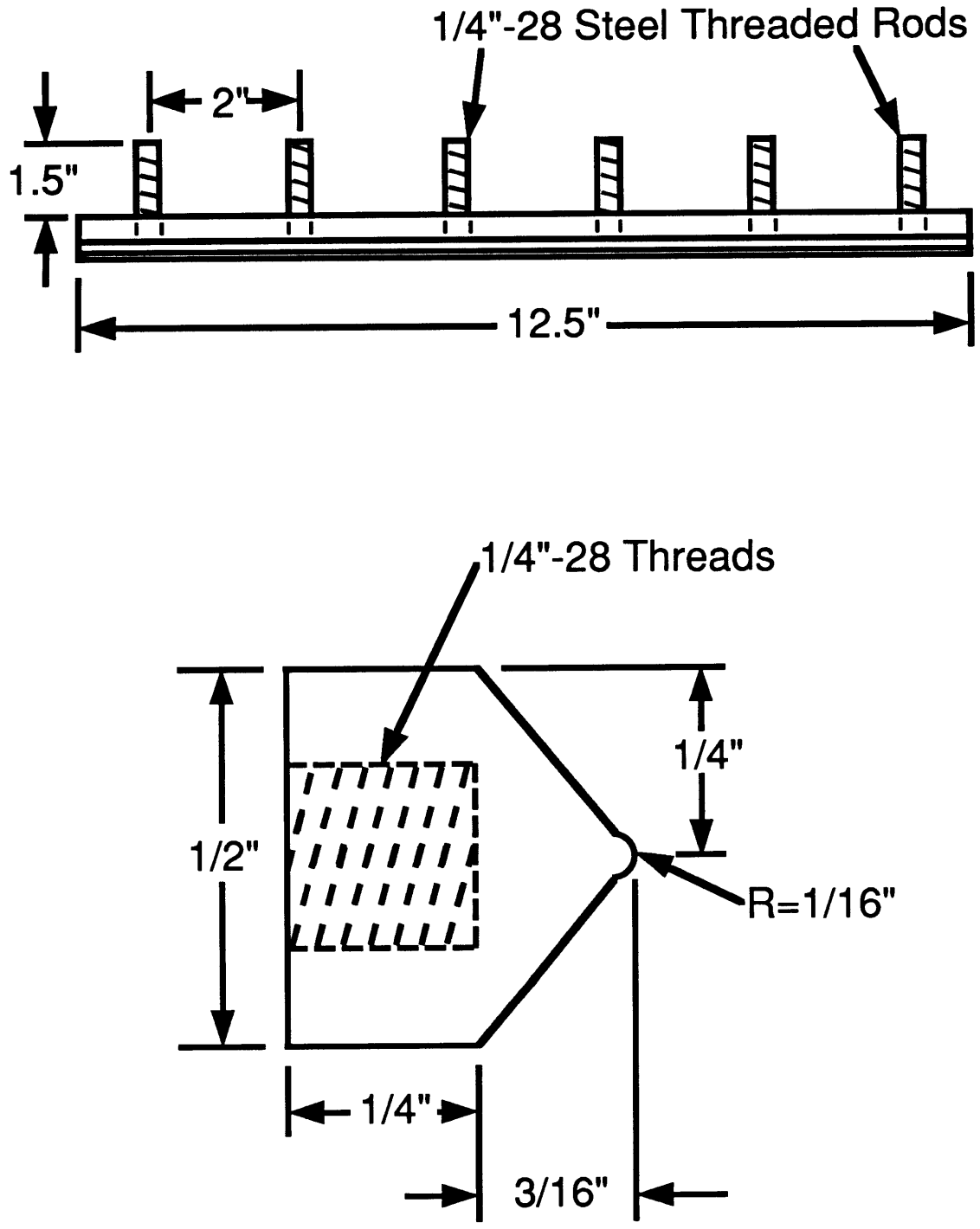

Figure 4.16 Illustration of steel knife edge: (*top*) steel knife edge with threaded rod attachments used for adjusting the boundary condition for different thickness shells, and (*bottom*) cross-section showing geometry of rounded 'knife' edge.

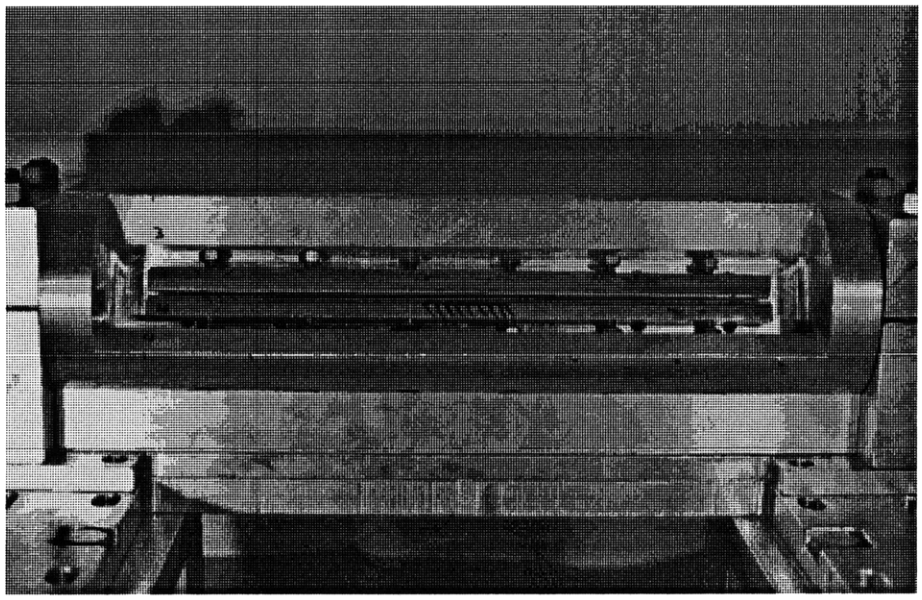

Figure 4.17 Close-up photograph of rod mounted in test fixture.

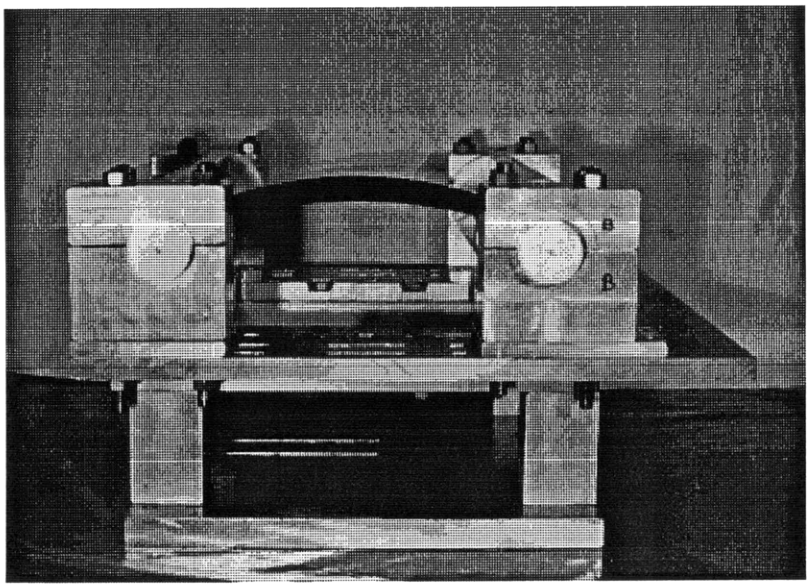

100 mm

Figure 4.18 Photograph of convex shell mounted in the rods of the test fixture.

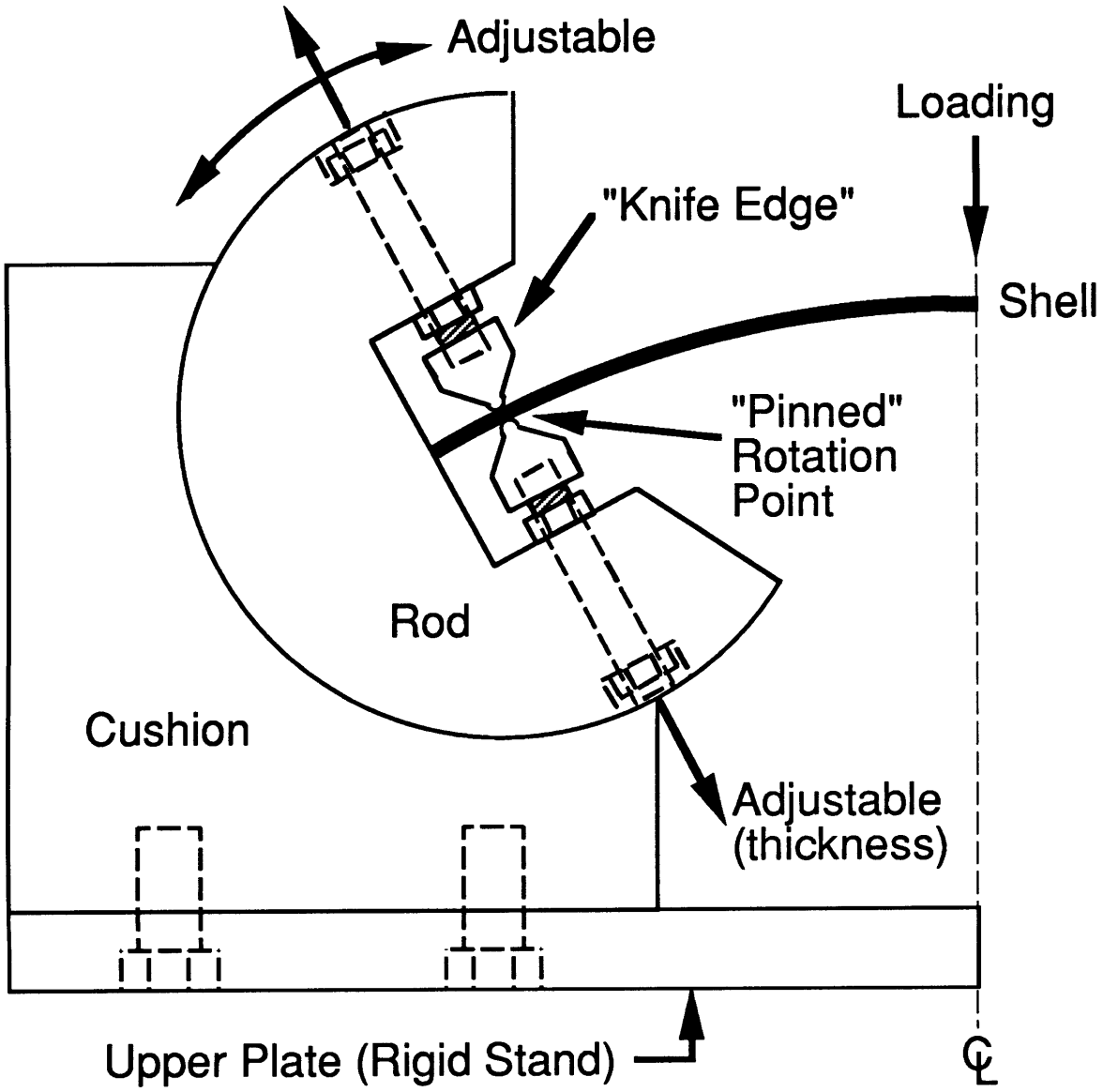

Figure 4.19 Illustration of test fixture cross-section showing specimen orientation for convex loading of a shell.

out of the knife edge supports during loading because of the tensile in-plane forces that are generated. The plates or concave shells 'pull-out' in-plane during loading whereas convex shells 'push-in' against the rods. 'Pull-out' would violate the no in-plane sliding condition. Knife edges, now only 102 mm (4") in length, are still used to maintain the out-of-plane condition of zero displacement but no resistive moment (pinned). However, the in-plane motion must be restrained while still allowing the shell to rotate. This requires attachments to the axial edges of the shells and plates and additional parts to be mounted in the rods of the test fixture.

The shell attachments are illustrated in Figure 4.20. A clamping bar is used to bolt the shell edge to the extended knife edge through holes drilled through the shell edge. The extended knife edges have the same cross-section as the knife edges in Figure 4.16 and are restrained by placing them in half-cylinder steel blocks which are screwed into tapped holes (heli-coils) located on the flat inside face of the test fixture rods. Thus, the extended knife edges can rotate in the half-cylinder steel restraining blocks but the shell cannot pull the extended knife edge past this point of rotation in the half-cylinder blocks. This provides the no in-plane condition and allows rotation. The extended knife edge point of rotation of the attached shell is coincident with the rotation point of the knife edges that restrain the out-of-plane motion, as in Figure 4.19. Therefore, the shells/plates rotate about a common point and the rods can still be adjusted prior to testing so that specimens are perpendicular to the out-of-plane knife edge restraints.

Figure 4.21 is an illustration of how the in-plane and out-of-plane conditions are combined to achieve the pinned/no in-plane sliding condition for concave and plate loading configurations. Cross-sections A-A and B-B from Figure 4.20 are shown in the upper and lower portions of Figure 4.21

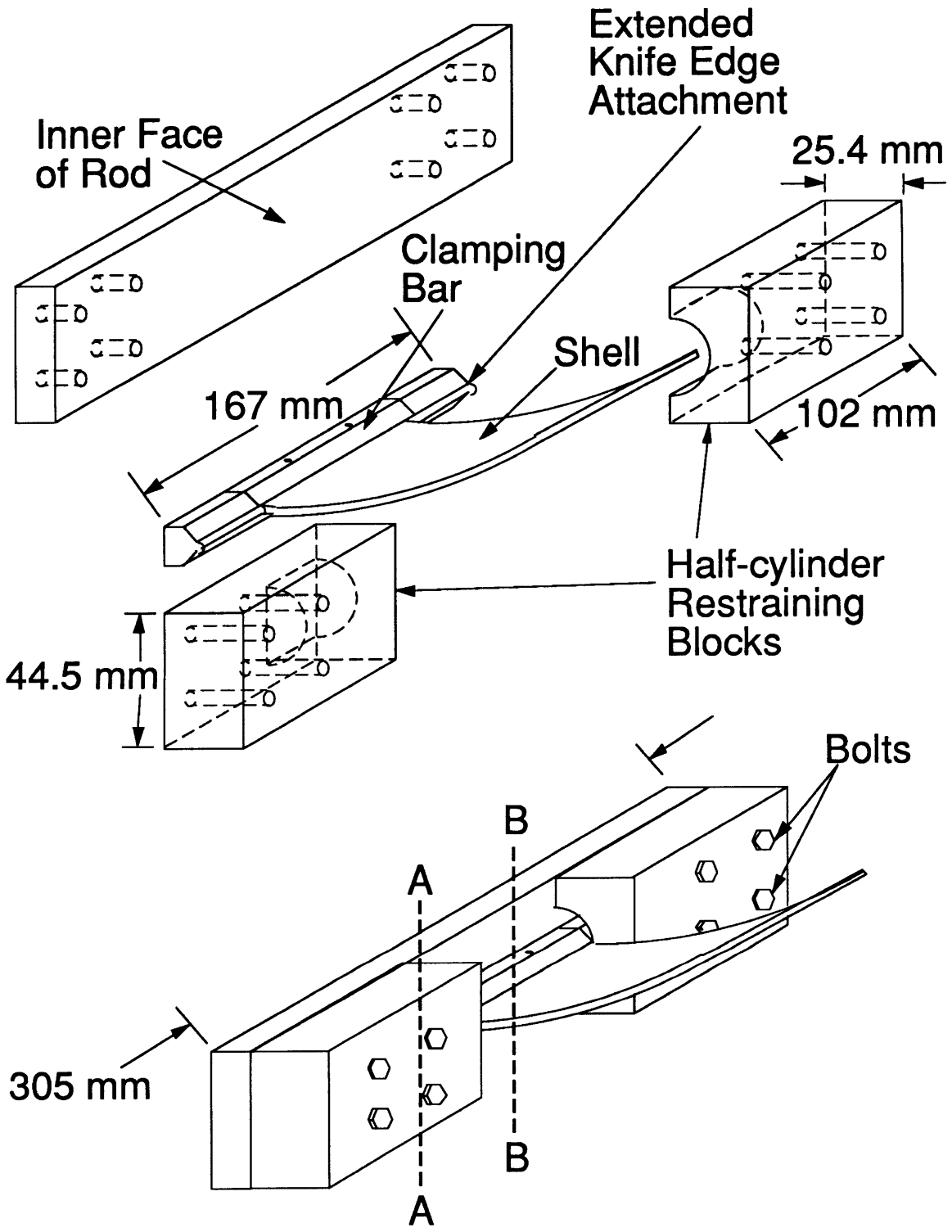

Figure 4.20 Illustration of shell attachments with extended knife edges and half-cylinder steel restraining blocks.

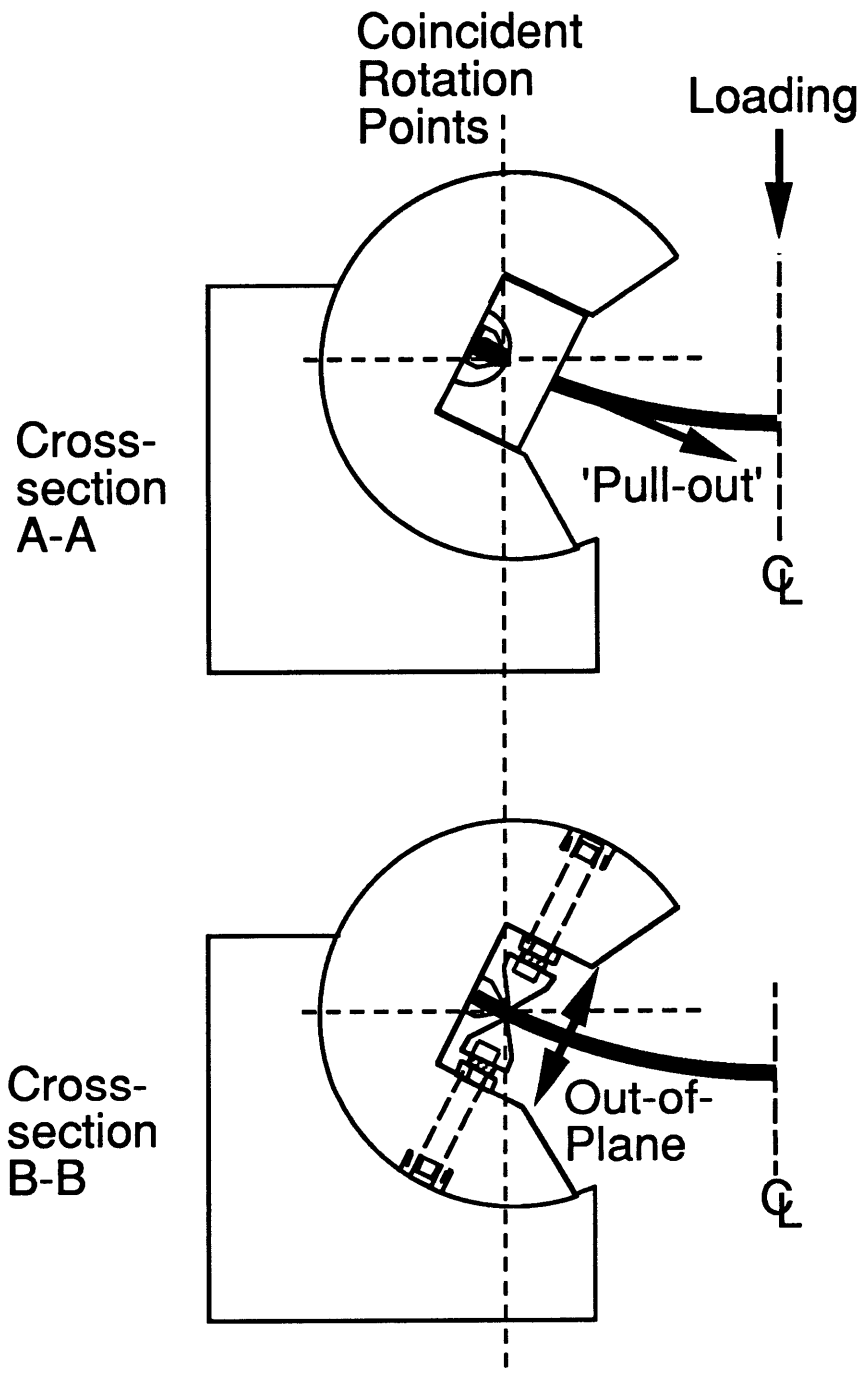

Figure 4.21 Illustration of how restraints are combined to achieve the (*top*) in-plane and (*bottom*) out-of-plane experimental boundary conditions for concave shells and plates (cross-sections refer to Figure 4.20).

respectively. The upper portion of Figure 4.21 contains the half-cylinder in-plane restraint against 'pull-out'. The half-cylinder blocks restrain the extended knife edges on either side of the shell. The lower portion of Figure 4.21 has the standard knife edges restraining the out-of-plane motion of the shell (the extended knife edge on the shell is also shown). The standard knife edges are 102 mm (4") in length and contact the shell between the half-cylinder restraining blocks. These restraints are combined to obtain the pinned/no in-plane sliding restraint for concave and flat shells. Figure 4.22 is a three-view dimensioned schematic of the extended knife edges, clamping bars, and half-cylinder restraining blocks.

It should be noted that the test fixture is used for all loading configurations and test types (impact and quasi-static) except for the full cylinders. Full cylinders are 'floor' supported at three points along the entire length (axial direction) of the cylinder. The arrangement is illustrated in cross-section in Figure 4.23. The bottom of the cylinder rests against the base of the support and the two steel triangles that are welded to the support. The cylinder is held in place using three elastic cords wrapped through the cylinder and around the support at the three contact points. One cord goes through the cylinder and around the floor support in the center, and the other two wrap through the center of the steel triangles shown in Figure 4.23. This arrangement is used for both impact and quasi-static testing and allows for the full cylinder deformation mode.

A discussion of the appropriateness of the achieved experimental boundary conditions (test fixture) is given in chapter 6. Additionally, other results from the experimental investigation are discussed that indicate the test fixture achieves the designed boundary condition.

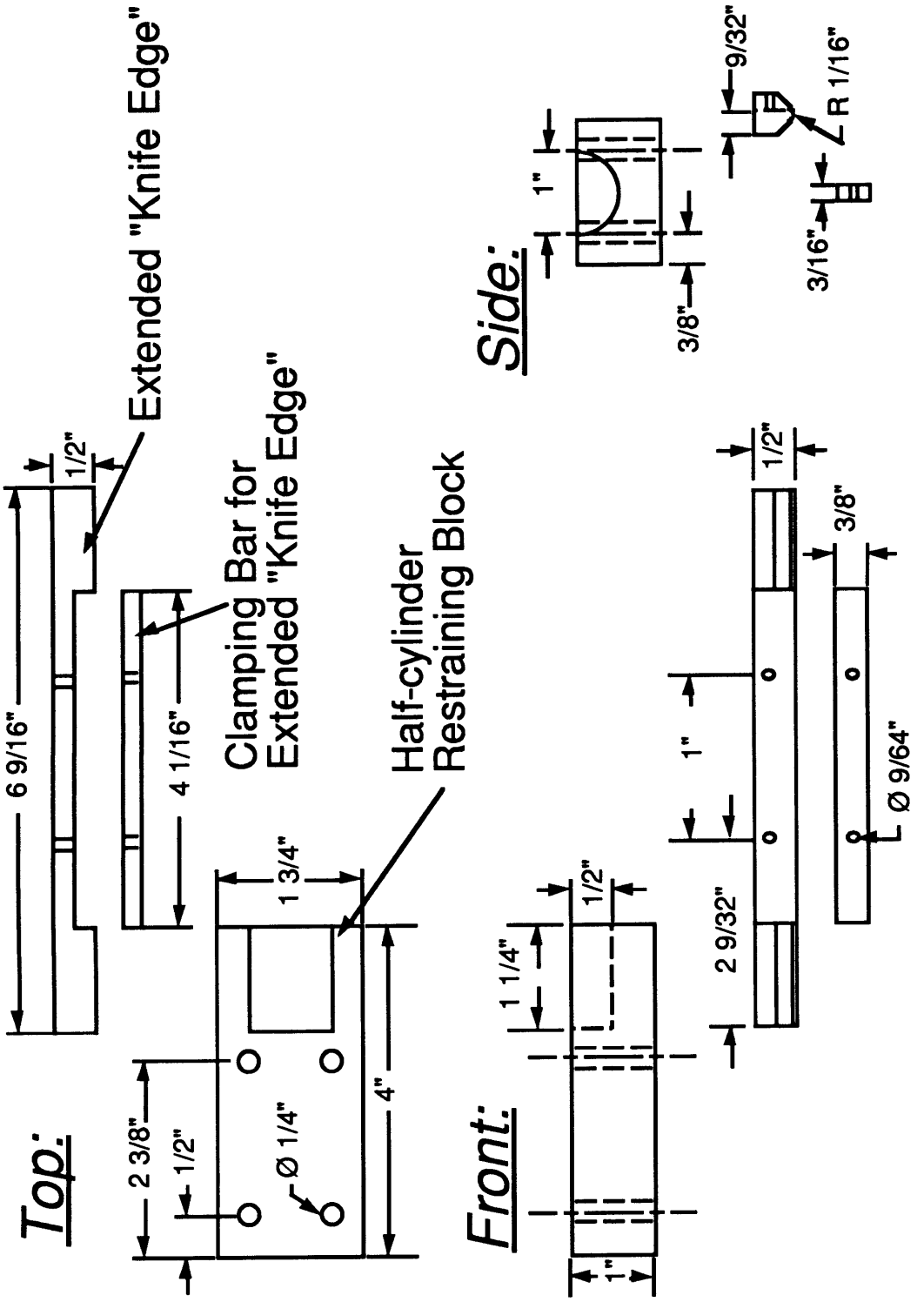

Figure 4.22 Three-view schematic of steel shell attachments: extended knife edges with clamping bars and half-cylinder restraining blocks.

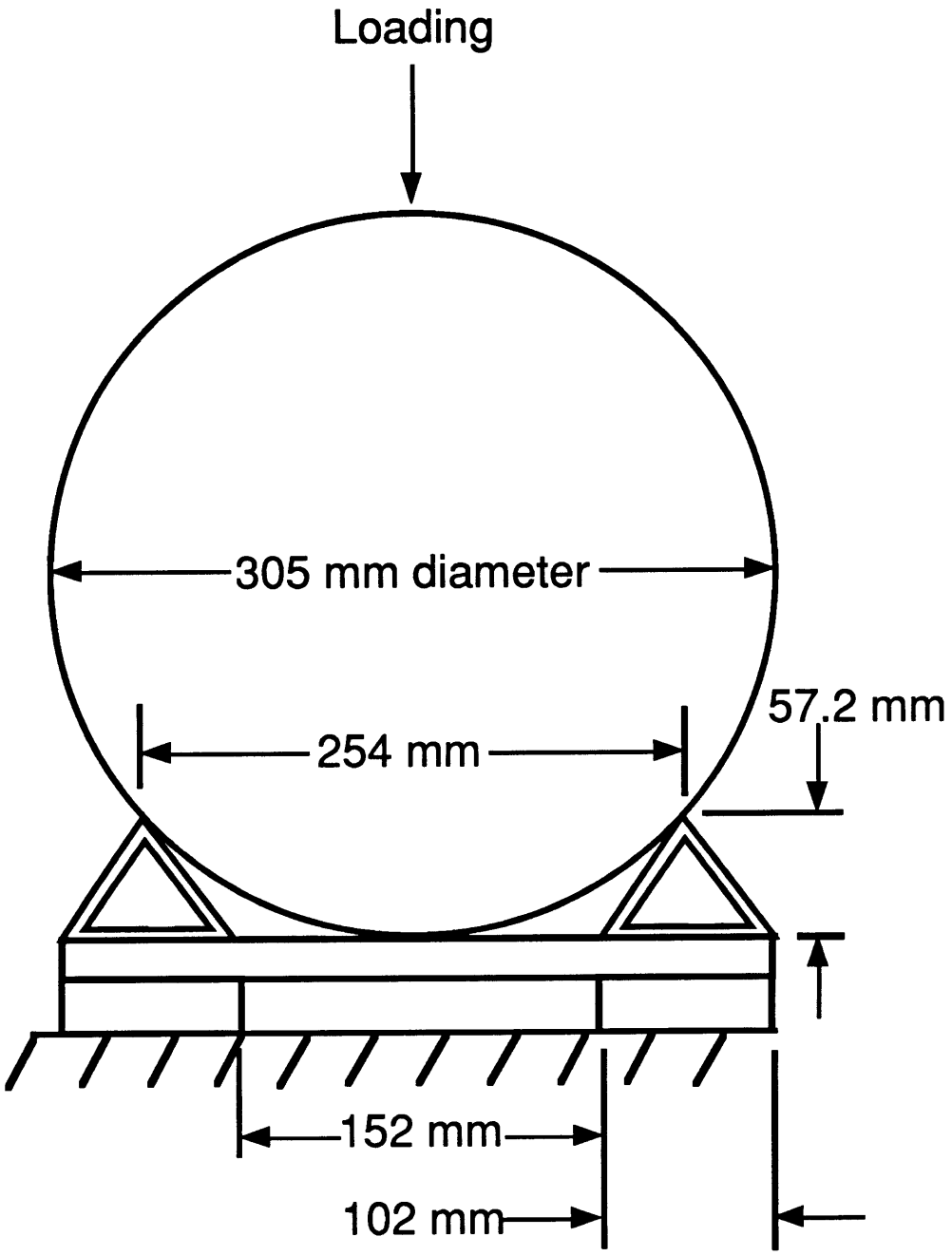

Figure 4.23 Illustration of boundary condition for full cylinders.

4.4 Testing Procedures

In this section, the experimental procedures used in the testing of the composite shells, plates, and cylinders are described. General procedures associated with the test fixture (i.e. mounting the specimens) are reviewed before moving on to an outline of impact and quasi-static test procedures. Impact testing was completed before quasi-static testing to determine the upper limit on load for the quasi-static tests. As discussed in chapter 3, this limit load is taken from the peak force measured during impact testing at 3 m/s for each structural configuration.

4.4.1 Specimen Set-up in Fixture

Some general considerations regarding the use of the test fixture are given in this section. Placement of convex shells in the test fixture is rather straightforward whereas concave and plate specimens require more steps. Therefore, set-up for the convex loading geometry is described before moving on to the more complicated concave and plate geometries.

For the convex loading case, the lower knife edge of each rod support is first fixed in place by bolting it to the rod using the threaded rod supports described in section 4.3. The upper knife edges are left free and the shell is allowed to rest on the lower knife edges. The rods are separately rotated until the shell is visually perpendicular to the inner face and lower knife edge of both rods. One rod/cushion assembly is spanwise adjustable as outlined in section 4.3. This assembly is moved toward the fixed rod/cushion assembly until the shell impinges on the inner face of both rods. At this time, the rods are locked in place (rotation and spanwise) by tightening the clamps at the end of each rod. The upper knife edges are brought in contact with the shell

and locked in place using the 6.35 mm (1/4") diameter threaded rods described in section 4.3. The shell is then ready to be tested. After preliminary impact testing, it was found that the fixed brace described in section 4.3 was not needed to reinforce the spanwise adjustable rod/cushion assembly because the clamps held the assembly rigidly in place. Thus, the fixed brace was not used in this work.

Convex and plate specimens require additional attachments for mounting in the test fixture. These additional attachments are described in section 4.3 and illustrated in Figure 4.20. First, the extended knife edge attachments must be placed on the axial edge of each shell. The attachments are first used as guides to drill two holes along each edge of the shell or plate. A 3.57 mm (9/64") diameter diamond-grit core drill is used to make holes in the specimens. The extended knife edge attachments are then bolted to the specimen. A double-stick transfer tape, Dry-Stik® Self-Adhesive, is used to improve the contact at all interfaces of the steel attachments and the composite specimens.

The specimen with the extended knife edges is now ready to be placed in the test fixture. Again, the lower knife edges are fixed prior to shell placement. Additionally, one half-cylinder restraining block (as illustrated in Figure 4.20) is bolted to the inside of each rod. The specimen is allowed to rest on the lower knife edges with the knife edge extensions inside the two opposing half-cylinder restraining blocks. The second set of half-cylinder restraining blocks are now bolted to each rod over the exposed extended knife edge attachments. The rods are rotated so that the specimen is perpendicular to the out-of-plane knife edges. Now, the spanwise adjustable rod/cushion assembly is moved away from the fixed rod/cushion assembly until the extended knife edge attachments impinge upon the half-cylinder

restraining blocks. The rods are then clamped and finally the upper knife edges are brought to rest against the specimen and locked in place.

4.4.2 Impact Test Procedure

All impact testing was done with the Free-Rolling Energy Device (FRED) developed in TELAC [77]. The specimens are constrained in the experimental boundary conditions as described in section 4.4.1. The rigid stand (test fixture) is bolted to a heavily weighted drill-press stand to provide a solid support for the specimens. The specimen orientation for the convex impact of a shell is shown in Figure 4.19 and the location of the shell with respect to the impactor is shown in Figure 4.24. Central impacts are insured by marking the center of each specimen prior to placement in the test fixture. This is done by flash-taping over the center region of the specimen and marking the center on the tape with paint marker. Prior to impact, the drill press stand is positioned so that the impacting tup contacts the specimen center and then the flash tape is removed.

The striker and impactor units that comprise FRED are shown in Figure 4.24. The striker unit consists of a linear spring that can be compressed with the hand winch. The electromagnets are energized prior to compressing the spring and the striker is accelerated toward the impacting rod when the magnets are released. The impacting rod is in turn propelled toward the specimen by the striker. The impactor unit allows the impacting rod to move freely on linear motion bearings and also houses the anti-rebound lever and light gates. The anti-rebound lever triggers the data acquisition system to begin taking data and also restrains the impacting rod after impact to prevent multiple impacts.

The light gates form part of the data acquisition apparatus for the

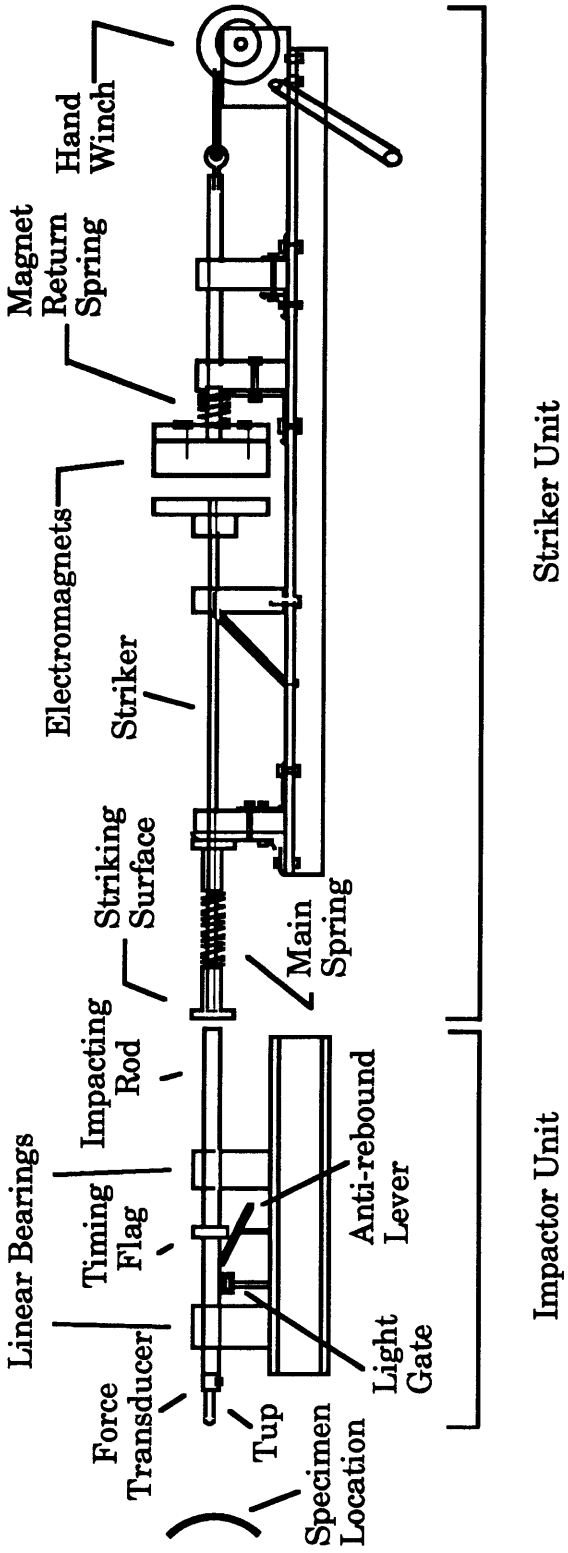

Figure 4.24 Illustration of Free-Rolling Energy Device (FRED).

impact tests and are illustrated in Figure 4.25. The light gates are used to determine the impact velocity. A black donut on the impacting rod breaks the first light beam and, just prior to the impact rod contacting the specimen, the second light beam is broken. The time difference between the beams being interrupted is recorded using a Fluke 1953A Counter-Timer. Knowing the distance between the light beams (36 mm), this time difference is used to calculate the velocity of the impacting rod.

Force-time histories are recorded using a PCB Model 208A04 force transducer having a measured response from the manufacturer of 5.16 mV/lb. The force transducer is mounted behind the 12.7 mm (1/2") diameter stainless steel tup as shown in Figure 4.25. The voltage from the force transducer is fed into a PCB Signal Conditioner Model 484B designed for use with the 208A04 force transducer. The amplified voltage is then sent to a GW Instruments MacADIOS II analog/digital converter connected to a Macintosh IIx computer which records the data. Voltages are sampled every 20 μs and converted to force units using the conversion factor of 862 N/V.

The force on the specimen is calculated from the force measured by the force transducer mounted behind the tup on the impacting rod. The inertia of the tup must be accounted for in calculating the force on the specimen. The force on the specimen is thus calculated using the derivation given in [72]. This modification to the force is expressed as:

$$F_{tot} = \left(\frac{M_{tup} + M_{ft} + M_{rod}}{M_{rod} + \frac{M_{ft}}{2}} \right) \times F_{ft} \tag{4.4}$$

where F_{tot} is the contact force experienced by the specimen, F_{ft} is the force experienced by the force transducer, M_{tup} is the mass of the tup (125 g), M_{ft}

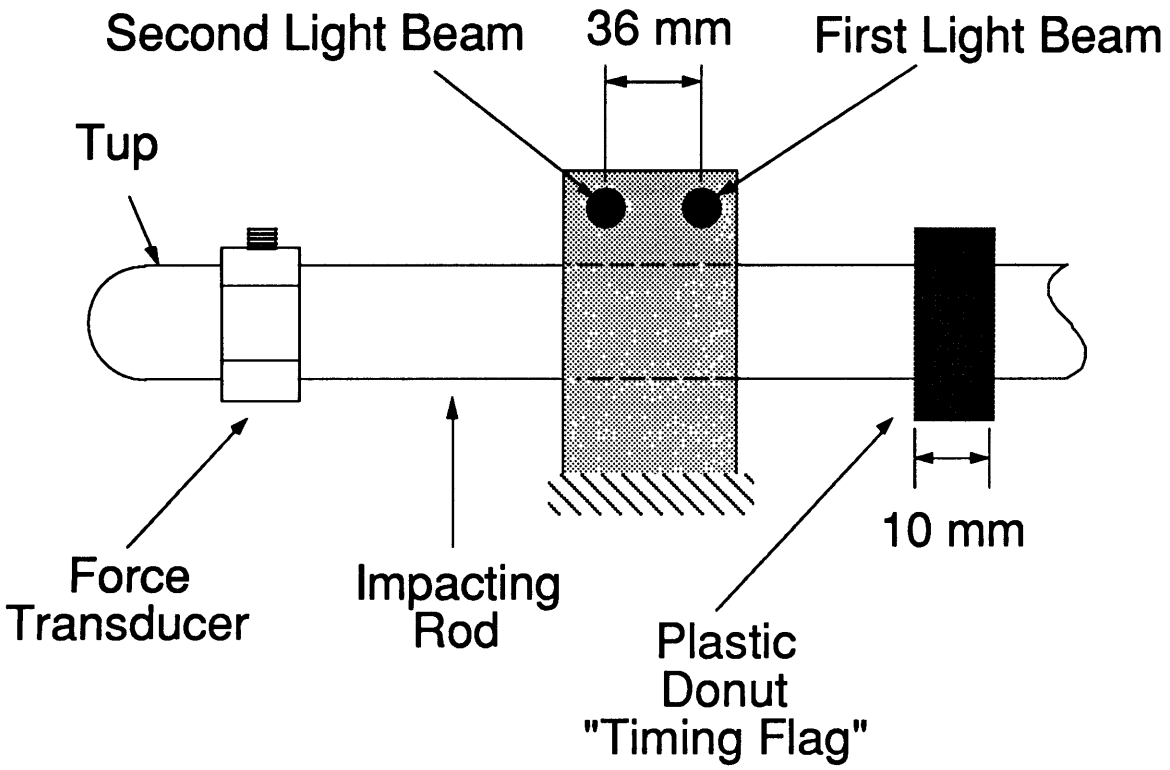

(total impacting mass = 1.60 kg)

Figure 4.25 Illustration of impactor rod and light-gates.

is the mass of the force transducer (25 g), and M_{rod} is the mass of the rod (1450 g). In this investigation, the force on the specimen is 1.09 times the force measured by the force transducer. The total mass of the assembly that impacts the specimens (impacting rod, tup, and force transducer) is 1.60 kg.

4.4.3 Quasi-Static Test Procedure

Quasi-static testing is performed using the same 12.7 mm stainless steel tup (indentor) used in the impact tests. The endpoint of the quasi-static tests is the peak force experimentally measured during impact testing at 3 m/s. The same test fixture used in impact tests is also used for quasi-static testing. All quasi-static tests were completed using an MTS-810 uniaxial testing machine. The set-up for the tests is shown in Figure 4.26.

The test fixture that holds the specimen is bolted to the lower grip of the testing machine. An MTS 8896 N (2000 lb) load cell and the indentor are mounted in the upper grip. A Trans-Tek 0350-0000 Linearly Variable Displacement Transducer (LVDT) is attached to the upper grip and positioned under the specimen directly below the indentor. This is accomplished using the centering assembly illustrated in Figure 4.27. The alignment jig precisely aligns the LVDT beneath the indentor so that the reduction in laminate thickness (indentation) is measured during loading. The tup has a threaded rod inserted into it which passes through a hole in the upper half of the alignment jig and screws into a threaded aluminum cylinder which is held in the upper grip. Thus, the alignment jig is held fixed in the upper grip with the tup while the specimen is inserted between the two forks of the alignment jig, as shown in Figure 4.27. The upper grip is stationary during testing and the shell is pushed into the indentor by the lower grip which is moving up.

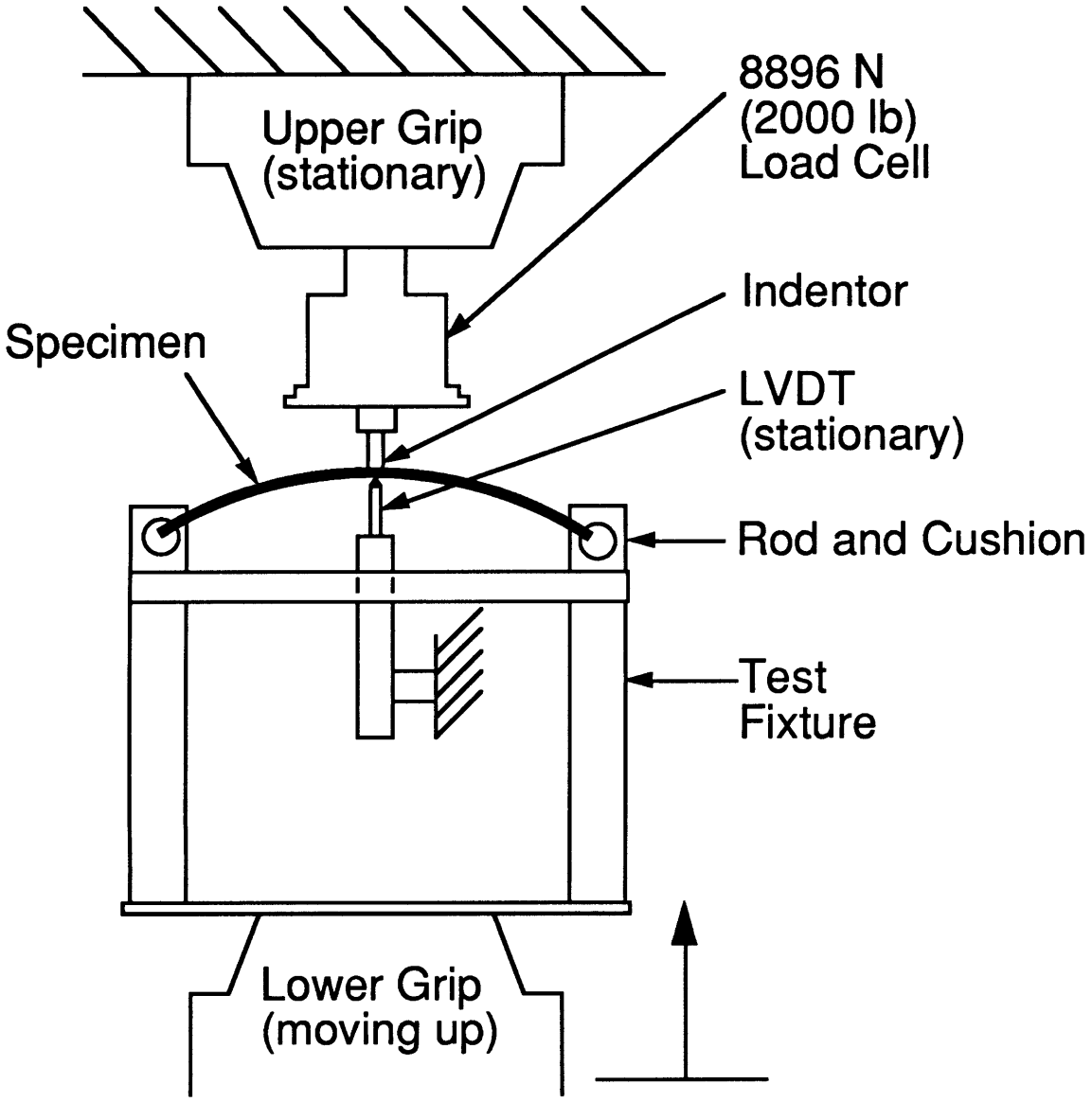

Figure 4.26 Illustration of test set-up for quasi-static testing.

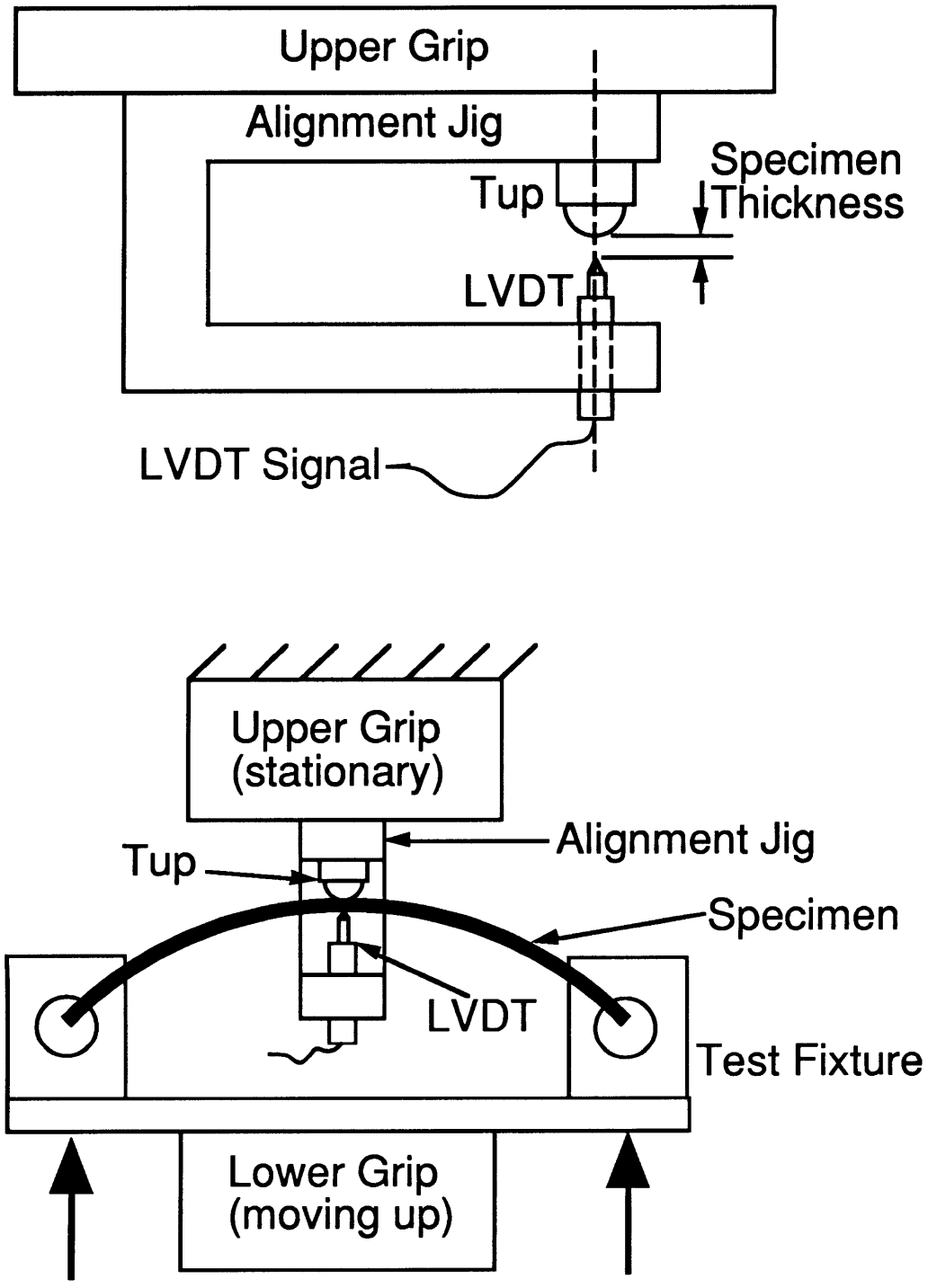

Figure 4.27 Illustration of centering assembly: (*top*) alignment jig mounted in upper grip with the tup and LVDT, and (*bottom*) alignment jig placement for quasi-static testing.

Specimen deflection is measured using the stroke of the testing machine, i.e. the motion of the test fixture. Resolution of the stroke varies between tests, as is subsequently explained, because the stroke range changes. Resolution varies from 0.006 mm to 0.06 mm depending on the shell being tested. Using the data acquisition system described in section 4.4.2, the resolution of the LVDT is 0.002 mm (0.0508") and the resolution of the load cell is 0.869 N (0.195 lb). Compliance of the test fixture, as it relates to measured values, i.e. stroke, is negligible. This is discussed quantitatively in chapter 6.

Testing is performed by raising the lower crosshead (grip) which moves the test fixture and specimen toward the stationary indentor. This is done by adjusting the stroke until a preload of not more than 1 N is seen. The LVDT is stationary, so as the specimen is pushed into the indentor, the LVDT measures the thickness reduction of the laminate. The MTS machine was run in compression mode under stroke control and then manually stopped at the desired peak load and unloaded immediately at the same rate as loading. The different structural configurations of the tests in this research gave a wide range of maximum deflection and force levels. A heuristic was developed to take full advantage of the resolution of all the measured quantities.

Although the peak load was known *a priori*, the maximum stroke, which defines the choice of stroke range, was not known. For each specimen, maximum stroke was estimated by twice integrating force-time histories from the 3 m/s impact tests of similar shells. The procedure for integrating the force-time histories to obtain displacements is described in chapter 5. Six minute tests (3 minutes of loading and 3 minutes of unloading) with a sampling frequency of 2 Hz were deemed appropriate based on previous

quasi-static/indentation research in TELAC. Since stroke rate is determined on the testing machine by setting a maximum stroke and an elapsed time, both needed to be calculated keeping in mind that the actual stroke could be larger than the one estimated by integrating the force-time histories. Thus, a factor of 1.5 was applied to both the estimated stroke and the desired test time so that the desired peak load would be reached.

4.5 Damage Evaluation Procedure

All specimens were evaluated for damage after completion of testing, whether impact or quasi-static. Two methods were used to evaluate such damage. The first was visual inspection. After testing, the front and back sides of the specimen were closely examined for damage. Matrix splits are visible on the back surface of some specimens as well as "marring" on the front surface from the indentor contact. Matrix splits are simply matrix cracks occurring in the fiber direction between the fibers. The length of the matrix splits were measured to the nearest 10 mm because the exact beginning and end of the crack is difficult to distinguish visually. Front surface damage (indentor/impactor side) is quantified by measuring the length, to the nearest millimeter, of the marring of the composite. The length of the marring was measured in both the axial and circumferential direction because some shells had elliptic, rather than circular, marred regions. Specimens that exhibit penetration can only be evaluated visually. Penetration occurs when the impactor/indentor passes entirely through the specimen.

The second type of damage evaluation is dye-penetrant enhanced X-radiography. X-radiography provides a view of the damage state that is

integrated though-the-thickness. After testing, a small hole 0.79 mm (1/32") is drilled through the thickness of the specimen at the center of the impact site. Flash tape is applied to the back surface (opposite impact) and a dye is injected with a syringe into the hole on the front surface. The x-ray opaque penetrating dye is 1,4 Diiodobutane (DiB) which seeps into cracks and delaminations in the specimens through capillary action. A small excess bubble of DiB is maintained on the specimen for approximately half an hour. This allows the DiB to fully penetrate into the damaged region. The excess dye bubble and flash tape are removed and the specimen x-rayed. A Scanray® Torrex 150D X-ray Inspection System used in "TIMERAD" mode and 50 kV potential is used to x-ray the specimens along with Polaroid Type 52 PolaPan Film.

The x-ray machine allows 260 mR (milliRoentgens) of radiation to penetrate each specimen which provides for a consistent damage characterization regardless of specimen thickness. DiB soaked portions of the specimen show up as dark areas in the x-rays. A sample x-ray photograph showing a large delamination is provided in Figure 4.28. The x-ray photograph is of the damage state looking down at the convex side of the shell. The 0° direction in Figure 4.28 is along the vertical axis of the page (circumferential shell direction) and positive angles are taken counterclockwise from that axis. All x-ray photographs in this work maintain this orientation and are shown to scale. This is true for specimens impacted on the concave side as well as cylinders.

The large damage (delamination) axis is along the 45° ply in this particular figure. The small, light, circular region at the center of the x-ray in Figure 4.28 is the hole drilled through the center of the impact site to inject the penetrating dye. The large light region in the photo is

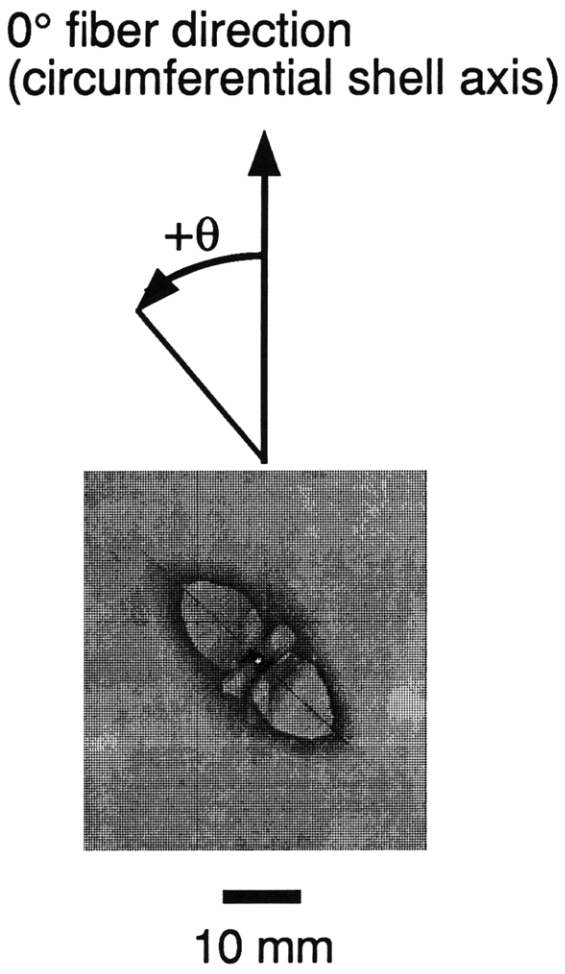

Figure 4.28 Typical x-ray photograph (to scale) with ply angle convention indicated.

characteristic of a delamination. In this photo, a larger delamination can be seen at 45° and a much smaller one at -45°. The dark line at 45° is a long matrix split in the ply on the side of the shell opposite impact. Shorter matrix splits can also be seen at -45° and 0°.

Damage in the x-ray photographs gives an integrated planar view of damage through-the-thickness of the shell. The damage picture for curved shells is slightly smaller than the actual damage area, due to the curvature. A damage area along the arc length of the shell is projected onto the flat photograph. This reduction in damage area is only 0.5% for the shell with the smallest radius (largest effect). This geometric effect on the measured versus actual damage area is considered negligible. Damage metrics used with the x-ray damage evaluation technique will be discussed in chapter 5.

CHAPTER 5

RESULTS

Results from impact and quasi-static testing are presented in this chapter. Impact test data consists of force-time histories which can be integrated to provide deflection information. Quasi-static test data includes force-deflection and force-indentation information. After testing, all specimens were evaluated both visually and with x-ray photography to determine the damage state.

A description of the observed instability behavior in the impact and quasi-static response is first given in section 5.1. Examples from experimental data are used to characterize this behavior. Terminology is clearly defined to facilitate descriptions of the loading responses in the following sections. Impact test data, including damage characteristics, is presented for different structural configurations (convex shell, concave shell, plate, and cylinder) in section 5.2. Following a similar format as in section 5.2, the quasi-static test data is presented in section 5.3.

5.1 Instability Description and Significance

The characteristics of many of the experimental loading responses for convex specimens are fundamentally different than those for plates and concave shells. A typical quasi-static force-deflection response is presented in Figure 5.1 for convex shell R1S1T1. Load and unload data was taken for all

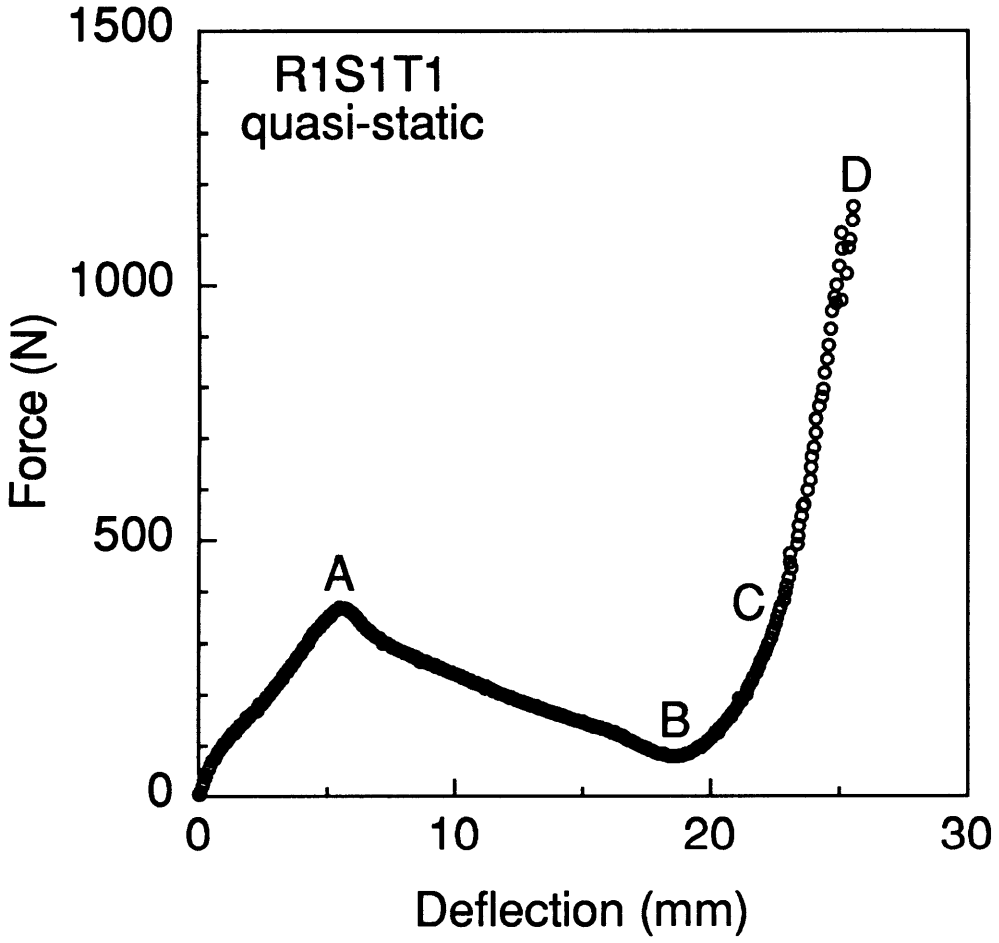

Figure 5.1 Force-deflection response for quasi-static loading of specimen R1S1T1.

specimens, but loading data only is generally presented for clarity in this chapter. The entire loading history, including unloading, is presented for all specimens in the appendices. The force-deflection response in Figure 5.1 is noted to be quite nonlinear and to contain a region where the load decreases as the deflection is increased. These characteristics are not typical of those found in plates, concave shells, and even some convex shells in this investigation. However, these characteristics are typical of shell instability behavior. Following the definitions used by previous authors [36, 78], terminology can be defined to describe the type of loading response observed in Figure 5.1.

Four key points on the force-deflection response are noted in Figure 5.1. In this deflection-controlled test (all specimens were tested under stroke control), the load is seen to increase with deflection up to an inflection point (point A) indicating a local load maximum. At this point, a further increase in deflection results in a decrease in load. The load continues to decrease until a second inflection point (point B), indicating a local load minimum, is reached. At this point of inflection, the load begins to increases again, this time more rapidly than before, up to the global load maximum (point D). The importance of point C (the load is equivalent to the load at point A) is explained subsequently. Qualitatively, the shell reaches an instability at point A and the load path proceeds into what is termed an unstable region. At point B, the shell reaches a second equilibrium path and the load again begins to increase.

In load control situations, convex shell response can look very similar to Figure 5.1 but contains important differences. Instability in low arches and general shells is well-documented, e.g. [36, 78, 79]. A general shell force-deflection response, after [78], is given in Figure 5.2 to illustrate the shell

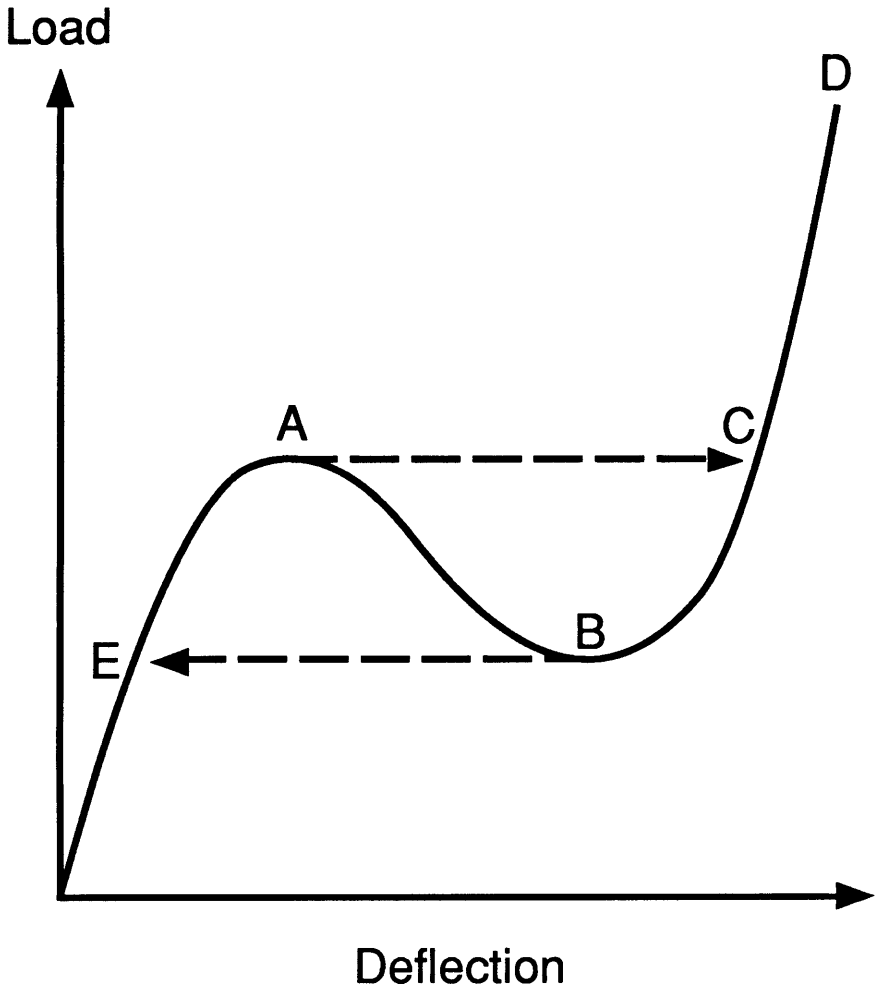

Figure 5.2 Illustration of force-deflection response for a general shell (after [78]).

behavior for load-control situations. Point A in Figure 5.2 is termed the "critical snapping load". In load control situations, convex shells can respond by following the loading path in Figure 5.2 up to point A and then the shell instantaneously 'jumps' from point A to point C and continues loading up to point D along the second equilibrium path. This 'jump' in the shell response is termed "snap-buckling" or "snap-through buckling". In the unloading of such a shell, the load path would decrease from point D to point B and then instantaneously jump to point E on the first stable equilibrium path. It would then follow this path down to zero deflection. With classic snap-buckling, two portions of the load path in Figure 5.2, one during loading and the other during unloading, are considered unstable. In loading, the jump of the load path in Figure 5.2 from point A to point C is considered unstable. During unloading of the specimen, the jump between B and E is considered unstable. Under load control, the region between points A and B is considered unstable in both loading and unloading for the snap-buckling phenomenon.

Quasi-static tests herein were conducted under deflection control and, as stated previously, snap-buckling was not observed. The entire loading path is stable for the convex specimens tested in this investigation including the region between points A and B in Figure 5.2 whereas snap-buckling would be observed for load-control situations. However, the loading response in Figure 5.1 is clearly very similar to that described by the snap-buckling illustration in Figure 5.2. Thus, for clarity, it is appropriate to use the same terminology associated with the snap-buckling phenomenon to describe force-deflection histories observed in this investigation. Referring back to Figure 5.1, the load at point A where the onset of instability occurs is defined as the critical snapping load. Considering loading, the loading path before point A

is defined as the first equilibrium path, the region between points A and B is defined as the instability region, and the loading between points B and D is defined as the second equilibrium path. These definitions are summarized in Figure 5.3 for the loading history given in Figure 5.1.

The second equilibrium path corresponds to loading in the inverted or "snapped-through" equilibrium position. An illustration of both equilibrium positions is given in Figure 5.4. In Figure 5.4, a cross-section of the shell is illustrated at the point of load application. The first equilibrium position corresponds to the shell in the convex position. The second, or inverted, equilibrium position, corresponds to loading the shell in a concave sense, i.e. loading the shell past point B in Figure 5.2. The inverted equilibrium position was observed during many of the quasi-static tests. This is shown in the upper photograph of Figure 5.5 for specimen R2S3T1 during quasi-static loading in the inverted equilibrium position. White paint marker was applied to the shell edges so that the mode shapes could be more easily distinguished in the photographs. The lower photograph in Figure 5.5 is of specimen R1S1T1 after quasi-static loading. In Figure 5.5, specimen R1S1T1 remained in the inverted equilibrium position after load was removed. The complete loading response for specimen R1S1T1 is shown in Figure 5.6. The unloading response in Figure 5.6 does not follow the loading path but returns to zero load after reaching the peak force. This type of response characterizes a stable postbuckled state for the shell, i.e. the shell remains in the inverted configuration after the load is completely removed.

The definition of a peak load for specimen response is extremely important because it is used as a damage resistance metric for impact and quasi-static comparisons in this investigation. As will be shown later in this chapter for the case of convex shells with an instability region, there is a clear

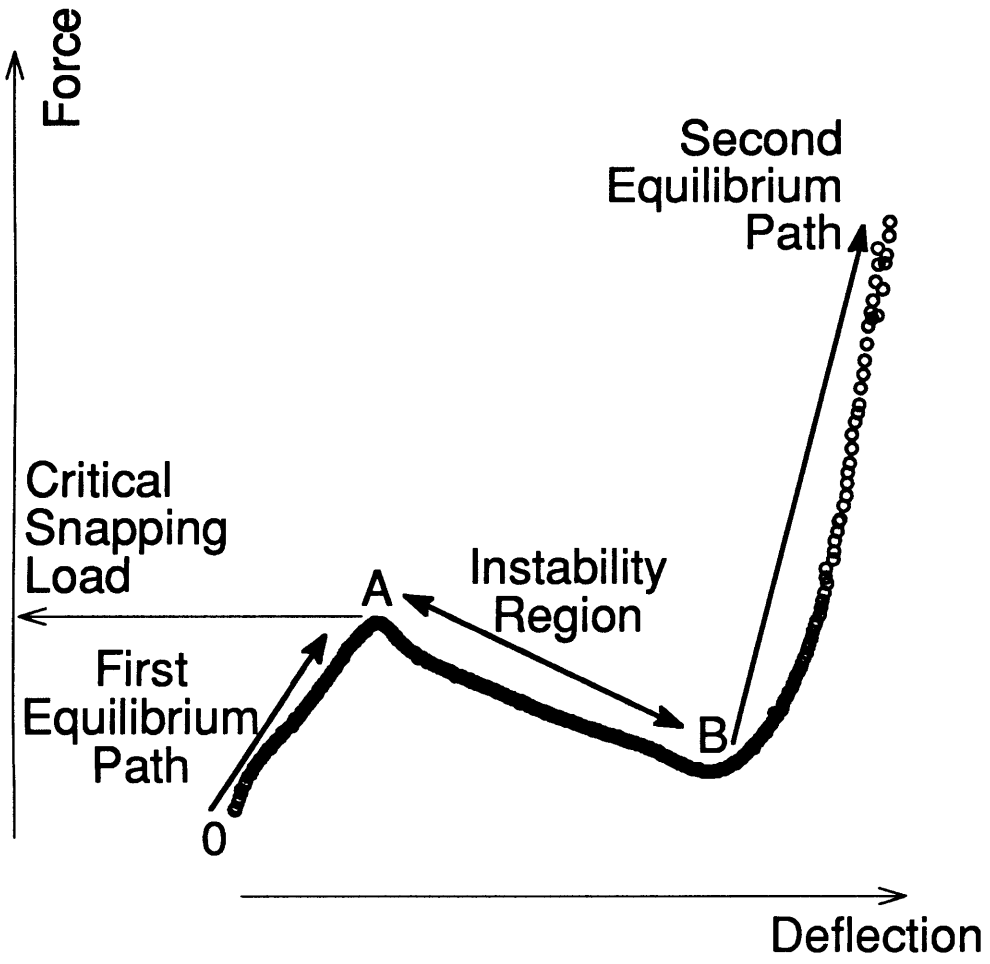

Figure 5.3 Illustration of definitions used to describe instability characteristics in load-deflection behavior of convex shells (data from Figure 5.1).

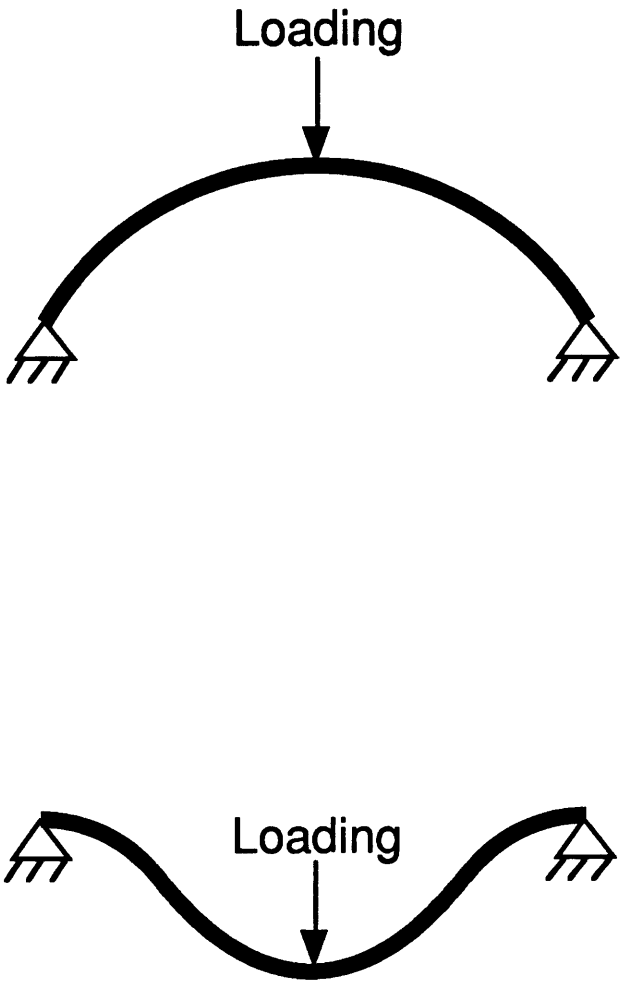

Figure 5.4 Illustration of convex shell loading: (*top*) in the first equilibrium position, and (*bottom*) in the second (inverted) equilibrium position.

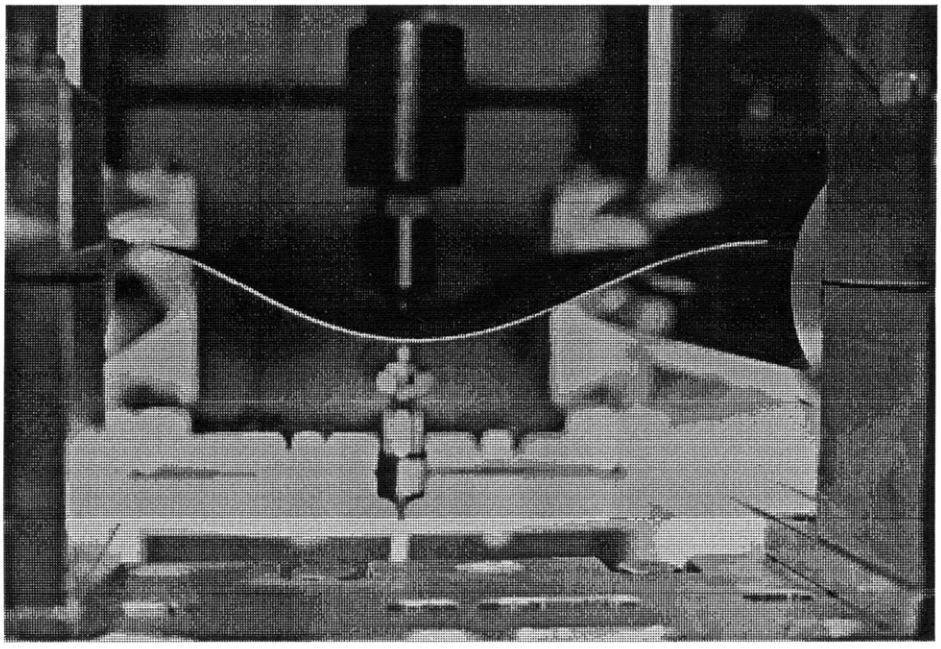

100 mm

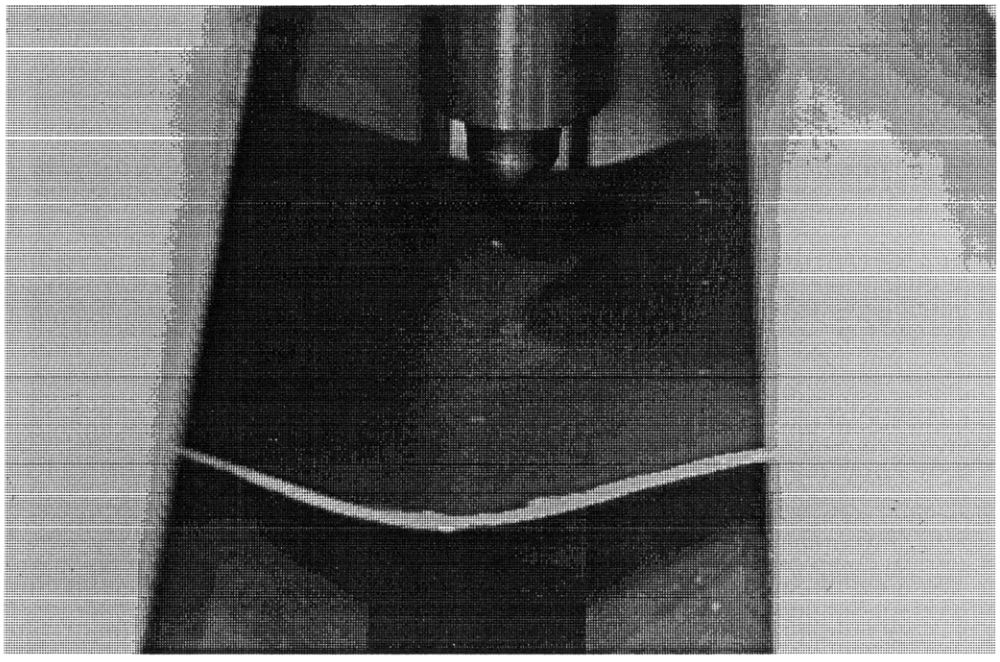

25 mm

Figure 5.5 Photographs of inverted convex shells: (*top*) specimen R2S3T1 during quasi-static loading, and (*bottom*) specimen R1S1T1 in stable postbuckled state after quasi-static loading.

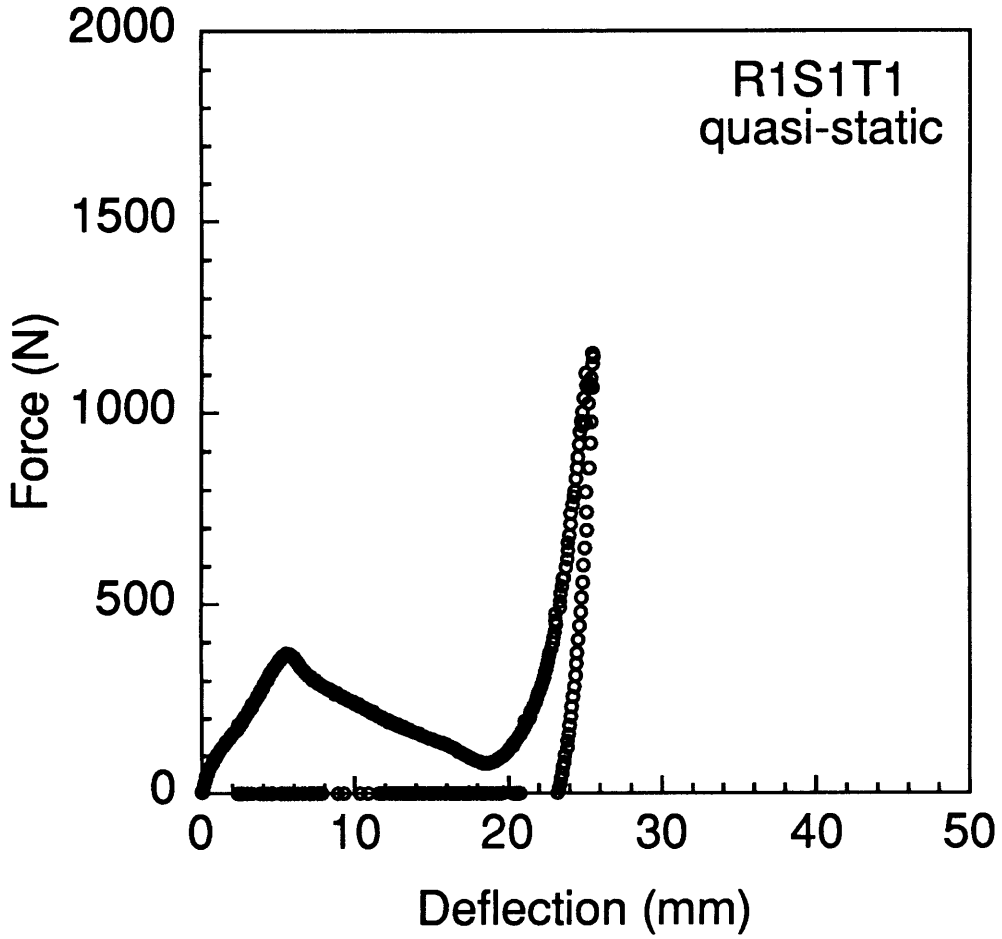

Figure 5.6 Force-deflection response for quasi-static loading and unloading of specimen R1S1T1.

need to distinguish on which equilibrium path the peak force occurred. Considering Figure 5.2 again, it is clear that from the start of the loading until point C is reached, the peak force is the critical snapping load. After the instability region and past the equivalent critical snapping load on the second equilibrium path, the peak force again increases. For specimens such as R1S1T1 that have increased loading past point C on the second equilibrium path, the peak load will be cited with "instability" noted. Thus, if the peak force occurs on the secondary equilibrium path, the notation for the peak force will include the word "instability". The overall peak force for the quasi-static testing of specimen R1S1T1 in Figure 5.6 is therefore 1160 N (instability) whereas the overall peak force for the response of specimen R1S2T1, shown in Figure 5.7, is 360 N. The latter overall peak force is also the critical snapping load because the shell response moved into the instability region.

The distinction between peak force and peak force (instability) warrants some examples and further discussion because of the large number of convex specimens that display the instability (10 of 22 specimens tested quasi-statically). The manner in which the instability is treated when citing overall peak force has already been defined. However, it is clear from the data (and intuition) that the instability will also affect other response parameters, such as peak deflection. For all response parameters, the parameter will include "instability" if the response progressed past point C in Figure 5.2. Thus, the peak deflection for specimen R1S1T1 (see Figure 5.6) is 26 mm (instability) and the peak deflection for specimen R1S2T1 (see Figure 5.7) is 51 mm. It is clear that the instability region will affect the contact time and peak deflection for specimens such as R1S2T1 in Figure 5.7. All parameters relating to loading response, including damage metrics, will

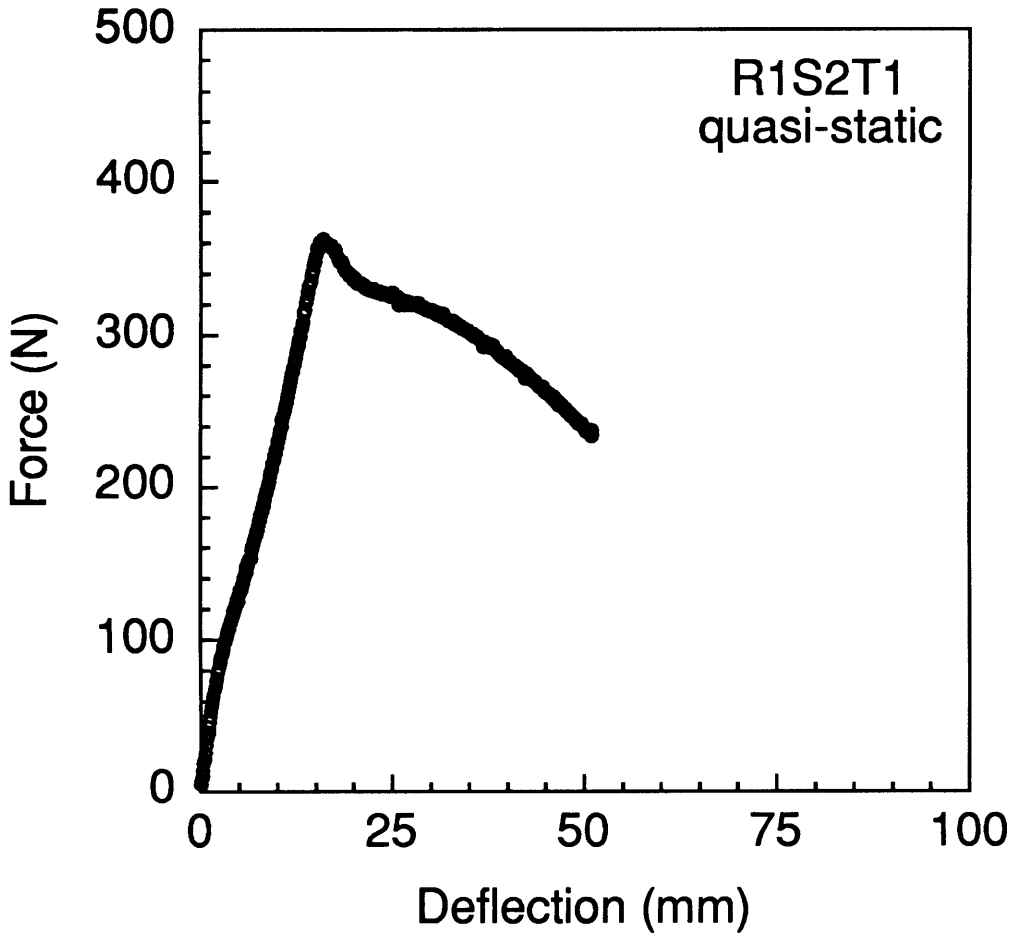

Figure 5.7 Force-deflection response for quasi-static loading of specimen R1S2T1.

maintain the same (instability) convention to indicate loading past point C in Figure 5.2. Plates and concave shells, as well as some convex shells, do not evidence the instability behavior described thus far and the peak force is simply cited. For example, the peak force for specimen R1S1T2 (concave) in Figure 5.8 tested quasi-statically is simply 1990 N.

It is clear that the instability plays an important role in the response of the convex shells tested quasi-statically. It remains to be determined what role, if any, the instability plays in the impact response of the convex shells that were tested. Force-time histories were taken to characterize the response of impacted specimens, not force-deflection histories. The first direct observation of the instability was that several shells maintained stable postbuckled states after impact. Specimen type R2S1T1 impacted at 2.9 m/s and 3.8 m/s and specimen type R3S1T1 impacted at 2.9 m/s and 4.0 m/s exhibited stable postbuckled states. A photograph of specimen type R3S1T1 after impact at 2.9 m/s is presented in Figure 5.9 to illustrate this stable postbuckling for impacted convex shells. This photograph is similar to the photograph in Figure 5.5 (quasi-static loading) indicating a similar phenomenon in the impact response for these convex specimens. The four postbuckled specimens snapped back to the normal convex shape when the in-plane restraint was relaxed as the specimens were being removed from the test fixture. This would indicate that the in-plane restraint is required to maintain the postbuckled configuration. Further evidence of the instability behavior is observed in the characteristics of many convex shell force-time histories. These characteristics are not observed in the force-time histories for any of the plates and concave shells.

The force-time histories for a number of convex shells are typical of those seen in plate and concave shell specimens and are oftentimes referred

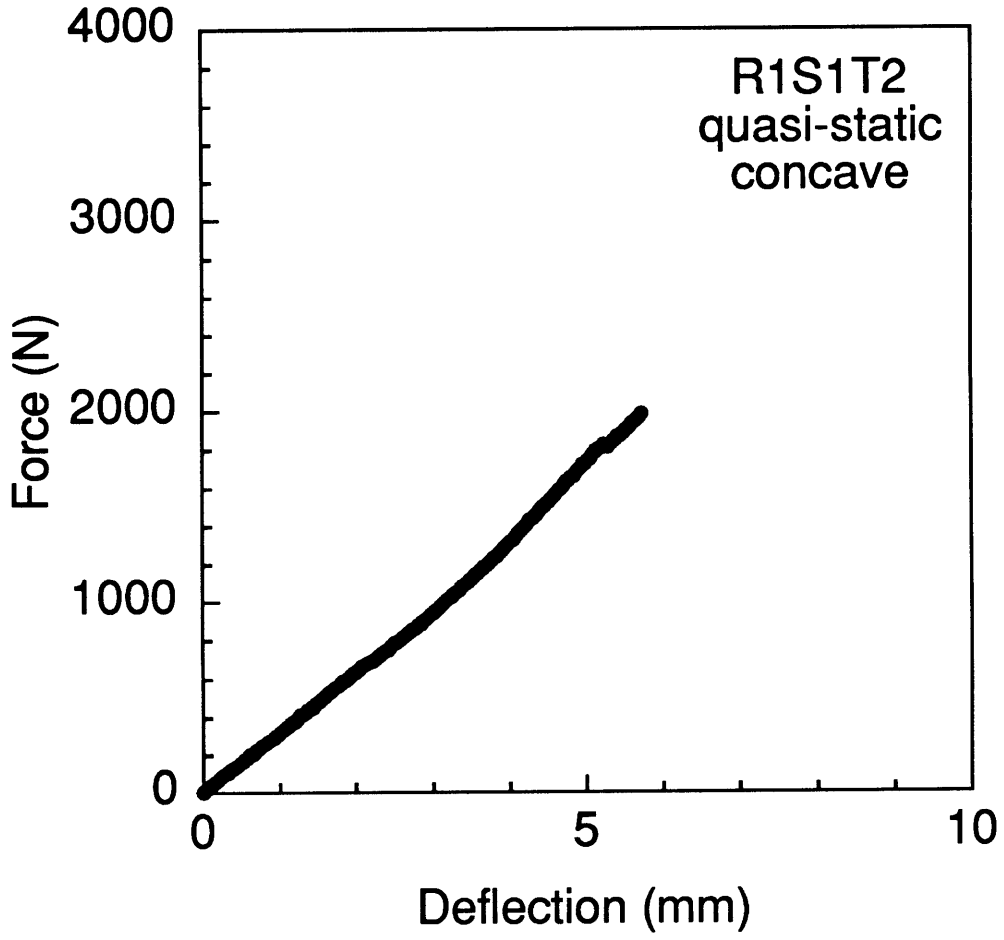

Figure 5.8 Force-deflection response for quasi-static loading of specimen R1S1T2 (concave).

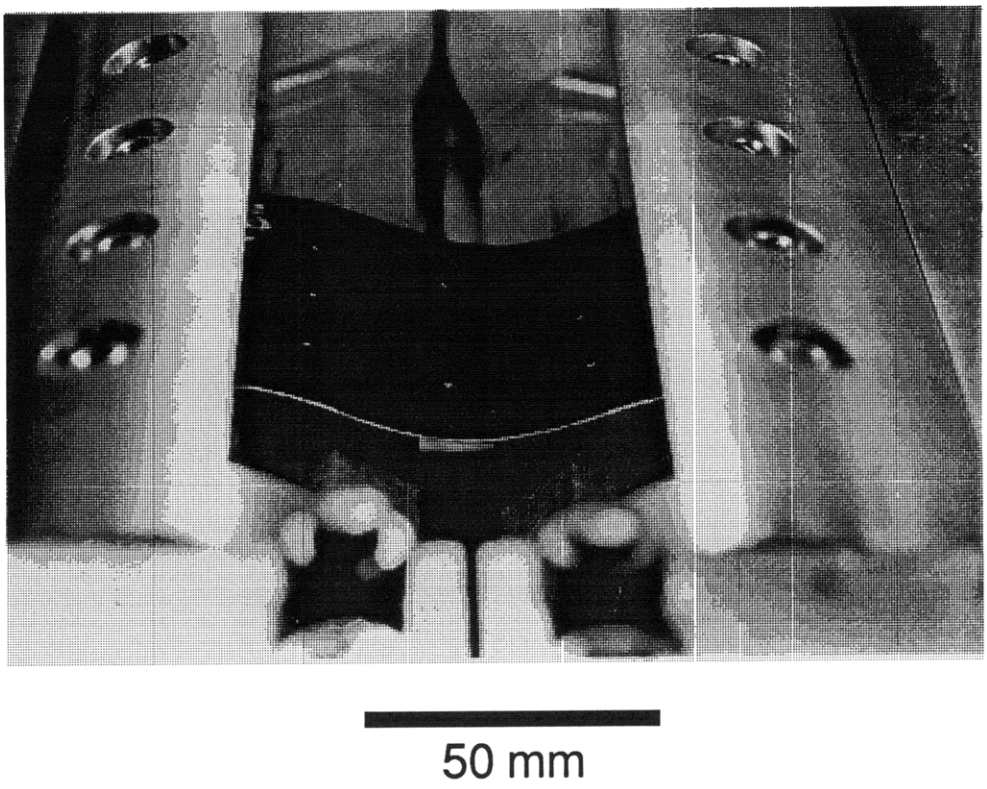

Figure 5.9 Photograph of convex shell specimen R3S1T1 impacted at 2.9 m/s showing resulting stable postbuckled state.

to as a half-sinusoid type response. An example of this is the force-time history measured during testing for convex specimen R1S1T1 impacted at 1.0 m/s as presented in Figure 5.10. The shape of the primary response is typical of force-time histories observed for plate specimens in previous investigations, e.g. [15]. However, the response shapes for the same shell configuration impacted at higher velocities are observed to be quite different as shown in the force-time histories for the 2.1 m/s and 3.0 m/s impacts of specimen type R1S1T1 presented in Figures 5.11 and 5.12. In Figure 5.11, a region in the middle of the impact event shows a drop in the load from a local maximum of 340 N after approximately 3 ms. The load drops until about 12 ms where it reaches a local minimum of 120 N and then increases to approximately 200 N at 18 ms. There is an approximate symmetry in the response around 18 ms. The load again drops after 18 ms, then increases to another local maximum of 300 N, approximately the peak force observed in the first half of the response (340 N). The load decreases after this point to zero where the contact ends at approximately 39 ms. The overall peak force is observed to occur before the initial drop in load. The response shape in Figure 5.11 is clearly much different than the 'half-sinusoid' response such as the one found in Figure 5.10.

An even further departure from the response shown in Figure 5.10 is observed in the force-time history for this specimen type impacted at 3.0 m/s as shown in Figure 5.12. The overall contact time has decreased, and the peak force is now observed to occur after the first drop in load. By comparison to Figure 5.11, the small increase in load after the first load-drop has given way to a much larger increase in Figure 5.12. The R1S1T1 specimen types impacted at 1.0 m/s and 2.1 m/s were not damaged, whereas the impact at 3.0 m/s did cause damage, as evidenced by the x-ray

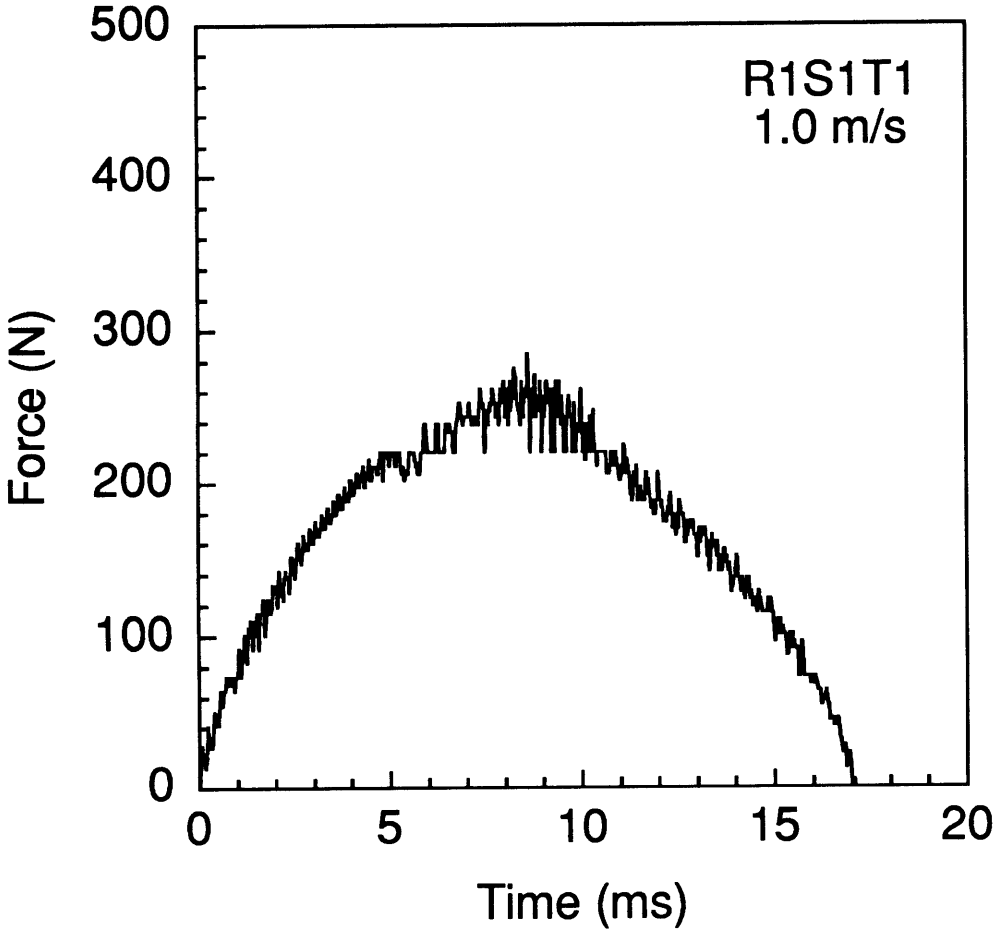

Figure 5.10 Force-time response of specimen R1S1T1 impacted at 1.0 m/s.

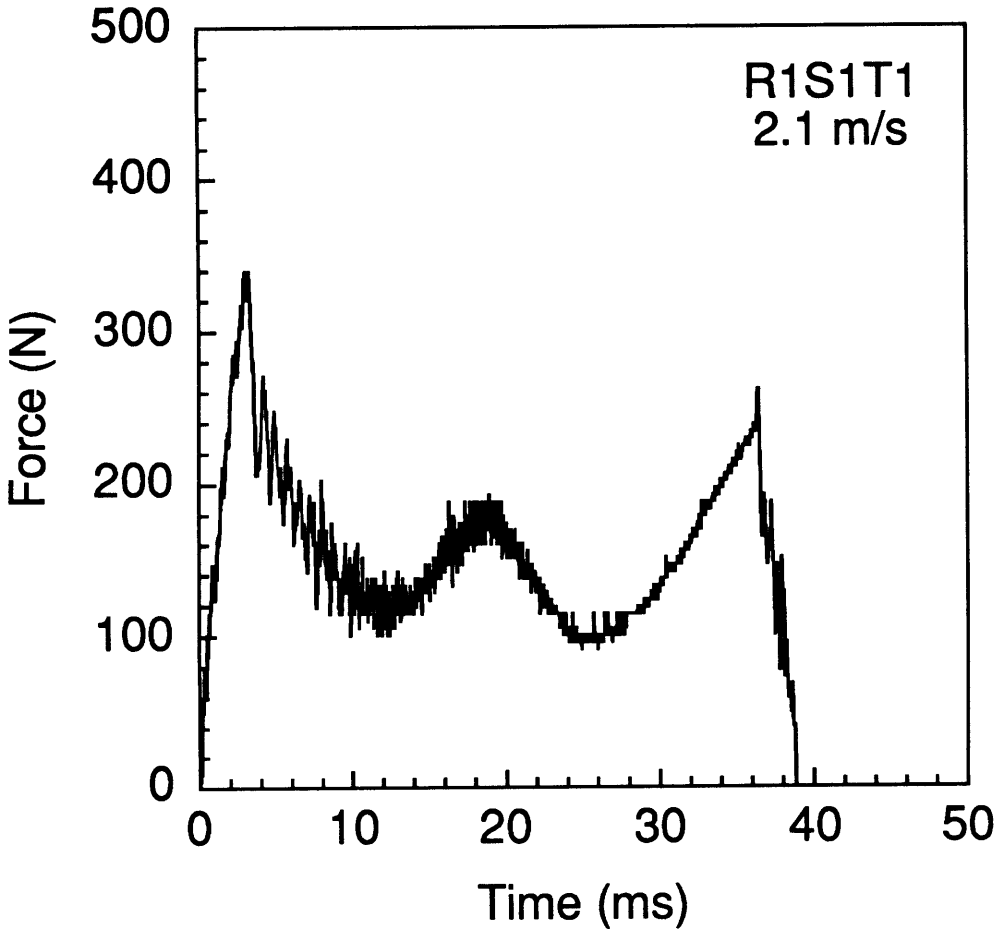

Figure 5.11 Force-time response of specimen R1S1T1 impacted at 2.1 m/s.

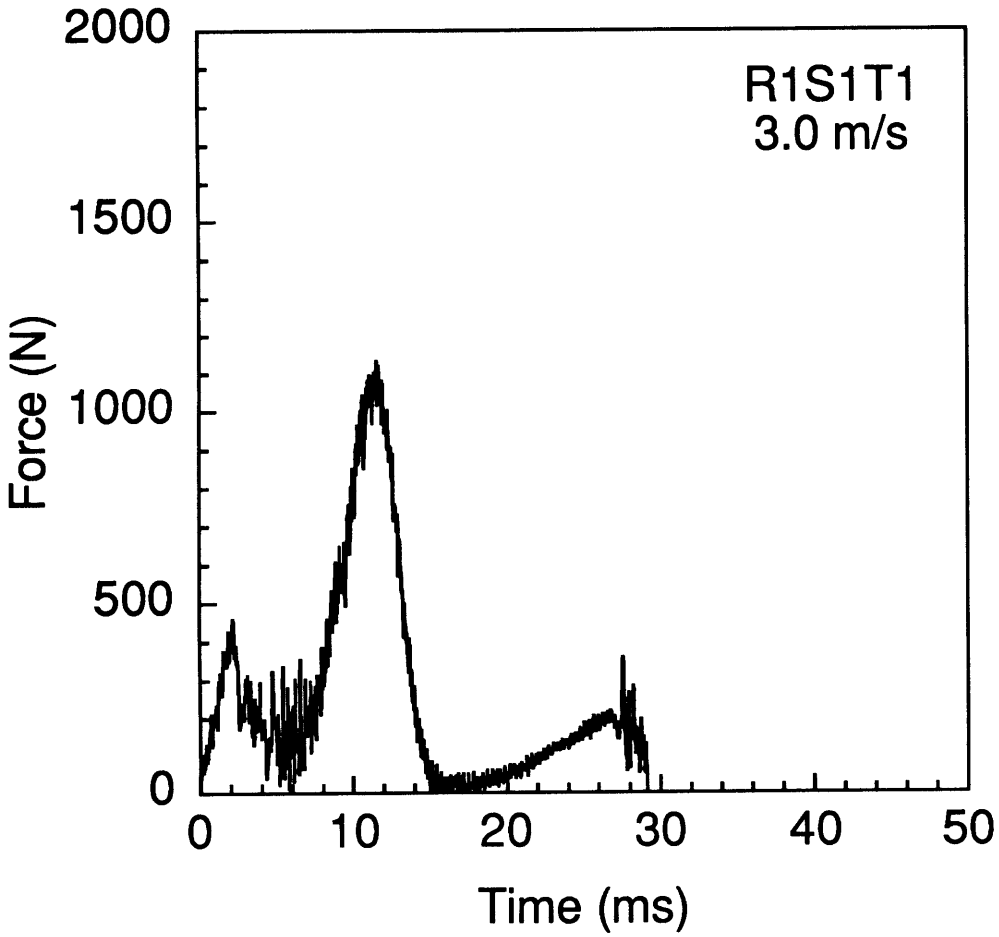

Figure 5.12 Force-time response of specimen R1S1T1 impacted at 3.0 m/s.

photography method. The shape of the force-time histories in Figures 5.11 and 5.12 can be interpreted as evidence of the same instability phenomenon observed in quasi-static tests of convex shells.

For better evidence of the instability event in an impact test, force-deflection results are needed. To obtain this information, force-time histories measured during testing can be twice-integrated to give deflection information at the center of the impacted specimen. By assuming that the impacting tup displaces the same distance as the specimen (it is in contact with the specimen) during the impact, the displacement of the impactor is equal to the displacement of the shell. This assumption is not valid after penetration occurs or if contact is lost during the impact. The shell and impactor displacement would differ if the indentation is significant relative to the displacement of the shell. This effect is shown to be negligible by considering indentation data taken from quasi-static tests where the largest effect from indentation is found to be less than 1.5% of the deflection. Thus, the acceleration-time history of the tup is found simply by dividing the measured force by the mass of the impacting assembly (1.60 kg) in the force-time history. The acceleration-time history is then integrated twice. The initial velocity is assumed to be the velocity measured using the light-gate apparatus described in chapter 4 with the initial displacement taken as zero. The double-integration takes the form:

$$w(t) = \int_0^t \left(\int_0^t a(t)dt + v_o \right) dt + x_o \tag{5.1}$$

where w(t) is the deflection at any time t, a(t) is the acceleration at t, v_0 is the initial velocity, and x_0 is the initial deflection of the specimen, taken to be zero. Again, a(t) is simply the measured force-time history divided by the

mass of the impacting assembly. The integrations are performed using the trapezoidal rule where the time-step is equal to the data sampling interval of 0.02 ms.

Using this integration procedure, the force-time histories in Figures 5.10 to 5.12 are integrated to determine the displacement of the shell center at any time t. The displacement-time history for convex shell R1S1T1 impacted at 1.0 m/s is shown in Figure 5.13. The curve follows the same trend as the force-time history in Figure 5.10, with the maximum deflection occurring in the middle of the contact where the force is maximum. This behavior is typical of all plate and concave specimens tested, which will be shown later. Figure 5.14 contains the deflection-time history for the specimen impacted at 2.1 m/s found in Figure 5.11. The shape of the displacement-time history is the same as the one found for the impact at 1.0 m/s even though the force-time history is clearly very different than the response in Figure 5.10. The response for specimen type R1S1T1 impacted at 3.0 m/s gives a deflection-time history, shown in Figure 5.15, which has nearly the same shape as the two previous cases although the force-time history is markedly different. The deflection-time history for this specimen (see Figure 5.15) is not quite symmetric with respect to the time of peak deflection, and there appears to be a discontinuity in the slope near the peak deflection. However, the shape of the three deflection-time histories are approximately the same with the peak deflection occurring approximately midway through the contact in Figures 5.13 through 5.15. It is observed that the instability is not as clearly evident, if at all, in the derived deflection-time histories as it is in the force-time histories for any of the convex shell specimens tested.

The deflection-time and force-time histories can be cross-plotted to give

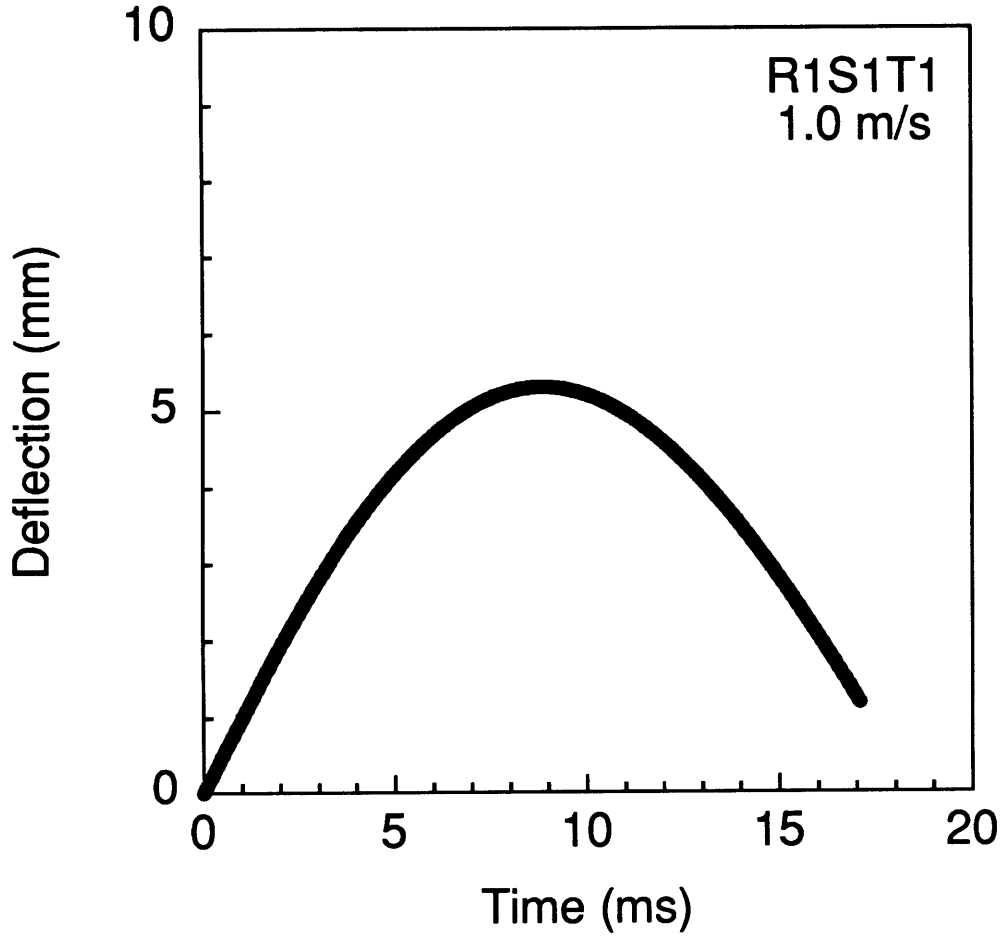

Figure 5.13 Deflection-time response of specimen R1S1T1 impacted at 1.0 m/s.

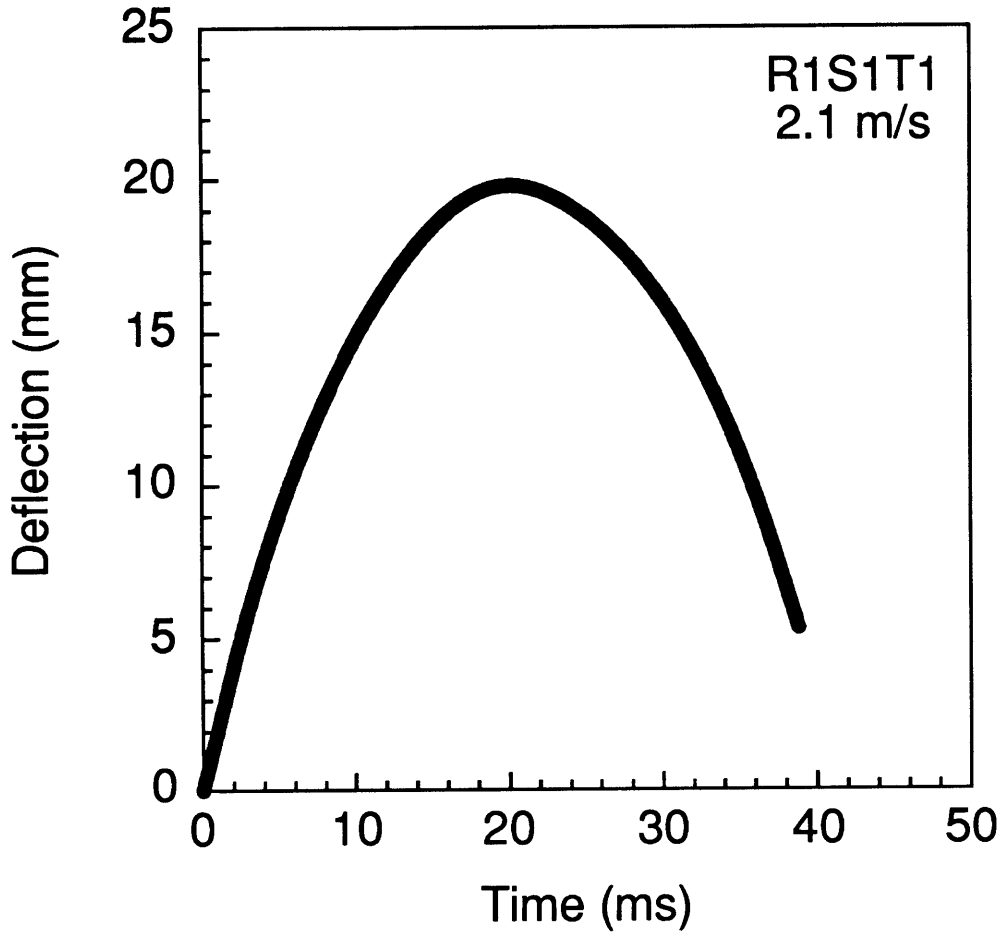

Figure 5.14 Deflection-time response of specimen R1S1T1 impacted at 2.1 m/s.

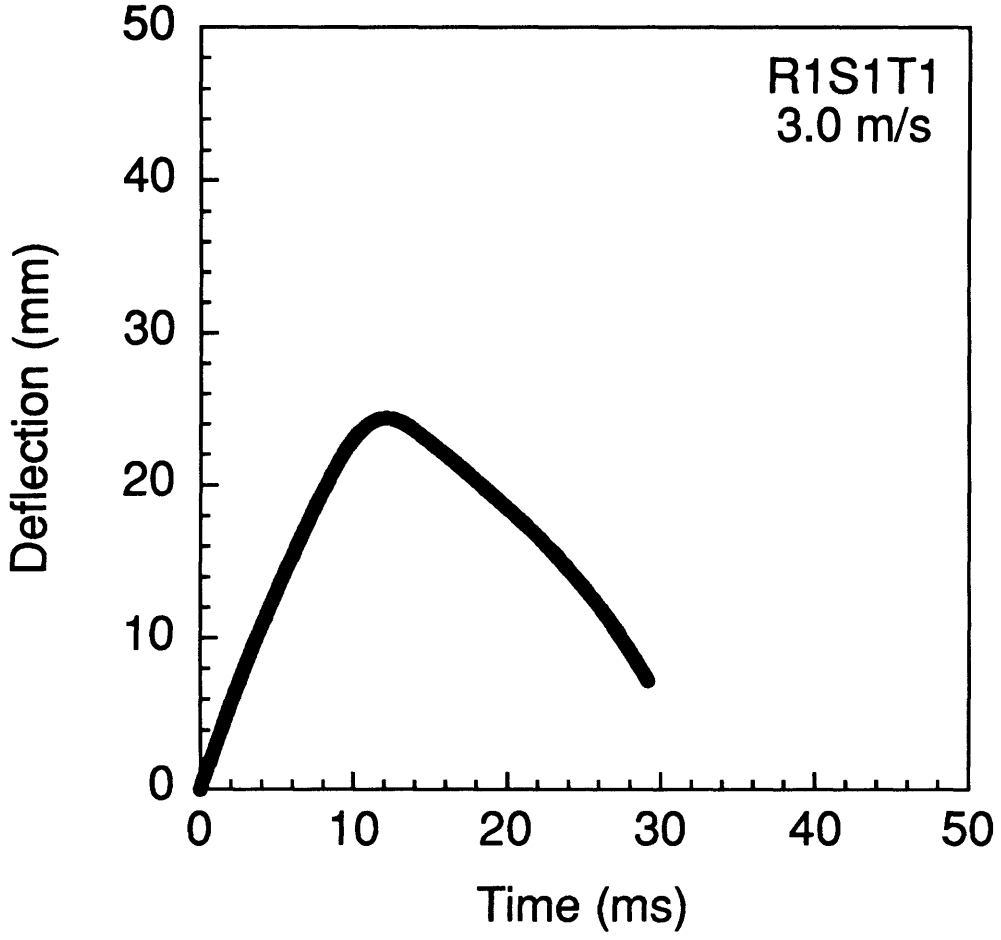

Figure 5.15 Deflection-time response of specimen R1S1T1 impacted at 3.0 m/s.

force-deflection histories for the impact tests. The force-deflection history for specimen type R1S1T1 impacted at 1.0 m/s is presented in Figure 5.16. None of the characteristics of instability are observed in this load-deflection response. This is expected since no load-drop is observed in the force-time history for this specimen in Figure 5.10. However, the force-deflection histories for the same specimen type impacted at 2.1 m/s and 3.0 m/s, presented in Figures 5.17 and 5.18, do exhibit instability characteristics.

The response in Figure 5.17 indicates that this specimen moved into the instability region but did not load above the critical snapping load along the second equilibrium path. At the higher impact velocity of 3.0 m/s, the response for this specimen type, shown in Figure 5.18, indicates that the response moved through the instability region and loaded past the magnitude of the critical snapping load along the second equilibrium path. These plots indicate that the impact response of many of the convex shells contain the same instability characteristics found in the quasi-static tests. Using the terminology defined previously, the peak forces for specimen type R1S1T1 impacted at 1.0 m/s and 2.1 m/s are, respectively, 290 N and 340 N. The peak force for this specimen type impacted at 3.0 m/s is 1130 N (instability). The contact times for specimen type R1S1T1 impacted at 1.0 m/s, 2.1 m/s, and 3.0 m/s from Figures 5.10 through 5.12 are, respectively, 17 ms, 39 ms, and 29 ms (instability).

The force-deflection response in Figures 5.17 and 5.18 can be used, along with the definitions based on snap-buckling given previously, to interpret the force-time histories for these specimens. The load at which the response first drops off corresponds to the critical snapping load, and the subsequent decrease in force with time is the shell moving through the instability region. Further, the increase in force after the first load-drop is

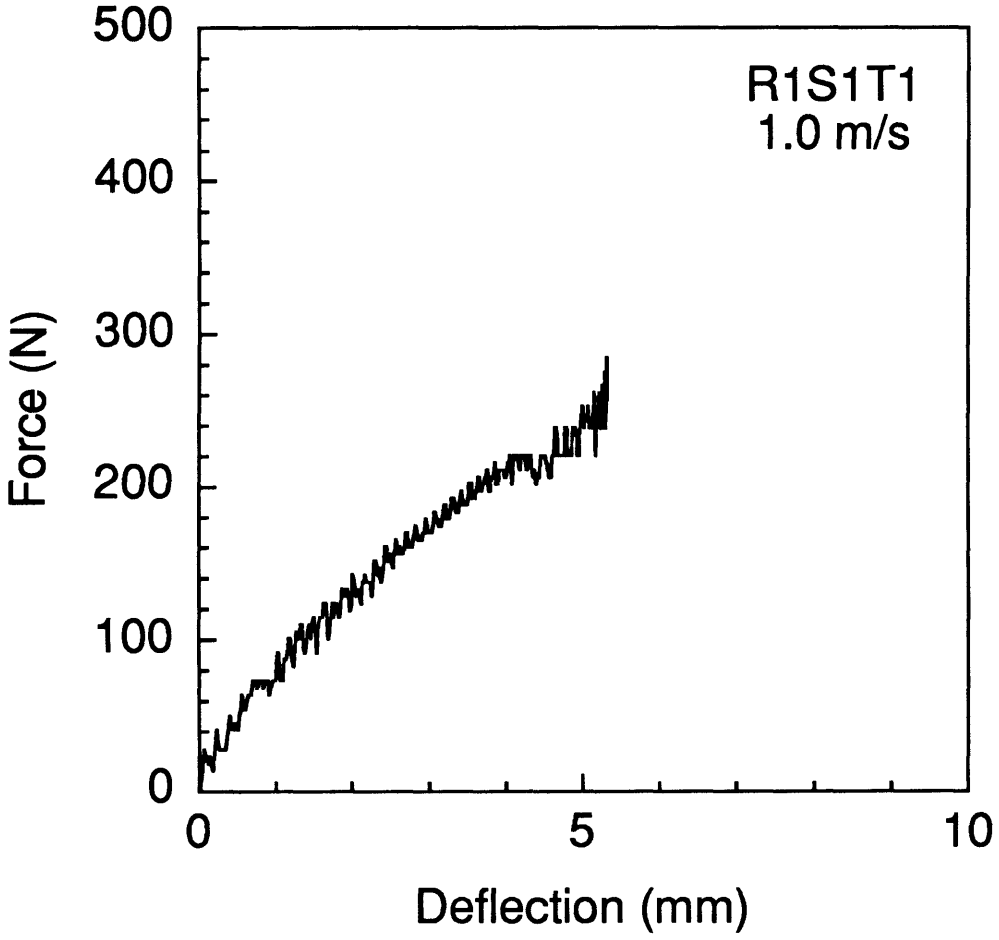

Figure 5.16 Force-deflection response of specimen R1S1T1 impacted at 1.0 m/s plotted up to peak deflection.

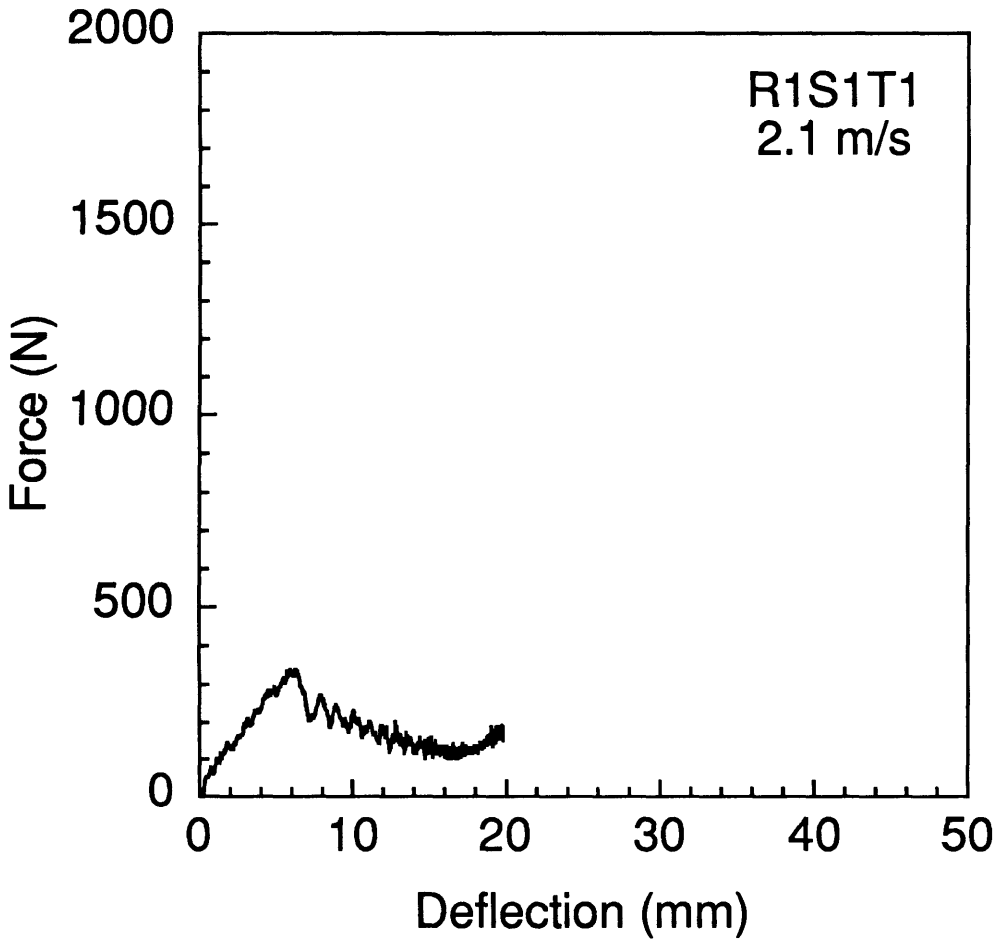

Figure 5.17 Force-deflection response of specimen R1S1T1 impacted at 2.1 m/s plotted up to peak deflection.

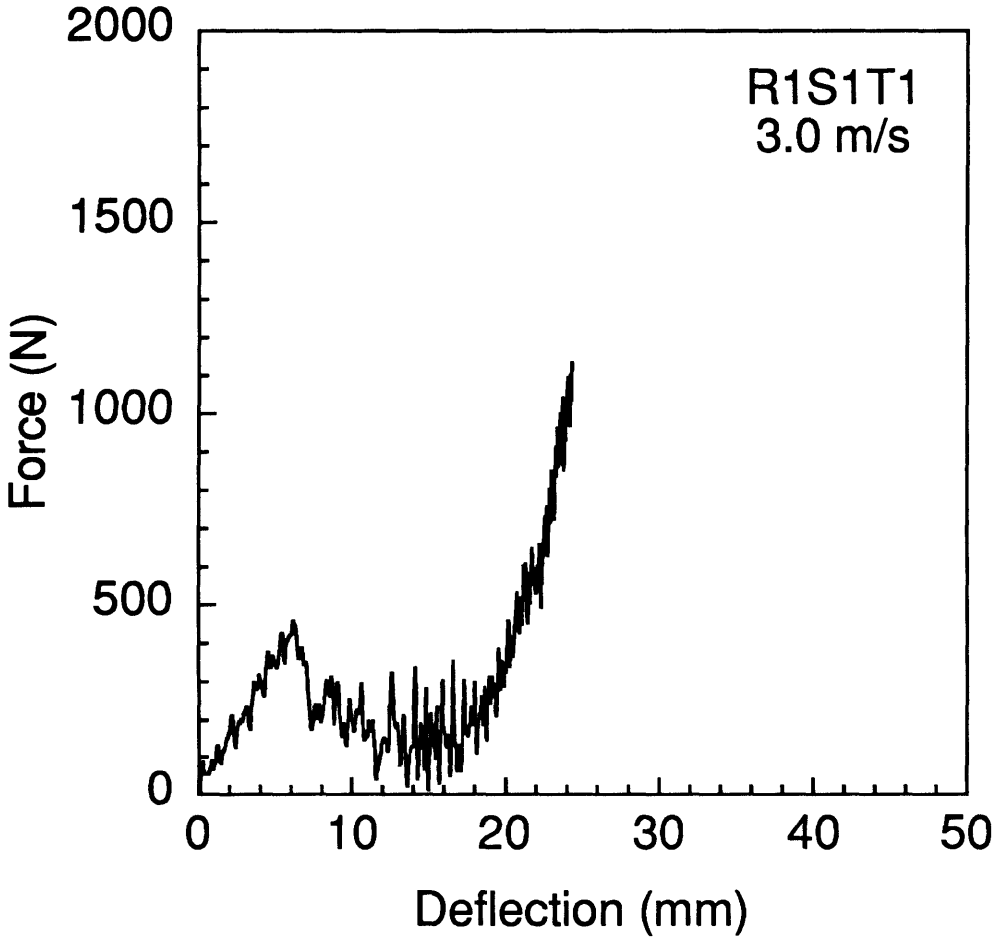

Figure 5.18 Force-deflection response of specimen R1S1T1 impacted at 3.0 m/s plotted up to peak deflection.

the shell loading along the second equilibrium path. The symmetry noted in Figure 5.11 can now be regarded as unloading along the same path as was observed for loading. Other convex shell specimens that exhibit an instability in the quasi-static response also evidence the instability in the impact force-time and force-deflection histories. It should be noted that the integrated force-deflection plots for impacted specimens do not indicate an instability unless a load-drop is present in the force-time history. Thus, the existence of an instability, and information about the instability, can be inferred from specimen force-time histories.

It is expected that the characteristics of the instability for impact and quasi-static testing of the same specimen type might be quite similar. This is indeed observed to be true. The force-deflection histories for the quasi-static test and the impact test at 3.0 m/s for specimen type R1S1T1 are plotted on the same scale in Figure 5.19 to illustrate this point. The response is nearly identical except for the vibrations superposed on the impact history. Both tests show approximately the same critical snapping load and instability region.

The same terminology defined for quasi-static tests is used to describe the impact response. Peak force and peak force (instability) are distinguished as before as are the other impact parameters. As with quasi-static tests, a large number of convex shells exhibit instability characteristics. For the 68 convex shells impacted and tested quasi-statically, 31 (46%) of the specimens indicate an instability. Shells that display an instability are typically thin (T1 or T2) and shallow. Shallow is a combination of span and radius which gives a small (relative) shell center height. Critical snapping loads associated with impact and quasi-static testing are presented in sections 5.2 and 5.3, respectively.

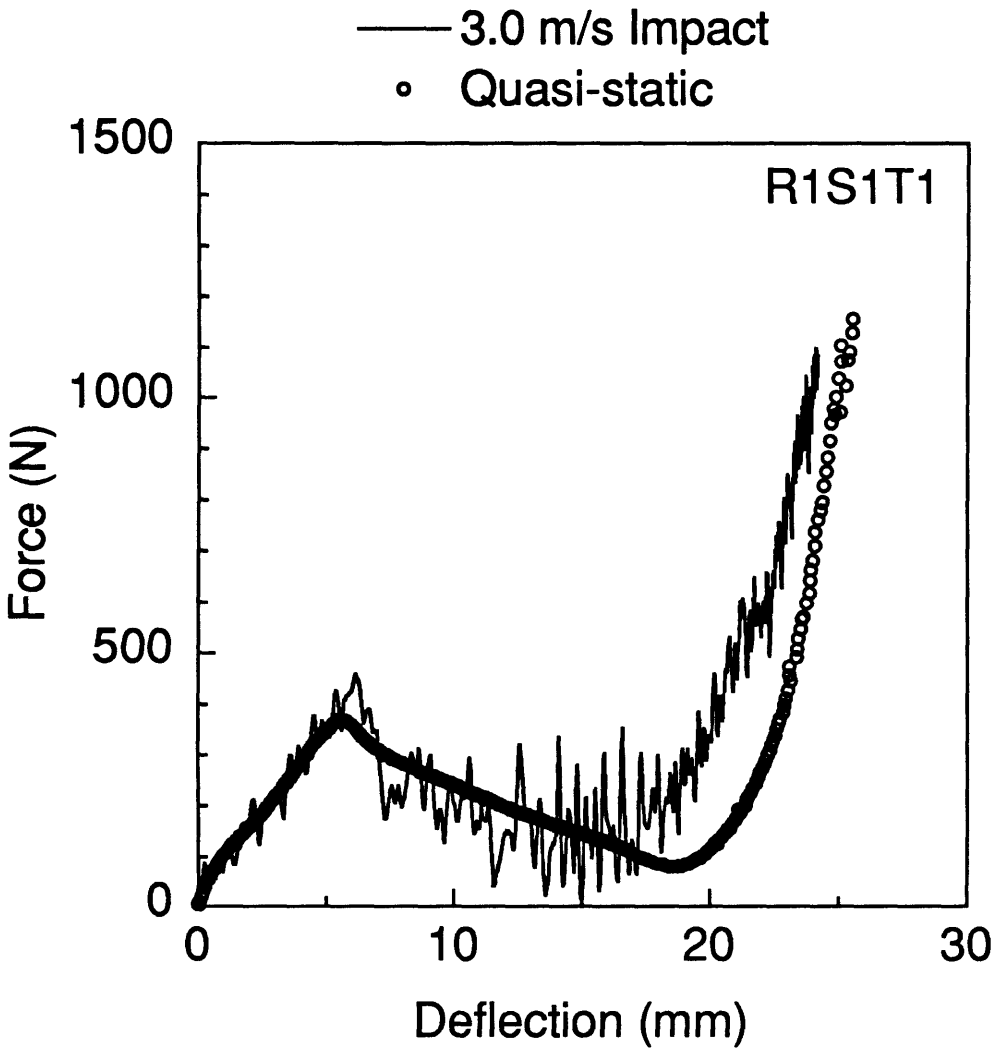

Figure 5.19 Force-deflection response of specimen type R1S1T1 impacted at 3.0 m/s and loaded quasi-statically.

5.2 Impact Testing

Impact force-time histories are presented in this section. Force-deflection and deflection-time information at the center of an impacted specimen can be obtained using the integration scheme outlined in section 5.1. Impact force-deflection information is useful for comparison with quasi-static force-deflection data and is presented for various specimens to characterize the impact response. Damage states evaluated visually and by x-ray photography are presented for specimens impacted at different velocities. Two shells in the test matrix, RPS1T1 and R1S1T1 concave, were not impacted at 4 m/s (nominal) because penetration occurred for these specimen types at 3 m/s (nominal) impact velocity.

5.2.1 Loading Response

Representative force-time histories are presented for the various structural configurations: plates, cylinders, convex, and concave shell sections. Typically, four force-time histories are available covering the range of impact velocities tested. Force-time histories for all specimens tested can be found in Appendix B. X-ray photographs for each impact are also presented in Appendix B. Force-deflection histories for all specimens can be found in Appendix C. The velocity of the impactor just prior to contacting the specimen is observed to be within ±0.1 m/s of the nominal (desired) value for all specimens tested except for three: specimens R2S1T1, R2S1T2, and R2S1T3 which were tested at impact velocities of 3.8 m/s, 3.2 m/s, and 2.8 m/s, respectively. Therefore, nominal values for the impact velocities, i.e. 1 m/s, 2 m/s, 3 m/s, and 4 m/s, are used to compare the impact response of the specimens.

Force-time histories for most specimens typically have a primary response with a higher frequency, lower amplitude, response superposed upon the primary response. This is visible in the force-time history for convex specimen R1S1T1 impacted at 1.0 m/s shown in Figure 5.10. The primary response, nearly a half-sinusoid shape in this case, is evident with a much lower amplitude, higher frequency secondary response superposed on the primary response. The amplitude of the secondary response typically increases very little with velocity (e.g. Figures 5.10 to 5.12 for specimen R1S1T1). This type of secondary response has previously been attributed to the vibration modes of the impacting assembly (rod, force transducer, and tup) [72]. The lowest mode for the impacting assembly was previously measured to be approximately 3.7 kHz [72]. A Fast Fourier Transform (FFT) was performed on the data shown in Figure 5.10 and frequency spikes at approximately 3.4 kHz, 6.4 kHz, 9.2 kHz, 12.4 kHz, and 16.0 kHz are observed. The spacing and magnitude of these frequencies are approximately equal to the frequencies found previously for the impacting assembly. Thus, this low amplitude, high frequency secondary response is attributed to the vibration of the impacting assembly and is not part of the specimen response. Most specimens exhibited the characteristics (frequency and magnitude relative to the primary response) of the secondary response just described. However, a small number of convex shells with large span (S2, S3, and SC) and small thickness (T1) displayed a notably different type of secondary response.

The force-time history for specimen R1S3T1 impacted at 3.1 m/s is presented in Figure 5.20 to illustrate the second type of response noted for convex shells. This specimen was not damaged during testing. It is seen that an approximate half sinusoid still exists for the impact of this specimen but

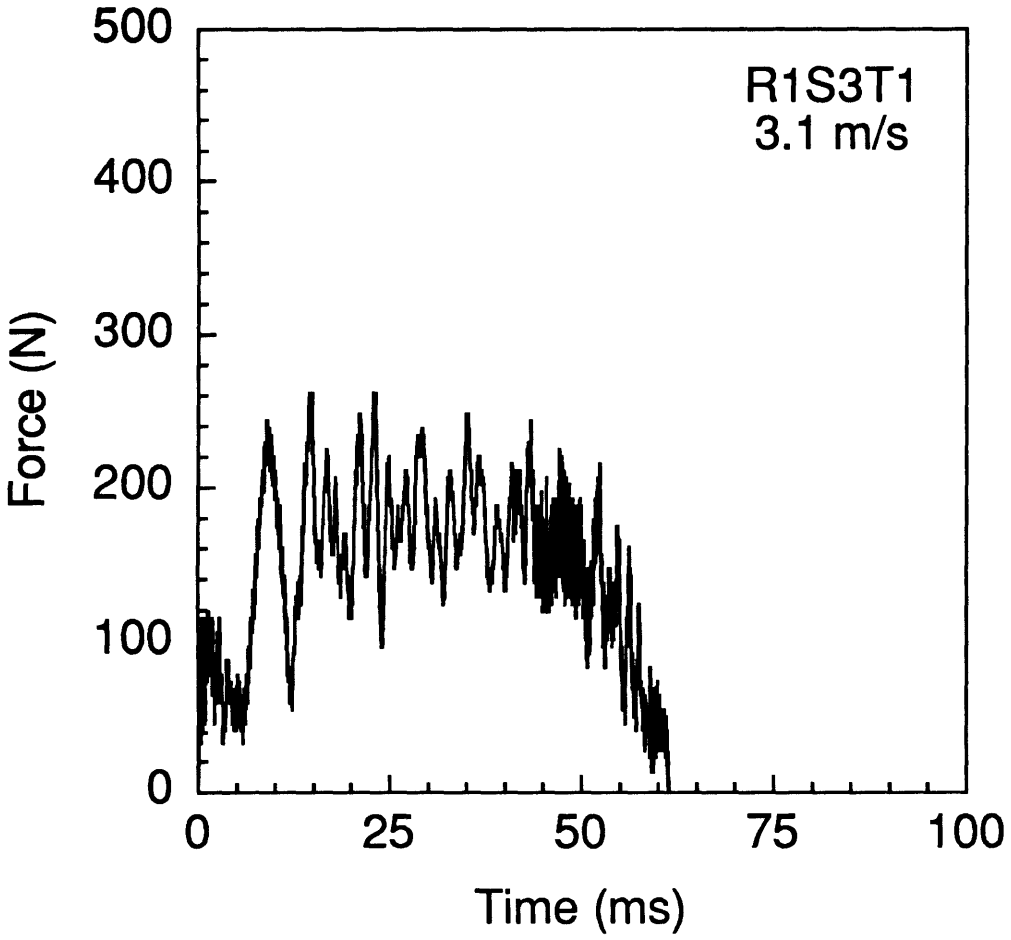

Figure 5.20 Force-time response of specimen R1S3T1 impacted at 3.1 m/s.

there now exists a secondary response of much greater relative magnitude than described previously, e.g. specimen R1S1T1 in Figure 5.10. The frequency of this larger amplitude secondary response is also noted to be much lower than the secondary response cited above and cannot be attributed to the first mode of the impacting assembly. The presence of a third possible response is observed to be superposed on the first two. This third response has the same characteristics as the high frequency secondary response cited in the previous paragraph and is seen better in the partial force-time history given in Figure 5.21 for specimen R1S3T1 (full history is given in Figure 5.20). Thus, a second, lower frequency response has joined the higher frequency response associated with the impacting assembly natural frequency. Specimen types with large span and thickness T1 display this behavior to varying degrees: R1S2T1, R1S3T1, R1SCT1, R2S3T1, and R3S3T1. Specimen types R2S3T2 and R3S3T2 may also display a lower frequency secondary response.

Characteristics of this lower frequency response are most clearly evident (and more exaggerated) in the force-time histories for specimen type R1SCT1 (full cylinder) in Figures 5.22 to 5.25. Full cylinders are a special case of convex shells in that the boundary condition for the full cylinders is floor-supported as explained in chapter 4, i.e. the cylinders are not mounted in the test fixture. These cylinders exhibited no damage in any of the x-ray photographs for any of the impact velocities tested. Compared to other convex shells, the primary response of the cylinders, much like specimen type R1S3T1 (half cylinder), are characterized by low peak forces and long contact durations. It is difficult to identify the half-sinusoid behavior in Figures 5.22 to 5.25 because the response contains a very large amplitude (relative to the primary response), low frequency, secondary response. Force-deflection

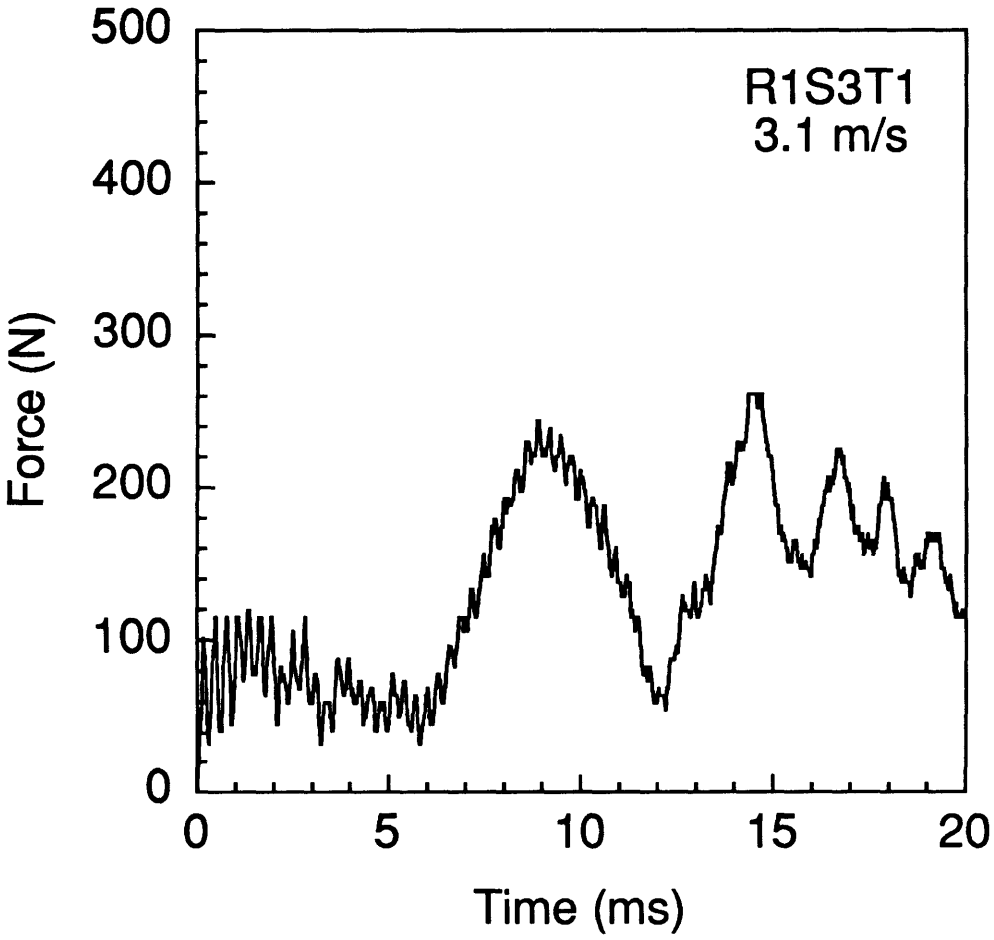

Figure 5.21 Blow-up of Figure 5.20: Force-time response of specimen R1S3T1 impacted at 3.1 m/s.

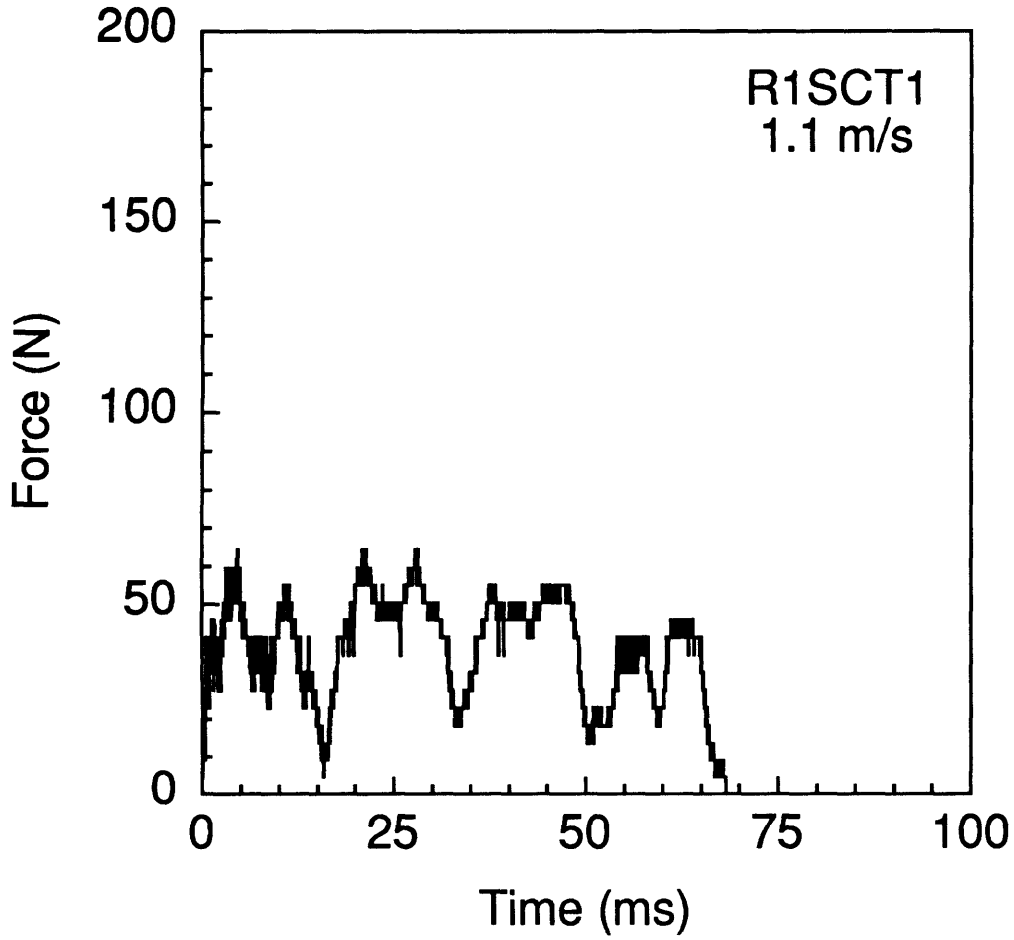

Figure 5.22 Force-time response of specimen R1SCT1 impacted at 1.1 m/s.

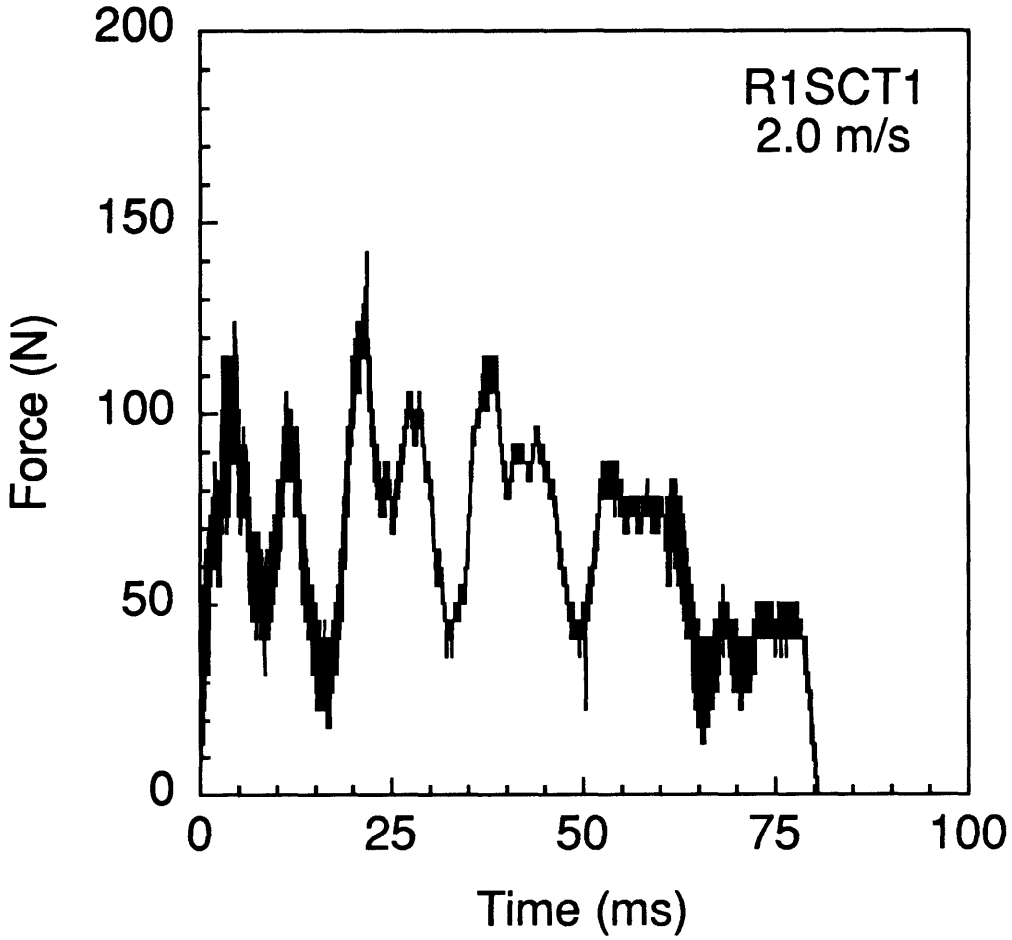

Figure 5.23 Force-time response of specimen R1SCT1 impacted at 2.0 m/s.

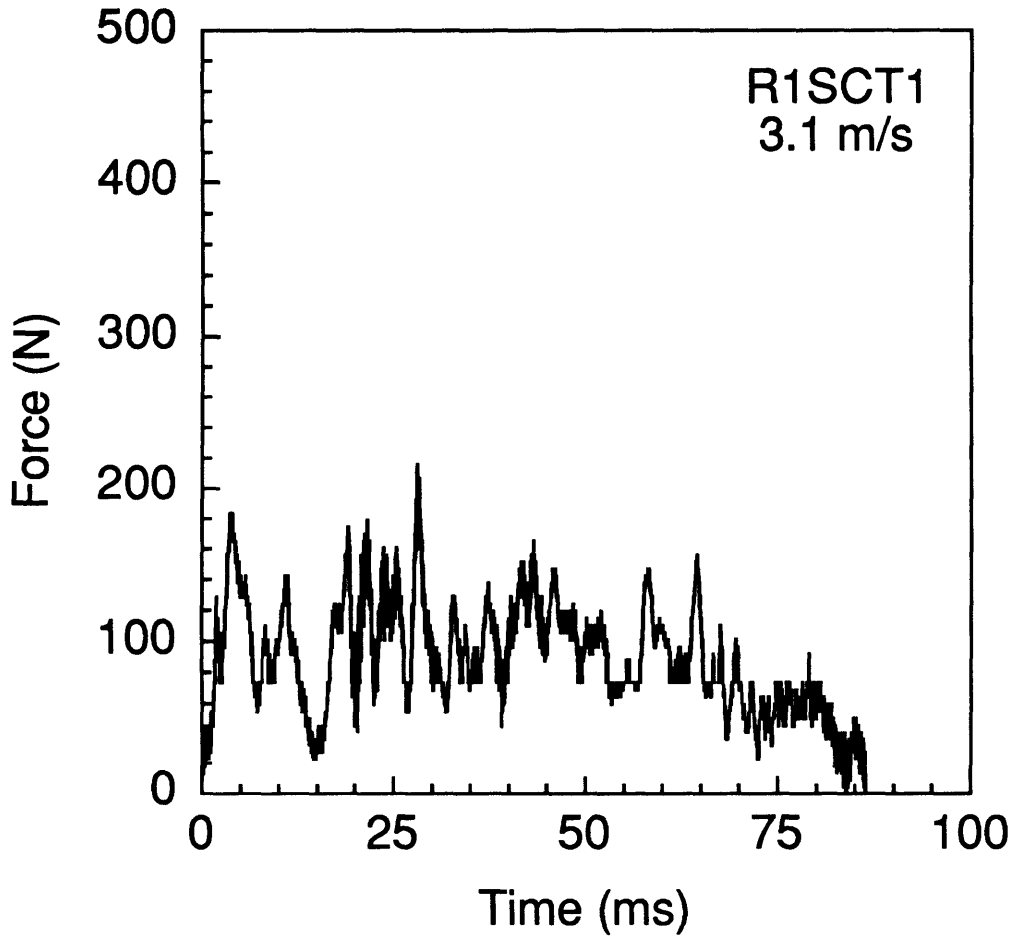

Figure 5.24 Force-time response of specimen R1SCT1 impacted at 3.1 m/s.

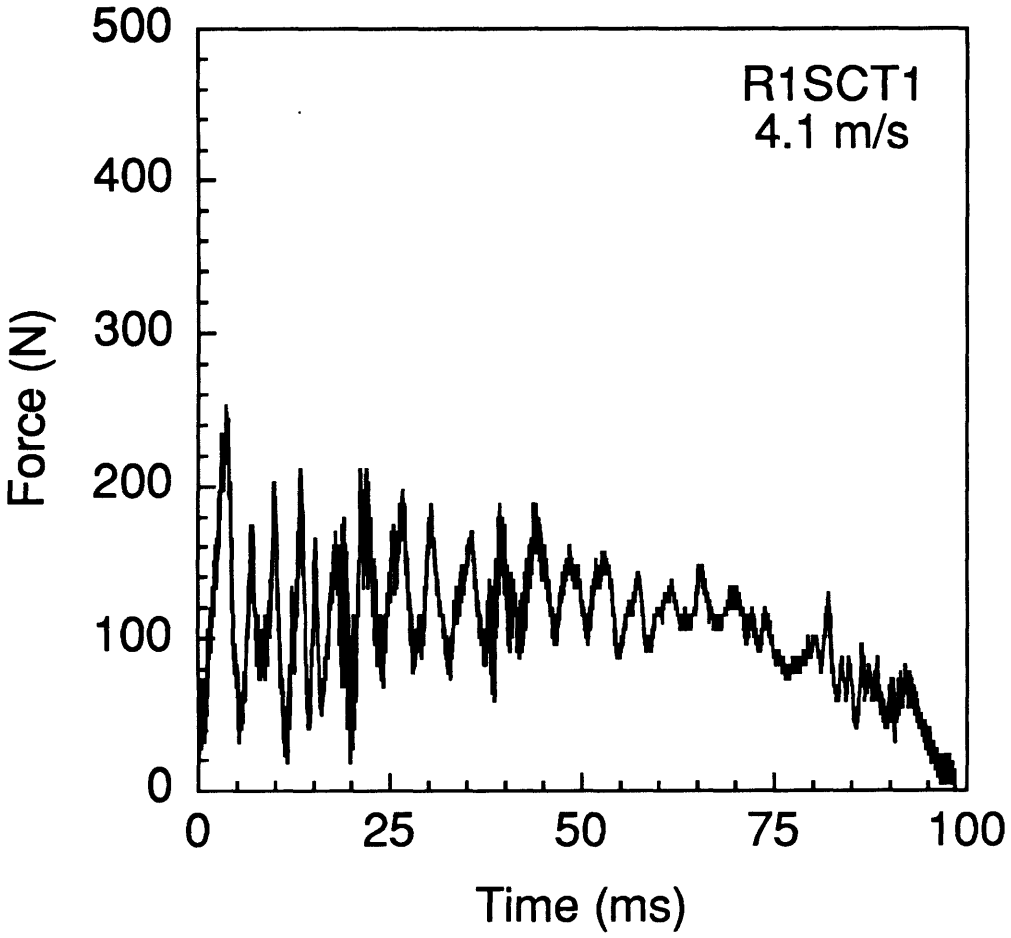

Figure 5.25 Force-time response of specimen R1SCT1 impacted at 4.1 m/s.

histories also exhibit the low frequency nature and shape of the secondary response.

The high frequency response associated with the impacting assembly natural frequencies is observed in all the force-time signatures for impacted specimens. The vibration of the impacting assembly, although present in the force-time histories of impacted specimens, is not a part of the specimen response to impact loading. Thus, further discussion of the response of specimens to impact loading will ignore this high frequency response.

Most convex specimens, as noted in section 5.1, display a primary response with a load drop typical of an instability. The shape of the primary response (instability) displays a progression with velocity for many convex shell specimens. The force-time histories for convex shell specimen type R1S1T1 impacted at 1 m/s, 2 m/s, and 3 m/s (nominal) appear in Figures 5.10 to 5.12 and the response at 4 m/s (nominal) is presented in Figure 5.26 to fully illustrate the progression. As noted in section 5.1, the shape of the primary response of convex shell R1S1T1 impacted at 1.0 m/s in Figure 5.10 is typical of force-time histories observed for plate specimens in this and previous investigations, e.g. [15]. However, the primary response of this shell at higher velocities displays the instability characteristics outlined in section 5.1 (see Figures 5.16 through 5.18). At an impact velocity of 1.0 m/s, the response is restricted to the first equilibrium path. The response at 2.1 m/s indicates that the load has moved through the instability and has started to load along the second equilibrium path. Then, at 3.0 m/s, the load progresses up the second equilibrium path past the magnitude of the critical snapping load to approximately 1130 N (instability). Finally, at an impact velocity of 3.9 m/s, the load increases further up the second equilibrium path up to approximately 1300 N (instability) as shown in Figure 5.26. Again, the peak

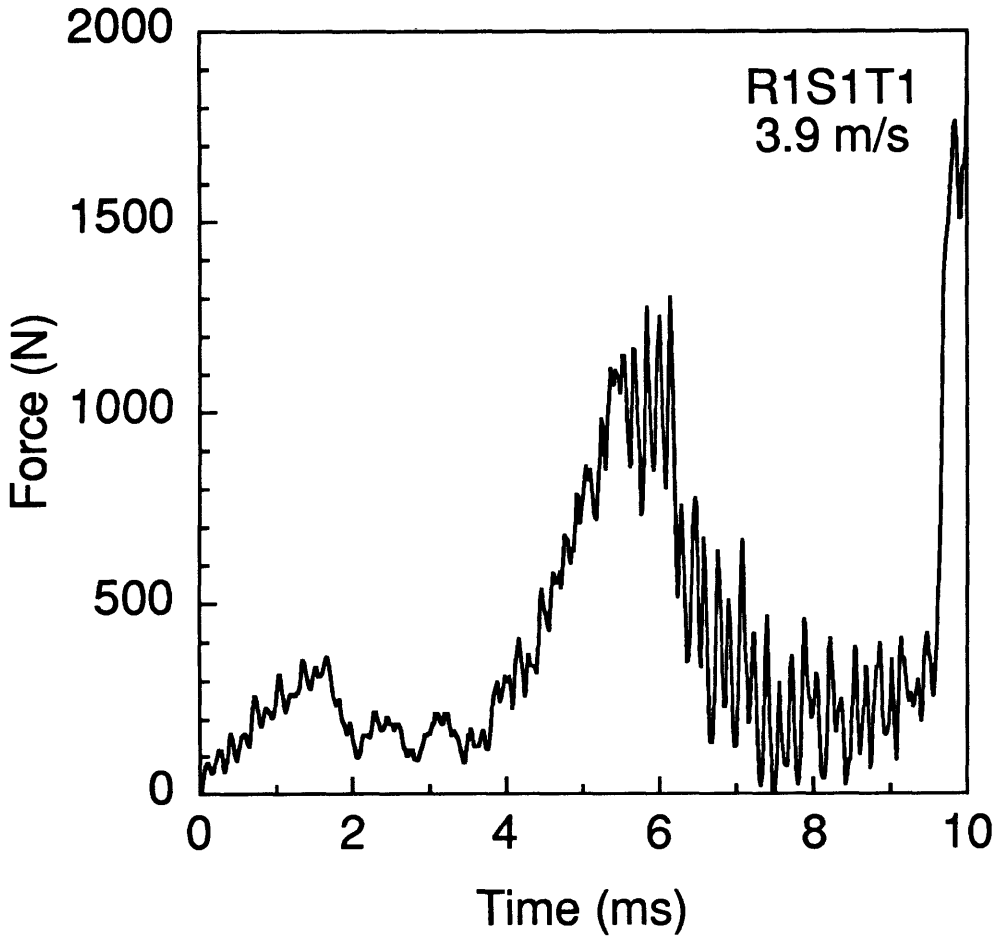

Figure 5.26 Force-time response of specimen R1S1T1 impacted at 3.9 m/s.

force is observed to occur after the first drop in load, at approximately 6 ms, in Figure 5.26. The large force spike in Figure 5.26 near 10 ms is from the impactor hitting the test fixture after penetrating the specimen and should be disregarded. A metallic ringing was noted during the impact test at 3.9 m/s and the test fixture was dented after the impact test indicating that the impactor had contacted the fixture.

The force-deflection history for specimen type R1S1T1 impacted at 3.9 m/s is presented in Figure 5.27 to illustrate the further increase in load (as compared with Figure 5.18) along the second equilibrium path to approximately 1300 N (instability) as a result of the increased impact velocity. Figures 5.27 and 5.18 have nearly the same shape except that in Figure 5.27 the load progresses further up the second equilibrium path. The critical snapping loads in Figures 5.11, 5.12, and 5.26 for specimen type R1S1T1 are observed to be nearly constant (approximately 400 N) with impact velocity. This behavior is also observed for the other four specimen types that display the instability progression behavior: specimen types R1S2T1 (1.9 m/s, 2.9 m/s, 4.0 m/s), R2S1T1 (2.0 m/s, 2.9 m/s, and 3.8 m/s), R2S1T2 (2.1 m/s, 3.2 m/s and 3.9 m/s), and R3S1T1 (1.0 m/s, 1.9 m/s, 2.9 m/s, and 4.0 m/s). It is unclear whether specimen types R1S3T1 (half cylinder) and R1SCT1 (full cylinder) also exhibit the instability progression behavior found for many other convex shells. This is due to the large (relative to the primary response) amplitudes of the secondary response.

As noted in section 5.1, four convex specimens exhibited stable postbuckled states after impact. Loading in the inverted (snapped-through) configuration can violate the in-plane boundary conditions imposed by the test fixture. The test fixture was not designed to restrain convex shells in the inverted configuration. The in-plane condition of the convex shell under

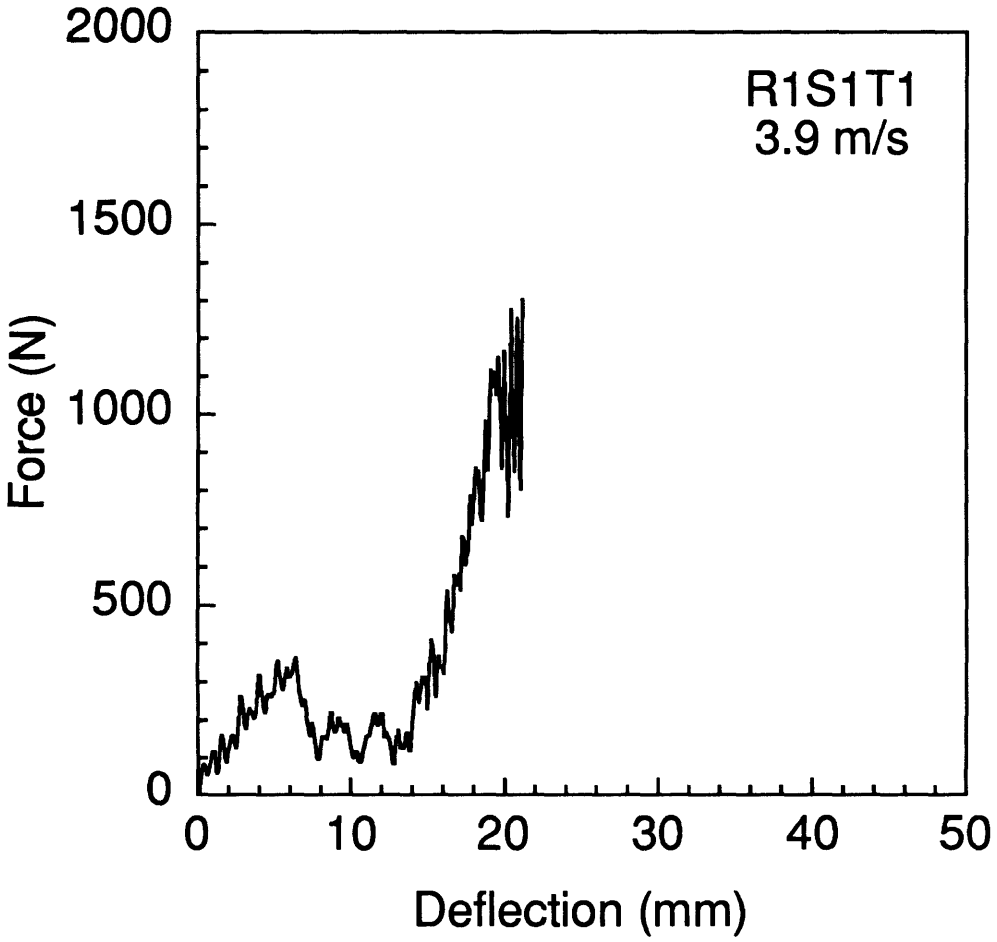

Figure 5.27 Force-deflection response of specimen R1S1T1 impacted at 3.9 m/s plotted up to the penetration force.

transverse loading is one of 'push-in' against the rods of the test fixture along the first equilibrium path. In the inverted configuration, this condition changes to 'pull-out'. Loading in the two configurations is illustrated in Figure 5.4. Although the test fixture is designed to restrain 'pull-out' for loading of plates and concave shells, and 'push-in' for convex shells, it was not designed to accommodate an instantaneous change in the in-plane boundary condition. Thus, the boundary condition for convex shells after the instability region is not guaranteed to be pinned/no in-plane sliding. It was noted that although no specimens fully pulled out of the test fixture, some were found to slip in-plane when loaded in the inverted configuration. Slipping was determined by visually inspecting the shells in the area where the knife-edge (out-of-plane) restraints impinge on the shells. When the shells rotate on the steel knife edges during loading, a visually distinguishable line is marked on the shells at the point of contact. Shells that clearly slip have smeared lines whereas shells that do not appear to have slipped have straight and uniform lines marked along the axial edges of the shell. Only three shells exhibited clear slipping during impact testing.

For specimens that clearly slipped, information from the force-time histories after the instability must be disregarded. Data for slipped specimens after the critical snapping load is always noted in tables and in the text, but is not used in plots of the response parameters. Three of the four shells with stable postbuckled states slipped during impact testing: specimen type R2S1T1 impacted at 2.9 m/s and specimen type R3S1T1 impacted at 2.9 m/s and 4.0 m/s. Large oscillations around the peak force for specimens that slipped are noted in the force-time histories. These oscillations are not evident in the response before the approximate peak load where penetration is noted to occur. These oscillations can be seen in the response in Figure

5.28 for specimen type R2S1T1 impacted at 2.9 m/s. However, the same specimen type impacted at 3.8 m/s did not slip but was penetrated. Oscillations around the peak force are also noted in the force-time history for this specimen as shown in Figure 5.29. Specimen type R3S1T1 impacted at 4.0 m/s exhibits both slipping and penetration. The force-time history for this specimen is given in Figure 5.30 to show these oscillations. Thus, it is observed that a sudden increase in the amplitude of the secondary response (oscillation) in the force-time histories of convex shells seems to indicate either penetration or slipping.

Penetration has previously been characterized, e.g. [15], by increased oscillations in the force-time history. In this work, specimens with penetration damage are noted to always exhibit the visible characteristic of increased oscillations. These large oscillations, relative to the rest of the response, are observed for all specimen configurations around the peak force when penetration damage is observed. A drop in load around the peak force is also observed for specimens that are penetrated. For example, this is observed in Figure 5.26 for specimen R1S1T1 impacted at 3.9 m/s, at approximately 6 ms. If penetration of convex specimens occurred, it occurred on the second equilibrium path, past the magnitude of the critical snapping load.

Out of 46 convex shell specimens impacted, 21 (46%) displayed instability behavior in the force-time histories. In addition to the five convex shell types described earlier, specimens R2S2T1, R2S3T1, R3S1T2, R3S2T1, and R3S3T1 impacted at 3 m/s (nominal) also display some degree of the instability progression behavior. The remaining convex specimens did not display this instability behavior. Convex specimens that do not display the instability behavior are considered to remain on the first equilibrium path, as

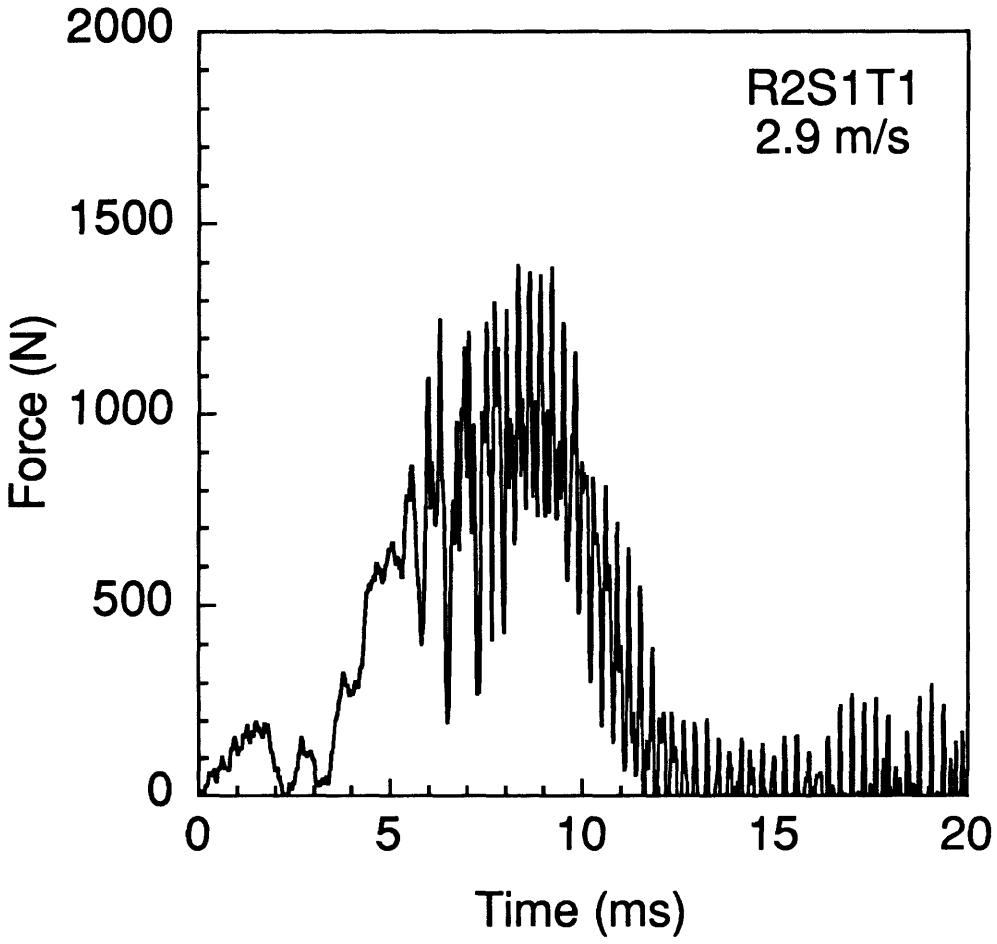

Figure 5.28 Force-time response of specimen R2S1T1 impacted at 2.9 m/s which was found to exhibit stable postbuckling and in-plane slipping.

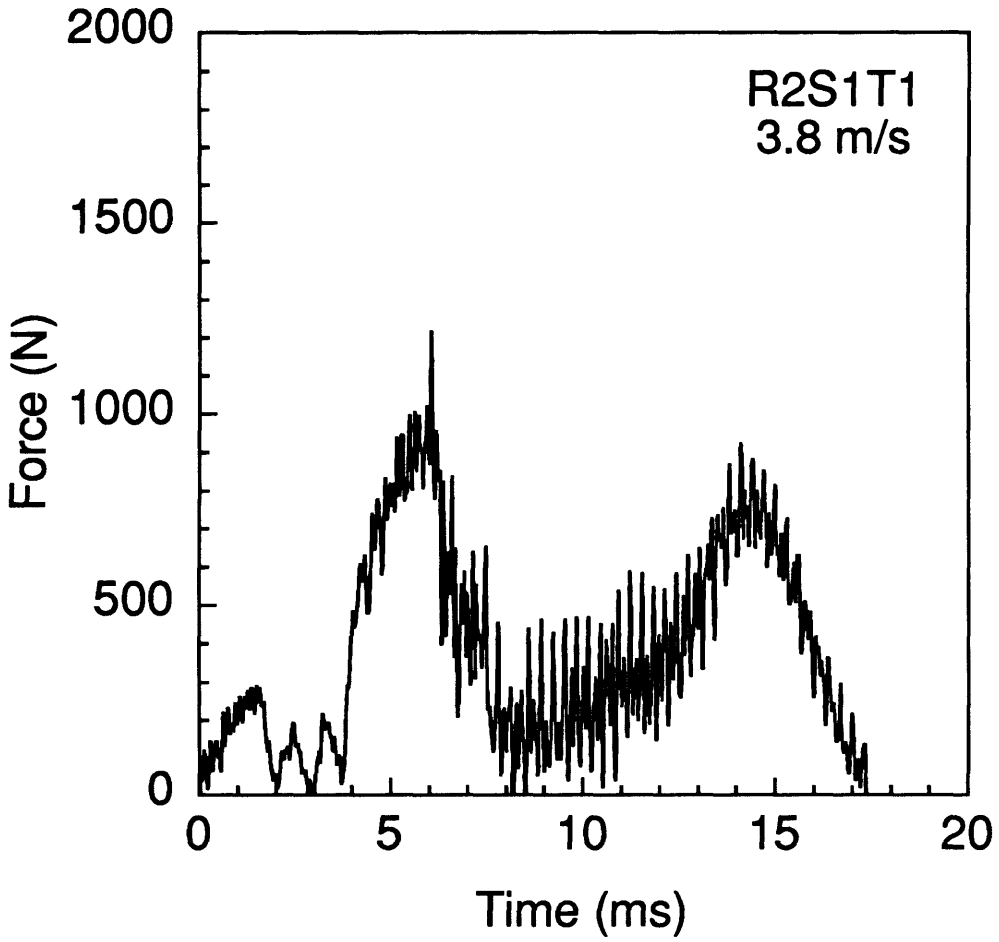

Figure 5.29 Force-time response of specimen R2S1T1 impacted at 3.8 m/s which was found to exhibit stable postbuckling and penetration.

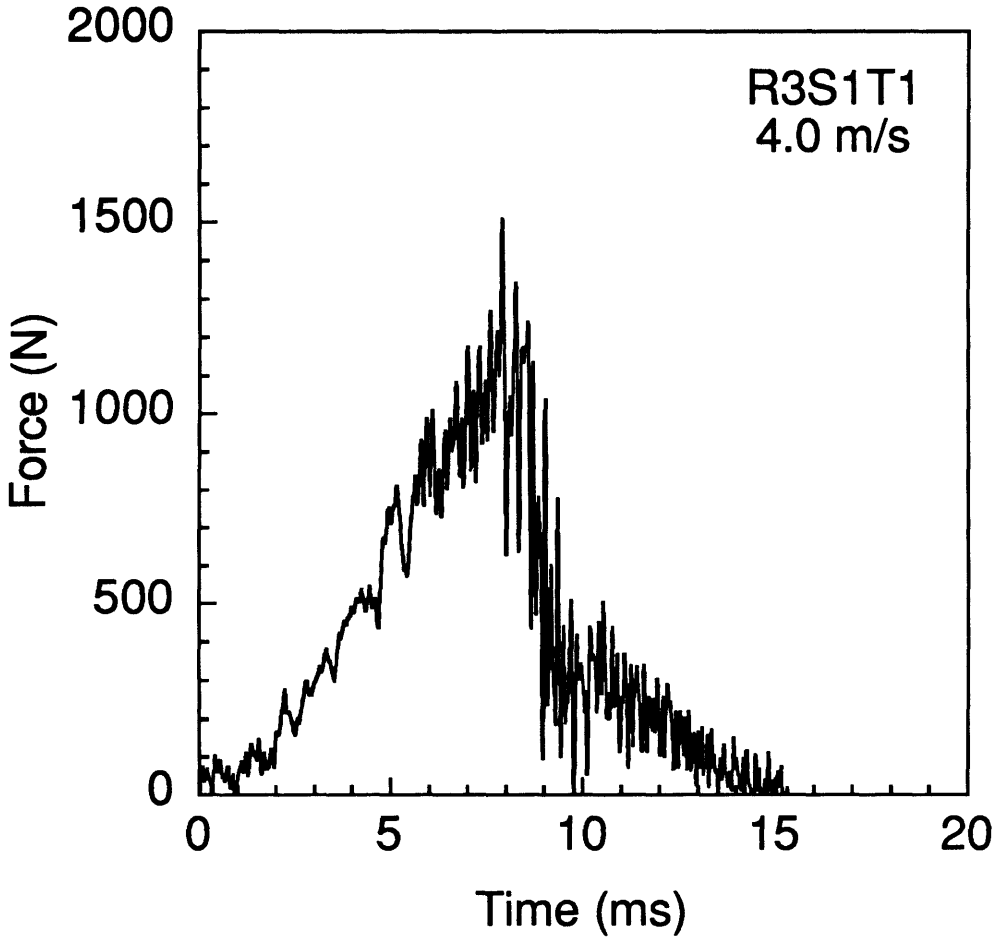

Figure 5.30 Force-time response of specimen R3S1T1 impacted at 4.0 m/s which was found to exhibit stable postbuckling, penetration, and in-plane slipping.

in Figures 5.10 and 5.16. The force-time history for convex specimen R1S1T2 impacted at 2.9 m/s is presented in Figure 5.31 to illustrate the half-sinusoid response behavior observed for many of the convex specimens. Convex specimens that exhibit the instability are typically thin (T1) and/or have intermediate (S2) or large (S3) spans. Thus, the convex shells that exhibit the instability are thin and/or shallow, i.e. the height of the shell is small compared with the radius and span. Instability behavior is not observed for plate or concave specimens.

Concave and plate specimens have force-time histories nearly identical to the one shown in Figure 5.31 for convex specimen type R1S1T2. Typical force-time histories for concave and plate specimens appear in Figures 5.32 and 5.33 for comparison to Figure 5.31. The force-time histories in Figures 5.32 and 5.33 also have much the same shape as in Figure 5.10 for convex specimen R1S1T1 impacted at 1.0 m/s. Unlike many convex specimens, the force monotonically increases with time and does not have any instability characteristics. The unloading is nearly symmetric around the contact time associated with the peak impact force for the concave and plate specimens. Concave and plate specimens either showed penetration (R1S1T1, R2S1T1, R3S1T1, and RPS1T1 impacted at 3 m/s nominal) or a force-time history with a primary response approximating a half sinusoid. The plate specimens have the same response shape as those from previous investigations, e.g. [15]. Deflection-time histories for cylinders, concave shells, and plates are all similar in shape to the deflection-time histories for the convex shells shown in Figures 5.13 and 5.14. Figures 5.34 through 5.36 contain typical deflection-time histories for cylinders, concave shells, and plates, respectively, to illustrate these observation.

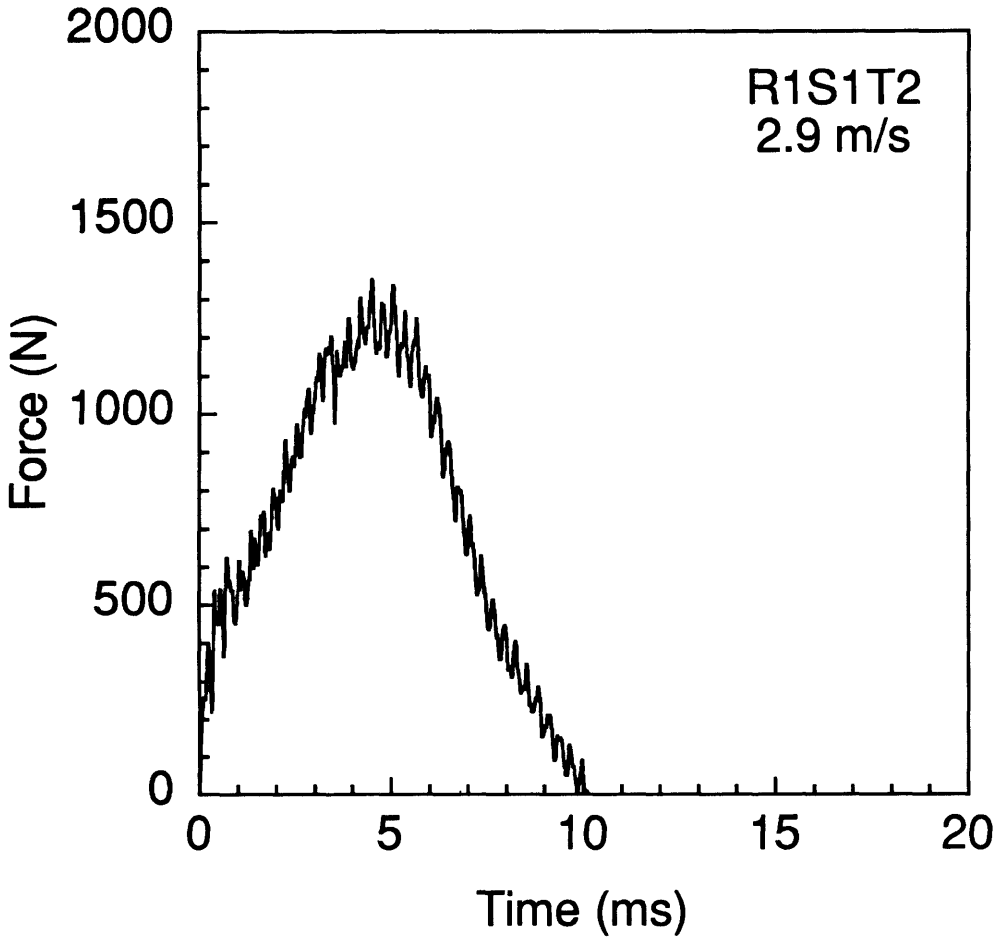

Figure 5.31 Force-time response of specimen R1S1T2 impacted at 2.9 m/s.

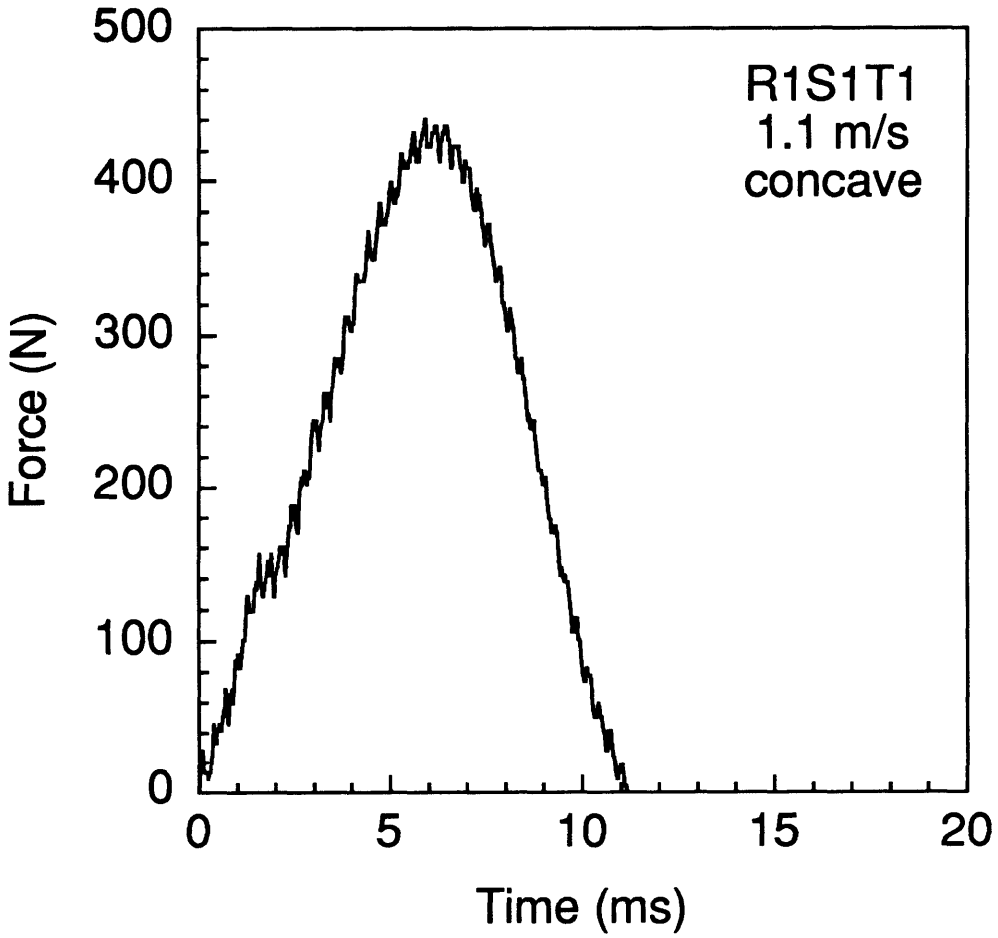

Figure 5.32 Force-time response of specimen R1S1T1 (concave) impacted at 1.1 m/s.

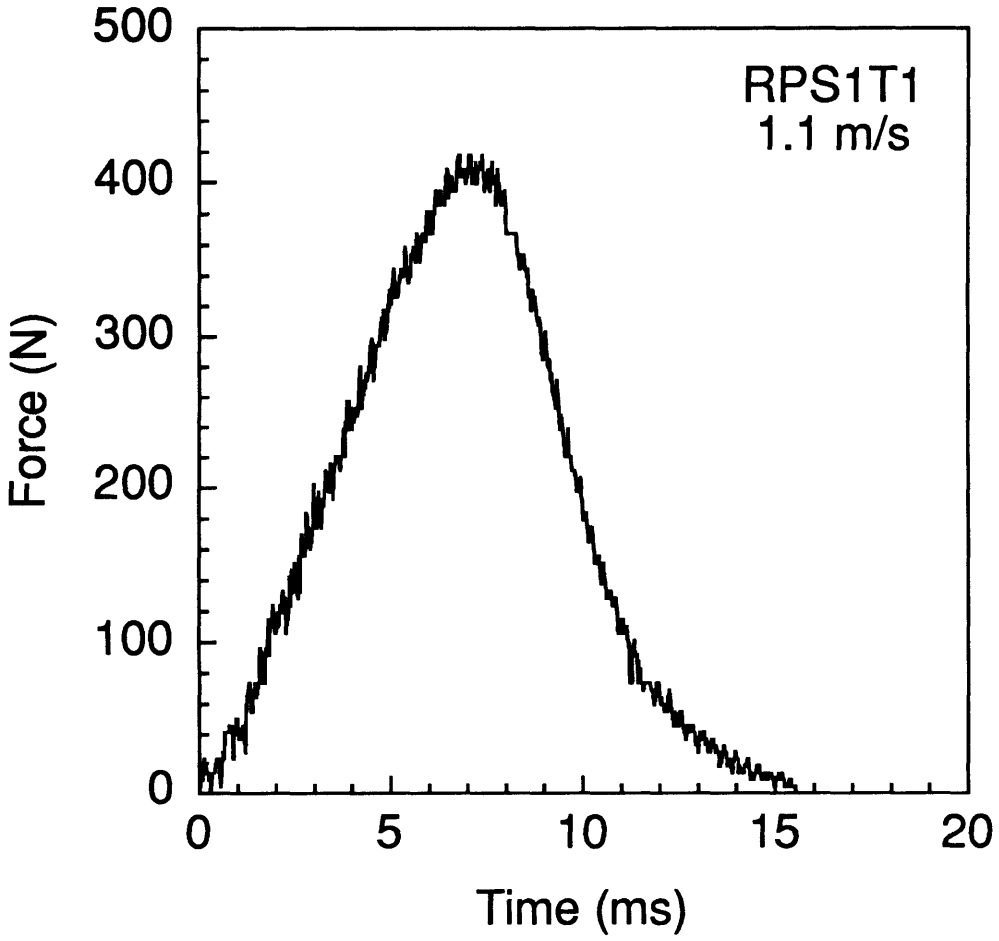

Figure 5.33 Force-time response of specimen RPS1T1 impacted at 1.1 m/s.

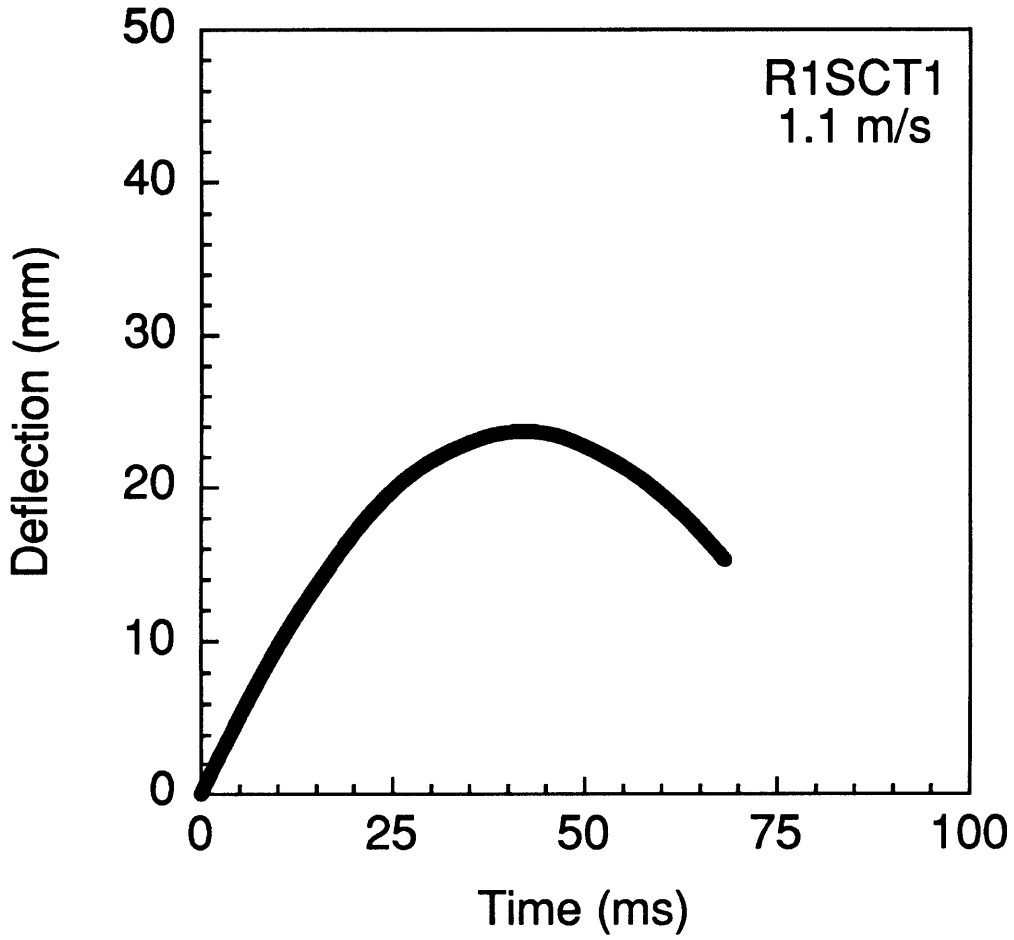

Figure 5.34 Deflection-time response of specimen R1SCT1 impacted at 1.1 m/s.

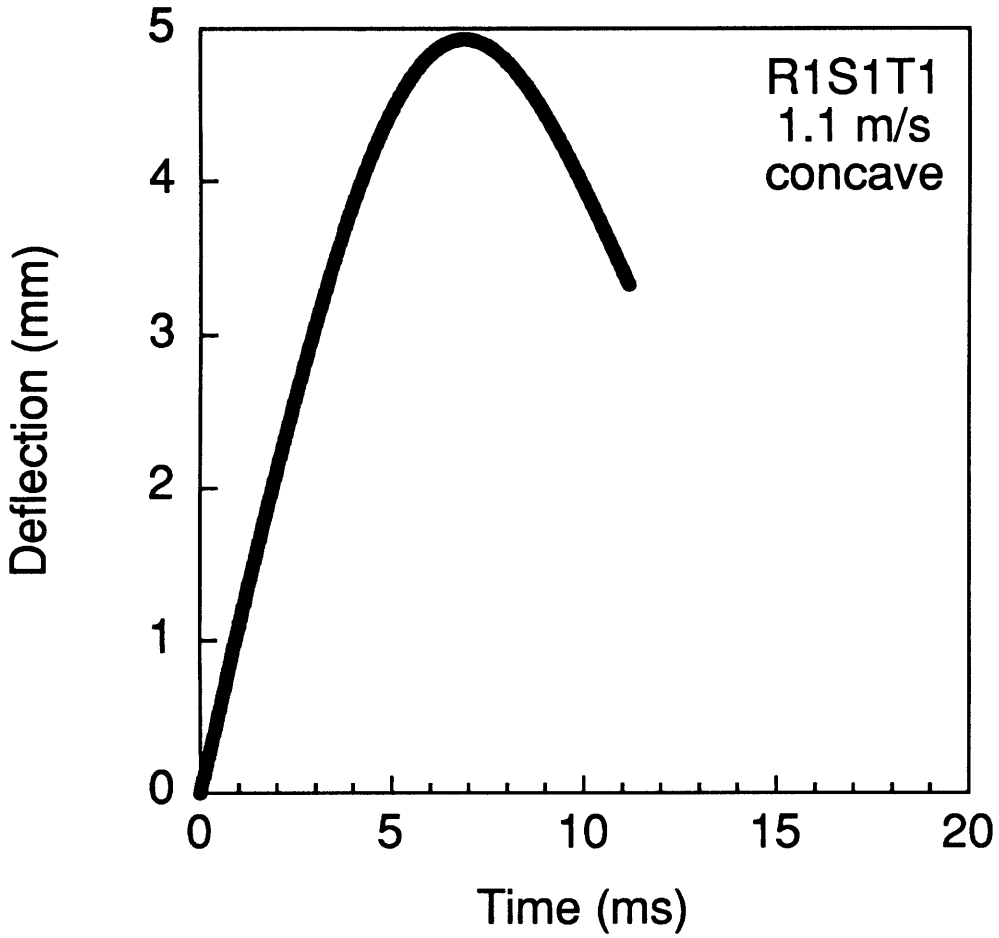

Figure 5.35 Deflection-time response of specimen R1S1T1 (concave) impacted at 1.1 m/s.

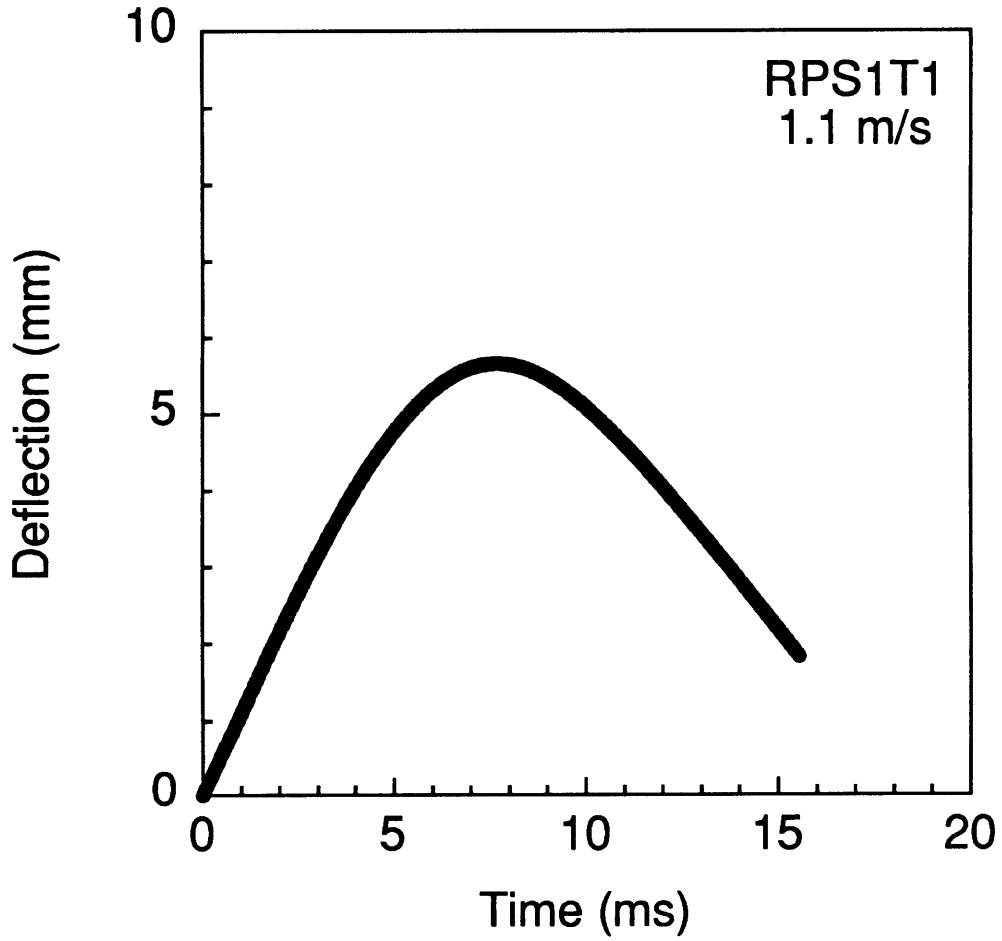

Figure 5.36 Deflection-time response of specimen RPS1T1 impacted at 1.1 m/s.

The instability in the response for many of the convex shells allows for two important forces to be defined in the response of these specimens: the overall peak force and the critical snapping load. The critical snapping loads for impacted convex specimens (see Figure 5.3) are presented in Table 5.1 for all the impacts at 3 m/s (nominal) and in Table 5.2 for the range of impact velocities. The critical snapping load is difficult to precisely determine from the force-time and force-deflection plots due, in part, to the high-frequency nature of the secondary response for these specimens. As explained in section 5.1, the load-drop in the force-time histories corresponds to the critical snapping load. Therefore, the critical snapping loads were estimated from the force-time histories to the nearest 50 N by noting at what force level the load-drop occurs.

As indicated previously, approximately half of the convex specimens tested have a response instability. Some trends are quickly discerned from Tables 5.1 and 5.2. In all cases except S3 in Table 5.1, the critical snapping load decreases as the radius increases. It is approximately constant for the S3 row in Table 5.1. No discernible trend is evident with respect to varying the span but increasing the thickness significantly increases the critical snapping load in all cases and is noted to most strongly influence the critical snapping load. The data in Table 5.2 indicates that the critical snapping load is approximately constant with respect to varying the impact velocity.

The critical snapping load is also associated with a deflection, and this deflection also shows some interesting trends. The deflection at the critical snapping load is also difficult to determine precisely from the force-time and force-deflection histories because of the high frequency secondary response. The center deflections at the critical snapping load are estimated to the nearest millimeter and are presented in Tables 5.3 and 5.4. As with the

Table 5.1 Critical Snapping Load[a] for Impact Tests[b] at 3 m/s (nominal)

	T1			T2			T3		
Span	R1	R2	R3	R1	R2	R3	R1	R2	R3
S1	400	150	100	-	650	450	-	-	-
S2	350	300	300		-			-	-
S3	-	200	250		-	-			-

[a] All values in N.

[b] Blanks indicate no test was conducted, and "-" indicates instability was not observed.

Table 5.2 Critical Snapping Load[a] for Impact Tests[b] at Various Velocities

		T1			T2	T3
Span	Velocity[c]	R1	R2	R3	R2	R3
S1	1	-	-	50	-	-
	2	350	150	100	750	-
	3	400	150	100	650	-
	4	350	250	100	800	-
S2	1	-				
	2	300				
	3	350				
	4	300				
S3	1	-				
	2	-				
	3	-				
	4	-				

[a] All values in N.

[b] Blanks indicate no test was conducted, and "-" indicates instability was not observed.

[c] Nominal velocity in m/s.

Table 5.3 Deflection[a] at Critical Snapping Load for Impact Tests[b] at 3 m/s (nominal)

	T1			T2			T3		
Span	R1	R2	R3	R1	R2	R3	R1	R2	R3
S1	6	4	4	-	5	5	-	-	-
S2	14	9	8		-			-	-
S3	-	12	9		-	-			-

[a] All values in mm.

[b] Blanks indicate no test was conducted, and "-" indicates instability was not observed.

Table 5.4 Deflection[a] at Critical Snapping Load for Impact Tests[b] at Various Velocities

		T1			T2	T3
Span	Velocity[c]	R1	R2	R3	R2	R3
S1	1	-	-	2	-	-
	2	6	5	3	6	-
	3	6	4	4	5	-
	4	6	5	2	6	-
S2	1	-				
	2	13				
	3	14				
	4	13				
S3	1	-				
	2	-				
	3	-				
	4	-				

[a] All values in mm.

[b] Blanks indicate no test was conducted, and "-" indicates instability was not observed.

[c] Nominal velocity in m/s.

critical snapping load itself, the deflection associated with the critical snapping load decreases as the radius is increased. The increase in deflection with increased thickness is not as significant as the increase for the critical snapping load. Deflection at the critical snapping load are noted to increase as the span is increased. Again, as with the critical snapping load itself, no trend with deflection at the critical snapping load is evident with respect to impact velocity.

The overall peak force, as indicated in section 5.1, is an important parameter for quantifying the impact response. This parameter is used as the damage resistance metric in this investigation. The distinction between peak force and peak force (instability) makes comparisons more tractable for convex shell specimens in Tables 5.5 and 5.6. An intuitive but important trend is that the peak force increases with velocity for all cases except specimen type R2S1T1 and specimen type R1S2T1. Specimen type R2S1T1 impacted at 3 m/s (nominal) slipped in-plane and this specimen type impacted at 4 m/s (nominal) was penetrated, making these data points inconclusive. The response for specimen R1S2T1 is noted to progress from the first equilibrium path for an impact velocity of 1 m/s (nominal) into the instability region for impact velocities of 2 m/s, 3 m/s, and 4 m/s (nominal) but not onto the second equilibrium path (compare Tables 5.2 and 5.6). Therefore, the peak force for these three latter impact velocities is the critical snapping load and the peak force does not increase with velocity. As with specimen type R1S2T1, specimen types R1S1T1 and R2S1T2 first show a force-deflection response in the instability region for impact velocities of 2 m/s (nominal). However, in both these cases, the load does not go past the magnitude of the critical snapping load on the second equilibrium path.

Table 5.5 Peak Force[a] for Impact Tests[b] at 3 m/s (nominal)

	T1				T2				T3			
Span	R1	R2	R3	RP	R1	R2	R3	RP	R1	R2	R3	RP
S1	*1.13*	*1.39*	*1.25*	**1.25**	1.35	*1.46*	*1.57*	1.95	1.69	1.54	1.44	2.43
S2	0.38	*0.85*	*1.10*			1.12				1.64	1.51	
S3	0.26	*0.28*	*0.75*			1.00	0.93				1.45	
S1 concave	**1.13**	**1.08**	**1.10**		1.98	2.04			2.69		2.35	
SC	0.22											

[a] All values in kN.

[b] Blanks indicate no test was conducted, *Italics* indicate peak force occurred on the second equilibrium path (instability), underline indicates specimen slipped in-plane after instability, and **bold** indicates penetration.

Table 5.6 Peak Force[a] for Impact Tests[b] at Various Velocities

Span	Velocity[c]	T1 R1	T1 R2	T1 R3	T1 RP	T2 R2	T3 R3
S1	1	0.29	0.22	*0.31*	0.42	0.44	0.54
	2	0.34	*0.94*	*0.87*	0.97	0.81	1.16
	3	*1.13*	*1.39*	*1.25*	**1.25**	*1.46*	1.44
	4	***1.30***	***1.22***	***1.51***		*1.73*	2.57
S2	1	0.18					
	2	0.33					
	3	0.38					
	4	0.34					
S3	1	0.10					
	2	0.24					
	3	0.26					
	4	0.38					
S1 concave	1	0.44					
	2	1.13					
	3	**1.13**					
	4						
SC	1	0.06					
	2	0.14					
	3	0.22					
	4	0.25					

[a] All values in kN.

[b] Blanks indicate no test was conducted, *Italics* indicate peak force occurred on the second equilibrium path (instability), underline indicates specimen slipped in-plane after instability, and **bold** indicates penetration.

[c] Nominal velocity in m/s.

These examples illustrate the importance of distinguishing between specimens that have an instability and those that do not.

The instability significantly affects the trend of increasing force with velocity. The variation of force with velocity for the S1-T1 convex specimen submatrix in Table 5.6 is presented in Figure 5.37 to illustrate the effect of the instability on the peak force. The force increases with velocity up to penetration for each of these specimens. However, the increase in peak force between 1 m/s and 2 m/s (nominal) for specimen R1S1T1 is not nearly as great as for the other specimens. The loading for this specimen is still in the instability region at 2 m/s (nominal) and the load has not yet progressed past the magnitude of the critical snapping load on the second equilibrium path. This makes the increase in peak force between 1 m/s and 2 m/s (nominal) almost insignificant, but it is apparent what is happening when the effect of the instability is considered.

Another obvious comparison for peak force is the impact tests for concave, convex, and plate specimens (S1T1 specimen types). These specimens all have the same aspect ratio and thickness but different curvatures and in the case of concave specimens, orientation with respect to the impact event. Concave specimens at every impact velocity have higher peak loads than corresponding convex shells, neglecting penetration. Concave shells also have higher peak forces than corresponding plate specimens as well. Also, the R1S1T1 (concave) specimen type impacted at 3 m/s (nominal) was penetrated while the corresponding convex shell type was not penetrated until 4 m/s (nominal). The data in Tables 5.5 and 5.6 indicate that all T1 specimens were penetrated at a peak force of approximately 1200 N, whether convex (instability), plate, or concave. It is interesting to note that for all velocities, the peak force for plates falls between those for all the

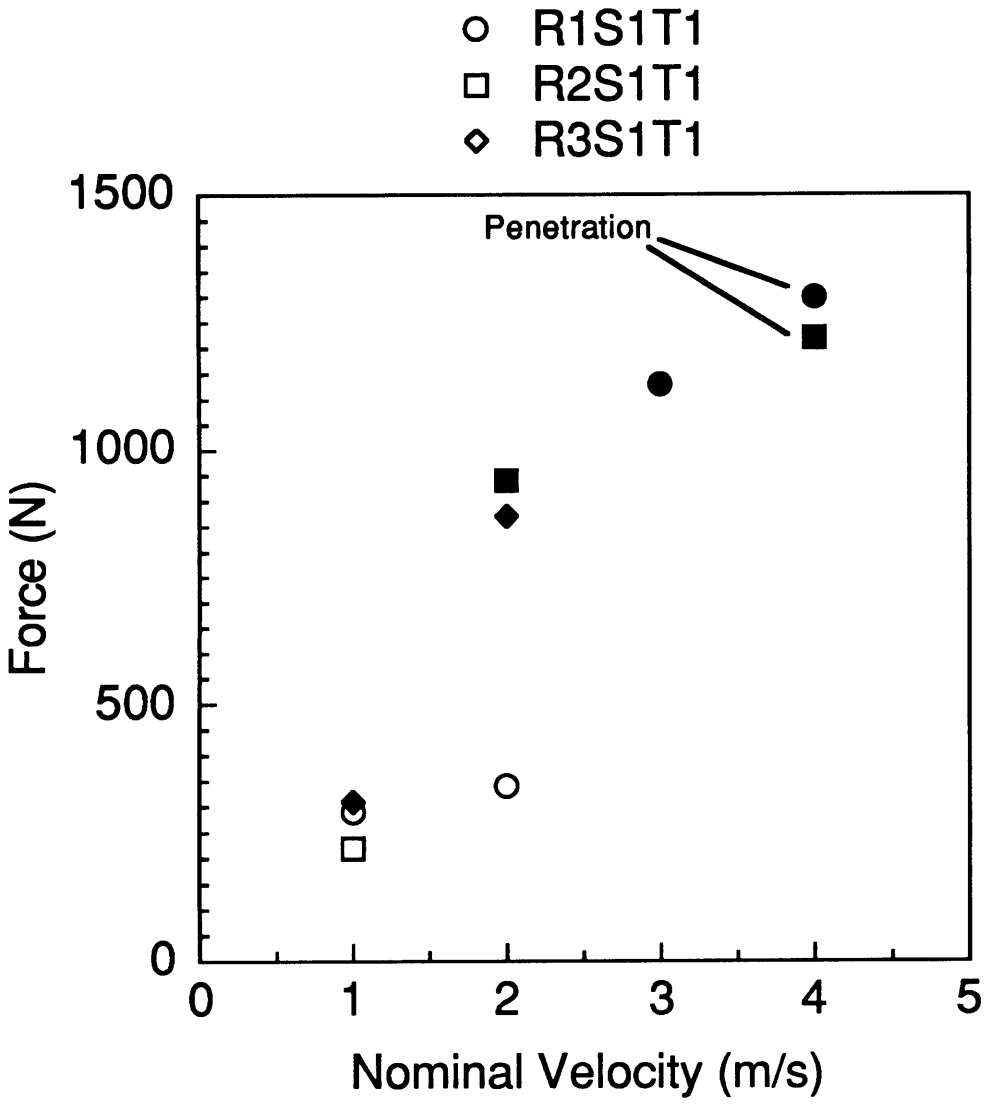

Note: filled data points indicate instability

Figure 5.37 Peak impact force versus nominal impact velocity for convex specimens indicating effect of instability.

convex specimens and those for the concave tests in the S1T1 portion of Table 5.6.

The effect of the three structural parameters (radius, span, and thickness) that were varied in this investigation on the peak force can also be examined. In Figure 5.38, the effect that varying the radius has on the peak force for various convex shells impacted at 3 m/s (nominal) is presented. Increasing the radius for specimen type S1T3 decreases the peak force while the opposite is true for specimen type S1T2 and the other convex shells that display the instability. The instability phenomenon was not observed for the S1T3 specimen type. Thus, if the force has not yet reached the critical snapping load, increasing the radius results in a decrease in the peak force while the opposite is true if the load has reached the magnitude of the critical snapping load on the second equilibrium path. The instability is therefore noted to reverse the trend with radius depending on which equilibrium path the peak force occurs. This again indicates the importance of the instability in the response. The data in Figure 5.38 also indicate that in the absence of the instability, the effect of varying the radius on the peak impact force is small. The results for the concave specimens shown in Table 5.5 have no obvious trend with radius but each T1 concave specimen was penetrated at approximately 1100 N.

The effect of span on the peak impact force can be determined by considering Table 5.5 for specimens impacted at 3 m/s (nominal). Increasing the span has the effect of lowering the peak force for 3 m/s impact tests for specimen types R1T1 and R2T2 but not for specimen type R3T3. The peak force for specimen type R3T3, the only specimen type in Table 5.5 with no instability behavior, was fairly insensitive to span. Again, as was the case for radius, the instability is noted to be extremely important. With the

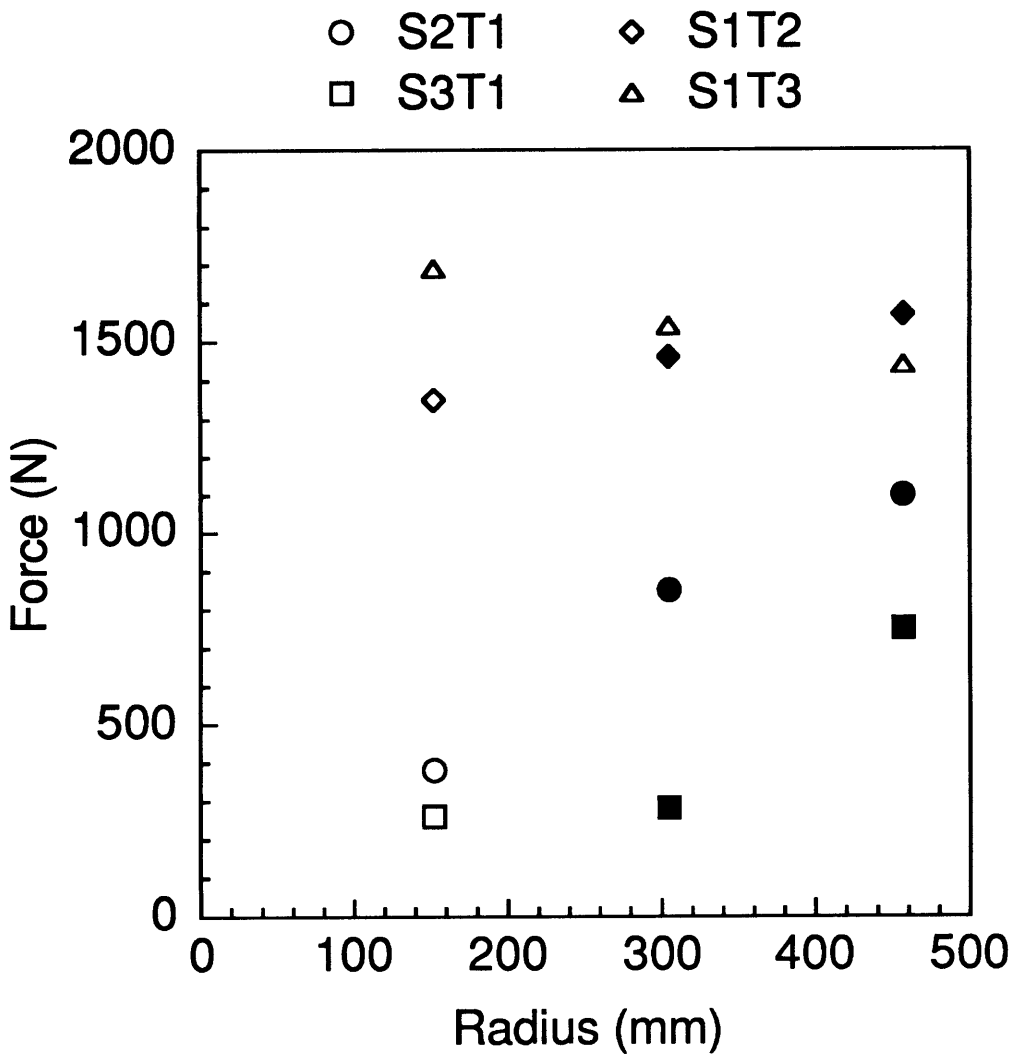

Note: filled data points indicate instability

Figure 5.38 Effect of radius on peak impact force for convex specimens impacted at 3 m/s (nominal).

instability present (S1), specimen types R1T1 and R2T2 are noted to have higher peak forces than specimens without the instability (S2). Larger peak forces associated with the instability are also noted in Figure 5.39 where peak impact force for convex specimens is plotted versus span for different velocities. The peak force is noted to increase significantly for specimens where the impact response has moved onto the second equilibrium path (instability) and past the magnitude of the critical snapping load. The increase in force with the instability is so dramatic for specimen R1S1T1 impacted at 4 m/s (nominal) as compared with the specimen impacted at 3 m/s (nominal), that the specimen was penetrated. Specimen types R2T1 and R3T1 show the decrease of peak force with increasing span for S2 and S3 in Table 5.5 but cannot be compared with the S1 specimen types because specimens R2S1T1 and R3S1T1 impacted at 3 m/s (nominal) slipped in-plane during testing.

The effect of increasing the thickness on the peak impact force can be determined from Tables 5.5 and 5.6. The peak impact force increases with thickness for cases with and without the instability, except in the range where the peak force transitions from the first to the second equilibrium path. It can be seen in Figure 5.40 that the peak impact force also increases with thickness for concave and plate specimens. Figure 5.41 is presented to illustrate the effect of varying the thickness on the peak impact force for all convex specimens tested. As the thickness increases, the force increases at a higher rate with velocity, regardless of the loading path on which the peak force occurred. The effects of thickness and the instability are even more apparent when Figure 5.41 is compared with Figure 5.42. The datapoints associated with the second equilibrium path (instability) have been removed from Figure 5.41 in Figure 5.42. It is clear in Figure 5.42 that the peak

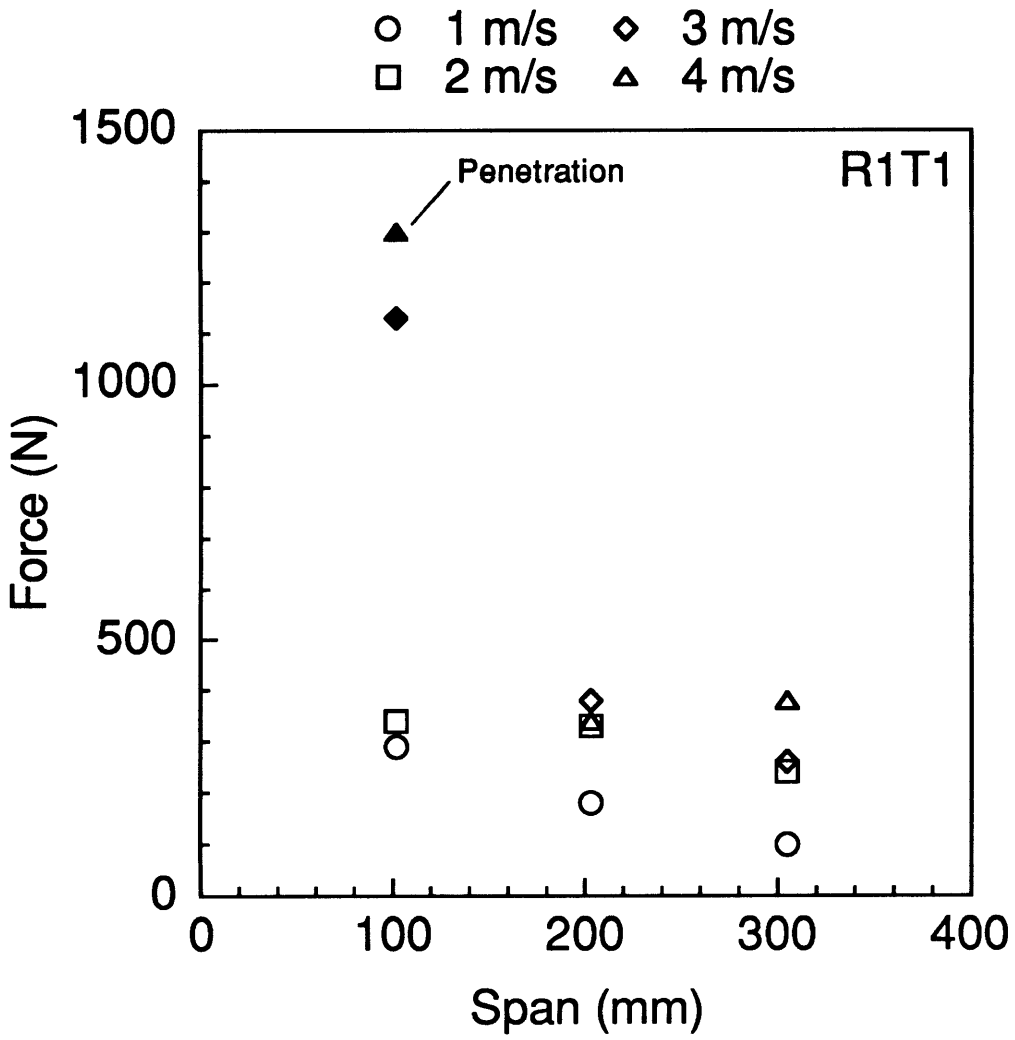

Note: filled data points indicate instability

Figure 5.39 Effect of span on peak impact force for convex specimen types R1T1 for range of impact velocities.

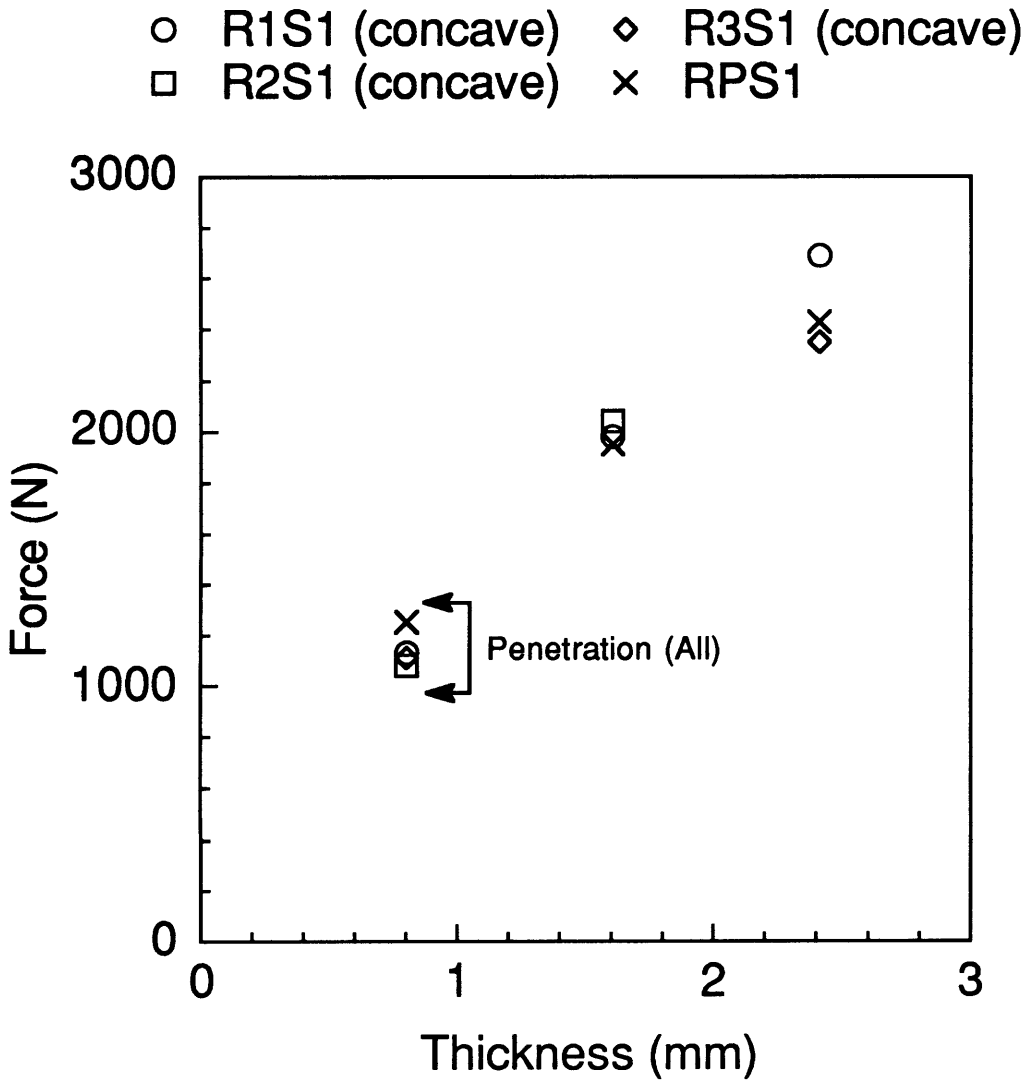

Figure 5.40 Effect of thickness on peak impact force for concave and plate specimens impacted at 3 m/s (nominal).

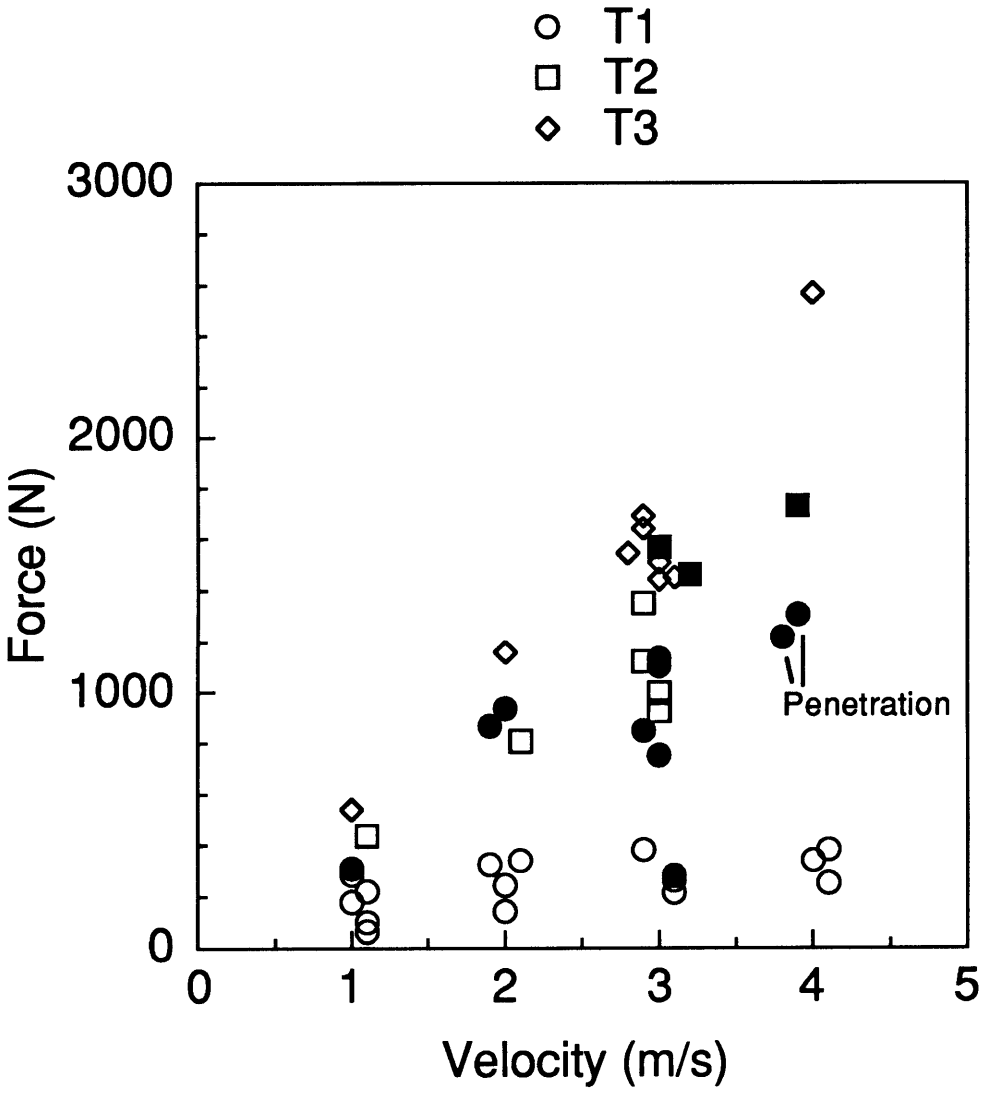

Note: filled data points indicate instability

Figure 5.41 Peak impact force versus impact velocity for various thicknesses for convex specimens.

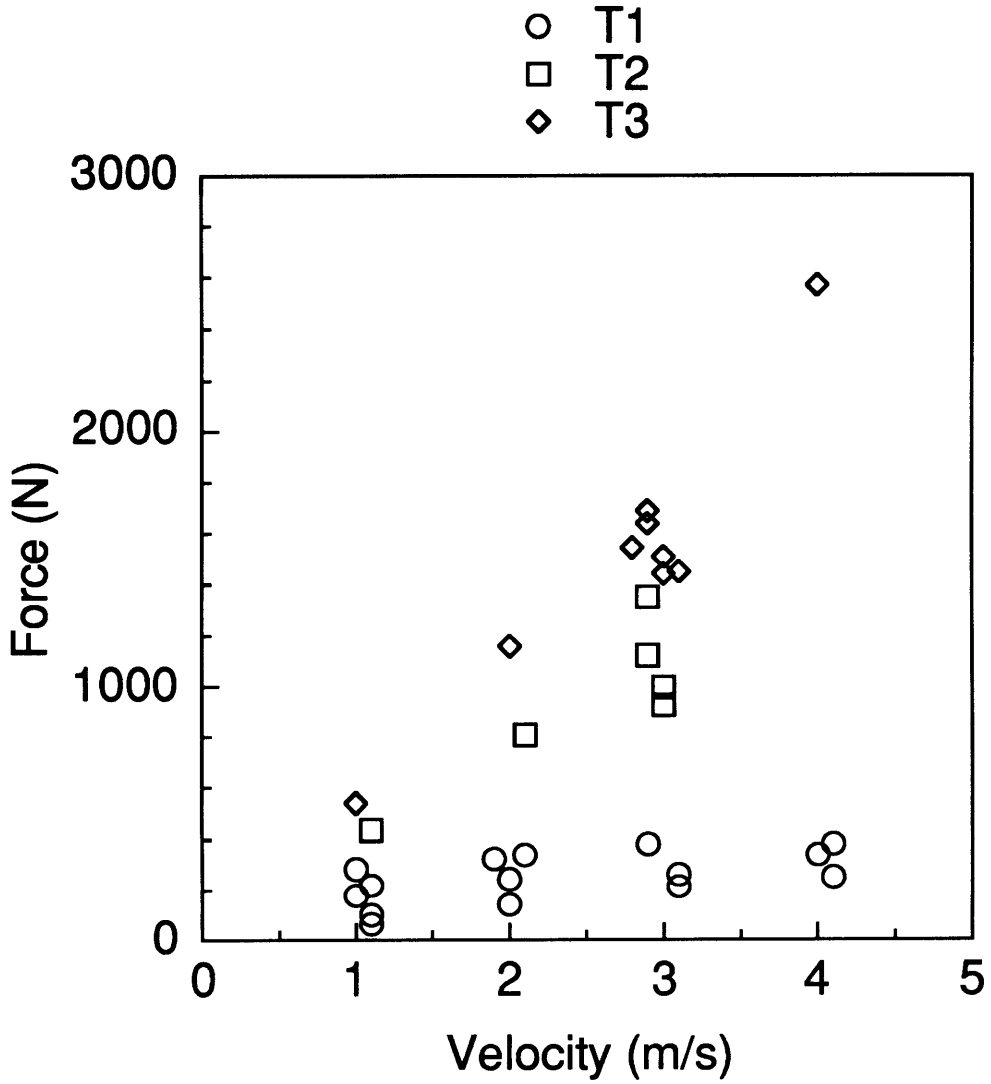

Figure 5.42 Peak impact force versus nominal impact velocity for various thicknesses for convex specimens not having the instability.

impact force increases at a higher rate as the thickness increases. By comparison to Figure 5.41, the increase in peak impact force with loading on the second equilibrium path is noted to move the datapoints closer to the peak impact forces for the next thickness, e.g. the datapoints for T1 (instability) are very close to the datapoints for the T2 specimens without the instability. The same can be said for T2 (instability) and T3 specimens. No T3 specimens displayed instability behavior. Plots similar to Figures 5.41 and 5.42 for radius and span do not display any trends like the one for thickness.

The test matrix design also allows the effects of structural parameter ratios on the impact response to be evaluated. The three important structural ratios to be evaluated are radius-to-thickness (R/T), radius-to-span (R/S), and span-to-thickness (S/T). As described in chapter 3, the structural ratios can be scaled using the scaling parameter n (e.g. nR1/T1 = Rn/T1 as per equation 3.1). The ratios can be varied by varying either of the structural parameters in the ratio, e.g. R or T in the radius-to-thickness ratio. The effect of varying the radius-to-thickness-ratio is presented in Figure 5.43 for convex specimens impacted at 3 m/s (nominal). Although the peak force may decrease as the radius-to-thickness ratio increases, no clear trend is evident due to scatter in the data. This is typical for concave specimens and convex specimens impacted at other velocities. The instability is noted not to occur below a radius-to-thickness ratio of 190.

The effect of varying the radius-to-span ratio on the peak impact force is presented in Figure 5.44. Although the peak force may be increasing with radius-to-span ratio, scatter in the data makes this observation uncertain. This is also true for convex specimens impacted at the three other impact velocities. The peak impact force for concave specimens is noted to be

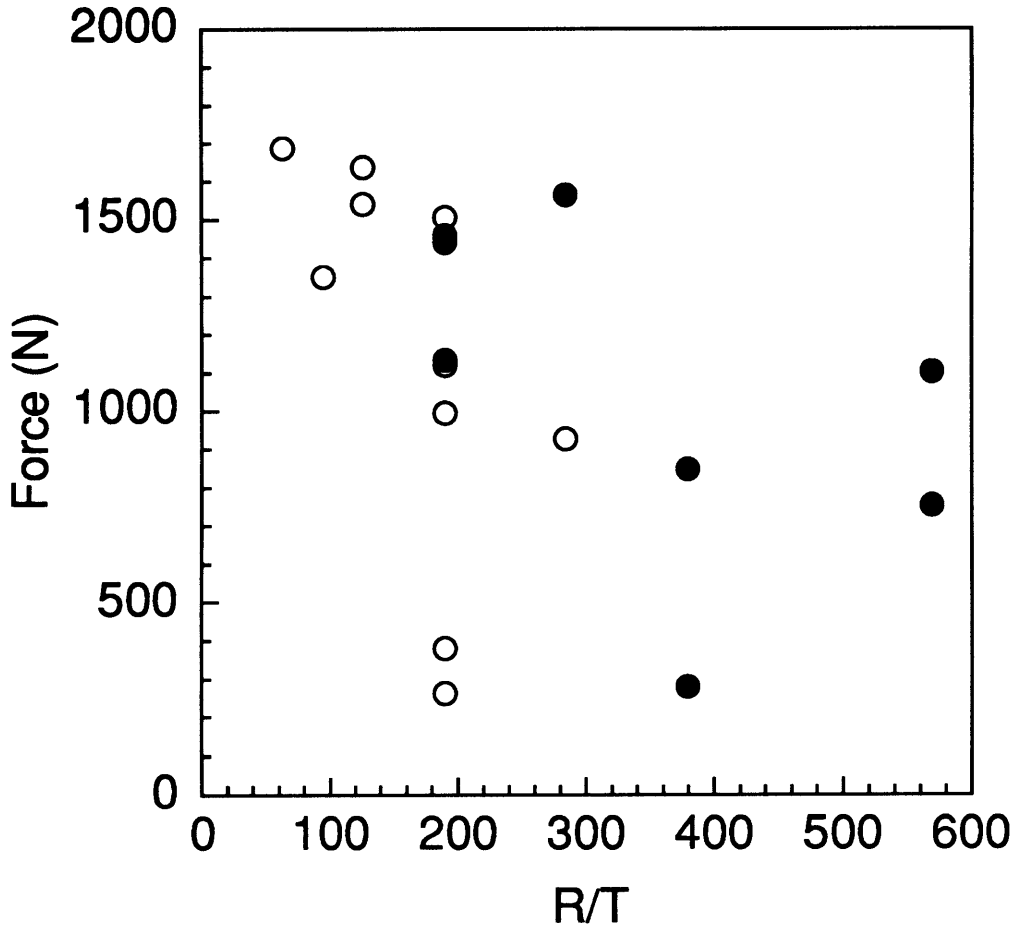

Note: filled data points indicate instability

Figure 5.43 Effect of radius-to-thickness ratio on peak impact force for convex specimens impacted at 3 m/s (nominal).

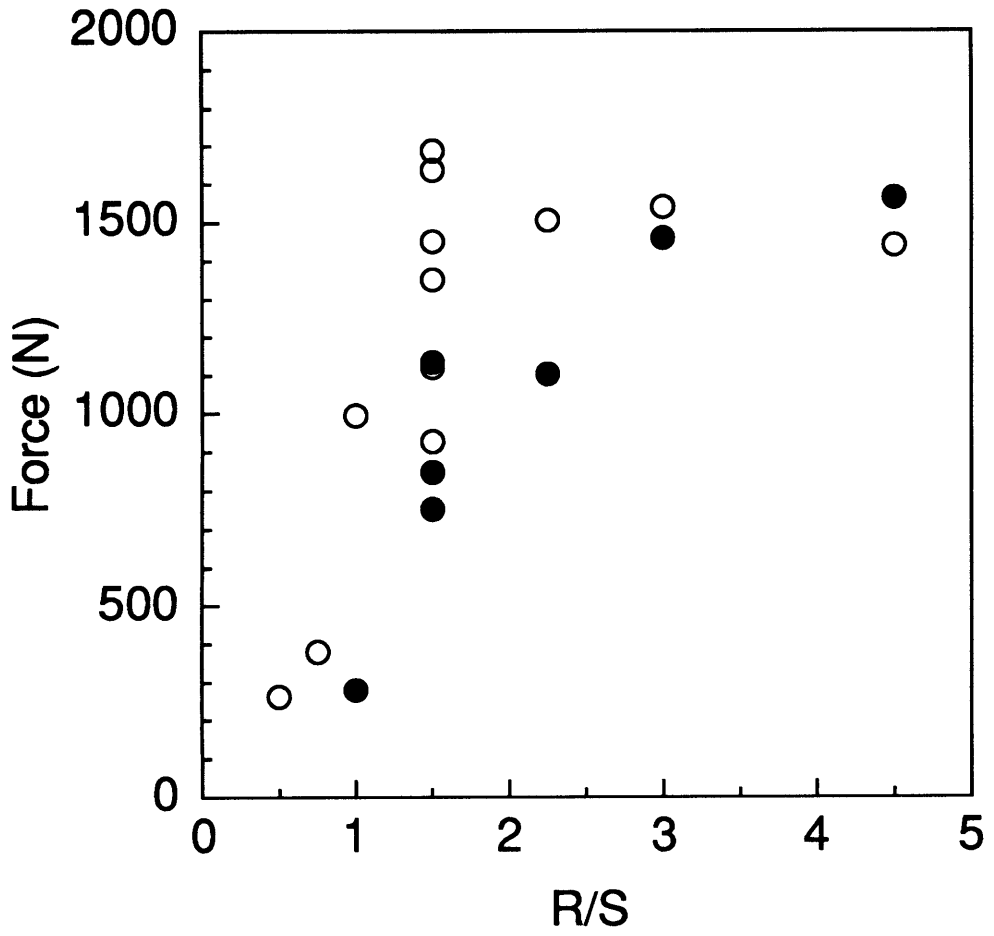

Note: filled data points indicate instability

Figure 5.44 Effect of radius-to-span ratio on peak impact force for convex specimens impacted at 3 m/s (nominal).

relatively insensitive to variations in the radius-to-span ratio, as shown in Figure 5.45. However, the effect of thickness is clearly evident again for concave specimens in Figure 5.45 which is a plot of peak impact force versus radius-to-span ratio for various thicknesses. In Figure 5.45, the impact force at each radius-to-span ratio is noted to be higher as the thickness increases. In comparison to the other ratios, the span-to-thickness ratio seems to have a discernible trend with the peak impact force as shown in Figure 5.46 for convex specimens impacted at 3 m/s (nominal). Regardless of instability, the peak impact force decreases significantly as the span-to-thickness ratio increases. This trend is repeated for convex specimens impacted at 1 m/s, 2 m/s, and 4 m/s (nominal) as shown in Figure 5.47. Concave and plate specimens also follow the same trend with the span-to-thickness ratio for specimens impacted at 3 m/s (nominal) as shown in Figure 5.48. It should be noted that all concave and plate specimens have span of S1 and thus only thickness varies in Figure 5.48.

Maintaining a constant structural ratio, and comparing the peak impact force, is another comparison that can be made from the design of the test matrix. The relative effect of the three structural parameters can be evaluated using the trends previously established for the structural parameters and making comparisons based on constant structural ratios. The relative effects of radius and thickness on the peak impact force can be evaluated by considering a constant radius-to-thickness ratio. Peak impact forces for a constant radius-to-thickness ratio (equal to 190) are shown for convex specimens impacted at 3 m/s (nominal) in Figure 5.49. The increase in peak force with scaling parameter follows the same trend as with thickness. The trend of peak impact force with radius was previously observed to be small and to switch directions depending on which equilibrium

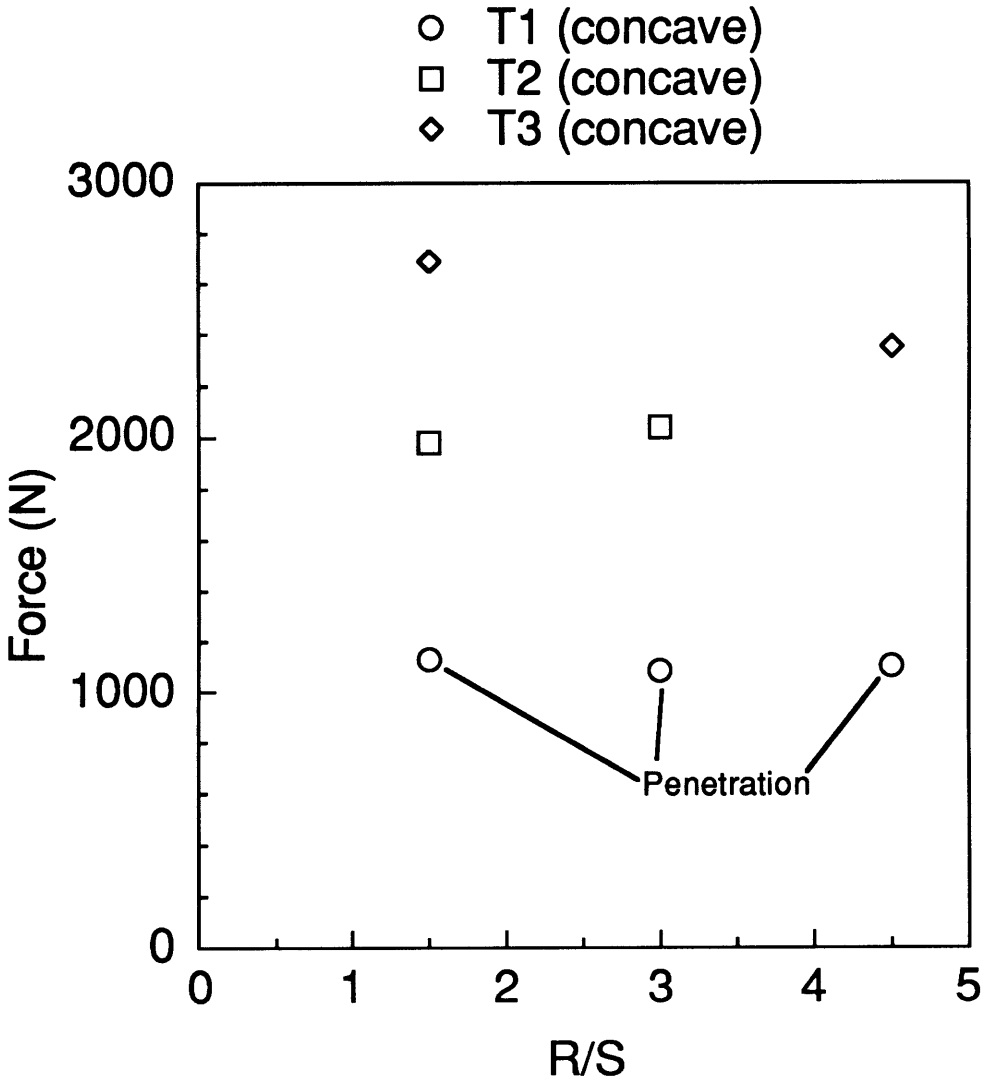

Figure 5.45 Effect of radius-to-span ratio on peak impact force for concave specimens impacted at 3 m/s (nominal).

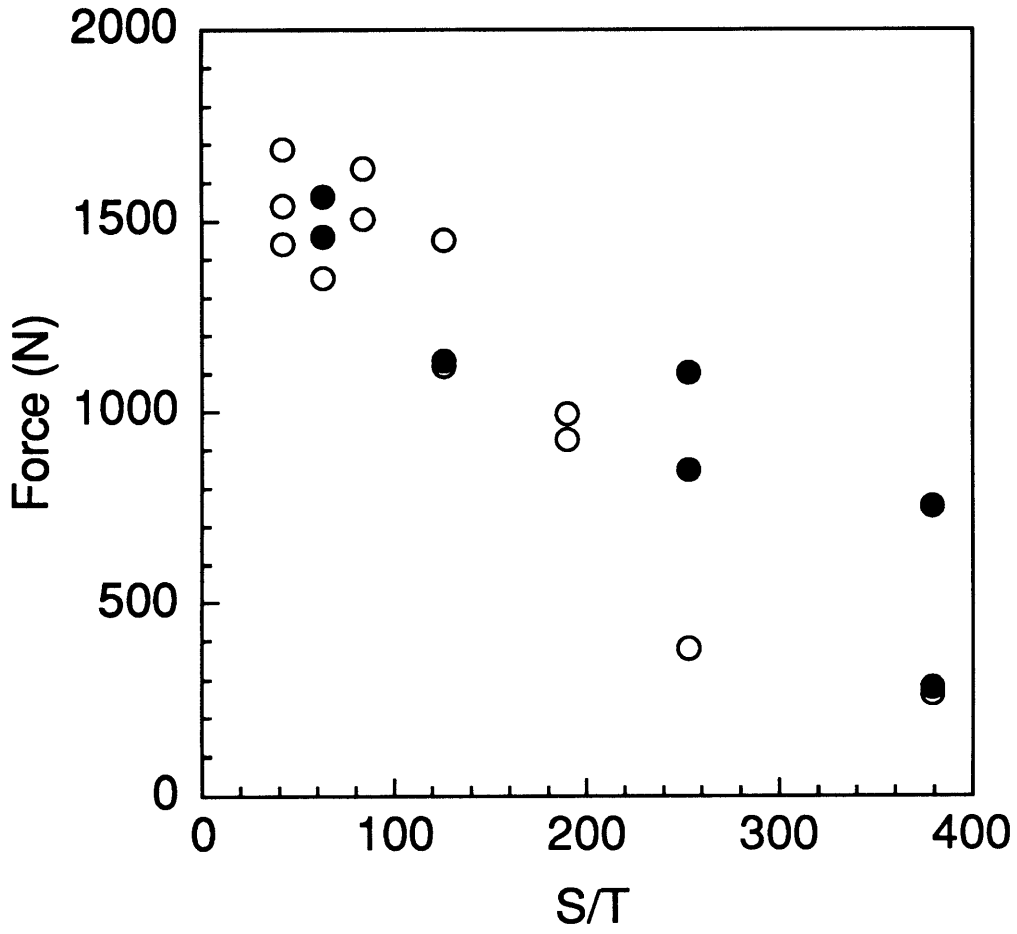

Note: filled data points indicate instability

Figure 5.46 Effect of span-to-thickness ratio on peak impact force for convex specimens impacted at 3 m/s (nominal).

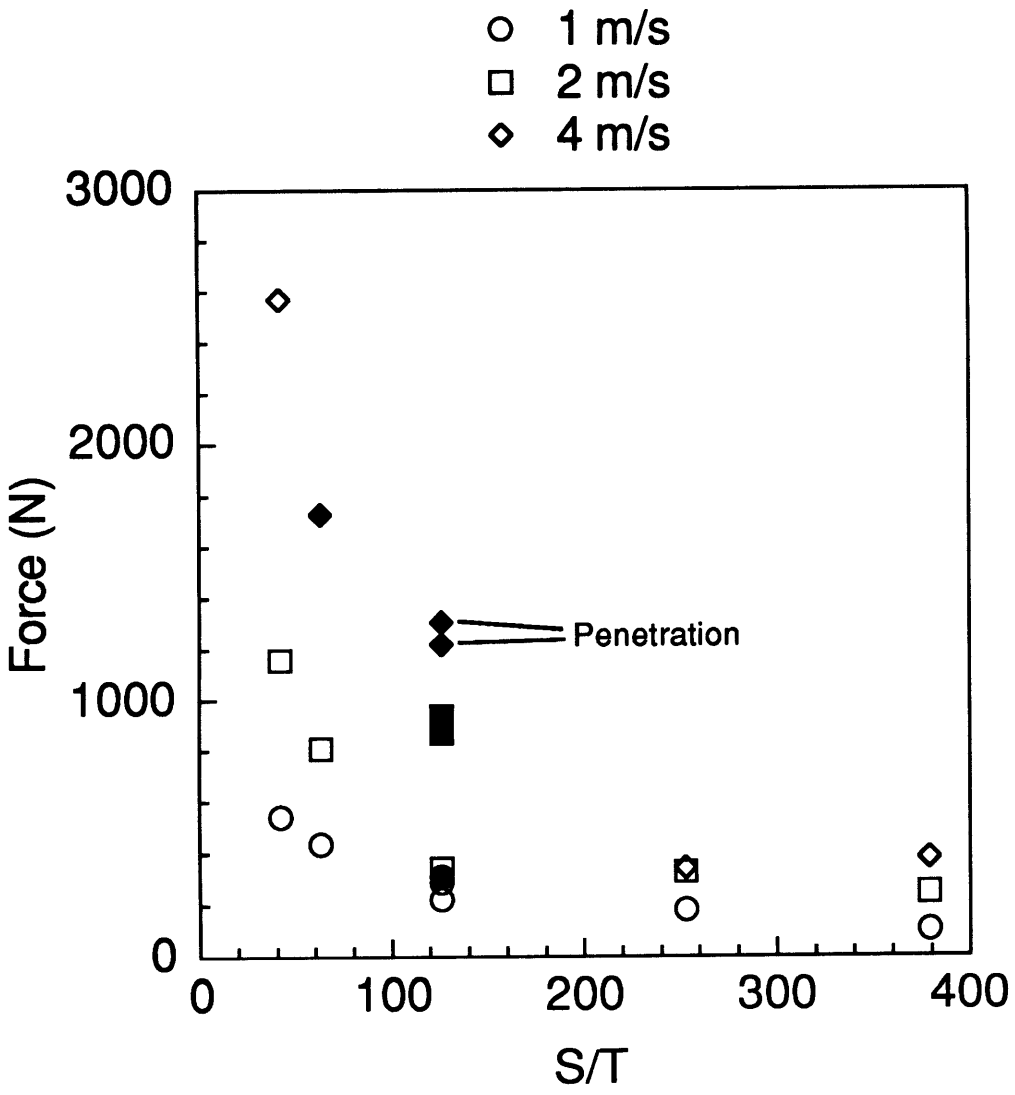

Note: filled data points indicate instability

Figure 5.47 Effect of span-to-thickness ratio on peak impact force for convex specimens impacted at 1 m/s, 2 m/s, and 4 m/s (nominal).

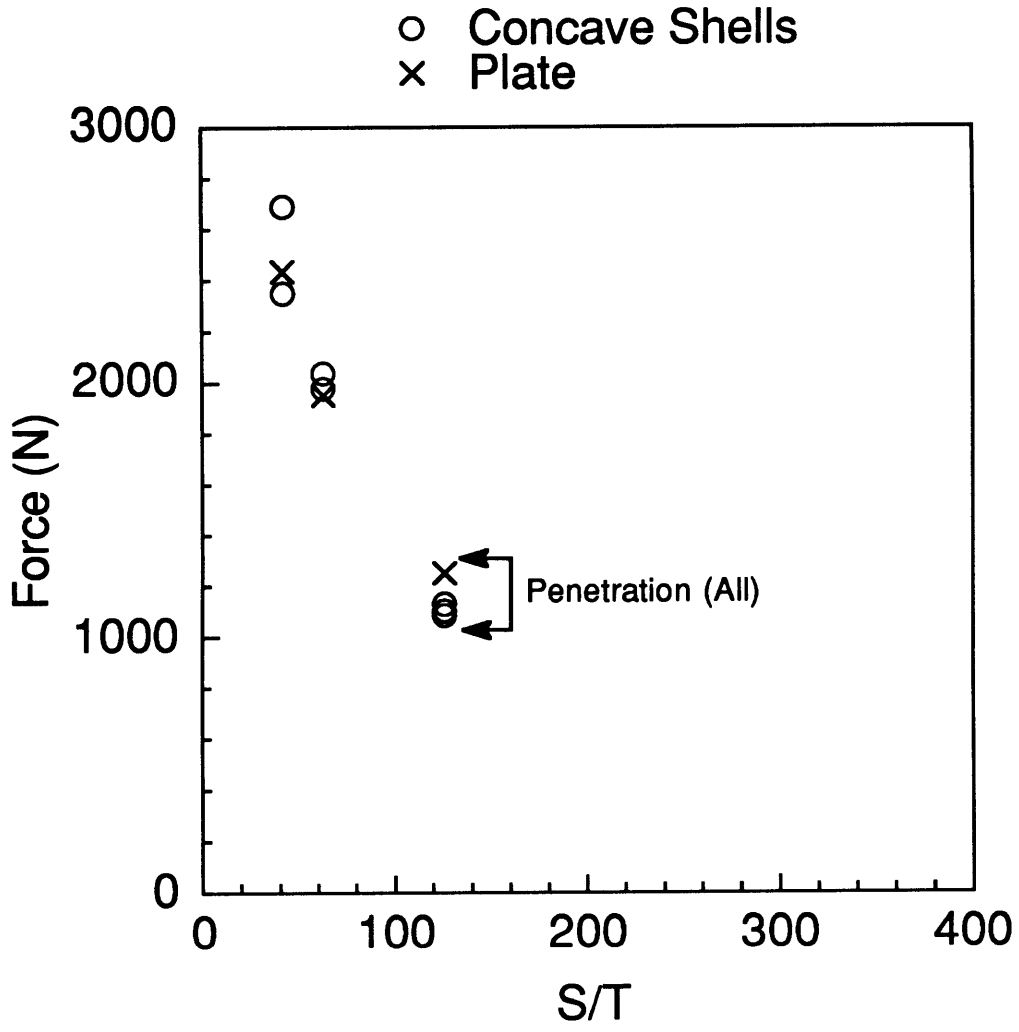

Figure 5.48 Effect of span-to-thickness ratio on peak impact force for concave and plate specimens impacted at 3 m/s (nominal).

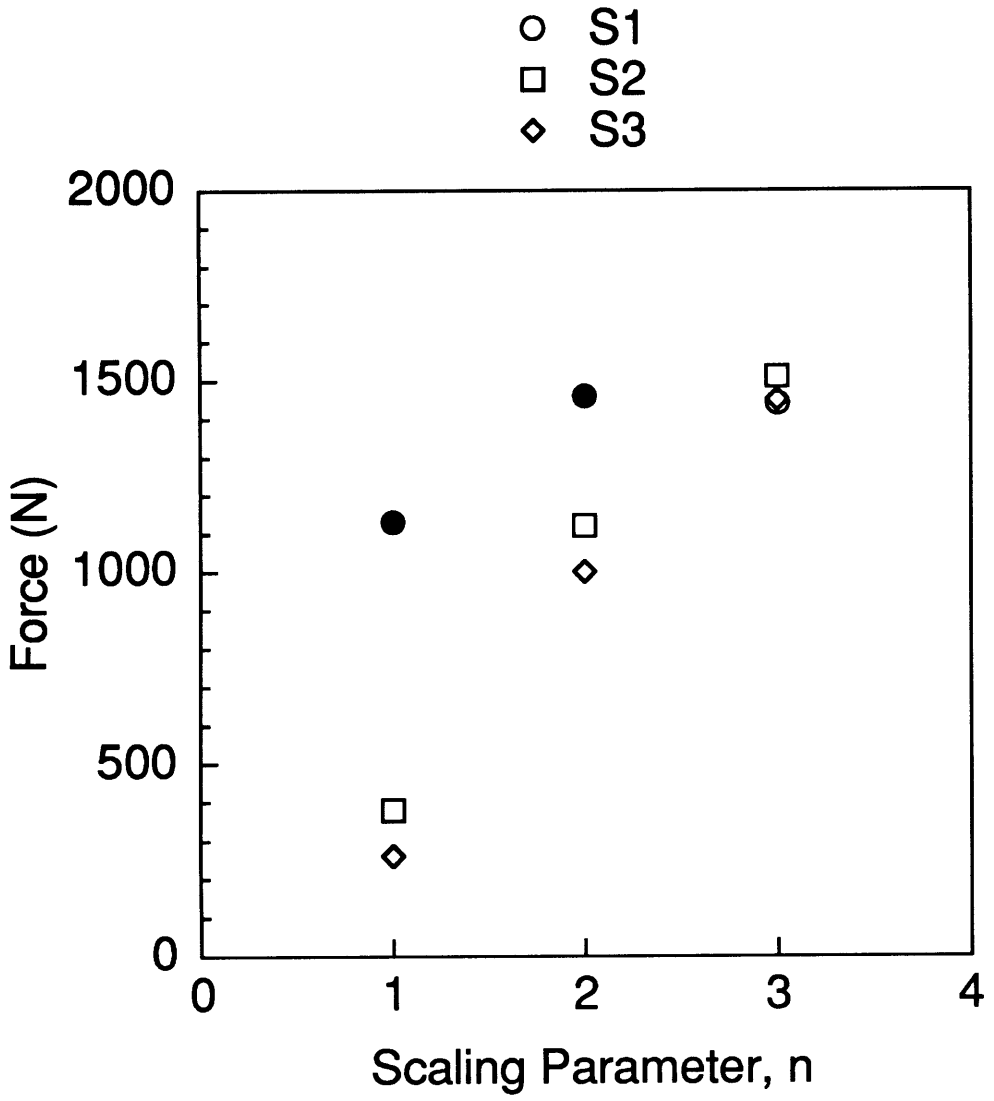

Note: filled data points indicate instability

Figure 5.49 Effect of scaling on peak impact force for convex specimens with constant radius-to-thickness ratio (190) impacted at 3 m/s (nominal).

path the peak force occurs, while increased thickness was previously observed to result in an increase in the peak impact force on both equilibrium paths. Thus, the trend of increasing peak impact force with increased thickness is maintained for specimens in Figure 5.49 even though both radius and thickness vary with the scaling parameter. This is noted to be true for the other three impact velocities, regardless of the instability effect, as shown for convex specimens in Figure 5.50. The trend is even maintained for concave specimens with a radius-to-thickness ratio of 190 impacted at 3 m/s (nominal) as can be seen in Table 5.5 by comparing specimens R1S1T1 (concave), R2S1T2 (concave), and R3S1T3 (concave). It is observed, from Figure 5.50, that the scaling parameter has a greater effect on the peak impact force at higher impact velocities. This follows the trend for thickness established earlier (see Figure 5.42).

The test matrix design also allows for a constant radius-to-span ratio of 1.5 to be used to investigate the effect of the scaling parameter on the peak impact force for convex specimens impacted at 3 m/s (nominal). The peak impact force is noted to decrease with increased scaling parameter (n) when a constant radius-to-span ratio is maintained as shown in Figure 5.51. This trend occurs regardless of which equilibrium path the peak force occurs on. A slight decrease in the peak impact force is noted in the response as the scaling parameter is increased. Also, the increase in peak impact force with increased thickness is again also evident in Figure 5.51.

The instability phenomenon also manifests itself in deflection and contact time magnitudes. Contact time and maximum deflection data are provided for all impact tests in Tables 5.7 through 5.10. For cases where penetration occurred, and the load drop signifying penetration is easily discernible in the force-time histories as described previously, the force-time

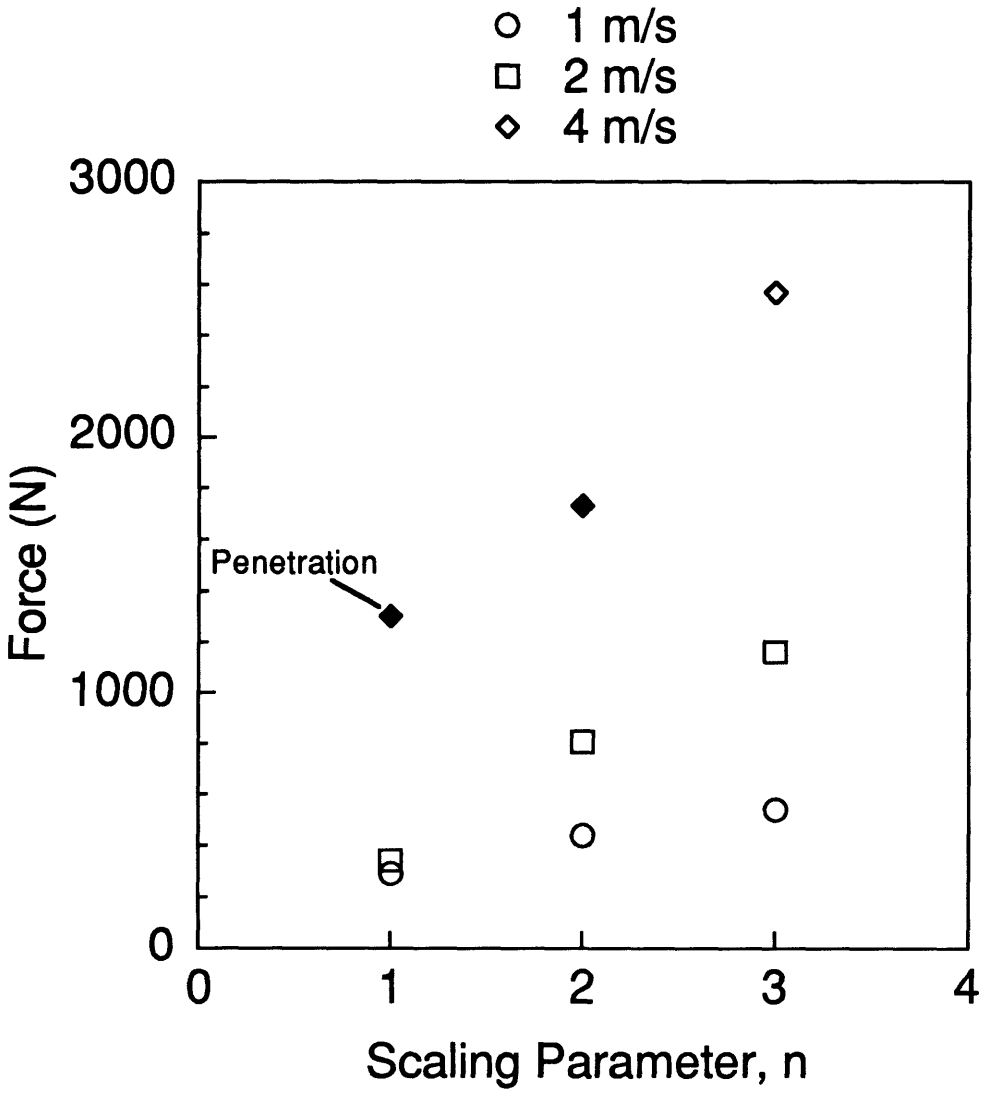

Note: filled data points indicate instability

Figure 5.50 Effect of scaling on peak impact force for convex specimens with constant radius-to-thickness ratio (190) and constant span impacted at 1 m/s, 2 m/s, and 4/ m/s (nominal).

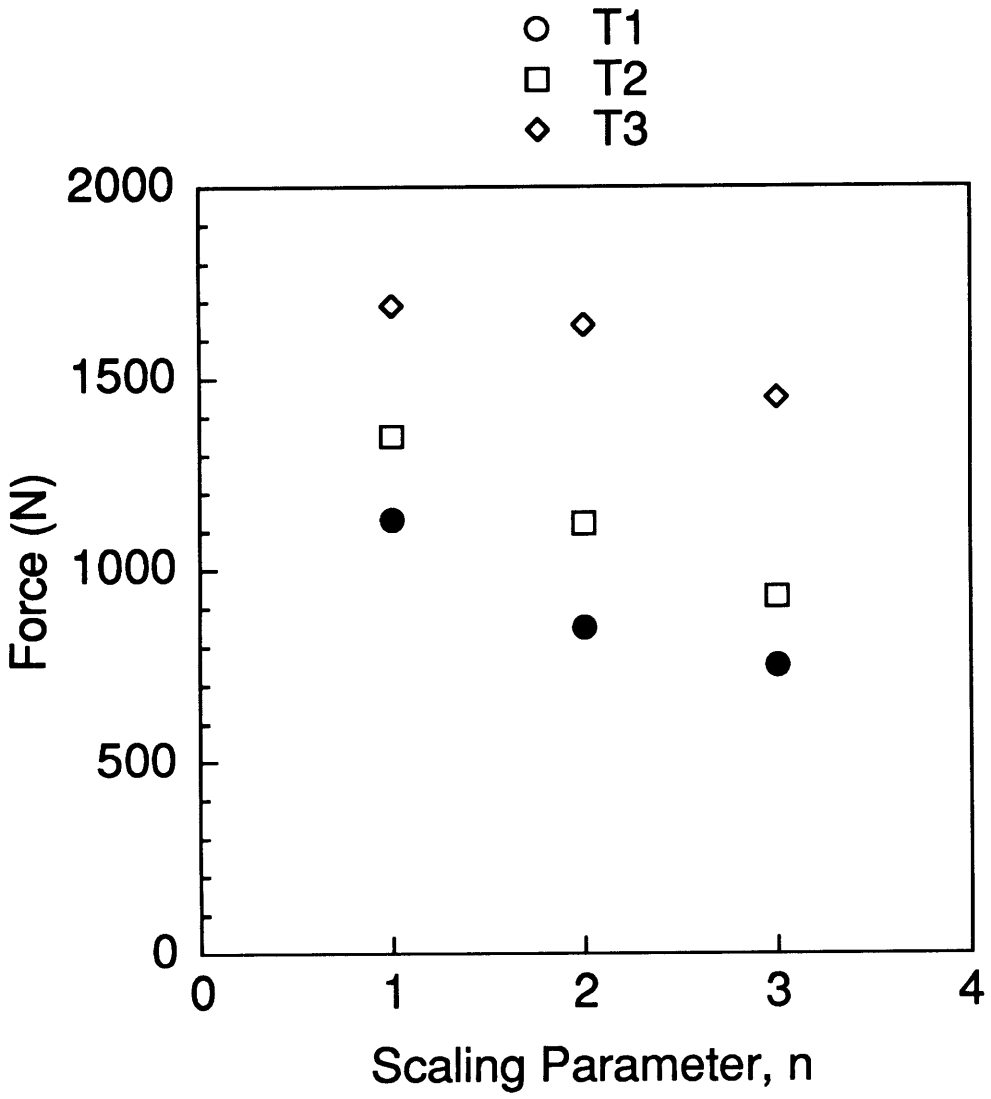

Note: filled data points indicate instability

Figure 5.51 Effect of scaling on peak impact force for convex specimens with constant radius-to-span ratio (1.5) impacted at 3 m/s (nominal).

Table 5.7 Time of Contact[a] for Impact Tests[b] at 3 m/s (nominal)

	T1				T2				T3			
Span	R1	R2	R3	RP	R1	R2	R3	RP	R1	R2	R3	RP
S1	*29*	*<u>12</u>*	*<u>13</u>*	**4.7**	10	*13*	*12*	8.1	7.6	8.0	10	6.6
S2	36	*54*	*42*			11				7.6	8.7	
S3	61	*88*	*51*			15	15				9.1	
S1 concave	**2.2**	**2.0**	**3.5**		7.3	6.8			5.1		6.9	
SC	86											

[a] All values in ms.

[b] Blanks indicate no test was conducted, *Italics* indicate peak force occurred on the second equilibrium path (instability), <u>underline</u> indicates specimen slipped in-plane after instability, and **bold** indicates penetration.

Table 5.8 Time of Contact[a] for Impact Tests[b] at Various Velocities

Span	Velocity[c]	T1 R1	T1 R2	T1 R3	T1 RP	T2 R2	T3 R3
S1	1	17	20	*25*	16	9.5	9.5
	2	39	*19*	*17*	13	11	8.9
	3	*29*	*12*	*13*	**4.7**	*13*	10
	4	***7.5***	***6.0***	***7.9***		*12*	8.3
S2	1	26					
	2	27					
	3	36					
	4	62					
S3	1	56					
	2	48					
	3	61					
	4	72					
S1 concave	1	11					
	2	7.9					
	3	**2.2**					
	4						
SC	1	68					
	2	80					
	3	86					
	4	98					

[a] All values in ms.

[b] Blanks indicate no test was conducted, *Italics* indicate peak force occurred on the second equilibrium path (instability), underline indicates specimen slipped in-plane after instability, and **bold** indicates penetration.

[c] Nominal velocity in m/s.

Table 5.9 Maximum Deflection[a] for Impact Tests[b] at 3 m/s (nominal)

	T1				T2				T3			
Span	R1	R2	R3	RP	R1	R2	R3	RP	R1	R2	R3	RP
S1	*24*	*<u>18</u>*	*<u>20</u>*	**12**	9.1	*13*	*12*	8.5	6.4	6.8	10	6.3
S2	31	*47*	*39*			10				6.8	8.3	
S3	57	*76*	*51*			14	15				8.8	
S1 concave	**6.1**	**5.9**	**8.8**		6.9	5.1			5.2		6.8	
SC	78											

[a] All values in mm.

[b] Blanks indicate no test was conducted, *Italics* indicate peak force occurred on the second equilibrium path (instability), <u>underline</u> indicates specimen slipped in-plane after instability, and **bold** indicates penetration.

Table 5.10 Maximum Deflection[a] for Impact Tests[b] at Various Velocities

		T1				T2	T3
Span	Velocity[c]	R1	R2	R3	RP	R2	R3
S1	1	5.3	6.9	*8.4*	5.7	3.5	3.0
	2	20	*13*	*11*	9.1	7.1	6.0
	3	*24*	*18*	*20*	**12**	*13*	10
	4	***24***	***21***	***25***		*16*	11
S2	1	8.4					
	2	17					
	3	31					
	4	64					
S3	1	20					
	2	32					
	3	57					
	4	88					
S1 concave	1	4.9					
	2	5.5					
	3	**6.1**					
	4						
SC	1	24					
	2	44					
	3	78					
	4	113					

[a] All values in mm.

[b] Blanks indicate no test was conducted, *Italics* indicate peak force occurred on the second equilibrium path (instability), underline indicates specimen slipped in-plane after instability, and **bold** indicates penetration.

[c] Nominal velocity in m/s.

history integration is performed only up to the time of penetration. This results in the maximum deflection data reported in Tables 5.9 and 5.10 for specimens that were penetrated. Accordingly, contact time is also given up to the time the load drops for penetrated specimens in Tables 5.7 and 5.8. Although the same definitions used for peak force are applied to contact time and peak deflection to indicate the instability, caution must be applied in interpreting this data. The contact time and/or peak deflection will increase significantly if the response progresses past the critical snapping load into the instability region. Therefore, the instability phenomenon can manifest itself in the contact time and peak deflection data before it is noted in italics in Tables 5.7 through 5.10.

The peak deflection is noted to increase in all cases in Table 5.10 as the velocity increases and the effect of the instability can be illustrated by considering specimen types R1S1T1 and R3S1T3. The peak deflection is noted to increase for specimen type R3S1T3 at a moderate rate compared to the initial large jump for specimen type R1S1T1. This large initial jump in deflection for specimen type R1S1T1 occurs between impact velocities of 1 m/s and 2 m/s (nominal) where the response is indicated in Table 5.10 not to have exceeded the magnitude of the critical snapping load on the second equilibrium path. The deflection for specimen type R1S1T1 experiences only a moderate increase in magnitude between impact velocities of 2 m/s and 3 m/s (nominal) even though this is where the response is noted to have exceeded the magnitude of the critical snapping load on the second equilibrium path (instability) in Table 5.10. Large deflections occur in the instability transition region but this behavior is not noted in the tables. In Table 5.10 (and other tables in this chapter) the instability is indicated only if the load has exceeded the magnitude of the critical snapping load on the

second equilibrium path. For specimen type R1S1T1, the increase in deflection associated with the instability occurs before the instability is indicated in Table 5.10. Thus, the data in Tables 5.7 through 5.10, and similar data for any shell response with an instability, must be used carefully.

There is no obvious trend in Tables 5.7 and 5.8 with respect to radius. However, for T1 specimens, the contact time is noted to increase for nearly all specimen types if the span increases, with the data for T2 and T3 specimens being inconclusive. Increasing the thickness is noted to decrease the contact time in all cases (excluding penetration and slipping). The contact times to penetration are noted to be relatively short, as are the contact times for concave and plate specimens relative to convex specimens. The variation of contact time with impact velocity is affected by convex shell instability, as previously outlined for maximum deflection, in Table 5.8. However, even in the absence of any instability, the contact times for convex specimens do not follow a definite trend. Some specimen types have increasing contact times with increasing velocity (e.g. R1S2T1), while others are approximately constant (e.g. R3S1T3). Previous investigators, e.g. [15], have demonstrated that the contact time decreases nonlinearly with increased impact velocity for plate specimens. This is supported by the data in Table 5.8 for plate specimens and is also the case for concave specimens. It is interesting to note that the contact times for shells with large span (S2, S3, and SC) and small thickness (T1) exhibit increased contact times as the impact velocity increases. This is opposite the trend for plate specimens observed in this work and by previous authors, e.g. [15].

An interesting comparison in contact times is for specimens with convex, concave, and plate geometries: R1S1T1, R1S1T1 (concave), and

RPS1T1. This comparison can be seen in the data presented in Figure 5.52. Concave and plate specimens display decreasing contact times with increasing velocity while the convex specimens display a markedly different behavior as a result of the instability. The contact time first increases as a result of the instability region for the convex specimen impacted at 2 m/s (nominal) as compared with the impact at 1 m/s (nominal) where no instability occurs. The contact time then decreases dramatically for the specimen impacted at 3 m/s (nominal), and then drops again for the impact at 4 m/s (nominal). The maximum deflection is noted to increase with velocity for every specimen in Table 5.10. Larger deflections are associated with increased span and, in general, plates and concave specimens have relatively small peak deflections compared with the convex specimen types regardless of the existence of instability regions. R1T1 specimen types in Table 5.10 indicate that the deflection increases at each velocity as the span is increased. This trend continues if the span of the full cylinder (SC), having a flexible in-plane boundary, is considered to be larger than the span of the half cylinder. The deflections vary by over a full order of magnitude in Tables 5.9 and 5.10.

5.2.2 Damage

Damage is characterized using two methods, visual and x-ray photography. X-ray photographs for all specimens are presented in Appendix B along with the force-time histories. In this section, results from visual damage characterization are presented first followed by the results of the x-ray photography method. As noted in section 5.2, penetration damage is the only discernible type of damage in the force-time histories. Penetration is manifested in the force-time histories as a sudden drop in load with large

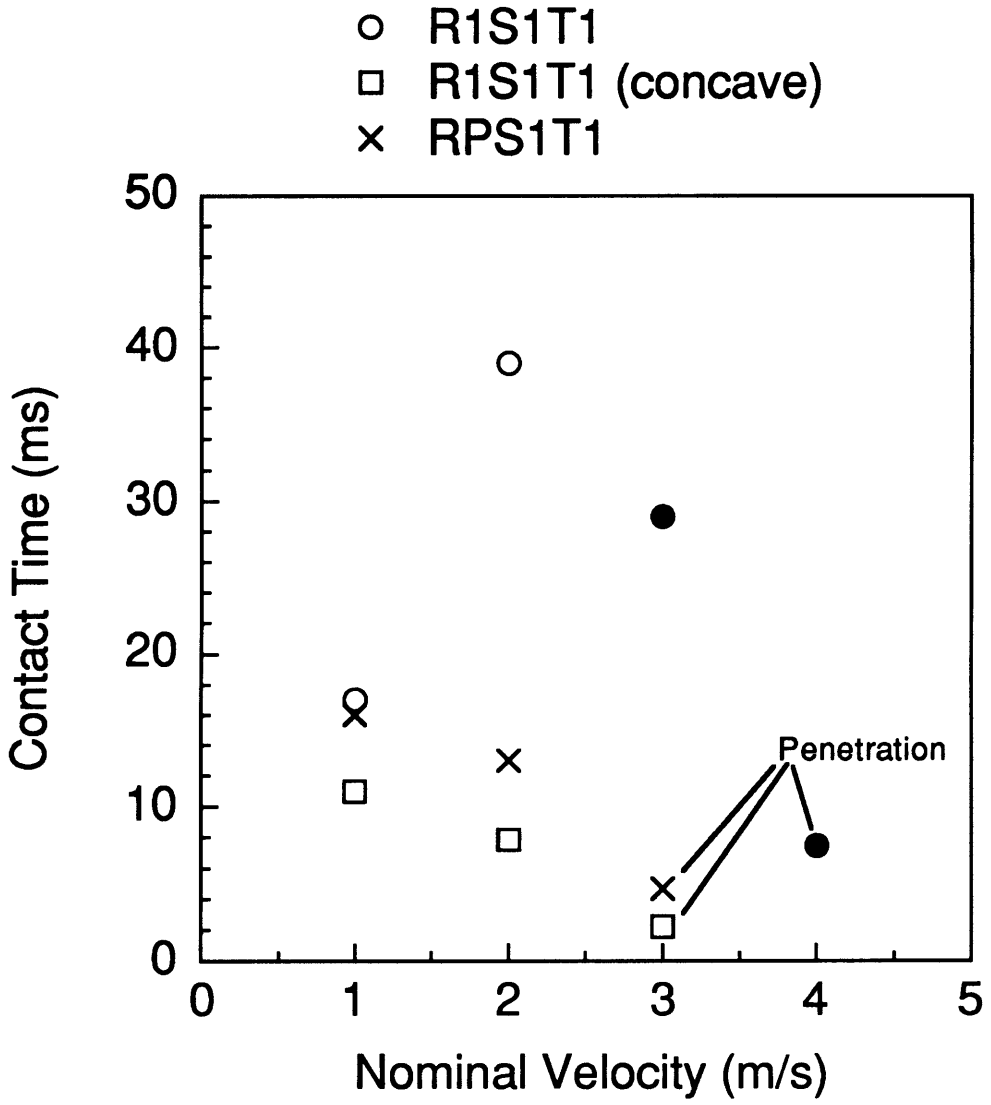

Note: filled data points indicate instability

Figure 5.52 Contact time versus nominal impact velocity for three different structural configurations (convex, concave, and plate).

(relative to the response before penetration) secondary oscillations around the drop in load.

Comparisons of impact damage based on varying the structural parameters, as done for peak impact force, is not addressed in this chapter. Peak force, which has previously been shown to be an excellent damage resistance metric for plate specimens [17-20], is used as the damage resistance metric for this investigation. As observed in section 5.2.1, varying structural parameters changes the specimen response, including peak force. There is therefore a two-step link between the structural parameters and the resultant damage with the peak force as the intermediate step. Discussion of damage resistance requires assessment of both steps. This is undertaken in chapter 6.

Visually, front and back surface damage can oftentimes be discerned after impact. Front-surface (side contacted by tup) incipient damage consists of a "marred" region, where contact occurs, that is smoother and slightly more reflective of light than the bulk of the specimen surface. This is visible with the naked eye under close scrutiny and laboratory lighting for many of the specimens, i.e. barely visible impact damage (BVID). At higher impact velocities, matrix cracking and fiber breaks are observed on the front surface of some specimens (denting), and at even higher velocities the specimen is penetrated. The length of the damaged region in both the axial and circumferential directions of the specimens was measured to the nearest millimeter, i.e. the lengths of the marred or damaged region are measured along the specimen axial and circumferential directions and not with respect to the fiber directions of the outermost (45°) plies. Typically, the region of front-surface damage was nearly circular with only a slight eccentricity. However, for specimens with elliptic visual damage, the axes of the ellipse

are observed to be along the axial and circumferential shell directions, and not along the fiber directions. Dimensions of the damaged region on the front surface are given in Appendix D as well as a calculated elliptical area of the region. The data is presented in the same order as the manufacturing data in Appendix A. The direction of the major axis for the ellipse switches orientation dependent on specimen type and impact velocity.

Visually, the incipient damage mode on the back surface of impacted specimens is a single matrix split/crack running along the fiber direction of the +45° ply. This single matrix crack is the only visible damage on the back surface of some specimens. Matrix splitting is visually observed on the back surface (side opposite impact) for many specimens and configurations. The length of each matrix split is presented in Appendix D for all impacted specimens. The start and termination of the matrix split are difficult to observe visually, therefore the matrix split lengths are measured to within 10 mm. The first matrix split is typically observed behind the point of contact of the specimen and the impactor, and is typically symmetric about the center of the shell. With increasing impact velocity, the matrix split is seen to extend and/or be joined by other matrix splits slightly to either side of the original. Spalling is sometimes observed to form between parallel matrix splits. Spalling occurs when a compressive through-thickness wave generated by the impact is reflected into a tensile wave at the back-surface of the impacted specimen. This reflected tensile wave causes the specimen to delaminate in a mode parallel to the fiber direction of the back ply. The spalled area is typically several times larger than the diameter of the impacting tup. The quantity and lengths of the visually observed matrix splits are presented in Appendix D along with the front-surface damage data. Spalling is indicated in Appendix D by placing parentheses around the matrix split lengths

associated with the delamination. As a general observation, the extent of the damage, whether it was front-surface marring or back-surface matrix splitting, increased with increasing impact velocity up to penetration.

A total of seven specimens were penetrated during impact testing. These specimens include convex and concave shells, and plates. All specimens penetrated were of thickness T1 and span S1, and specimens with all three radii were penetrated in both the convex and concave configuration. All concave and plate specimens were penetrated at an impact velocity of 3 m/s (nominal) whereas convex specimens penetrated at 4 m/s (nominal). Penetrated convex specimens all had peak forces on the second equilibrium path above the magnitude of the critical snapping load. Penetration is characterized by a large number of fiber breaks and matrix cracks through the specimen thickness, approximately the diameter of the impacting tup, 12.7 mm. Penetration damage for convex, concave, and plate specimens is visually observed to be quite similar. Front-surface photographs of penetrated convex, concave, and plate specimens are presented in Figure 5.53 to illustrate this similarity. Penetrated specimens are also characterized by extensive back-surface delaminations. The delaminations begin at the center of the shell, behind the contact region, and propagate towards the circumferential edges of the shell at 45° in a band centered behind the contact region with a width of approximately the diameter of the tup, 12.7 mm. Damage (penetration) as viewed from the back-side of specimen R1S1T1 (concave) is shown in Figure 5.54 for the case of impact at 3.0 m/s to illustrate delamination damage. As with front-surface damage, back-surface damage for penetrated specimens (convex, concave, and plate) is also visually observed to be quite similar.

The information from the x-ray photographs of impacted specimens can

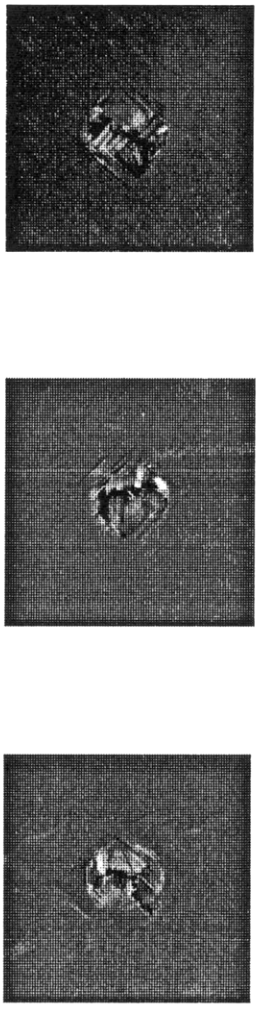

Figure 5.53 Photographs of front surface of typical penetrated specimens: (*top*) R2S1T1 impacted at 3.8 m/s; (*middle*) R1S1T1 (concave) impacted at 3.0 m/s; and (*bottom*) RPS1T1 impacted at 3.0 m/s.

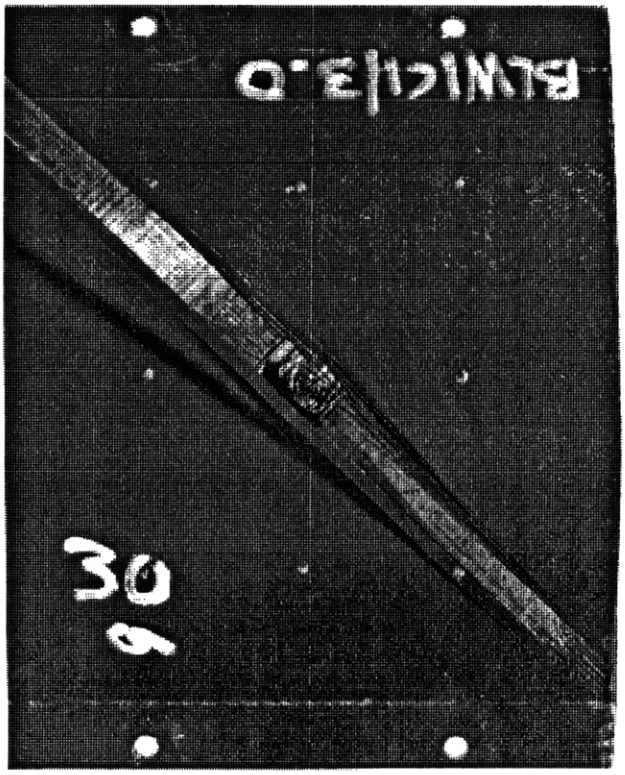

Figure 5.54 Photograph of back-surface penetration damage of specimen R1S1T1 (concave) impacted at 3.0 m/s showing extensive delamination.

be categorized into three broad types: no damage, where damage is not evident in the x-ray photographs; damage, where damage is evident in the x-ray photographs; and penetration. In Appendix B, x-ray photographs are not provided for specimens that display no damage. Figure 5.55 is an x-ray photograph of specimen R2S1T1 impacted at 1.1 m/s which is an example of a case with no damage. The light circle at the center of the photograph is the hole where the dye-penetrant is injected into the contact region. Aside from this hole, nothing is visible in the photograph. Damage is visible in the x-ray photograph for specimen type R1S1T1 impacted at 3.0 m/s shown in Figure 5.56. Specimens that are severely damaged from penetration are not evaluated using x-ray photography because the damage is too severe to inject dye into the specimen.

In Tables 5.11 and 5.12, specimens are classified into the three categories noted above: specimens that exhibit no damage (N), damage visible in the x-ray photograph (D), or penetration (P). Again, specimens that have the peak impact force on the second equilibrium are distinguished in the tables from those that do not by putting the damage classification in italics. It should be noted that specimens with visual back-surface matrix splits and/or spalling always show damage (D) in the x-ray photographs. Incipient damage in the x-ray photographs of all specimen types, regardless of orientation, is observed to be delamination and matrix crack formation along the 45° and/or -45°, and 0° directions. It is unclear from the specimens tested whether or not matrix cracking or delaminations constitute incipient damage. Previous investigations using more complete damage characterization schemes have shown that matrix cracking precedes delaminations [15]. At higher impact velocities, delamination and matrix cracking extends in all three fiber directions. Finally, at even higher impact velocities, severe

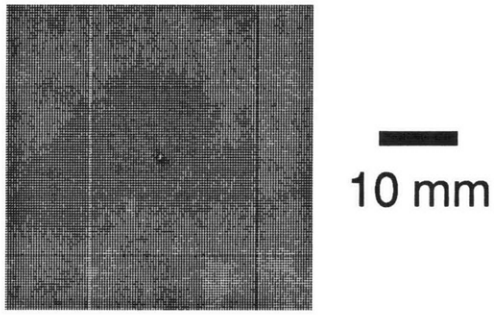

Figure 5.55 X-ray photograph of specimen R2S1T1 impacted at 1.1 m/s showing no damage.

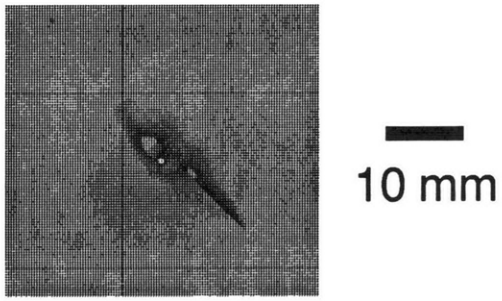

Figure 5.56 X-ray photograph of specimen R1S1T1 impacted at 3.0 m/s.

Table 5.11 Damage Severity[a] Chart for Impact Tests[b] at 3 m/s (nominal)

	T1				T2				T3			
Span	R1	R2	R3	RP	R1	R2	R3	RP	R1	R2	R3	RP
S1	*D*	*D*	*D*	P	D	*D*	*D*	D	D	D	D	D
S2	N	*D*	*D*			D				D	D	
S3	N	*N*	*D*			D	D				D	
S1 concave	P	P	P		D	D			D		D	
SC	N											

[a] "N" indicates no damage in the x-ray photographs, "D" indicates damage in the x-ray photographs, and "P" indicates penetration.

[b] Blanks indicate no test was conducted, *Italics* indicate peak force occurred on the second equilibrium path (instability), and underline indicates specimen slipped in-plane after instability.

Table 5.12 Damage Severity[a] Chart for Impact Tests[b] at Various Velocities

		T1				T2	T3
Span	Velocity[c]	R1	R2	R3	RP	R2	R3
S1	1	N	N	*N*	D	D	N
	2	N	*D*	*D*	D	D	D
	3	*D*	*D*	*D*	P	*D*	D
	4	*P*	*P*	*P*		*D*	D
S2	1	N					
	2	N					
	3	N					
	4	N					
S3	1	N					
	2	N					
	3	N					
	4	N					
S1 concave	1	D					
	2	D					
	3	P					
	4						
SC	1	N					
	2	N					
	3	N					
	4	N					

[a] "N" indicates no damage in the x-ray photographs, "D" indicates damage in the x-ray photographs, and "P" indicates penetration.

[b] Blanks indicate no test was conducted, *Italics* indicate peak force occurred on the second equilibrium path (instability), and underline indicates specimen slipped in-plane after instability.

[c] Nominal velocity in m/s.

damage indicated by fiber breaks through the entire specimen thickness is observed (penetration). Penetration was never observed below an impact velocity of 3 m/s (nominal).

For a given specimen type, there is an ordering of damage with velocity for the categories of damage outlined here. For impact of identical specimens, no damage is followed at higher velocities by damage which can be seen in the x-ray photographs which is followed at even higher velocities by penetration. Damage order with velocity is apparent in Table 5.12, e.g. specimen type R1S1T1. No damage at impact velocities of 1 m/s and 2 m/s (nominal) is followed by damage at 3 m/s (nominal). This specimen type was penetrated at 4 m/s (nominal). The order of no damage (N), damage (D), and penetration (P) with increasing velocity is never violated by any of the specimens. It should be noted that specimen types R1S3T1 (half cylinders) and R1SCT1 (full cylinders) were not damaged at any of the impact velocities.

The x-ray photography method of damage visualization can be used to show damage progression with increasing impact velocity for a given specimen type. For example, consider the damage observed in the x-ray photographs for convex specimen type R3S1T3 at different velocities. No damage occurred at an impact velocity of 1.0 m/s but damage extent increased as the impact velocity increased from 2.0 m/s to 4.0 m/s as can be seen in the x-ray photographs of the damaged specimens in Figure 5.57. At an impact velocity of 2.0 m/s, damage is observed to be a matrix crack along the 45° direction of the composite through the center of the specimen (this matrix split was visually observed on the back side of the specimen as well). A delamination extends along and around this matrix crack. In the actual photograph, matrix cracks extending approximately the length of the delamination can be seen in the 0° and -45° directions. At an impact velocity

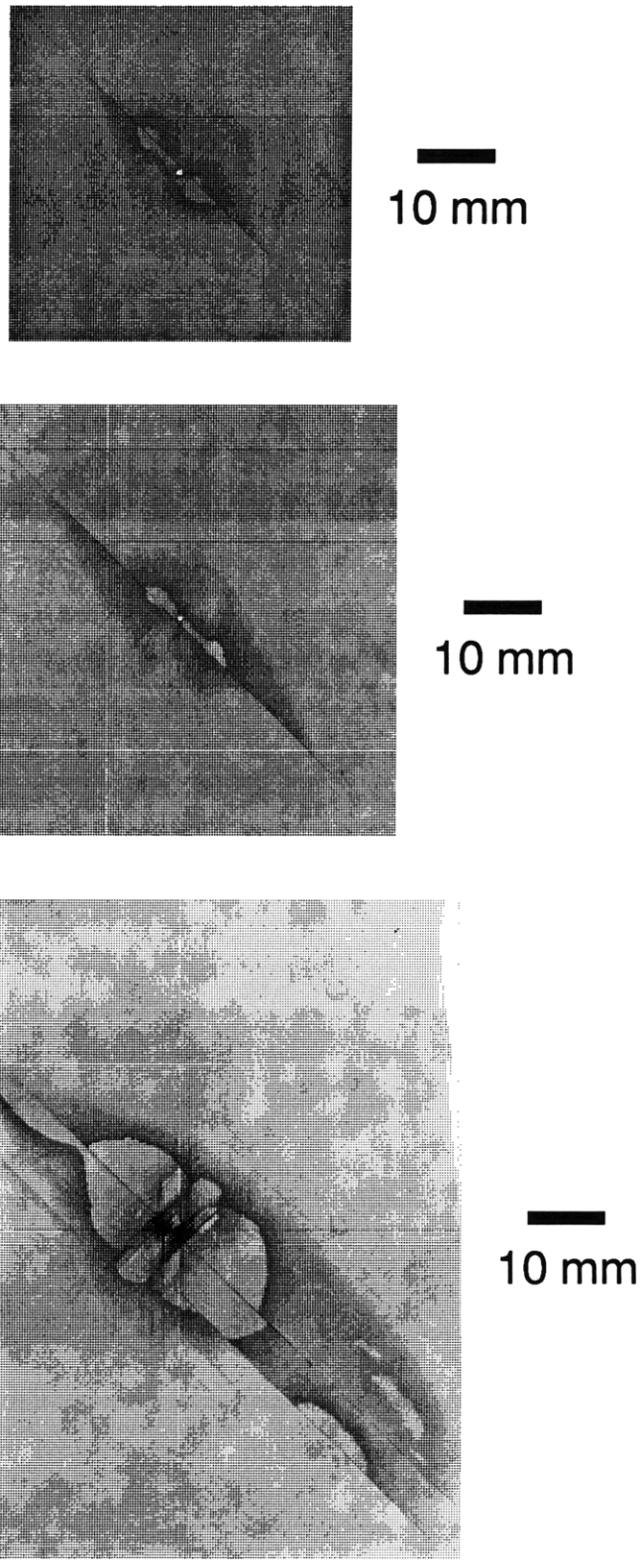

Figure 5.57 X-ray photographs of specimen type R3S1T3 impacted at: (*top*) 2.0 m/s, (*middle*) 3.0 m/s, and (*bottom*) 4.0 m/s.

of 3.0 m/s, these same damage modes are seen to extend further in all directions with the 45° matrix crack extending to nearly 100 mm in length. The other matrix cracks have also extended slightly and become more densely spaced while the delamination has also extended. Finally, at an impact velocity of 4.0 m/s, specimen type R3S1T3 shows a significant extension of all the previous damage modes as well as formation of large delaminations oriented at -45°. Matrix cracks at 0° are also clearly visible. Delaminations away from the central delamination area can also be seen to form near the matrix cracks which have themselves extended. A matrix split is visually observed on the back surface of specimen R3S1T3 impacted at 2.0 m/s and 3.0 m/s and two larger matrix splits for the impact at 4.0 m/s.

Although the velocity where damage is first observed may vary, as well as the extent of the damage, the damage modes, and the damage extent progression for specimen R3S1T3 are typical of all specimens up to penetration. Concave specimens typically display a larger damage extent (all modes and directions) for a given impact velocity than identical shells in the convex orientation. The damage x-ray photographs for impacts at different velocities for specimen R1S1T1 (concave) are presented in Figure 5.58 for comparison to Figure 5.56. The only difference between the two cases is the structural orientation (convex or concave) of the specimens. The damage x-ray photograph at 1.1 m/s for specimen R1S1T1 (concave) is difficult to see in Figure 5.58. Four equally sized delaminations (each is approximately 3 mm long) in the 45° and -45° directions can be seen in the actual photograph. Specimen type R1S1T1 was not damaged at impact velocities of 1 m/s or 2 m/s (nominal), whereas specimen type R1S1T1 (concave) was damaged. The concave specimen is noted to be penetrated at an impact velocity of 3 m/s (nominal) while the convex specimen was first observed to have damage at

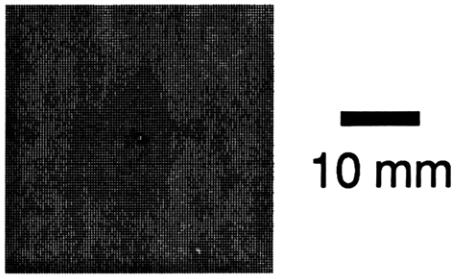

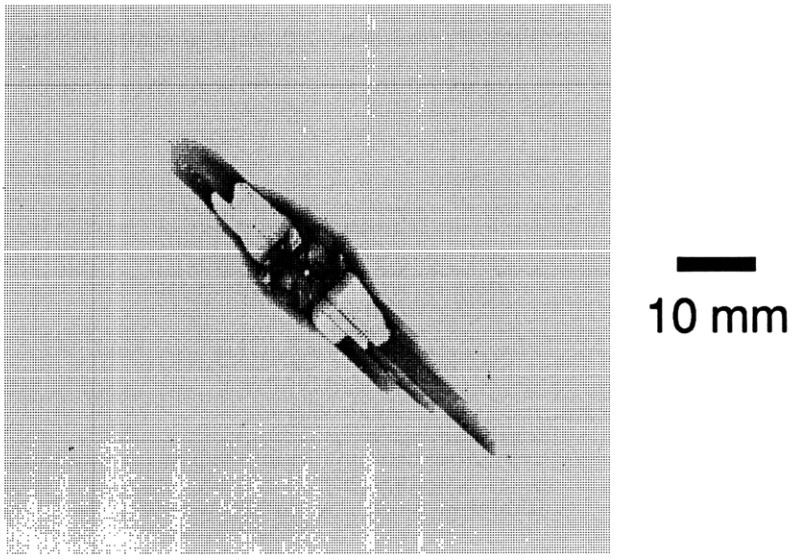

Figure 5.58 X-ray photographs of specimen R1S1T1 (concave) impacted at: (*top*) 1.1 m/s, and (*bottom*) 2.0 m/s. This specimen type was penetrated at an impact velocity of 3.0 m/s.

this impact velocity (see Figure 5.56). It is observed in Tables 5.11 and 5.12 that concave specimens are more extensively damaged and also penetrated at lower impact velocities than corresponding convex specimens. Convex specimen type R1S1T1 was penetrated at an impact velocity of 3.9 m/s while specimen type R1S1T1 (concave) penetrated at an impact velocity of 3.0 m/s. The plate specimen for the same thickness and span shows damage similar to specimen type R1S1T1 (concave). The x-ray photographs of the damage state for specimen type RPS1T1 are shown in Figure 5.59. A small delamination (5 mm long total) at 45° can be seen in the damage photo of the specimen impacted at 1.1 m/s accompanied by a 5 mm long matrix crack also at 45° in Figure 5.59. As with specimen type R1S1T1 (concave), specimen RPS1T1 was penetrated at an impact velocity of 3.0 m/s. Although the damage extent is slightly different, specimen types R1S1T1 (concave) and RPS1T1 have the same damage classifications at each velocity.

Most specimens exhibited the modes and shapes of damage shown thus far. Either a single large delamination at 45° or two delaminations, another at -45° also, are found in the x-ray photographs in Appendix B. The damage is typically accompanied by matrix cracking at 45°. Figure 5.60 contains three x-ray photographs of damaged specimens that have different structural geometries and impact velocities but still display the same general damage modes and extents as discussed up to this point. Specimen R3S1T1 impacted at 1.9 m/s shows a single 'peanut' shaped delamination at 45° while specimen R1S1T2 (concave) impacted at 2.9 m/s and specimen R2S3T2 impacted at 3.0 m/s both show a double-peanut delamination because the single peanut has now been joined by a delamination at -45°. Specimen R1S1T2 also displays a barely visible delamination along the 0° fiber direction. Delaminations along

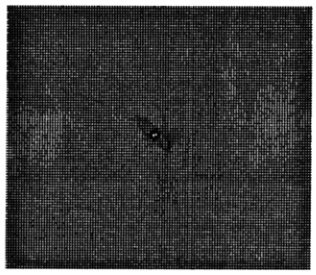

10 mm

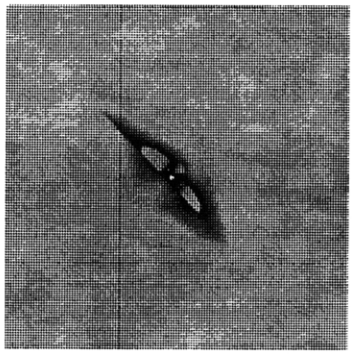

10 mm

Figure 5.59 X-ray photographs of specimen RPS1T1 impacted at: (*top*) 1.1 m/s, and (*bottom*) 2.1 m/s. This specimen type was penetrated at an impact velocity of 3.0 m/s.

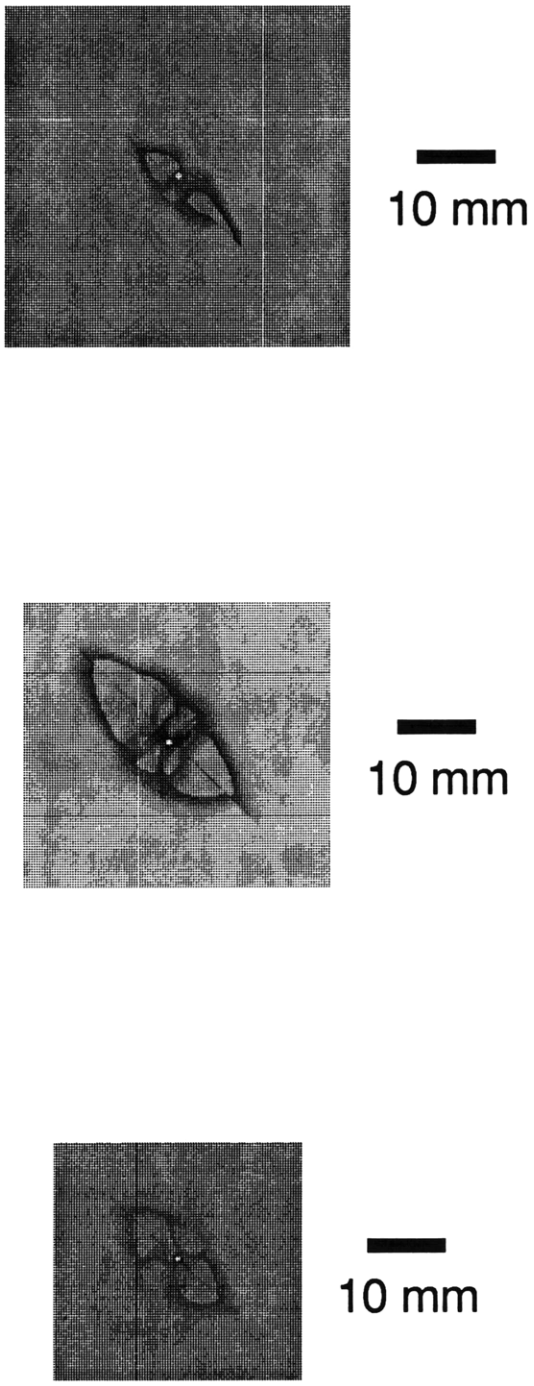

Figure 5.60 X-ray photographs of specimens with typical damage states: (*top*) R3S1T1 impacted at 1.9 m/s, (*middle*) R1S1T2 (concave) impacted at 2.9 m/s, and (*bottom*) R2S3T2 impacted at 3.0 m/s.

the 0° fiber direction are difficult to see in the x-ray photographs because of the typically larger delaminations in the 45° and -45° directions.

Based on the typical damage states observed in the x-ray photographs for all specimen types, a damage metric is introduced to quantify the damage extent observed in the x-ray photographs. The typical delaminations and associated matrix cracking in the 45° and -45° direction, as illustrated in Figure 5.60, are used to quantify the extent of the damage in the x-ray photographs. Appendix D contains the lengths of the delaminations for each specimen in the 45° and -45° directions, as well as the average of these two lengths. The damage length in the 45° and -45° directions is approximated to the nearest millimeter in the x-ray photographs, e.g. specimen R1S1T2 (concave) impacted at 2.9 m/s (top photograph in Figure 5.60) has measured damage lengths of 26 mm and 10 mm in the 45° and -45° directions, respectively. Spalling-type delaminations cannot be distinguished from other delamination damage in the x-ray photographs and thus are included in the damage length measurements. It should be noted that the actual x-ray photographs were measured and not the scanned pictures presented in Appendix B. The average of the two damage lengths in the 45° and -45° directions is used as a metric for quantifying damage extent. The average damage extent in the x-ray photograph for each specimen is presented in Tables 5.13 and 5.14. In general, for a given specimen type, the average damage extent increases with increasing impact velocity up to penetration, as can be seen in Table 5.14. This is observed for convex, concave, and plate specimens and has previously been reported for plate specimens, e.g. [15]. Trends relating the average damage extent to peak impact force will be discussed in chapter 6.

Damaged specimens always contain damage in the 45° direction and

Table 5.13 Average of Damage Extent[a] in 45° and -45° Directions from X-ray Photographs for Impact Tests[b] at 3 m/s (nominal)

	T1				T2				T3			
Span	R1	R2	R3	RP	R1	R2	R3	RP	R1	R2	R3	RP
S1	*13*	*<u>30</u>*	*<u>11</u>*	P	65	*21*	*24*	28	65	43	14	29
S2	0	*7*	*34*			15				55	20	
S3	0	0	*8*			13	13				18	
S1 concave	P	P	P		18	27			20		25	
SC	0											

[a] All values in mm.

[b] "P" indicates penetration, blanks indicate no test was conducted, *Italics* indicate peak force occurred on the second equilibrium path (instability), and <u>underline</u> indicates specimen slipped in-plane after instability.

Table 5.14 Average of Damage Extent[a] in 45° and -45° Directions from X-ray Photographs for Impact Tests[b] at Various Velocities

		T1				T2	T3
Span	Velocity[c]	R1	R2	R3	RP	R2	R3
S1	1	0	0	0	3	8	0
	2	0	*10*	*10*	8	11	12
	3	*13*	*30*	*11*	P	*21*	14
	4	*P*	*P*	*P*		*24*	49
S2	1	0					
	2	0					
	3	0					
	4	0					
S3	1	0					
	2	0					
	3	0					
	4	0					
S1 concave	1	6					
	2	19					
	3	P					
	4						
SC	1	0					
	2	0					
	3	0					
	4	0					

[a] All values in mm.

[b] "P" indicates penetration, blanks indicate no test was conducted, *Italics* indicate peak force occurred on the second equilibrium path (instability), and underline indicates specimen slipped in-plane after instability.

[c] Nominal velocity in m/s.

this damage extent is always greater than in the -45° direction. Therefore, the 45° direction is considered the principal damage direction. Damage extent (in the 45° and -45° directions) in x-ray photographs for convex specimens with a response that remains on the first equilibrium path (no instability) is observed to be larger in the -45° direction, relative to the 45° direction, than for specimens that have the peak impact force on the second equilibrium path (instability). Convex specimens that have an instability typically have the damage extent primarily in the 45° direction. These observations translate into higher -45°/45° damage extent ratios for convex specimens that have peak forces on the first equilibrium path. This "damage extent ratio" is the ratio of the damage extent in the -45° direction to the damage extent in the 45° direction (principal damage direction). This defines the second damage metric (damage extent ratio) to be used with the average damage extent (first metric) for quantifying damage. Damage extent ratios are provided in Tables 5.15 and 5.16. The average damage extent ratio for convex specimens with the instability is 0.34. This compares to the average for convex specimens without the instability of 0.63, nearly twice that of convex specimens that progress past the magnitude of the critical snapping load on the second equilibrium path. In comparison, concave specimens and plates have average damage extent ratios of 0.49 and 0.30, respectively. Appendix D also contains the ratio of the -45° damage extent to the 45° damage extent for all impacted specimens. No trends are evident in Table 5.16 for the damage extent ratio with regard to velocity. As with average damage extent, trends relating the damage extent ratio to peak impact force will be discussed in chapter 6.

It is not true that all the specimens damaged in the typical fashion described thus far. There were four impacted specimens which showed

Table 5.15 Ratio of -45° to 45° Damage Lengths from X-ray Photographs for Impact Tests[a] at 3 m/s (nominal)

	T1				T2				T3			
Span	R1	R2	R3	RP	R1	R2	R3	RP	R1	R2	R3	RP
S1	*0.24*	*<u>0.20</u>*	*<u>0.38</u>*	P	0.86	*0.35*	*0.26*	0.27	0.86	0.55	0.87	0.41
S2	-	*0.56*	*0.18*			0.43				0.57	0.56	
S3	-	-	*0.60*			0.63	0.67				0.57	
S1 concave	P	P	P		0.38	0.33			0.44		0.67	
SC	-											

[a] "P" indicates penetration, blanks indicate no test was conducted, *Italics* indicate peak force occurred on the second equilibrium path (instability), and <u>underline</u> indicates specimen slipped in-plane after instability.

Table 5.16 Ratio of -45° to 45° Damage Lengths from X-ray Photographs for Impact Tests[a] at Various Velocities

Span	Velocity[b]	T1 R1	T1 R2	T1 R3	T1 RP	T2 R2	T3 R3
S1	1	-	-	-	0.20	0.50	-
	2	-	*0.36*	*0.25*	0.33	1.00	0.53
	3	*0.24*	*0.20*	*0.38*	P	*0.35*	0.87
	4	*P*	*P*	*P*		*0.27*	0.21
S2	1	-					
	2	-					
	3	-					
	4	-					
S3	1	-					
	2	-					
	3	-					
	4	-					
S1 concave	1	0.71					
	2	0.41					
	3	P					
	4						
SC	1	-					
	2	-					
	3	-					
	4	-					

[a] "P" indicates penetration, blanks indicate no test was conducted, *Italics* indicate peak force occurred on the second equilibrium path (instability), and underline indicates specimen slipped in-plane after instability.

[b] Nominal velocity in m/s.

atypical x-ray photographs of the damage area. Specimens R1S1T2 and R2S2T3, both impacted at 2.9 m/s, show asymmetric and extensive damage states as shown in Figure 5.61. Specimen R1S1T2 shows extensive delamination and matrix cracking at 45°, -45°, and 0°. The damage extends only to one side of the specimen, the lower half of the top photograph in Figure 5.61. The lower photograph shows that specimen R2S2T3 has a biased extent of delamination and matrix cracking at 45°, and again only to one side. Specimens R1S1T3 and R2S1T3, impacted at 2.9 m/s and 2.8 m/s, respectively, also have atypical and large damage states as shown in Figure 5.62. Multiple delaminations and matrix cracks in the 0°, 45°, and -45° directions are observed in the upper photo for specimen R1S1T3. Matrix cracks that have formed in the 0°, 45°, and -45° directions for specimen R2S1T3 are also observed. However, for specimen R2S1T3, the delaminations are noted to form along the 0° direction of the shell instead of in the 45° or -45° directions.

Some other general observations concerning the damage states and evaluation techniques can be made. Front-surface damage, although more difficult to observe visually, is oftentimes not accompanied by visual back-surface damage. Specimens that are visually evaluated as marred oftentimes do not have any damage as evidenced by the x-ray photography method. However, back-surface damage in the form of fiber splits is never found without also observing damage in the x-ray photograph. Spalling-type delaminations are easily visible, as is penetration. Relative to the front-surface marred region of damage, the back-surface matrix splits and spalling are more easily discerned visually. Matrix splitting was the only visible damage (no marring) for convex specimen types R3S1T3 (2.0 m/s and 3.0 m/s) and R3S3T3 (3.1 m/s). Only 6-ply specimens (T1) were fully penetrated

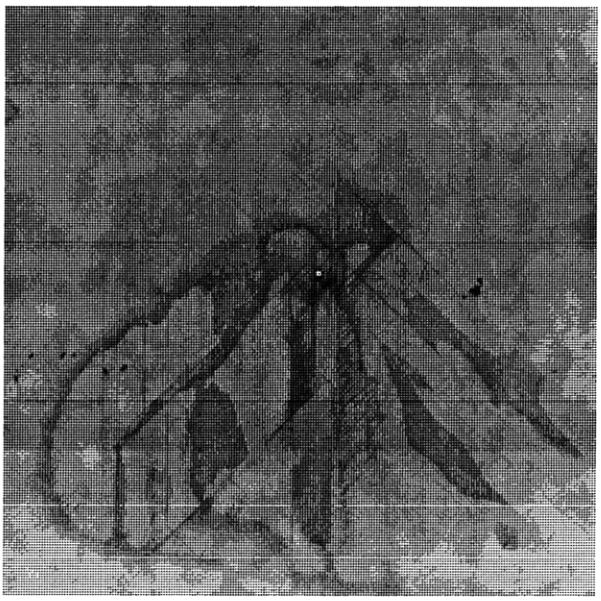

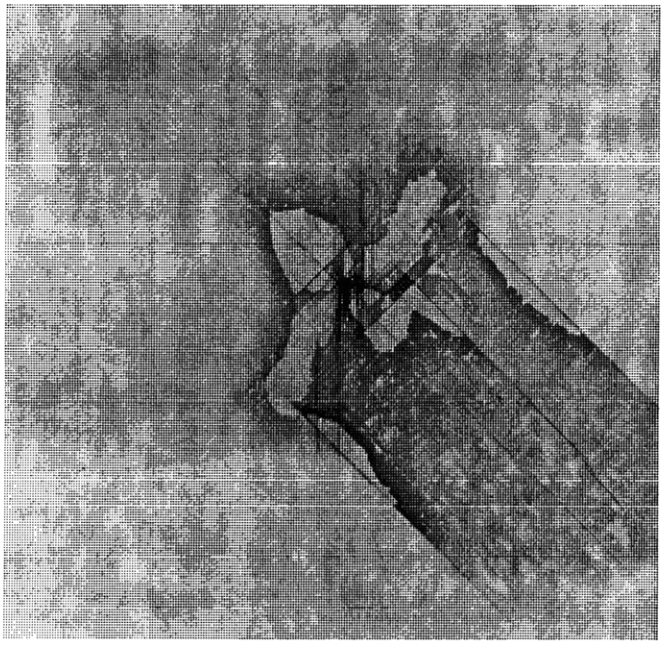

Figure 5.61 X-ray photographs of specimens with atypical damage states: (*top*) R1S1T2 impacted at 2.9 m/s, and (*bottom*) R2S2T3 impacted at 2.9 m/s.

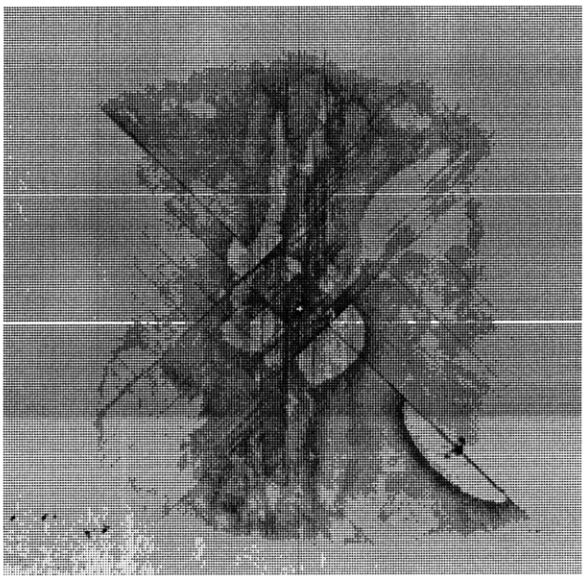

10 mm

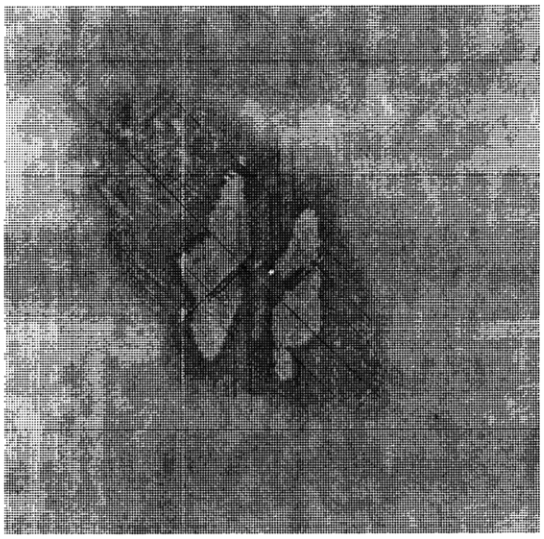

10 mm

Figure 5.62 X-ray photographs of specimens with atypical damage states: (*top*) R1S1T3 impacted at 2.9 m/s, and (*bottom*) R2S1T3 impacted at 2.8 m/s.

during impact testing. Some 12-ply (T2) specimens were nearly penetrated (fiber breaks on front-side and delaminations on the back surface were observed visually) but not fully penetrated. Lastly, it should be noted that the formation of damage, as evidenced by visual inspection and the x-ray photographs, does not visibly affect the force-time signatures; i.e. incipience and damage cannot be discerned in the force-time histories except for penetration. Penetration is indicated by an increase in the secondary oscillations and a substantial drop in load in the force-time history.

5.3 Quasi-Static Testing

Results from quasi-static testing of specimens are presented in this section. Specimens were tested quasi-statically under deflection control to the peak force measured in the tests of corresponding specimens impacted at 3 m/s (nominal). The same boundary conditions (test fixture) used in impact tests are utilized in the quasi-static tests as well. It should also be noted that the stroke of the testing machine is a good measure of the specimen deflection because the maximum difference in the stroke and deflection measurements will be shown to be less than 0.02 % in chapter 6.

Following the same format as section 5.2, force-deflection data is presented to characterize the response of the specimens to loading. Data for specimens with peak forces that occur on the second equilibrium path, above the critical snapping load, are distinguished by the "instability" notation as in sections 5.1 and 5.2. The global response characterization is then followed by the force-indentation results and the resulting contact parameters that can be calculated from this data and used to characterize the local behavior.

Lastly, visual and x-ray photography damage characterization results are presented.

5.3.1 Loading Response

Force-deflection histories for all specimens tested can be found in Appendix E. It should be noted that four specimens were not loaded to the peak force desired because the deflections of the shells exceeded the chosen stroke range of the testing machine. The method used to determine this range was given in chapter 3 and was based on maximum values of deflections calculated from impact data. The (desired/attained) peak forces for these specimens are 220/260 N (R1S3T1), 150/220 N (R1SCT1), 1180/1390 N (instability) (R2S1T1), and 1110/1250 N (instability) (R3S1T1). Specimen R2S1T1 is a special case because it was penetrated during quasi-static testing and the test stopped after the specimen was observed to penetrate. In section 5.2, it was observed that three specimens slipped in-plane during impact testing. No specimens tested quasi-statically were observed to slip in-plane. The loading response for convex specimens (shell sections and cylinders) is presented first, followed by concave shells and plates.

Generally, the force-deflection response of all the specimens can be grouped into three categories based on specimen configuration. Convex shells were observed to either possess an obvious instability or were observed to have two separate and approximately linear regions up to the peak force. Concave shells and plates were similar to one another in that load most often simply increased monotonically.

Force-deflection histories for many convex specimens exhibit the instability behavior discussed in sections 5.1 and 5.2. The force-deflection response and description have already been presented for specimen type

R1S1T1 tested quasi-statically (see Figure 5.6) in section 5.1. The unloading portion of this specimen is different than many of the other specimens tested in that the specimen maintained a stable postbuckled state and the force returns to zero at a large deflection (approximately 24 mm). Typically, the load returns to zero at, or very close to, zero deflection as shown in the response of specimen R2S3T1 in Figure 5.63. The unloading very closely follows the loading for this specimen with only a slight hysteresis in the response. It should also be noted that the unloading curve is always below the loading curve for all specimens tested quasi-statically.

Specimens R2S1T1 and R3S1T1 also exhibited an instability but did not maintain the stable postbuckled condition that specimen R1S1T1 displayed. These shells were two of the four that were only approximately loaded to the peak desired force. Specimen R2S1T1 was penetrated during testing and maintained a stable postbuckled state for approximately one minute during unloading but then snapped back to the convex configuration. Penetration is evident in the discontinuous force-deflection response near the peak force of 1180 N (instability), as shown in Figure 5.64. The stable postbuckling and subsequent return to the convex configuration after approximately 1 minute is evident in the discontinuous unloading curve. After the force returns to zero at a deflection of approximately 13.5 mm (stable postbuckling, the tup loses contact with the specimen), the unloading is noted to resume at a deflection of approximately 6.5 mm. Specimen R3S1T1 also held a stable postbuckled configuration during unloading, but only for a few seconds. The discontinuity in the force-deflection curve for convex specimen R3S1T1 is evident at approximately 1000 N in Figure 5.65 and should not be interpreted as penetration but stable postbuckling.

Specimen R1SCT1 (full cylinder) is a special case of a convex shell and

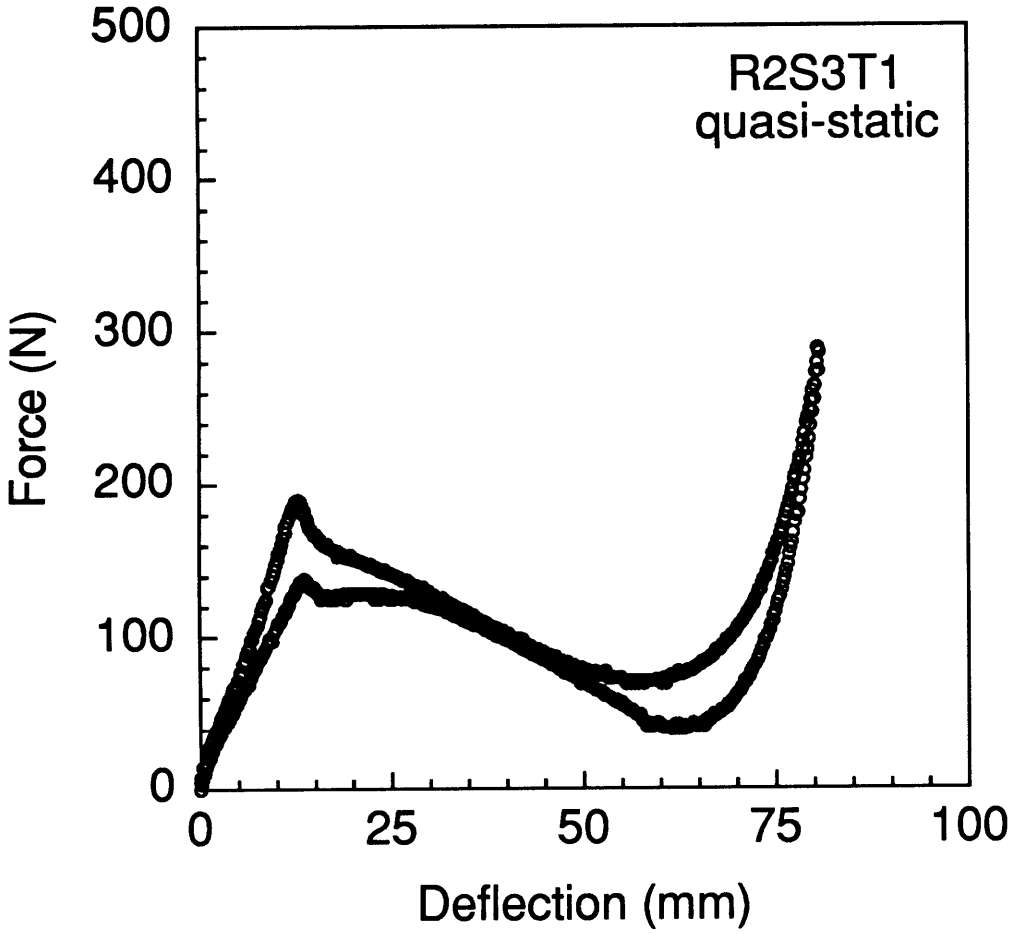

Figure 5.63 Force-deflection history for quasi-static loading and unloading of specimen R2S3T1.

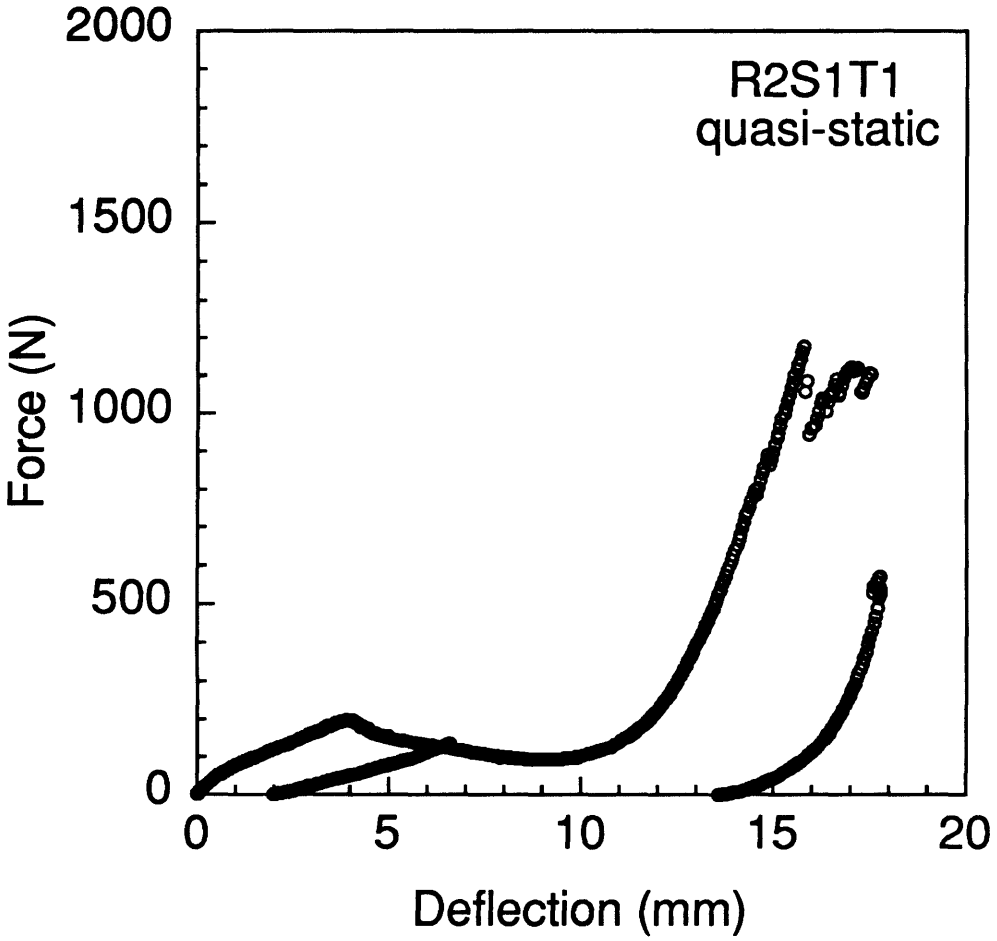

Figure 5.64 Force-deflection history for quasi-static loading and unloading of specimen R2S1T1.

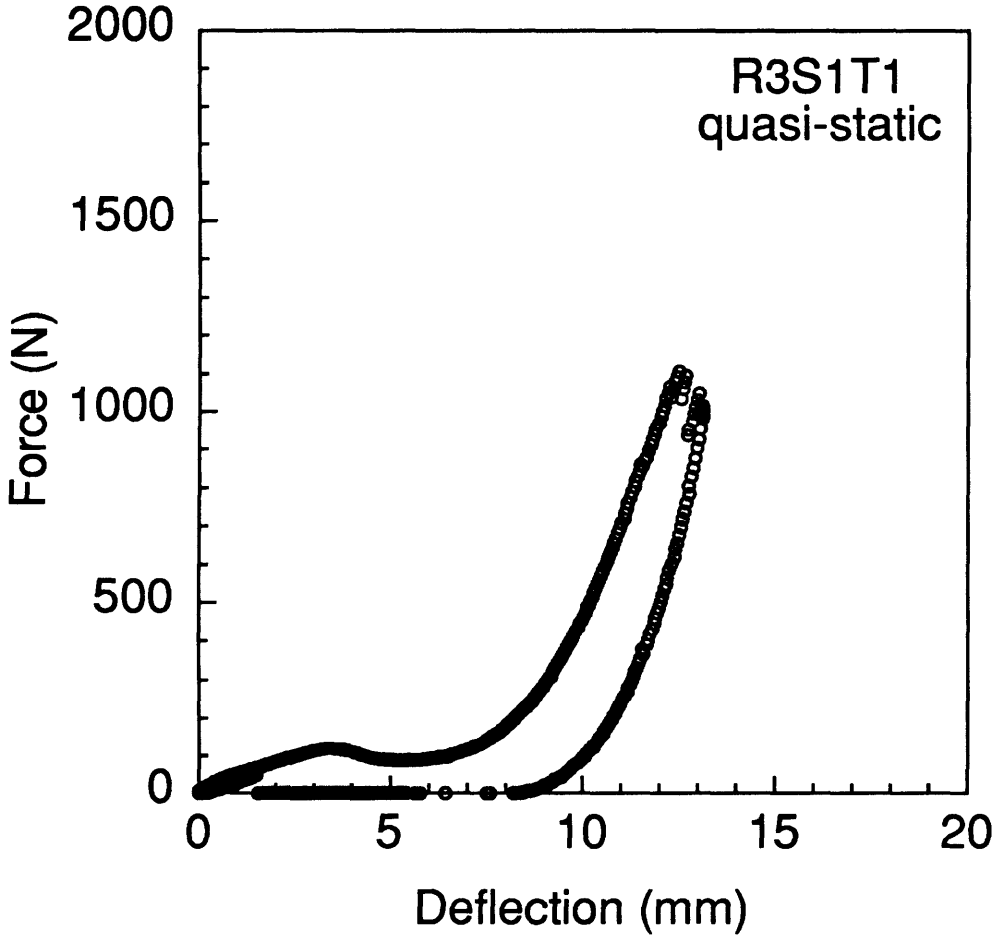

Figure 5.65 Force-deflection history for quasi-static loading and unloading of specimen R3S1T1.

compares to specimen R1S3T1 (half cylinder) supported in the test fixture. Convex shells R1S3T1 and R1SCT1 (full cylinder) do not display the instability behavior, as shown in Figure 5.66. The half cylinder, supported in the test fixture, is noted to have a stiffer response than the full cylinder. The force-deflection response for these specimens displays two distinct loading regions. The first region is nearly linear and lies between 0 mm and approximately 80 mm deflection for the full cylinder and 0 mm and 30 mm for the half cylinder. The second region, which makes up the rest of the loading curves for these two specimens, is nearly linear for the full cylinder but not for the half cylinder. The desired peak force was not obtained for either of these specimens and no damage was observed in the x-ray photographs.

Specimen R1SCT1 deflected a total of 125 mm (nearly equal to the cylinder radius of 152 mm) during loading. Figures 5.67 and 5.68 contain four photographs of the progression of the cylinder cross-sectional deformation under loading. Load levels for the deformation shapes in the photographs were not recorded. Again, white paint has been applied to the shell edge to better visualize the deformation mode shape. The upper photo in Figure 5.67 is of the upper half of the cylinder cross-section in the undeformed configuration. The tup and LVDT (directly beneath the tup) are clearly visible. In the bottom photo in Figure 5.67, the cylinder has deformed in a mode where the cylinder diameter (span) has elongated substantially. Antisymmetry is noticeable in the cross-sectional deformation shape. The antisymmetric cross-sectional deformation is more easily discerned after further displacement of the tup in the upper photograph of Figure 5.68. The diameter of the cylinder is noted to elongate even further by comparison of Figure 5.68 (upper photo) with Figure 5.67. The lower, close-up photograph of the cross-section in Figure 5.68 is presented to more clearly identify the

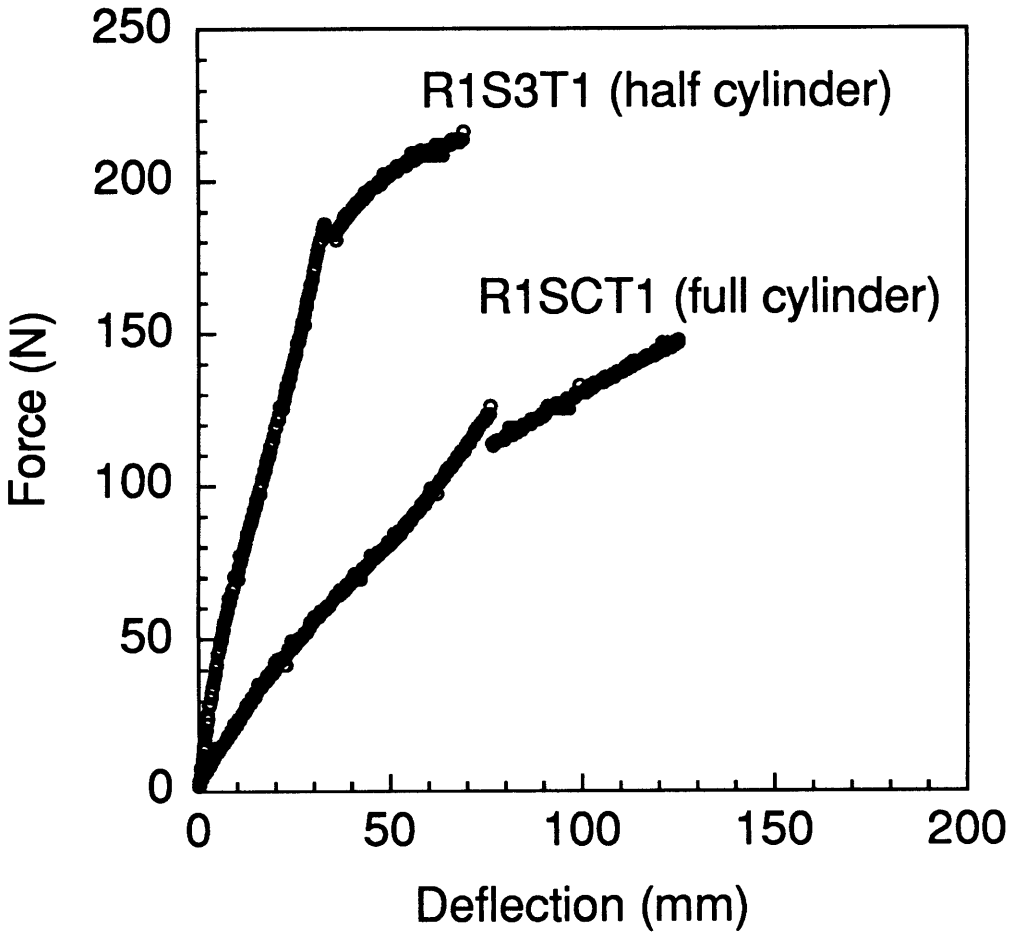

Figure 5.66 Force-deflection histories for quasi-static loading of specimens R1S3T1 and R1SCT1.

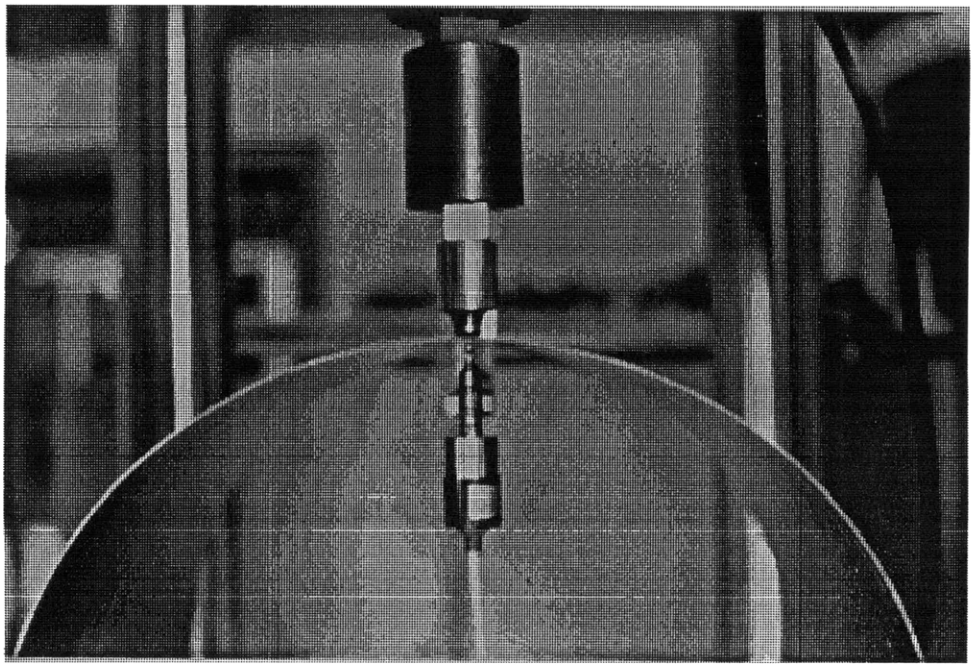

50 mm

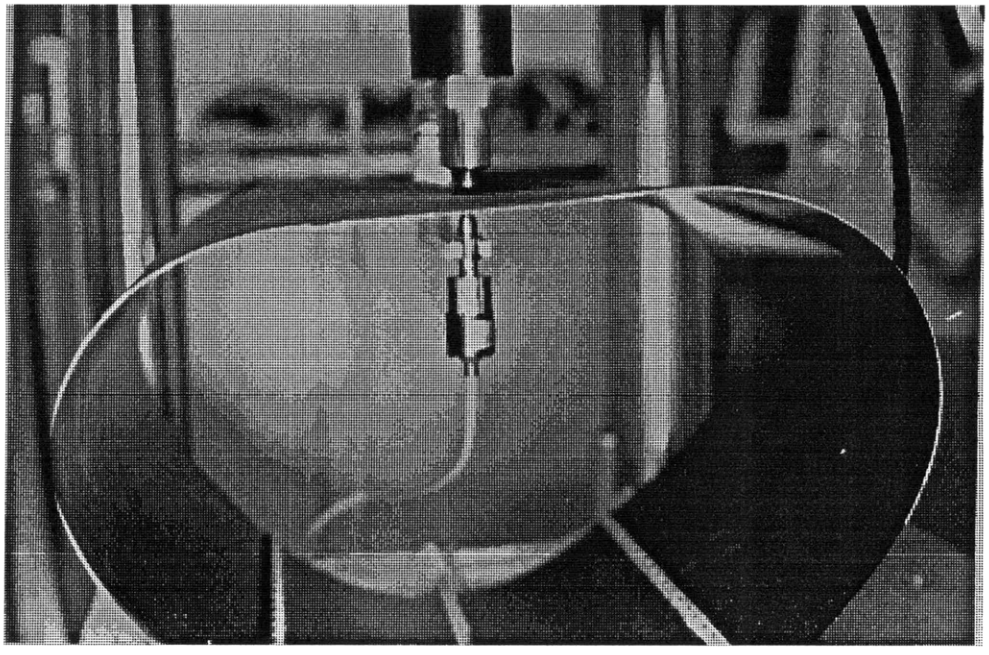

50 mm

Figure 5.67 Photographs of progression of the cross-sectional deformation of specimen R1SCT1 under quasi-static loading.

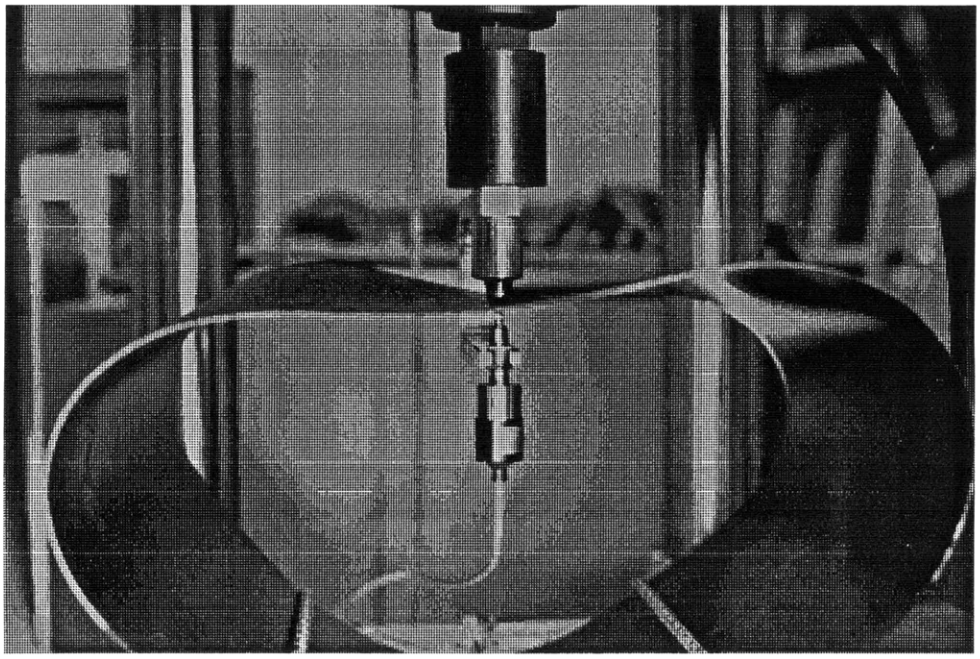

50 mm

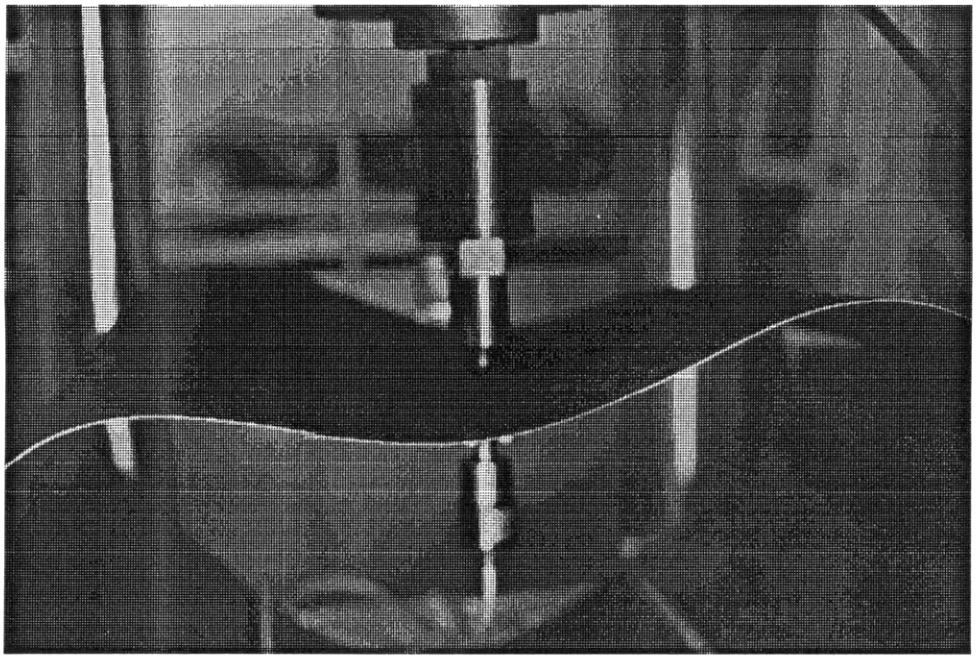

50 mm

Figure 5.68 Photographs of further progression of the cross-sectional deformation of specimen R1SCT1 under quasi-static loading.

shape of the cross-sectional deformation. The antisymmetry is also evident in the deformation along the length of the cylinder. Figure 5.69 contains two photographs showing the same cylinder under loading but from a top/side view. The deformation mode of the half cylinder, specimen R1S3T1, is shown for comparison in Figure 5.70. Antisymmetry along the circumferential edge can be seen in the top photo and also along the length in the bottom photo. The elongation along the diameter is suppressed for the half cylinder by the test fixture boundary condition. Many convex specimens were observed during testing to have antisymmetric deformation shapes, but to a lesser degree than the cylinder and half cylinder as shown in Figures 5.67 through 5.70.

In addition to convex specimens R1S1T1, R2S1T1, and R3S1T1, convex shell specimens R1S2T1, R2S1T2, R2S2T1, R2S3T1, R3S1T2, R3S2T1, and R3S3T1 tested quasi-statically display the instability. All of these specimens were damaged in the x-ray photographs except specimens R1S2T1 and R2S3T1. As with impacted convex specimens in section 5.2, the characteristics of shells with an instability is generally thin and/or shallow. Out of 22 convex shells tested, 10 (45%) of the shells displayed some degree of the instability in the force-deflection response. The force-deflection curve for specimen R1S1T2, presented in Figure 5.71, is a typical example of convex shells that do not display the instability. The curve does not display any of the load-drop behavior characteristic of an instability and yet it is nonlinear. The curve appears nearly linear up to 500 N and then appears to have another linear response, different from the first and with reduced slope, from 500 N to approximately 1400 N. Hysteresis in the force-deflection response is clearly evident. The quasi-static loading response of specimen R3S3T2 given in Figure 5.72 is an example of a specimen that has very little hysteresis.

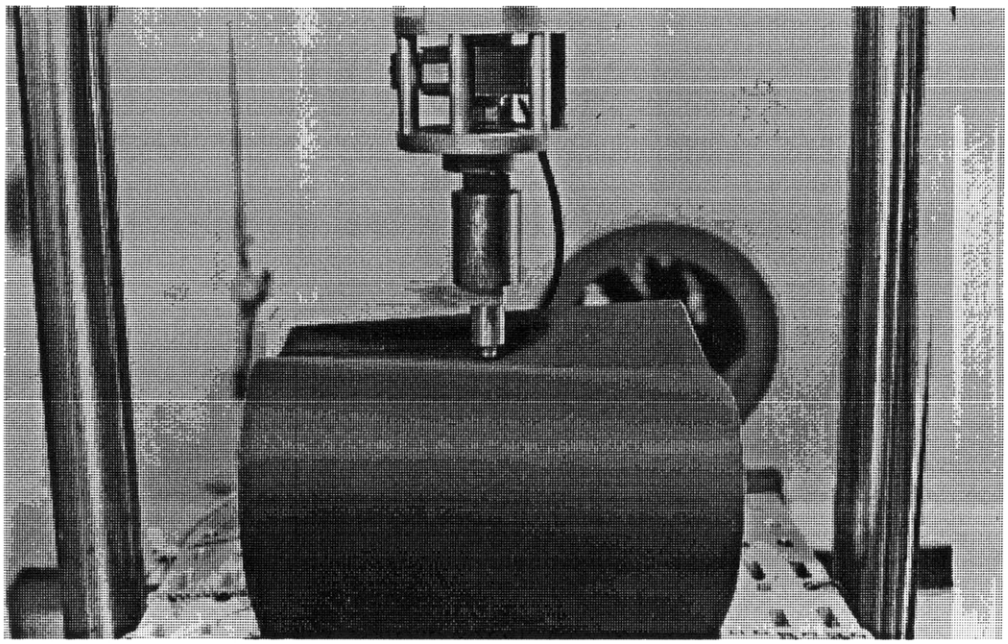

100 mm

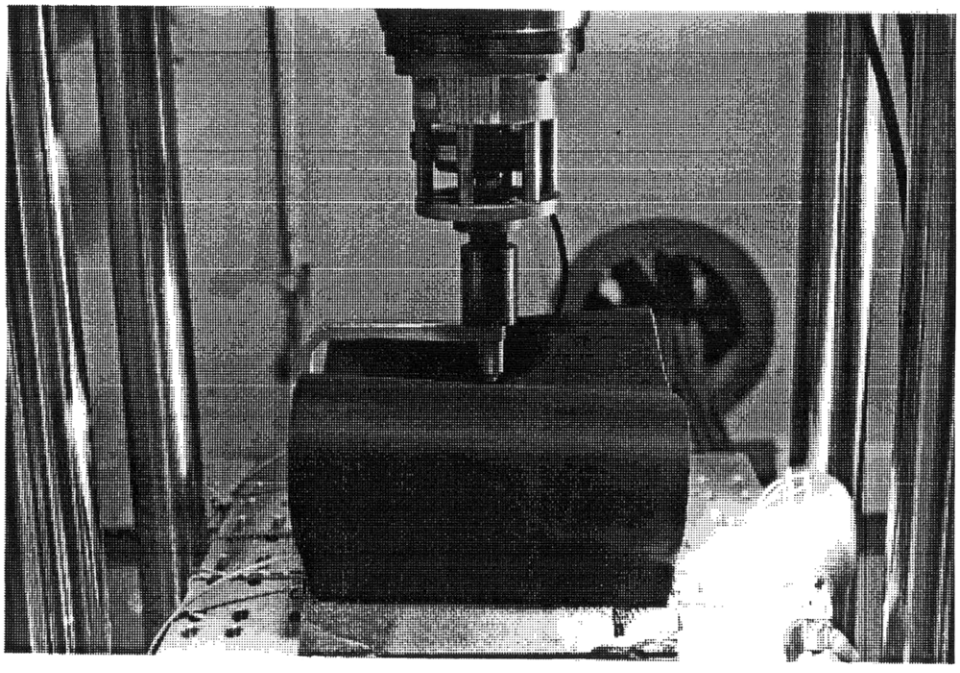

100 mm

Figure 5.69 Side/top view photographs of progression of the deformation of specimen R1SCT1 under quasi-static loading.

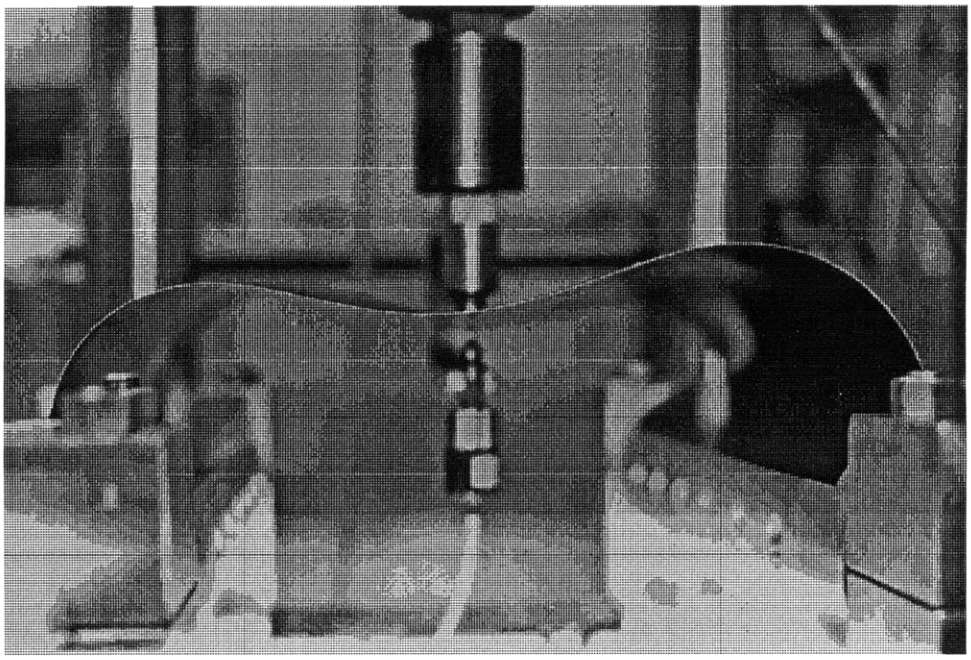

100 mm

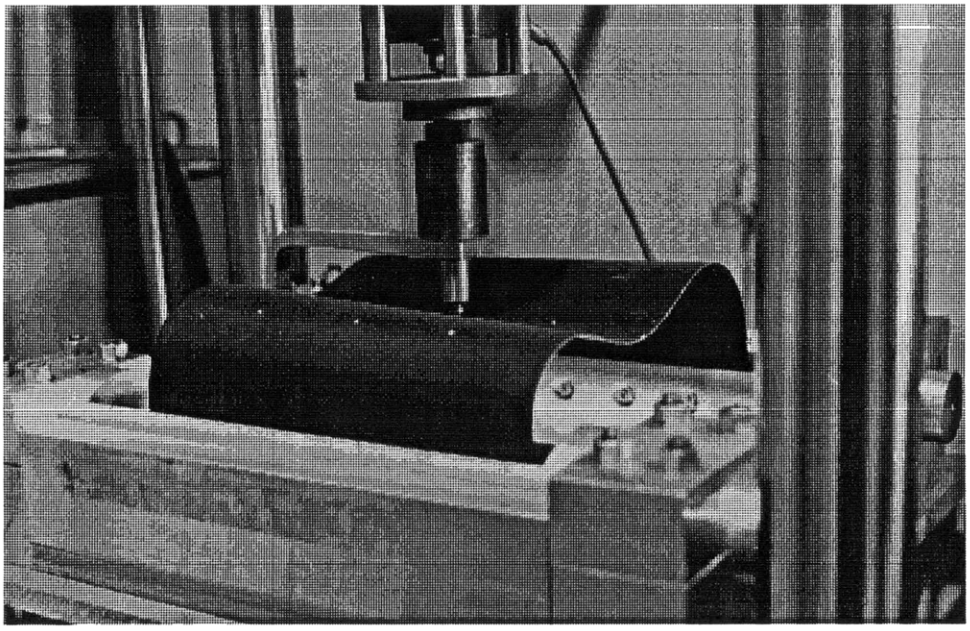

100 mm

Figure 5.70 Photographs of the deformation of specimen R1S3T1 under quasi-static loading.

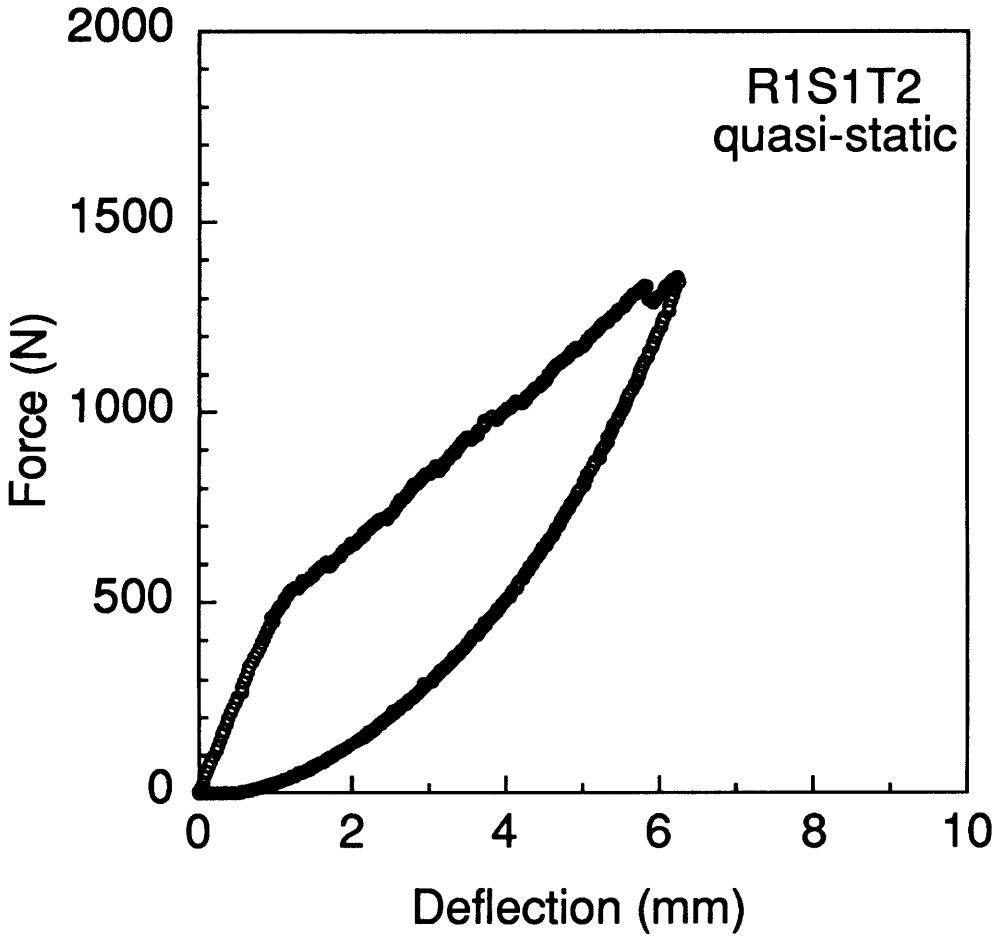

Figure 5.71 Force-deflection history for quasi-static loading and unloading of specimen R1S1T2.

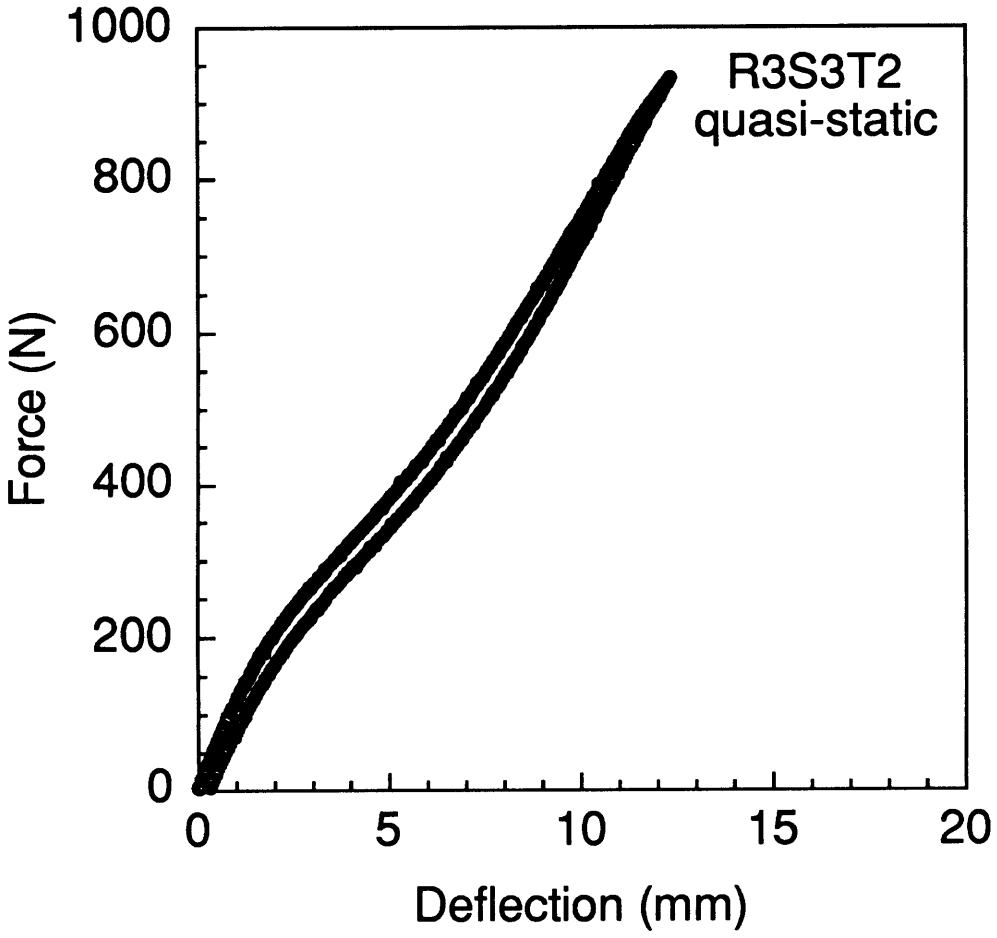

Figure 5.72 Force-deflection history for quasi-static loading and unloading of specimen R3S3T2.

This specimen is also an example of several specimens that did not display the instability behavior but that did show a decrease in stiffness followed by an increase in stiffness after further loading (to approximately the same initial stiffness). Convex specimens R2S2T2, R2S3T2, R3S1T3, R3S3T2, and R3S3T3 were observed to regain stiffness after an initial decrease but did not display the instability. To varying degrees, convex specimens that did not display the instability did display two distinct regions of nearly linear behavior as well as some degree of hysteresis. All convex specimens (excluding specimens R1S3T1 and R1SCT1) that did not display the instability, display damage in the x-ray photographs.

The force-deflection response for concave shells and plates is very similar. No instability is observed in any of the concave shells or plates as might be expected. Figure 5.73 is the force-deflection curve for specimen R1S1T1 (concave) and Figure 5.74 is the response for specimen RPS1T1. Specimen R1S1T1 (concave) has damage in the x-ray photograph and specimen RPS1T1 was penetrated during loading. Figure 5.73 can be compared to Figure 5.6 to illustrate the difference between the concave and convex orientation in the shape of the force-deflection response, i.e. the instability is noted in Figure 5.6 but not in Figure 5.73. Specimen R1S1T1 (concave) is noted to have a stiffer initial response than specimen RPS1T1, and both have greater initial stiffness than specimen R1S1T1. These trends are typical of all specimens tested. The force-deflection curves for specimens R1S1T1 (concave) and RPS1T1 indicate a nonlinear region (stiffening) followed by slight fluctuations in the response along a nearly linear path until the peak force is reached. Considering Figure 5.74, penetration of specimen RPS1T1 is evidenced by the discontinuity near the peak force. Figures 5.73 and 5.74 are two typical examples of concave and plate loading response.

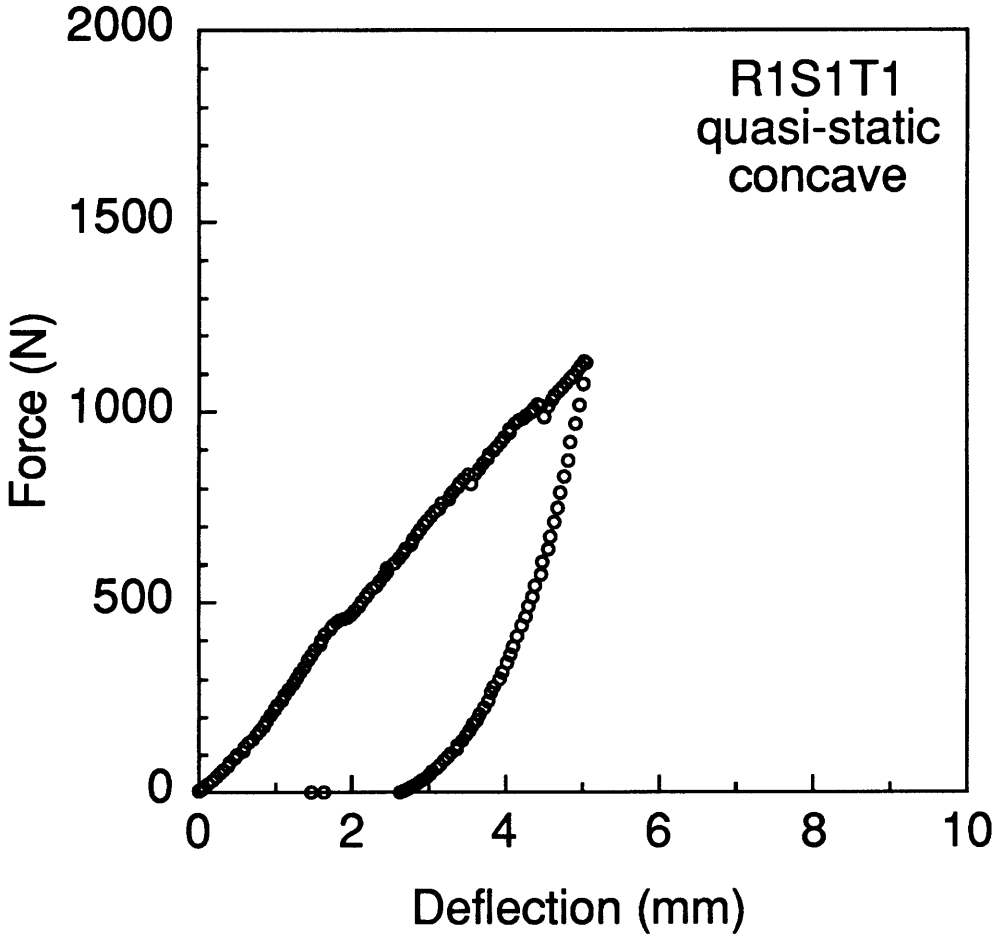

Figure 5.73 Force-deflection history for quasi-static loading and unloading of specimen R1S1T1 (concave).

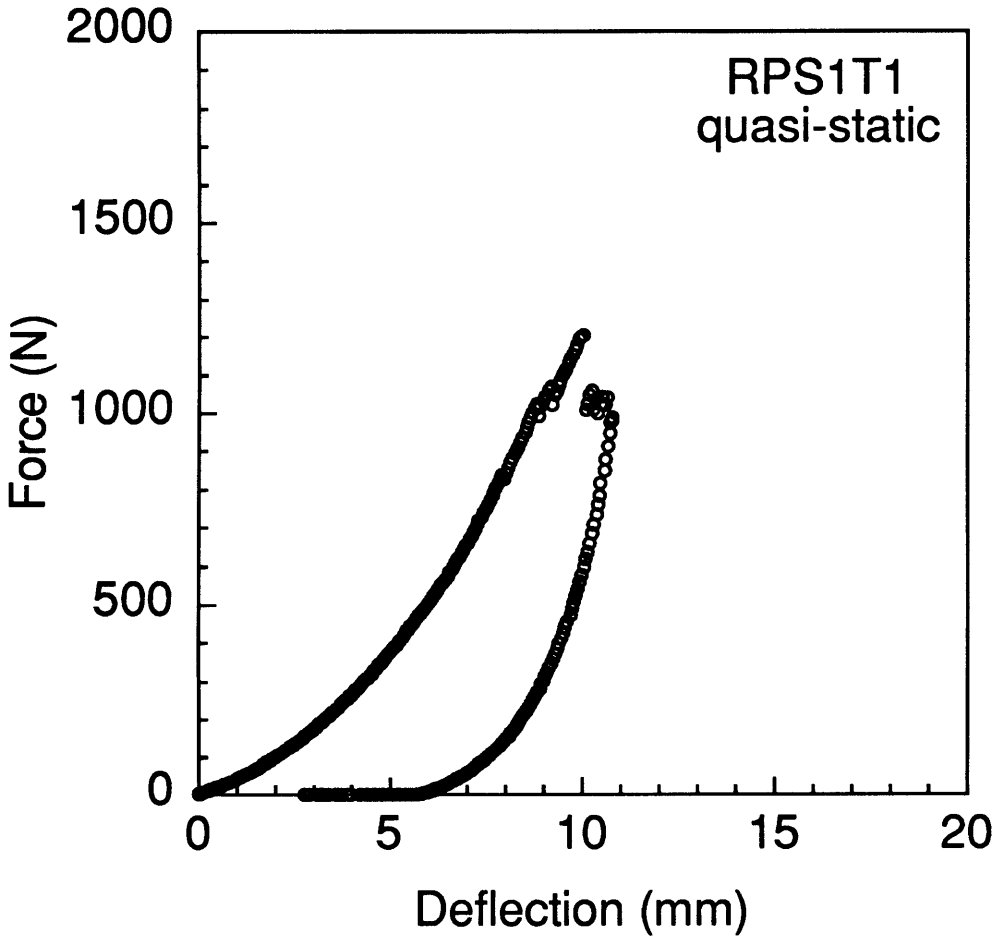

Figure 5.74 Force-deflection history for quasi-static loading and unloading of specimen RPS1T1.

Concave and plate specimens have varying degrees of hysteresis in the unloading curves and it should be noted that all concave and plate specimens were either damaged or penetrated during quasi-static testing.

The test matrix design allows the effects of individual structural parameters (radius, span, and thickness), and ratios of these parameters, on the response shape of specimens tested quasi-statically to be considered. Force-deflection data for impact tests is also available for this same type of comparison, however the high frequency secondary response makes comparisons extremely difficult and inconclusive; the quasi-static data is much easier to compare. The response for S1T1 specimens is presented in Figure 5.75 for the four possible radii in this investigation. All of these specimens had an instability (except RPS1T1) and were damaged during quasi-static testing. There is an observed development of the instability region as radius decreases (increased curvature). The plate specimen (infinite radius) is noted to have no instability region. For specimens with progressively smaller radii, the instability region increases in magnitude both with regard to force and deflection. The critical snapping load and deflection both also increase as specimen radius decreases. This development of the instability region with respect to radius is noted for all convex specimens tested.

Figure 5.76 is a blow-up of Figure 5.75 and allows the initial stiffness of the specimens to be evaluated. The initial stiffness is noted to increase with decreasing radius in Figure 5.76, with the plate having the lowest initial stiffness. This trend of increasing initial stiffness with decreasing radius is noted for all convex and plate specimens tested, regardless of the instability, except for specimen types S3T1. The initial quasi-static response of the S3T1 specimen types is presented in Figure 5.77. The initial stiffness for the R2

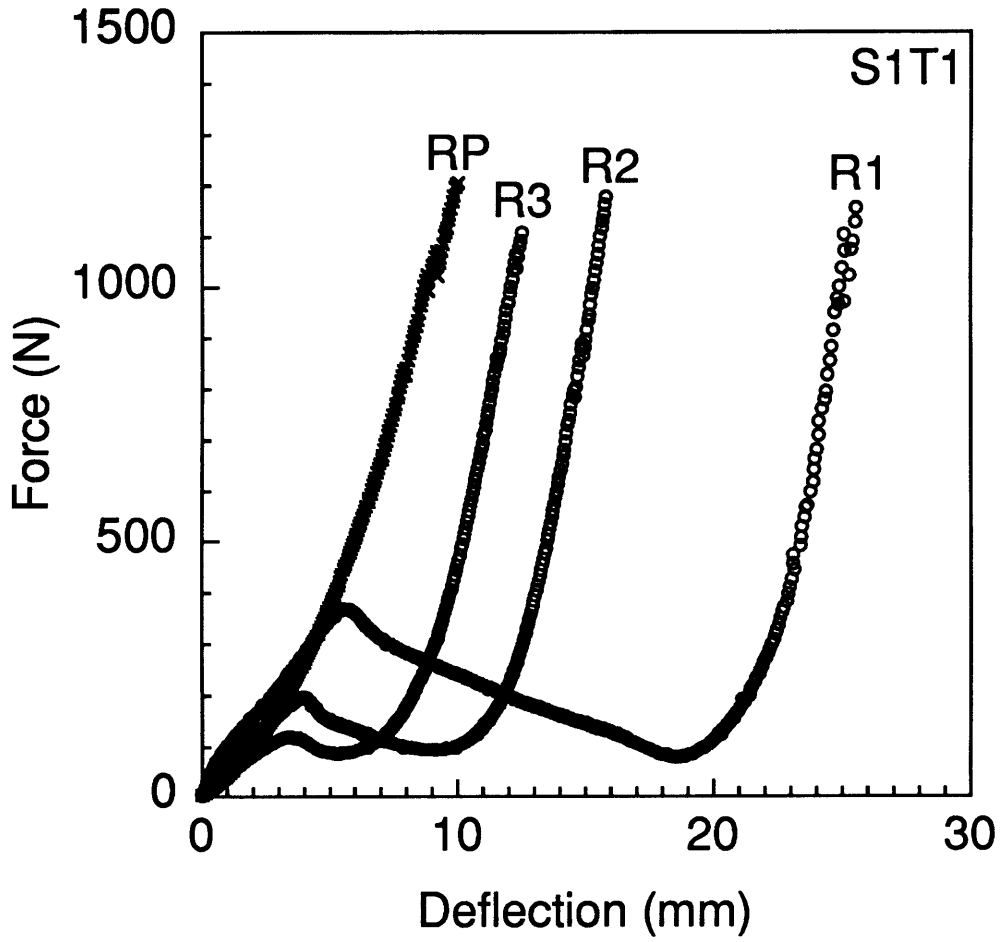

Figure 5.75 Quasi-static loading response of S1T1 plate specimen and convex specimens of various radii.

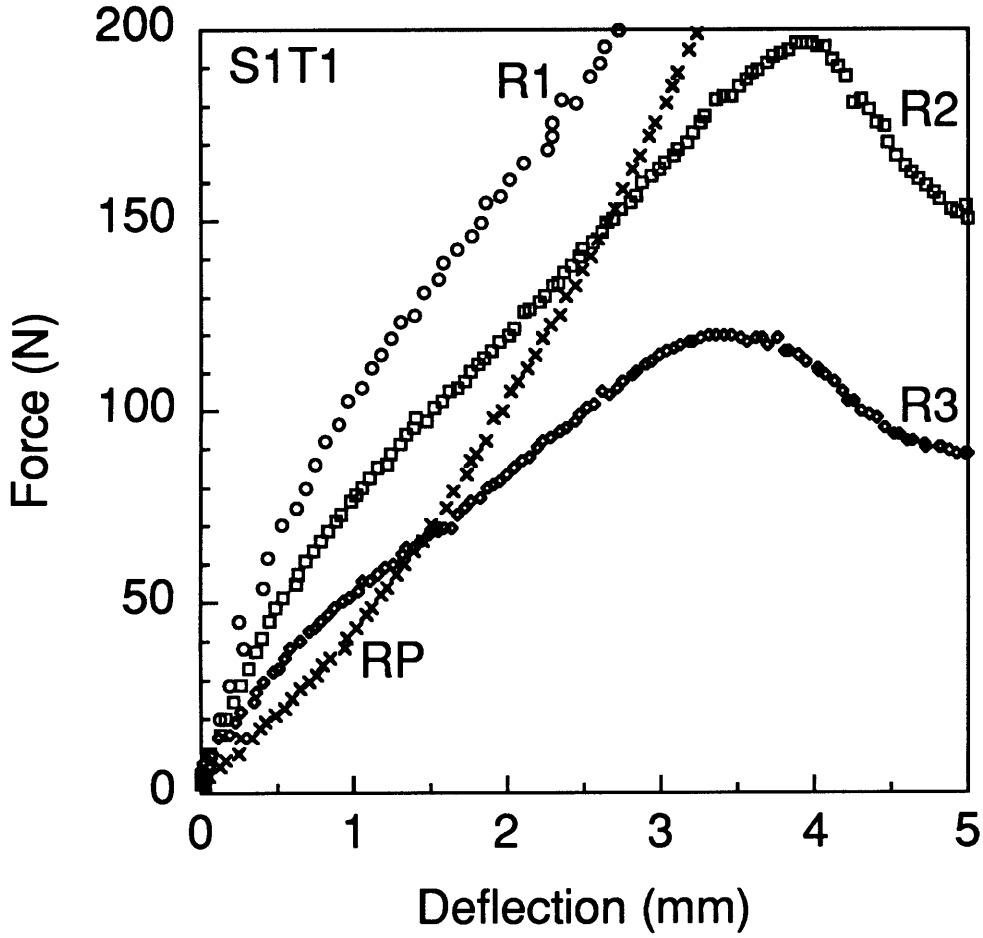

Figure 5.76 Blow-up of Figure 5.75: Quasi-static loading response of S1T1 plate specimen and convex specimens of various radii.

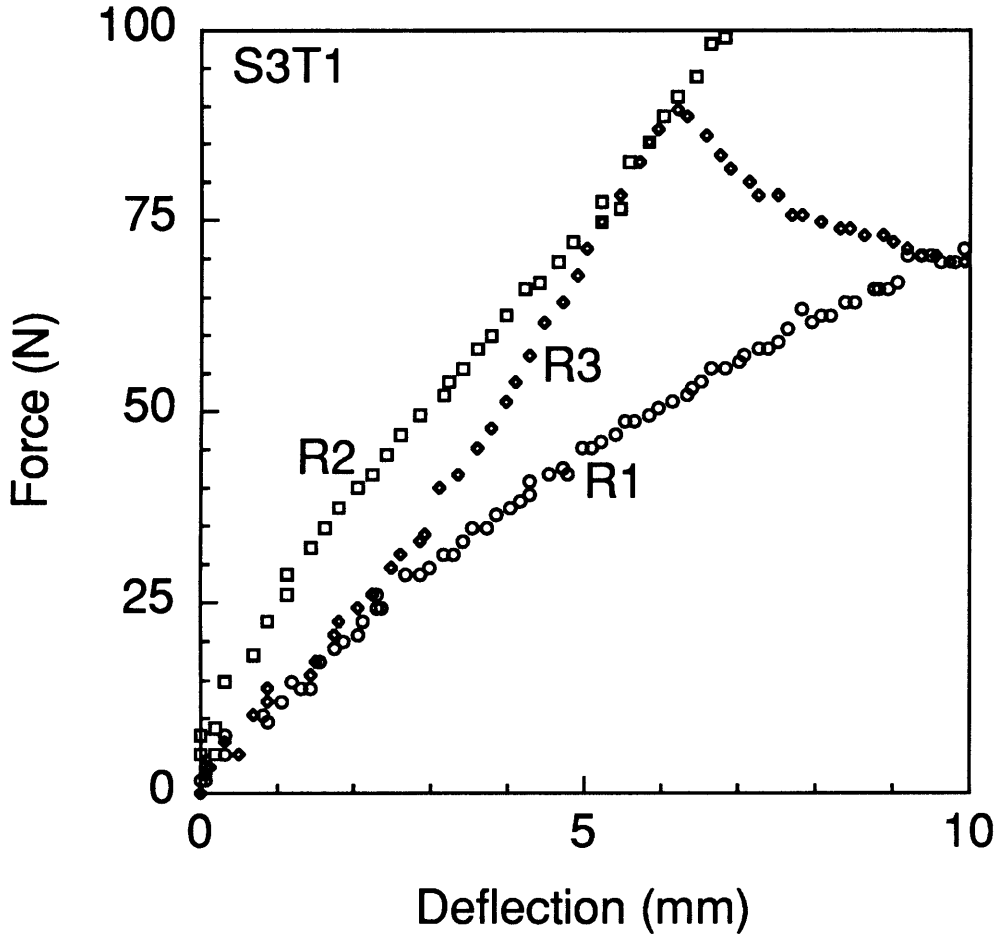

Figure 5.77 Blow-up of quasi-static loading response of S3T1 convex specimens of various radii.

and R3 specimen types is seen to follow the trend of increasing initial stiffness with decreasing radius. However, the R1 specimen type (half cylinder) has an initial stiffness lower than both the R2 and R3 specimen types which does not agree with the previous trend. The effect of radius on the response of concave specimen types S1T1 is shown in Figure 5.78. The initial stiffness increases with decreasing radius for these specimens which is the same trend for identical convex specimens.

The effect of varying the span on the response shape of convex shells is presented in Figures 5.79 and 5.80 for specimen types R2T1 and R2T2, respectively. Increasing the span is noted to have little effect on the critical snapping load in Figure 5.79, but the critical snapping deflection is noted to increase as are the deflections associated with the instability region (deflection between the two equilibrium paths). The initial structural stiffness decreases as the span is increased in both figures, regardless of the instability (initial stiffness decreases slightly from S1 to S2 in Figure 5.80). These trends are repeated for all convex specimens tested.

The effect of thickness is also consistent between specimens with and without the instability. The effect of thickness is evident in the force-deflection histories for specimen types R3S1 and R3S3 in Figures 5.81 and 5.82, respectively. The initial stiffness, critical snapping load, and critical snapping deflection all increase as thickness is increased for convex specimens. Increasing the thickness also increases the initial structural stiffness for concave and plate specimens in all cases.

The effects of maintaining constant radius-to-thickness and radius-to-span ratios on the response shape of convex specimens can also be considered. The response curves of three specimens (all S1) with a constant radius-to-thickness ratio equal to 190 are presented in Figure 5.83. The effect of

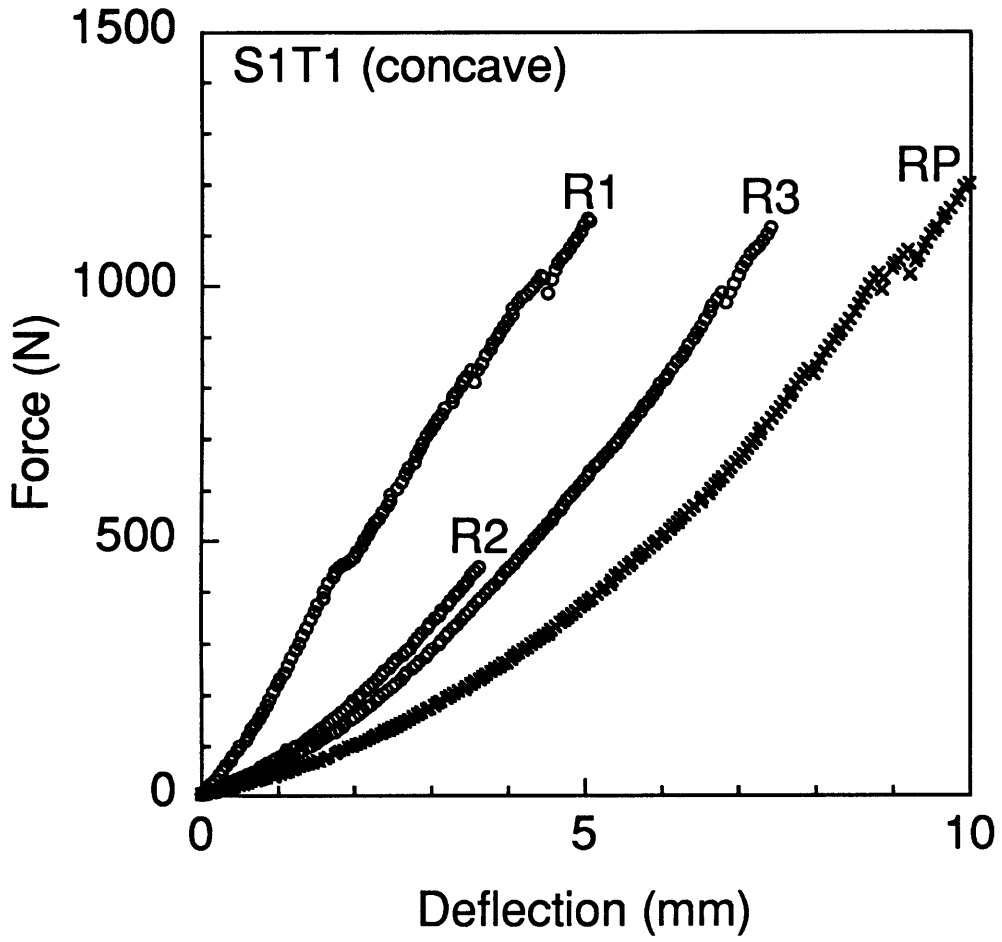

Figure 5.78 Quasi-static loading response of S1T1 plate specimen and concave specimens of various radii.

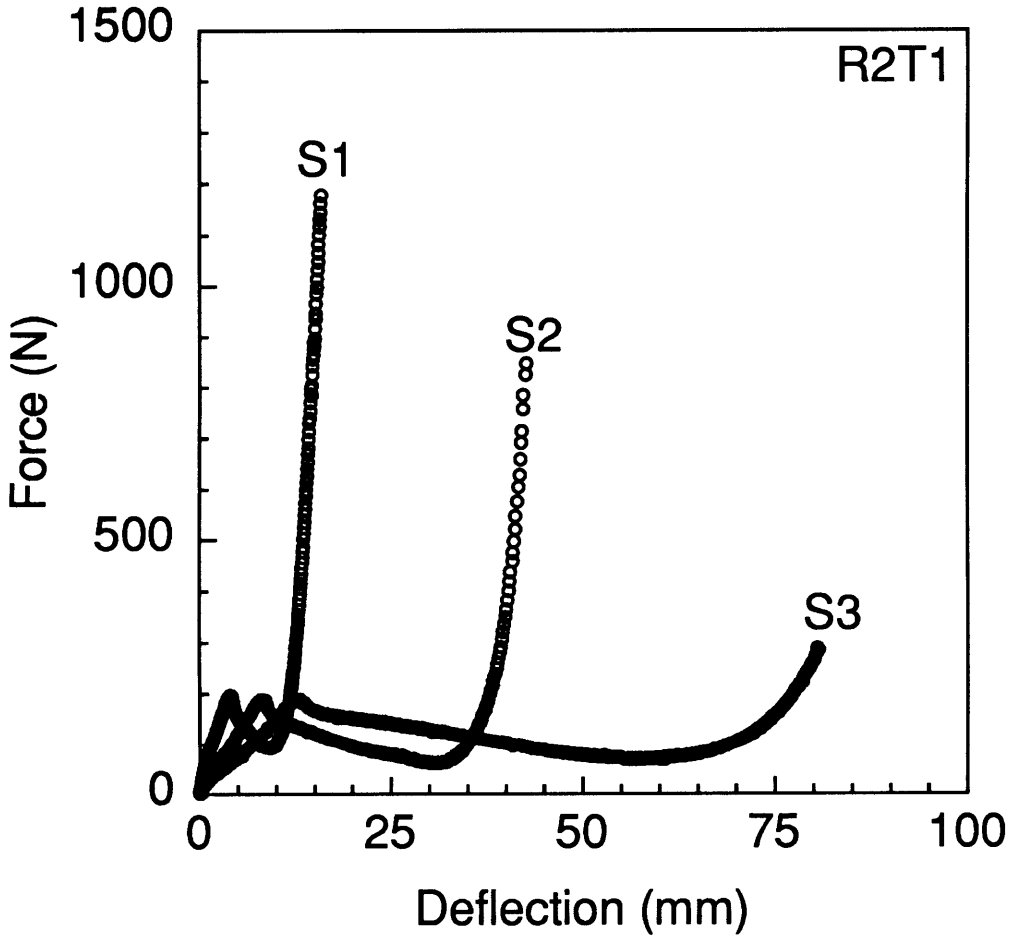

Figure 5.79 Quasi-static loading response of R2T1 convex specimens of various spans.

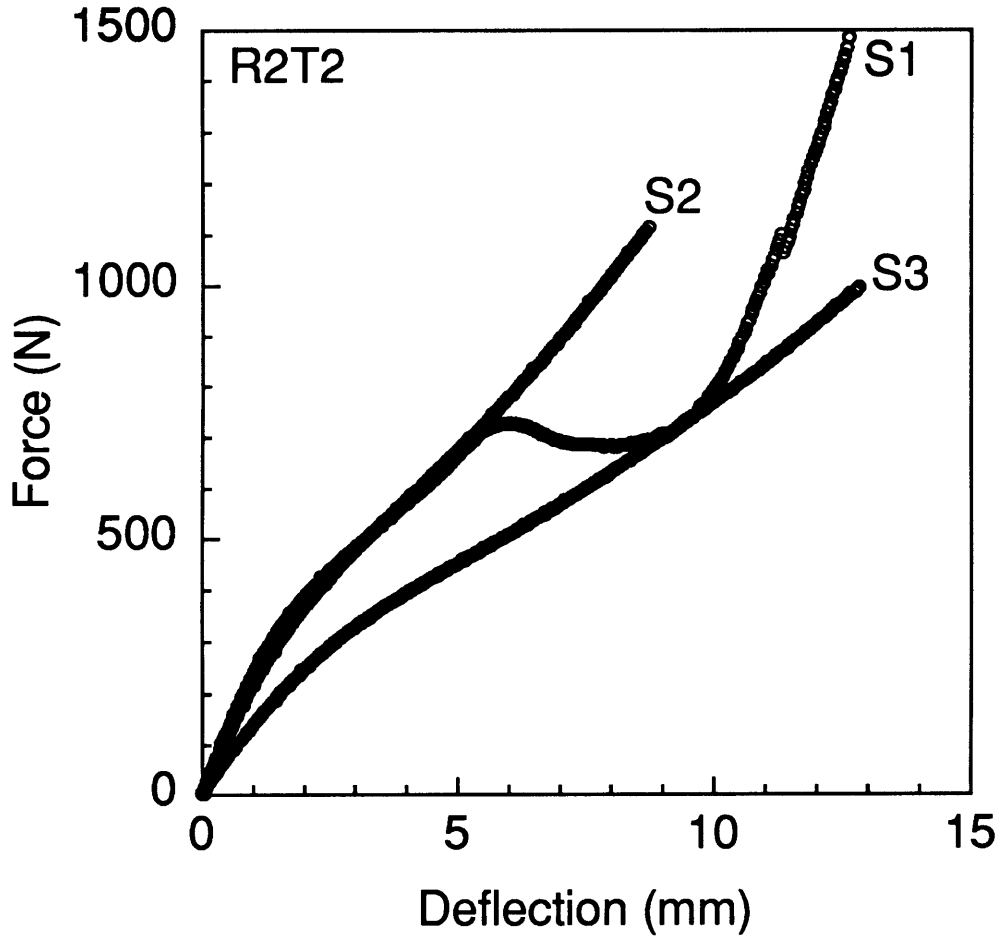

Figure 5.80 Quasi-static loading response of R2T2 convex specimens of various spans.

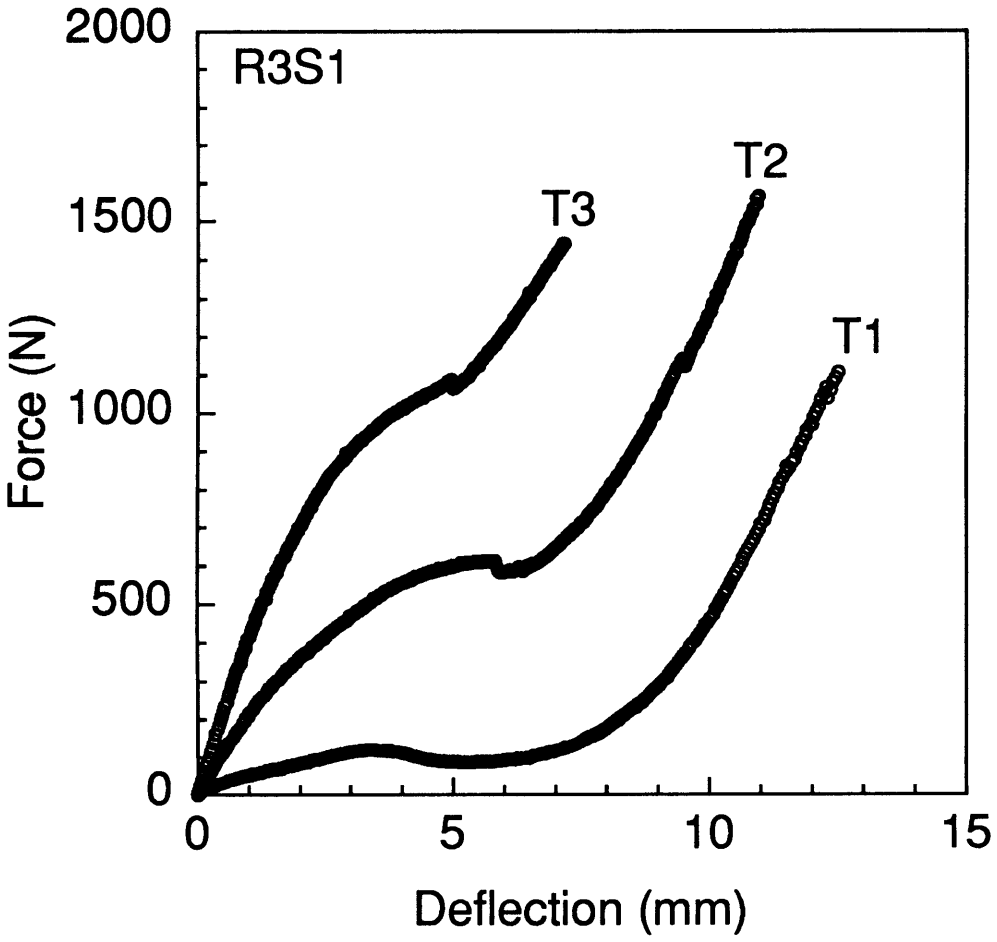

Figure 5.81 Quasi-static loading response of R3S1 convex specimens of various thicknesses.

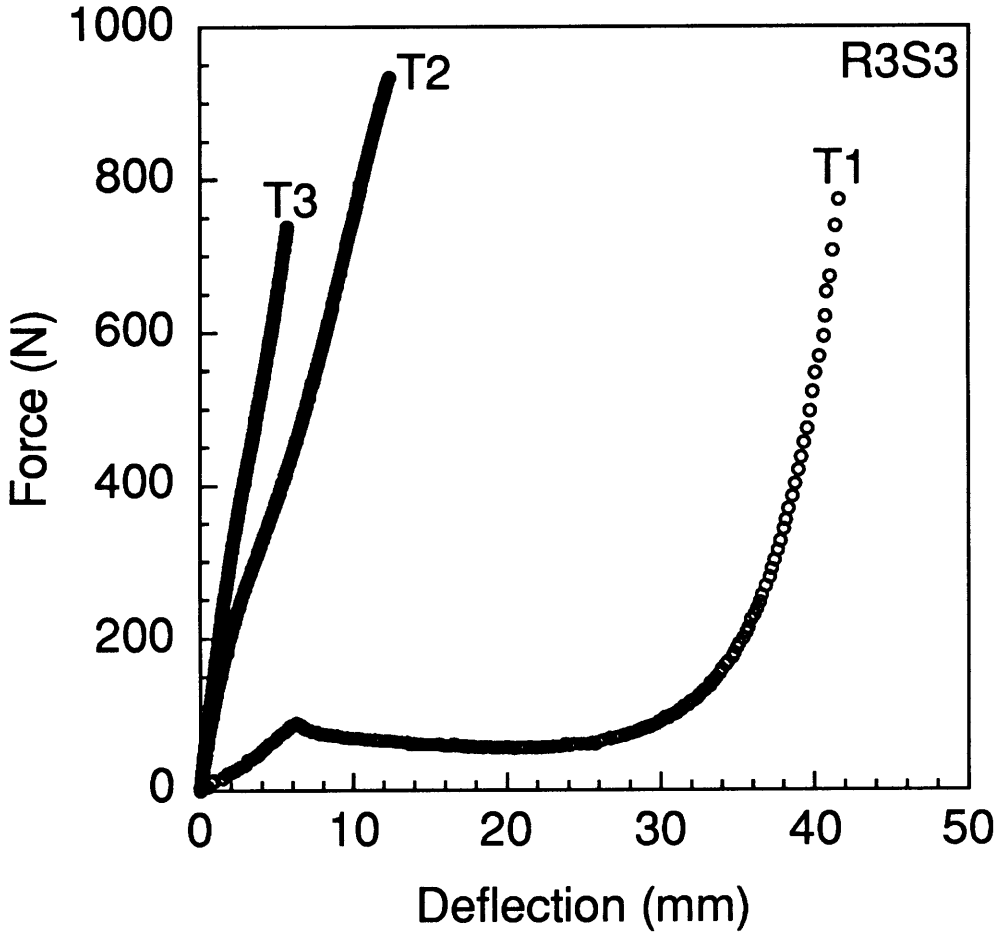

Figure 5.82 Quasi-static loading response of R3S3 convex specimens of various thicknesses.

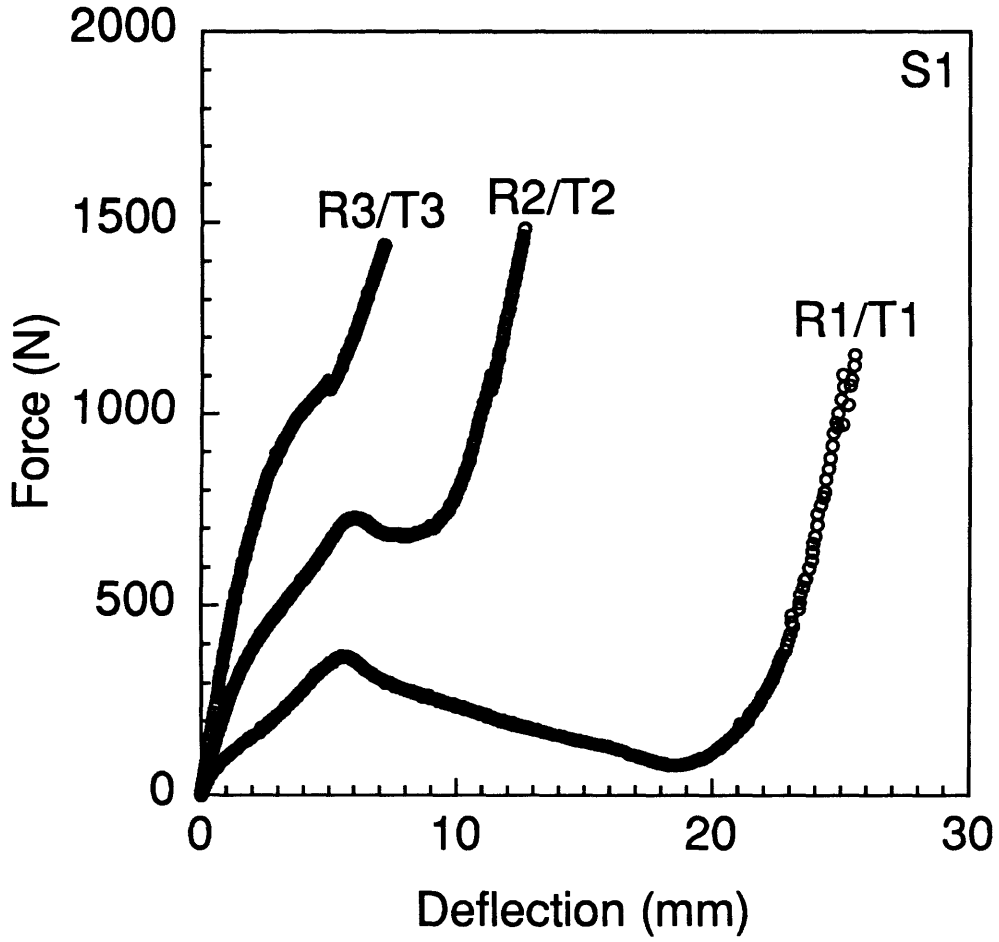

Figure 5.83 Effect of scaling on quasi-static loading response of convex specimens with constant radius-to-thickness ratio (190) and span (S1).

increasing the scaling parameter is noted to change the response significantly, i.e. keeping the radius-to-thickness ratio constant does not give similar shell response. The initial structural stiffness is noted to increase as the scaling parameter increases which follows the trend of increasing the thickness and not the trend for increasing radius. Concave specimens also follow this trend with regard to increasing initial structural stiffness. Other convex specimens with constant radius-to-thickness ratios display the same trends.

The response of specimens with a constant radius-to-span ratio of 1.5 and thickness T1 are presented in Figure 5.84. The response is again noted to change significantly even though the radius-to-span ratio is kept constant. The initial structural stiffness is observed to decrease as the scaling parameter increases which follows the trend of increasing both the radius and span. Other specimens with constant radius-to-span ratio display this same behavior. For a constant radius-to-span ratio, the critical snapping load is noted to decrease with increasing scaling parameter. This follows the trend with respect to increasing radius. The critical snapping load was previously shown to be nearly insensitive to span. Thus, the trend of decreasing critical snapping load with increasing radius and span (increasing the scaling parameter) is actually following the trend with radius.

As described in sections 5.1 and 5.2, two important forces are associated with convex specimens that have a response instability: the peak force and critical snapping load. Critical snapping loads are provided in Table 5.17 for quasi-static tests and the deflections at the critical snapping load are given in Table 5.18. It should be noted that the critical snapping load and deflection are more easily and accurately extracted from quasi-static force-deflection curves than from impact test data. The impact tests have the

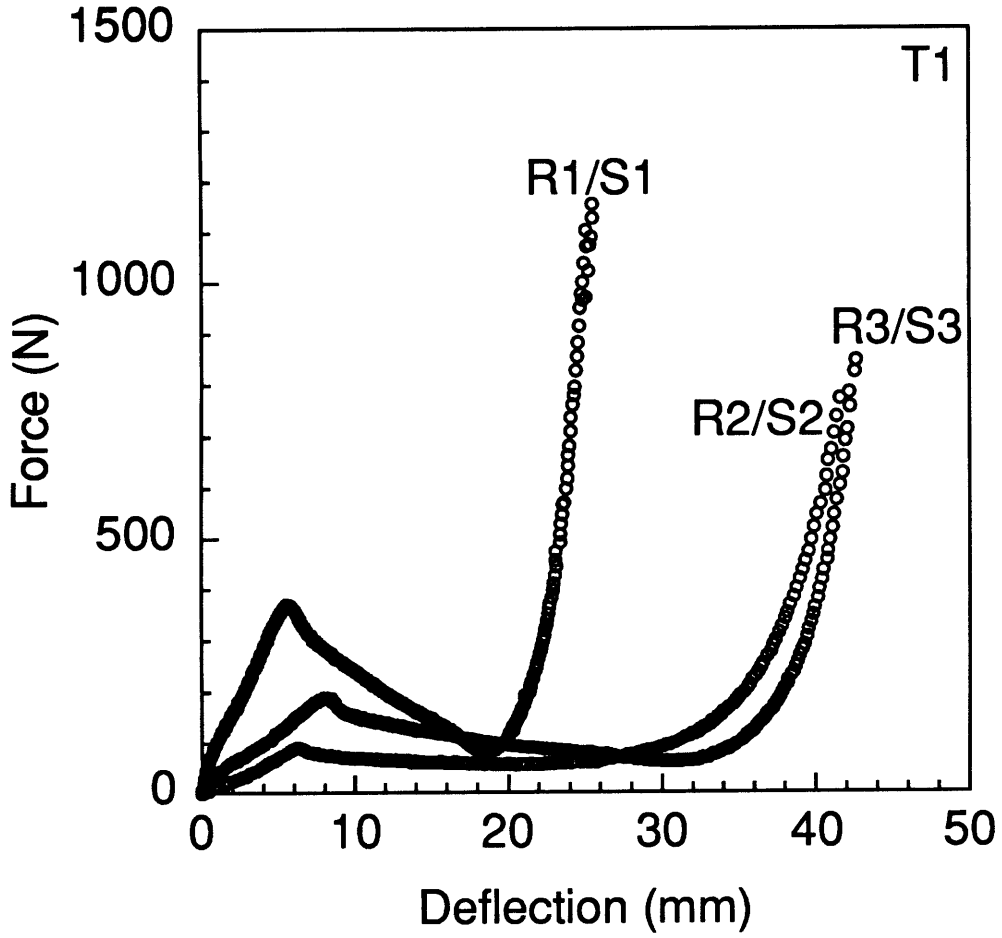

Figure 5.84 Effect of scaling on quasi-static loading response of convex specimens with constant radius-to-span ratio (1.5) and thickness (T1).

Table 5.17 Critical Snapping Load[a] for Quasi-static Tests[b]

	T1			T2			T3		
Span	R1	R2	R3	R1	R2	R3	R1	R2	R3
S1	400	200	120	-	750	600	-	-	-
S2	360	200	150		-			-	-
S3	-	190	100		-	-			-

[a] All values in N.

[b] Blanks indicate no test was conducted, and "-" indicates instability was not observed.

Table 5.18 Deflection[a] at Critical Snapping Load for Quasi-static Tests[b]

	T1			T2			T3		
Span	R1	R2	R3	R1	R2	R3	R1	R2	R3
S1	5	4	3	-	6	6	-	-	-
S2	13	8	6		-			-	-
S3	-	11	6		-	-			-

[a] All values in mm.

[b] Blanks indicate no test was conducted, and "-" indicates instability was not observed.

associated high frequency secondary response which makes it difficult to obtain the critical snapping load and deflection. For example, the critical snapping loads from the impact tests can only be determined to ±50 N while the quasi-static tests are known within ±10 N. Tables 5.17 and 5.18 can be compared to Tables 5.1 and 5.3 for impact tests at 3 m/s (nominal). These tables indicate that the same specimen types that evidence an instability in quasi-static tests also have the instability in impact loading. The data in Tables 5.17 and 5.18 indicate that both the critical snapping load and deflection decrease with increasing radius. The critical snapping load generally decreases with span (except for specimen R3S2T1) and the critical snapping deflection increases. Increasing the thickness has the effect of increasing the critical snapping load and deflection although there are only two specimens that allow this conclusion to be drawn. Keeping any of the structural ratios (R/T, R/S, and S/T) constant does not result in a constant critical snapping load or deflection. However, for a constant radius-to-thickness ratio, the critical snapping load is noted to increase significantly with scaling parameter, n. This follows the trend with increasing the thickness, but not the trend with radius.

Peak force is the second important force associated with testing convex specimens and is equally important for plate and concave specimens. Peak forces for specimens tested quasi-statically are given in Table 5.19, and Table 5.20 contains the maximum deflections for these tests. Table 5.19 can be compared with Table 5.5 which contains the peak impact forces measured during impact tests at 3 m/s (nominal). The desired peak forces for the quasi-static tests were achieved in all cases except for the four specimens cited at the beginning of section 5.2 that were not loaded to the desired peak force because of limitations on the stroke range of the testing equipment. This can

Table 5.19 Peak Force[a] for Quasi-static Tests[b]

	T1				T2				T3			
Span	R1	R2	R3	RP	R1	R2	R3	RP	R1	R2	R3	RP
S1	*1.16*	***1.18***	*1.11*	**1.21**	1.35	*1.49*	*1.57*	1.96	1.69	1.54	1.44	2.43
S2	0.36	*0.85*	*1.14*			1.11				1.65	1.51	
S3	0.22	*0.29*	*0.78*			1.00	0.93				1.35	
S1 concave	1.13	1.09	1.12		1.99	2.01			2.71		2.37	
SC	0.15											

[a] All values in kN.

[b] Blanks indicate no test was conducted, *Italics* indicate peak force occurred on the second equilibrium path (instability), and **bold** indicates penetration.

Table 5.20 Maximum Deflection[a] for Quasi-static Tests[b]

	T1				T2				T3			
Span	R1	R2	R3	RP	R1	R2	R3	RP	R1	R2	R3	RP
S1	*26*	***16***	*13*	**10**	6.3	*13*	*11*	8.0	5.1	5.5	7.2	5.8
S2	51	*43*	*33*			8.7				5.4	6.2	
S3	77	*81*	*42*			13	12				10	
S1 concave	5.1	6.7	7.4		5.7	6.3			4.6		5.3	
SC	125											

[a] All values in mm.

[b] Blanks indicate no test was conducted, *Italics* indicate peak force occurred on the second equilibrium path (instability), and **bold** indicates penetration.

be seen by comparison of Tables 5.5 and 5.19. The data for maximum deflection in the quasi-static tests (Table 5.19) generally agrees with the impact deflection data in Table 5.9. Comparisons of peak force and deflection with regard to varying the structural parameters is not useful because, as stated previously, the peak forces were determined *a priori* from the impact tests at 3 m/s (nominal).

5.3.2 Force-indentation Results and Contact Parameters

Indentation data taken during each quasi-static test is used to study the local behavior of the specimens with the data presented in the form of force-indentation plots. These results can be used to determine the Hertzian-type contact relation discussed in chapters 2 and 3. Force-indentation curves for all specimens can be found in Appendix F. These figures were all plotted up to the maximum load of the test, and the unloading data was not plotted. This was done because the majority of specimens showed large deviations from a smooth force-indentation curve during the test. Thus, the unloading curves displayed widely scattered and nonuniform behavior. This behavior can be attributed to many factors such as the formation of damage (e.g. matrix cracks and delaminations) in the region where the LVDT measuring the indentation contacts the specimen.

The force-indentation data taken for the quasi-static loading of convex specimen R1S1T1 is presented in Figure 5.85. The data is noted to be widely scattered and even to show negative values of indentation (expansion of the laminate thickness). This aspect will be discussed in chapter 6. A small region in the lower portion of Figure 5.85, between 0 mm and 0.015 mm (between 0 N and 150 N) is considered useful information for analyzing the local contact behavior. Widely scattered data is typical of the majority of the

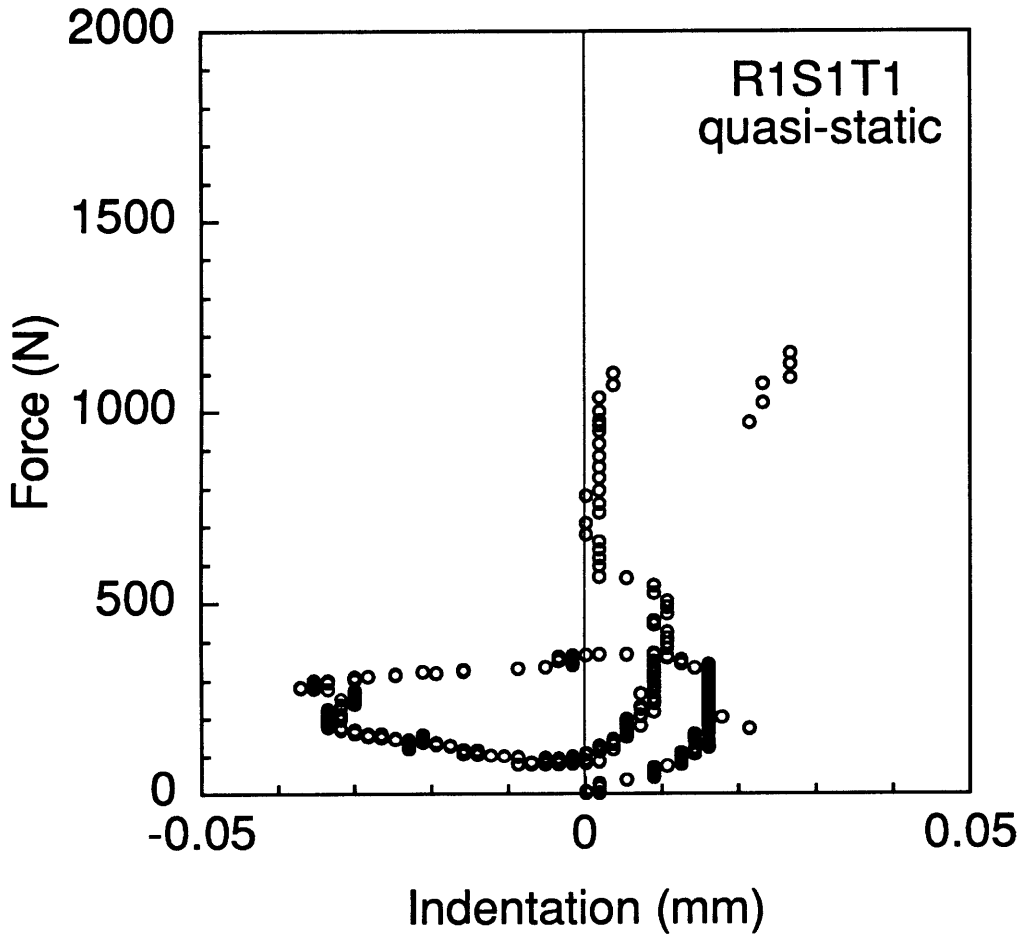

Figure 5.85 Force-indentation response for quasi-static loading of specimen R1S1T1.

force-indentation results, with only a region at the beginning of the curve representing classical contact behavior. Figure 5.86 contains the force-indentation results for specimen R3S3T3. For this specimen, there is a much greater range of useful data with which to work and it will be used as an example to illustrate how the constants for the contact relation are extracted from the force-indentation data.

The constants for the contact relation can be extracted from the force-indentation results using a least-squares curve-fitting approach. First, a useful range of data for each specimen must be determined. Useful information is defined as the force-indentation data at the beginning of the loading before any sharp deviations from the exponential contact law behavior are noted. The useful region is defined by coordinates of the last useful point in the data, starting from zero indentation and zero force. In Figure 5.86, this point has coordinates of force equal to 740 N and indentation equal to 0.06 mm. The maximum force, indentation, and deflection of the last point in the data used for the curve fits are given in Appendix F. These values may later be useful in determining if the data lies within the range of classical Hertzian assumptions. The data can be fit to the Hertzian type contact relation in two ways. The general Hertzian contact relation can be represented as:

$$F = K\alpha^m \tag{5.2}$$

where F is the contact force, K is the contact stiffness, α is the indentation, and m is the exponential parameter. In the classical Hertzian derivation for an infinite isotropic half-space, the parameter m takes on the value of 1.5. Thus, the data can be fit to equation 5.2 either by leaving m as a fitting

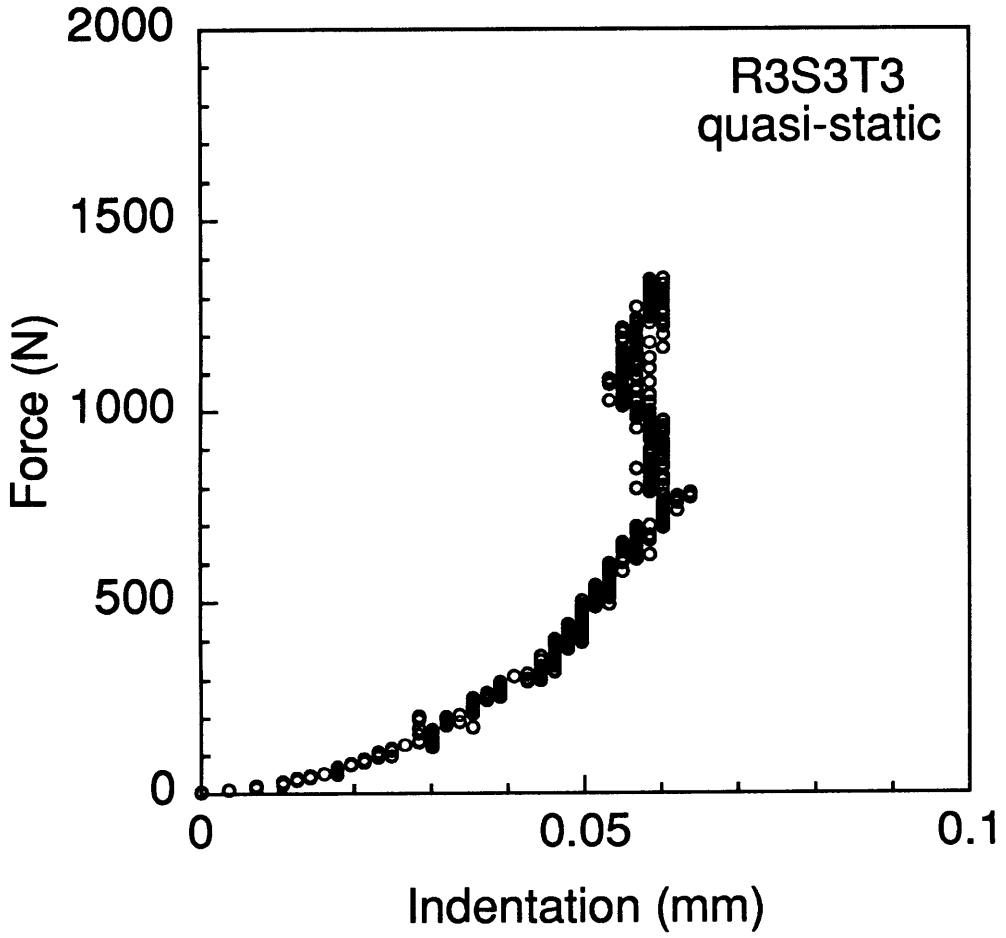

Figure 5.86 Force-indentation response for quasi-static loading of specimen R3S3T3.

parameter or by constraining m to be 1.5 and fitting the data using only the contact stiffness.

In the constrained case, equation 5.2 can simply be fit to the force-indentation data using a least-squares approach where K is the only unknown variable (m is set equal to 1.5). This yields a value for K of 43.1 $kN/mm^{1.5}$ with a linear correlation factor, R, of 0.964 for the R3S3T3 data in Figure 5.86. The linear correlation factor (also called Pearson's R) will have a value close to 1.0 when the curve fit matches the data very well [10]]. The same data can also be fit using the least-squares method when m is unconstrained. Taking the logarithm of both sides of equation 5.2 yields:

$$log(F) = logK + mlog(\alpha) \tag{5.3}$$

This equation is a straight line with a slope of m and y-intercept equal to log(K). The plot of this straight line, with the corresponding curve fit, is presented in Figure 5.87 for the useful range of data for specimen R3S3T3. This yields a value of m of 1.85 and K of 117 $kN/mm^{1.85}$ with a linear correlation factor for the log-log fit of 0.986.

Tables 5.21 through 5.23 contain the contact relation constants determined via the constrained (m = 1.5) and unconstrained curve fits. Omissions in the tables indicate that a useful range of data could not be determined for the curve fits. Appendix F contains the contact constants, linear correlation factors, as well as the maximum force, deflection, and indentation for the curve fits. It should be noted that the forces in the useful ranges of data that were defined for the curve fits were all below the critical snapping load.

The values of the exponent for the unconstrained curve fit in Table 5.22 are noted to be very close to 1.5. Given this observation, the contact

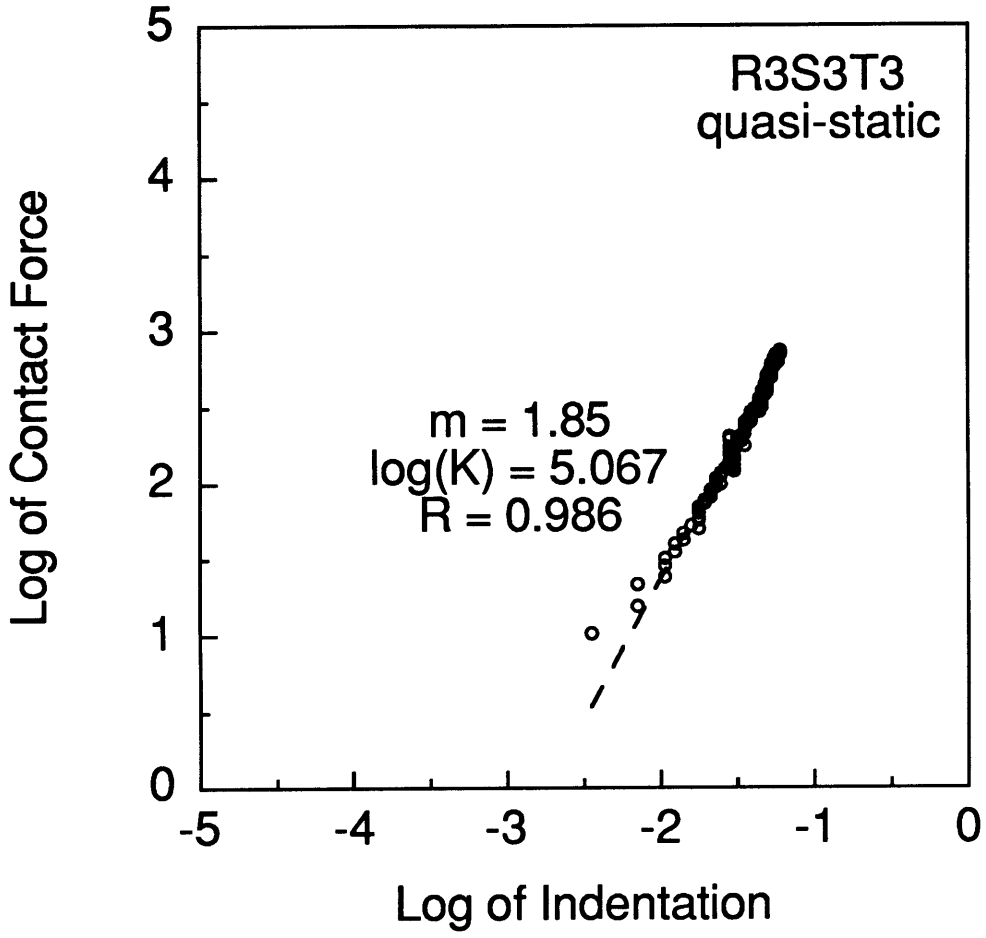

Figure 5.87 Log-log plot of force-indentation response for quasi-static loading of specimen R3S3T3 used to calculate contact relation constants for the unconstrained fit.

Table 5.21 Values of Contact Stiffness, K[a], for the Constrained Curve Fit[b]

	T1				T2				T3			
Span	R1	R2	R3	RP	R1	R2	R3	RP	R1	R2	R3	RP
S1	74.2	39.1	34.5	26.3	32.1	42.5	39.3	48.4	-	43.8	48.1	42.8
S2	27.3	-	23.9			57.2				40.7	33.9	
S3	52.1	54.3	17.2			39.8	43.0				43.1	
S1 concave	61.9	54.2	24.8		34.7	41.1			50.0		46.6	
SC	27.7											

[a] All values in $kN/mm^{1.5}$.

[b] Blanks indicate no test was conducted, and "-" indicates a useful range of data for the curve fit could not be determined.

Table 5.22 Values of Exponent m for the Unconstrained Curve Fit[a]

	T1				T2				T3			
Span	R1	R2	R3	RP	R1	R2	R3	RP	R1	R2	R3	RP
S1	1.48	1.58	1.08	1.41	1.90	1.68	1.64	1.44	-	1.50	1.48	1.52
S2	1.44	-	1.62			1.44				1.68	1.55	
S3	1.46	1.58	1.64			1.42	1.73				1.85	
S1 concave	1.31	1.65	1.61		1.65	1.56			1.57		1.65	
SC	1.73											

[a] Blanks indicate no test was conducted, and "-" indicates a useful range of data for the curve fit could not be determined.

Table 5.23 Values of Contact Stiffness, K^a, for the Unconstrained Curve Fit[b]

	T1				T2				T3			
Span	R1	R2	R3	RP	R1	R2	R3	RP	R1	R2	R3	RP
S1	67.0	51.6	6.13	17.3	115	75.3	57.8	37.5	-	41.5	44.2	44.2
S2	21.5	-	37.1			45.7				64.8	35.4	
S3	43.5	74.3	27.3			28.7	97.4				117	
S1 concave	26.4	80.1	34.0		53.1	47.0			58.9		69.3	
SC	65.5											

[a] All values in kN/mm^m (m from Table 5.22).

[b] Blanks indicate no test was conducted, and "-" indicates a useful range of data for the curve fit could not be determined.

stiffness for the constrained curve fit (Table 5.21) is used to characterize the local response. With m set equal to 1.5, the contact stiffness, K, can be directly compared. This is not true for the unconstrained case where both m and K are fitting variables and K will be dimensionally inconsistent for comparison if m varies. No definite trends are observed in Table 5.21 that relate the contact stiffness to any of the structural parameters (radius, span, and thickness), or ratios of the parameters.

5.3.3 Damage

Damage to the specimens resulting from quasi-static loading is presented in this section. Again, visual and x-ray photography were used to evaluate damage to the specimens. X-ray photographs of damaged specimens can be found in Appendix E along with the force-deflection histories. Generally, the same types of damage observed both visually and with x-ray photography for impact tests are found for specimens tested quasi-statically. The same types of damage characterization for impact tests are used in this section. The data for the damage characterization of specimens tested quasi-statically is given in Appendix G, following the same format as Appendix D (impact test damage data).

The specimens were closely scrutinized (visually) under laboratory lighting conditions. Most of the damage observed visually should be considered barely visible impact damage (BVID). Penetration damage is the only type that would not be considered BVID. Visually, front-surface damage modes were typified by marring, matrix cracking and fiber breaks, and/or penetration at the point of contact of the tup and the specimen. Specimen types R2S1T1 and RPS1T1 were penetrated during testing and showed the same front-surface signs of penetration as discussed in section 5.2 for the

impact loading case, e.g. fiber breaks and matrix cracks extending through the specimen thickness. Back-surface damage was noted to be matrix splitting along the fiber direction (45°) behind the point of contact between the tup and specimen. Delaminations (spalling) observed between matrix splits for the impact tests were not observed for any of the specimens tested quasi-statically which indicates that spalling is dynamic in nature. Back-surface penetration damage displayed the same modes of damage found for the impact tests (fiber breaks, matrix cracking, and delamination) but to a lesser extent. During testing, stroke was reversed when the sudden drop in load associated with penetration was observed. This may contribute to the lesser extent of penetration damage because the tup would not pass as far through the laminate during the deflection-controlled quasi-static test if the stroke is reversed as soon as penetration is observed.

Again, much like the damage found in impacted specimens, x-ray photography of quasi-statically loaded specimens can be grouped into three broad categories; no damage, damage that is visible in the x-ray photographs, and penetration damage. The results of the x-ray photography damage evaluation method with regard to these three categories for quasi-static tests is summarized in Table 5.24 and can be compared to Table 5.11 (impact tests). Tables 5.11 (impact) and 5.24 (quasi-static) are noted to be identical except for four entries. Specimen R2S1T1 was penetrated during quasi-static testing but was only damaged during impact testing. However, this specimen slipped in-plane during impact testing making this data point inconclusive. The three remaining differences are the concave S1T1 specimen types. During impact testing at 3 m/s (nominal) these three specimens were penetrated. However, they were only damaged during quasi-static testing.

Table 5.24 Damage Severity[a] Chart for Quasi-static Tests[b]

	T1				T2				T3			
Span	R1	R2	R3	RP	R1	R2	R3	RP	R1	R2	R3	RP
S1	*D*	*P*	*D*	P	D	*D*	*D*	D	D	D	D	D
S2	N	*D*	*D*			D				D	D	
S3	N	*N*	*D*			D	D				D	
S1 concave	D	D	D		D	D			D		D	
SC	N											

[a] "N" indicates no damage in the x-ray photographs, "D" indicates damage in the x-ray photographs, and "P" indicates penetration.

[b] Blanks indicate no test was conducted, and *Italics* indicate peak force occurred on the second equilibrium path (instability).

The excellent comparison between Tables 5.11 and 5.24 means that the same trends that exist for impact tests are repeated in the quasi-static results.

The same types (modes) of damage viewed in the x-ray photographs of impact damage are observed in the x-ray photographs for the quasi-static tests. Single or double peanut-shaped delaminations at 45° and -45° (fiber directions) are typically formed. Figure 5.88 contains two examples (R1S1T1 and R3S2T1) showing single peanut delaminations and Figure 5.89 contains x-ray photographs of double peanut-shaped delaminations (concave specimen R1S1T2 and specimen R2S2T2). The delamination at 45° is accompanied by a matrix crack in the 45° direction in the majority of the x-ray photographs. The double peanut-shaped delamination is often accompanied by matrix cracks in the 0° and -45° plies, which can be seen in the actual photographs of the damage but are difficult to see in Figure 5.89. Four specimens displayed atypical damage states in the x-ray photographs. Specimens R1S1T2 and R2S2T3, shown in Figure 5.90, have asymmetric and large damage states. Specimen R1S1T2 has matrix cracking and delamination at 45°, -45°, and 0° extending away from the point of contact in only one direction. Specimen R2S2T3 has a double peanut-shaped damage state as well as extensive matrix cracking and delaminations at 45°, forming in only one direction away from the point where the tup contacts the specimen. Damage x-ray photographs of specimens R1S1T3 and R2S1T3, presented in Figure 5.91, also show extensive matrix cracking and delaminations forming around the cracks, with the damage being nearly equally distributed in the 45°, -45°, and 0° directions. All four of these specimen types impacted at 3 m/s also show atypical damage states (see Figures 5.61 and 5.62 for comparison).

The lengths of the 45° and -45° delaminations are again used as metrics for characterizing the damage found in the x-ray photographs. This

Figure 5.88 X-ray photographs of specimens tested quasi-statically showing single peanut-shaped delaminations at 45°: (*top*) specimen R1S1T1, and (*bottom*) specimen R3S2T1.

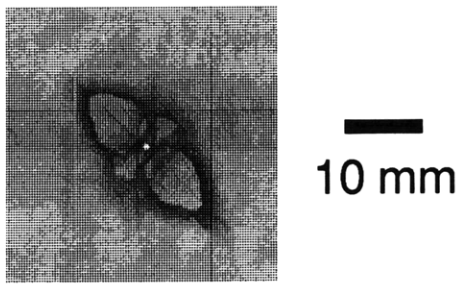

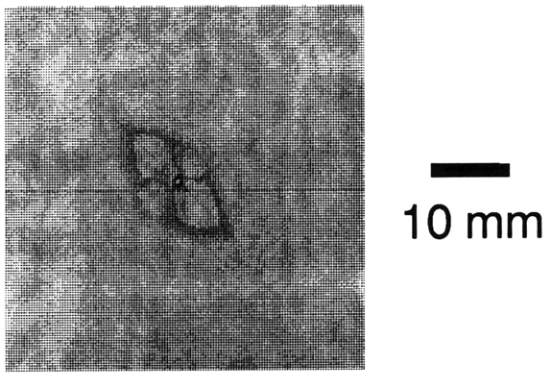

Figure 5.89 X-ray photographs of specimens tested quasi-statically showing double peanut-shaped delaminations at 45° and -45°: (*top*) specimen R1S1T2 (concave), and (*bottom*) specimen R2S2T2.

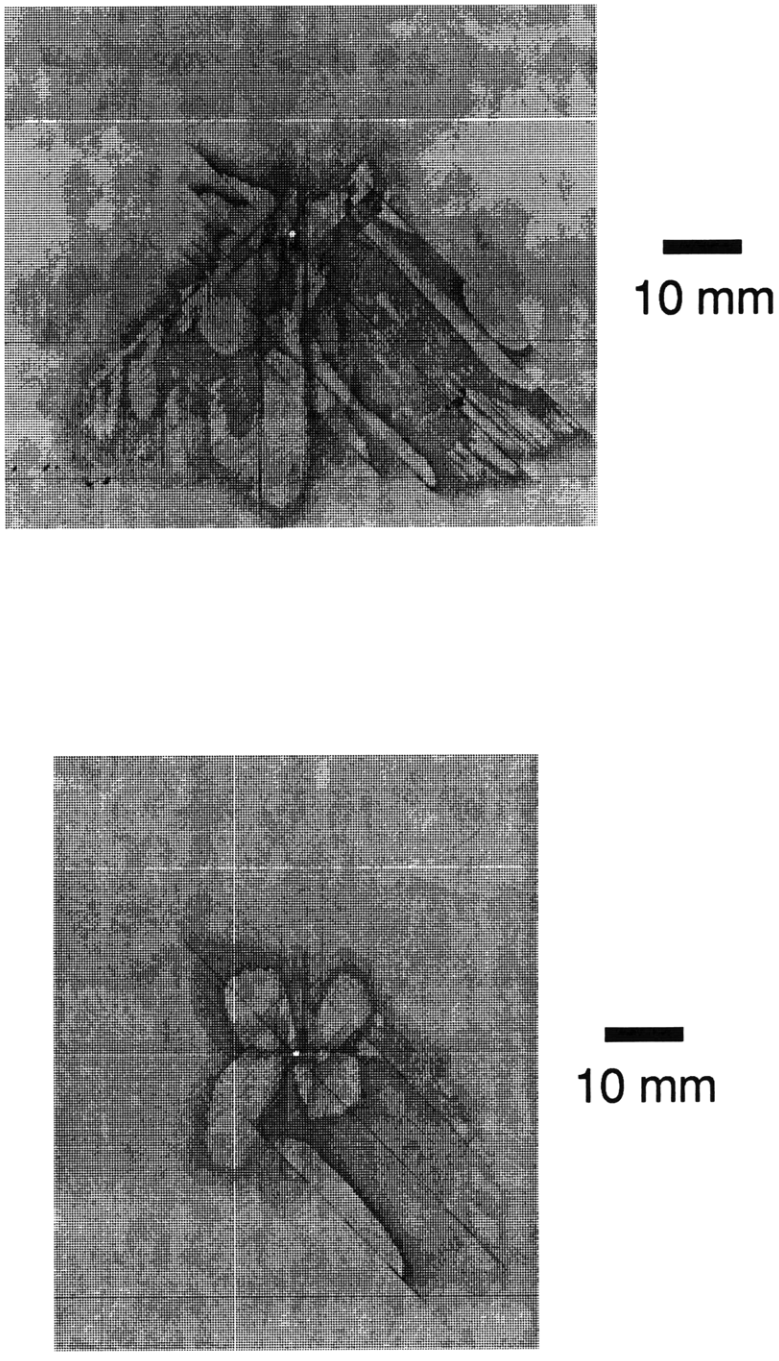

Figure 5.90 X-ray photographs of specimens tested quasi-statically showing atypical damage states: (*top*) R1S1T2, and (*bottom*) R2S2T3.

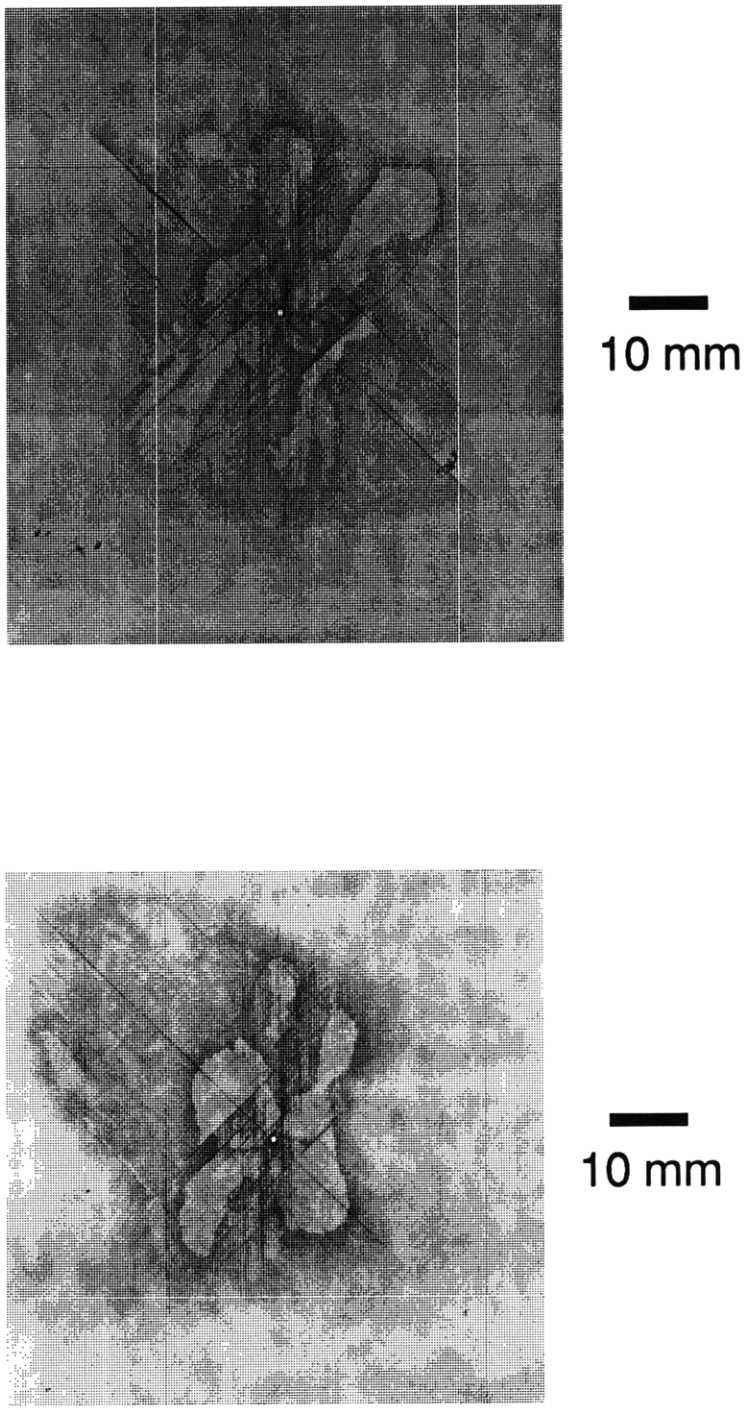

Figure 5.91 X-ray photographs of specimens tested quasi-statically showing atypical damage states: (*top*) R1S1T3, and (*bottom*) R2S1T3.

data is presented in Appendix G along with the average damage length and ratio. The average damage length is used as a metric to characterize the extent of damage and is presented in Table 5.25 for quasi-static tests. The ratio of damage lengths in the -45° and 45° directions is also utilized, as explained in section 5.2 for impact tests, to characterize the damage distribution and is provided in Table 5.26 for all specimens tested quasi-statically. The average damage extents and ratios in Tables 5.25 and 5.26 can be compared with Tables 5.13 and 5.15, respectively, for impact tests at 3 m/s (nominal). No trends were observed within Tables 5.13 and 5.15 for the impact tests and this is also the case for the quasi-static tests. The data for the impact and quasi-static tests generally compares quite well with the averages of the damage ratios comparing almost perfectly. The average ratio of damage lengths for convex shells with the instability is 0.34 while the average without the instability (first equilibrium path) is 0.64. These compare with values of 0.34 and 0.63, respectively, for the impact tests. The average ratio of damage lengths for concave shells and plates tested quasi-statically are 0.44 and 0.32, respectively. The corresponding values for concave shells and plates from the impact tests at 3 m/s (nominal) are 0.49 and 0.30, respectively. It is therefore easily noted that the average damage ratios for impact and quasi-static tests are comparable and even identical for the case of convex shells that progressed beyond the critical snapping load during testing.

General observations relating to the damage states evaluated visually and with x-ray photography can be made. Some specimens that were visually observed to be marred on the front surface were found to have no damage using the x-ray photography method, e.g. specimen R1S2T1. This behavior was also noted for the impact tests. Back-surface damage (matrix splits) was

Table 5.25 Average of Damage Extent[a] in 45° and -45° Directions from X-ray Photographs for Quasi-static Tests[b]

	T1				T2				T3			
Span	R1	R2	R3	RP	R1	R2	R3	RP	R1	R2	R3	RP
S1	*16*	*P*	*21*	P	65	*16*	*19*	26	65	58	30	28
S2	0	*7*	*11*			14				40	32	
S3	0	*0*	*6*			13	11				19	
S1 concave	16	11	9		16	18			18		23	
SC	0											

[a] All values in mm.

[b] "P" indicates penetration, blanks indicate no test was conducted, *Italics* indicate peak force occurred on the second equilibrium path (instability).

Table 5.26 Ratio of -45° to 45° Damage Lengths from X-ray Photographs for Quasi-static Tests[a]

	T1				T2				T3			
Span	R1	R2	R3	RP	R1	R2	R3	RP	R1	R2	R3	RP
S1	*0.19*	*P*	*0.27*	P	0.86	*0.41*	*0.31*	0.24	0.86	0.77	0.40	0.40
S2	-	*0.40*	*0.29*			0.59				0.60	0.58	
S3	-	-	*0.50*			0.63	0.57				0.54	
S1 concave	0.24	0.50	0.31		0.52	0.38			0.57		0.59	
SC	-											

[a] "P" indicates penetration, blanks indicate no test was conducted, *Italics* indicate peak force occurred on the second equilibrium path (instability).

not found without there also being damage in the x-ray photograph. Lastly, with respect to the force-deflection histories, it is not clear that incipient damage formation or further damage progression within the specimens can be seen in the force-deflection histories, except for penetration. Cracking was heard in specimens that penetrated during quasi-static testing, and other specimens were heard to crack as well near the maximum force of the tests. Some specimens show small variations in the force-deflection curves near the peak force and display damage in the x-ray photographs, e.g. the force-deflection history of specimen R1S1T1 (concave) in Figure 5.73. However, other specimens are found to have similar damage (both extent and mode) but display no distinct variations in the force-deflection history, e.g. specimen R3S3T2 in Figure 5.72. The x-ray damage states for specimens R1S1T1 (concave) and R3S3T2 tested quasi-statically are presented in Figure 5.92 to illustrate that the damage states for this comparison are indeed similar. Thus, except for penetration, damage can form with no visible indication in the quasi-static force-deflection curves. Lastly, spalling was not observed on the back surface of any of the specimens tested quasi-statically but was observed for some similar specimen types during impact testing.

Figure 5.92 X-ray photographs of specimens tested quasi-statically: (*top*) specimen R1S1T1 (concave), and (*bottom*) specimen R3S3T2.

CHAPTER 6

DISCUSSION

Important findings from the present work are discussed in this chapter with results from chapter 5 used to motivate and provide evidence for the discussion. Results from testing are first used to evaluate the performance of the test fixture in section 6.1. A comparison of the results from impact and quasi-static testing follows in section 6.2. Basic issues identified through the experimental test results in chapter 5 are outlined which relate structural parameters to the impact response, including damage, in section 6.3. In section 6.4, key results are discussed from a damage resistance perspective and used to highlight important implications in this area.

6.1 Test Fixture

Observations made during testing and presented in chapter 5 provide a basis for evaluating the performance of the test fixture. Providing a consistent boundary condition for shells with various structural configurations was a key consideration in the design of the test fixture. Experimental boundary conditions are never mathematically ideal. However, response comparisons are only practical if the boundary conditions are consistent between specimens and tests. Therefore, criteria for evaluating the performance of the test fixture include consistency from specimen to

specimen and test to test, as well as knowing the boundary conditions for modeling purposes.

Analyses of general shells having rectangular planform with simple (allowing in-plane sliding) or clamped supports along the axial edges, predict the instability response and stable postbuckling observed during testing [36, 78]. The pinned/no in-plane sliding boundary conditions used in the experiments are somewhere between clamped and simply supported. Stable postbuckling was observed for some convex shells during both impact and quasi-static testing. The instability region has been seen to develop in the response as the curvature of the specimen is increased from a plate (no curvature) to convex shells with curvature (see Figure 5.75). This has been observed in analysis of a sinusoidal arch subjected to transverse loads [79]. Trends observed in this work agree with such analysis. Specifically, the critical snapping load, the deflections associated with the instability region, and the initial stiffness increase as the curvature is increased. Also, at small values of curvature (approaching a plate), the analysis predicts that the load drop associated with the instability disappears and simply becomes an inflection point in the load-deflection response. This is in agreement with the trend observed in this experimental investigation. These observations indicate that characteristics of shells with mathematically ideal boundary conditions are qualitatively preserved in the current experiments.

The smooth force-deflection curves presented in chapter 5 and in Appendix E for quasi-static loading indicate that the pinned boundary conditions are allowing rotation as desired. If the boundary were interfering with rotation of the specimens, friction would restrain the axial shell edges from rotation until the moment causing the rotation exceeded the resisting moment. This would be evident in the force-deflection histories as drops in

load. However, except for penetration, drops in load were not observed. For example, large rotations were observed (e.g. Figure 5.5) for many convex shells of thickness T1 and the force-deflection histories for these specimens are typically smooth and regular. Additionally, the shell edges that contact the knife edges (pinned condition) were observed to be undamaged after testing. If the shell were kept from rotating, it is reasonable to assume that the shell edges would be damaged in the region of contact due to the moments produced by the transverse loading. Undamaged shell edges again indicate that the shells rotated at the pinned boundary.

The in-plane restraint for convex shells is known to be zero displacement because the shell is restrained from 'push-in' by the rod and cushions as described in chapter 4. The no in-plane sliding restraint for plate and concave specimens ('pull-out') can be qualitatively evaluated based on observations of the specimen edges after testing. During preliminary testing, impacted plates were noted to slip out of the extended knife edges which provide the in-plane restraint. In these preliminary test cases, the holes in the plate edges where the extended knife edges mount through, were broken during impact as the plate 'pulled-out' of the knife edges. This was rectified by addition of the double-stick transfer tape as described in chapter 4. None of the specimens in the subsequent work had the axial-edge holes broken during testing which indicates that the in-plane condition was maintained.

The out-of-plane restraint (knife edges) can be evaluated based on forces measured during testing. Geometric coupling in the transverse loading of shells makes the loading indeterminate at the pinned boundaries. However, a critical case can be considered to show that the out-of-plane restraint is acceptably rigid. Relative to the rigidity of the rods and cushions, the 6.35 mm (0.25") diameter threaded steel rods that support the knife edges

which provide the out-of-plane restraint for the plates and shells are the least rigid aspect of the out-of-plane restraint. The critical case is therefore defined by assuming the knife edges carry the entire load during testing of the specimen that reaches the highest load for the smallest center deflection (stiffest specimen). This is a conservative estimate because much of the transverse load is also carried by the in-plane restraint after deflections on the order of half a specimen thickness occur [81]. By comparing Tables 5.19 and 5.20 for peak force and maximum deflection, it is easy to see that specimen type R1S1T3 (concave) has both the highest force (2710 N) and lowest maximum deflection (4.6 mm) of all specimens tested quasi-statically. Assuming all the load (compression) is carried by the threaded rods supporting the knife edges, the deformation of the out-of-plane restraint is calculated to be approximately 0.02 % of the deflection at the peak force for this specimen. Thus, the out-of-plane boundary condition is observed to be effectively zero displacement. These results indicate that the desired out-of-plane boundary conditions were achieved by the test fixture design.

Consistency in the boundary conditions provided by the test fixture can be qualitatively evaluated by considering several characteristics of the response curves for specimens during impact and quasi-static loading. The deformation shapes of shells that underwent large rotations were observed to be perfectly antisymmetric which indicates that the boundary conditions were consistent between both shell edges (side to side), i.e. no unsymmetric deformation shapes were observed. Consistency between tests is demonstrated by noting that quasi-static and impact tests of the same specimen type follow the same force-deflection path, e.g. specimen type R1S1T1 in Figure 5.19. Additionally, the force-deflection response progression with velocity for impacted convex shells of the same specimen

type shows consistency from test to test. The response progresses along the same load path regardless of velocity, e.g. specimen type R1S1T1 in Figures 5.16, 5.17, 5.18, and 5.27. These observations indicate that the rate of rotation at the pinned boundary does not alter the response. This would indicate that friction (or lack of it) at the boundary does not appreciably affect the shell response.

The discussion and evidence presented in this section show that the boundary conditions are consistent and provide the desired boundary conditions. However, one difficulty encountered during testing, as described in chapter 5, involves maintaining the no in-plane sliding restraint when a convex shell passes through the instability region and begins loading on the second equilibrium path. Although the test fixture can accommodate either 'push-in' or 'pull-out' at the in-plane boundary, it was not designed to handle the instantaneous change ('push-in' to 'pull-out') in the boundary condition which results from the instability. However, it should be noted that the test fixture was designed so that modifications to the shell boundary condition can easily be made. Thus, if it is desired to maintain the no in-plane sliding restraint when the shell passes through the instability, modifications to the test fixture are easily made.

Although only three impacted specimens were noted to slip in-plane after the instability, the in-plane boundary conditions for convex shells on the second equilibrium path is not known as precisely as in the other cases. Nevertheless, aside from the three specimens that were observed to slip, the effect of this in-plane uncertainty on the response along the second equilibrium path is likely to be insignificant because the force-deflection response for different specimens (same specimen type) impacted at different velocities follow the same loading curve along the second equilibrium path,

e.g. specimen type R1S1T1 in Figures 5.18 and 5.27. Also, as noted in chapter 5, force-deflection histories for specimens which exhibit slipping have load drops on the second equilibrium path and an increased oscillatory response not associated with penetration (see Figures 5.28 and 5.30). Except for the three shells that slipped, this behavior was not observed in the force-deflection histories for unpenetrated convex shells. Therefore, it is likely that the in-plane restraint of no in-plane sliding was maintained for the majority of the convex shells on the second equilibrium path.

6.2 Comparison of Impact and Quasi-static Response

The comparison between impact and quasi-static tests is motivated by the consideration that, as explained in chapter 3, quasi-static testing is cheaper and more repeatable than impact tests. Therefore, it is of interest to note the appropriateness and limitations of quasi-static testing as it relates to impact testing. The comparison is based on the response of the specimens to loading (force-deflection histories) and also damage (extent and mode). In this investigation, quasi-static tests were performed under stroke (deflection) control up to the peak impact force observed for specimens of the same type impacted at 3 m/s (nominal). This was done because peak force has been shown to be a key parameter in the impact damage response of plates [17-20]. It should be noted that specimens which have the critical snapping load as the peak force must have the additional criterion that the peak deflection be the same when loaded quasi-statically. Specimen R1S2T1 is an example where the peak force does not define the end of the loading history for the impact test as expected. The impact loading history for this specimen terminates in the instability region and thus the peak force is equal to the

critical snapping load. The quasi-static loading of this specimen should have been stopped after a deflection of 31 mm instead of 50 mm. This specimen is unique among the specimens tested quasi-statically in this investigation but it should be noted that characterizing the response of a convex shell simply by the peak impact force is not always sufficient.

As noted in chapter 5, force-deflection response curves for all specimens impacted and tested quasi-statically can be found in Appendices C and E, respectively. The response shape of impacted composite convex shells has been shown in chapter 5 to possess the same instability behavior observed in the force-deflection response for the same specimen type tested quasi-statically. An example of this is the impact and quasi-static response for specimen type R1S1T1 shown in Figure 5.19. The shape of the curves compare almost identically, except for the secondary oscillations evident in the impact response curve which have been attributed to the vibration of the impacting assembly. The load drop associated with the instability, a clear indicator of the response, is noted in both curves. Plates and concave shells also compare similarly. The force-deflection impact and quasi-static response for specimen type RPS1T1 is presented in Figure 6.1 to illustrate this comparison for plates.

It is generally observed that the response shape (force-deflection curves) of specimens impacted and tested quasi-statically are similar. This is true for convex shells, concave shells, and plates except for convex specimens that have a low frequency, high amplitude secondary response. The large secondary response visible in the force-deflection histories for impacted shells with large span (S2, S3, and SC) and small thickness (T1) is not present in the quasi-static response. The large amplitude, low frequency response can be easily seen in the impact force-deflection history presented in Figure 6.2

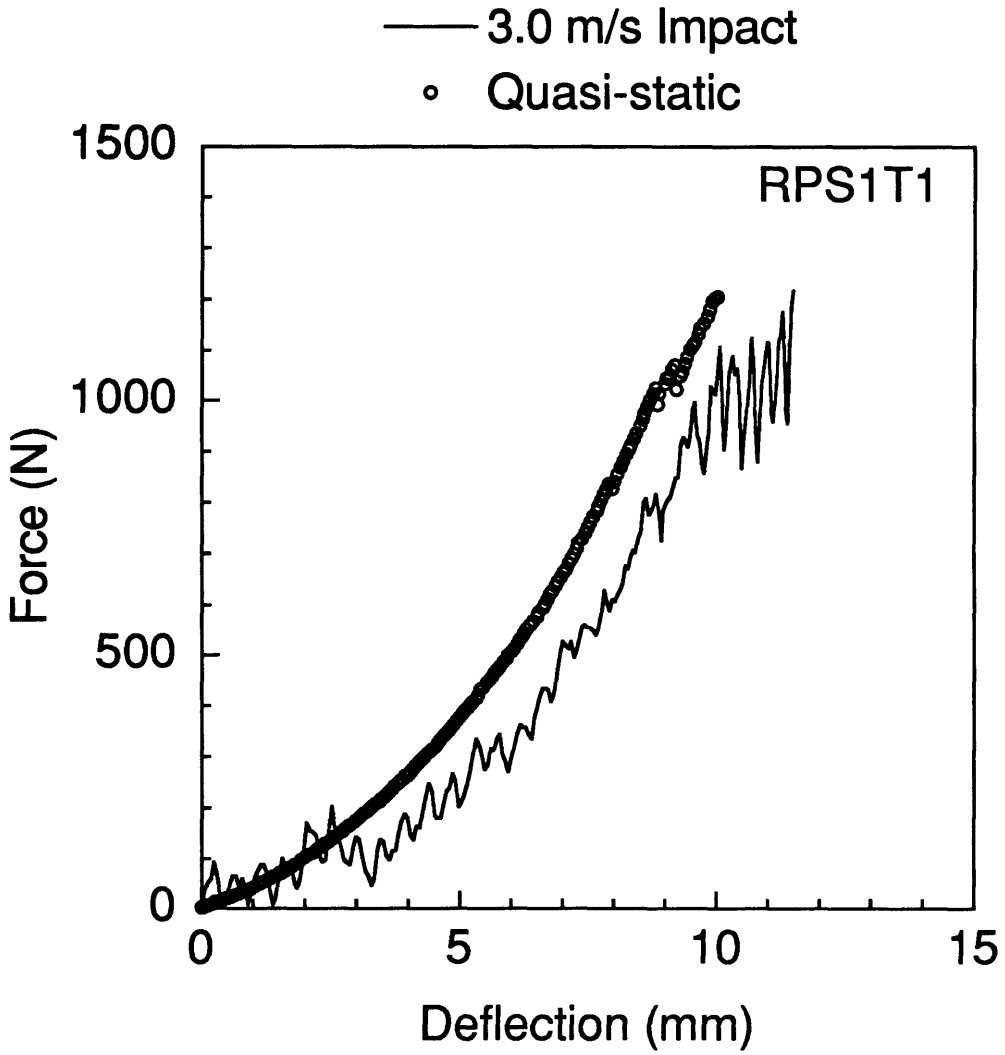

Figure 6.1 Force-deflection response of specimen type RPS1T1 impacted at 3.0 m/s and loaded quasi-statically.

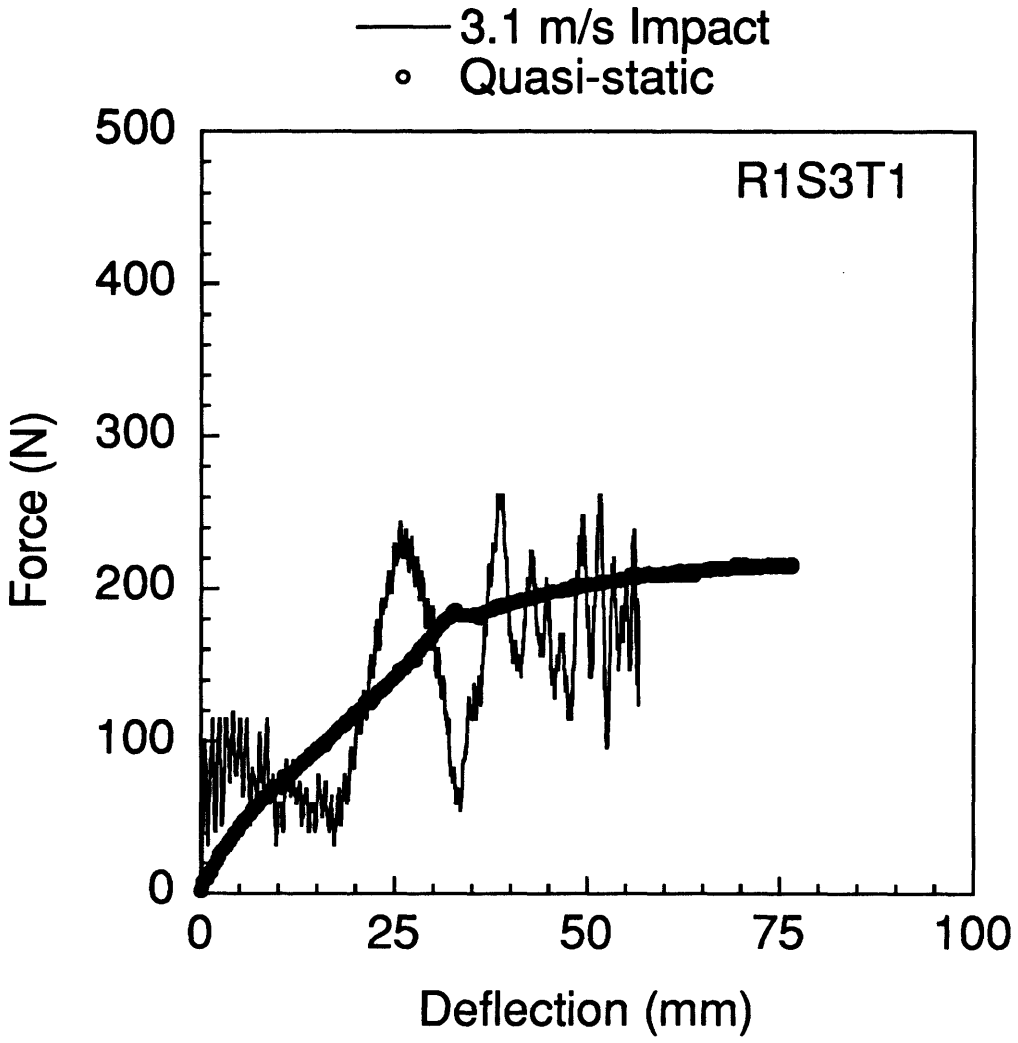

Figure 6.2 Force-deflection response of specimen type R1S3T1 impacted at 3.1 m/s and loaded quasi-statically.

(along with the quasi-static response) for specimen type R1S3T1. This difference is further addressed in section 6.3.

It is important to note that because a stable path through the instability region is observed in the force-deflection plots for impact tests, it can be ascertained that the impact loading behaves like a deflection-controlled experiment rather than a load-controlled experiment. In a load-controlled experiment, there is no stable path through the instability region between the first and second equilibrium paths; i.e. the response would have a snap-through instability and instantaneously jump from the critical snapping load on the first equilibrium path to the same force magnitude on the second equilibrium path. Stable force-deflection response curves were observed in the impact force-deflection histories. This observation directly points to the conclusion that, for the impact velocities in this investigation, the response of the shells is quasi-static in nature.

Response parameters (peak force, maximum deflection, and the critical snapping load and deflection), presented in chapter 5, can also be used to compare impact and quasi-static tests. Peak force is set *a priori* for quasi-static tests so this parameter is constrained to match between the two types of tests. The comparisons in chapter 5 indicate that the other parameters agree between the impact and quasi-static tests. Comparisons of critical snapping load and maximum deflection for impact and quasi-static tests are provided in Figures 6.3 and 6.4. Buckling (critical snapping load) for suddenly loaded general structures, such as in the impact tests, is generally thought to be a percentage (~70%) of the buckling load for quasi-static tests [82]. However, the data presented in Figure 6.3 and in chapter 5 indicate that virtually no difference is observed in critical snapping load between the impact and quasi-static tests. There was some difficulty in determining the

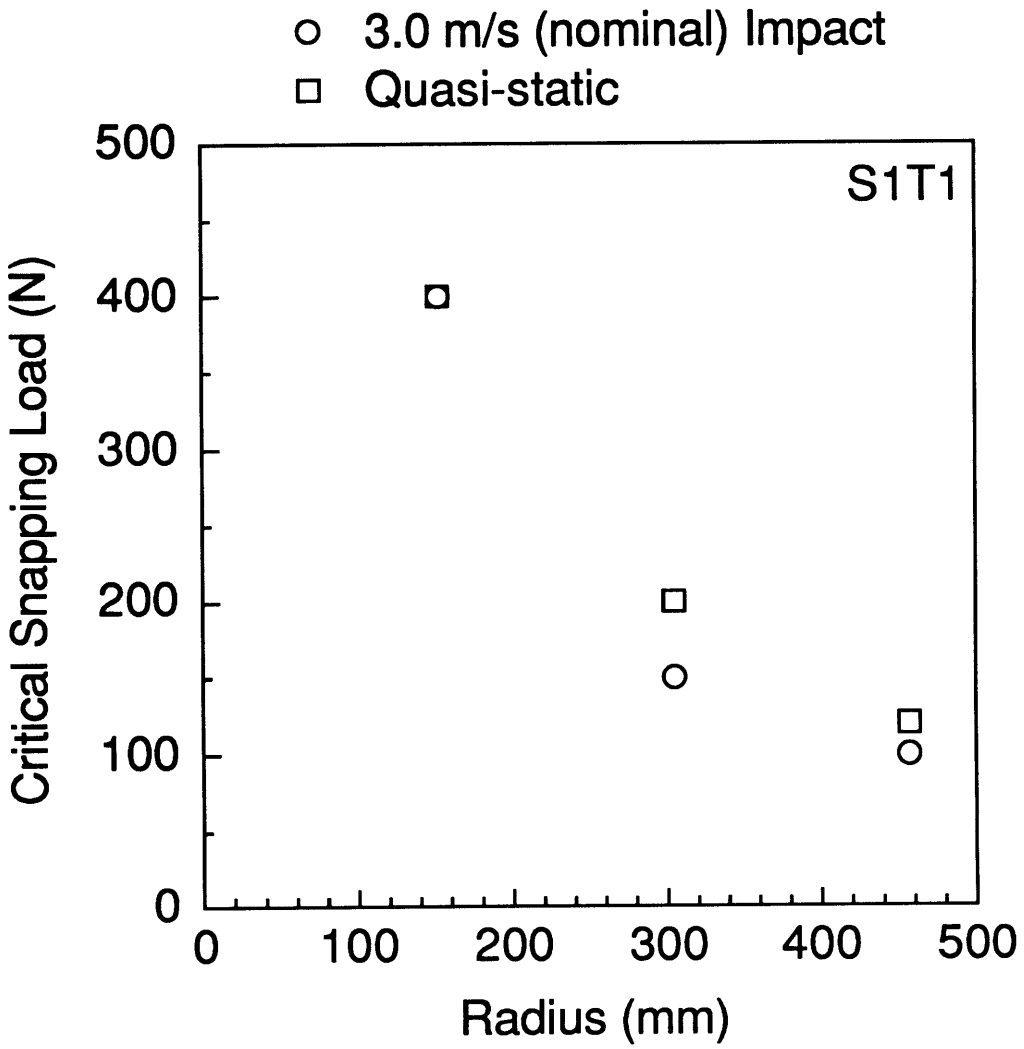

Figure 6.3 Critical snapping load versus radius for convex specimen types S1T1 impacted at 3.0 m/s (nominal) and loaded quasi-statically.

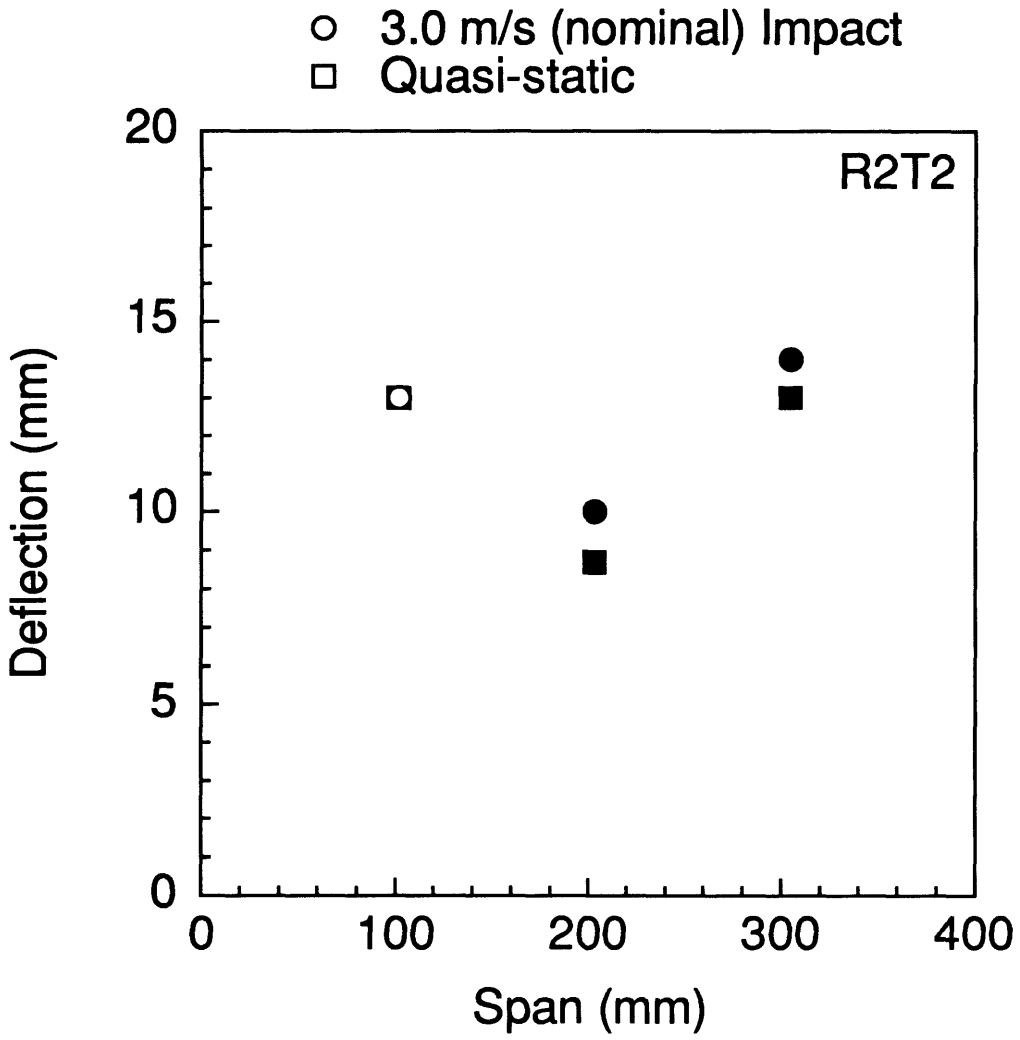

Note: filled data points indicate instability

Figure 6.4 Maximum deflection versus span for convex specimen types R2T2 impacted at 3.0 m/s (nominal) and loaded quasi-statically.

critical snapping load from impact tests, as explained in chapter 5, due to the oscillatory secondary response of the impacted specimens. Since the critical snapping load is noted to be higher or lower in impact tests than in quasi-static tests, it is likely that the critical snapping loads are approximately equal, i.e. scatter in the data centers around the conclusion that the critical snapping loads are approximately equal (compare Tables 5.1 and 5.17).

The data presented in Figures 6.3 and 6.4 illustrate that the response parameters from impact tests at 3.0 m/s (nominal) and quasi-static tests agree. This also implies that trends relating the structural variables to these response parameters are in agreement. An example is the relation between the critical snapping load and the radius of curvature (see Figure 6.3). In chapter 5, the results from testing indicate that the critical snapping load generally decreases with increasing radius for convex shells impacted and tested quasi-statically. Thus, based on the response parameters presented in chapter 5, impact and quasi-static tests are noted to have similar response characteristics and trends.

In addition to the equivalence in force-deflection characteristics, specimens impacted and loaded quasi-statically to the same peak force have damage states that are similar in mode, shape, and extent. The data presented in chapter 5 provides the evidence which points to the conclusion that peak force is the appropriate damage resistance metric regardless of the structural configurations as the same specimen types impacted and loaded quasi-statically to the same peak force have the same damage states. This statement applies to convex shells both with and without the instability, concave shells, and plates. The comparison of damage states in this section relies on the assumption that the peak forces during loading are the same. As noted in chapter 5, four specimens did not reach the desired peak load

during quasi-static testing because of limitations on the range of the testing equipment and two specimens slipped in-plane during testing at an impact velocity of 3 m/s (nominal). Therefore, specimens R1S3T1, R1SCT1, R2S1T1 and R3S1T1 are justifiably ignored for the purposes of the damage comparison discussion.

Qualitatively, the damage categories outlined in chapter 5 based on x-ray photographs of the damaged specimens (see Tables 5.11 and 5.24) are the same for impact and quasi-static tests with two differences. First, spalling is observed only in impact tests, and second, three specimens which were penetrated during impact testing were not penetrated quasi-statically. This is true for all three concave specimens of thickness T1, R1S1T1 (concave), R2S1T1 (concave), and R3S1T1 (concave). It is possible that the specimens tested quasi-statically would have penetrated at a load just slightly higher than the desired load. There is approximately equal scatter in the quasi-static data for specimens that were penetrated during impact testing. Of the five specimens that penetrated during impact testing that were tested quasi-statically, three specimens were not penetrated (penetration may have occurred at a slightly higher load) and two specimens were penetrated at slightly lower loads. The (impact/quasi-static) penetration forces for these specimens are 1220/1180 N (instability) (R2S1T1), 1250/1210 N (RPS1T1). Therefore, it is likely that the penetration difference observed for the impact and quasi-static tests is simply scatter in the data. It should be noted that at the other damage extreme, specimens which were not damaged during impact testing were also undamaged after quasi-static tests.

Since it is known (except for the three penetrated concave specimens discussed above) that the damage categories described in chapter 5 are the same for quasi-static and impact tests at 3 m/s (nominal), the average

damage extent ("damage" category) for each specimen type can be compared. By comparing Tables 5.13 and 5.25, the average damage extents in the 45° and -45° directions are noted to be similar and even identical in some cases. The comparison can be made more easily by considering Figure 6.5 where the average damage extent is plotted versus peak force for impact tests at 3 m/s (nominal) and quasi-static tests. This helps to show that the average damage extent for convex shells impacted at 3 m/s (nominal) and tested quasi-statically follow the same trend with respect to peak force. The same is true for plates and concave shells.

Comparison of x-ray photographs of the damage states is another way to compare quasi-static and impact tests. First, consider the damage states of specimen R1S1T1 presented in Figure 6.6. This specimen has been used to discuss the instability in chapter 5 and much of the response data for this specimen has already been presented in chapter 5. The damage states in Figure 6.6 are noted to be quite similar in both shape, extent, and distribution for this convex shell that had the peak force (both cases) on the second equilibrium path. In both x-ray photographs in Figure 6.6, matrix cracks and delaminations run primarily in the 45° direction, with only a very small delamination in the -45° direction. As another case, consider the damage x-rays for specimen R2S3T2 presented in Figure 6.7. The loading for convex shell R2S3T2 did not progress past the critical snapping load on the first equilibrium path. The two damage states are again noted to be quite similar, with a large matrix crack (dark line) at 45° in both photographs. The damage x-ray photographs for specimen type R3S1T3 (concave) are presented in Figures 6.8 to illustrate that the damage states are similar for concave specimens as well. The same is true for plate specimens, e.g. RPS1T3 in Figure 6.9.

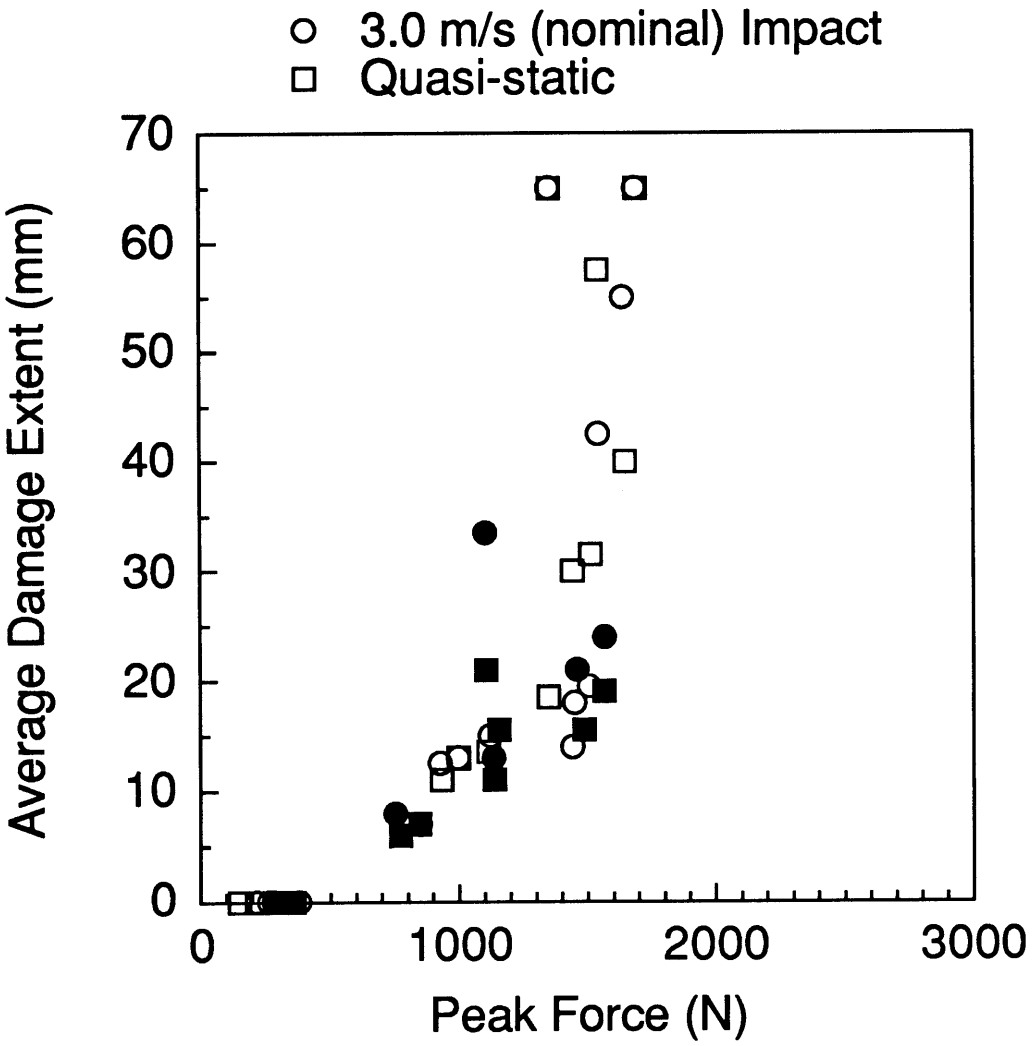

Note: filled data points indicate instability

Figure 6.5 Average damage extent versus peak force for convex shells impacted at 3 m/s (nominal) and tested quasi-statically.

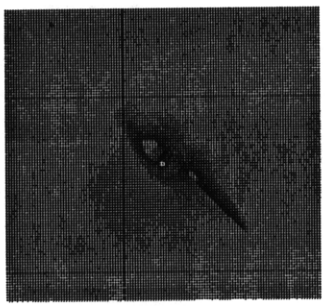

10 mm

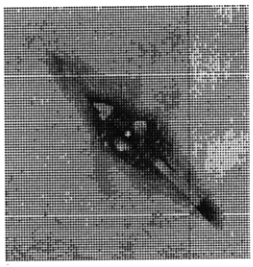

10 mm

Figure 6.6 X-ray photographs of specimen type R1S1T1 loaded nominally to the same peak force of 1150 N (instability) via: (*top*) impact at 3.0 m/s, and (*bottom*) quasi-static test.

Figure 6.7 X-ray photographs of specimen type R2S3T2 loaded nominally to the same peak force of 1000 N via: (*top*) impact at 3.0 m/s, and (*bottom*) quasi-static test.

10 mm

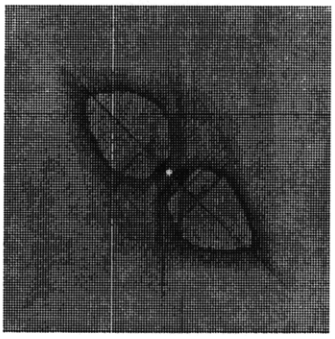

10 mm

Figure 6.8 X-ray photographs of specimen type R3S1T3 (concave) loaded nominally to the same peak force of 2360 N via: (*top*) impact at 3.0 m/s, and (*bottom*) quasi-static test.

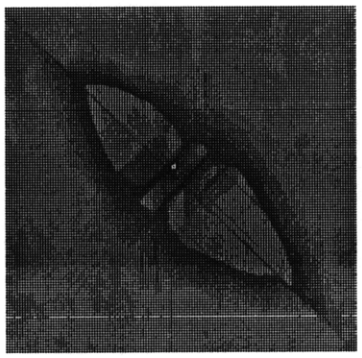

10 mm

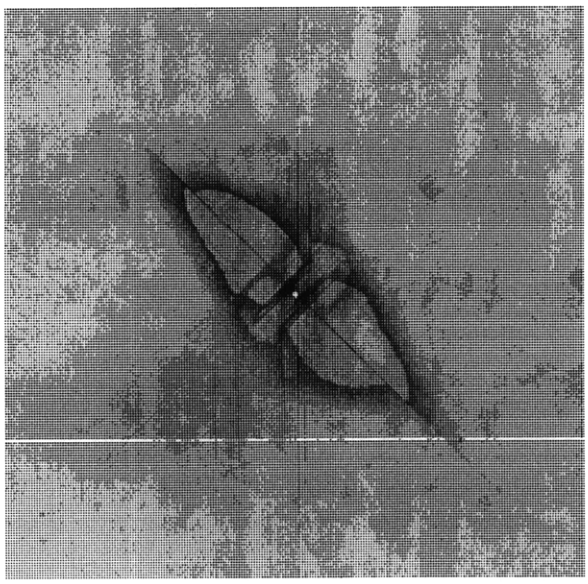

10 mm

Figure 6.9 X-ray photographs of specimen type RPS1T3 loaded nominally to the same peak force of 2430 N via: (*top*) impact at 3.0 m/s, and (*bottom*) quasi-static test.

Compelling evidence of the similarity in damage states with the same peak force is found by considering the atypical damage states discussed in chapter 5. The atypical damage states, although unsymmetric and/or having damage distributions different than the typical peanut-shaped delaminations, are still consistent between quasi-static and impact tests. The x-ray photographs for the damage states of these specimens have already been presented in Figures 5.61, 5.62, 5.90, and 5.91 but are presented together in Figures 6.10 and 6.11 for direct comparison for specimens R1S1T2 and R2S2T3. The damage states, although unsymmetric and atypical, are still consistent in shape, mode, and extent between the impact and quasi-static tests for each specimen.

The damage extent ratios presented in Tables 5.15 and 5.26 for impact and quasi-static tests, respectively, can also be used to compare the two types of tests. The ratios are noted to be similar and the average damage extent ratios, presented in chapter 5, for concave shells, plates, and convex shells with peak forces on the first and second equilibrium paths agree very well. The average damage extent ratios for impact and quasi-static tests are, respectively: convex shells with peak force on the first equilibrium path (0.63 and 0.64), convex shells with peak force on the second equilibrium path above the critical snapping load (0.34 and 0.34), concave shells (0.49 and 0.44), and plates (0.30 and 0.32). It should be noted that the coefficients of variation for each of these ratios is approximately 30%, which is very high. This high percentage may partially be a result of the coarseness of the average damage ratio metric.

Response parameters, force-deflection response characteristics, and damage data indicate that for the range of impact velocities tested, impact and quasi-static tests are nearly identical. The only limitations appear to be

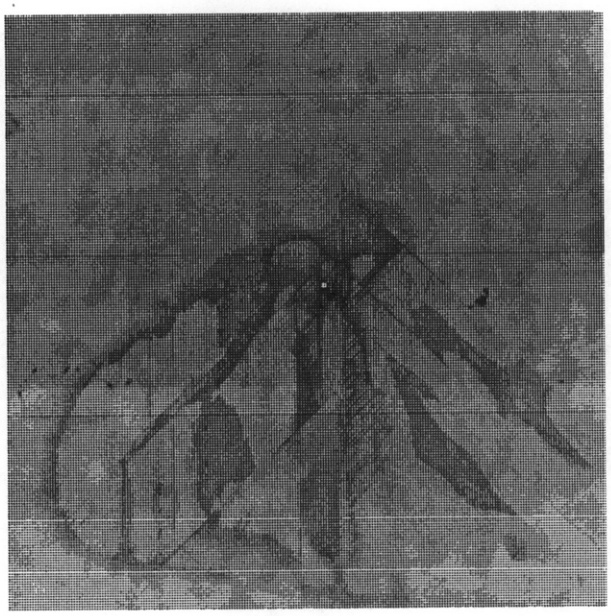

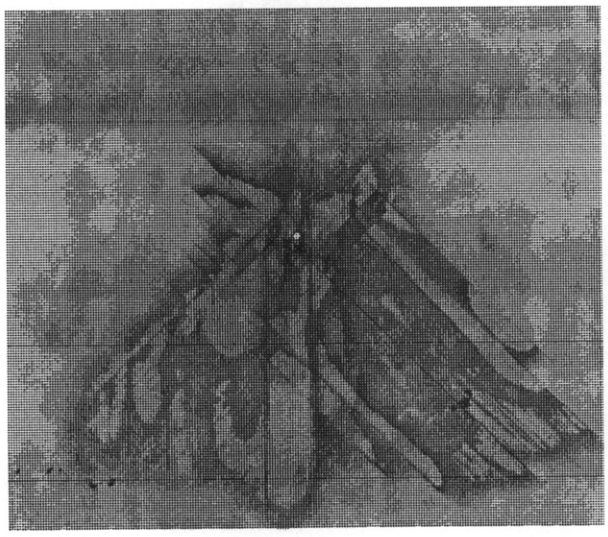

Figure 6.10 X-ray photographs of specimen type R1S1T2 loaded nominally to the same peak force of 1350 N via: (*top*) impact at 2.9 m/s, and (*bottom*) quasi-static test.

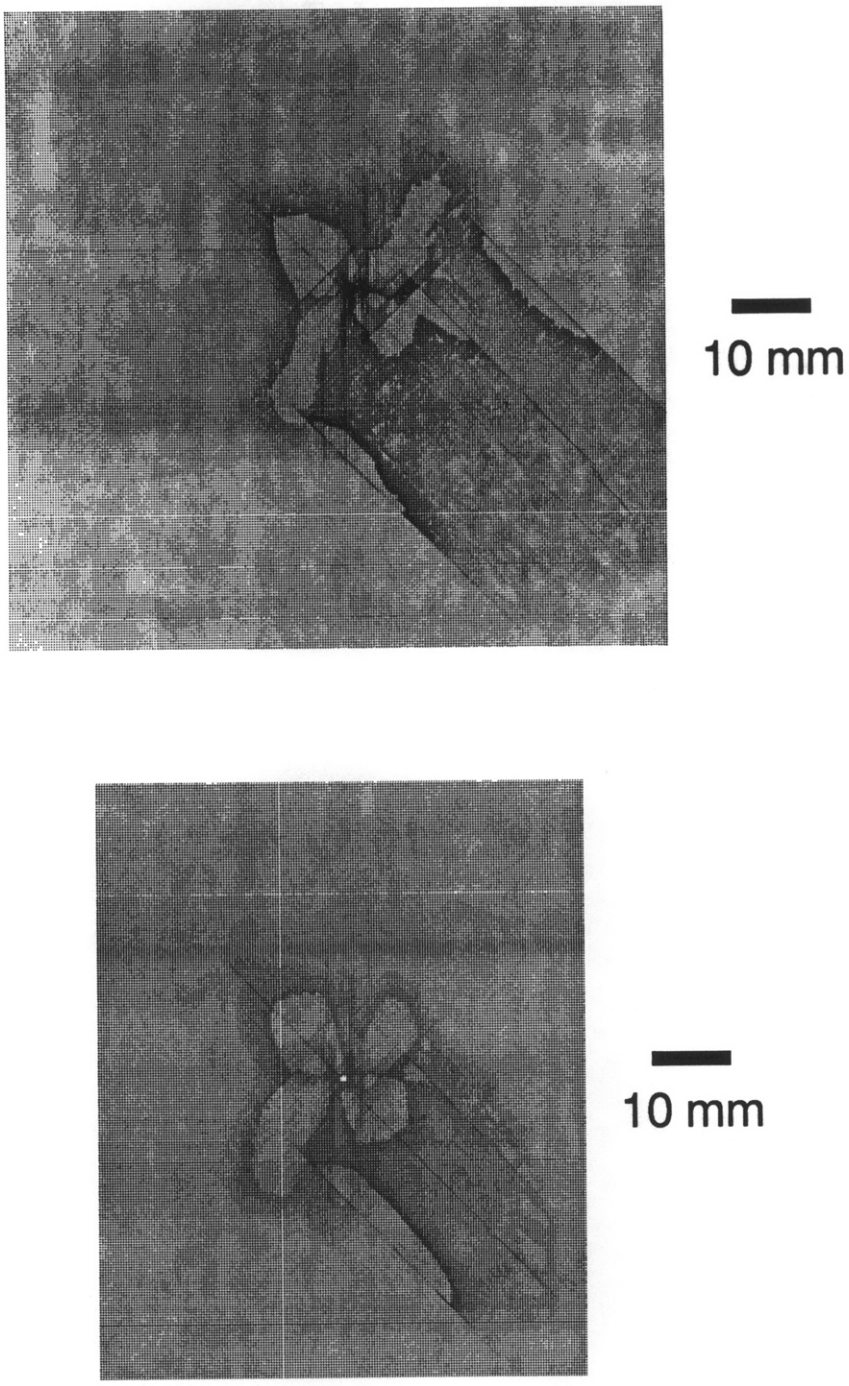

Figure 6.11 X-ray photographs of specimen type R2S2T3 loaded nominally to the same peak force of 1650 N via: (*top*) impact at 2.9 m/s, and (*bottom*) quasi-static test.

spalling in some of the impact tests, the peak force associated with penetration, and the low frequency (large relative amplitude) secondary response observed for convex specimens with large span (S2, S3, and SC) and small thickness (T1). It was shown that impact tests behave like deflection-, rather than load-, controlled quasi-static tests because of the observed stable path through the instability region in the impact force-deflection histories of convex shells. One of the strongest indications of the similarity in response comes from the comparisons of the damage states, especially the atypical damage states, for the two types of tests. Not only are impact and quasi-static tests in this investigation comparable, but the peak impact force is noted to be a key damage resistance and response metric. Based on the evidence presented in this section, it is assumed that results from quasi-static tests can be applied to the discussion of impact response. Thus, the rest of this chapter draws together the data from quasi-static and impact tests to form conclusions about how the structural parameters influence the response, i.e. response refers to either impact or quasi-static response.

6.3 Effects of Structural Parameters

Structural parameters were varied (scaled as discussed in chapter 3) to investigate the effect of these parameters on the loading response of composite structures. The structural parameters affect the response of the specimen to loading. Thus, for a given impact event (velocity in this investigation), varying any of the three structural parameters will affect the response metrics, e.g. peak force. This section provides a discussion of the results of this aspect of the present work using data presented in chapter 5. This section is broken up into two parts. First, the effect of varying

structural parameters on specimen response, e.g. peak force, is discussed. In the second section, the effects of structural parameters on the resultant damage state (response) are discussed.

6.3.1 Loading Response

The instability has been shown, in chapter 5, to have a significant effect on the response of convex shells. Concave and plate specimens, as expected, do not display any of the characteristics of the instability phenomenon. Thus, the instability behavior in the response of convex shells is significantly different from the response of plates noted in previous investigations. This instability phenomenon is noted to have a significant effect on the response parameters. Trends observed for convex specimens in this investigation can be very different from trends observed in this and previous work for plates, due to the instability. An example is that for plates, peak impact force increases with velocity up to penetration, while for convex shells there is a range of velocities (not associated with penetration) where the peak impact force is noted to remain constant because of the instability region. For convex specimen type R1S2T1, the velocity range associated with a constant peak impact force was noted to span from 2 m/s to 4 m/s (nominal). Additionally, trends affected by the instability phenomenon for convex shells are different than those observed previously for convex shells [35]. For example, peak force was noted to increase for larger radii shells in [35], whereas peak impact force was observed in this investigation to decrease on the first equilibrium path and increase on the second. The instability phenomenon thus has a strong effect on the response of convex shells to impact and quasi-static loading.

For shells with an instability (or inflection point), one author has suggested that the impact force-deflection response of composite shells should be normalized using the Budiansky-Roth type criterion [35]. In this approach, the force is normalized by the critical snapping load and the deflection by the shell height. The shell height is illustrated in Figure 6.12 (see equation 6.1 presented later) along with the radius and span for a generic convex shell. This normalization is done to allow comparison of force-deflection plots for different impact events and shell geometries. The criterion was originally developed for clamped spherical isotropic caps under uniform pressure loading [83] but has been applied [35] to impacted rectangular planform cylindrical composite shells. The normalization is shown for the force-deflection response of two different shell types with varying radius in Figures 6.13 and 6.14. The normalization works fairly well in Figure 6.13 for S2T1 specimen types but clearly is not sufficient for the S1T1 specimen types in Figure 6.14. The normalization does not capture much of the behavior for shells with an instability, especially after the critical snapping load. The normalization also does not capture the behavior before the critical snapping load, on the first equilibrium path. Therefore, the results from this investigation indicate that this normalization does not capture the characteristics of cylindrical composite shell response, particularly when an instability is observed.

An interesting comparison between convex shells with the instability and concave shells can be made if the origin for deflection is shifted such that the deflection origin is the initial deflection of a plate specimen (zero shell height, see Figure 6.12). Quasi-static response curves for specimen types R2S1T1 and R2S1T1 (concave) are presented in Figure 6.15 and for specimen types R3S1T1 and R3S1T1 (concave) in Figure 6.16. It can be seen from the

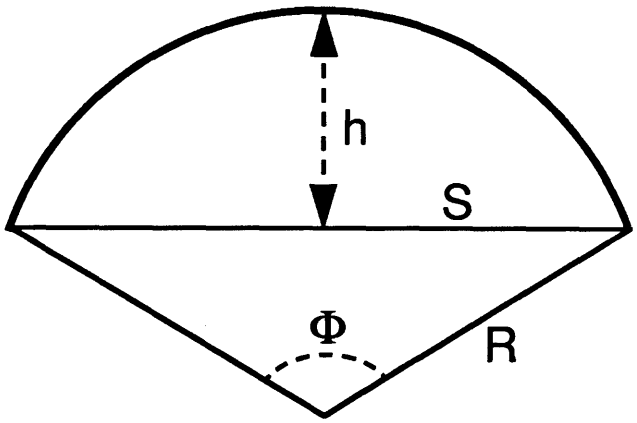

Figure 6.12 Illustration of shell height and the included angle, Φ.

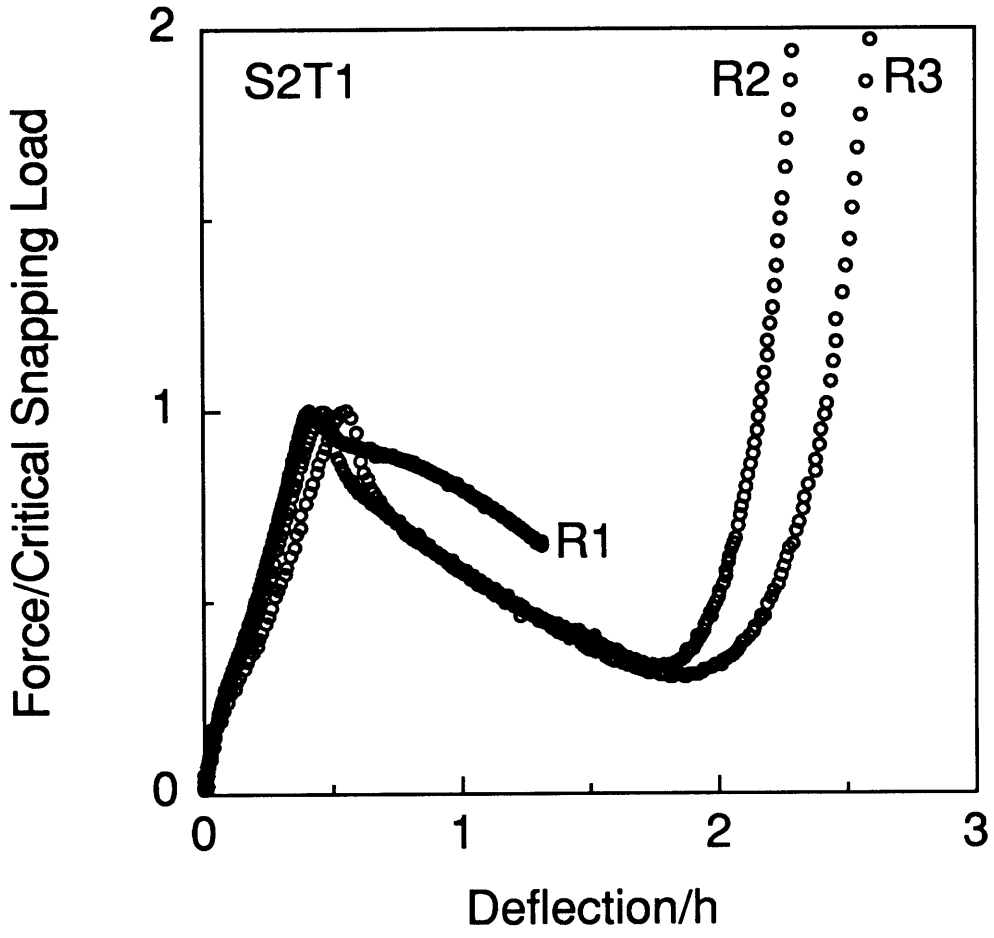

Figure 6.13 Force-deflection response normalization based on Budiansky-Roth criterion [83] for S2T1 type convex shells.

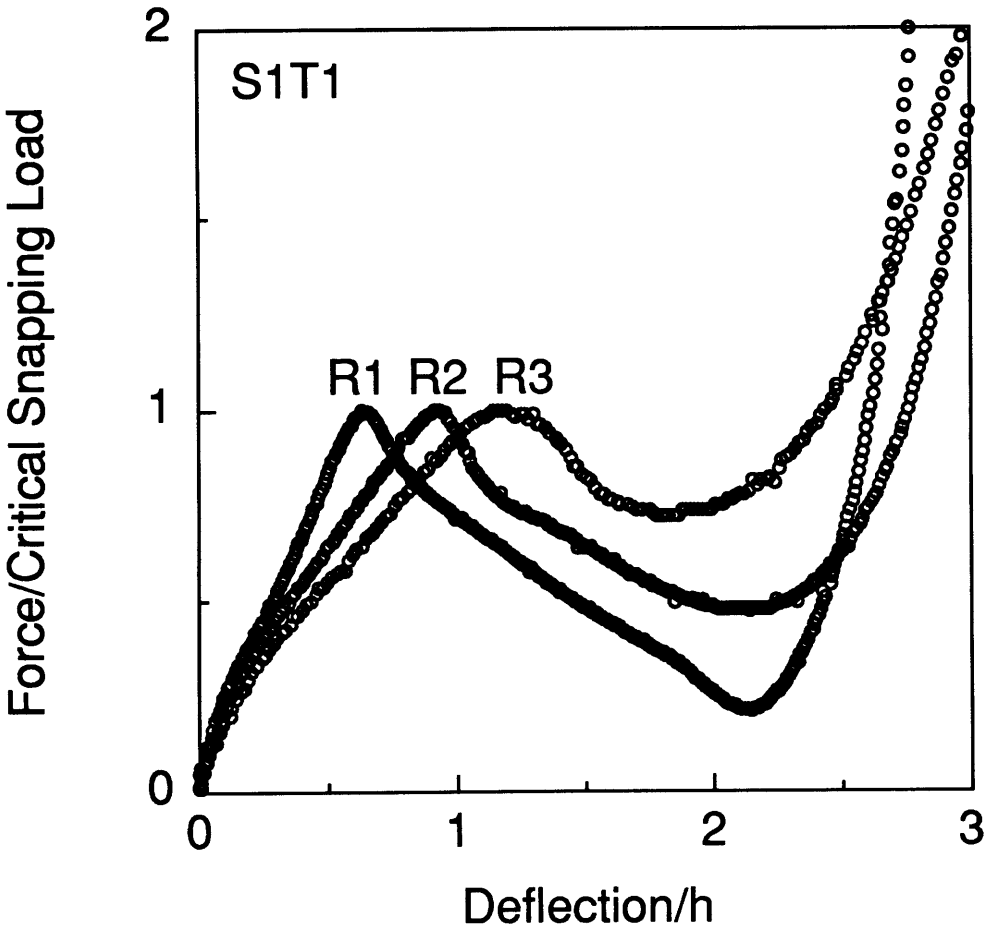

Figure 6.14 Force-deflection response normalization based on Budiansky-Roth criterion [83] for S1T1 type convex shells.

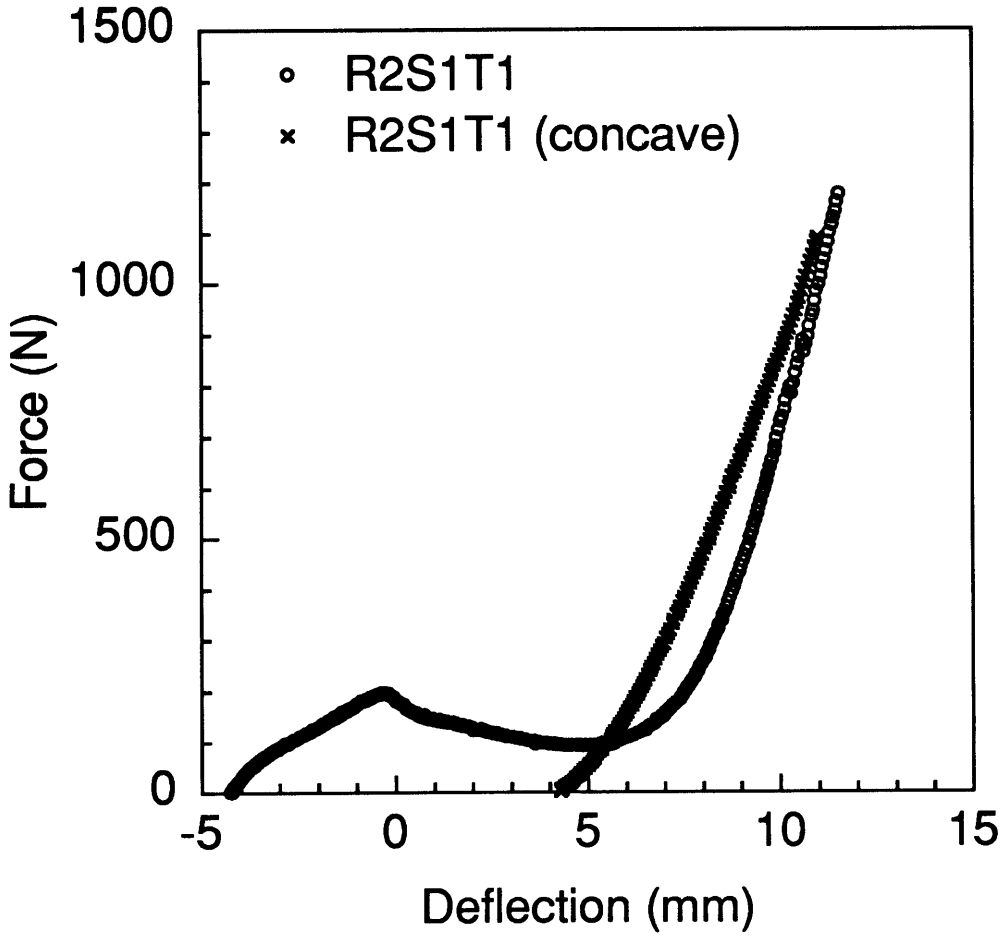

Figure 6.15 Quasi-static force-deflection response with shifted deflection origin for specimen types R2S1T1 and R2S1T1 (concave).

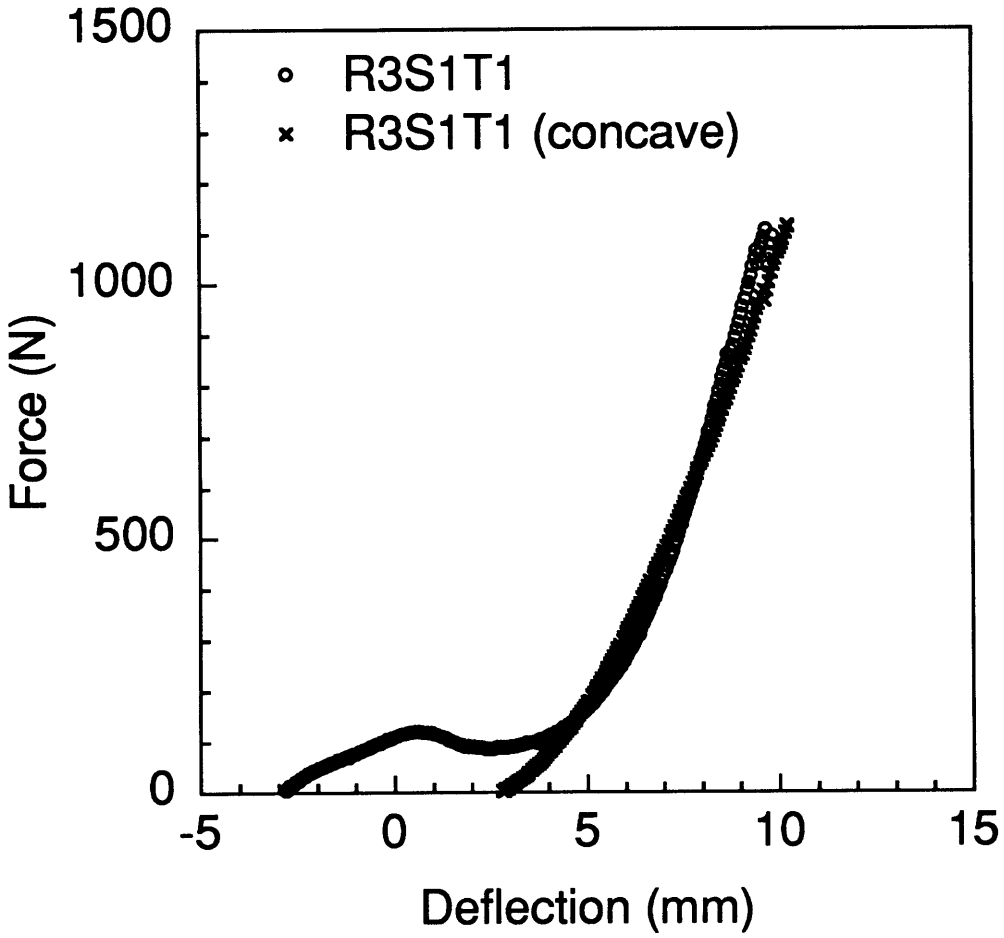

Figure 6.16 Quasi-static force-deflection response with shifted deflection origin for specimen types R3S1T1 and R3S1T1 (concave).

figures that the loading along the second equilibrium path for the convex shell is nearly identical in shape and magnitude to that of the concave shell. This behavior is also noted for convex and concave specimen type R1S1T1. If a pure membrane shell were loaded transversely in the convex and concave position, the loading along the second equilibrium path for the convex shell would be identical to the loading of the concave shell with this shift of deflection origin. Thus, the S1T1 specimen types that have the instability in this investigation show significant contributions of membrane stiffness to the loading response. It is likely that specimens with higher bending stiffness will not have overlapping responses such as those shown in Figures 6.15 and 6.16 because the relative importance of the membrane stiffness with respect to the bending stiffness decreases. Results from this investigation indicate that the relative contribution of membrane stiffness versus bending stiffness is thus a key parameter in the response of convex shells. As the structural parameters change, the relative contributions of membrane stiffness and bending stiffness to the response are also expected to change. Understanding the effects of varying the structural parameters on this aspect of the shell response is necessary to understand the overall behavior of shells subjected to transverse loading. This understanding will help to identify regimes where either the bending or membrane stiffness dominates the response as well as to understand the regime where both effects contribute to the overall response.

It was shown in chapter 5 that all structural parameters affect both the response shape (force-time and force-deflection histories) as well as the response parameters. For example, the trend of peak impact force with radius actually reverses depending on which equilibrium path the peak force occurs on. Radius was shown to be an extremely important parameter

because it has a strong effect on the development of the instability region; also, without curvature, there is no instability. The development can be seen in Figure 6.17 where force-deflection responses for S1T1 shells of various radii and specimen RPS1T1 are presented. The effect of the instability on the response is noted to increase as the radius is decreased (curvature is increased). As the radius gets larger for the specimens in Figure 6.17, the instability region is noted to become smaller and approach the monotonic type response of the plate specimen. Thus, increasing the curvature of the specimen has the effect of increasing the effect of the instability on the response. Increasing the specimen span or decreasing the thickness increases the effect of the instability region as well. Decreasing the thickness decreases the bending stiffness significantly which allows the instability to develop more quickly.

Some authors, e.g. [83], cite shell height as an important parameter in governing the response of shells to transverse loading. Shell height is defined as the initial height of the convex shell at its center. An illustration of the shell height is given in Figure 6.12. The geometrical relation between shell height, radius, and span is given by:

$$h = R - \sqrt{R^2 - \left(\frac{S}{2}\right)^2} \tag{6.1}$$

where h is the shell height, R is the shell radius, and S is the span of the shell. Thus, increasing the radius decreases shell height and increasing the span increases the height (with the restriction that $S \leq 2R$). The instability region will become larger as the shell height is increased since an increase in shell height is equivalent to a decrease in radius (see Figure 6.17). The instability region also becomes larger with an increase in span (see Figure

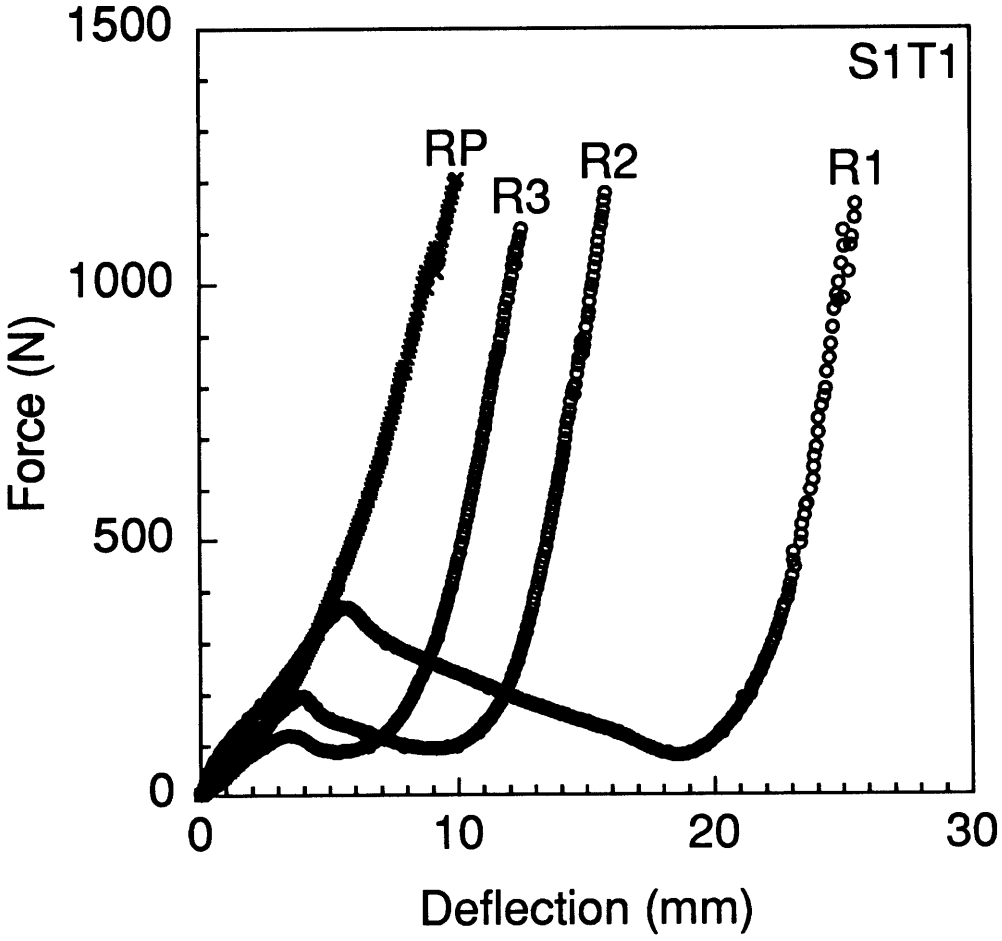

Figure 6.17 Force-deflection loading response of S1T1 plate specimen and convex shells of various radii.

5.79) and an increase in shell span is also equivalent to an increase in shell height. However, shell height alone does not define a shell: another structural parameter such as radius, span, arcspan, or the included angle (Φ in Figure 6.12) must also be specified. Arcspan and included angle will also likely affect the response according to their relation to the radius and span.

The trends of the response parameters (such as peak force) with the shell height follow the trends previously established for radius and span given the relation between shell height, radius, and span (see equation 6.1). For example, decreasing the radius was shown to increase the critical snapping load (see Figure 6.3). Increasing the shell height, which is equivalent to decreasing the radius for these specimens, thus has the same effect on the response. This is shown in Figure 6.18 where the critical snapping load for specimen type S1T1 is plotted versus shell height for both impact tests at 3.0 m/s (nominal) and quasi-static tests (compare to Figure 6.3). There are too few specimens in the test matrix (for a given thickness) that have the same shell height with different radii and span to make a comparison based solely on shell height. Therefore, although the shell height will capture trends with radius and span when each is varied independently, it is not known (because of lack of data) whether shell height is an important parameter or if it simply captures radius and span effects. It is important to determine whether shell height captures trends in the data whether radius or span is varied and this should therefore be investigated more fully.

Ratios of the shell height with radius and span simply provide a different way of varying the radius-to-span ratio due to the geometric relation between height, radius, and span. In Figure 6.19, the peak impact force for convex shells impacted at 3.0 m/s (nominal) is plotted versus the radius-to-height ratio. This plot is quite similar to the one found in Figure 5.44 for the

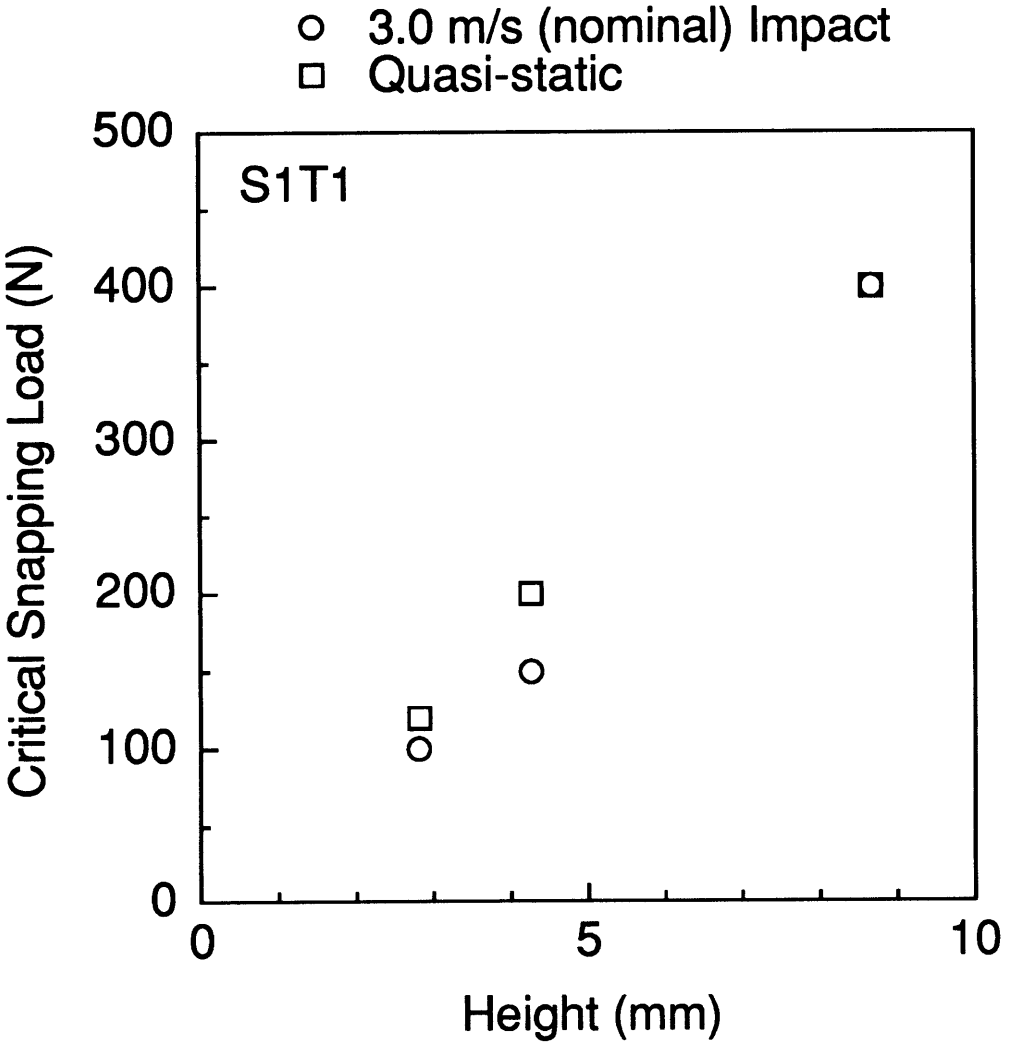

Figure 6.18 Critical snapping load versus height for convex specimen types S1T1 impacted at 3.0 m/s (nominal) and loaded quasi-statically.

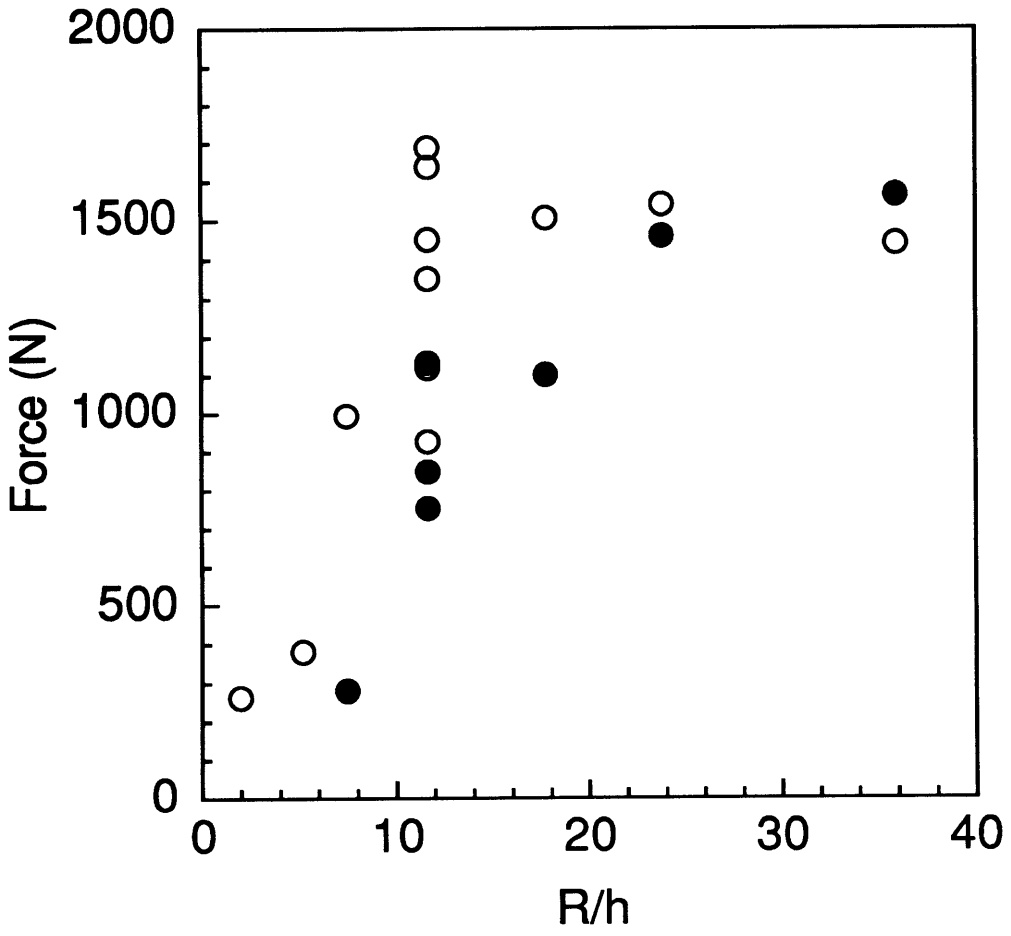

Note: filled data points indicate instability

Figure 6.19 Effect of radius-to-height ratio on peak impact force for convex specimens impacted at 3 m/s (nominal).

same data plotted versus the radius-to-span ratio. Additionally, the plot of this data versus the span-to-height ratio is also similar to Figure 5.44. As noted in chapter 5, no clear trends over the range of impact velocities tested were observed for the radius-to-span ratio. The same can be said of the radius-to-height and span-to-height ratios.

The height-to-thickness ratio combines both radius and span into one parameter (h) along with thickness. The plot of peak impact force versus the height-to-thickness ratio for convex shells impacted at 3 m/s (nominal) is given in Figure 6.20. For small values of the height-to-thickness ratio, the peak impact force is noted to decrease nearly linearly as shown in the blow-up of Figure 6.20 presented in Figure 6.21. Plots of peak impact force versus the height-to-thickness ratio for impact velocities of 1 m/s, 2 m/s, and 4 m/s (nominal) are presented in Figures 6.22 to 6.24 to illustrate that the peak impact force follows approximately the same nearly linear trend for small values of the height-to-thickness ratio. This nondimensional parameter may capture the behavior of convex shells when the height-to-thickness ratio is small. However, for large values of this nondimensional ratio, the data does not lie along this line. This is shown in each of the graphs in Figures 6.20, 6.22, 6.23, and 6.24. In each case, at a height-to-thickness ratio of approximately 190, the damage has leveled off from the earlier linear trend. Thus, no clear trend is evident with respect to peak impact force over the entire range of the height-to-thickness ratio but there may be a regime (small height-to-thickness ratio) where this parameter captures the response. The results presented in Figures 6.20 to 6.24 (especially Figure 6.21 where much data is available) indicate that the height-to-thickness ratio should be further investigated to determine the effect this parameter has on the response.

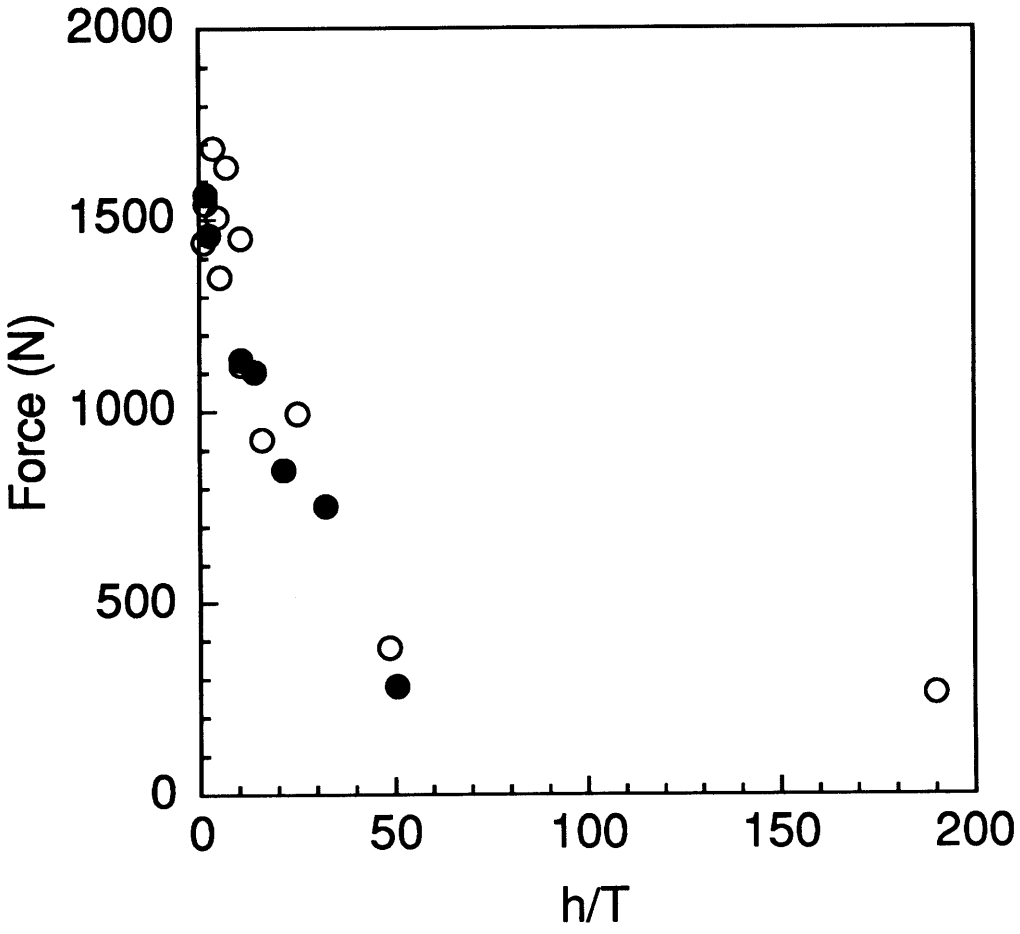

Note: filled data points indicate instability

Figure 6.20 Effect of height-to-thickness ratio on peak impact force for convex specimens impacted at 3 m/s (nominal).

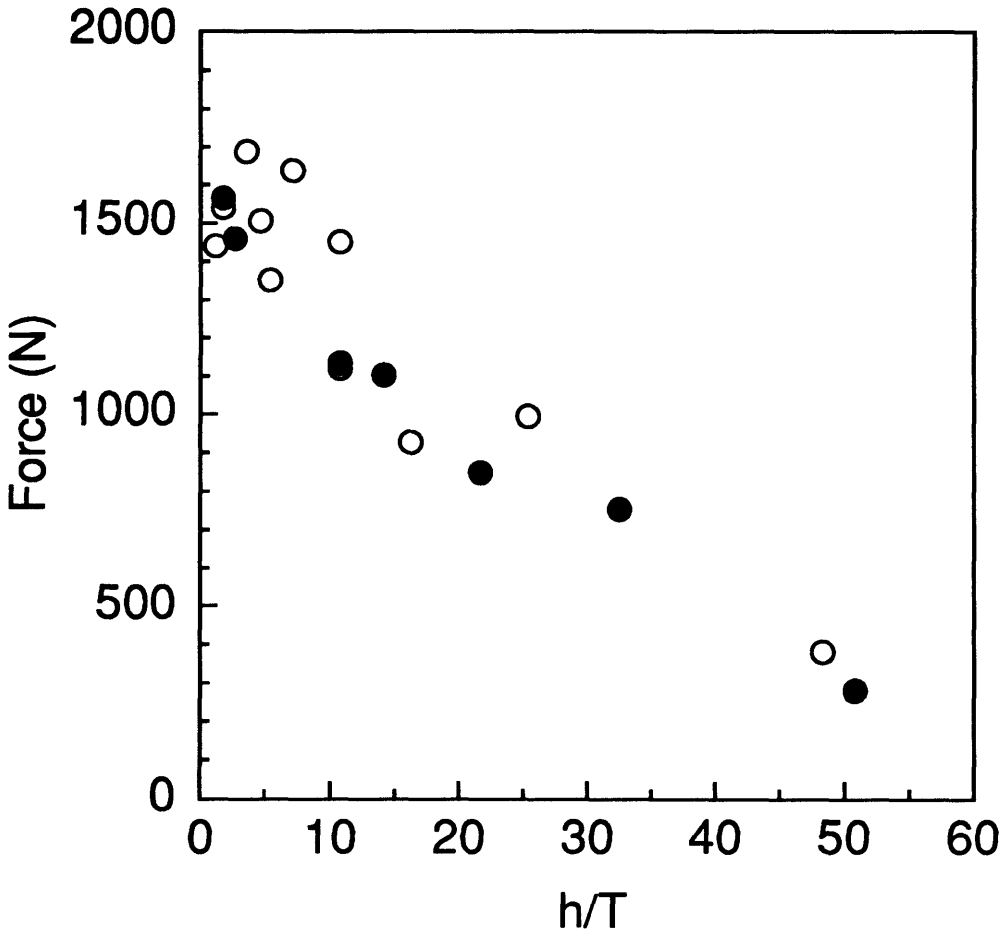

Note: filled data points indicate instability

Figure 6.21 Blow-up of Figure 6.20: Effect of height-to-thickness ratio on peak impact force for convex specimens impacted at 3 m/s (nominal).

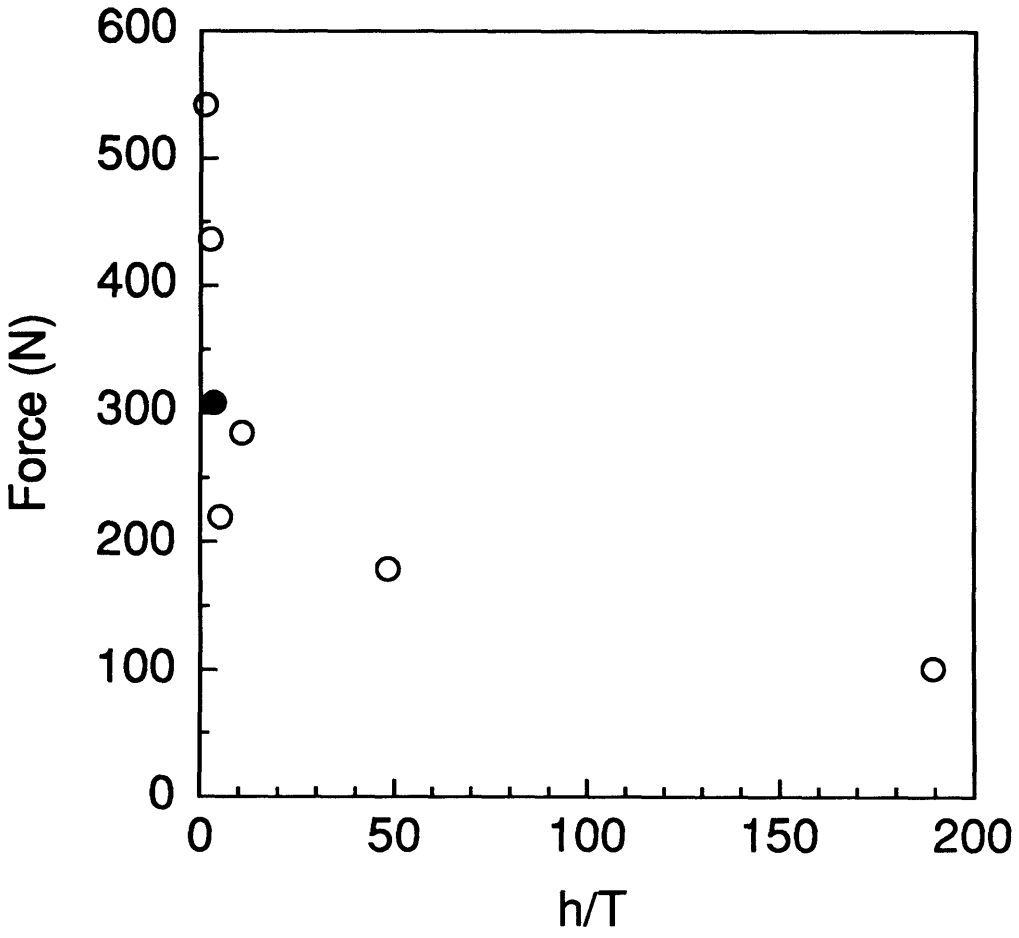

Note: filled data points indicate instability

Figure 6.22 Effect of height-to-thickness ratio on peak impact force for convex specimens impacted at 1 m/s (nominal).

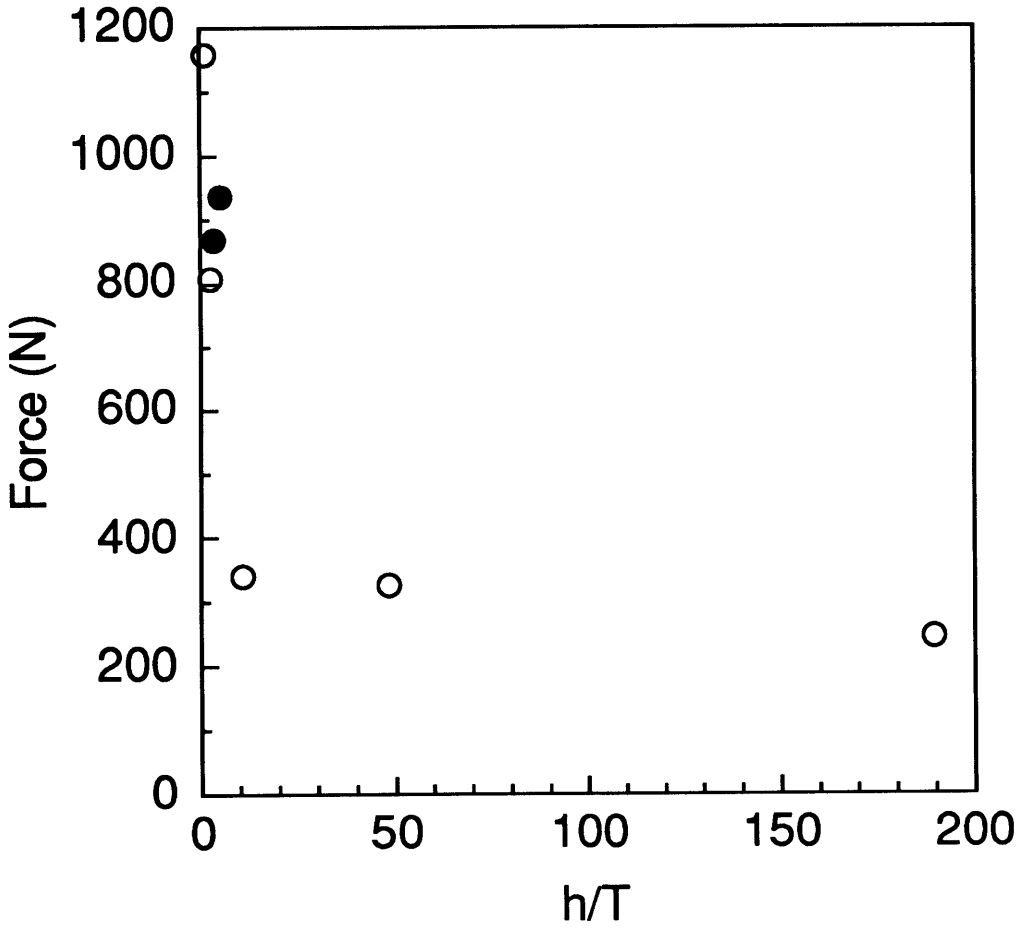

Note: filled data points indicate instability

Figure 6.23 Effect of height-to-thickness ratio on peak impact force for convex specimens impacted at 2 m/s (nominal).

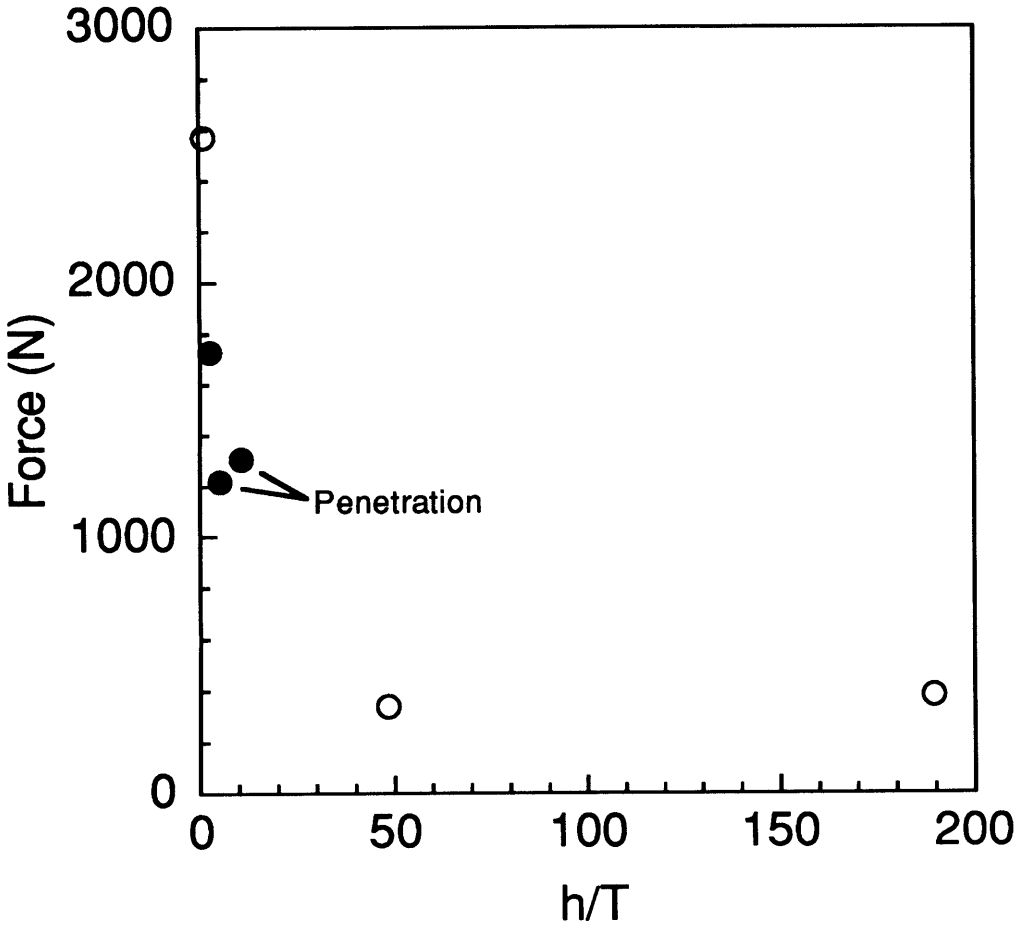

Note: filled data points indicate instability

Figure 6.24 Effect of height-to-thickness ratio on peak impact force for convex specimens impacted at 4 m/s (nominal).

Specifically, more data is needed in the region between the small height-to-thickness ratio (linear trend) and the datapoints at a height-to-thickness ratio near 190 to better characterize the behavior.

It was found that the scaled structural parameters (radius, span, and thickness) all affect the shell response and response parameters and that the same can be said for the shell height (which can be derived from the radius and span). Of the three structural variables, thickness is observed to have the strongest effect on the response of convex shells, regardless of the instability. As the thickness increases, the peak impact force increases regardless of the instability (see Figures 5.40 to 5.42). Increasing the thickness increases both the bending stiffness and the membrane stiffness of the specimen and also alters the relative contributions of each to the overall response. It was shown in chapter 5 (by comparing constant structural ratios) that trends with thickness prevailed over trends with radius and span which indicates that radius and span affect the response to a lesser degree than thickness. Thickness is noted to be a key parameter in the impact response of all specimens tested. Shell height was shown in this chapter to capture trends with radius and span following the geometrical relation between radius, span, and shell height. It is not known whether shell height is an important parameter due to lack of data to compare shells with different radius and span that have the same shell height. As found with the structural ratios, ratios involving shell height do not show any clear trends in the data over the entire range of impact velocities tested. However, the data indicates that there may be a region (or regions) where the height-to-thickness ratio may be a key parameter in the response of convex shells (small height-to-thickness ratio regime). Thus, both the height and height-to-thickness ratio warrant further investigation.

Shells with large span (S2, S3, and SC) and small thickness (T1) are noted to have a low frequency, large amplitude, secondary response as compared with other convex shells. This large secondary response in the force-time histories for cylinders does not compare very well with the half-sinusoid type response predicted by previous authors [57]. However, it is interesting to note that for an impact by what these authors considered a medium mass, a low frequency secondary response was generated in their analysis on top of the primary half-sinusoid type response, much like the force-time histories observed in this investigation. This behavior was not discussed as being different than other plots in the paper which displayed only the typical half-sinusoid response. This low frequency, large amplitude secondary response may be another manifestation of the relative importance of bending versus membrane stiffness in the response of convex shells. These specimens have the largest membrane stiffening effect relative to bending stiffness of all specimens tested. The large amplitude response of these large shell sections, being different than smaller sections which behave more like quasi-static tests, may indicate that the larger shell specimens are not representative of a real structural component such as a wing. These considerations are important in scaling if future work shows that low frequency oscillatory response characteristics are not a part of the response of actual structural components.

The impact response of cylinders is noted to be different than for the half cylinders restrained in the test fixture. The boundary condition of pinned/no in-plane sliding seems to have a significant effect on the response. Cylinders have lower peak forces for a given impact event, longer contact durations, and larger deflections than similar half cylinders. The effect of the boundary condition is to restrain the half cylinder from deforming in a mode

that would increase the half cylinder diameter (compare Figures 5.68 and 5.70). Cylinders do not have this restraint. The stiffening effect on the force-deflection response can be easily noted by comparing the quasi-static force-deflection curves (see Figure 5.66) for the cylinder and half-cylinder. The difference in the response for these specimens indicates that the stiffening effect of the no in-plane sliding boundary condition is an important aspect of the response of shells restrained in the test fixture. The full cylinder deformation mode (response) is not likely be excited by projectile impact of a typical aerospace structure such as a fuselage due to stiffeners in the fuselage structure. The shell sections restrained in the test fixture are probably more representative of a fuselage or wing which have stiffeners and other internal support structures. Therefore, the boundary conditions are very important in modeling the response of actual structures and using full cylinders to model shell impact likely will not accurately characterize the response.

Initial stiffness (force-deflection response) of the various specimens tested gives an indication of the initial force-deflection response of convex shells to loading (along the first equilibrium path). The initial stiffness is nonlinear due to geometric coupling in the shells and thus quantitative comparisons are not possible. However, trends are evident from the force-deflection data presented in chapter 5, e.g. Figure 5.76. Initial stiffness of the shells tends to increase as the radius decreases (curvature increases). Plates have zero curvature and concave specimens can be considered to have negative curvature. The initial stiffness is generally observed to increase with increasing absolute curvature, whether the shell is convex or concave with the plate having the lowest initial stiffness of all the specimens tested. This trend is not surprising because of the membrane stiffening effect associated with curvature, and has been documented for convex isotropic

shells by previous authors, e.g. [79]. It should be noted, however, that the trend of initial stiffness with radius (or other structural parameters) does not necessarily apply to the overall response of the shell. For example, an initially stiffer shell may actually be more structurally compliant at higher loads due to the instability region that develops as the response progresses. Therefore, the initial stiffness is not a good way to characterize the overall response of convex shells.

Results from this investigation also provide important conclusions about the contact stiffness of composite shells. It was noted in chapter 5 that only a very small region of the contact response, in the initial part of the loading, can be accurately modeled by the nonlinear Hertzian contact law. In the small region where the response is nearly Hertzian, the exponent in the contact law is typically very close to the value of 1.5 predicted for an isotropic half-space. The large deflections of the convex shells, relative to plates, which cause large membrane stresses and possible "'wrapping" of the indentor around the specimen, makes the assumptions surrounding the contact law invalid after only a small part of the shell response. This is evident in the force-indentation plots (see Appendix F).

It is further interesting to note that negative values of indentation (laminate expansion through-the-thickness) were measured during testing of some convex shells. This might be explained by the formation of damage such as delaminations on the back surface of the specimen. However, another explanation seems equally valid. A laminate under compressive in-plane membrane loads will generally expand through-the-thickness due to Poisson's effect (except for special cases [84]), thus causing negative values of indentation. Compressive membrane stresses are generated from transverse loading of the convex shells. In the region of contact, it would seem likely

that the local contact behavior of the indentor compressing the specimen through-the-thickness would overcome the Poisson effect causing expansion through-the-thickness. However, in the instability region, the contact force (stress) decreases significantly while the compressive membrane forces remain large. Comparison of force-indentation data and force-deflection data (to define the instability region) for specimens R1S1T1, R2S1T1, and R3S2T1 seems to substantiate this hypothesis. The force-indentation response for specimen R1S1T1 is presented in Figure 6.25 to illustrate the laminate expansion behavior. The force (and indentation) increase to approximately 400 N (the critical snapping load) following a nearly Hertzian stiffening response. However, the indentation moves to negative values as the load decreases slightly (through the instability region). At approximately 150 N, the indentation reverses trend and again moves toward positive values which corresponds to loading on the second equilibrium path and an increase in the contact force. It is evident from this discussion that the Hertzian type model of contact is only valid in a very small region of shell response and is not adequate to characterize the local behavior of the indentor contacting the shell. The wide variation in the local contact response, especially in that it differs markedly from the classical Hertzian approximation, makes modeling of the local problem difficult.

In summary, the instability region has been noted to be a key phenomenon in the loading response of convex shells. Trends in response parameters such as peak impact force are affected by the instability and differ from those observed for plates and concave shells. Thickness has been shown to affect the shell response to a greater degree than radius or span. Membrane stiffening in many convex shells has been noted to have a significant effect on the response for specimens with small thickness (T1). It

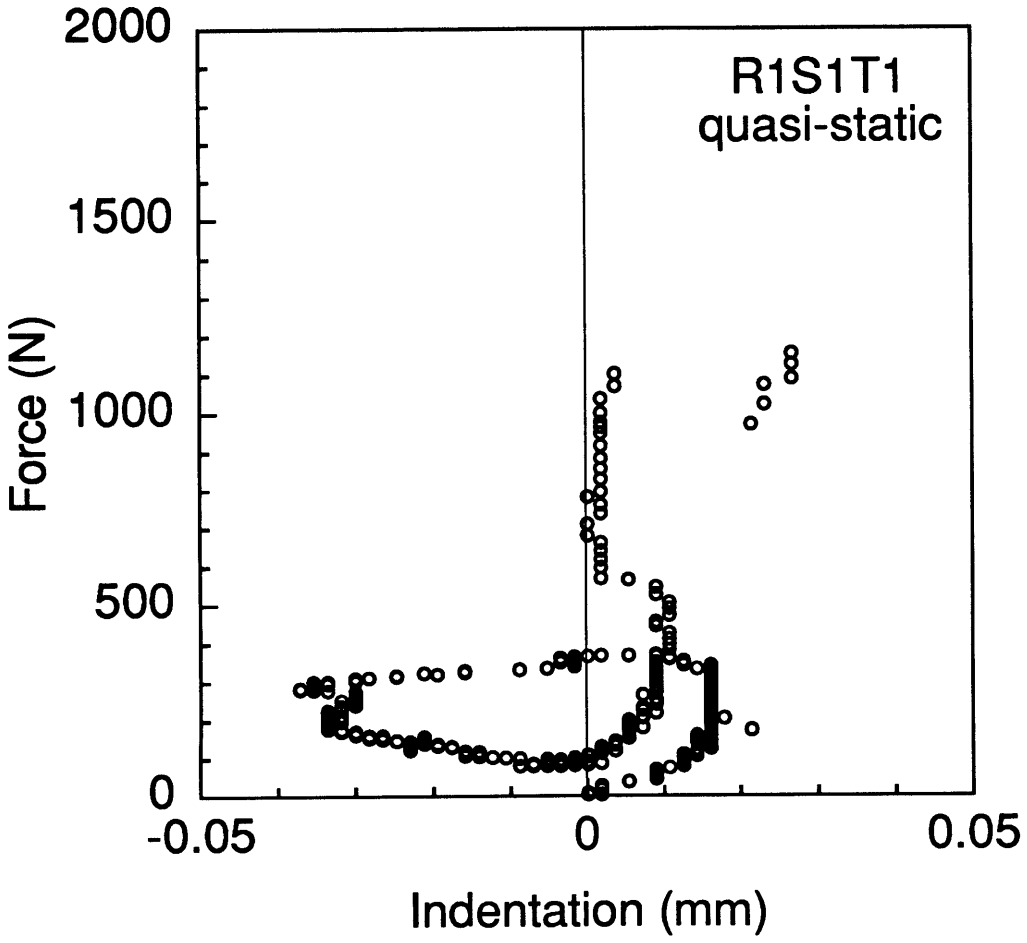

Figure 6.25 Force-indentation response for quasi-static loading of specimen R1S1T1.

is important to understand the relative importance of membrane stiffness to bending stiffness and define regimes where either of the two effects dominate the response and what happens when they both are important. The derived parameter, shell height, has been noted to capture the trends with both radius and span and increasing the shell height by varying either the radius or span has the effect of increasing the instability region in the force-deflection response for convex shells. The height-to-thickness ratio is potentially a key parameter in the response of convex shells. Another observed response phenomenon is that (S2, S3, or SC) convex shells with small thickness (T1) have a large amplitude secondary response in the impact tests that is not observed in the quasi-static tests. This is probably linked to the large relative importance of the membrane stiffness to bending stiffness of these shells. This effect may not need to be accounted for in modeling because this characteristic of the response is not noted in smaller shell sections which are thought to be more representative of a fuselage because of stiffeners. However, this effect should clearly be considered, particularly when structural scaling is undertaken. The local behavior of the indentor/impactor contacting the laminate is quite different than the classical Hertzian behavior and this will pose difficulties in modeling this aspect of the response. Finally, the present discussion indicates that the relative importance of membrane stiffness to bending stiffness, i.e. "ratio" of these effects, is a key parameter in characterizing the response of convex shells to transverse loading and should be more closely investigated.

6.3.2 Damage

The comparison of damage based on varying the structural parameters must be approached carefully. Damage has been shown to be a function of

the peak force, and peak impact force has been shown to be a function of the three structural parameters (radius, span, and thickness). Given an impact event (velocity in this investigation), varying any of the structural parameters changes the response, including the peak impact force. Thus, comparisons based on varying the structural parameters should look toward how the change in specimen geometry affects the peak force to determine how the damage will be affected. Therefore, the discussion of the effect of structural parameters on the damage extent focuses on how the response (peak force) has changed and what effect this change has on the resultant damage state.

It was noted in chapter 5 that, in general, damage extent increases with velocity. Also, peak force increases with velocity except in the region of the instability where it is approximately constant. Thus, damage increases with peak force. The average damage extent metric plotted versus peak force for all convex shells (impact and quasi-static) is presented in Figure 6.26 to illustrate how the damage extent increases with peak impact force. The average damage extent is noted to increase along a nearly linear path up to approximately 1500 N regardless of the instability or combinations of structural parameters that define the response (and peak force). This is illustrated in Figure 6.27 where a line indicating the nearly linear behavior is drawn. The convex shell that did progress into the instability region with approximately 35 mm average damage extent (see Figure 6.27) exhibited spalling (specimen R3S2T1 impacted at 3.0 m/s) which explains the large damage extent at this force. Around a peak force of approximately 1500 N, the average damage extents for some convex specimens are noted to increase significantly, clearly indicating a different behavior from the nearly linear trend.

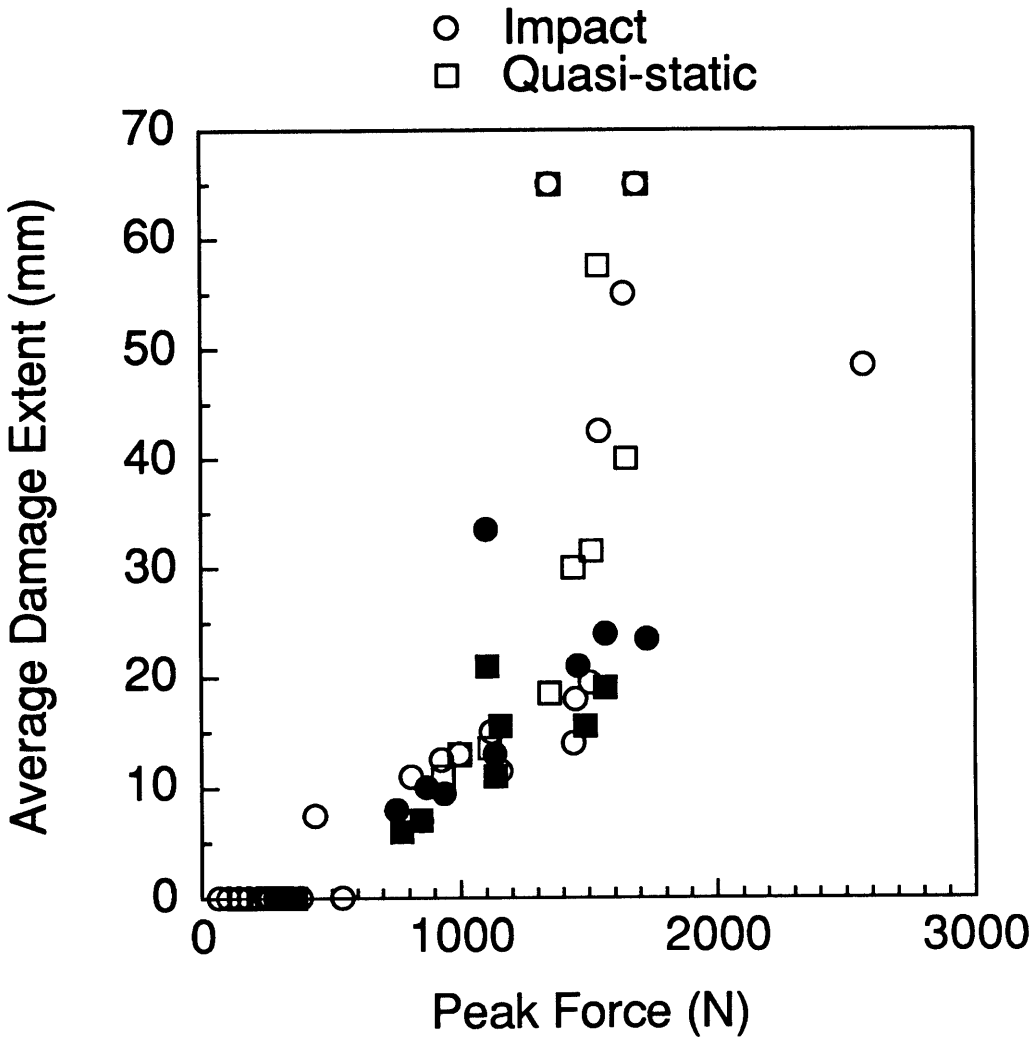

Note: filled data points indicate instability

Figure 6.26 Average damage extent versus peak force for convex shells impacted and tested quasi-statically.

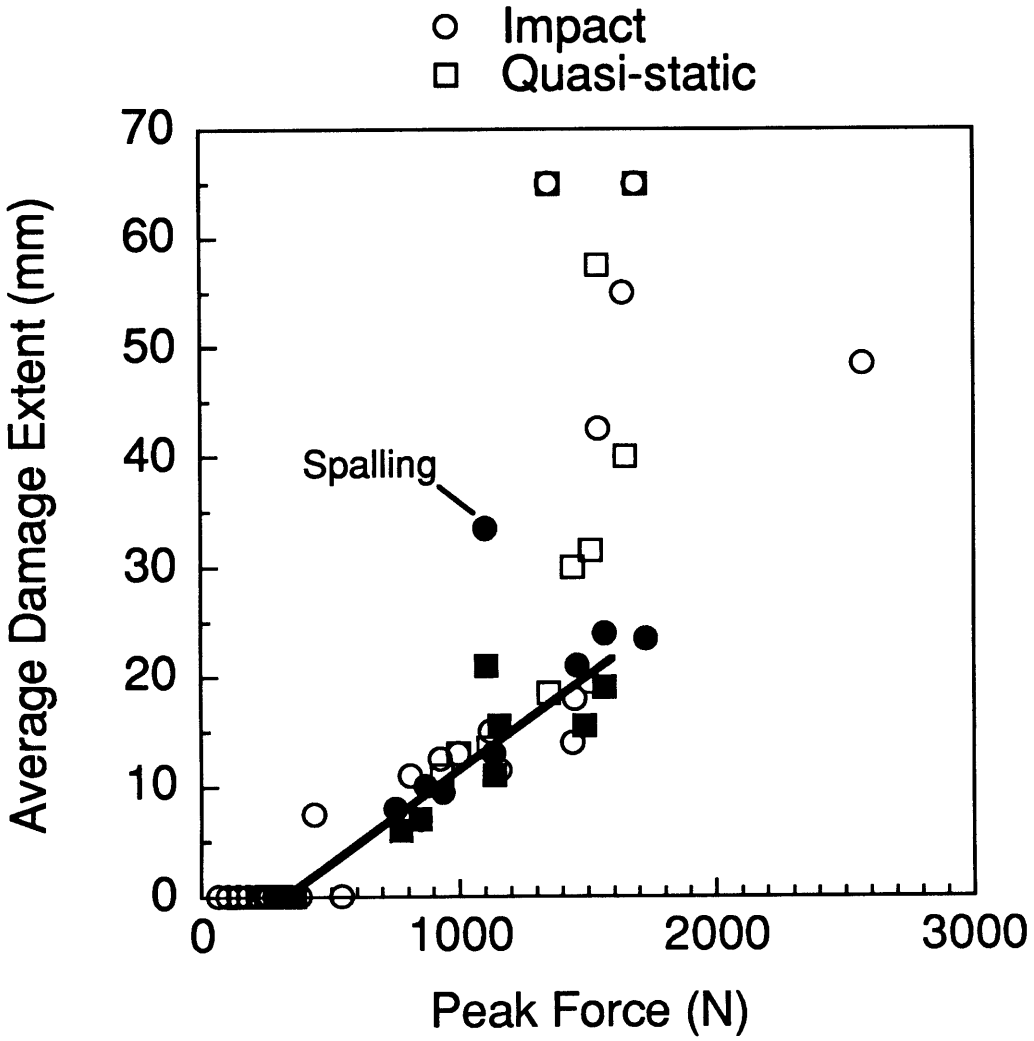

Note: filled data points indicate instability

Figure 6.27 Average damage extent versus peak force for convex shells impacted and tested quasi-statically illustrating nearly linear relationship below approximately 1500 N.

The specimens that deviate from the nearly linear behavior did not evidence an instability, i.e. the peak force occurred on the first equilibrium path for all these specimens. These specimens were all of thickness T2 or T3 and span S1 or S2 as shown in Figure 6.28. The characteristic that sets the response of these specimens apart from the majority of specimens is that these shells reach high peak loads on the first equilibrium path without reaching the critical snapping load. This is due to the shell structural parameters which govern the response. Except for specimen type R1S1T2, all these specimens have the highest thickness, T3, which contributes both bending and membrane structural stiffness to the convex shell which allows these shells to resist the instability. Small span also contributes to the structural stiffness of the shells. Specimen type R1S1T2 is a 'deep' shell which means this configuration has significant membrane stiffness contributions to the overall structural stiffness of the specimen. By contrast, specimen types R2S1T2 and R3S1T2, having larger radius (smaller shell height) as compared to specimen type R1S1T2, have less of a contribution from membrane stiffness and the same contribution to bending stiffness. These latter two specimens transition through the instability region and have average damage extents between 20 mm and 25 mm (these are the three filled impact datapoints above 1300 N in Figure 6.28). These datapoints lie along the nearly linear portion of the line drawn in Figure 6.28.

The membrane stress for specimens on the first equilibrium path is compressive whereas it is tensile on the second equilibrium path (and for plates and concave shells). Therefore, due to the structural parameters that cause high peak forces on the first equilibrium path, the convex shells which deviate from the near linear average damage extent versus force behavior have large compressive membrane stresses at peak load. Combined with

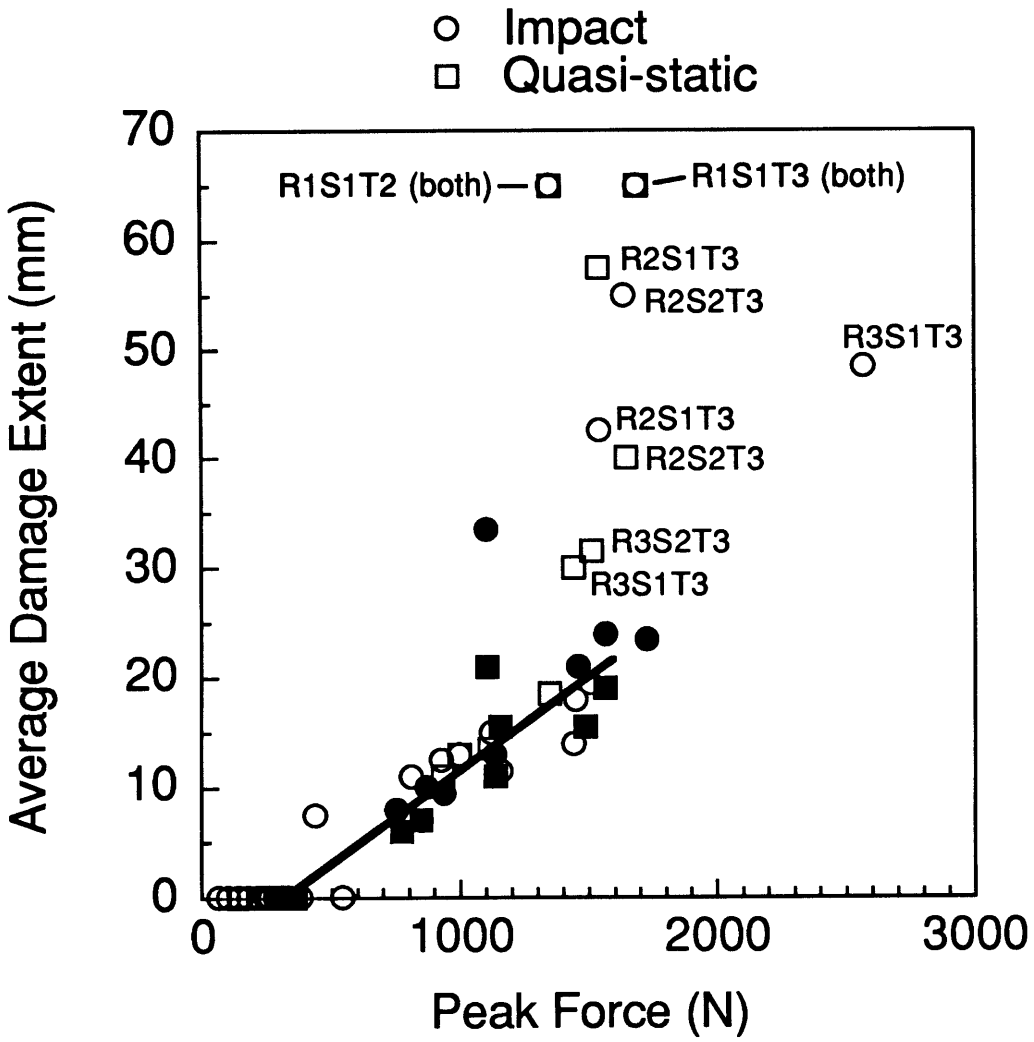

Note: filled data points indicate instability

Figure 6.28 Average damage extent versus peak force for convex shells impacted and tested quasi-statically indicating convex specimens with peak impact force on the first equilibrium path which deviate from the nearly linear relationship shown in Figure 6.27.

large bending stresses, the contribution from the compressive membrane stresses seems to be the reason for the large deviations in average damage extent from the nearly linear relationship. Further support for this hypothesis is provided by considering the average damage extent trend with radius for the specimens which deviated from the nearly linear behavior (these specimens are indicated in Figure 6.28). Aside from specimen type R1S1T2, two 'families' of specimens are observed to have large average damage extents: specimen types S1T3 and S2T3. It can be noted in Figure 6.28 that for the two families of convex shells, the average damage extent deviates to a greater extent from the near linear behavior as the specimen radius is decreased (specimen type R1S2T3 was not included in the test matrix). Contributions from membrane stiffness increase over bending stiffness contributions with increased curvature (decreased radius). Thus, the average damage extent of the specimens deviates further from the near linear damage extent behavior as the compressive membrane stress (membrane stiffening effect) increases. Therefore, it is probable that the in-plane compressive stresses of the specimens in Figure 6.28 that deviate from the nearly linear damage extent versus force trend contribute (along with high bending stresses) to the significantly increased damage extent. Analysis of this type of loading must be undertaken to understand the relative contributions of the bending and membrane stresses to determine how the damage state is affected.

Concave and plate specimens, like convex shells on the second equilibrium path, have tensile membrane stresses at peak load. The average damage extent for plate and concave specimens impacted and tested quasi-statically is presented in Figure 6.29 on the same scale as Figures 6.26 to 6.28 for comparison. Although high peak forces are reached (well above 1500

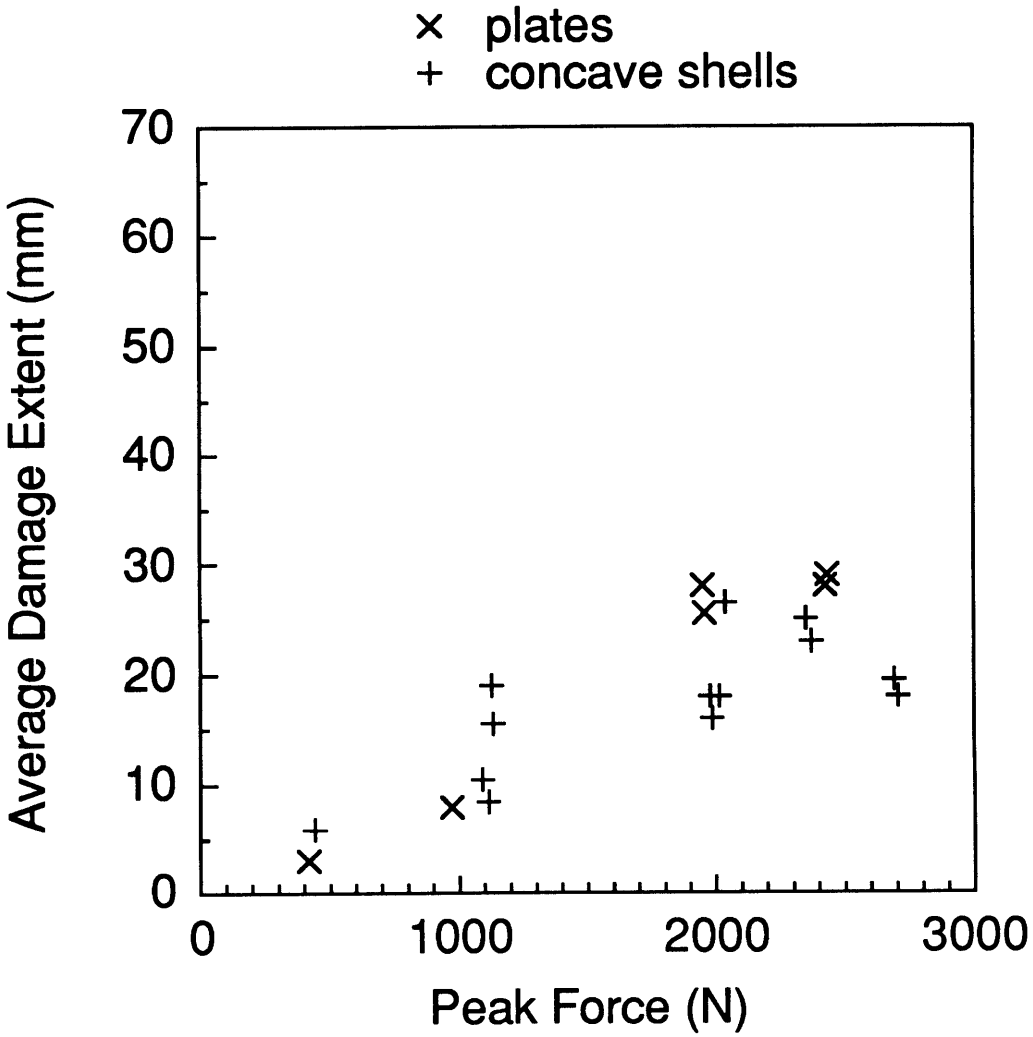

Figure 6.29 Average damage extent versus peak force for plates and concave shells impacted and tested quasi-statically.

N), the average damage extent is not noted to increase beyond approximately 30 mm for any of the specimens. By comparison, specimen type R3S1T3 has an average damage extent of approximately 50 mm. Specimen type R3S1T3 at approximately 2600 N was the only T3 convex specimen impacted at 4 m/s (nominal) which is the reason this datapoint is set apart from the rest of the data in Figure 6.28. This specimen has the peak force on the first equilibrium path and thus, unlike the plates and concave shells, would have a compressive membrane stress at peak load. The average damage extent trend for plates and concave shells, which have tensile membrane stresses at peak load, is small compared to the damage extent for convex shells on the first equilibrium path, even at high loads. This therefore also supports the hypothesis that compressive membrane stresses, combined with high bending stresses, play a large role in the significantly increased damage extent of convex shells on the first equilibrium path.

All of the specimens noted in chapter 5 to have atypical damage states are included in those specimens which deviate from the linear damage extent versus force trend. This would suggest that convex shells which have peak force on the first equilibrium path and resist passing through the instability (compressive membrane stresses) damage to a different extent and with a different planar distribution than convex shells that pass through the instability (tensile membrane stresses). These specimens were noted to have unsymmetric damage extents and delamination distributions different from the single- and double-peanut type delaminations noted for other convex shells. Again, compressive membrane stresses may contribute to the large damage extents noted for these specimens.

The observation that convex shells on the first equilibrium path have increased damage extents and different distributions than convex shells on

the second equilibrium path, possibly due to compressive membrane stress contributions to the overall stress state, leads into a discussion of the average damage extent ratios. The data presented in chapter 5 indicates that the damage distributions for convex shells on the first and second equilibrium paths are distinctly different. The average damage extent ratios for convex shells with peak force on the first equilibrium path is nearly twice that for specimens with peak forces on the second equilibrium path (0.63 compared to 0.34). Again, this may be an indication of tensile and compressive membrane stresses contributing to differences in the damage state. Also, the average damage extent ratios for plates and concave shells (which have tensile membrane forces) are 0.31 and 0.46, respectively. These ratios are very near the ratios for the convex shells on the second equilibrium path (0.34) which also have tensile membrane forces at peak load. This also indicates that the difference in damage states depends on the relative contribution of compressive or tensile membrane stresses to the overall stress state when the peak force is reached. The coefficients of variation for the average damage extents are noted to be very high (~30%). However, this large of a coefficient of variation does not explain the large difference in the average damage extent ratios for convex shells on the first and second equilibrium paths. These and other results discussed in this section strongly indicate that the damage extents/distributions are influenced differently by compressive and tensile membrane stresses at peak load.

It is not known whether the position of the damage through the laminate thickness is different for convex shells with peak forces on the first and second equilibrium paths, i.e. the atypical damage extents and distributions may be manifestations of damage occurring in (or between) different plies in the laminate. Analysis of these types of convex shells will

help determine the relative importance of the compressive membrane stresses on the overall stress state but further experimental work to characterize the damage more rigorously (through-the-thickness) is also required to understand the increased damage extent phenomenon for convex shells that have peak forces on the first equilibrium path.

Finally, there are reasons for the damage states observed for specimens R1S1T2 and R2S2T3 being unsymmetric (and atypical) (see Figures 6.10 and 6.11). Unsymmetric deformation modes are not only possible, but predicted, for some transversely loaded arches [85]. In relation to the observed unsymmetric damage states, the specimens may have deformed in an unsymmetric fashion and thus the resultant stress and damage are also unsymmetric. The deformation modes for specimens R1S1T2 and R2S2T3 were not easy to observe visually during testing due to the small displacements associated with the desired peak loads for these specimens so it is not known whether the deformations were unsymmetric. However, the unsymmetric damage states strongly indicate unsymmetric deformation and therefore unsymmetric deformation modes should be considered in modeling transversely loaded composite shell structures.

In this section, the average damage extent is noted to be a function of the peak impact force and to increase nearly linearly for convex shells up to a force of approximately 1500 N, regardless of the structural parameters that govern the response (peak force). At peak forces above approximately 1500 N, the average damage extent increases significantly for convex shells that remain on the first equilibrium path. These specimens have increased damage extent as well as atypical damage distributions. The observations in this section indicate that compressive membrane stresses in convex shells that are generated when the peak force occurs on the first equilibrium path

are likely a key mechanism in damage formation. These specimens damage to a greater extent than other convex shells with an instability (tensile membrane stresses) at an equivalent peak force. Furthermore, the average damage extent is noted to be larger for convex shells on the first equilibrium path than for any of the concave and plate specimens at equivalent peak forces. Structural parameters that cause the peak force to remain on the first equilibrium path, effectively delaying the onset of the instability, include increased curvature (decreased radius) and increased thickness. These parameters change the relative contributions of membrane and bending stresses which affects the response of convex shells to loading including the resulting damage state. Analytical modeling of the loading of composite shells is needed to quantify these effects and define parameters which govern this behavior, especially in relation to the relative contributions of membrane and bending stiffness to the response of convex shells and the effects of compressive and tensile membrane stresses on the resulting damage states.

6.4 Implications for Damage Resistance

Many factors affect statements about the damage resistance of shell specimens tested, e.g. convex specimens without the instability often have a greater damage extent at a given impact force than do plates and concave specimens. However, the key for damage resistance is to consider the damage given an impact event. In an impact event, energy from the impactor is transferred to the specimen but the total energy is conserved. The initial energy of the impactor is consumed by the rebound energy of the impactor, structural energy (work done in deforming the specimen), damage energy, and higher order terms such as heat and noise generation. It is easy to see

that increasing the energy consumed in deforming the structure leaves less energy available for damage formation.

The area under the force-deflection curve for a specimen is likely a good indicator of the energy associated with structural deformation. Convex shells, through large structural deformations under load as compared with plates and concave shells, can consume larger amounts of impact energy. By consuming large amounts of energy through structural deformation, convex shells reach lower peak forces than plates or concave shells. For specimen types S1T1 (all radii) impacted at 1 m/s (nominal), the convex shells were not damaged but the plate and concave shells were. The convex shells all had lower peak forces for the impact at 1 m/s (nominal) than the concave and plate specimens. This would seem to support the hypothesis that increased structural energy leaves less energy available for damage formation. It was also observed that convex specimens with large span (S2, S3, and SC) and small thickness (T1) experienced large deflections, low peak forces, and were also undamaged at all four impact velocities. This again indicates that structural deformation, peak force, and damage are related. Convex shells can also have an instability which has large deformations associated with this instability region. For example, specimen type R1S1T1 impacted at 2 m/s (nominal) progressed into the instability region and was not damaged during testing whereas specimens RPS1T1 and R1S1T1 (concave) were both damaged. The peak force attained for specimen R1S1T1 at an impact velocity of 2 m/s (nominal) was 340 N, whereas the peak forces for the plate and concave specimen were 970 N and 1130 N, respectively. The large deformations associated with the instability for convex shells consume impactor energy which results in lower peak forces and less damage extent.

The force-deflection loading histories of specimen types S2T1 are presented in Figure 6.30 so that a comparison of specimens with different instability regions can be made. The specimens are tested quasi-statically to the same peak forces measured during impact tests. As discussed in section 6.2, the quasi-static loading of specimen R1S2T1 should have been stopped after a deflection of 31 mm instead of 50 mm. Regardless, the energy associated with deforming this specimen to 31 mm deflection (matching the impact test) can be obtained by calculating the area (using the trapezoidal rule for integration as in chapter 5) under the force-deflection curve for this specimen. This calculation yields an energy of 8.1 J. Likewise, the energies under the curves for specimens R2S1T1 and R3S1T1 are calculated to be 6.0 J (instability) and 5.1 J (instability), respectively. Larger energies associated with structural deformation correspond to lower peak forces, as can be noted in Figure 6.30. The average damage extents for the R1, R2, and R3 impacted convex shells of type S1T1 are 0 mm, 7 mm (instability), and 34 mm (instability), respectively. Thus, increasing the effect of the instability region indicates a mechanism by which impact energy can be consumed which results in lower peak forces. This, in turn, leads to decreased damage extent.

The effects of structural parameters on the damage response of specimens can therefore be understood by considering the effects these parameters have on the consumption of impact energy through structural deformation. By examining Figure 6.30, it can be seen that as the radius decreases (curvature increases) and the instability becomes more prevalent, the shells consume more energy through structural deformation. It can therefore be seen that one significant way in which the structural parameters affect the damage state is through the development of the instability region which may also be linked to the relative contribution of membrane to bending

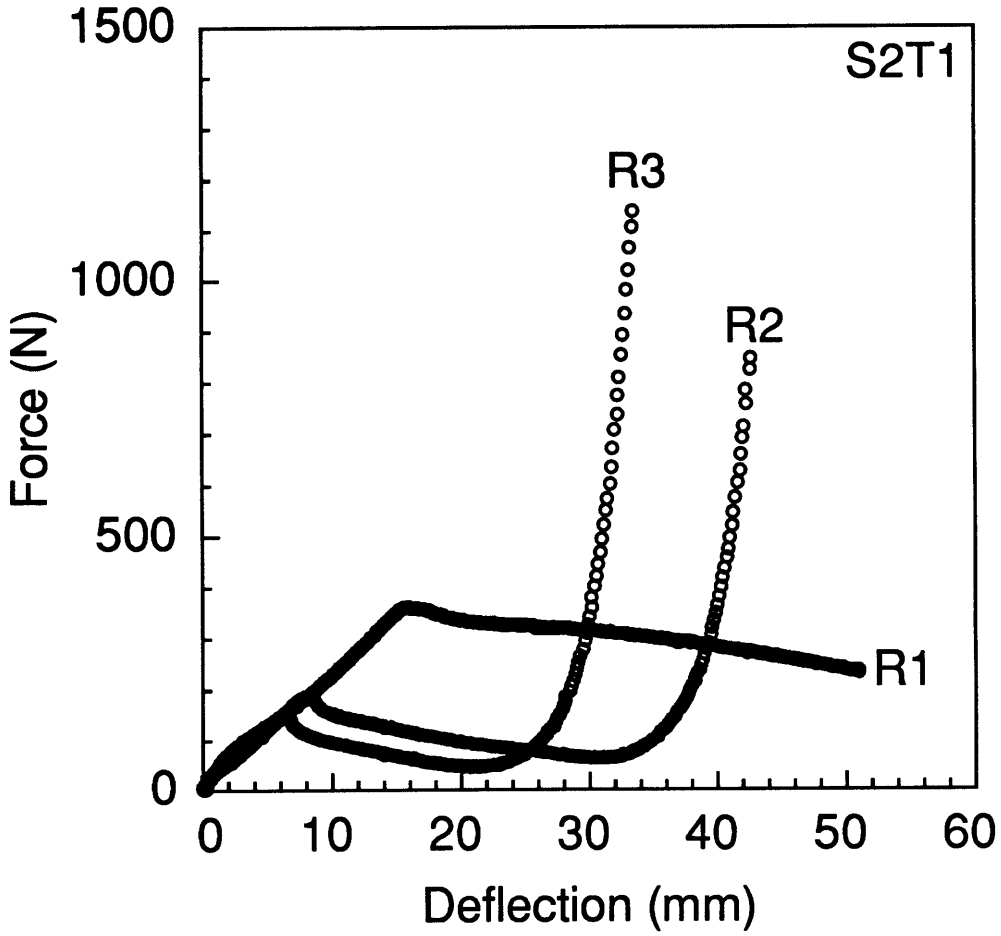

Figure 6.30 Force-deflection loading response of S2T1 specimens of various radii.

stiffness. It was previously noted that decreasing the radius (increasing the curvature), increasing the span, and decreasing the thickness leads to larger instability regions. As the radius or thickness decreases, the relative contribution of membrane stiffness to bending stiffness increases. Varying the structural parameters in this fashion should thus increase the energy consuming mechanism of the instability region and lead to lesser amounts of damage. For example, since peak force has been shown to correlate with damage extent, i.e. larger forces equal more damage, the energy consumed to a given force for two specimens can be compared to illustrate the effect of the instability region. Considering Figure 6.17, the energies consumed to reach a force of 400 N for the RP and R1 specimens are 0.8 J and 4.6 J (instability), respectively. Adding curvature, and thus an instability region, for the convex specimen increases the energy consumption by a factor of 5. More (impact) energy is consumed in taking the convex shell to 400 N than for the plate specimen. This can also noted by considering Figures 6.15 and 6.16. It is clear in these figures that the energy associated with structural deformation to an equivalent peak force is greater for the convex shell than for the concave shell. Concave shells, like plates, load monotonically and thus have poor (compared with convex shells) energy absorbing capability through structural deformation.

The observations in this section concerning absorbed energy and damage resistance lead to further discussion. It has been shown that given an impact event, convex shells can absorb more energy through structural deformation (sometimes through the instability phenomenon) than corresponding plate or concave specimens. Given an impact event, this results in improved damage resistance of convex shells over plates and concave shells. However, the results from section 6.3 indicate that convex

shells which do not progress into the instability region can incur greater amounts of damage than plates or concave shells at an equivalent force, not an equivalent impact event. This is important when addressing the issue of barely visible impact damage (BVID). BVID refers to an impact damage level in composite structures that has little visual indication of damage to the naked eye. Since impact damage to composite structures cannot be reliably characterized visually, there exists the possibility that substantial damage can be missed during inspection which needs to be taken into consideration when designing damage tolerant composite structures. Thus, convex shells have improved impact damage resistance in general, but may contain greater amounts of nonvisible subsurface damage of the BVID level than plates. This is shown by the deviation of some convex shells from the nearly linear damage extent versus force trend in Figure 6.28. There is thus a trade-off or even duality with respect to impacted composite shells in that convex shells have the ability to be more impact resistant than plates but also have the characteristic that hidden damage occurs to a greater extent. Essentially, convex shells on the first equilibrium path may incur more non-visible damage at equivalent forces than plate specimens (compare Figures 6.28 and 6.29). If convex specimens damage to a greater extent than plates, with the same visual cues (BVID), then this must be accounted for when defining design allowables for damage tolerant structural design.

Convex shells, through increased structural deformation (sometimes due to the instability region), can consume more impact energy than corresponding plate or concave specimens and reach lower peak forces as a result. For the instability region, this is simply because it takes more energy to reach a force on the second equilibrium path than on the first. Lower peak forces result in less damage, and convex shells effectively have a mechanism

by which to reduce damage formation from impact events. Therefore, convex shells have the advantage of possibly being more damage resistant than plates or concave shells. However, with the same visual cues identifying the damage as BVID, convex shells which experience peak loads on the first equilibrium path (which depends on the shell structural parameters) may incur larger amounts of hidden damage than plates or convex shells (at an equivalent peak force) which have loaded past the critical snapping load on the second equilibrium path. The increased damage extent of convex shells with high peak forces on the first equilibrium path may be due to the relative contribution of compressive membrane stresses as compared with bending stresses for these specimens. This relative contribution or "ratio" of membrane stiffness to bending stiffness effects is considered key to understanding the response of convex shells to transverse loading. Modeling of composite shells to determine the effects of both structural parameters and the instability region on the resulting damage state are required to fully understand the mechanisms that affect the damage resistance (such as membrane stresses and the energy consuming ability of convex shells) of convex shells.

CHAPTER 7

CONCLUSIONS AND RECOMMENDATIONS

The present work was conducted to experimentally investigate the impact response of composite shells with emphasis on characterizing damage resistance. To do this, the effects of basic structural parameters (radius, span, and thickness) on the impact and quasi-static response of cylindrical composite shells to transverse loading were investigated. Various structural configurations were considered, including convex and concave shell sections, cylinders, and plates. Experimental response data was taken and damage characterized for all specimens. Since this is preliminary work in a relatively new area, one major aim of this research was to establish basic trends to guide future work in the area of impact-damaged composite shells. In this chapter, conclusions are drawn from the results of this investigation and recommendations for future work are made.

7.1 Conclusions

The work conducted and the data and discussion presented herein lead to the following conclusions:

1. The instability observed in the response of many convex shells, but not for plates or concave shells, is a key phenomenon in the response of convex shells. The instability affects all response parameters and

trends, even reversing the trends in some cases, and also introduces the additional parameters of critical snapping load and deflection.

2. Due to factors such as the instability, the initial stiffness (or trends of initial stiffness with structural parameters) is not an accurate way to characterize the overall response of convex shells.
3. The Hertzian type contact relation is not sufficient to characterize the local behavior of indented convex shells except in a very small region of the initial response.
4. The relative contribution of membrane stiffness to bending stiffness is considered to be key in understanding the response of convex shells.
5. The test fixture designed and built for this research was shown to consistently provide the desired pinned/no in-plane sliding boundary condition for convex shells, concave shells, and plates. However, the test fixture did not restrain some convex shells in-plane after the instability.
6. The boundary condition of pinned/no in-plane sliding stiffens the response of shell specimens and, in general, the boundary conditions are found to have a strong influence on the response.
7. Full cylinder specimens, due to elongation of the cylinder diameter (full cylinder deformation mode) under load, have a different response than half cylinders restrained in the test fixture. Boundary conditions must be accurately characterized when modeling actual structures and using full cylinders to model structures such as a fuselage (which contains stiffeners) likely will not accurately capture the response due to the effects of boundary conditions.
8. Quasi-static loading of specimens (all geometries) to the peak load measured during impact testing was generally found to produce a

response equivalent to the impact tests including the damage states, even in cases where unsymmetric and atypical damage states occurred.

9. Backface spalling was noted in some cases for impacted specimens, but not for specimens tested quasi-statically.

10. Convex shells with large span (S2, S3, and SC) and small thickness (T1) have a large amplitude, low frequency secondary response in the impact tests that is not found in the quasi-static tests. These specimens have the largest contribution of membrane stiffness relative to bending stiffness of all specimens tested.

11. Thickness, as well as radius, were shown to be key parameters with regard to the response. Both these parameters directly contribute to determining the relative contribution of membrane stiffness to bending stiffness to the response of convex shells.

12. Shell height was shown to capture response parameter trends with respect to radius and span, but it could not be determined whether shell height is an important parameter in and of itself, or whether it simply captures radius and span trends through the geometric relation between radius, span, and shell height.

13. Although no nondimensional structural ratio was noted to have a definite trend over the entire range of specimens tested, there appear to be regimes where trends with these ratios are important. In particular, peak force was shown to have a nearly linear relationship with the height-to-thickness ratio for small values of the ratio.

14. Peak force is shown to be an excellent damage resistance metric.

15. Energy consumed through structural deformation is noted to be an important indicator of the damage resistance capability of composite specimens. For the same impact event, convex shells, through large

deformations (sometimes through the instability region), have improved damage resistance over concave shells and plates.

16. Unsymmetric damage modes were observed for some convex shells with peak load on the first equilibrium path and was explained by noting that unsymmetric deformation modes (and stress states) are possible for transversely loaded convex shells.
17. Convex shells with peak load on the first equilibrium path have significantly increased hidden damage extent and different damage distributions at a given force than plates. This is attributed to the relative importance of the membrane stiffness to the bending stiffness and differences due to compressive versus tensile membrane stress.

7.2 Recommendations

The present work raises a number of issues which need to be addressed by further investigation. The following recommendations are therefore made:

1. The test fixture was designed so that modifications, if necessary, could be easily made. Modifications to the test fixture to ensure the in-plane boundary for convex shells after the instability should be pursued.
2. Analyses, which include effects of the instability region (first and second equilibrium paths), must be undertaken to understand the local stress state, resulting damage, and the relative importance of membrane stiffness versus bending stiffness. Unsymmetric deformation modes should be included in such analyses because of the observed unsymmetric damage states for some convex shell specimens.
3. A means by which to quantify membrane stiffness and bending stiffness contributions to the response of convex shells needs to be

quantified in the form of metrics to yield a "ratio" which can be used to characterize the shell and its behavior, especially with regard to structural scaling considerations.

4. The Fast Fourier Transform (FFT) technique should to used to study the difference in impact and quasi-static response noted for convex shells with large span (S2, S3, and SC) and small thickness (T1). The relative importance of the membrane stiffness to bending stiffness for these specimens should be carefully considered.
5. Spalling, and the effects that cause it, need to be understood because this is a noted difference between some impact and quasi-static tests.
6. Modeling of the local contact behavior should be further considered because the Hertzian type relation is insufficient except in a very small region of the response.
7. The effects of structural parameters (and ratios of these parameters) on the shell response and resulting damage state should be further explored, analytically and experimentally, to fully understand the mechanisms that affect damage resistance, such as the energy consuming ability of convex shells.
8. Regimes need to be identified through analysis and experiment where the membrane stiffness or bending stiffness dominate the response, and where both are important. This will likely lead to insights into how structural ratios (e.g. height-to-thickness ratio) capture trends in the response parameters.
9. The significantly increased amount of hidden damage that can be sustained by convex shells, relative to plate specimens, needs careful consideration both experimentally and analytically to determine

parameters, such as contributions from tensile versus compressive membrane stresses, that affect this type of damage response.

10. Although differences in planar damage extent and distribution have been noted for specimens with different contributions from membrane and bending stresses, the through-thickness distribution of the damage needs to be experimentally quantified using techniques such as deply [86].

References

1. Nolet, S. C. and Sandusky, P. M., "Impact Resistant Hybrid Composite for Aircraft Leading Edges", *SAMPE Quarterly*, Vol. 17, No. 4, 1986, pp. 46-53.

2. Olivia, P. V., "SF-340 Airfoil Structure - A Unique Approach", *17th National SAMPE Technical Conference*, Kiamasha Lake, NY USA, 1985,

3. Smith, P. J., Thomson, L. W., and Wilson, R. D., "Development of Pressure Containment and Damage Tolerance Technology for Composite Fuselage Structures in Large Transport Aircraft", NASA-CR-3996, Boeing Aerospace Co., August, 1986.

4. "Military Specification: Airplane Damage Tolerance Requirements", MIL-A-83444, USAF, July, 1974.

5. "Damage Tolerance and Fatigue Evaluation of Structures", FAR Advisory Circular 25.571, FAA, September, 1978.

6. Cairns, D. S. and Lagace, P. A., "A Consistent Engineering Methodology for the Treatment of Impact in Composite Materials", *Journal of Reinforced Plastics and Composites*, Vol. 11, No. 4, 1992, pp. 395-412.

7. Lagace, P. A. and Wolf, E., "Impact Damage Resistance of Several Laminated Material Systems", *Proceedings of the AIAA/ASME/ASCE/AHS/ASC 34th Structures, Structural Dynamics, and Materials Conference*, LaJolla, CA, 1993, pp. 1863-1872.

8. Choi, H. Y., Downs, R. J., and Chang, F.-K., "A New Approach toward Understanding Damage Mechanisms and Mechanics of Laminated Composites Due to Low-Velocity Impact: Part I - Experiments", *Journal of Composite Materials*, Vol. 25, August, 1991, pp. 992-1011.

9. Choi, H. Y., Wu, H.-Y. T., and Chang, F.-K., "A New Approach toward Understanding Damage Mechanisms and Mechanics of Laminated Composites Due to Low-Velocity Impact: Part II - Analysis", *Journal of Composite Materials*, Vol. 25, August, 1991, pp. 1012-1038.

10. Abrate, S., "Impact on Laminated Composite Materials", *Composites*, Vol. 24, No. 3, 1991, pp. 77-99.

11. Cantwell, E. M. and Morton, E. R., "The Impact Resistance of Composite Materials", *Composites*, Vol. 22, No. 5, 1991, pp. 55-97.

12. Matsuhashi, H., Graves, M. J., Dugundji, J., and Lagace, P. A., "Effect of Membrane Stiffening in Transient Impact Analysis of Composite Laminated Plates", *AIAA/ASME/ASCE/AHS 34th Structures, Structural Dynamics, and Materials Conference*, LaJolla, CA, 1993, pp. 2668-2678.

13. Munjal, A. K., Rahnenfuehrer, E. W., Spencer, D. F., Pickett, B. E., and Maloney, E. F., "Impact Damage Evaluation of Graphite/Epoxy Composite Materials for Space Applications", *22nd International SAMPE Technical Conference*, Boston, MA, 1990, pp. 1200-1207.

14. Cairns, D. S., "Impact and Post-Impact Response of Graphite/Epoxy and Kevlar/Epoxy Structures", TELAC Report 87-15, Ph.D. Thesis, Massachusetts Institute of Technology, 1987.

15. Wolf, E., "Impact Damage Mechanisms in Several Laminated Material Systems", TELAC Report 92-3, S. M. Thesis, Massachusetts Institute of Technology, March, 1992.

16. Caprino, G., "Composite Materials Response Under Low-Velocity Impact", *Composite Structures*, Vol. 2, 1984, pp. 261-71.

17. Lagace, P. A., Williamson, J. E., Tsang, P. H. W., Wolf, E., and Thomas, S. A., "The Use of Force as a (Impact) Damage Resistance Parameter", *American Society for Composites Seventh Technical Conference*, 1992, pp. 991-1000.

18. Jackson, W. C. and Poe, C. C., Jr., "The Use of Impact Force as a Scale Parameter for the Impact Response of Composite Laminates", *Journal of Composites Technology & Research*, Vol. 15, No. 4, Winter, 1992, pp. 282-289.

19. Lagace, P. A., Williamson, J. E., Tsang, P. H. W., Wolf, E., and Thomas, S., "A Preliminary Proposition for a Test Method to Measure (Impact) Damage Resistance", *Journal of Reinforced Plastics and Composites*, Vol. 12, No. 5, May, 1993, pp. 584-601.

20. Swanson, S. R., "Impact of Composite Cylinders", *Composites; Proceedings of the 8th International Conference on Composite Materials (ICCM/8)*, Honolulu, HI, 1991, pp. 32-C-1 to 32-C-10.

21. Tan, T. M. and Sun, C. T., "Use of Statical Indentation Laws in the Impact Analysis of Laminated Composite Plates", *ASME Journal of Applied Mechanics*, Vol. 52, 1985, pp. 6-12.

22. Lee, S. and Zahuta, P., "Instrumented Impact and Static Indentation of Composites", *Journal of Composite Materials*, Vol. 25, February, 1991, pp. 204-222.

23. Gresczuk, L. B., "Damage in Composite Materials Due to Low Velocity Impact", in *Impact Dynamics*, ed. Zukas, J. A., Nicholas, T., Swift, H. F., and Curran, D. R., Wiley-Interscience, New York, 1982, pp. 55-94.

24. Cairns, D. S., "A Simple, Elasto-Plastic Contact Law for Composites", *Journal of Reinforced Plastics and Composites*, Vol. 10, July, 1991, pp. 423-433.

25. Yang, S. H. and Sun, C. T., "Indentation Law for Composite Laminates", *Composite Materials: Testing and Design (Sixth Conference), ASTM STP 787*, ASTM, 1982, pp. 425-449.

26. Wu, E. and Yen, C.-S., "An Analytical Method for Developing the Contact Law of Laminated Plates", *ASME Summer Mechanics and Materials Conference*, Tempe, AZ, 1992, pp. 55-60.

27. Wu, E., "The Contact Behavior Between Laminated Composite Plates and Rigid Spheres", *Journal of Applied Mechanics*, Vol. 61, March, 1994, pp. 60-66.

28. Tsai, S., "A Survey of Macroscopic Failure Criteria for Composite Materials", *Journal of Reinforced Plastics and Composites*, Vol. 3, January, 1984, pp. 40-62.

29. Nahas, M. N., "Survey of Failure and Post-Failure Theories of Laminated Fiber-Reinforced Composites", *Journal of Composite Technology and Research*, Vol. 8, No. 4, Winter, 1986, pp. 138-153.

30. Graves, M. J. and Lagace, P. A., "Damage Tolerance of Composite Cylinders", *Composite Structures*, Vol. 4, No. 1, 1985, pp. 75-91.

31. Ramkumar, R. L. and Thakar, Y. R., "Dynamic Response of Curved Laminated Plates Subjected to Low-velocity Impact", *Journal of Engineering Materials and Technology*, Vol. 109, No. 1, 1987, pp. 67-71.

32. Kraft, M. J., "Impact Damage Response of Graphite/Epoxy Fabric Structures", TELAC Report 88-9, S. M. Thesis, Massachusetts Institute of Technology, 1989.

33. Lin, H. J. and Lee, Y. J., "Inelastic Impact of Composite Laminated Plate and Shell Structures", *Composite Structures*, Vol. 14, No. 2, 1990, pp. 89-111.

34. Lin, H. J. and Lee, Y. J., "Use of Statical Indentation Laws in the Impact Analysis of Composite Laminated Plates and Shells", *Journal of Applied Mechanics*, Vol. 57, No. 3, 1990, pp. 787-789.

35. Kistler, L. S., "Experimental Investigation of the Impact Response of Cylindrically Curved Laminated Composite Panels", *35th AIAA/ASME/ASCE/AHS/ASC Structures, Structural Dynamics, and Materials Conference*, Hilton Head, SC, 1994, pp. 2292-2297.

36. Palazotto, A. N., Chien, L. S., and Taylor, W. W., "Stability Characteristics of Laminated Cylindrical Panels Under Transverse Loading", *AIAA Journal*, Vol. 30, No. 6, June, 1992, pp. 1649-1653.

37. Greer Jr., J., "The Numerical Considerations in Characterizing the Dynamic Response of a Composite Shell Structure", *AIAA/ASME/ASCE/AHS 34th Structures, Structural Dynamics, and Materials Conference*, LaJolla, CA, 1993, pp. 673-682.

38. Marshall, I. H., Rhodes, J., and Banks, W. M., "Experimental Snap-buckling Behaviour of Thin GRP Curved Panels Under Lateral Loading", *Composites*, Vol. 8, No. 2, April, 1977, pp. 81-86.

39. Marshall, I. H., Rhodes, J., and Banks, W. M., "The Nonlinear Behaviour of Thin, Orthotropic, Curved Panels Under Lateral Loading", *Journal of Mechanical Engineering Science*, Vol. 19, No. 1, 1977, pp. 30-37.

40. Johnson, E. R., Hyer, M. W., and Carper, D. M., "Response of Composite Material Shallow Arch to Concentrated Load", *AIAA/ASME/ASCE/AHS 25th Structures, Structural Dynamics, and Materials Conference*, Palm Springs, CA, 1984, pp. 310-321.

41. Christoforou, A. P., Swanson, S. R., and Beckwith, S. W., "Lateral Impact of Composite Cylinders", *ASTM STP 1012*, ASTM, 1989, pp. 313-325.

42. Christoforou, A. P., Swanson, S. R., Ventrello, S. C., and Beckwith, S. W., "Impact Damage of Carbon/Epoxy Composite Cylinders", *32nd International SAMPE Symposium and Exhibition*, Anaheim, CA, 1987, pp. 964-973.

43. Palazotto, A., Perry, R., and Sandhu, R., "Impact Response of Graphite/Epoxy Cylindrical Panels", *AIAA Journal*, Vol. 30, No. 7, 1992, pp. 1827-1832.

44. Perry, R. B., "Impact Damage in Curved Graphite/Epoxy Panels with Clamped Edges", Air Force Institute of Technology, M. S. Thesis, 1990.

45. Lin, H. J. and Lee, Y. J., "Impact-Induced Fracture in Laminated Plates and Shells", *Journal of Composite Materials*, Vol. 24, November, 1990, pp. 1179-1199.

46. Manders, P. W., Bader, M. G., Hinton, M. J., and Flower, P. Q., "Mechanics of Impact Damage in Filament Wound Glass-fibre/Epoxy-resin Tubes", *Third International Conference on Mechanical Behaviour of Materials*, Cambridge, England, 1979, pp. 275-284.

47. Meyer, P. I., "Low-velocity Hard-object Impact of Filament-wound Kevlar/Epoxy Composites", *Composite Science and Technology*, Vol. 33, No. 4, 1988, pp. 279-293.

48. Alderson, K. L. and Evans, K. E., "Failure Mechanisms During the Transverse Loading of Filament-wound pipes Under Static and Low Velocity Impact Conditions", *Composites*, Vol. 23, No. 3, May, 1992, pp. 167-173.

49. Senn, E. A., "Impact Damage Tolerance of Composite Cylindrical Panels", Air Force Institute of Technology, M. S. Thesis, 1989.

50. Gause, L. W., Rosenfeld, M. S., and Vining, R. E., "Effect of Impact Damage on the XFV-12A Composite Wing-box", *25th National SAMPE Symposium and Exhibition*, San Diego, CA, 1980, pp. 679-690.

51. Yener, M., Asce, M., and Wolcott, E., "Progressive Impact Damage Assessment in Composite Pressure Vessels", *Engineering, Construction, and Operations in Space: Proceedings of Space '88*, Albuquerque, NM, 1988, pp. 518-528.

52. Minnetyan, L., Chamis, C. C., and Murthy, P. L., "Damage and Fracture in Composite Thin Shells", *23rd International SAMPE Technical Conference*, Kiamesha Lake, NY, 1991, pp. 787-801.

53. Jegley, D. C. and Lopez, O. F., "Comparison of Hand Laid-up Tape and Filament Wound Composite Cylinders and Panels With and Without Impact Damage", *AIAA/ASME/ASCE/AHS 32nd Structures, Structural Dynamics, and Materials Conference*, Baltimore, MD, 1991, pp. 1144-1152.

54. Razi, H. and Lindsay, V. C., "Analysis of Simply Supported Orthotropic Cylinders Subjected to Low-velocity Impact", *AIAA/ASME/ASCE/AHS 28th Structures, Structural Dynamics, and Materials Conference*, Monterey, CA, 1987, pp. 438-442.

55. Yener, M. and Wolcott, E., "Damage Assessment Analysis of Composite Pressure Vessels Subjected to Random Impact Loading", *Journal of Pressure Vessel Technology*, Vol. 111, No. 2, 1989, pp. 124-129.

56. Swanson, S. R., "Mechanics of Transverse Impact in Fiber Composite Plates and Cylinders", *Journal of Reinforced Plastics and Composites*, Vol. 12, No. 3, March, 1993, pp. 256-267.

57. Christoforou, A. P. and Swanson, S. R., "Analysis of Simply Supported Orthotropic Cylindrical Shells Subject to Lateral Impact Loads", *Recent Advances in the Macro- and Micro-Mechanics of Composite Materials Structures - Winter Annual Meeting of the ASME*, Chicago, IL, 1988, pp. 77-84.

58. Swanson, S. R., Smith, N. L., and Qian, Y., "Analytical and Experimental Strain Response in Impact of Composite Cylinders", *Composite Structures*, Vol. 18, 1991, pp. 95-108.

59. Chang, F.-K. and Kutlu, Z., "Strength and Response of Cylindrical Composite Shells Subjected to Out-of-Plane Loadings", *Journal of Composite Materials*, Vol. 23, January, 1989, pp. 11-31.

60. Li, S., Rosen, P. D., Reid, S. R., and Hinton, M. J., "Indentation of Laminated Filament-wound Composite Tubes", *Composites*, Vol. 24, No. 5, 1993, pp. 407-421.

61. Mustafa, B., Li, S., Soden, P. D., Reid, S. R., Leech, C. M., and Hinton, M. J., "Lateral Indentation of Filament Wound GRP Tubes", *International Journal of Mechanics & Science*, Vol. 34, No. 6, 1992, pp. 443-457.

62. Minnetyan, L. and Rivers, J. M., "Structural Durability of Stiffened Composite Shells", *AIAA/ASME/ASCE/AHS 33rd Structures, Structural Dynamics, and Materials Conference*, Dallas, TX, 1992, pp. 2879-2886.

63. Wilder, B. and Palazotto, A., "A Study of Internal Delaminations in Curved Composite Panels", *AIAA/ASME/ASCE/AHS 29th Structures, Structural Dynamics, and Materials Conference*, Williamsburg, VA, 1988, pp. 341-350.

64. Wilder, B. L., "A Study of Damage Tolerance in Curved Composite Panels", Air Force Institute of Technology, M. S. Thesis, 1988.

65. Wilder, B. and Palazotto, A., "A Study of Damage in Curved Composite Panels", *Engineering, Construction, and Operations in Space: Proceedings of Space '88*, Albuquerque, NM, 1988, pp. 518-528.

66. Palazotto, A., Maddux, G. E., and Horban, B., "The Use of Stereo X-ray and Deply Techniques for Evaluating Instability of Composite Cylindrical Panels with Delaminations", *Experimental Mechanics*, Vol. 29, No. 2, 1989, pp. 144-151.

67. Horban, B. A., "The Effects of Through the Thickness Delaminations on Curved Composite Panels", Air Force Institute of Technology, M. S. Thesis, 1985.

68. Horban, B. and Palazotto, A., "Experimental Buckling of Cylindrical Composite Panels with Eccentrically Located Circular Delaminations", *AIAA Journal of Spacecraft and Rockets*, Vol. 24, No. 4, 1987, pp. 349-352.

69. Flaggs, D. L. and Kural, M. H., "Experimental Determination of the In Situ Transverse Lamina Strength in Graphite/Epoxy Laminates", *Journal of Composite Materials*, Vol. 16, March, 1982, pp. 103-115.

70. Ranniger, C. U., "Damage Tolerance and Arrest Characteristics of Pressurized Graphite/Epoxy Tape Cylinders", TELAC Report 91-11, S. M. Thesis, Massachusetts Institute of Technology, 1991.

71. Priest, S., "Damage Tolerance of Pressurized Graphite/Epoxy Tape Cylinders Under Uniaxial and Biaxial Loading", TELAC Report 93-19, S. M. Thesis, Massachusetts Institute of Technology, 1994.

72. Ryan, K. F., "Dynamic Response of Graphite/Epoxy Plates Subjected to Impact Loading", TELAC Report 89-13, S. M. Thesis, Massachusetts Institute of Technology, 1990.

73. Thomas, S., "Effects of Structural Parameters on the Static Indentation and Bending Behavior of Graphite/Epoxy Laminates", TELAC Report 93-9, S. M. Thesis, Massachusetts Institute of Technology, 1993.

74. Wong, M., "The Effects of Fabrication and Moisture on the Curvatures of Thin Unsymmetric Gr/Ep Laminates", TELAC Report 82-1, S. M. Thesis, Massachusetts Institute of Technology, 1982.

75. Lagace, P. A., Brewer, J. C., and Varnerin, C., "TELAC Manufacturing Course Notes", TELAC Report 88-4B, Massachusetts Institute of Technology, 1990.

76. Stover, D., "Coping with Spring-in in Composite Tools and Parts", *Advanced Composites*, Vol. 8, No. 2, March/April, 1993, pp. 38-45.

77. Lie, S. C., "Damage Resistance and Damage Tolerance of Thin Composite Facesheet Honeycomb Panels", TELAC Report 89-3, S. M. Thesis, Massachusetts Institute of Technology, 1989.

78. Marshall, I. H. and Rhodes, J., "Snap-buckling of Thin Shells of Rectangular Planform", in *Stability Problems in Engineering Structures and Components*, ed. Richards, T. H. and Stanley, P., Applied Science Publisher, London, 1979, pp. 249-264.

79. Fung, Y. C. and Kaplan, A., "Buckling of Low Arches or Curved Beams of Small Curvature", NASA TN 2840, California Institute of Technology, November, 1952.

80. Press, W. H., Flannery, B. P., Teukolsky, S. A., and Vetterling, W. T., *Numerical Recipes "Fortran Version"*, Cambridge University Press, New York, 1989, pp. 484-488.

81. Timoshenko, S., *Theory of Plates and Shells*, McGraw-Hill, New York, 1940, pp. 329-333.

82. Budiansky, B. and Hutchinson, J. W., "Dynamic Buckling of Imperfection-sensitive Structures", *International Congress of Applied Mechanics*, Munich, Germany, 1964, pp. 636-651.

83. Budiansky, B. and Roth, R. S., "Axisymmetric Dynamic Buckling of Clamped Shallow Spherical Shells", NASA TN D-1510, 1962.

84. Herakovich, C. T., "Composite Laminates with Negative Through-the-Thickness Poisson's Ratios", *Journal of Composite Materials*, Vol. 18, 1984, pp. 447-455.

85. Timoshenko, S., *Theory of Elastic Stability*, Engineering Societies Monographs, McGraw-Hill, New York, 1936, pp. 204-238.

86. Freeman, S. M., "Characterization of Lamina and Interlaminar Damage in Graphite/Epoxy Composites by the Deply Technique", *Composite Materials: Testing and Design, ASTM STP 787*, ASTM, 1982, pp. 50-62.

Appendix A

Specimen Manufacturing Data

Manufacturing data for all specimens is presented in this appendix. Three radii are calculated, as described in chapter 4, and their average reported. Thickness is averaged from nine points measured following the procedure given in chapter 4. The percent difference between the average and nominal values are presented as well as the coefficient of variation for the thickness data. Nominal values for the radius and thickness can be found in Table 4.1. As explained in chapter 4, 2 of the 94 specimens from the test matrix given in chapter 3 were not tested. This was due to penetration of two specimens at an impact velocity of 3 m/s (nominal) which made the impact tests at 4 m/s (nominal) unnecessary for these two specimen types.

Table A.1 Curvature and Thickness Data[a]

Specimen[b]	Test Velocity[c]	Radius[d] Average (mm)	Radius Difference (%)	Thickness Average (mm)	Thickness Difference (%)	C.V. (%)[e]
R1S1T1	1.0	146	4.0	0.807	-0.3	1.5
R1S1T1	2.1	145	5.1	0.821	-2.1	1.9
R1S1T1	q	153	-0.1	0.808	-0.5	1.5
R1S1T1	3.0	145	4.9	0.803	0.2	3.1
R1S1T1	3.9	143	6.0	0.810	-0.7	4.0
R1S1T1c	1.1	139	8.9	0.786	2.2	2.8
R1S1T1c	2.0	139	8.9	0.790	1.8	2.2
R1S1T1c	q	138	9.4	0.803	0.2	1.5
R1S1T1c	3.0	139	8.5	0.803	0.2	1.7
R1S1T2	q	150	1.4	1.565	2.7	0.7
R1S1T2	2.9	145	4.9	1.558	3.1	2.0
R1S1T2c	q	149	2.0	1.557	3.2	1.8
R1S1T2c	2.9	143	6.2	1.561	2.9	0.9
R1S1T3	q	146	4.4	2.195	9.0	1.2
R1S1T3	2.9	145	4.6	2.213	8.2	1.4
R1S1T3c	q	168	-10.	2.237	7.3	0.8
R1S1T3c	3.0	142	6.7	2.219	8.0	0.8
R1S2T1	1.0	150	1.3	0.821	-2.1	1.8
R1S2T1	1.9	151	0.8	0.805	-0.1	3.4
R1S2T1	q	141	7.5	0.803	0.2	1.5
R1S2T1	2.9	153	-0.5	0.826	-2.7	1.8
R1S2T1	4.0	139	8.9	0.807	-0.3	1.5
R1S3T1	1.1	140	8.4	0.822	-2.3	2.8
R1S3T1	2.0	140	8.4	0.801	0.4	3.3
R1S3T1	q	143	6.3	0.842	-4.7	2.2
R1S3T1	3.1	141	7.5	0.816	-1.5	2.4
R1S3T1	4.1	143	6.3	0.831	-3.3	2.3
R1SCT1	1.1	154	-1.1	0.851	-5.9	3.0
R1SCT1	2.0	154	-1.0	0.803	0.1	1.4
R1SCT1	q	154	-1.1	0.817	-1.6	1.6
R1SCT1	3.1	154	-1.1	0.817	-1.7	2.8
R1SCT1	4.1	154	-1.0	0.796	1.0	2.7
R2S1T1	1.1	302	1.0	0.837	-4.1	1.9
R2S1T1	2.0	296	2.8	0.824	-2.5	1.8
R2S1T1	q	285	6.3	0.827	-2.9	2.1
R2S1T1	2.9	301	1.1	0.825	-2.7	1.7
R2S1T1	3.8	298	2.3	0.835	-3.9	1.8
R2S1T1c	q	282	7.4	0.816	-1.4	2.1
R2S1T1c	3.1	298	2.3	0.828	-3.0	2.0
R2S1T2	1.1	293	4.0	1.542	4.1	1.0
R2S1T2	2.1	289	5.1	1.564	2.8	1.5
R2S1T2	q	288	5.4	1.591	1.0	2.4
R2S1T2	3.2	298	2.3	1.580	1.7	2.6
R2S1T2	3.9	280	8.1	1.557	3.2	2.1

Table A.1 Curvature and Thickness Data[a] (continued-2)

Specimen[b]	Test Velocity[c]	Radius[d] Average (mm)	Radius Difference (%)	Thickness Average (mm)	Thickness Difference (%)	C.V.[e] (%)
R2S1T2c	q	294	3.6	1.574	2.1	1.8
R2S1T2c	3.0	295	3.1	1.562	2.8	2.0
R2S1T3	q	283	7.1	2.273	5.8	1.4
R2S1T3	2.8	295	3.2	2.246	6.9	0.9
R2S2T1	q	283	7.3	0.814	-1.3	2.3
R2S2T1	2.9	284	6.8	0.809	-0.6	2.3
R2S2T2	q	296	2.8	1.621	-0.8	2.5
R2S2T2	2.9	300	1.4	1.602	0.4	2.2
R2S2T3	q	301	1.3	2.319	3.9	2.0
R2S2T3	2.9	294	3.6	2.276	5.6	2.0
R2S3T1	q	316	3.6	0.809	-0.6	2.1
R2S3T1	3.1	311	2.0	0.813	-1.2	1.6
R2S3T2	q	292	4.1	1.586	1.4	1.5
R2S3T2	3.0	296	2.8	1.582	1.6	1.1
R3S1T1	1.0	425	7.1	0.812	-1.0	1.2
R3S1T1	1.9	434	5.0	0.811	-0.8	1.3
R3S1T1	q	443	3.2	0.825	-2.6	2.4
R3S1T1	2.9	432	5.4	0.817	-1.6	2.7
R3S1T1	4.0	466	1.8	0.830	-3.2	1.7
R3S1T1c	q	501	9.6	0.826	-2.7	1.9
R3S1T1c	3.0	438	4.1	0.819	-1.9	1.6
R3S1T2	q	441	3.6	1.592	1.0	1.2
R3S1T2	3.0	434	5.0	1.572	2.3	1.5
R3S1T3	1.0	454	0.7	2.340	3.0	1.3
R3S1T3	2.0	437	4.4	2.331	3.4	1.2
R3S1T3	q	441	3.5	2.373	1.6	1.5
R3S1T3	3.0	449	1.7	2.346	2.8	2.4
R3S1T3	4.0	462	1.0	2.258	6.4	2.3
R3S1T3c	q	427	6.7	2.379	1.4	0.9
R3S1T3c	3.0	469	2.6	2.364	2.0	1.7
R3S2T1	q	468	2.4	0.862	-7.2	1.6
R3S2T1	3.0	455	0.5	0.826	-2.7	1.1
R3S2T3	q	452	1.2	2.378	1.4	0.5
R3S2T3	3.0	450	1.6	2.384	1.2	1.6
R3S3T1	q	496	8.5	0.865	-7.6	3.1
R3S3T1	3.0	502	9.8	0.829	-3.2	1.5
R3S3T2	q	430	5.9	1.636	-1.7	0.9
R3S3T2	3.0	448	1.9	1.562	2.9	1.5
R3S3T3	q	443	3.0	2.375	1.5	1.7
R3S3T3	3.1	445	2.7	2.361	2.1	1.2
RPS1T1	1.1	plate	plate	0.858	-6.7	1.6
RPS1T1	2.1	plate	plate	0.848	-5.5	1.4
RPS1T1	q	plate	plate	0.855	-6.3	0.9
RPS1T1	3.0	plate	plate	0.852	-6.0	1.2

Table A.1 Curvature and Thickness Data[a] (continued-3)

Specimen[b]	Test Velocity[c]	Radius[d] Average (mm)	Radius[d] Difference (%)	Thickness Average (mm)	Thickness Difference (%)	C.V.[e] (%)
RPS1T2	q	plate	plate	1.654	-2.9	1.3
RPS1T2	3.1	plate	plate	1.626	-1.1	1.6
RPS1T3	q	plate	plate	2.423	-0.5	1.3
RPS1T3	3.0	plate	plate	2.378	1.4	1.1

[a] 92 of 94 specimens from test matrix are reported.

[b] "c" after specimen identification indicates concave test.

[c] Impact velocity in m/s; "q" indicates quasi-static test.

[d] "plate" specimens were not measured for radius.

[e] Coefficient of Variation.

Appendix B

Impact Response Data

Impact test data for all specimens is presented in this appendix. The response is comprised of force-time histories measured during testing and scanned x-ray photographs of the resultant damage state. Axis scales for the force-time histories were chosen based on a compromise between showing specifics of each specimen response (smallest scale showing entire specimen response) and allowing the response of different specimens to be compared (one scale for all specimens). Five force scales and four time scales were found to provide a reasonable compromise. Specimens that did not evidence damage in the x-ray photographs are indicated by "No Damage" instead of an x-ray photograph. Specimens that were penetrated during impact were not x-rayed and are indicated by "Penetration Damage". As noted in chapter 5, three specimens are known to have slipped in-plane during impact testing. Slipping is indicated in the figure titles for these specimens.

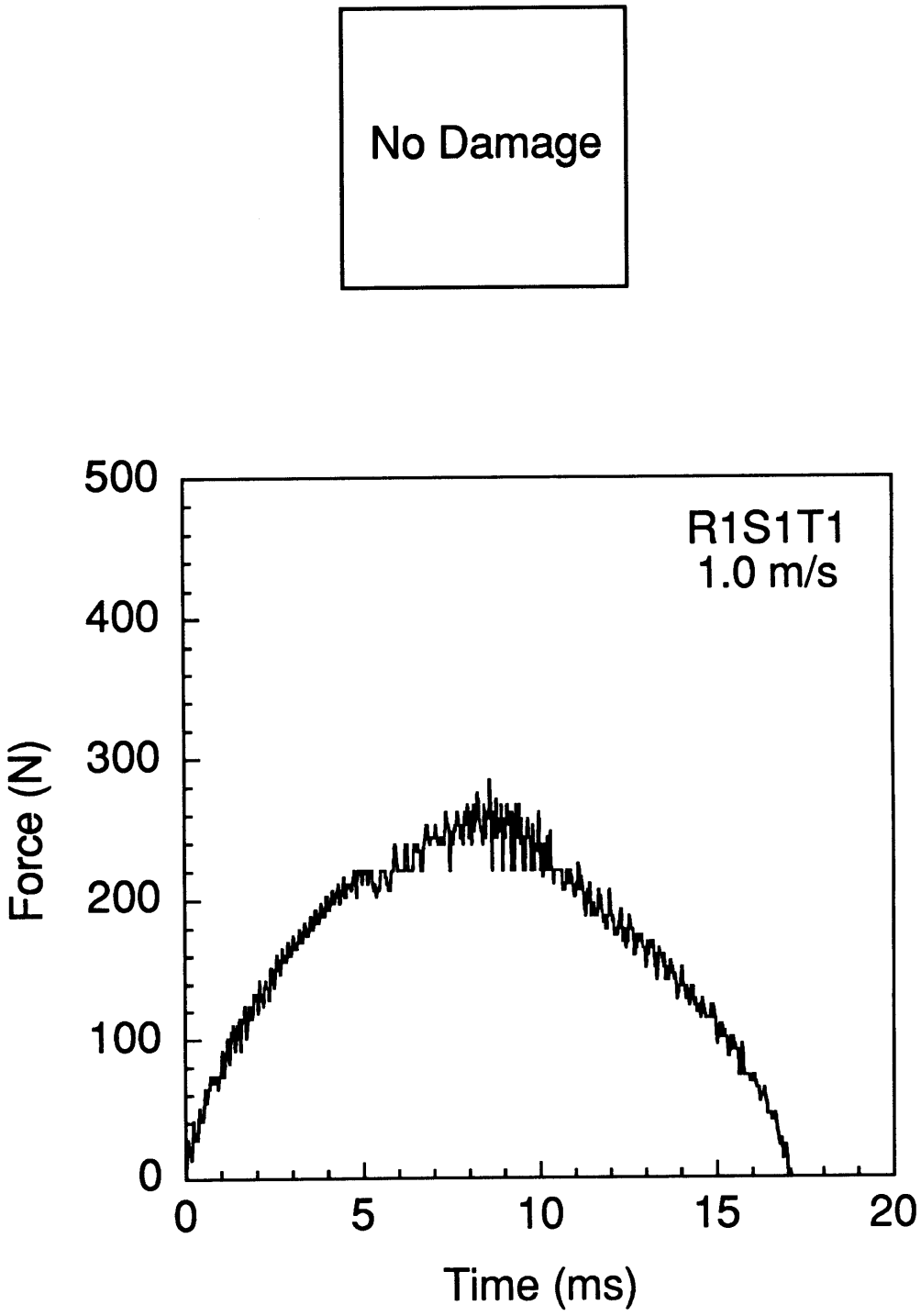

Figure B.1 Results of impact of 1.0 m/s on specimen R1S1T1: (*top*) no damage is observed in the x-ray photograph, and (*bottom*) force-time history.

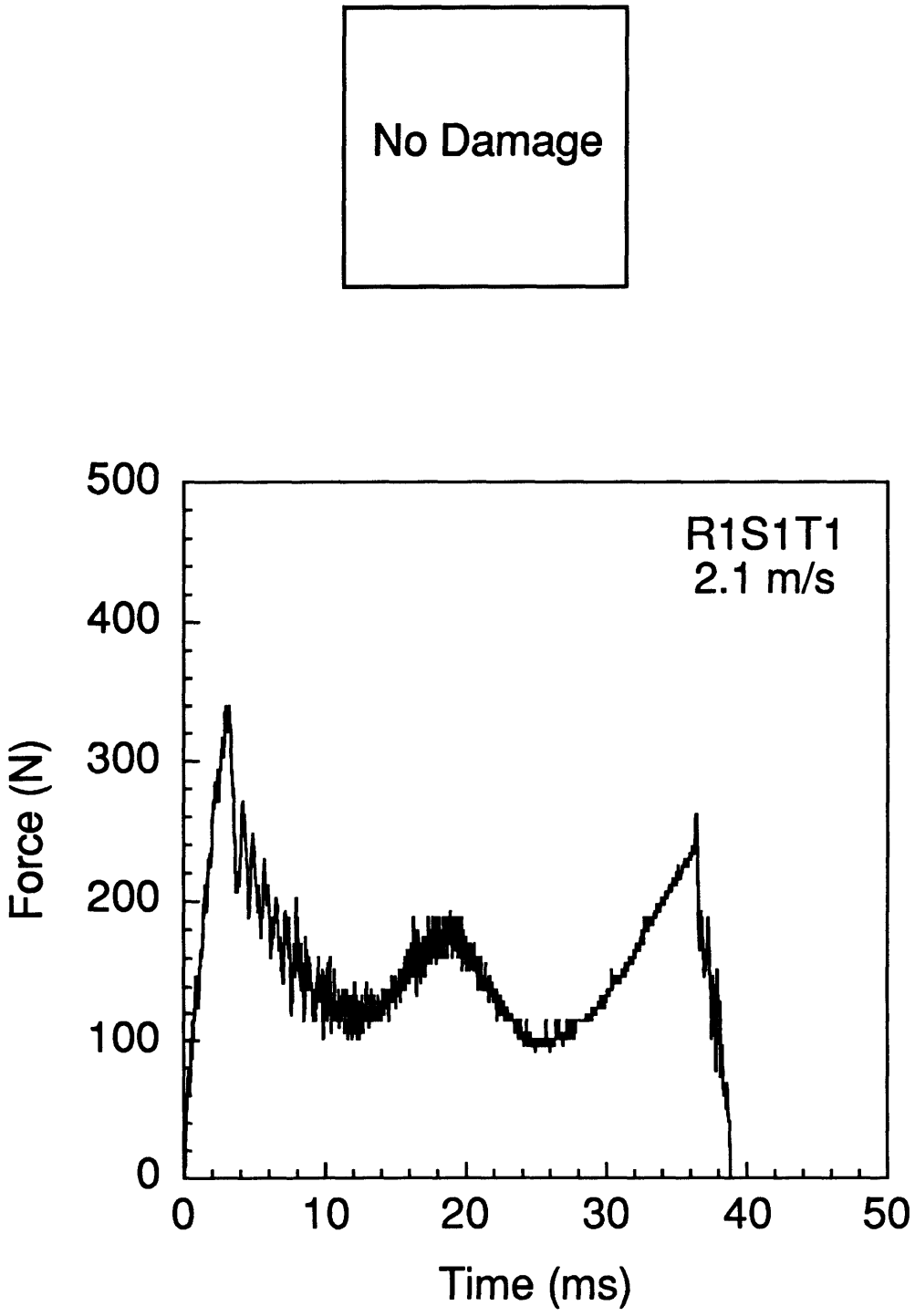

Figure B.2 Results of impact of 2.1 m/s on specimen R1S1T1: (*top*) no damage is observed in the x-ray photograph, and (*bottom*) force-time history.

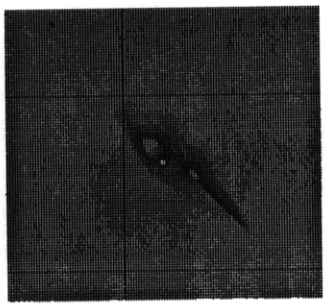

10 mm

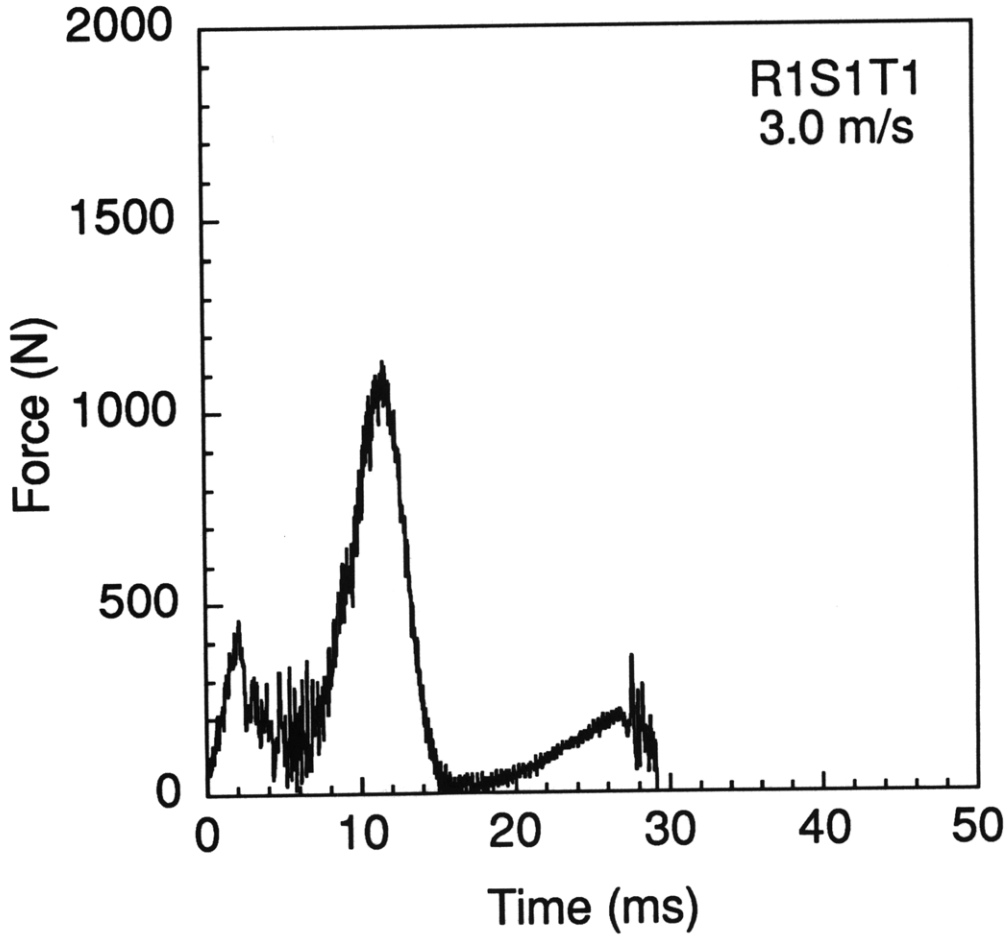

Figure B.3 Results of impact of 3.0 m/s on specimen R1S1T1: (*top*) x-ray photograph of damage state, and (*bottom*) force-time history.

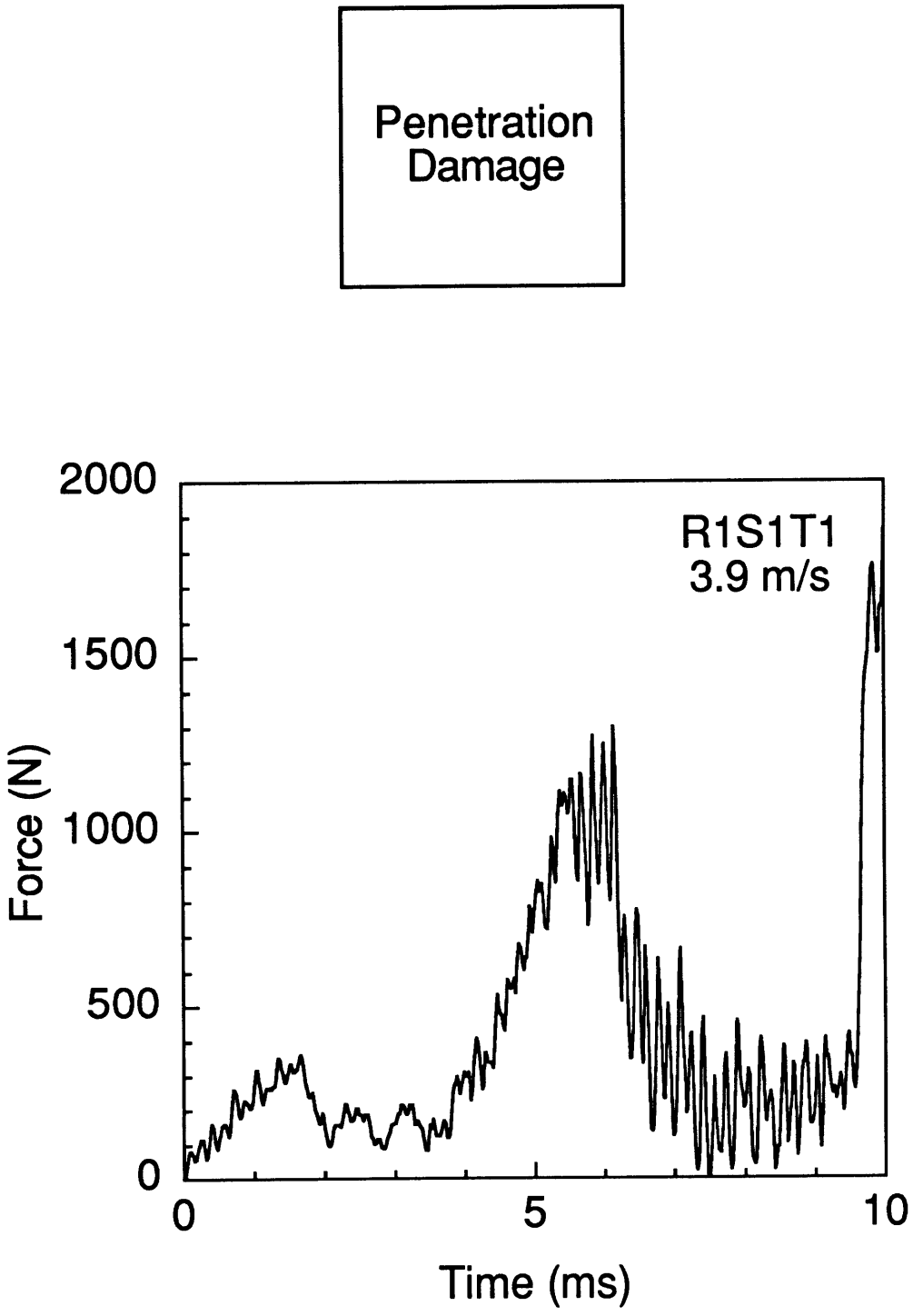

Figure B.4 Results of impact of 3.9 m/s on specimen R1S1T1: (*top*) penetration damage is observed for this specimen, and (*bottom*) force-time history.

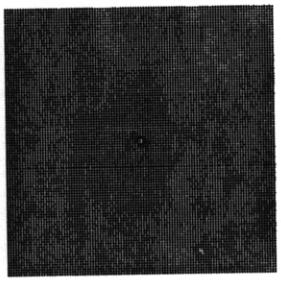

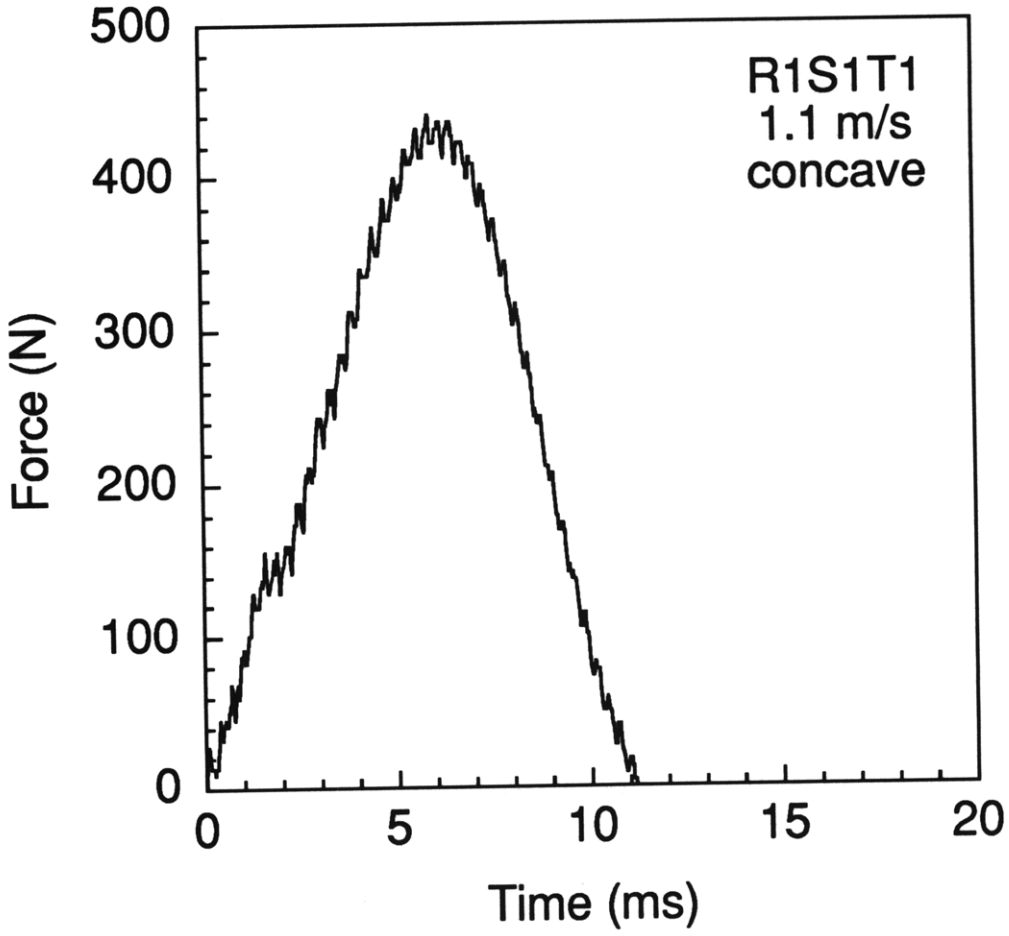

Figure B.5 Results of impact of 1.1 m/s on specimen R1S1T1 (concave): (*top*) x-ray photograph of damage state, and (*bottom*) force-time history.

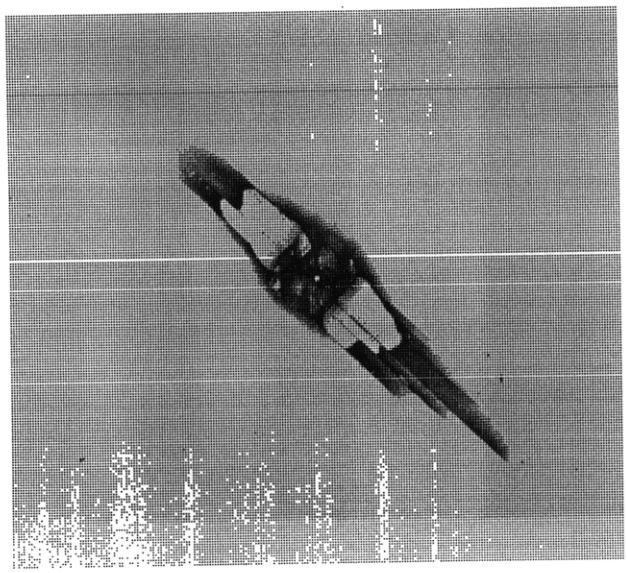

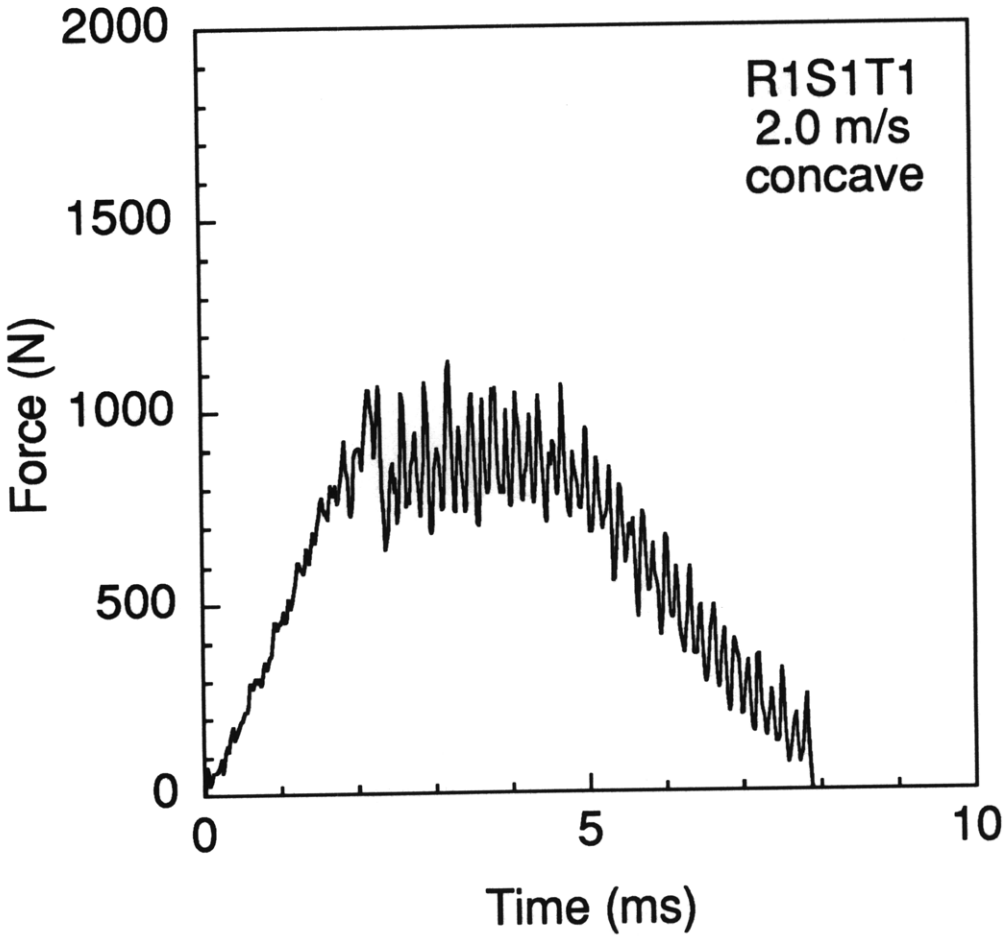

Figure B.6 Results of impact of 2.0 m/s on specimen R1S1T1 (concave): (*top*) x-ray photograph of damage state, and (*bottom*) force-time history.

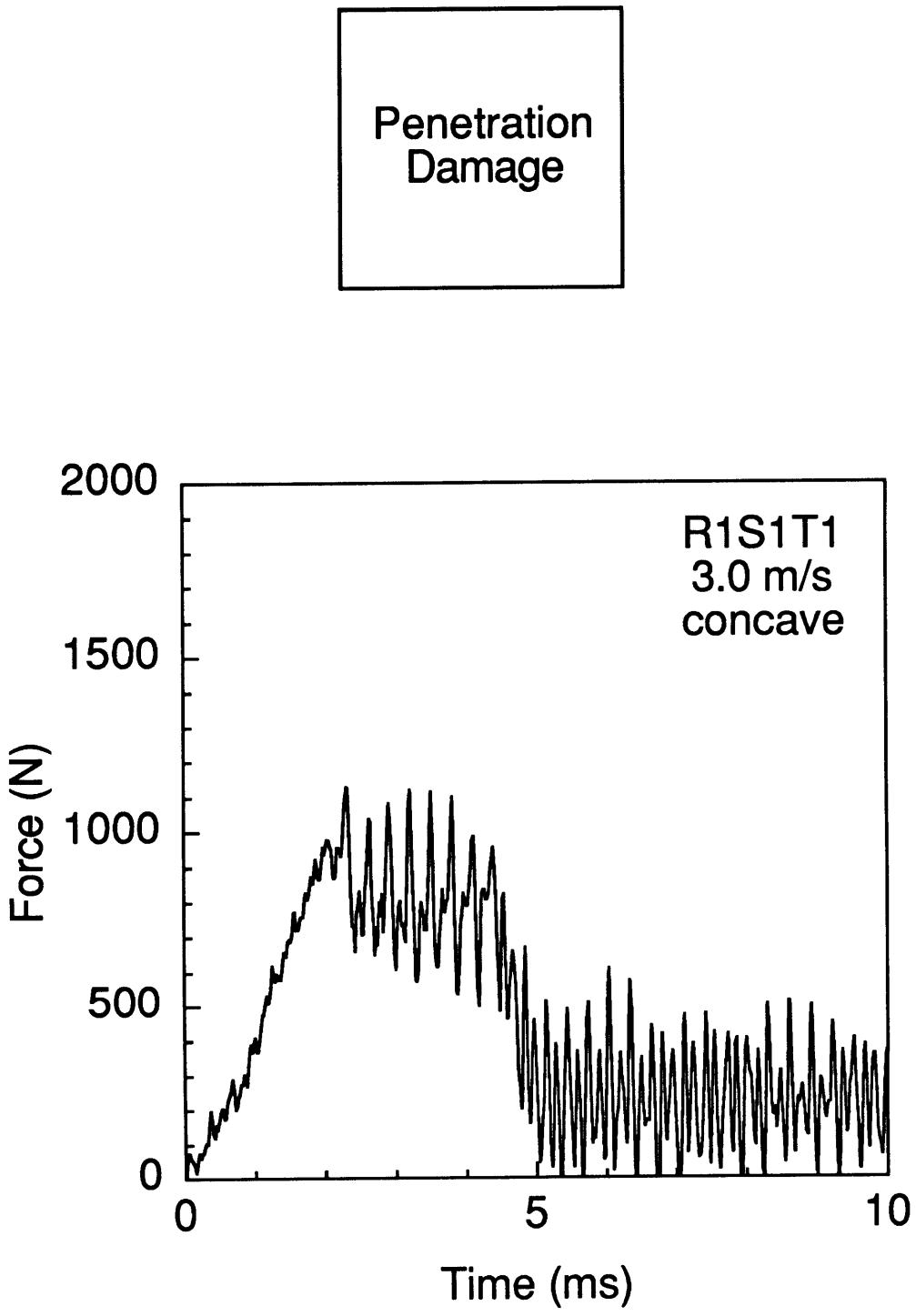

Figure B.7 Results of impact of 3.0 m/s on specimen R1S1T1 (concave): (*top*) penetration damage is observed for this specimen, and (*bottom*) force-time history.

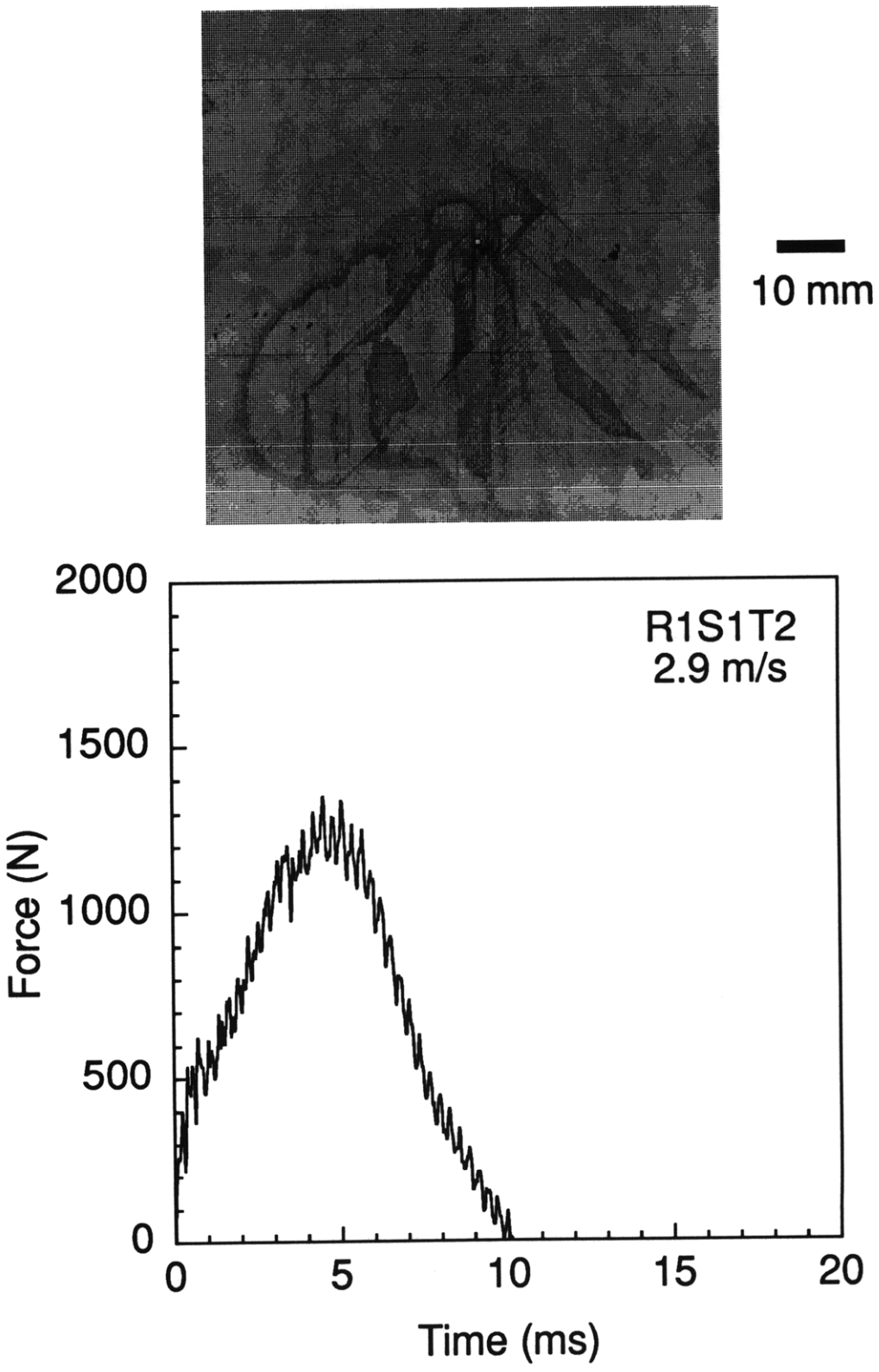

Figure B.8 Results of impact of 2.9 m/s on specimen R1S1T2: (*top*) x-ray photograph of damage state, and (*bottom*) force-time history.

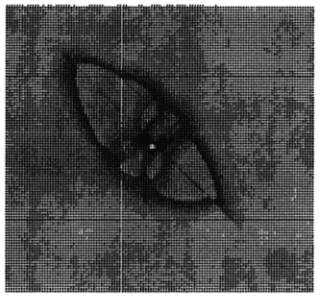

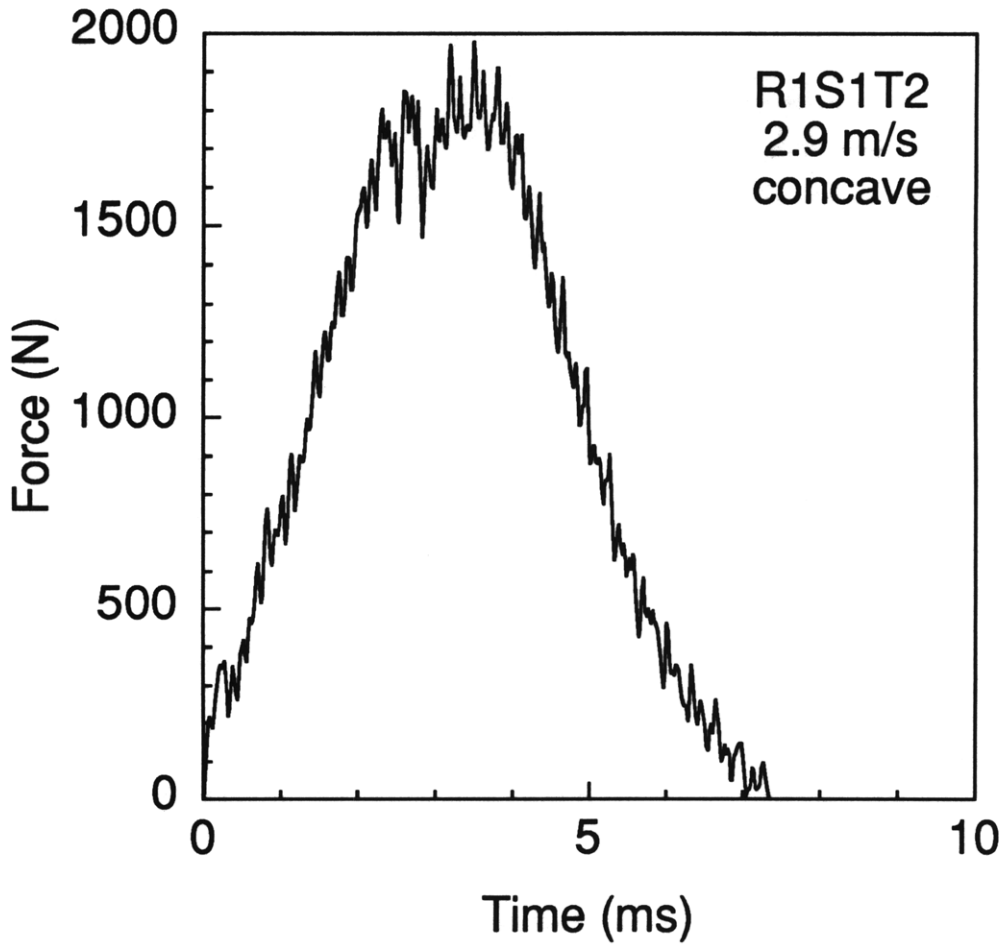

Figure B.9 Results of impact of 2.9 m/s on specimen R1S1T2 (concave): (*top*) x-ray photograph of damage state, and (*bottom*) force-time history.

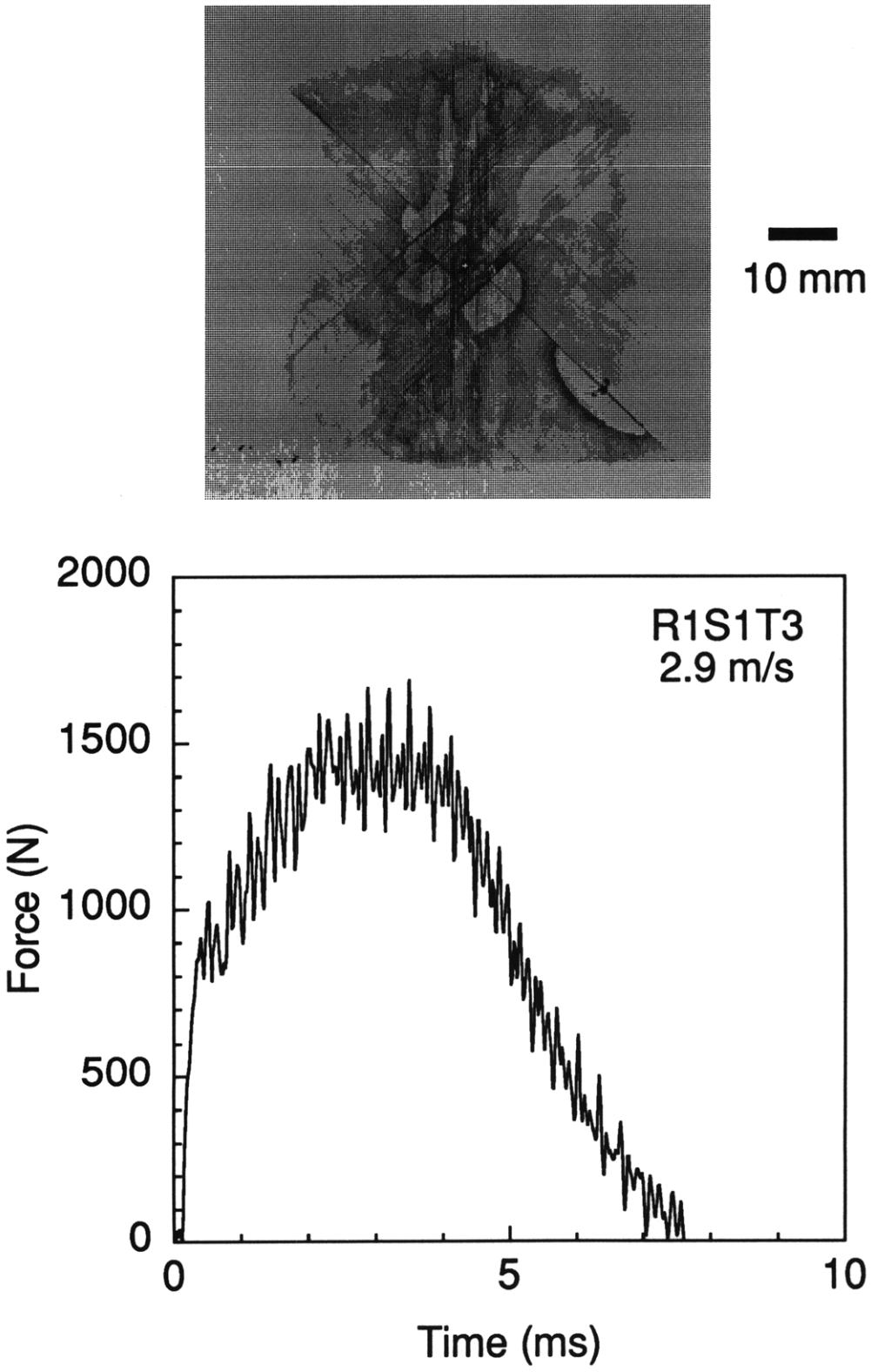

Figure B.10 Results of impact of 2.9 m/s on specimen R1S1T3: (*top*) x-ray photograph of damage state, and (*bottom*) force-time history.

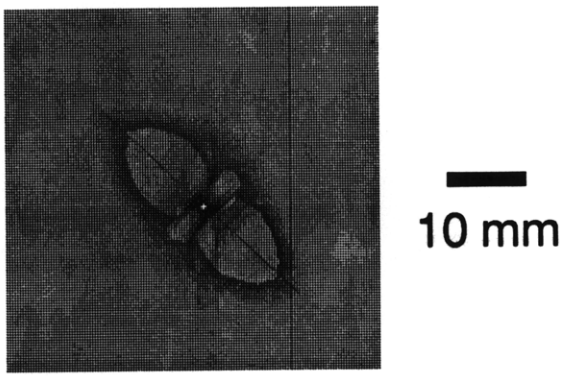

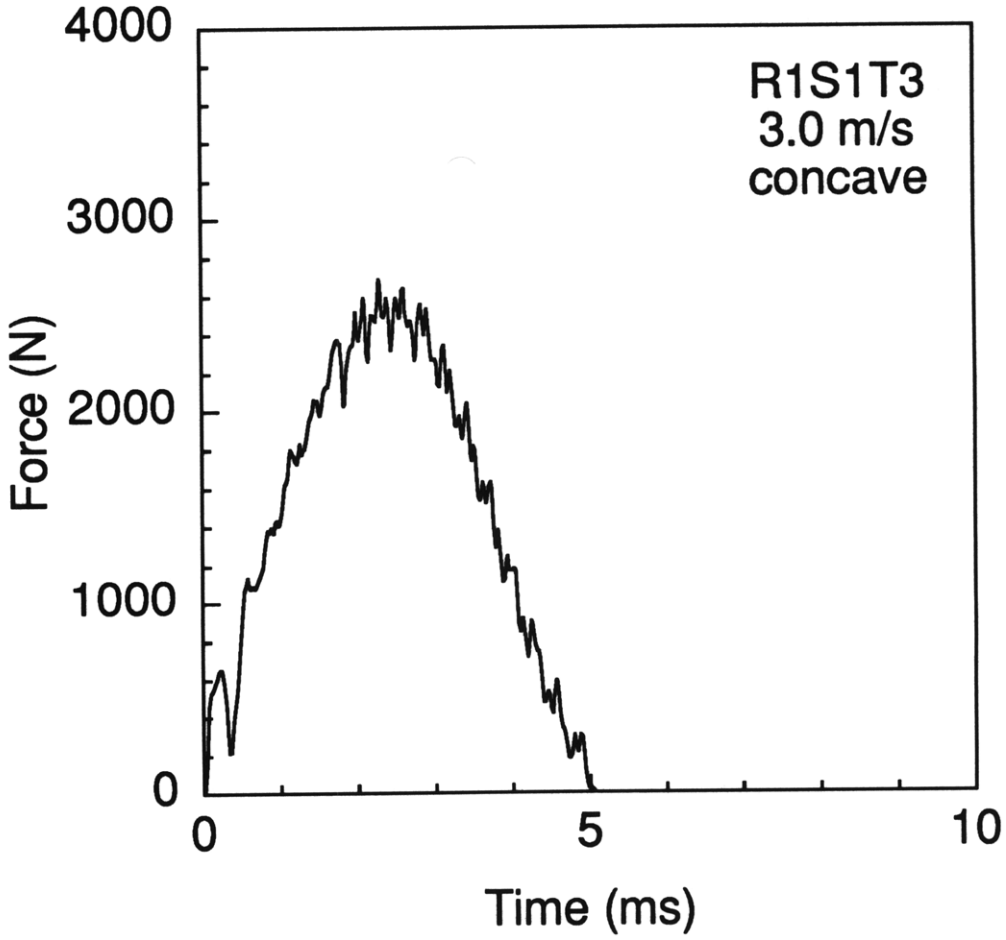

Figure B.11 Results of impact of 3.0 m/s on specimen R1S1T3 (concave): (*top*) x-ray photograph of damage state, and (*bottom*) force-time history.

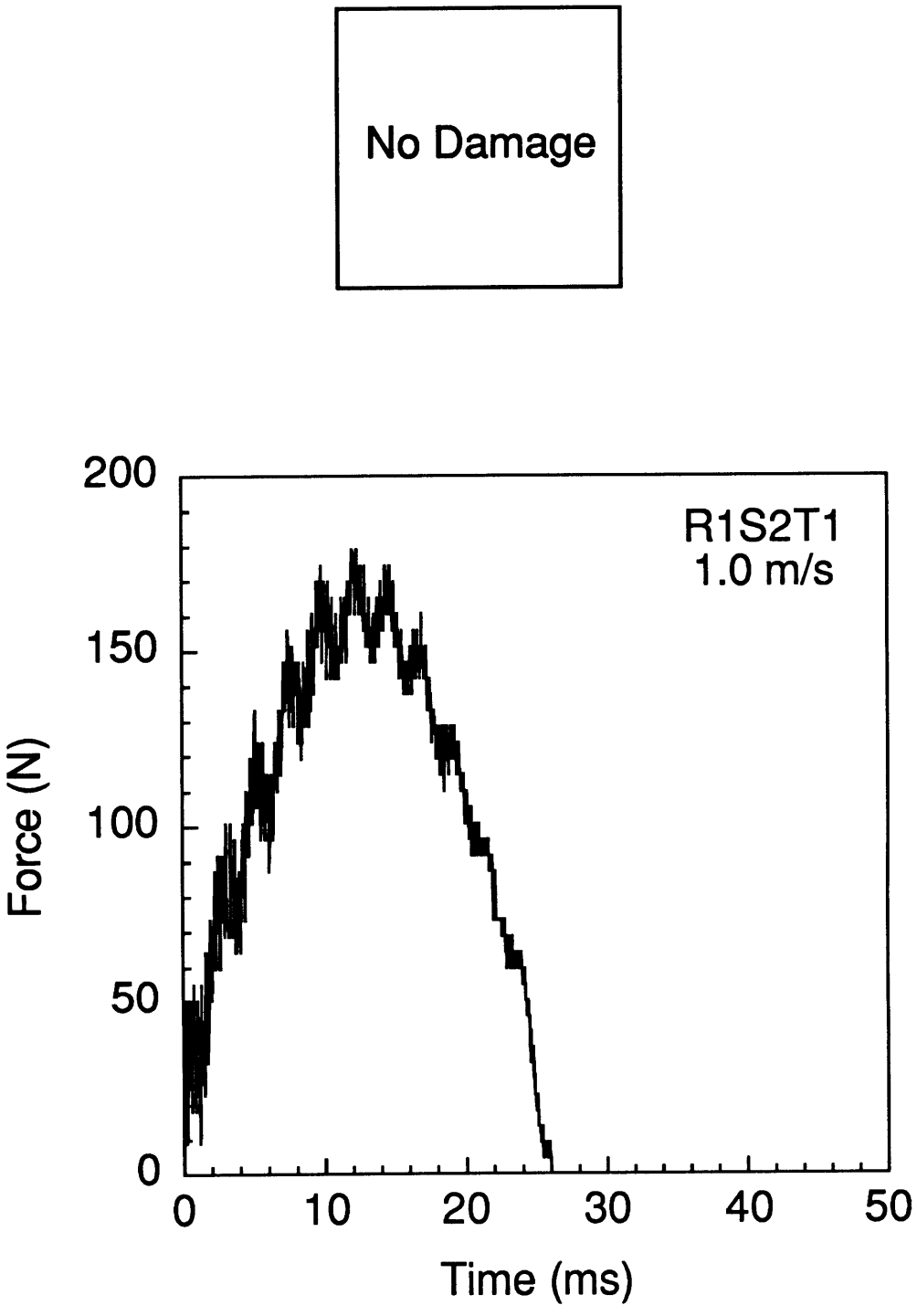

Figure B.12 Results of impact of 1.0 m/s on specimen R1S2T1: (*top*) no damage is observed in the x-ray photograph, and (*bottom*) force-time history.

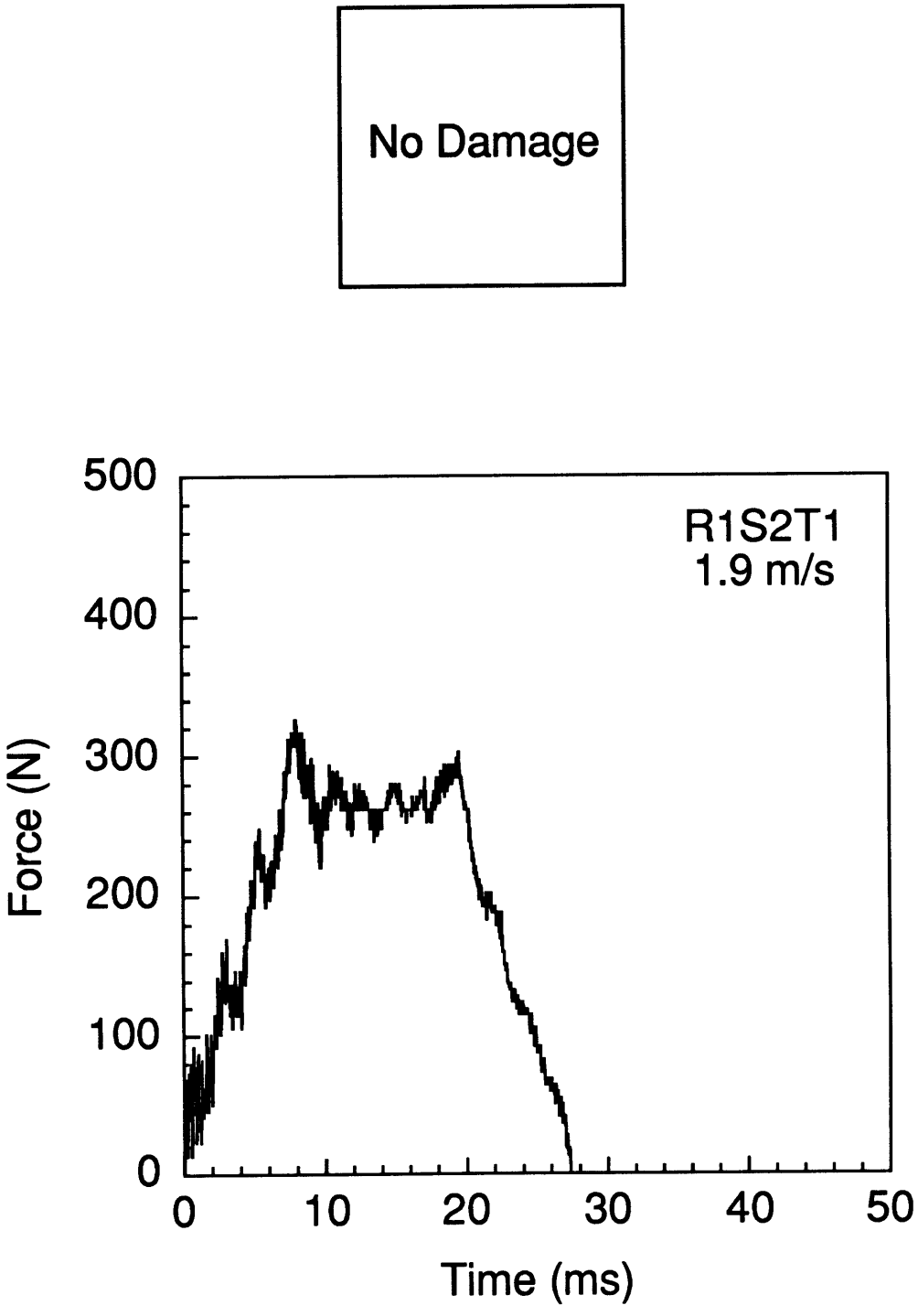

Figure B.13 Results of impact of 1.9 m/s on specimen R1S2T1: (*top*) no damage is observed in the x-ray photograph, and (*bottom*) force-time history.

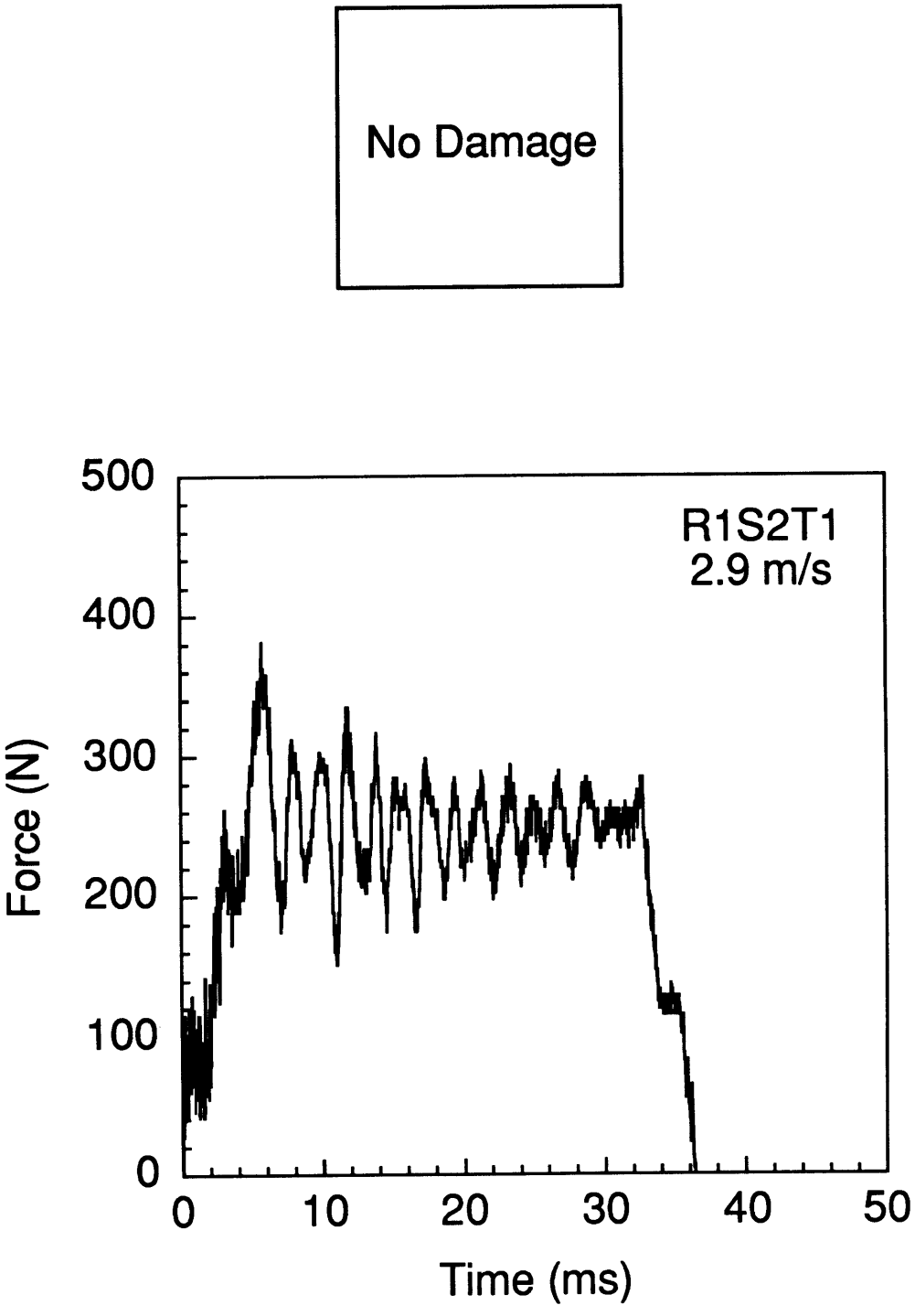

Figure B.14 Results of impact of 2.9 m/s on specimen R1S2T1: (*top*) no damage is observed in the x-ray photograph, and (*bottom*) force-time history.

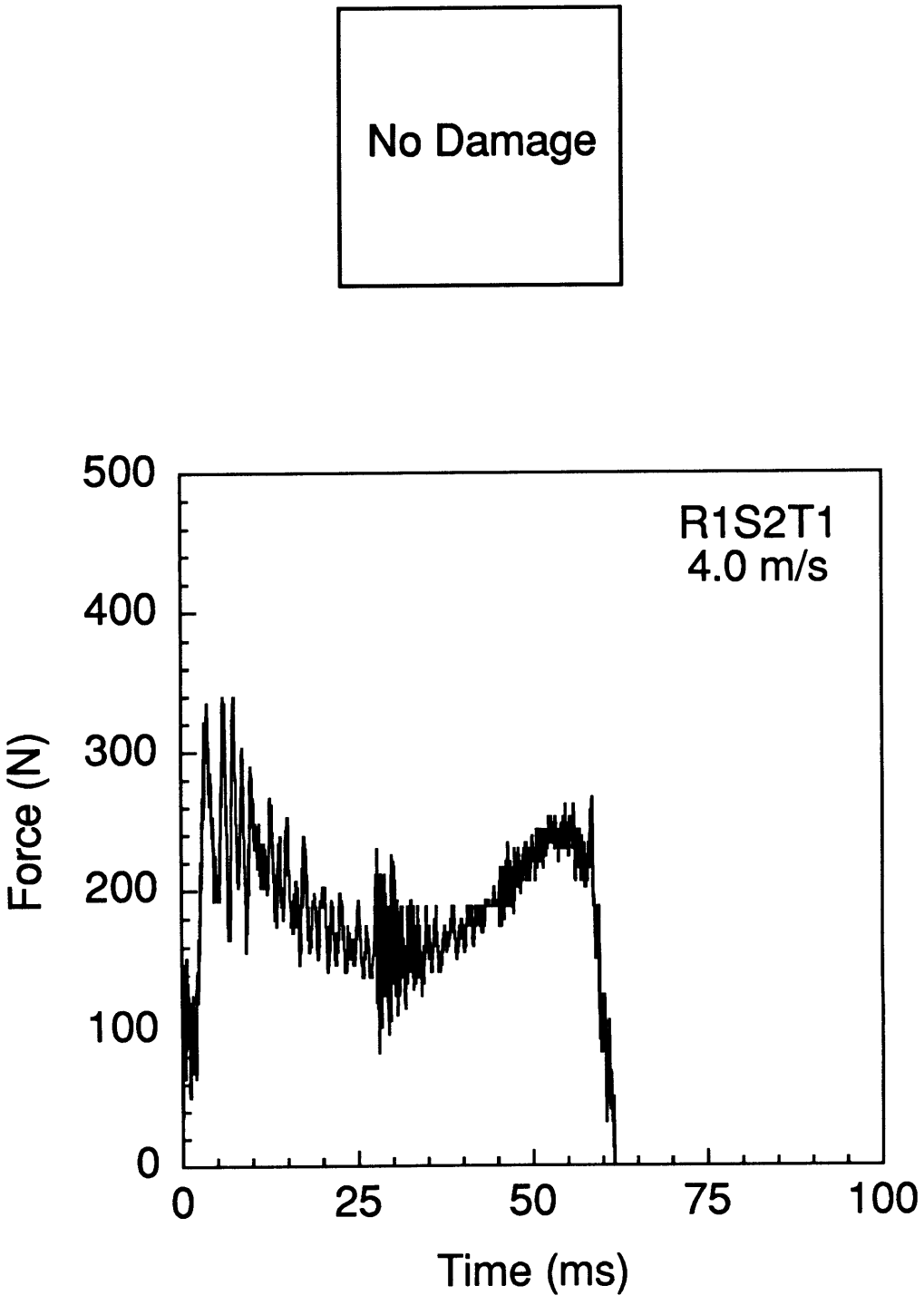

Figure B.15 Results of impact of 4.0 m/s on specimen R1S2T1: (*top*) no damage is observed in the x-ray photograph, and (*bottom*) force-time history.

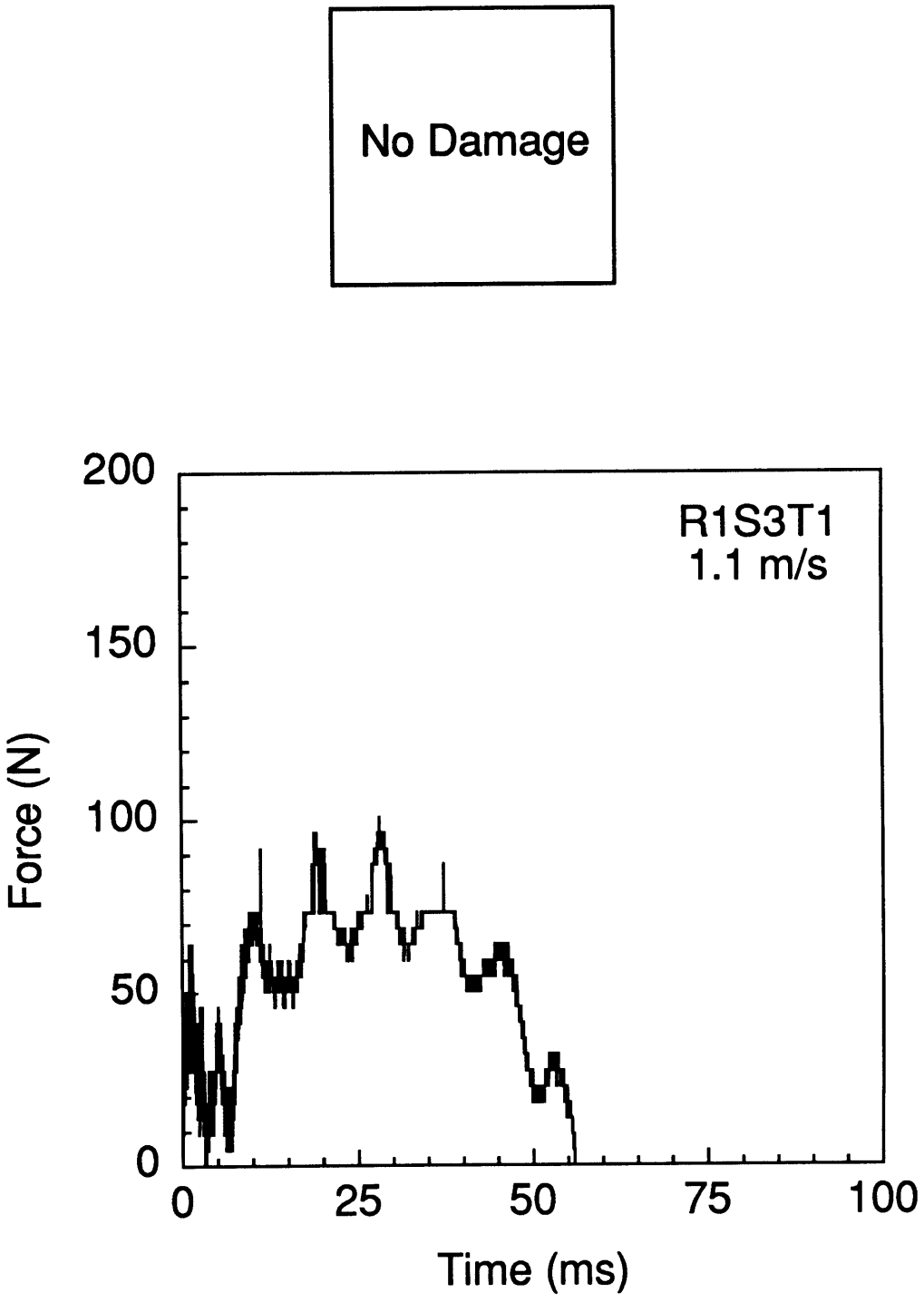

Figure B.16 Results of impact of 1.1 m/s on specimen R1S3T1: (*top*) no damage is observed in the x-ray photograph, and (*bottom*) force-time history.

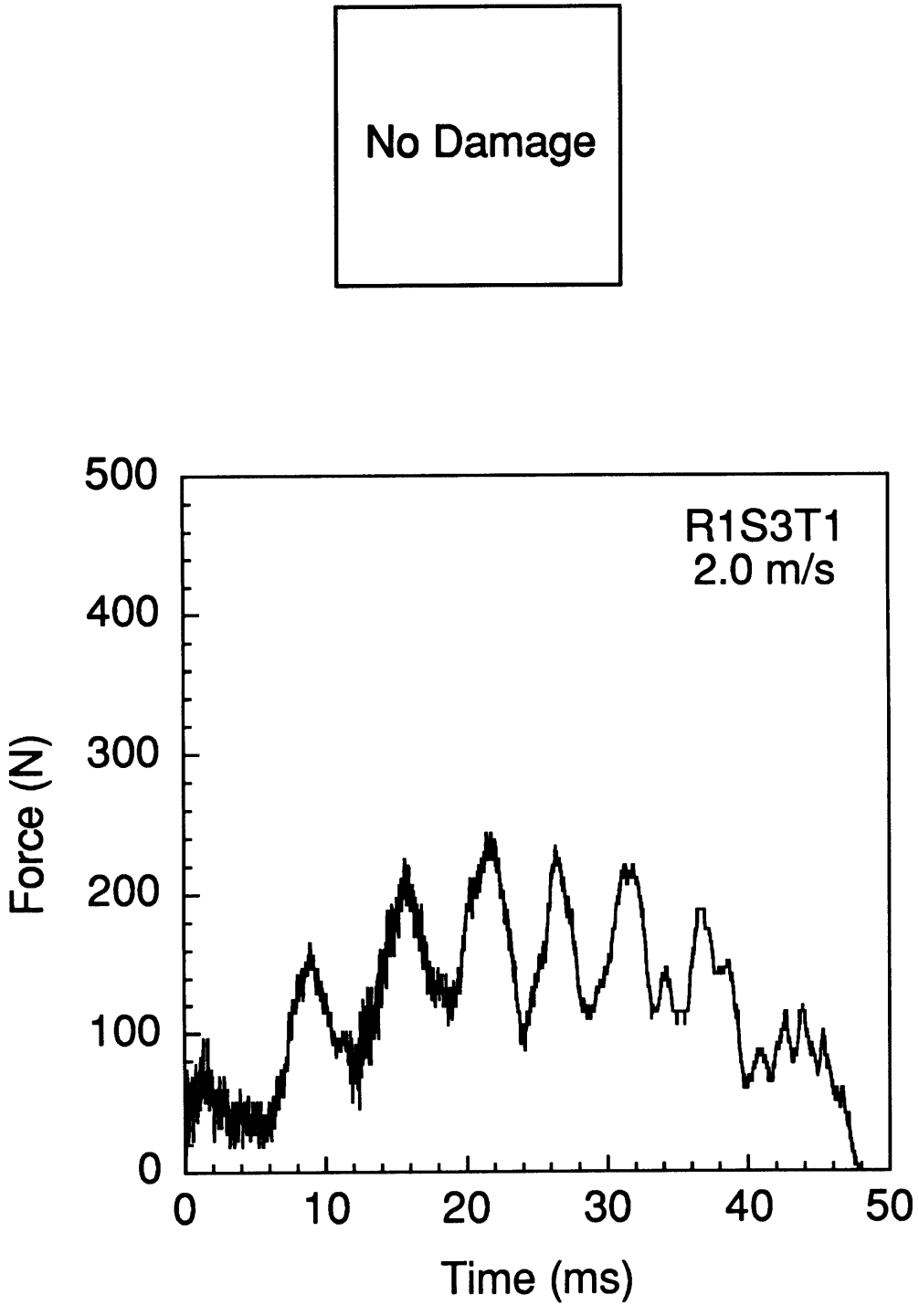

Figure B.17 Results of impact of 2.0 m/s on specimen R1S3T1: (*top*) no damage is observed in the x-ray photograph, and (*bottom*) force-time history.

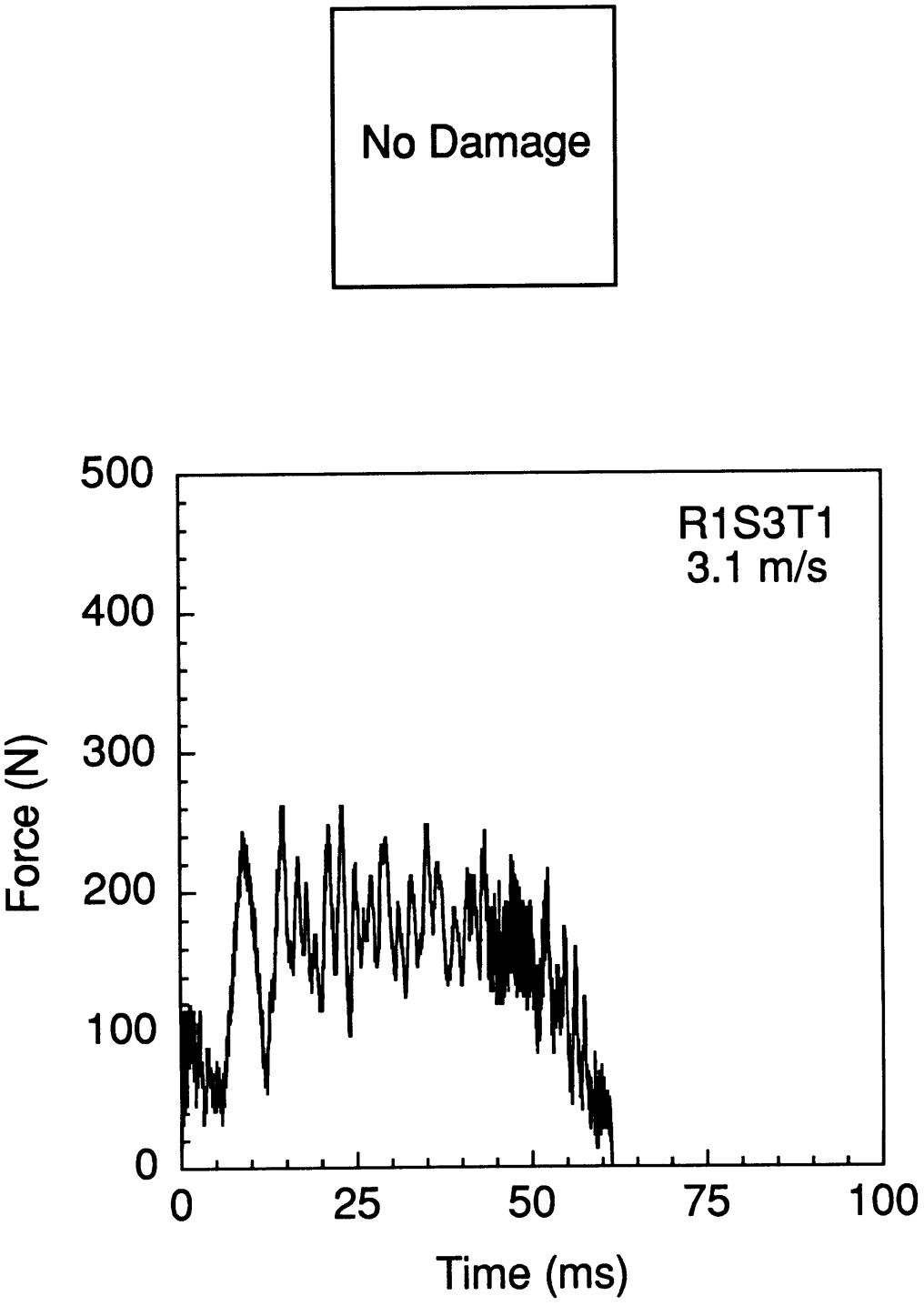

Figure B.18 Results of impact of 3.1 m/s on specimen R1S3T1: (*top*) no damage is observed in the x-ray photograph, and (*bottom*) force-time history.

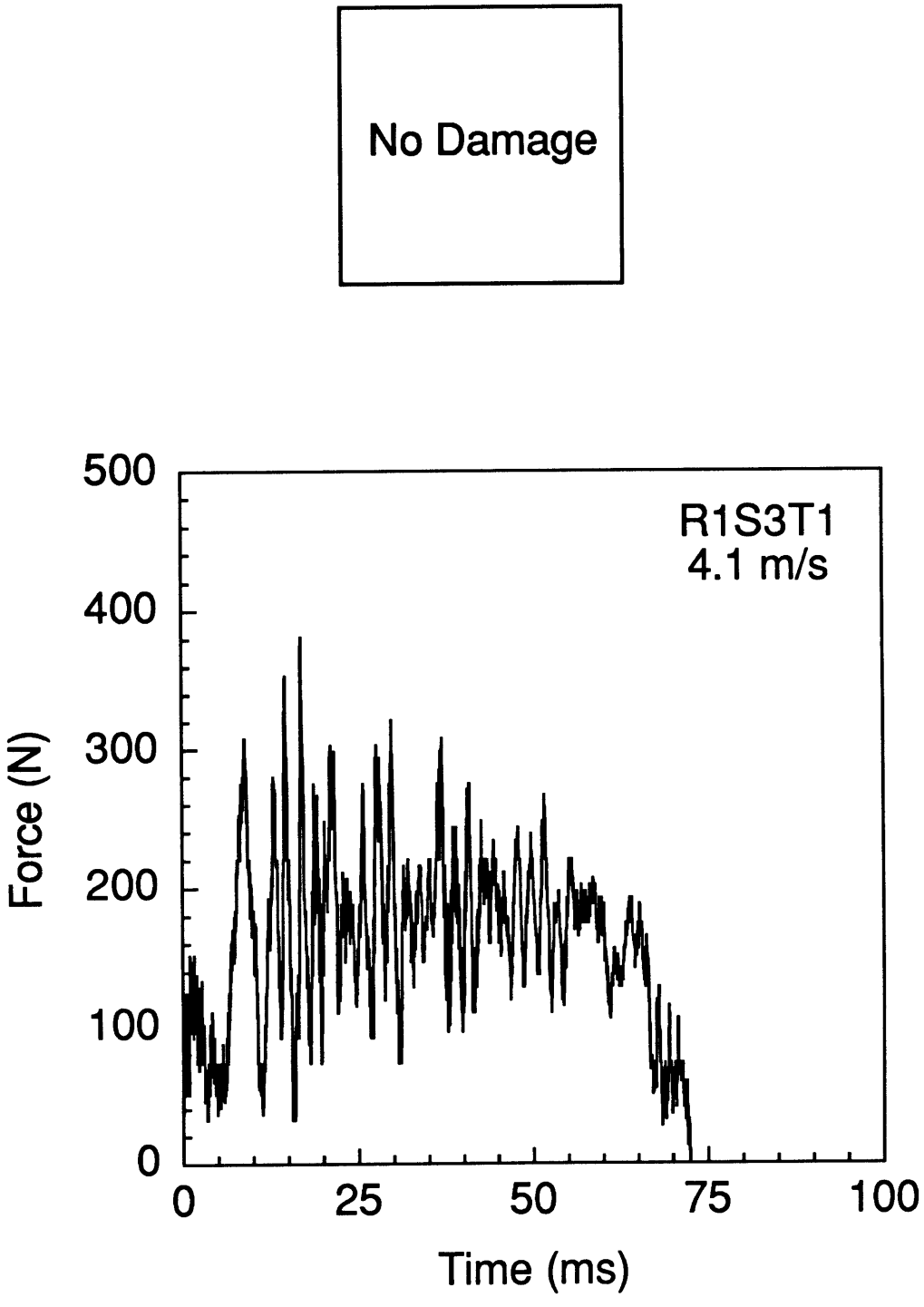

Figure B.19 Results of impact of 4.1 m/s on specimen R1S3T1: (*top*) no damage is observed in the x-ray photograph, and (*bottom*) force-time history.

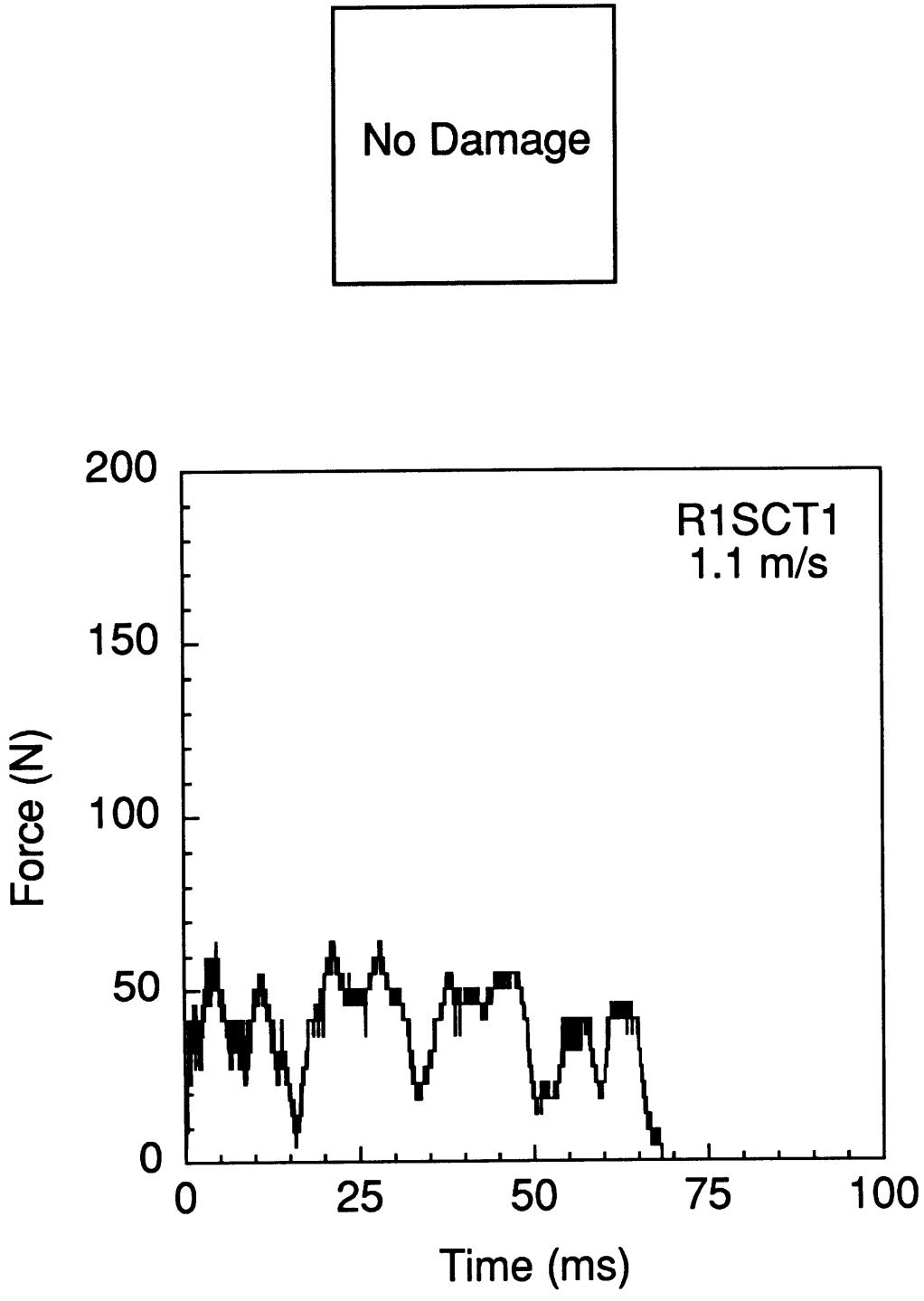

Figure B.20 Results of impact of 1.1 m/s on specimen R1SCT1: (*top*) no damage is observed in the x-ray photograph, and (*bottom*) force-time history.

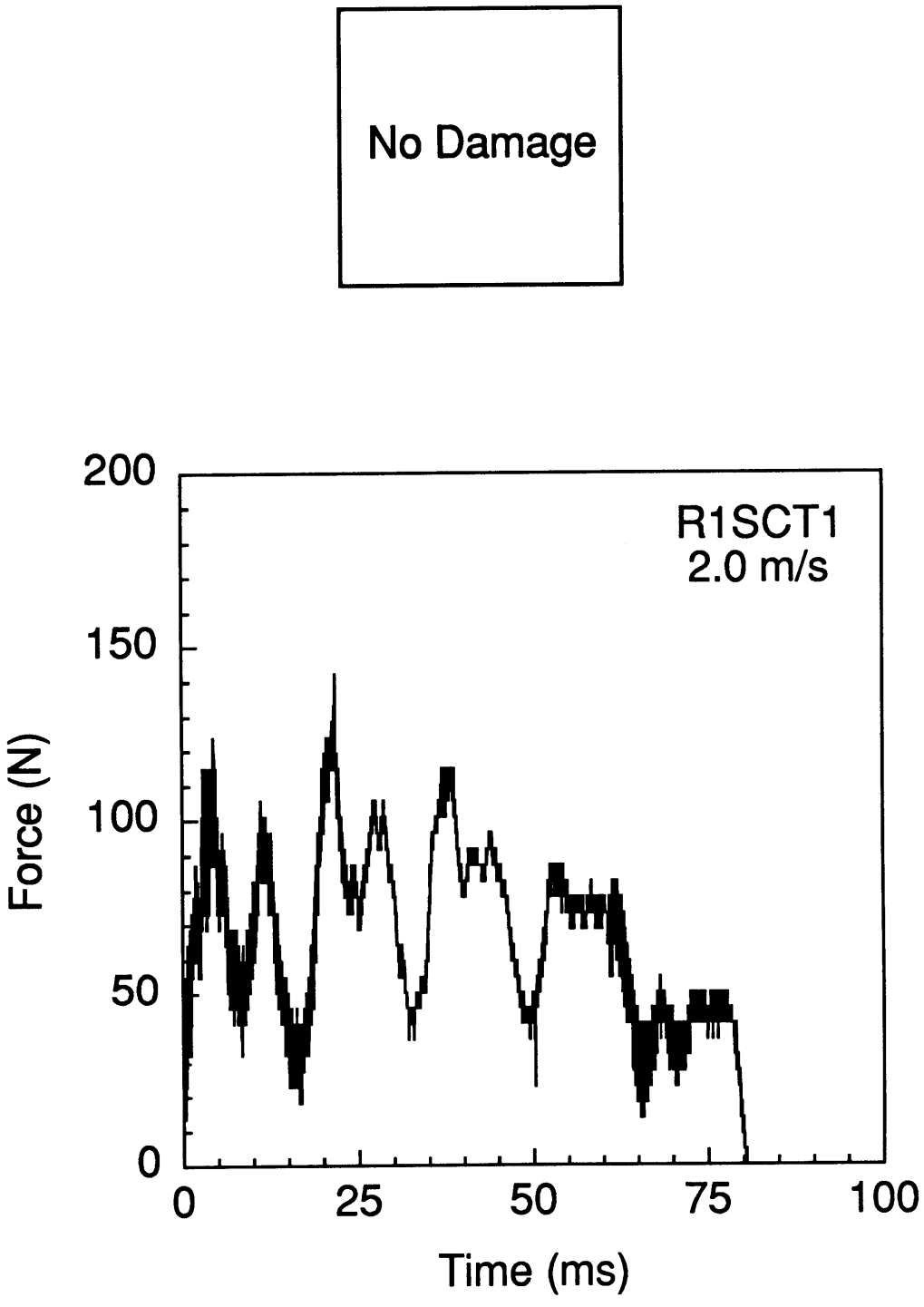

Figure B.21 Results of impact of 2.0 m/s on specimen R1SCT1: (*top*) no damage is observed in the x-ray photograph, and (*bottom*) force-time history.

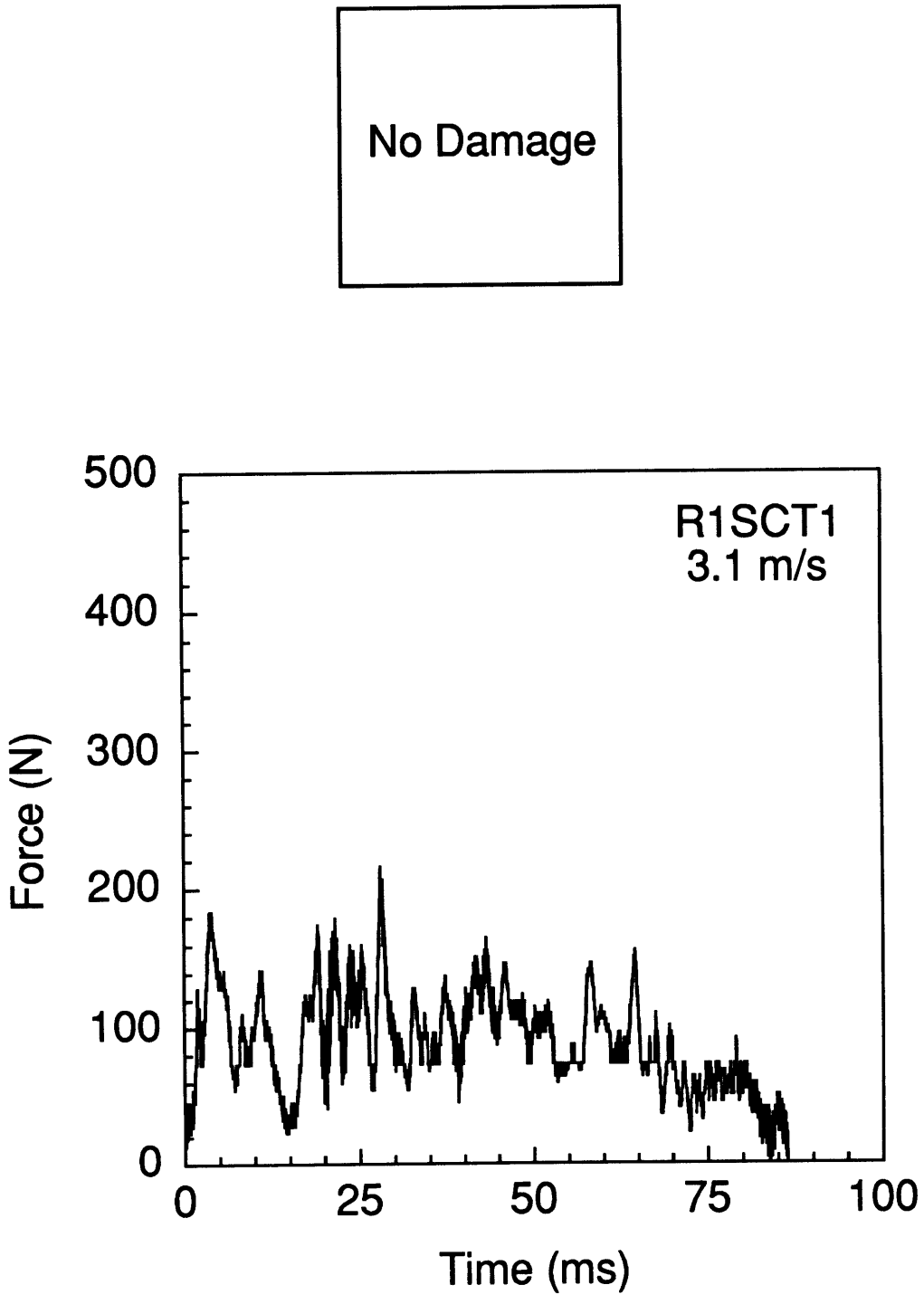

Figure B.22 Results of impact of 3.1 m/s on specimen R1SCT1: (*top*) no damage is observed in the x-ray photograph, and (*bottom*) force-time history.

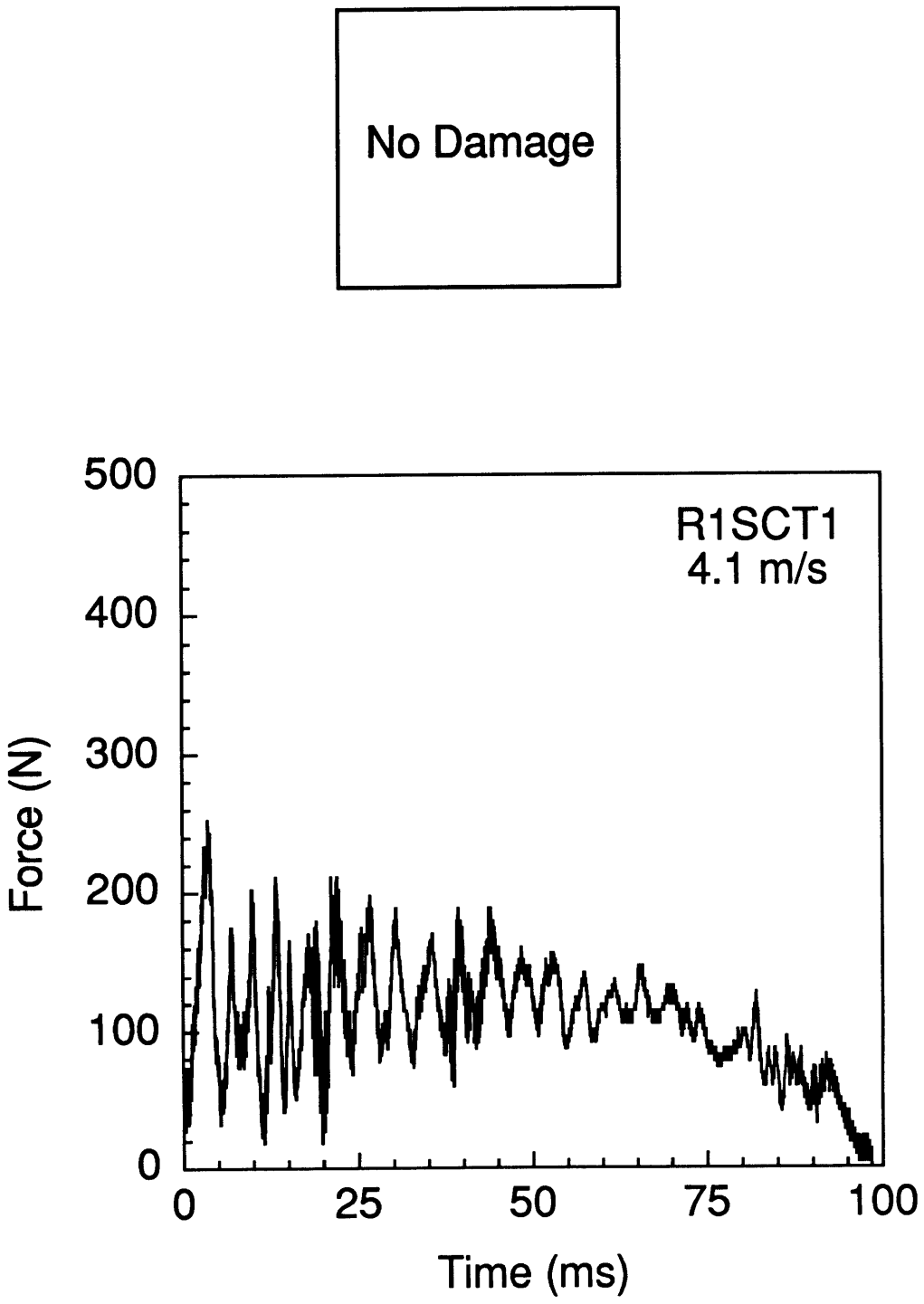

Figure B.23 Results of impact of 4.1 m/s on specimen R1SCT1: (*top*) no damage is observed in the x-ray photograph, and (*bottom*) force-time history.

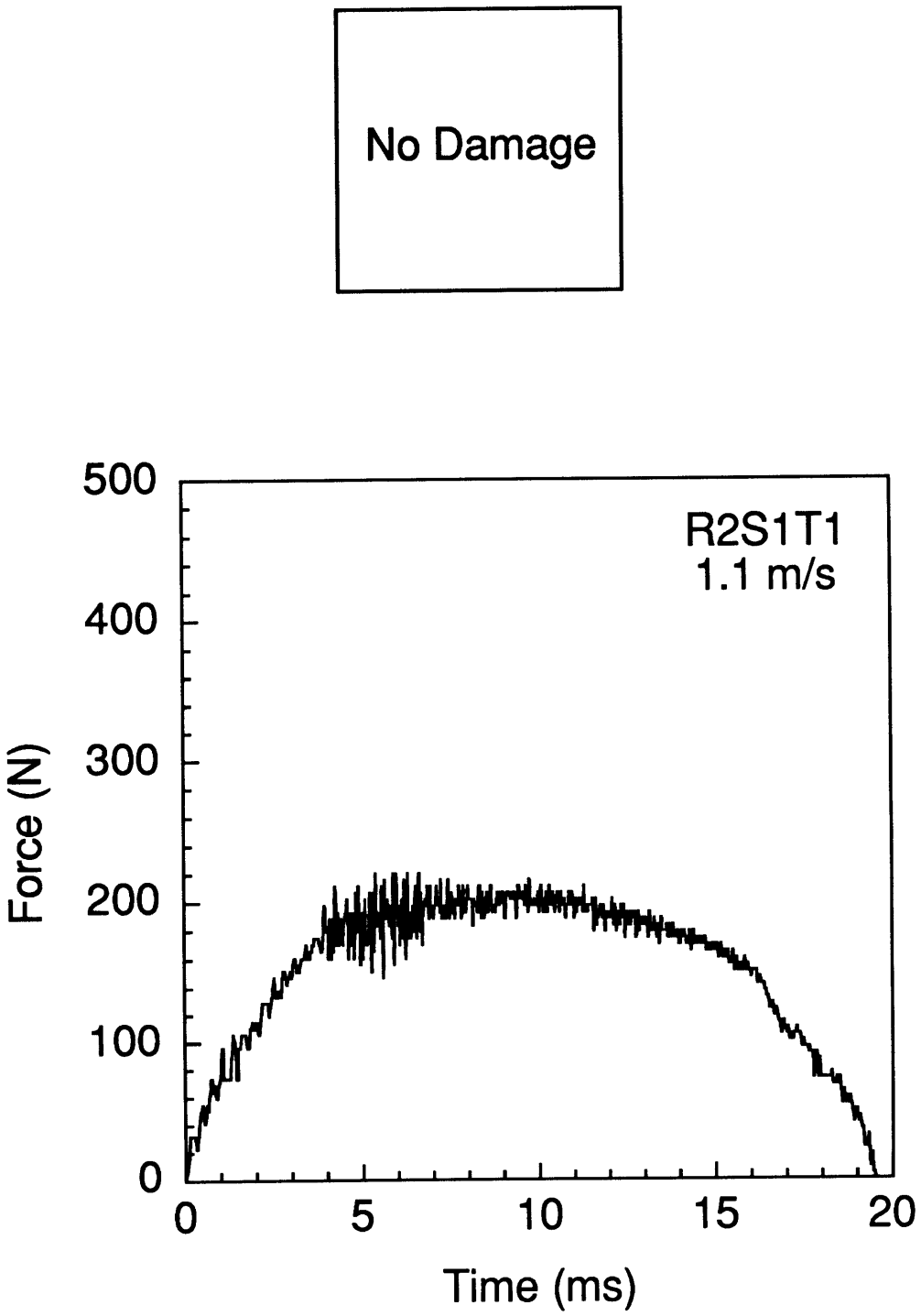

Figure B.24 Results of impact of 1.1 m/s on specimen R2S1T1: (*top*) no damage is observed in the x-ray photograph, and (*bottom*) force-time history.

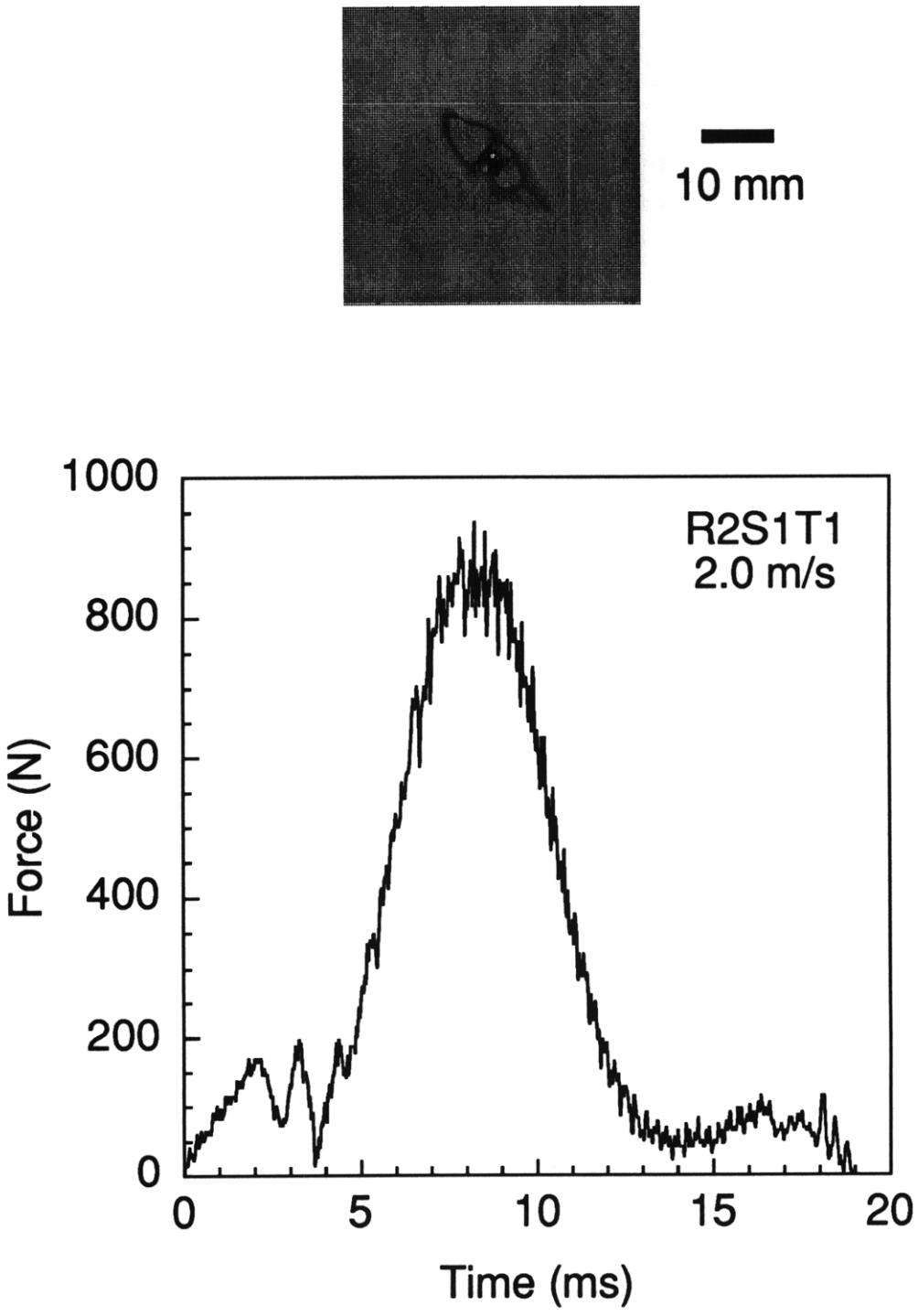

Figure B.25 Results of impact of 2.0 m/s on specimen R2S1T1: (*top*) x-ray photograph of damage state, and (*bottom*) force-time history.

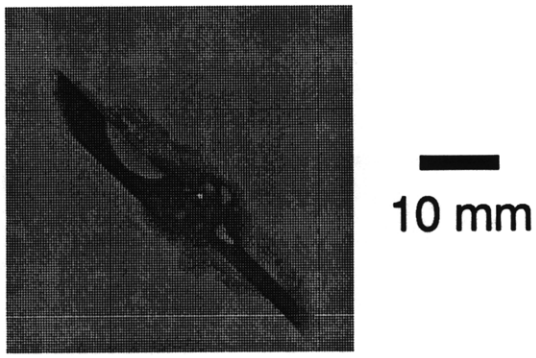

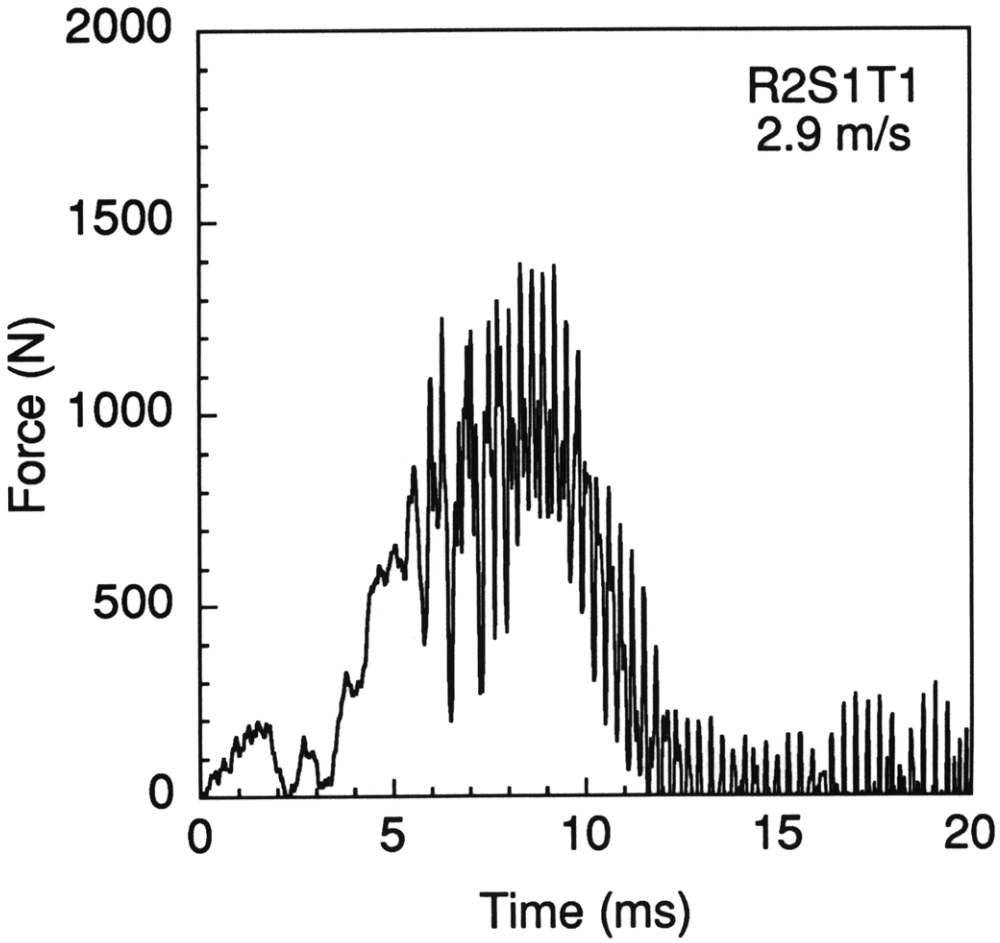

Figure B.26 Results of impact of 2.9 m/s on specimen R2S1T1: (*top*) x-ray photograph of damage state, and (*bottom*) force-time history. This specimen slipped in-plane during testing.

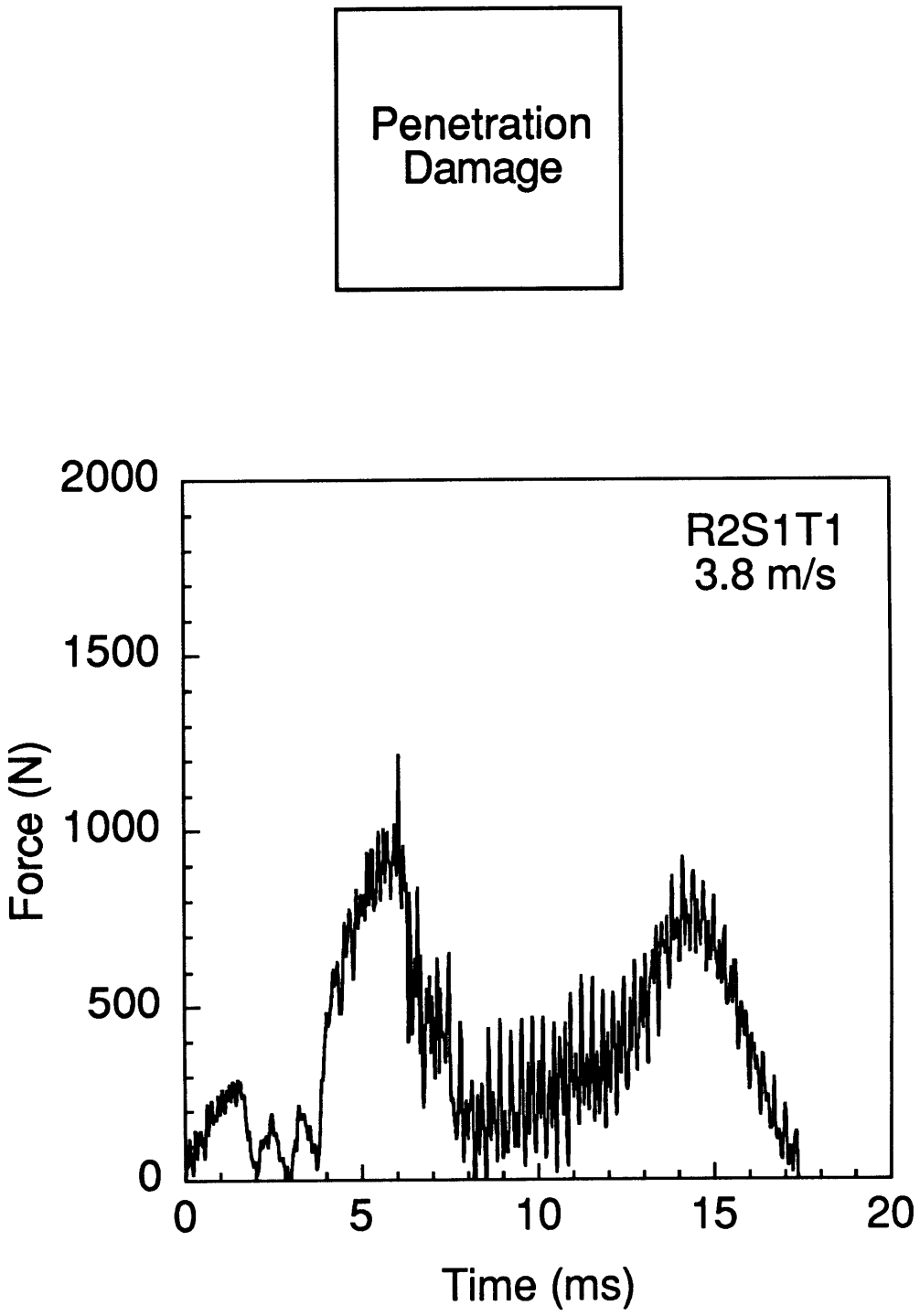

Figure B.27 Results of impact of 3.8 m/s on specimen R2S1T1: (*top*) penetration damage is observed for this specimen, and (*bottom*) force-time history.

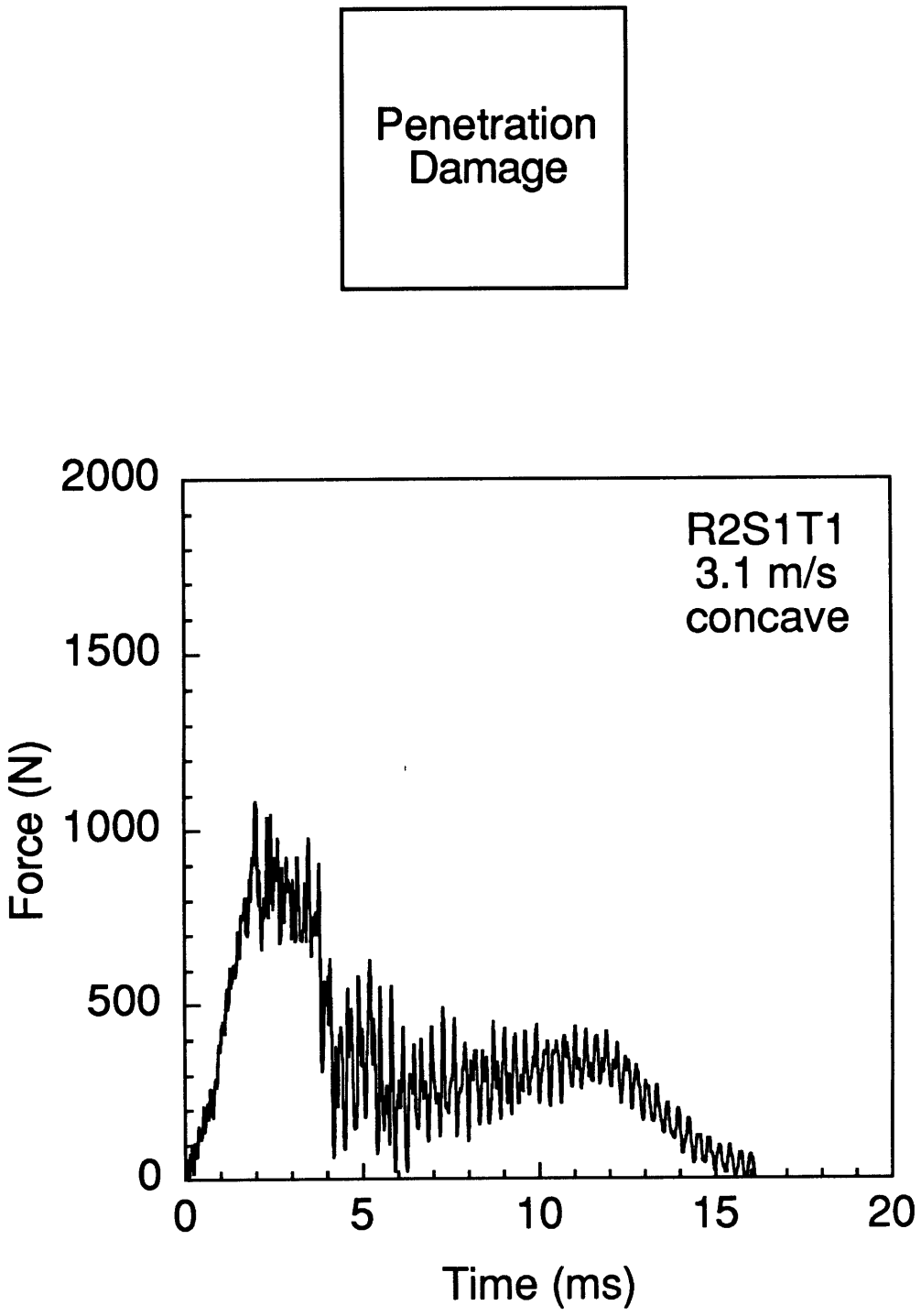

Figure B.28 Results of impact of 3.1 m/s on specimen R2S1T1 (concave): (*top*) penetration damage is observed for this specimen, and (*bottom*) force-time history.

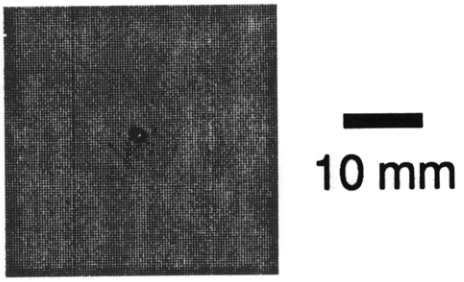

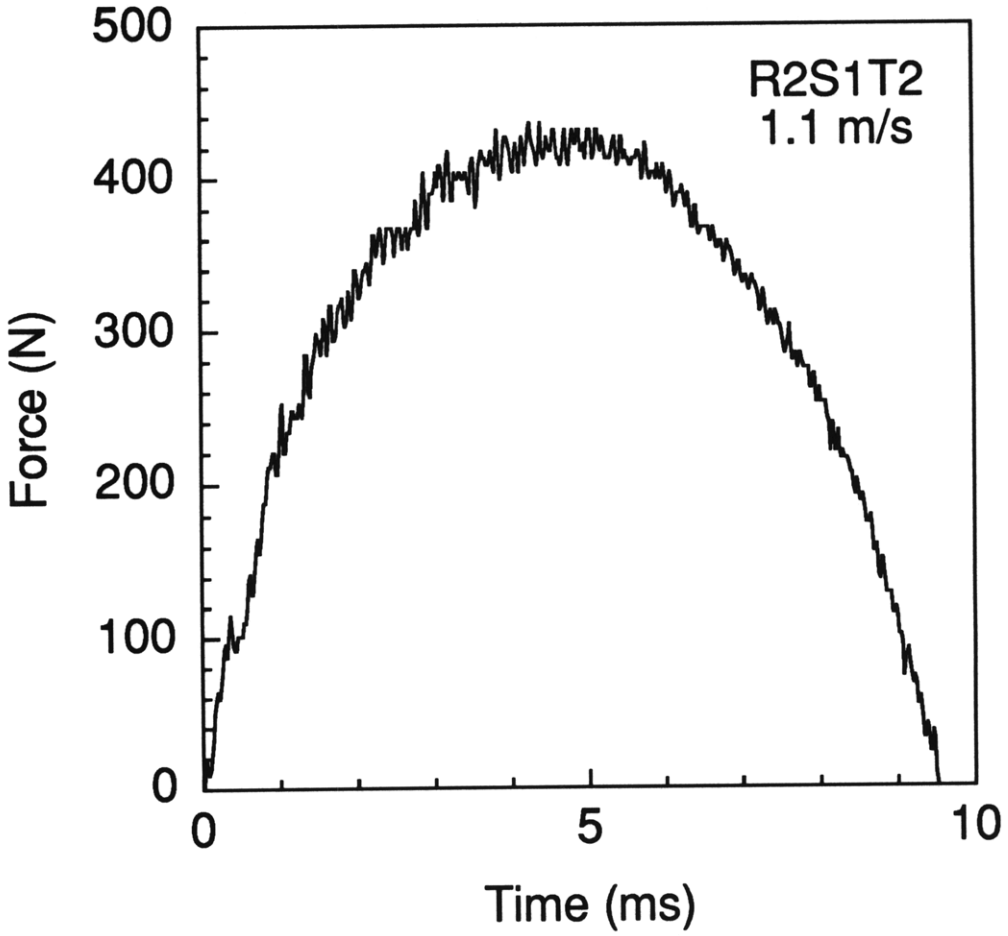

Figure B.29 Results of impact of 1.1 m/s on specimen R2S1T2: (*top*) x-ray photograph of damage state, and (*bottom*) force-time history.

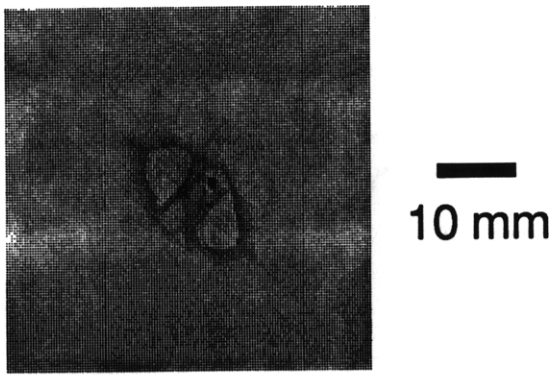

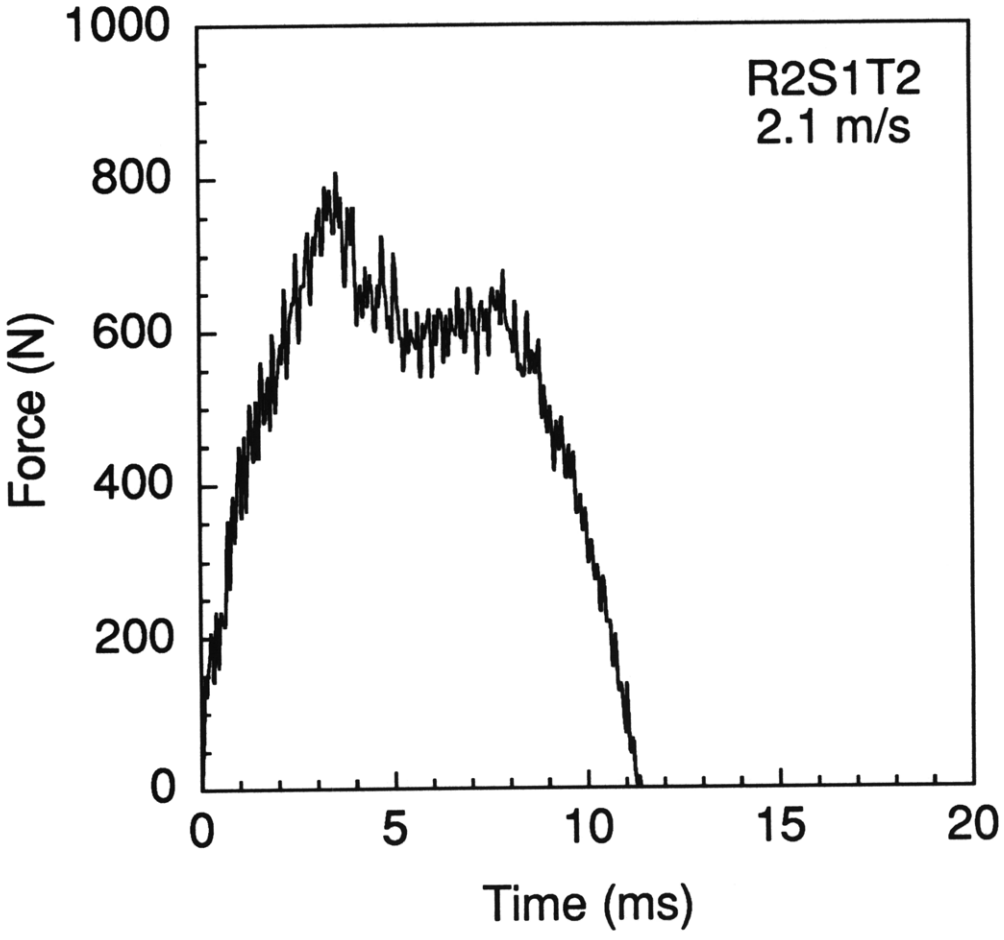

Figure B.30 Results of impact of 2.1 m/s on specimen R2S1T2: (*top*) x-ray photograph of damage state, and (*bottom*) force-time history.

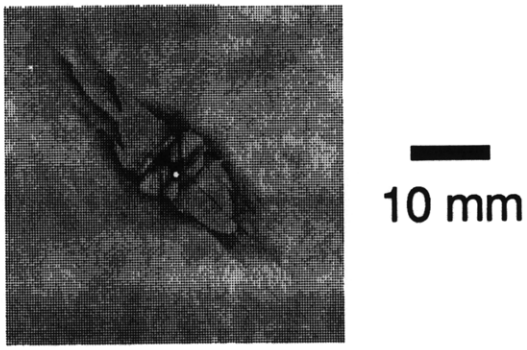

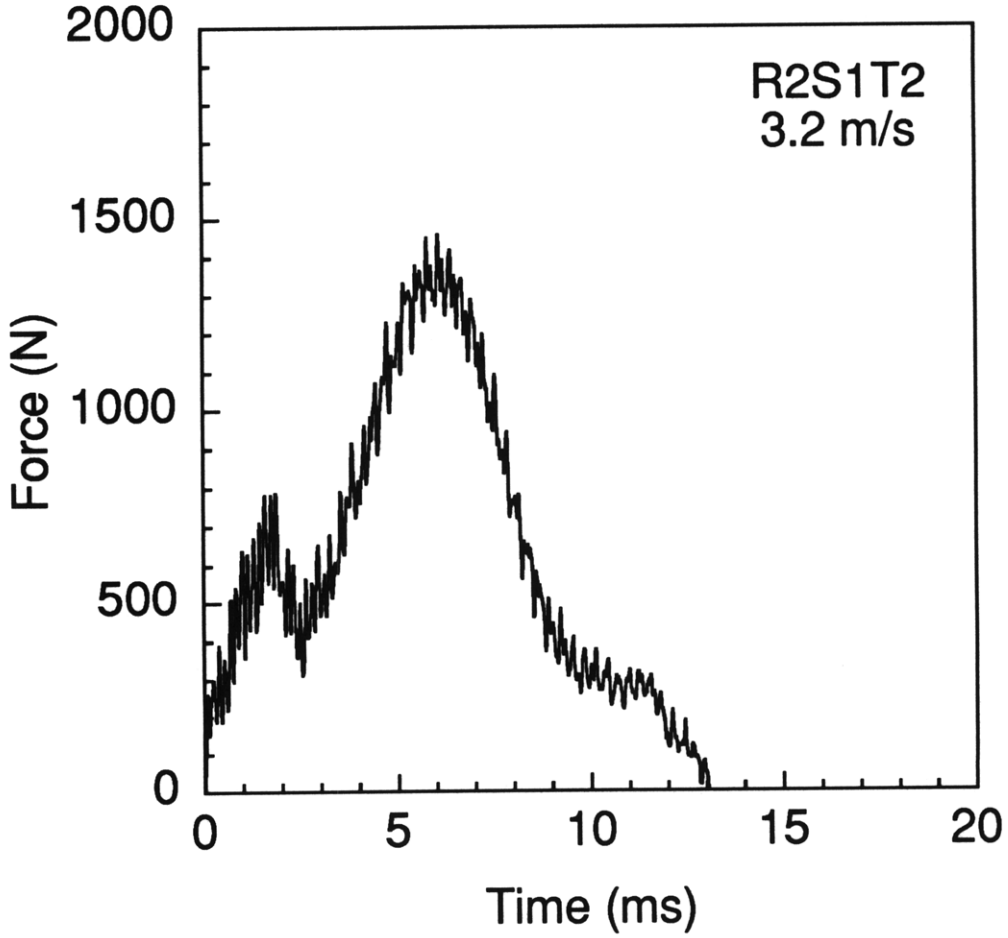

Figure B.31 Results of impact of 3.2 m/s on specimen R2S1T2: (*top*) x-ray photograph of damage state, and (*bottom*) force-time history.

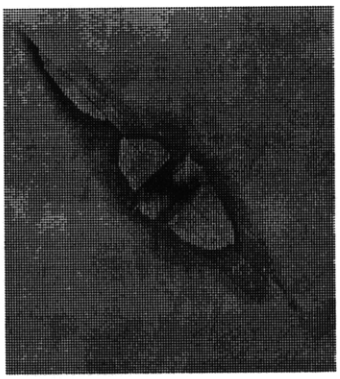

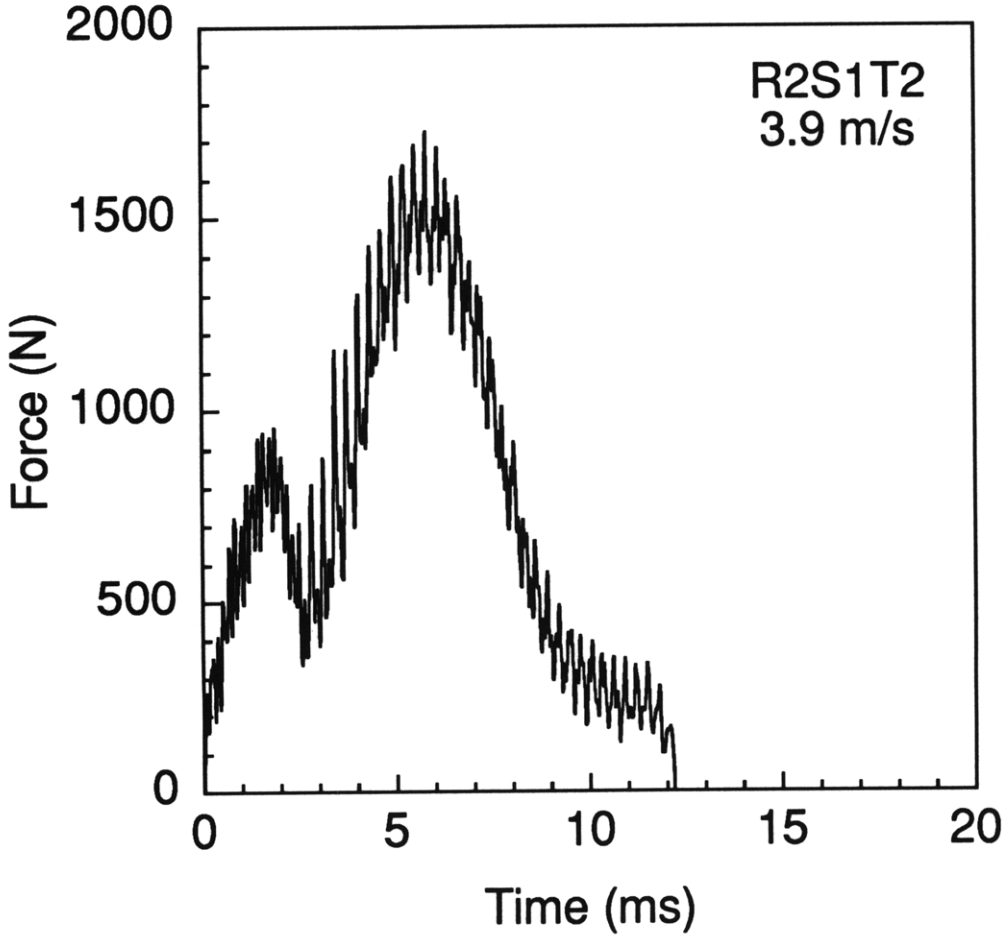

Figure B.32 Results of impact of 3.9 m/s on specimen R2S1T2: (*top*) x-ray photograph of damage state, and (*bottom*) force-time history.

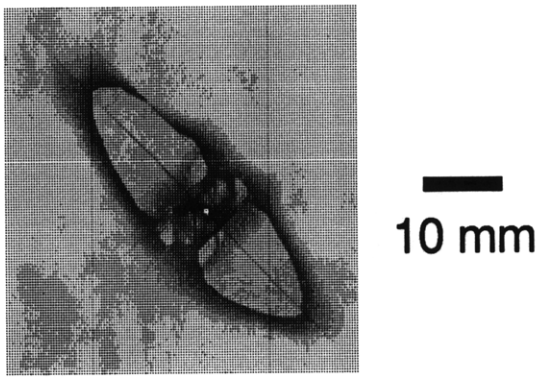

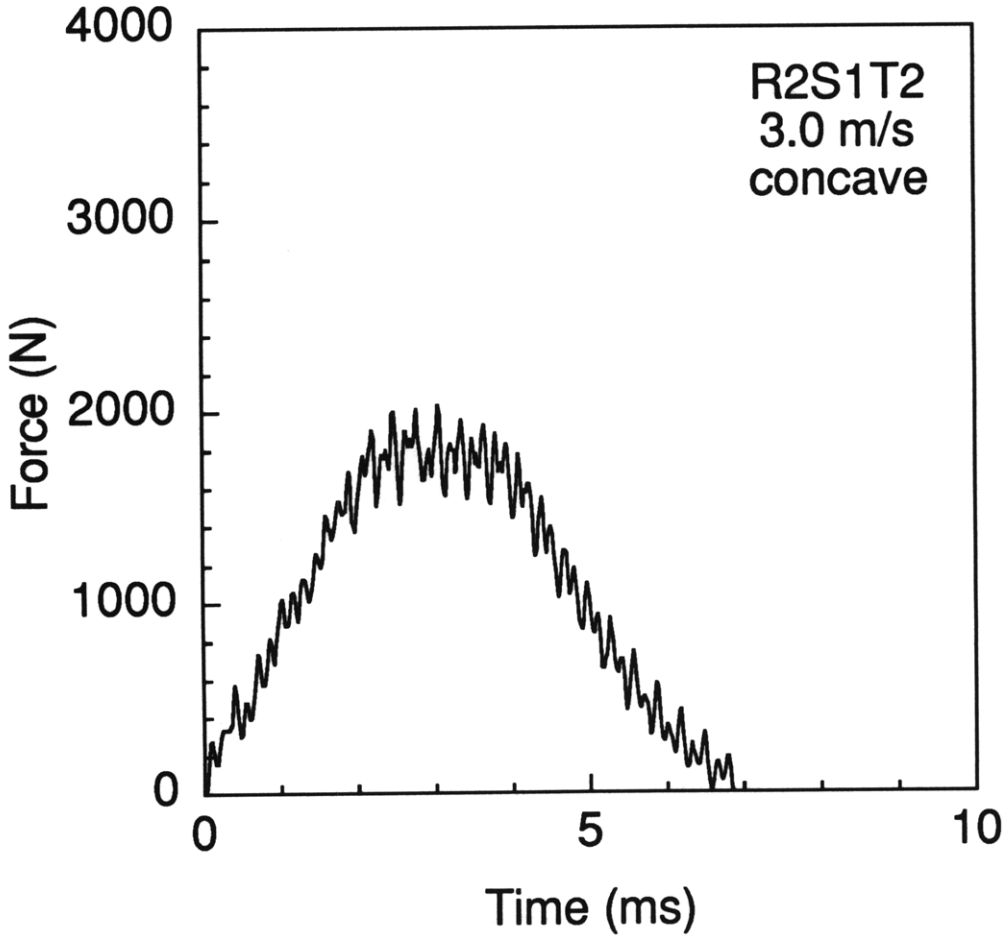

Figure B.33 Results of impact of 3.0 m/s on specimen R2S1T2 (concave): (*top*) x-ray photograph of damage state, and (*bottom*) force-time history.

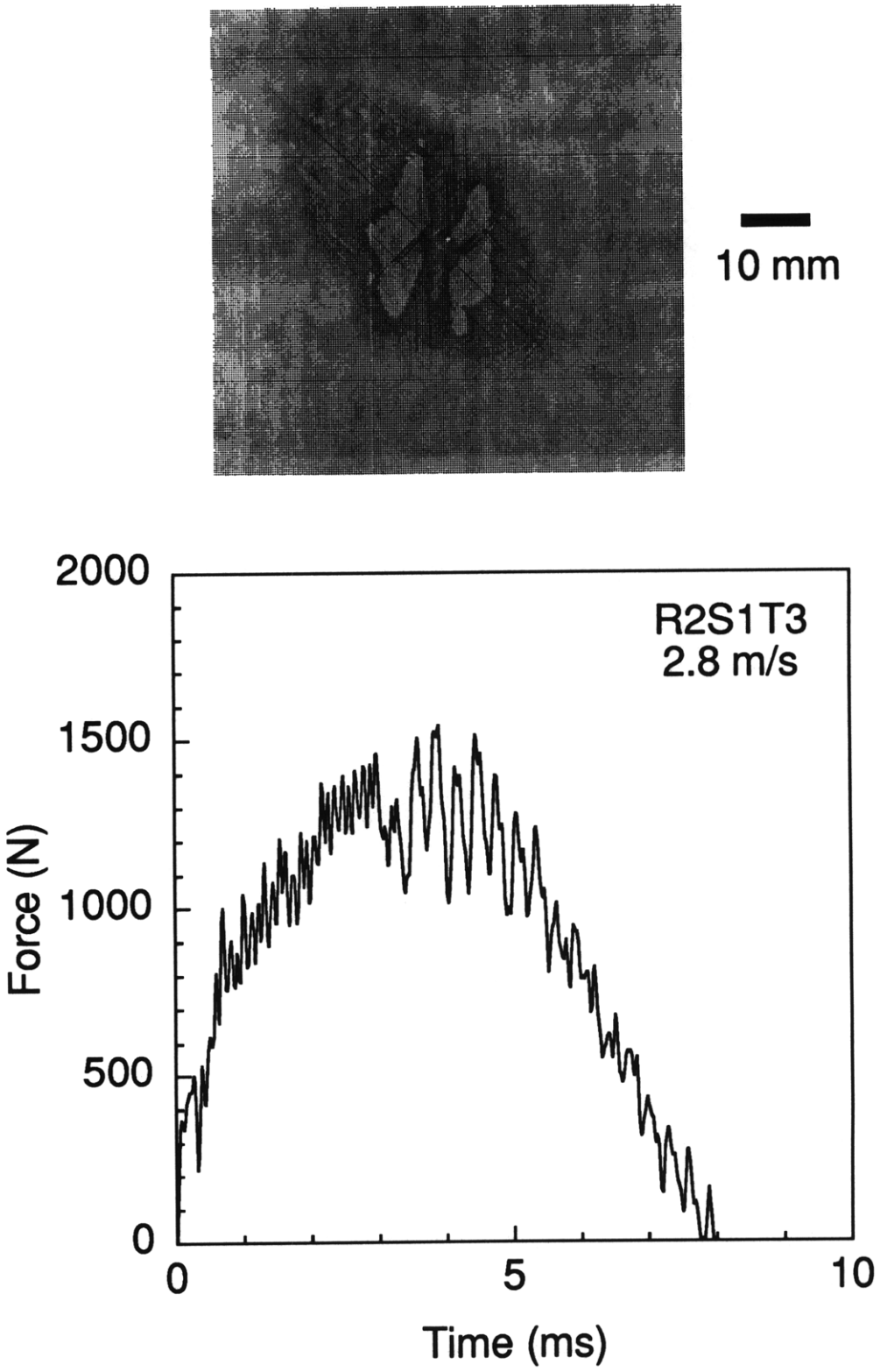

Figure B.34 Results of impact of 2.8 m/s on specimen R2S1T3: (*top*) x-ray photograph of damage state, and (*bottom*) force-time history.

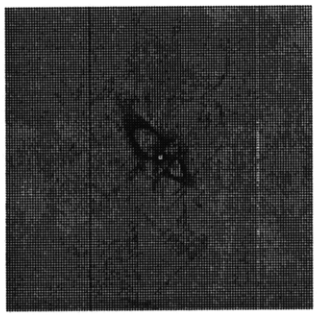

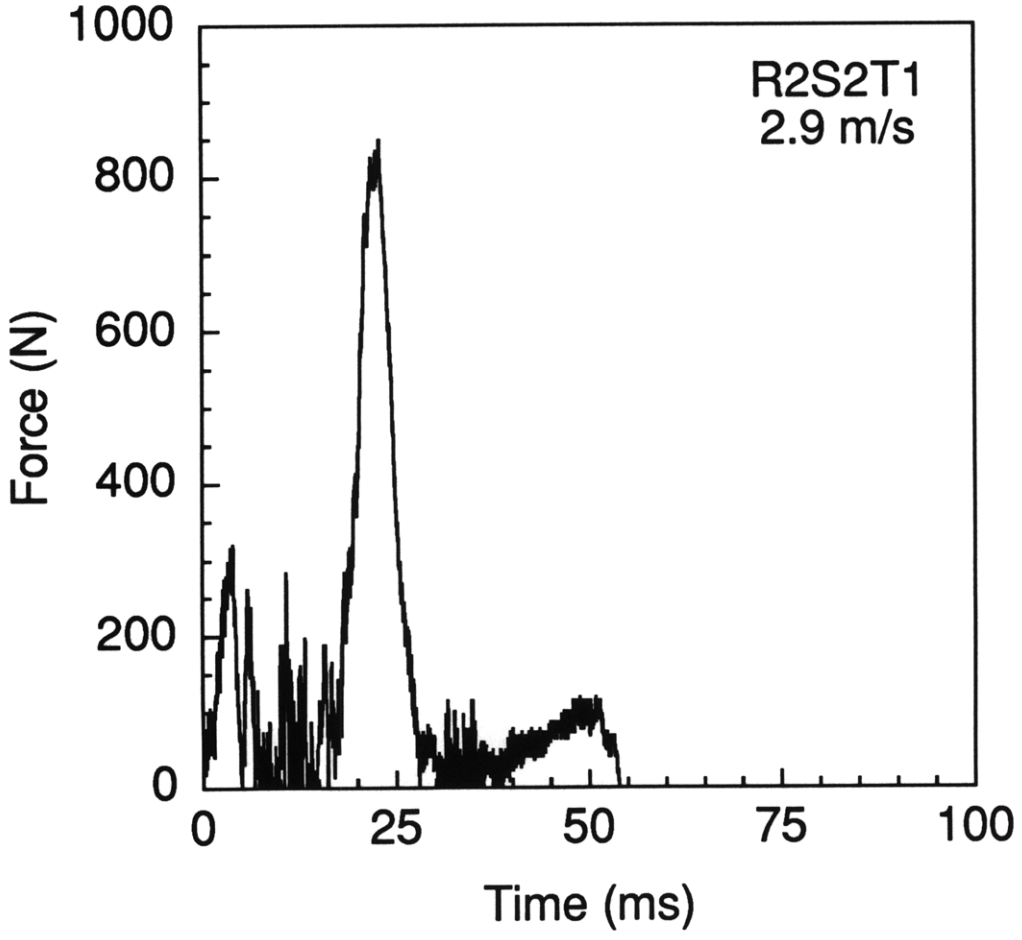

Figure B.35 Results of impact of 2.9 m/s on specimen R2S2T1: (*top*) x-ray photograph of damage state, and (*bottom*) force-time history.

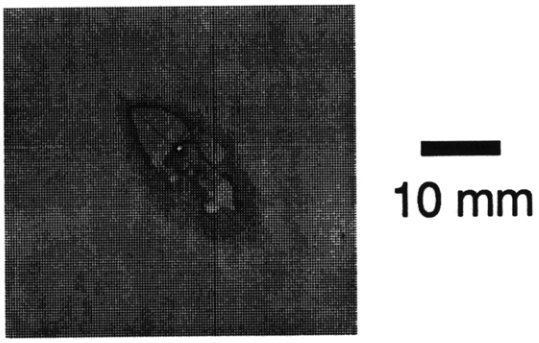

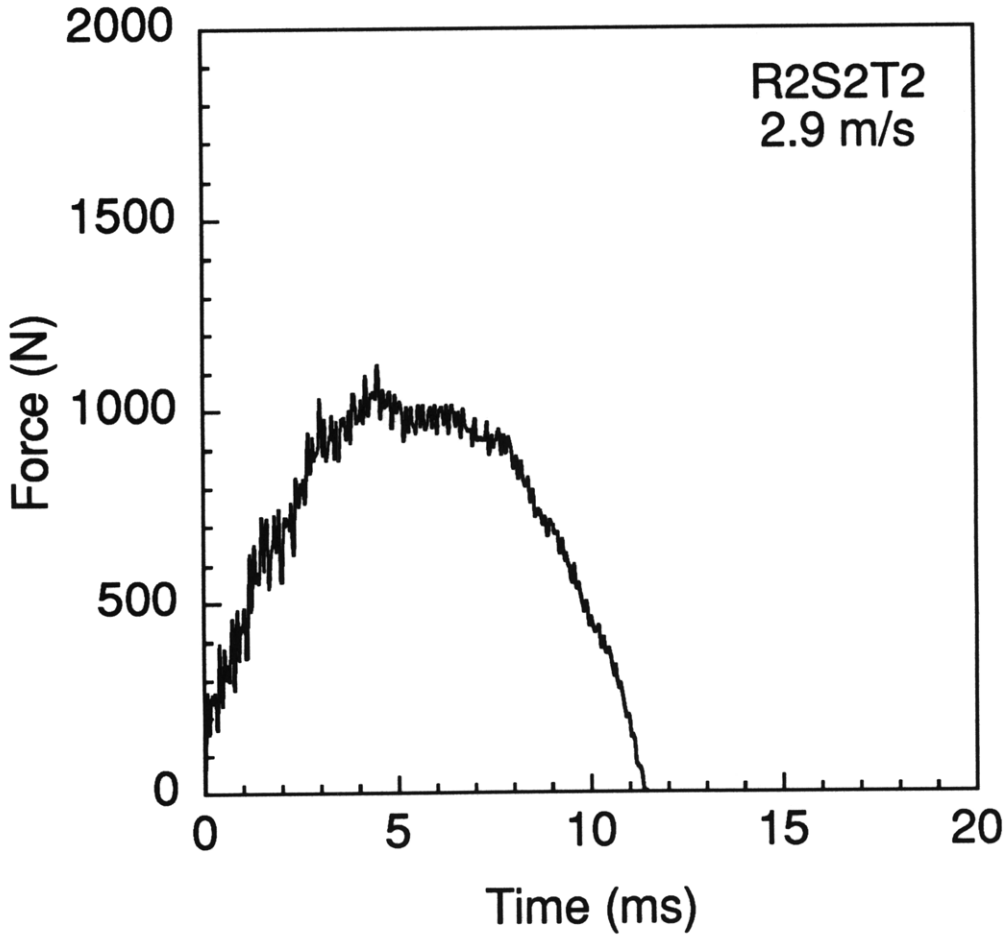

Figure B.36 Results of impact of 2.9 m/s on specimen R2S2T2: (*top*) x-ray photograph of damage state, and (*bottom*) force-time history.

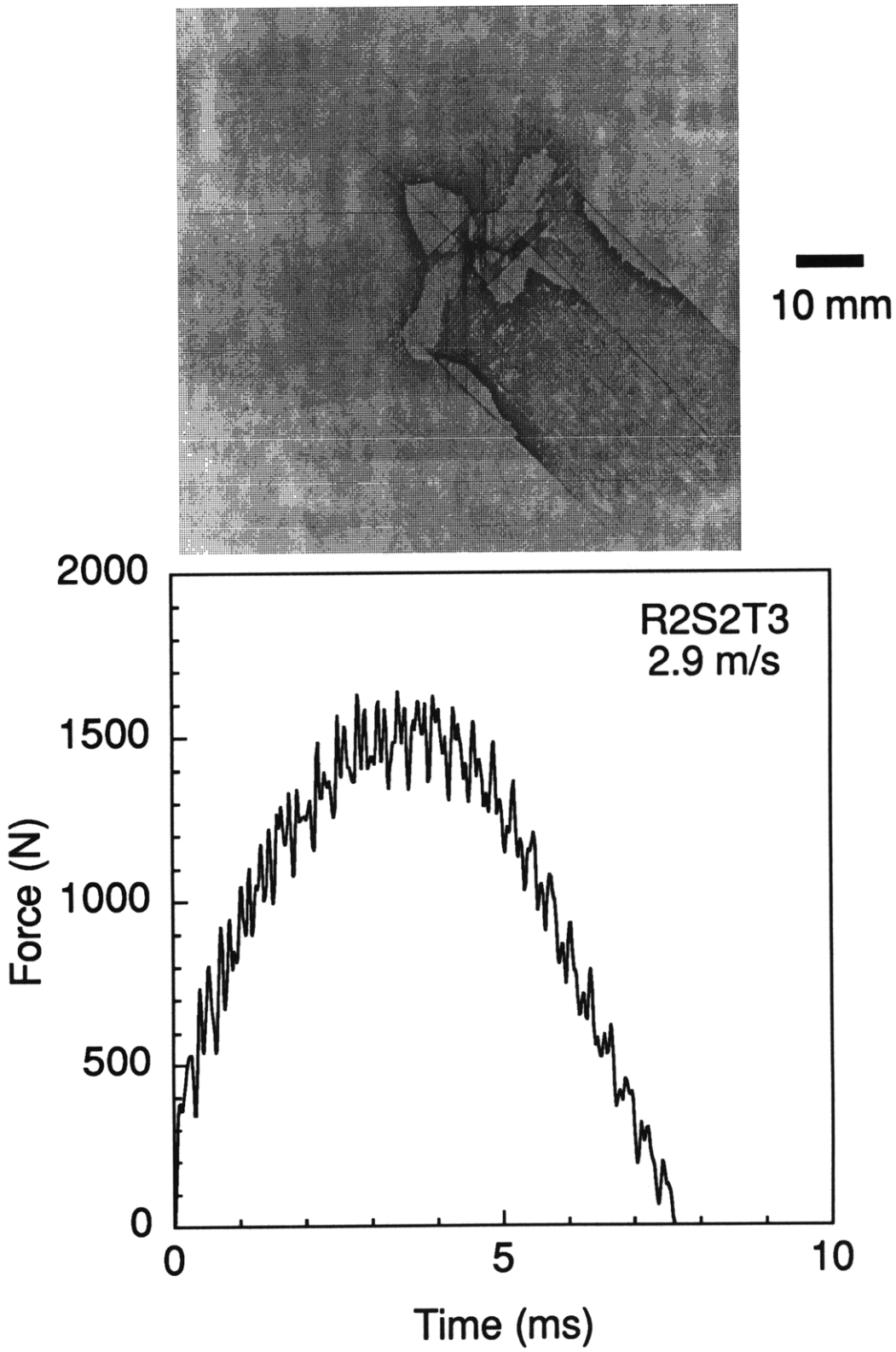

Figure B.37 Results of impact of 2.9 m/s on specimen R2S2T3: (*top*) x-ray photograph of damage state, and (*bottom*) force-time history.

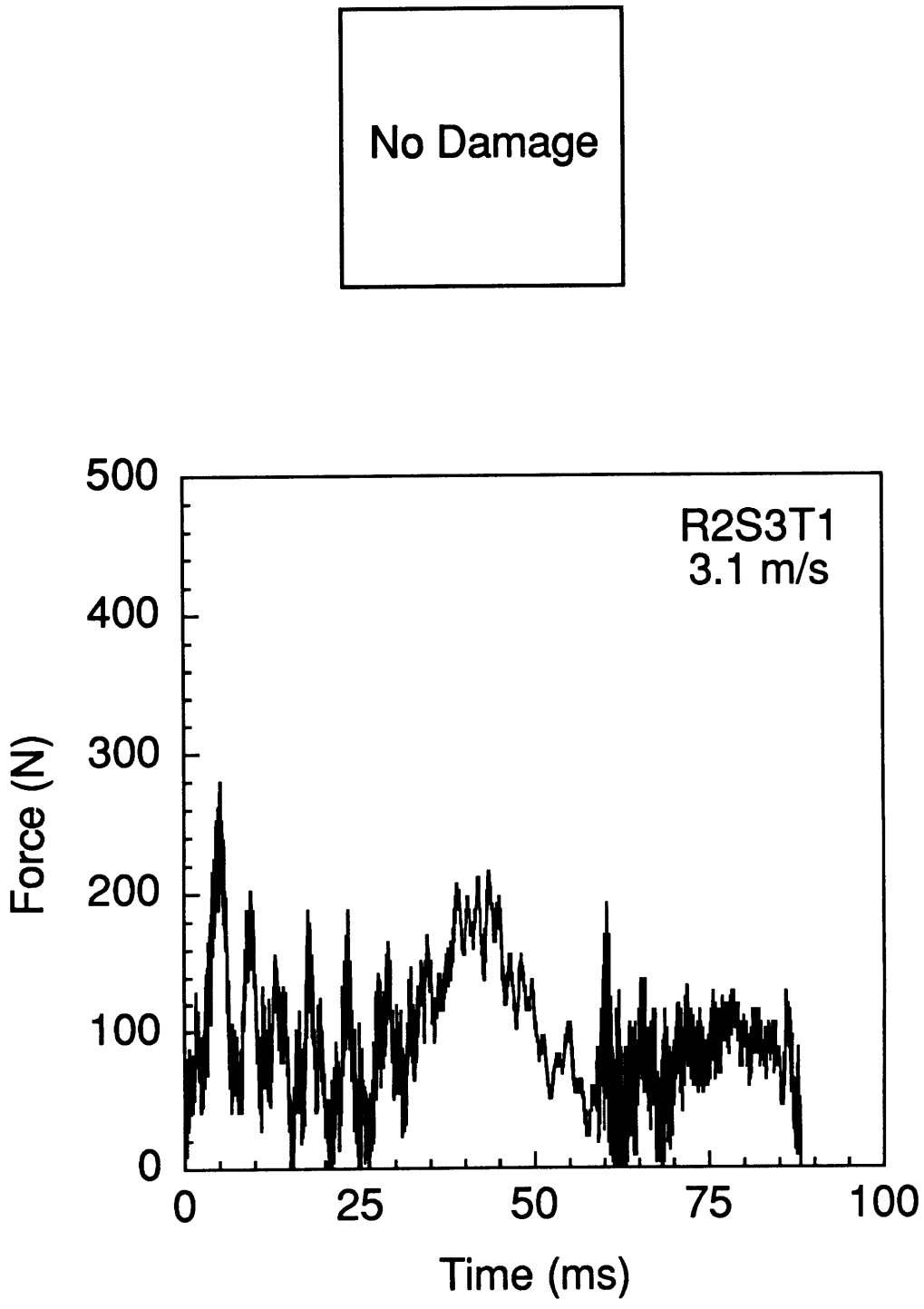

Figure B.38 Results of impact of 3.1 m/s on specimen R2S3T1: (*top*) no damage is observed in the x-ray photograph, and (*bottom*) force-time history.

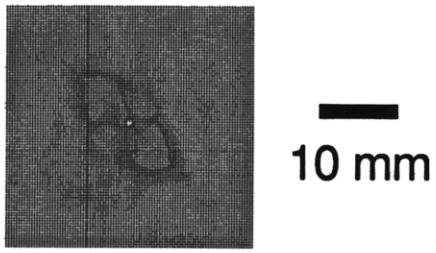

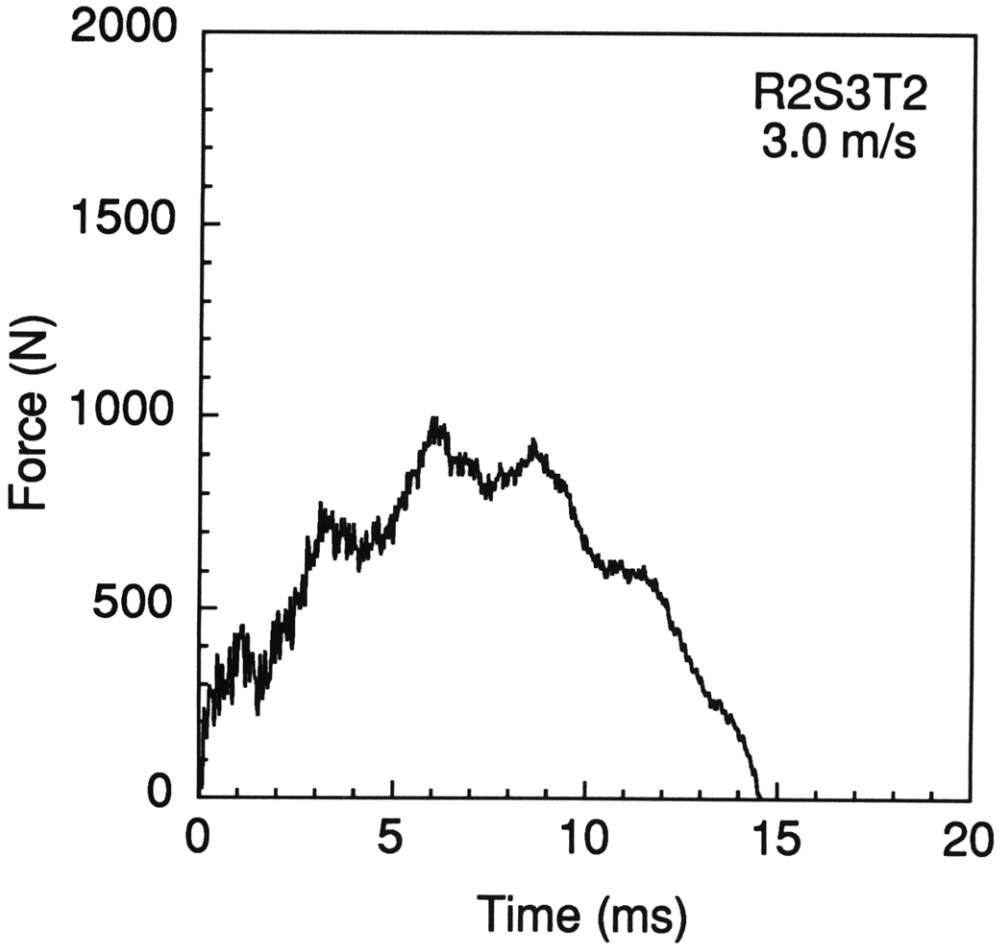

Figure B.39 Results of impact of 3.0 m/s on specimen R2S3T2: (*top*) x-ray photograph of damage state, and (*bottom*) force-time history.

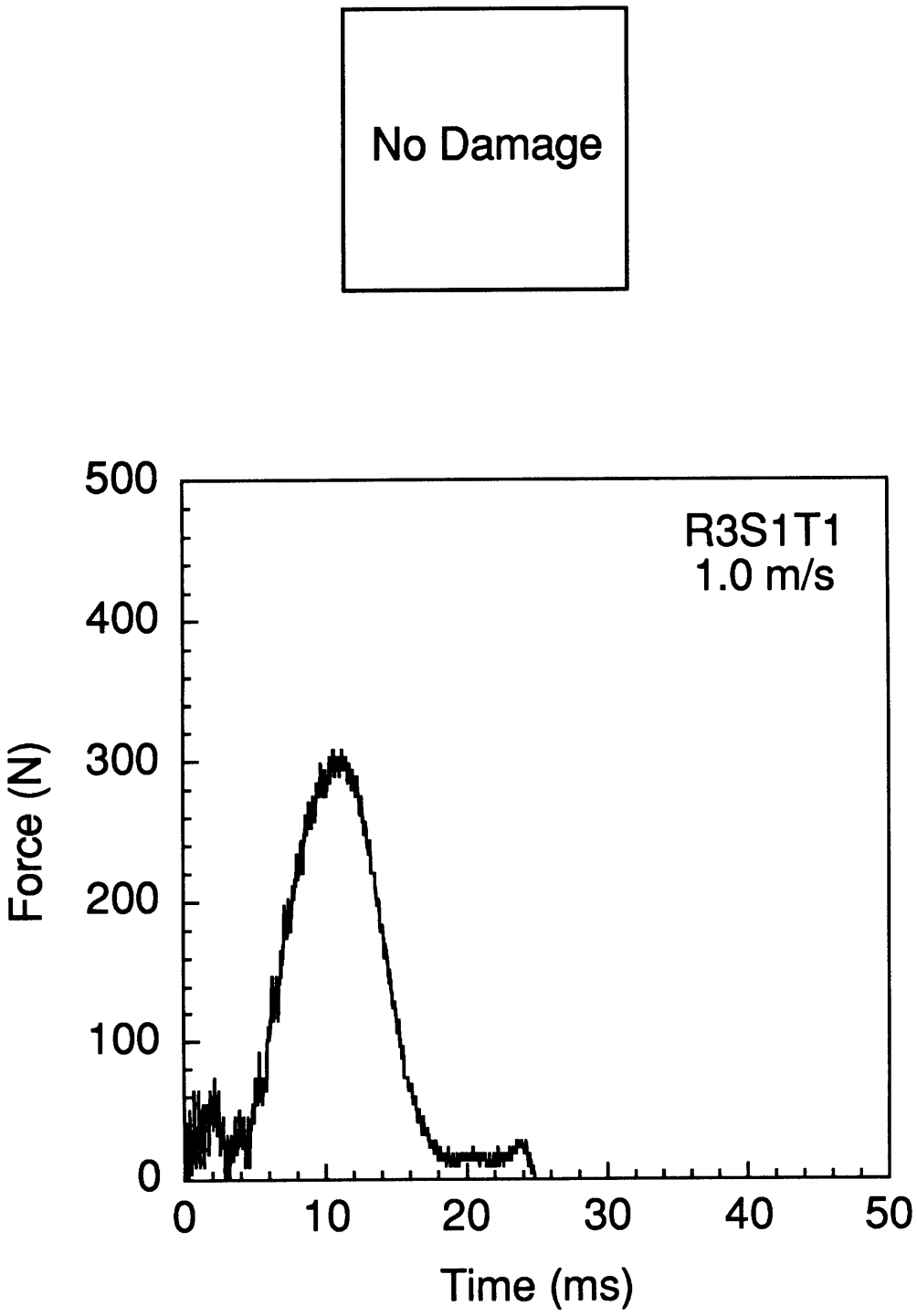

Figure B.40 Results of impact of 1.0 m/s on specimen R3S1T1: (*top*) no damage is observed in the x-ray photograph, and (*bottom*) force-time history.

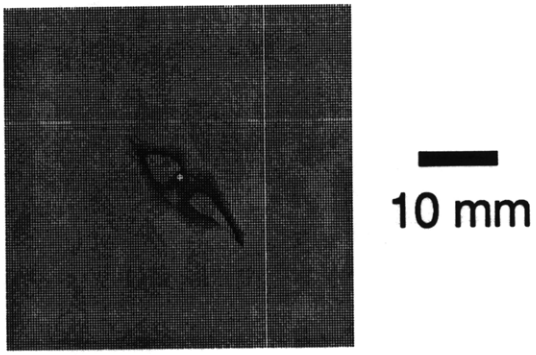

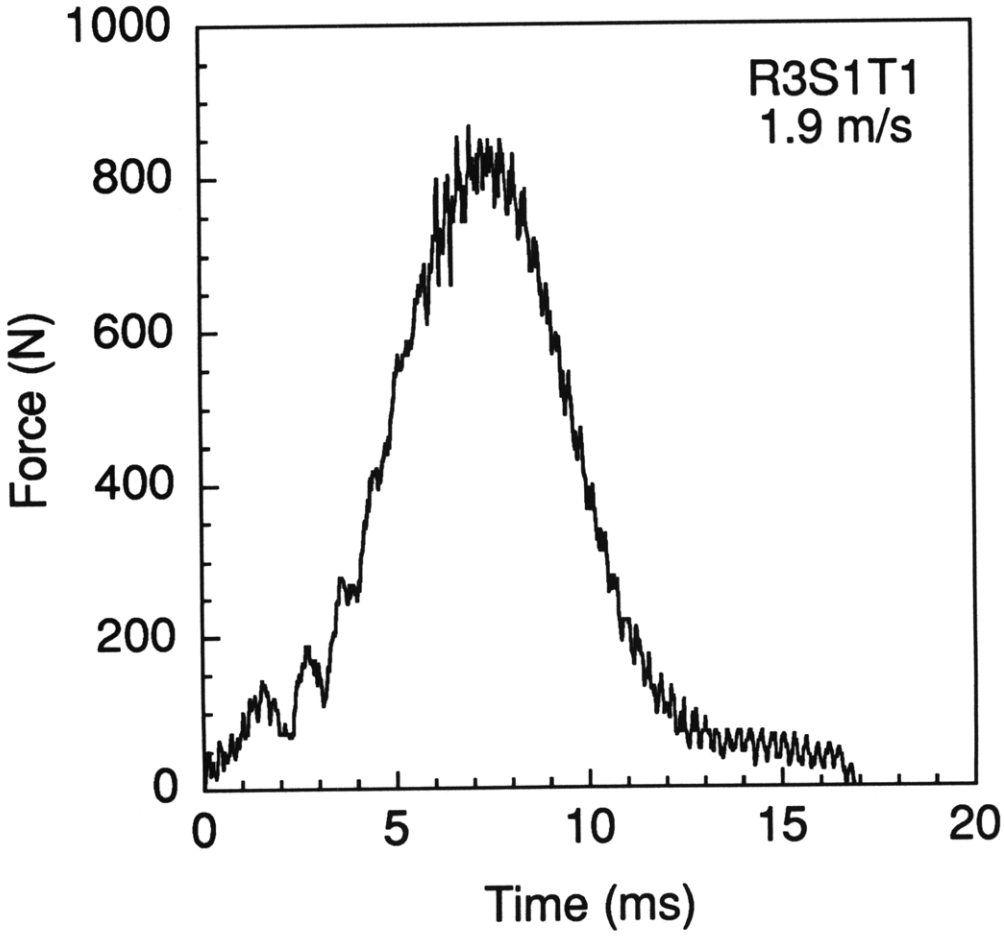

Figure B.41 Results of impact of 1.9 m/s on specimen R3S1T1: (*top*) x-ray photograph of damage state, and (*bottom*) force-time history.

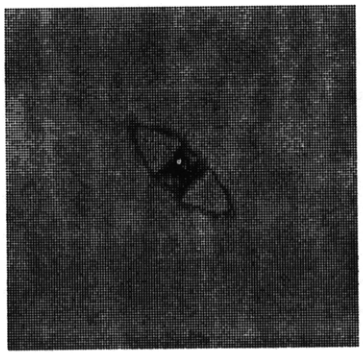

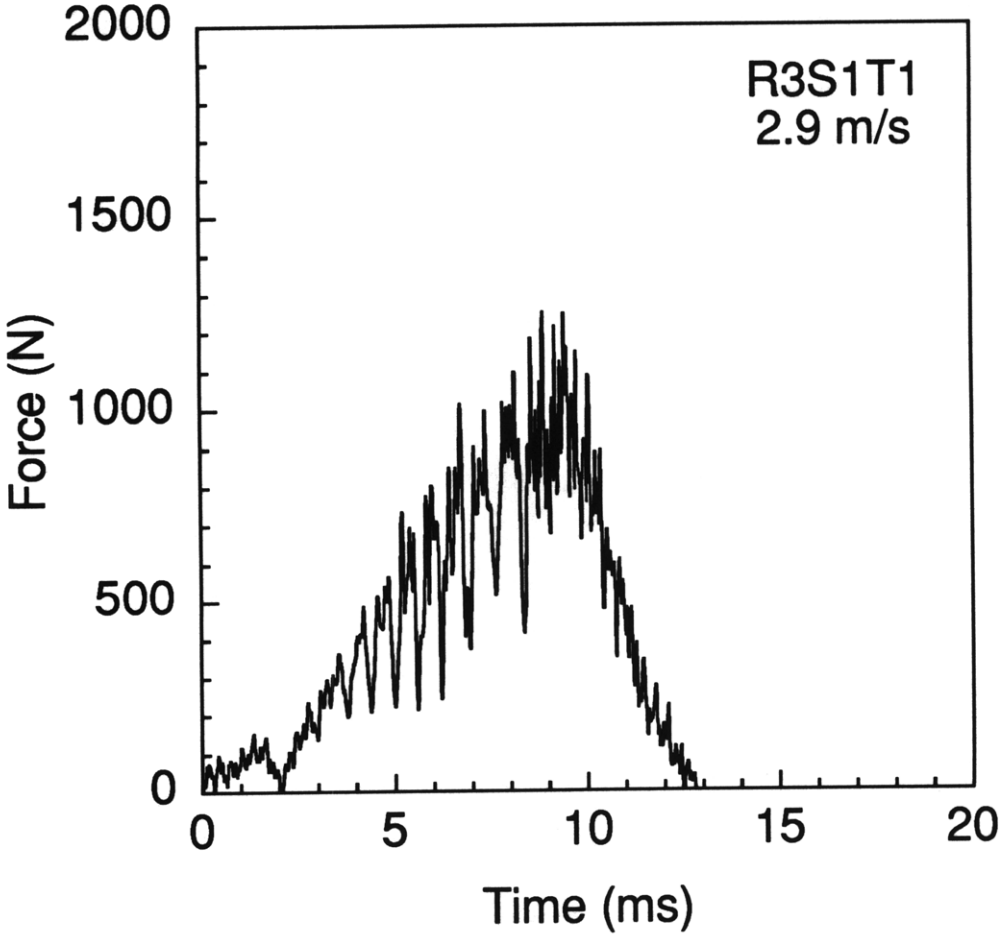

Figure B.42 Results of impact of 2.9 m/s on specimen R3S1T1: (*top*) x-ray photograph of damage state, and (*bottom*) force-time history. This specimen slipped in-plane during testing.

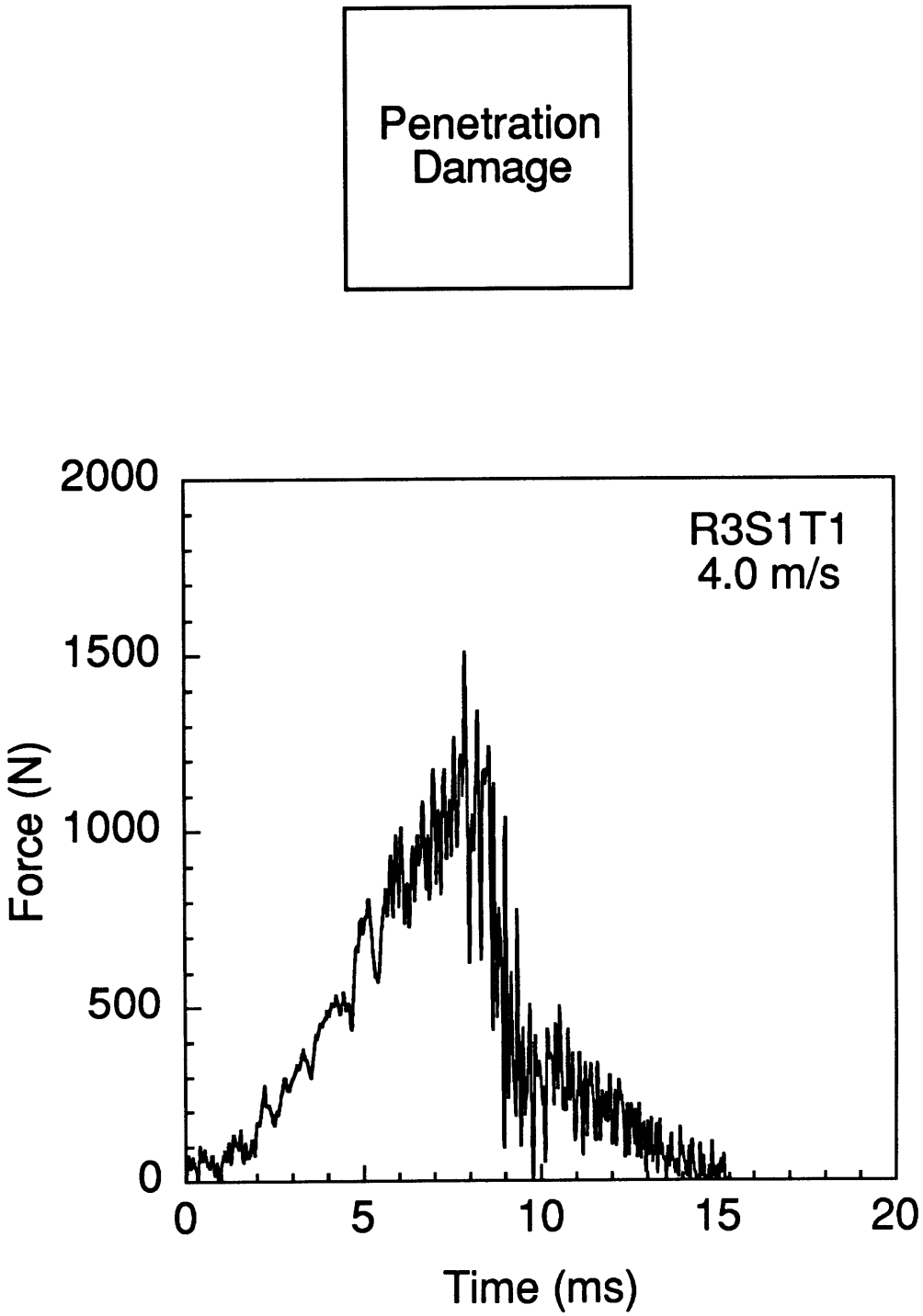

Figure B.43 Results of impact of 4.0 m/s on specimen R3S1T1: (*top*) penetration damage is observed for this specimen, and (*bottom*) force-time history. This specimen slipped in-plane during testing.

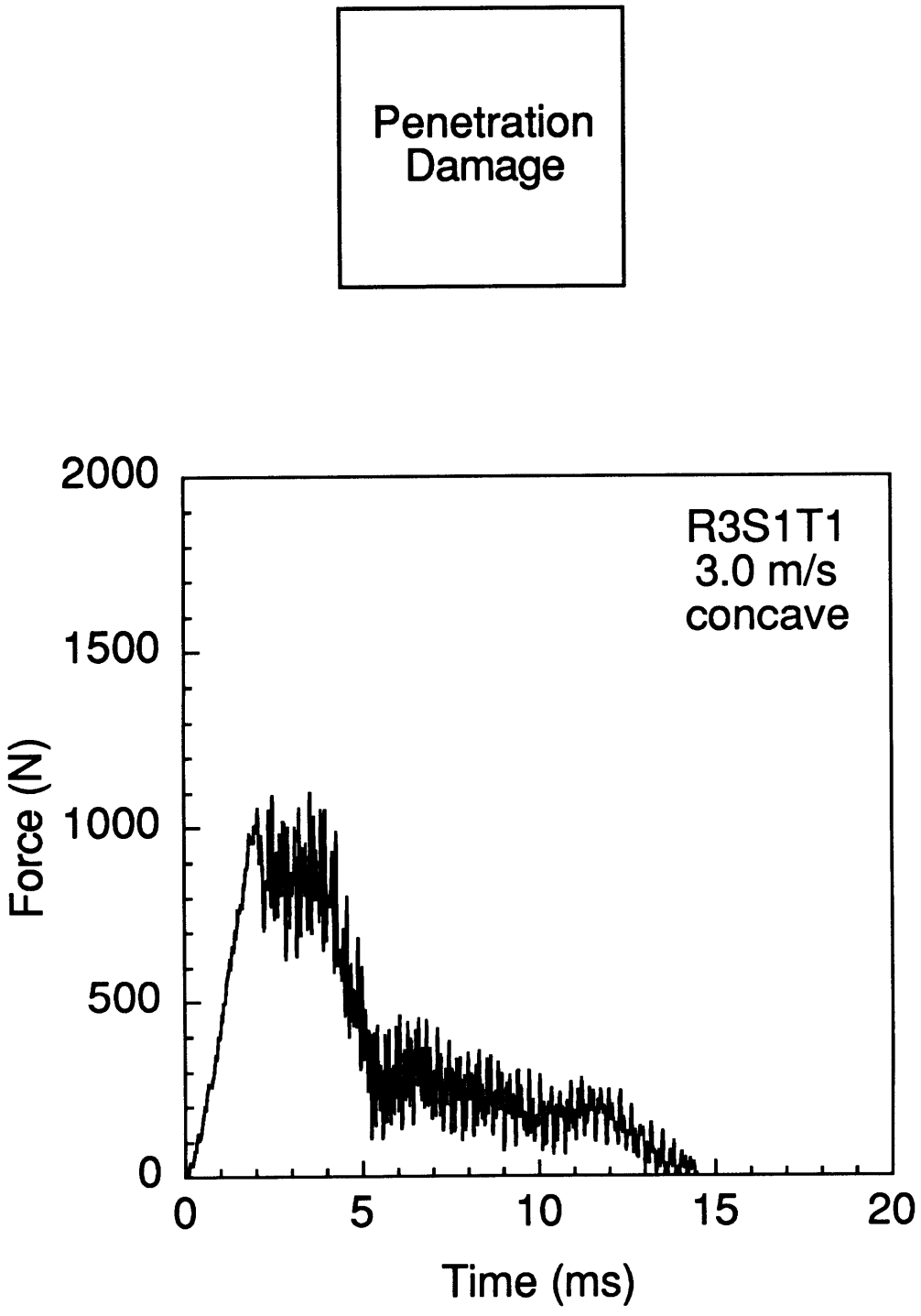

Figure B.44 Results of impact of 3.0 m/s on specimen R3S1T1 (concave): (*top*) penetration damage is observed for this specimen, and (*bottom*) force-time history.

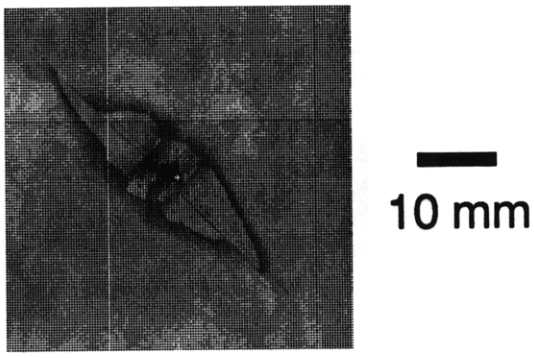

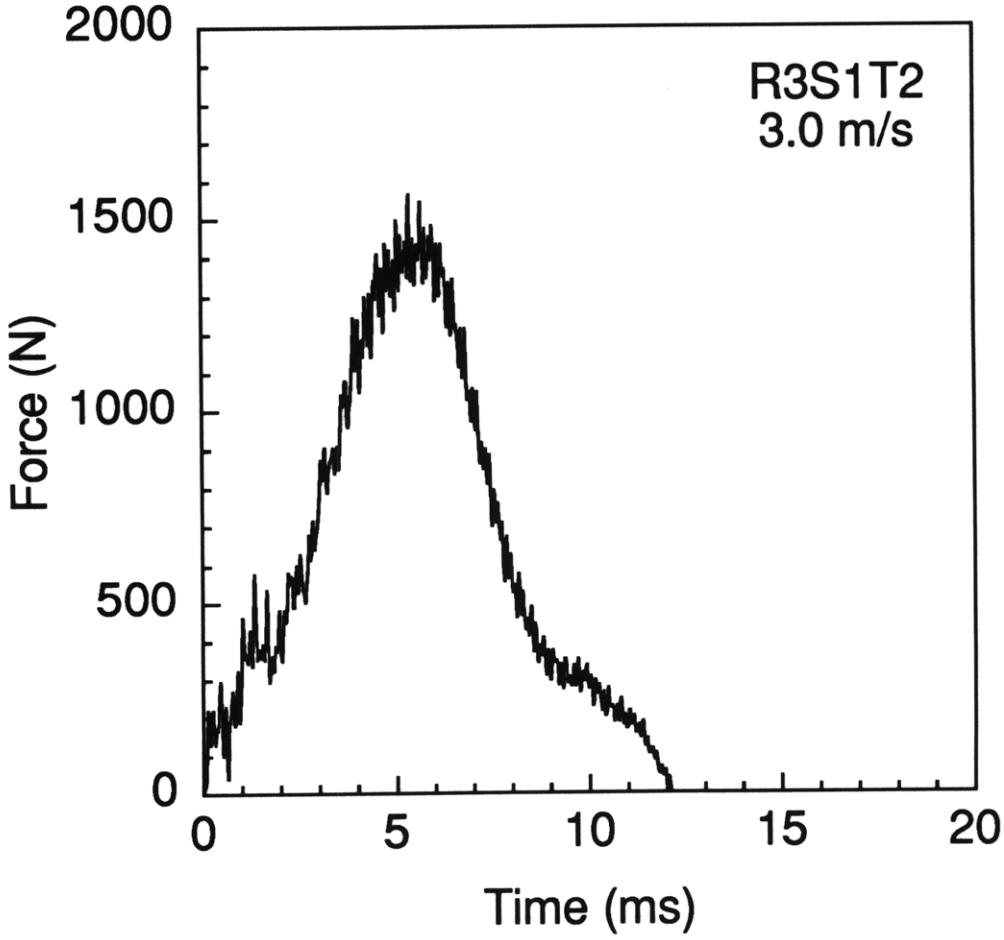

Figure B.45 Results of impact of 3.0 m/s on specimen R3S1T2: (*top*) x-ray photograph of damage state, and (*bottom*) force-time history.

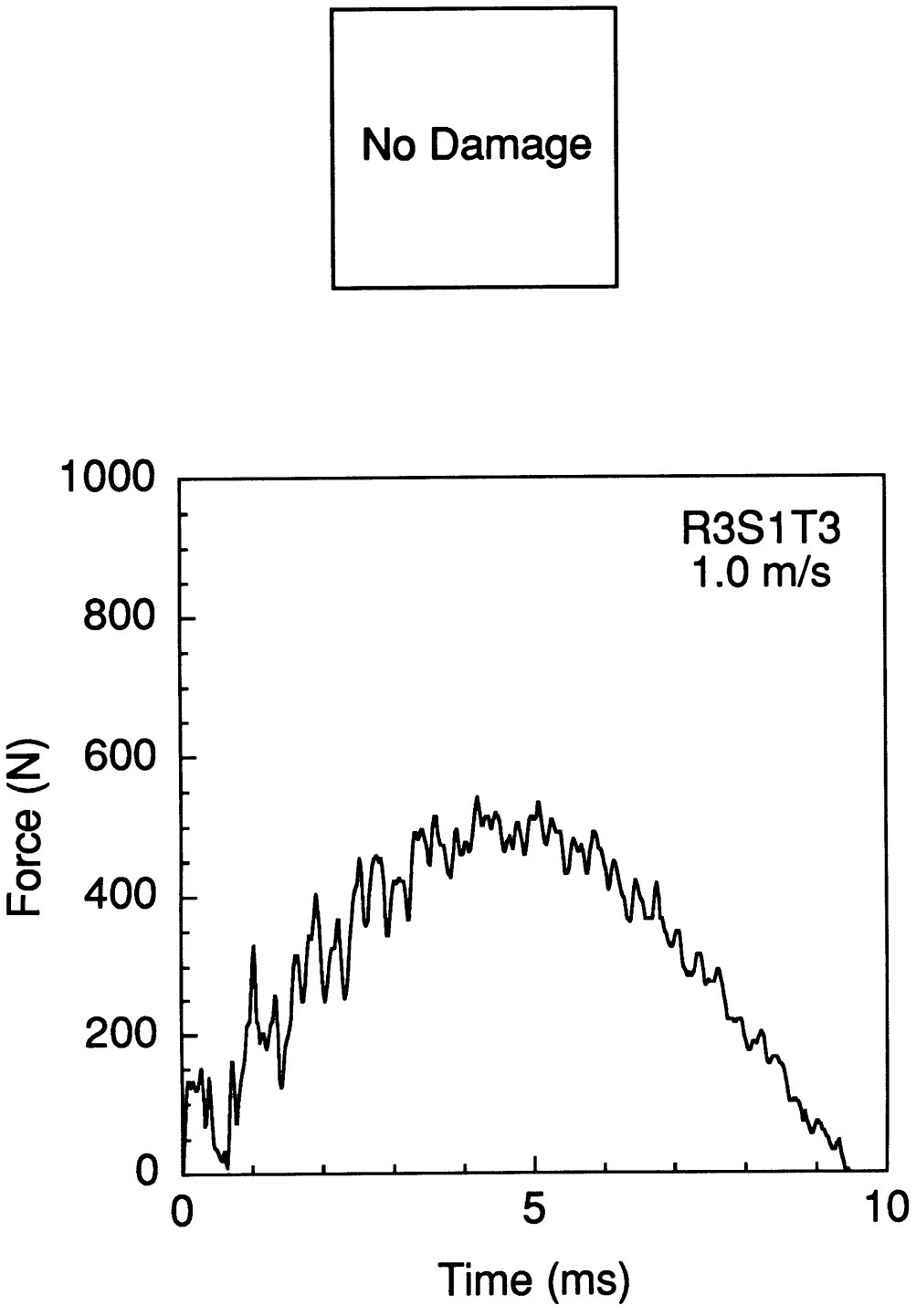

Figure B.46 Results of impact of 1.0 m/s on specimen R3S1T3: (*top*) no damage is observed in the x-ray photograph, and (*bottom*) force-time history.

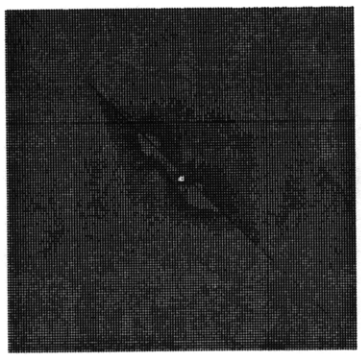

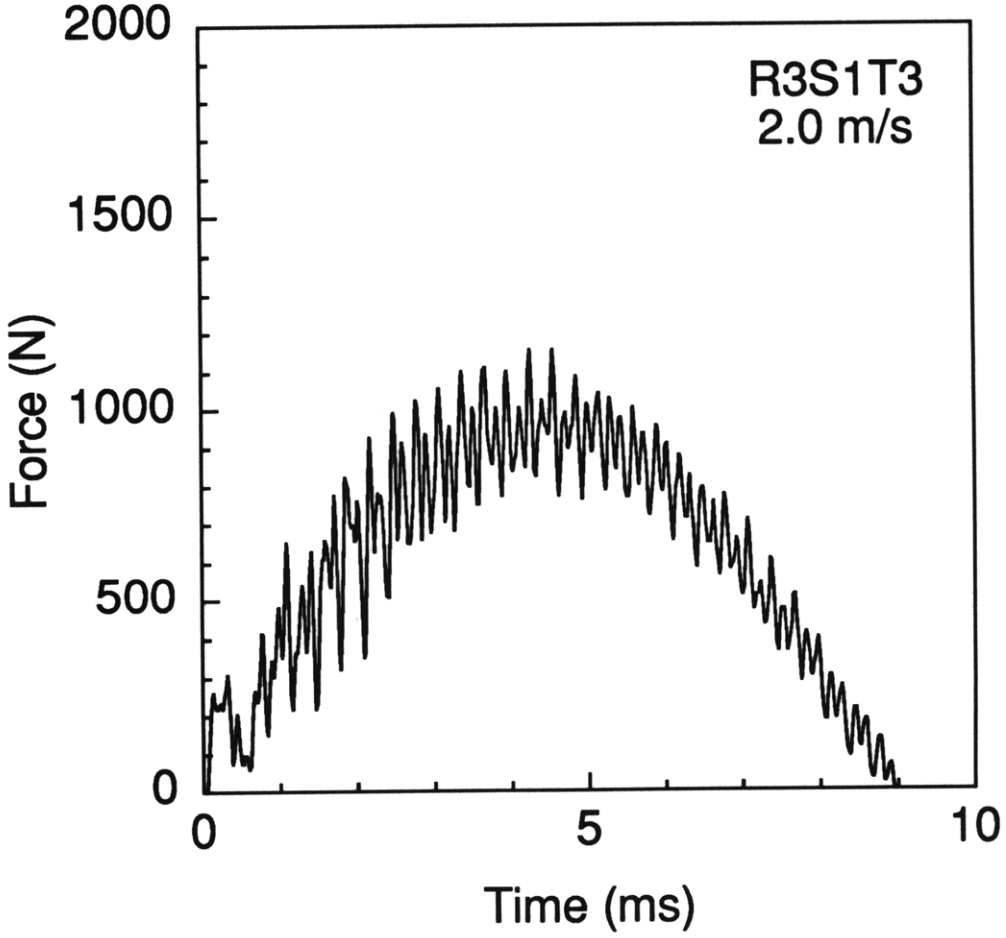

Figure B.47 Results of impact of 2.0 m/s on specimen R3S1T3: (*top*) x-ray photograph of damage state, and (*bottom*) force-time history.

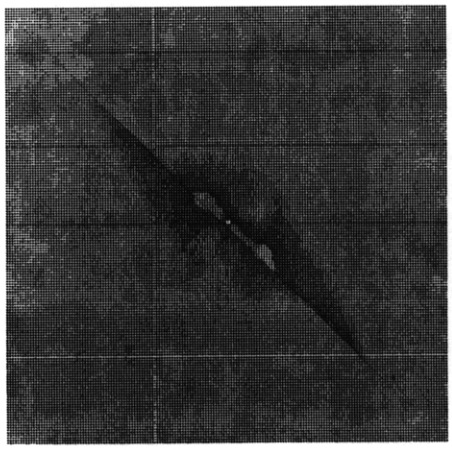

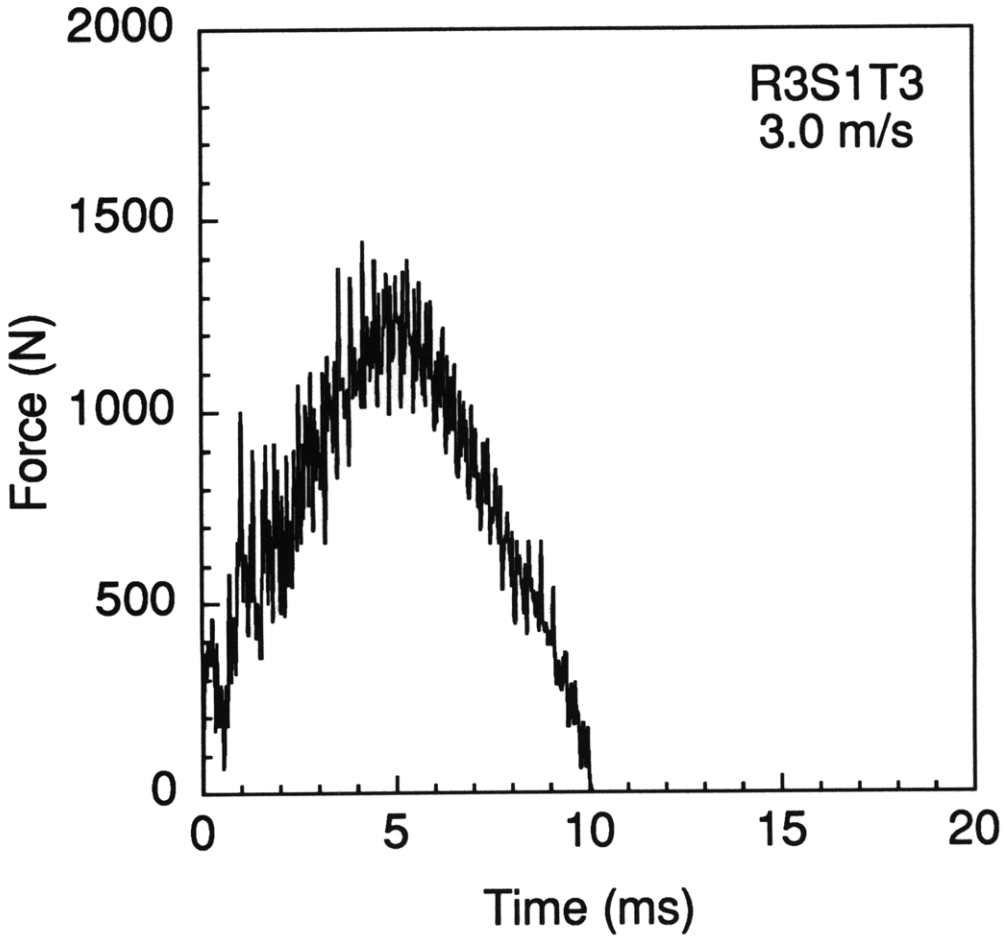

Figure B.48 Results of impact of 3.0 m/s on specimen R3S1T3: (*top*) x-ray photograph of damage state, and (*bottom*) force-time history.

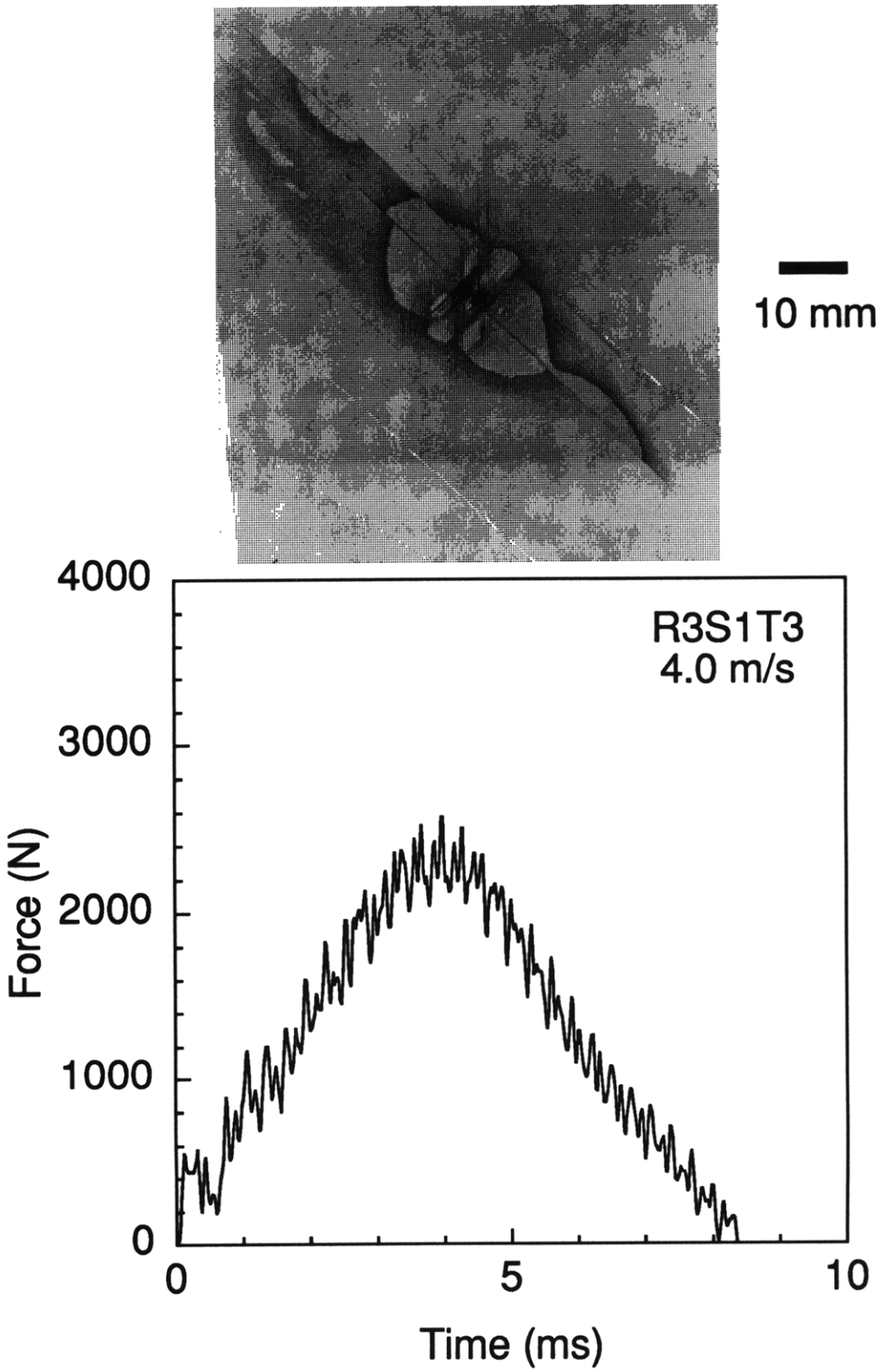

Figure B.49 Results of impact of 4.0 m/s on specimen R3S1T3: (*top*) x-ray photograph of damage state, and (*bottom*) force-time history.

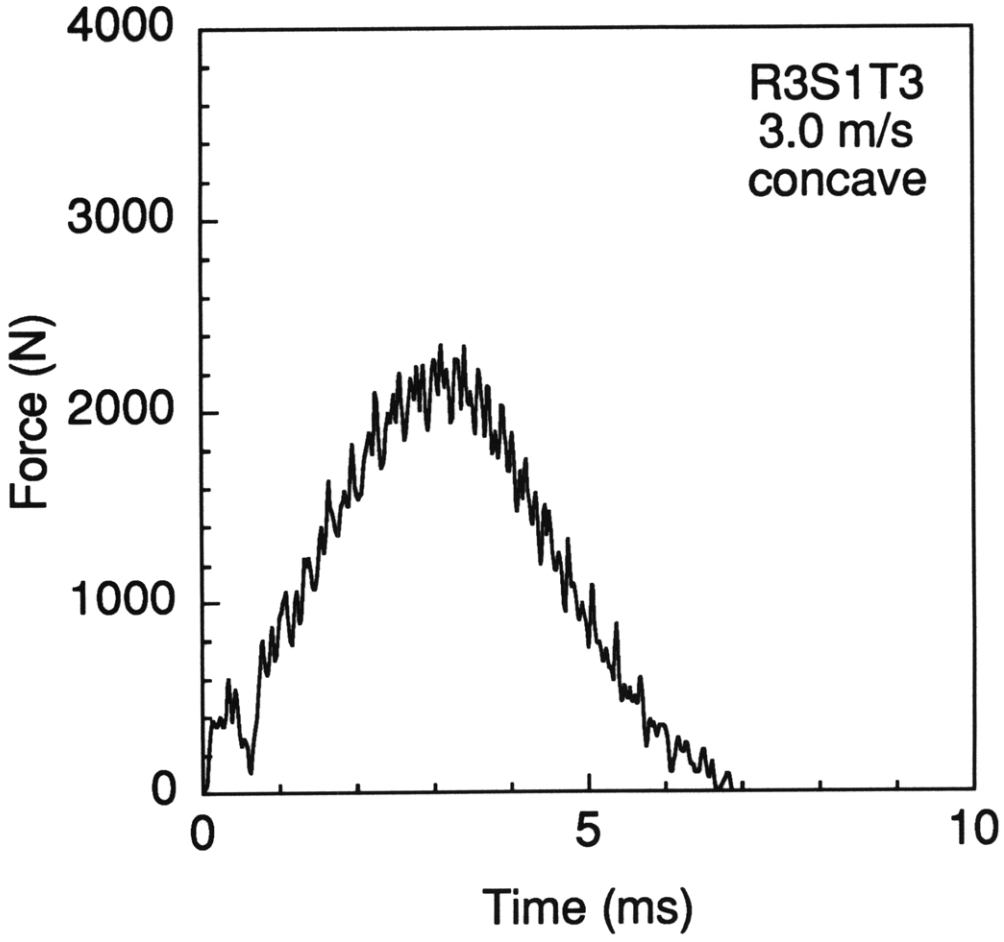

Figure B.50 Results of impact of 3.0 m/s on specimen R3S1T3 (concave): (*top*) x-ray photograph of damage state, and (*bottom*) force-time history.

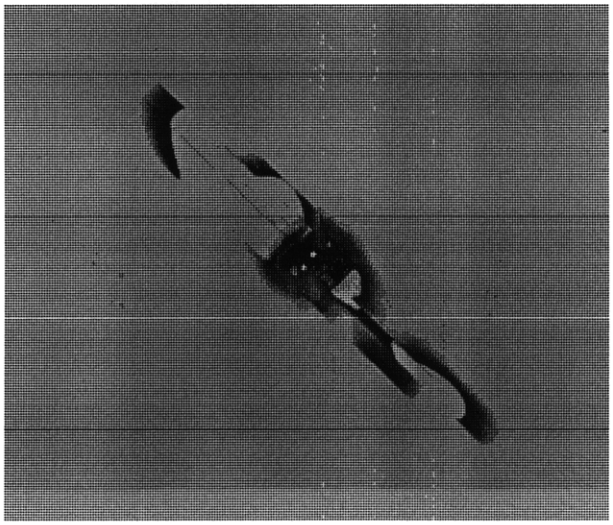

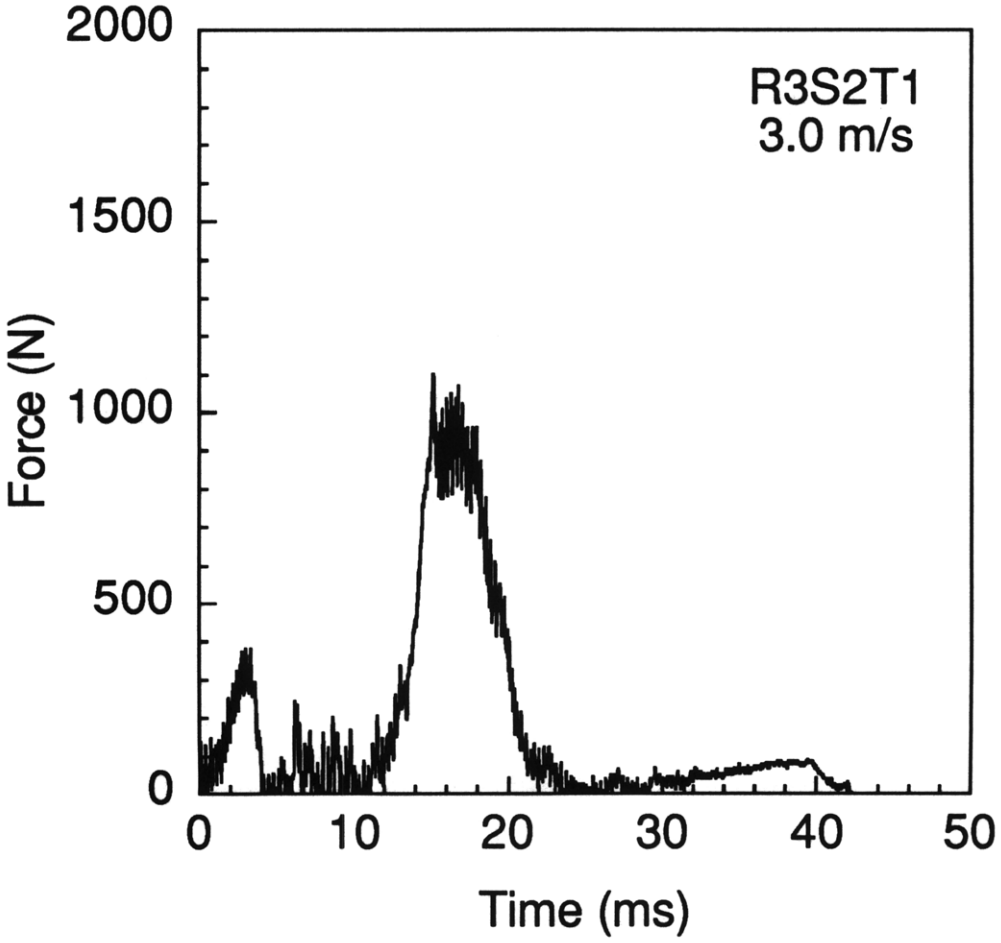

Figure B.51 Results of impact of 3.0 m/s on specimen R3S2T1: (*top*) x-ray photograph of damage state, and (*bottom*) force-time history.

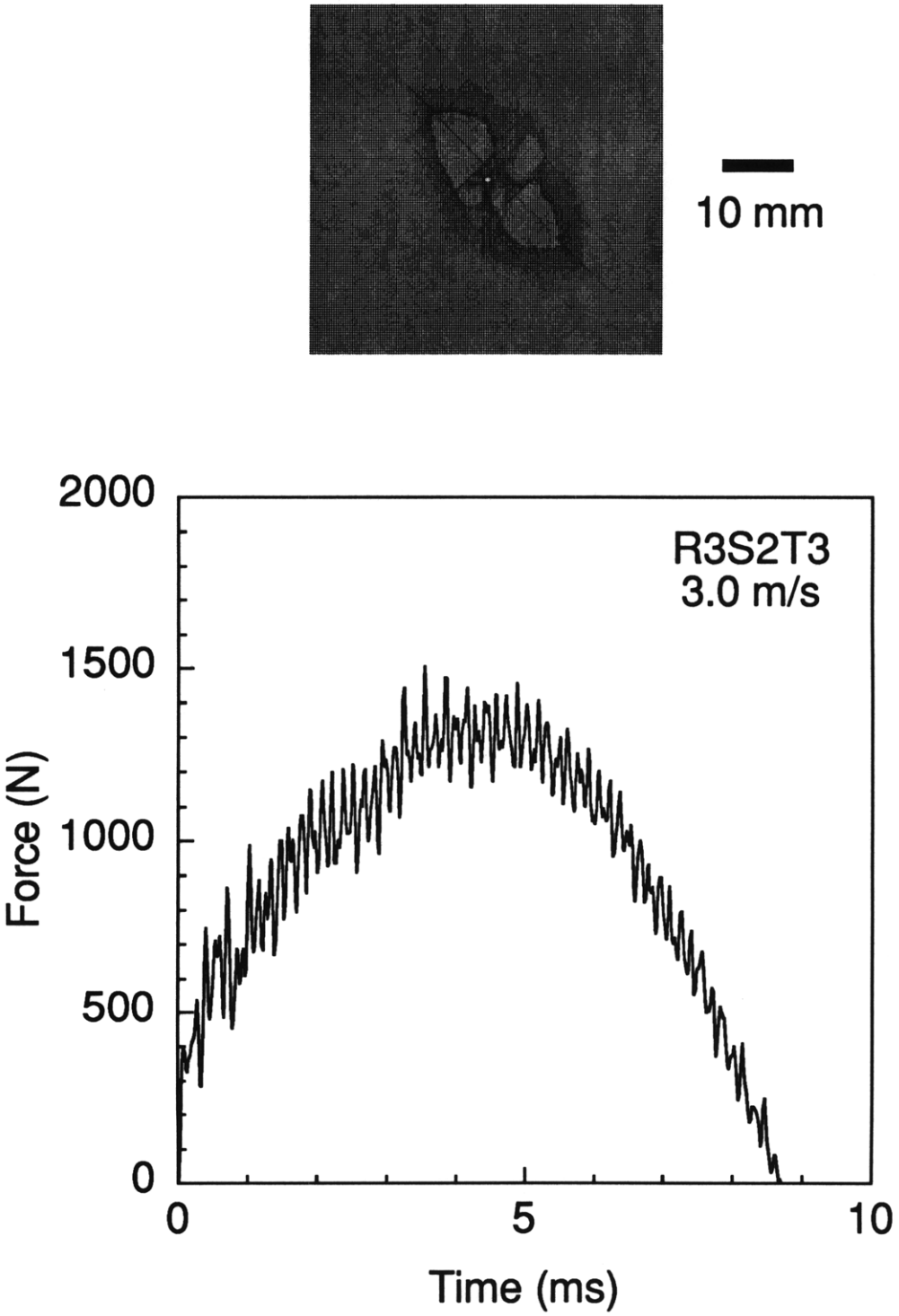

Figure B.52 Results of impact of 3.0 m/s on specimen R3S2T3: (*top*) x-ray photograph of damage state, and (*bottom*) force-time history.

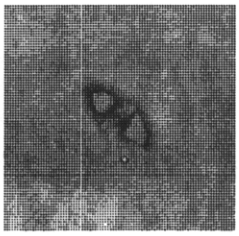

10 mm

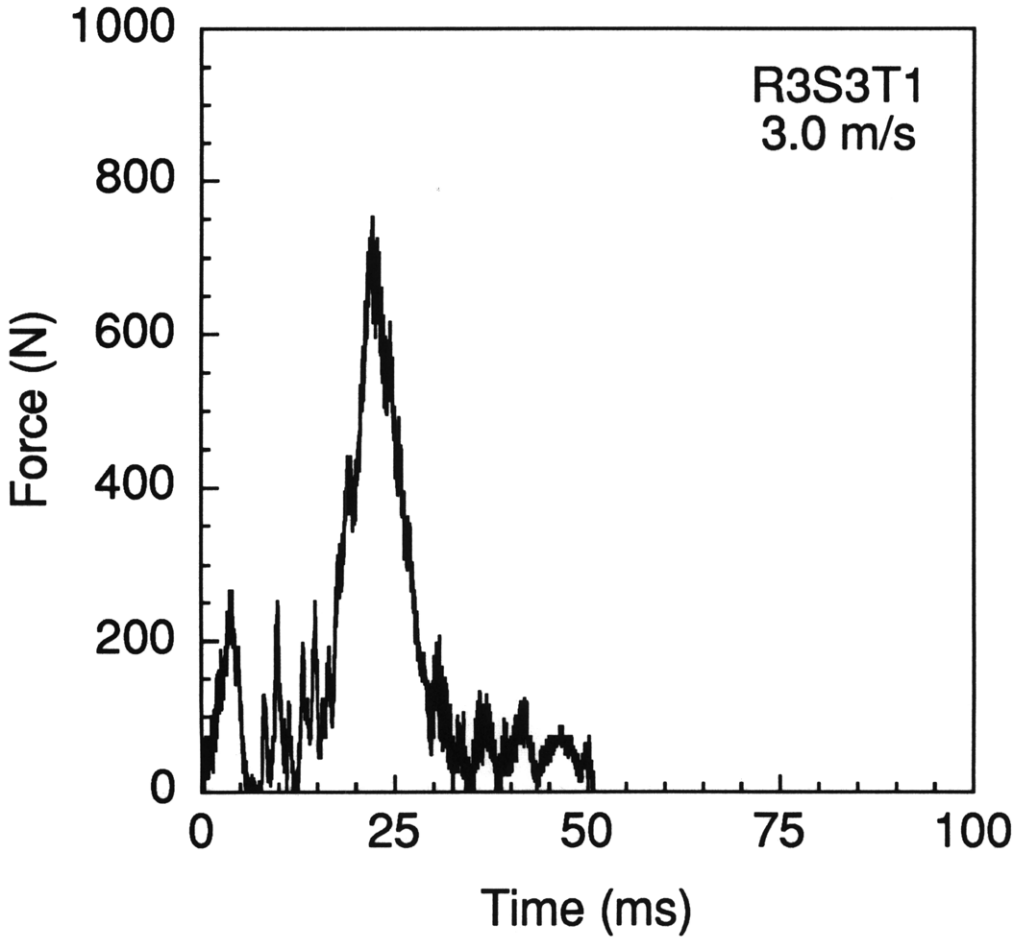

Figure B.53 Results of impact of 3.0 m/s on specimen R3S3T1: (*top*) x-ray photograph of damage state, and (*bottom*) force-time history.

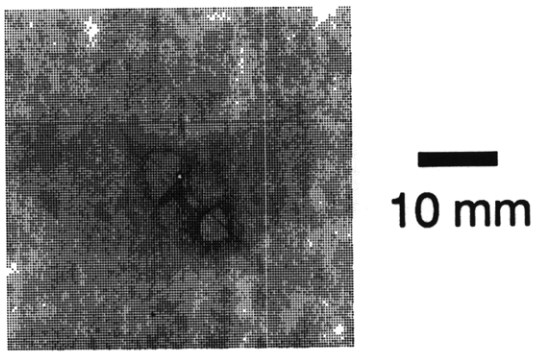

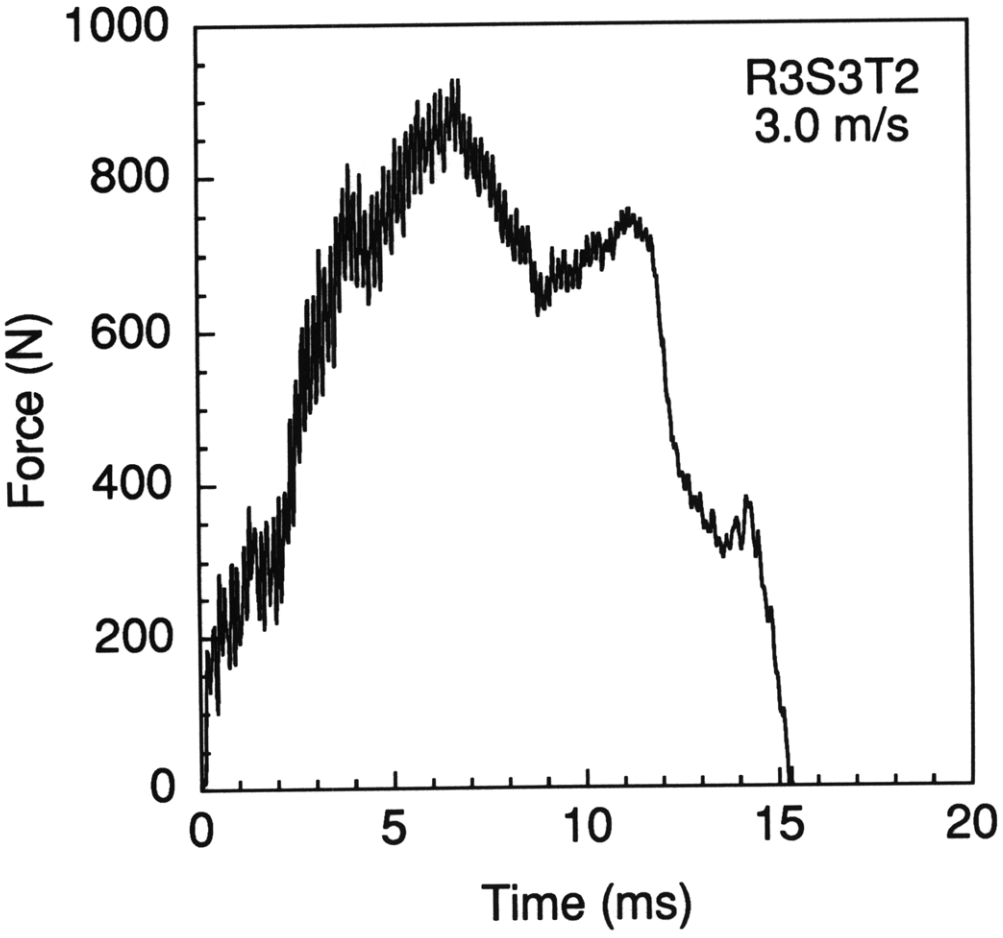

Figure B.54 Results of impact of 3.0 m/s on specimen R3S3T2: (*top*) x-ray photograph of damage state, and (*bottom*) force-time history.

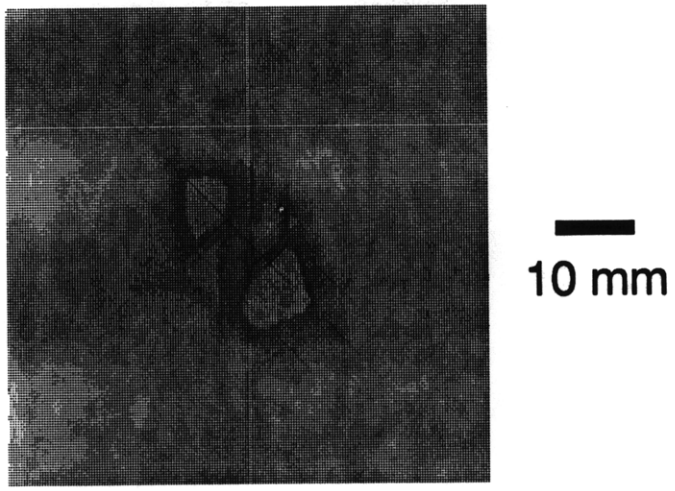

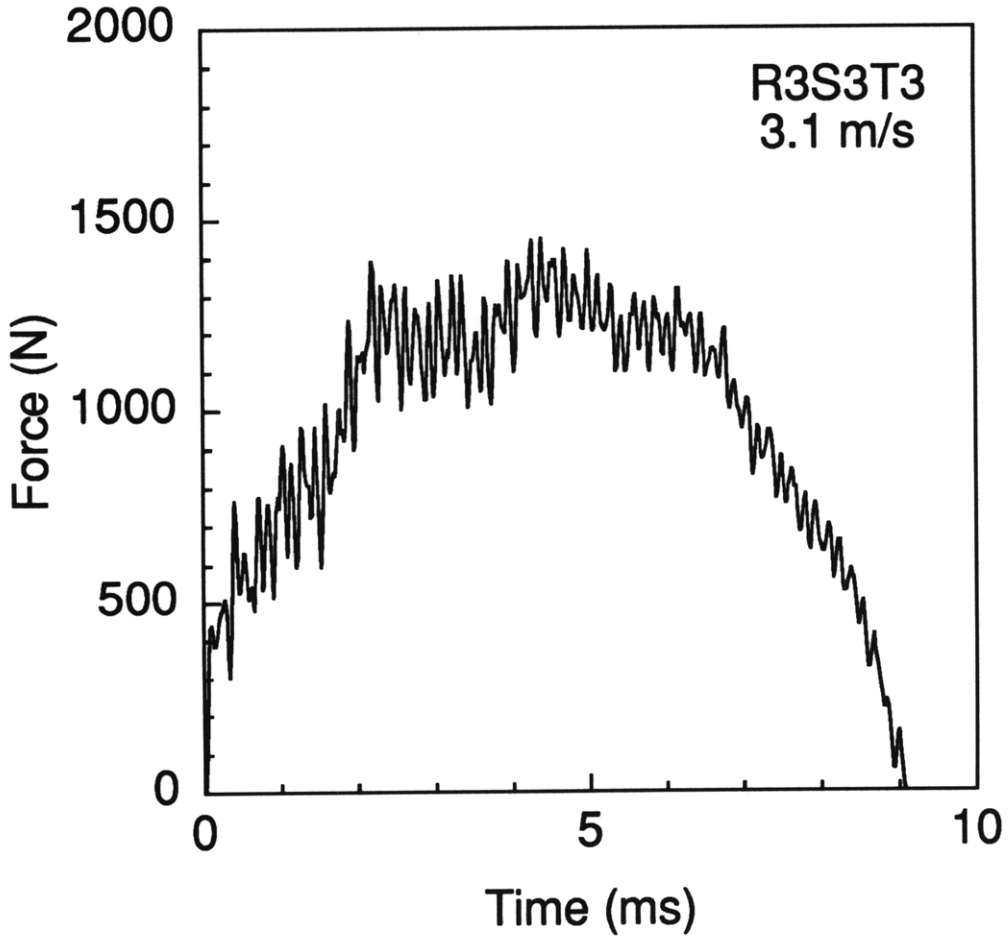

Figure B.55 Results of impact of 3.1 m/s on specimen R3S3T3: (*top*) x-ray photograph of damage state, and (*bottom*) force-time history.

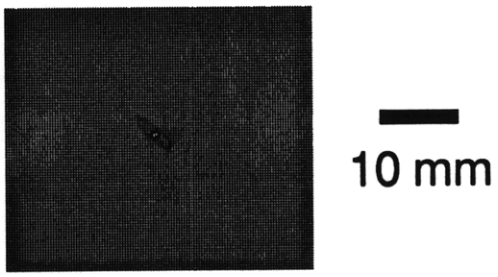

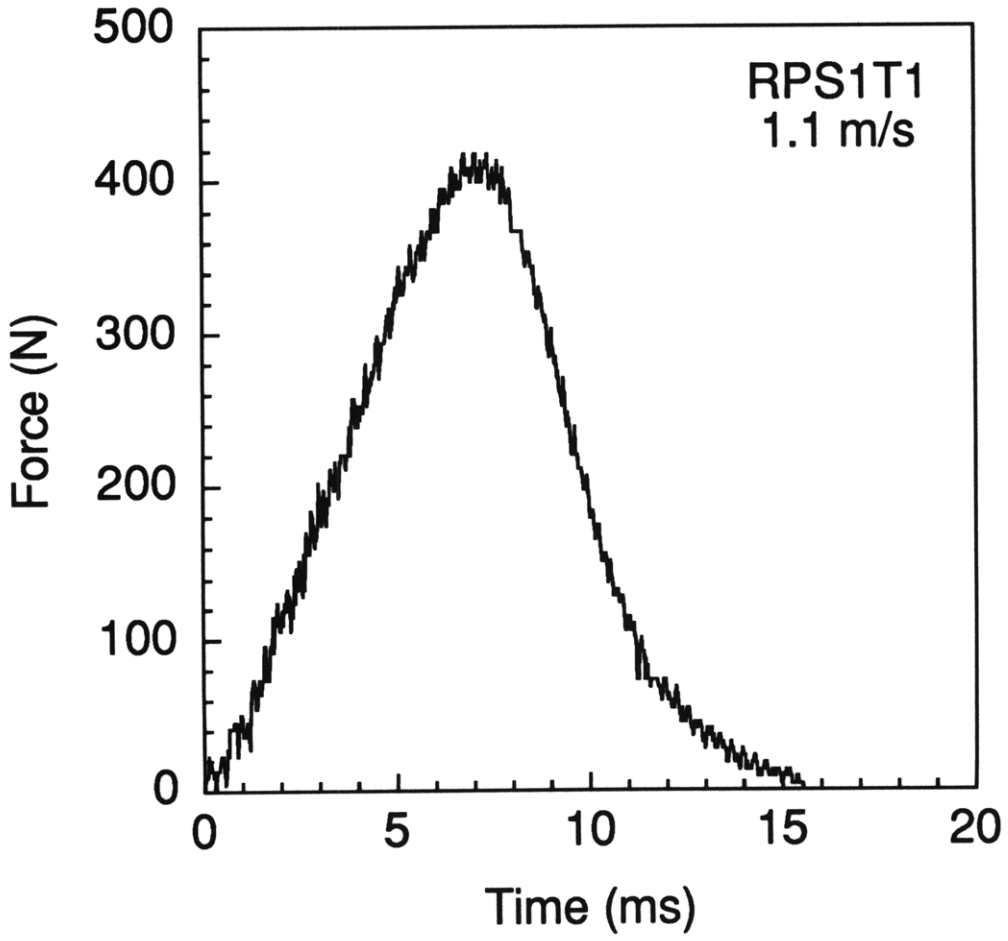

Figure B.56 Results of impact of 1.1 m/s on specimen RPS1T1: (*top*) x-ray photograph of damage state, and (*bottom*) force-time history.

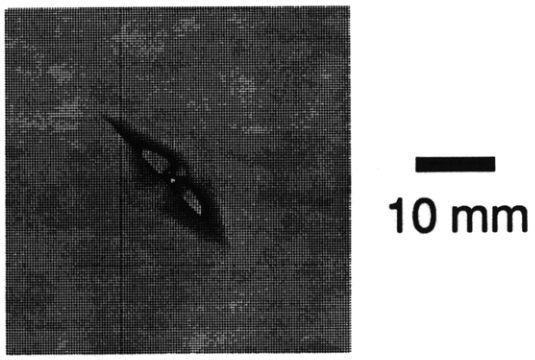

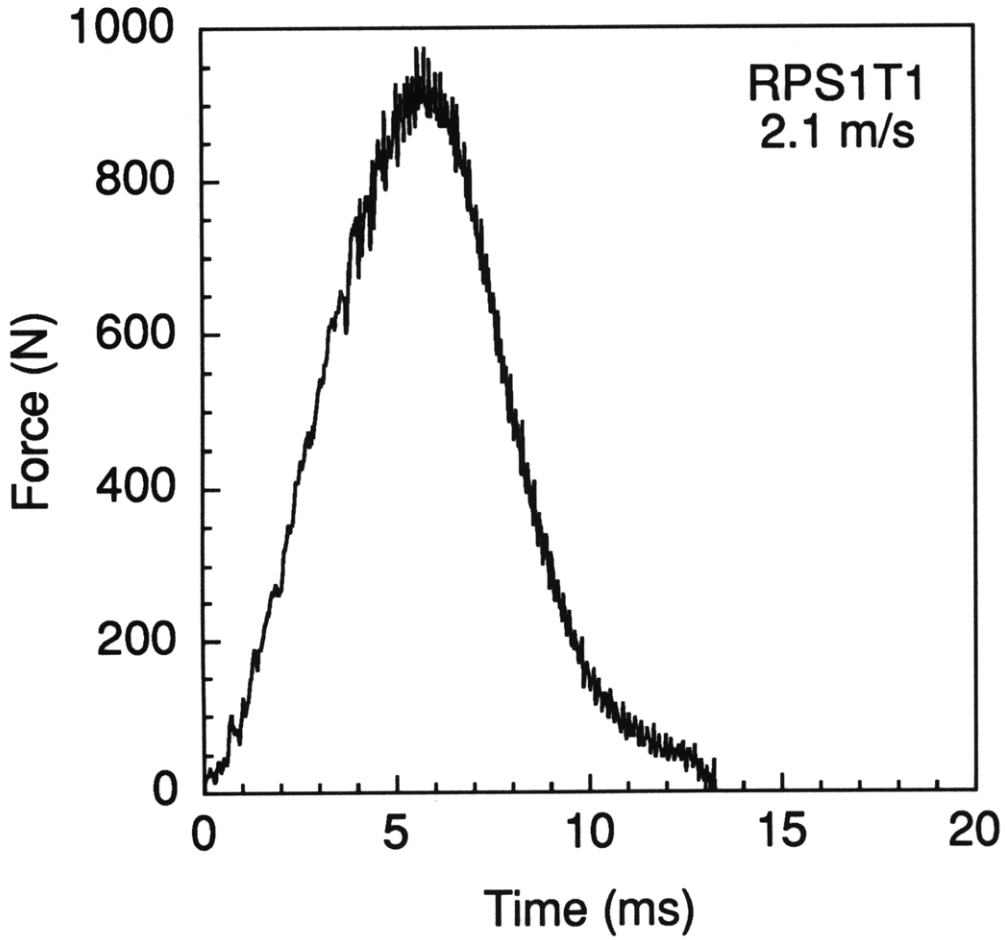

Figure B.57 Results of impact of 2.1 m/s on specimen RPS1T1: (*top*) x-ray photograph of damage state, and (*bottom*) force-time history.

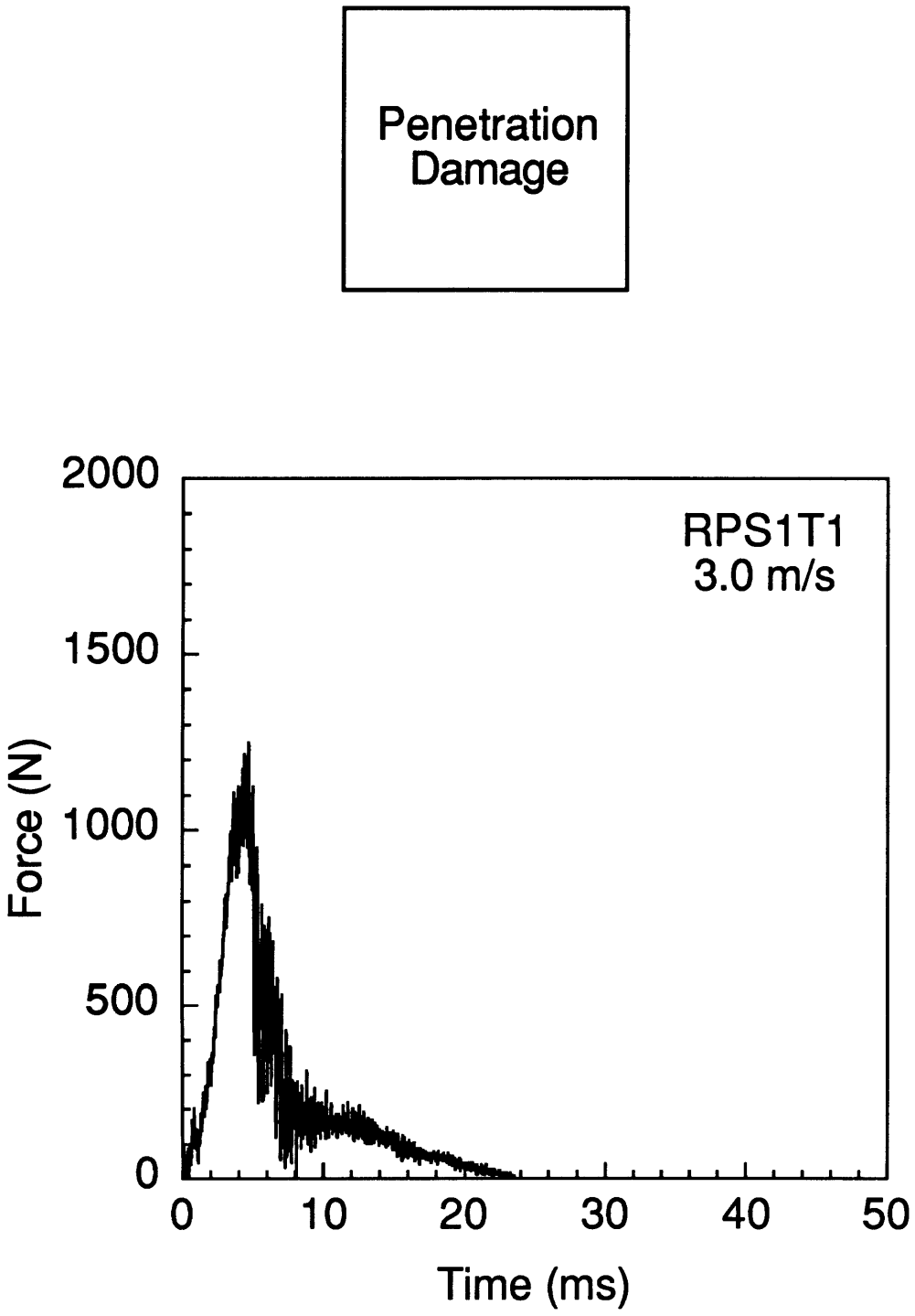

Figure B.58 Results of impact of 3.0 m/s on specimen RPS1T1: (*top*) penetration damage is observed for this specimen, and (*bottom*) force-time history.

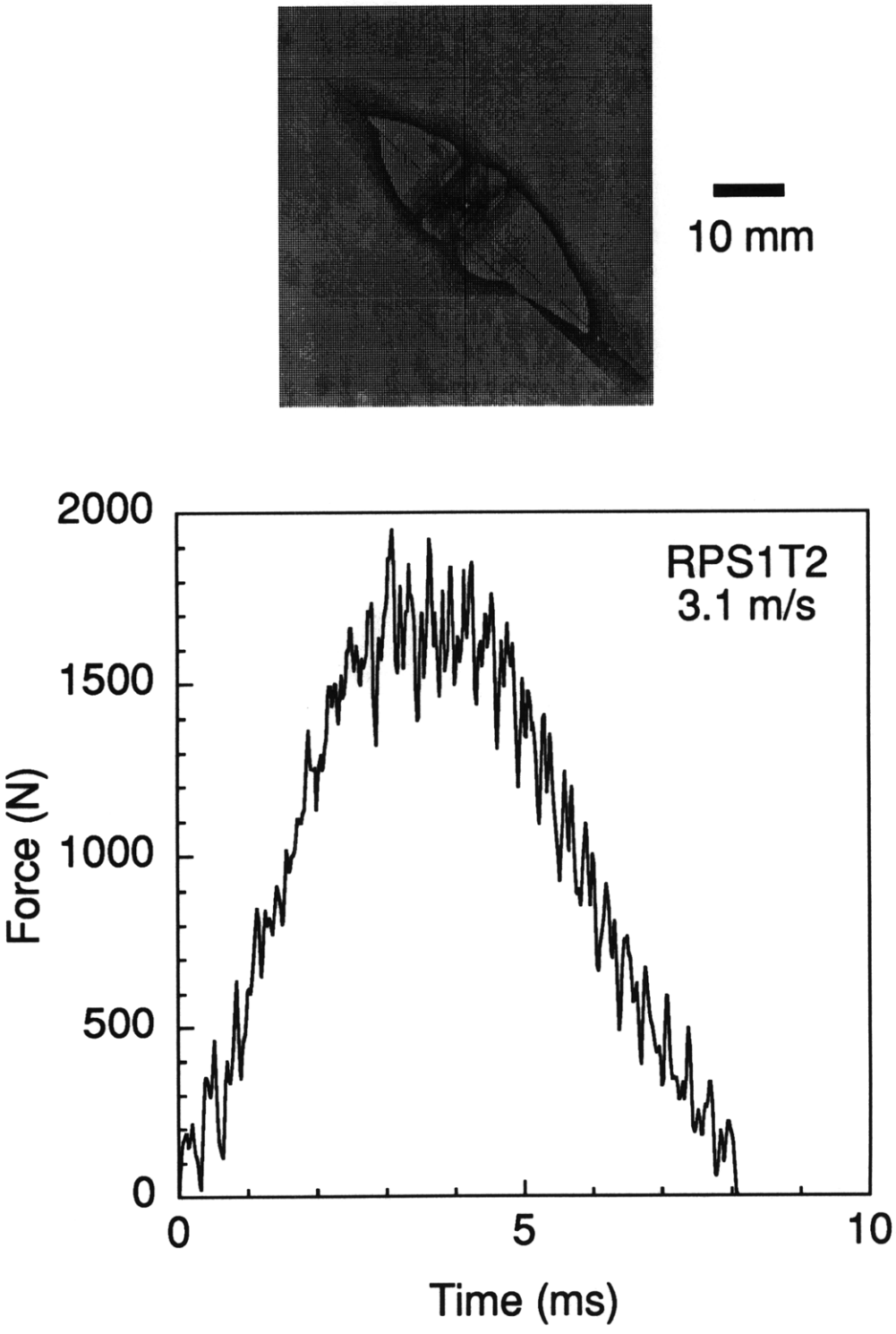

Figure B.59 Results of impact of 3.1 m/s on specimen RPS1T2: (*top*) x-ray photograph of damage state, and (*bottom*) force-time history.

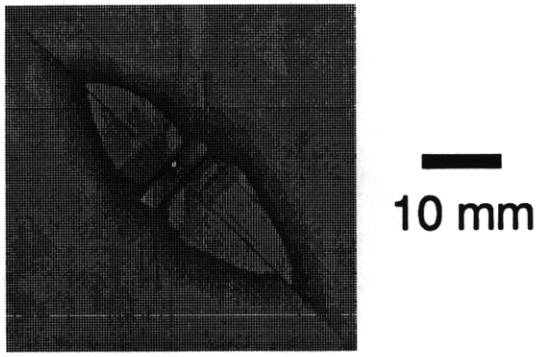

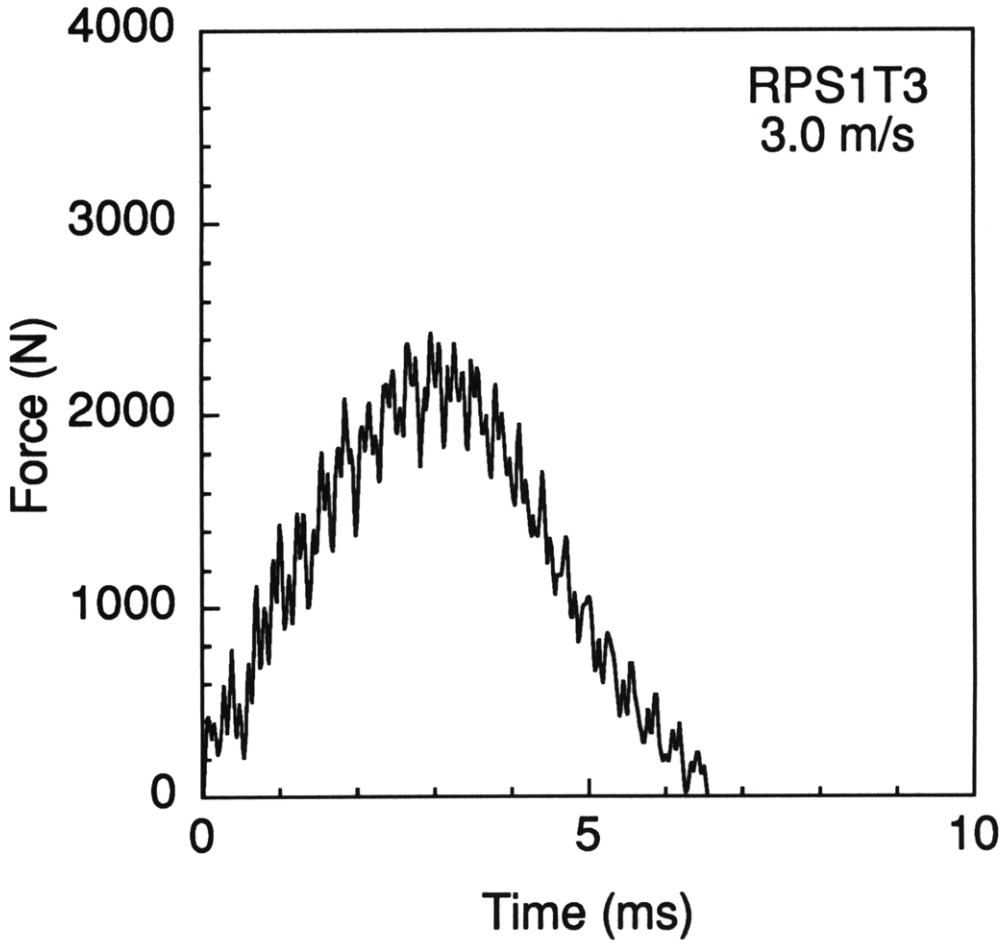

Figure B.60 Results of impact of 3.0 m/s on specimen RPS1T3: (*top*) x-ray photograph of damage state, and (*bottom*) force-time history.

Appendix C

Impact Force-deflection Histories

Force-deflection histories for all impacted specimens are presented in this appendix. The deflections are calculated from the experimental force-time histories, as described in chapter 5, and then cross-plotted with the force data. Axis scales for the force-deflection histories were chosen based on a compromise between showing specifics of each specimen response (smallest scale showing entire specimen response) and allowing the response of different specimens to be compared (one scale for all specimens). Five force scales (as in appendix B) and six deflection scales were found to provide a reasonable compromise. Typically, after the force-deflection response for an impacted specimen reaches peak deflection, the response follows nearly the same path back to zero deflection, i.e. the response overlaps. Thus, for clarity, force-deflection data is only plotted up to the peak deflection in the figures. However, in the case of penetration, the data is plotted up to the penetration force. As noted in chapter 5, three specimens are known to have slipped in-plane during impact testing. Slipping and penetration are indicated in the figure titles.

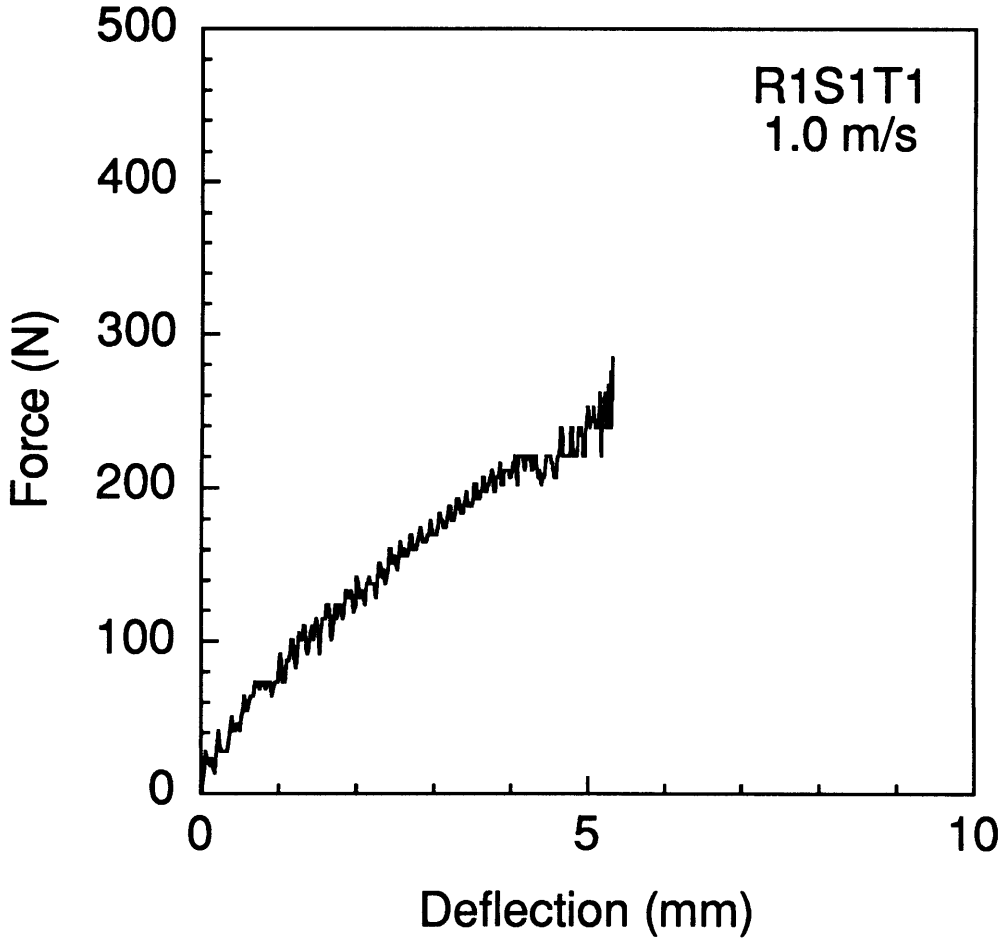

Figure C.1 Force-deflection response of specimen R1S1T1 impacted at 1.0 m/s.

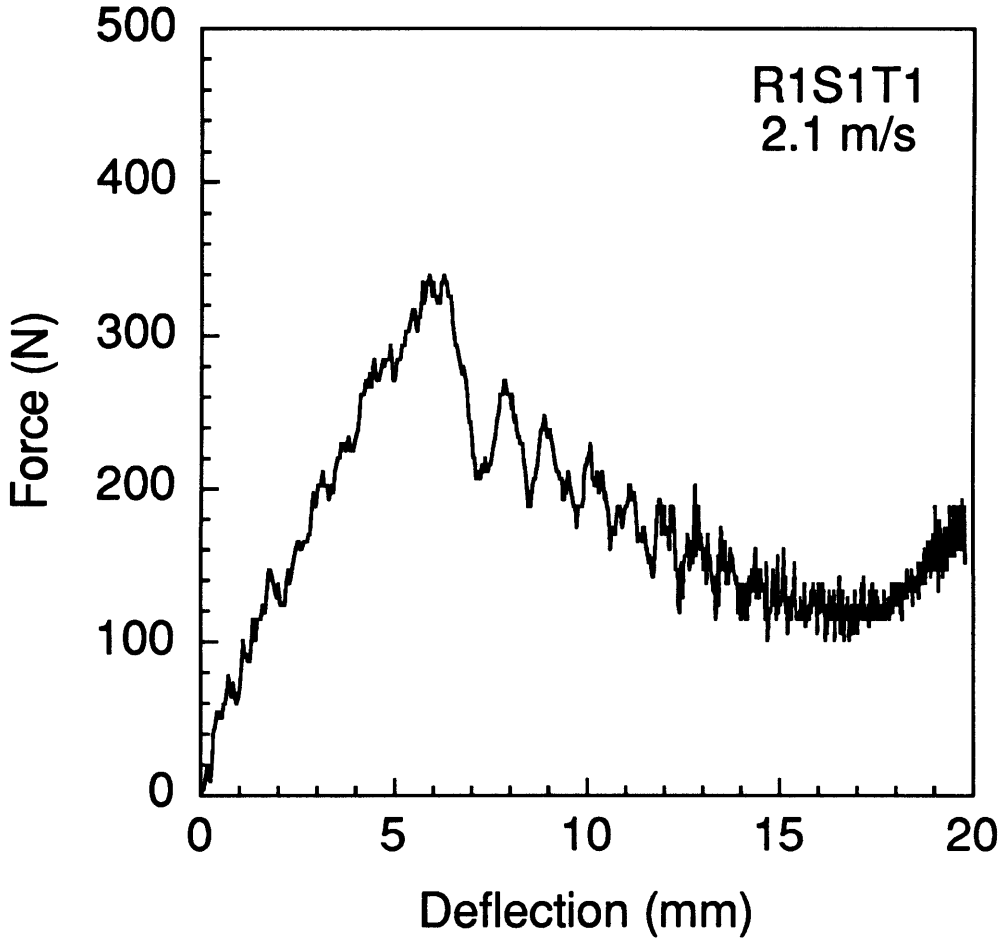

Figure C.2 Force-deflection response of specimen R1S1T1 impacted at 2.1 m/s.

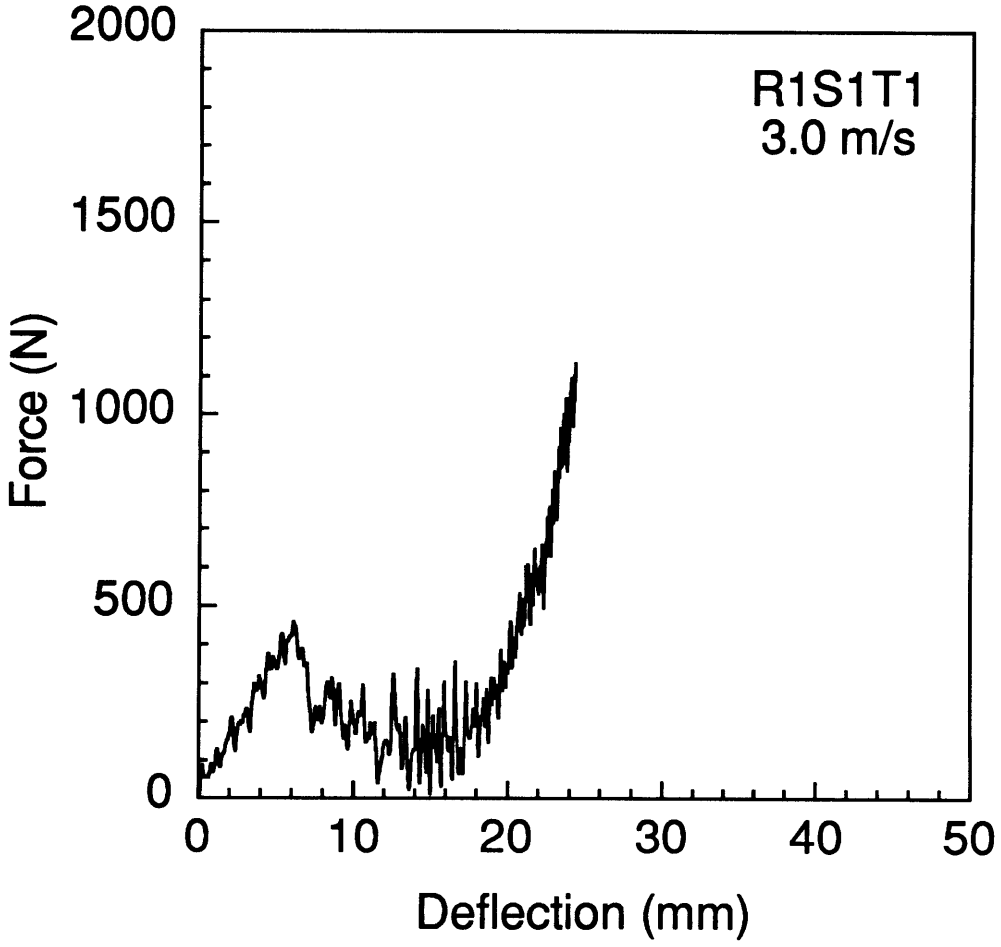

Figure C.3 Force-deflection response of specimen R1S1T1 impacted at 3.0 m/s.

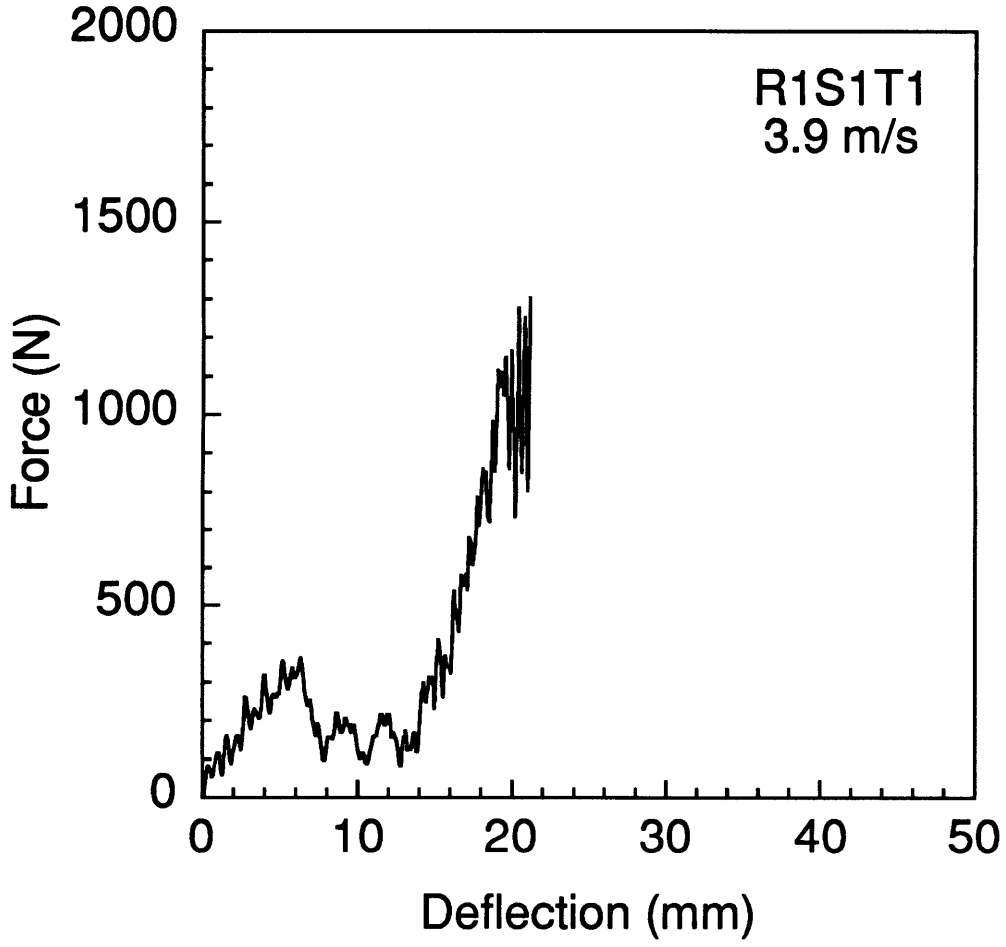

Figure C.4 Force-deflection response of specimen R1S1T1 impacted at 3.9 m/s. This specimen was penetrated during testing.

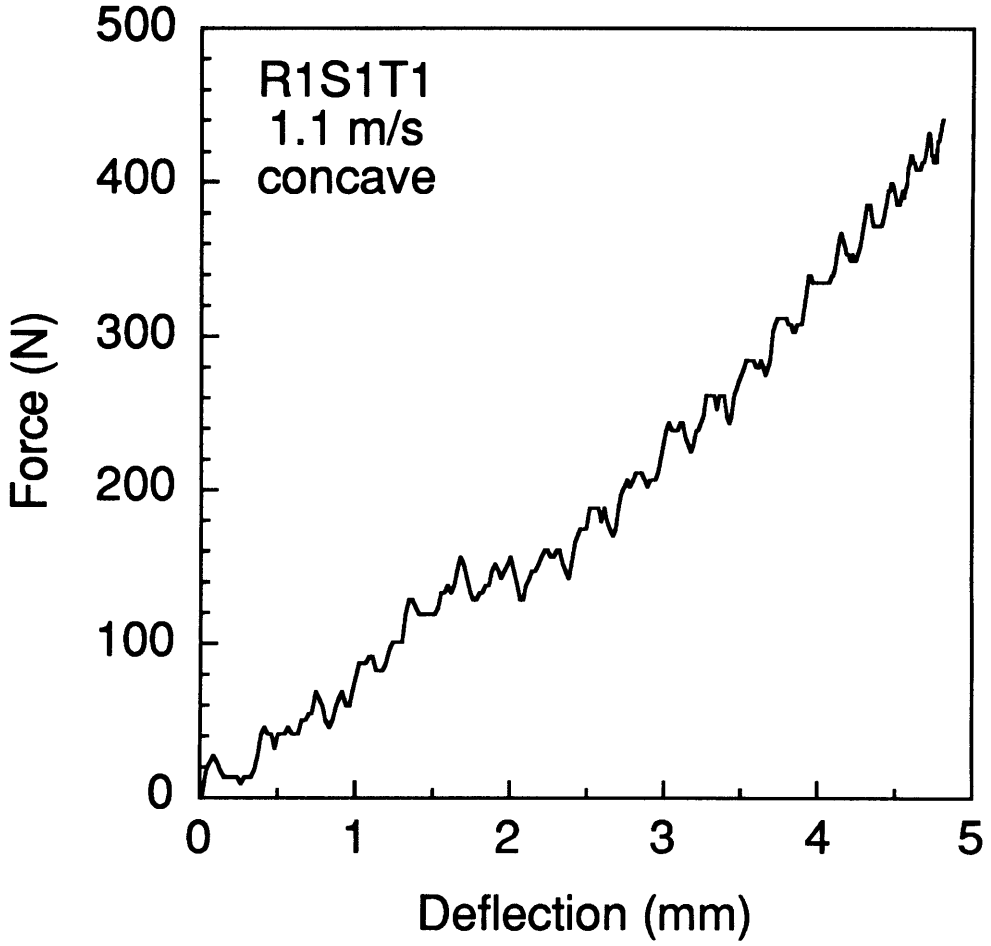

Figure C.5 Force-deflection response of specimen R1S1T1 (concave) impacted at 1.1 m/s.

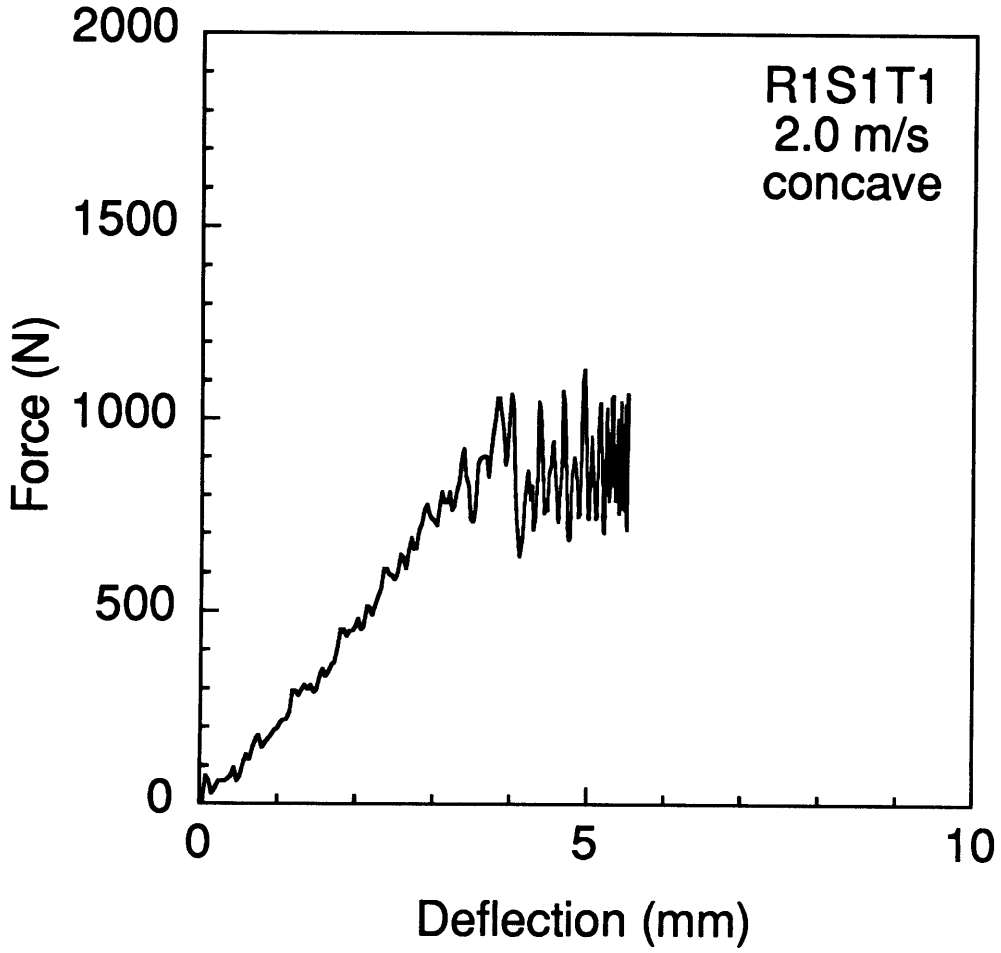

Figure C.6 Force-deflection response of specimen R1S1T1 (concave) impacted at 2.0 m/s.

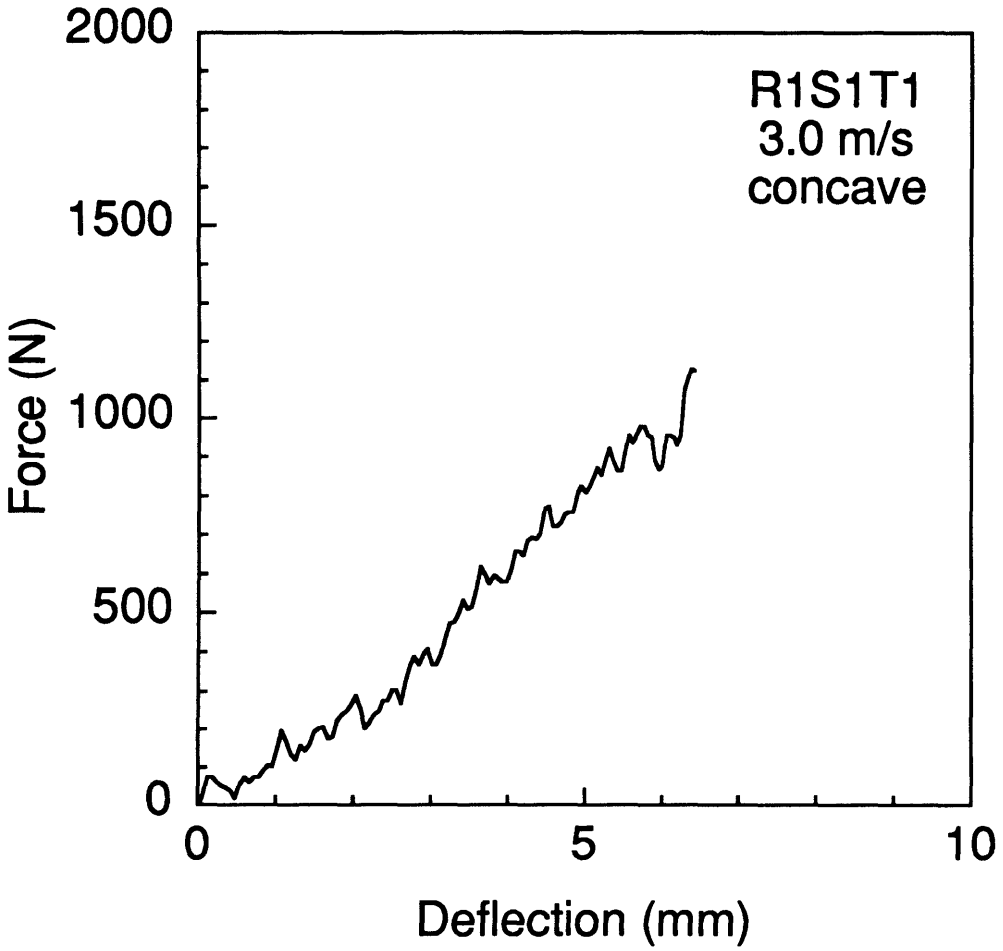

Figure C.7 Force-deflection response of specimen R1S1T1 (concave) impacted at 3.0 m/s. This specimen was penetrated during testing.

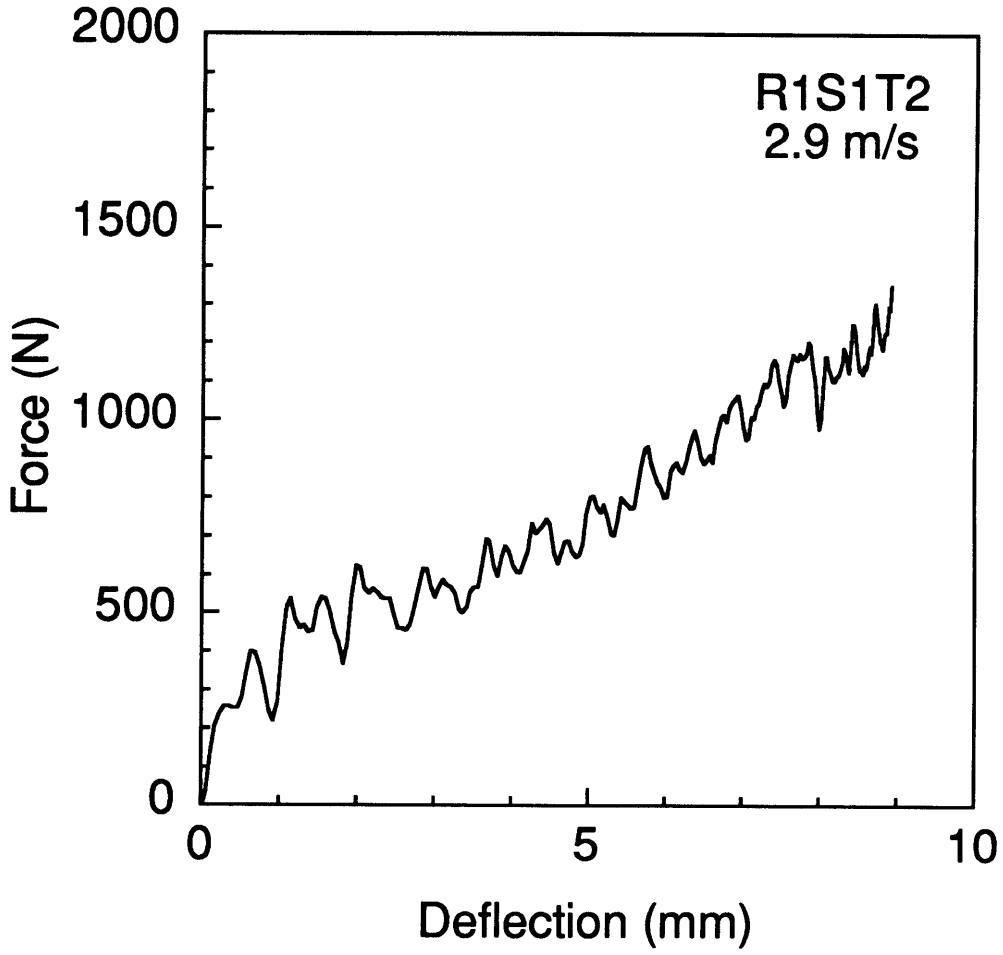

Figure C.8 Force-deflection response of specimen R1S1T2 impacted at 2.9 m/s.

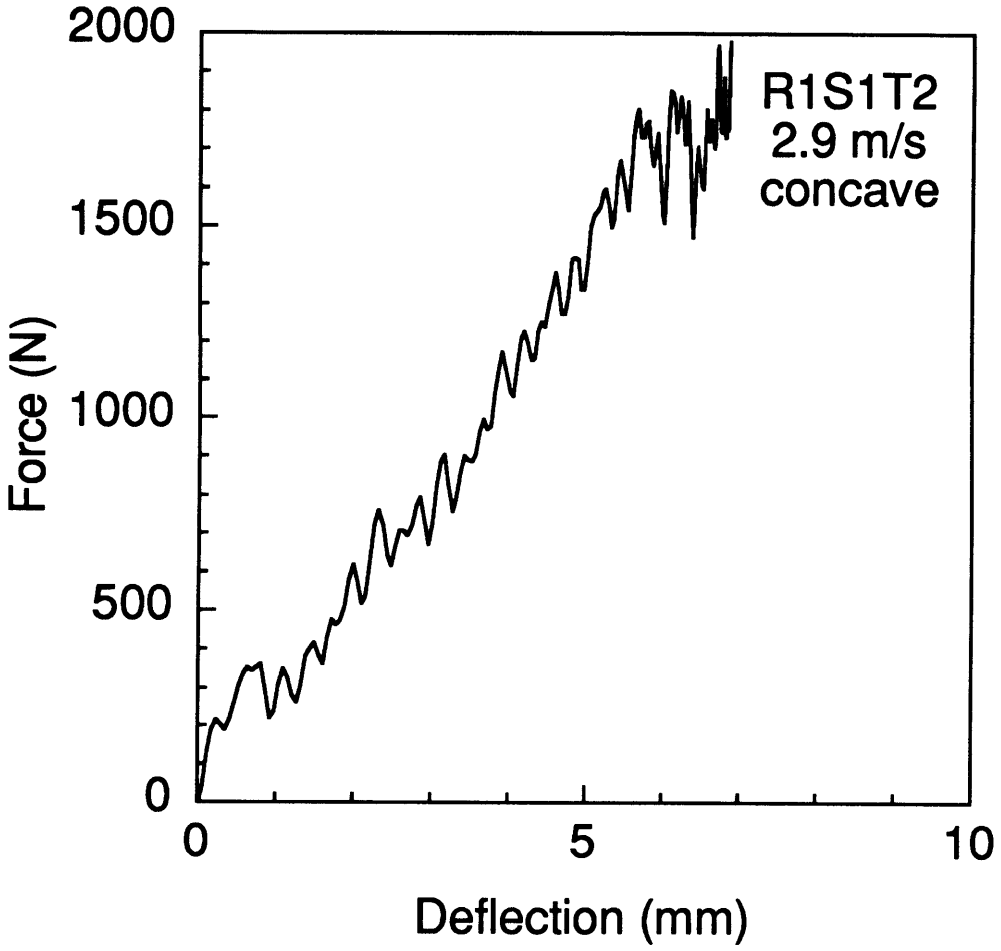

Figure C.9 Force-deflection response of specimen R1S1T2 (concave) impacted at 2.9 m/s.

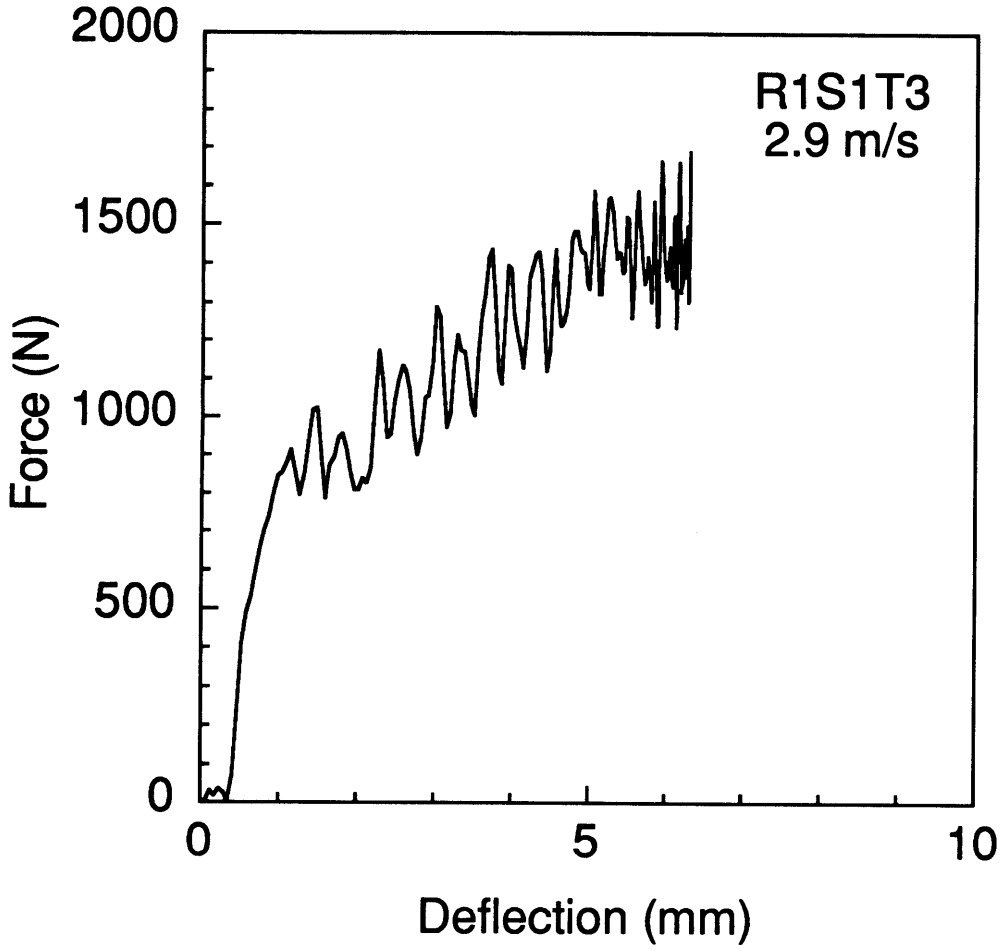

Figure C.10 Force-deflection response of specimen R1S1T3 impacted at 2.9 m/s.

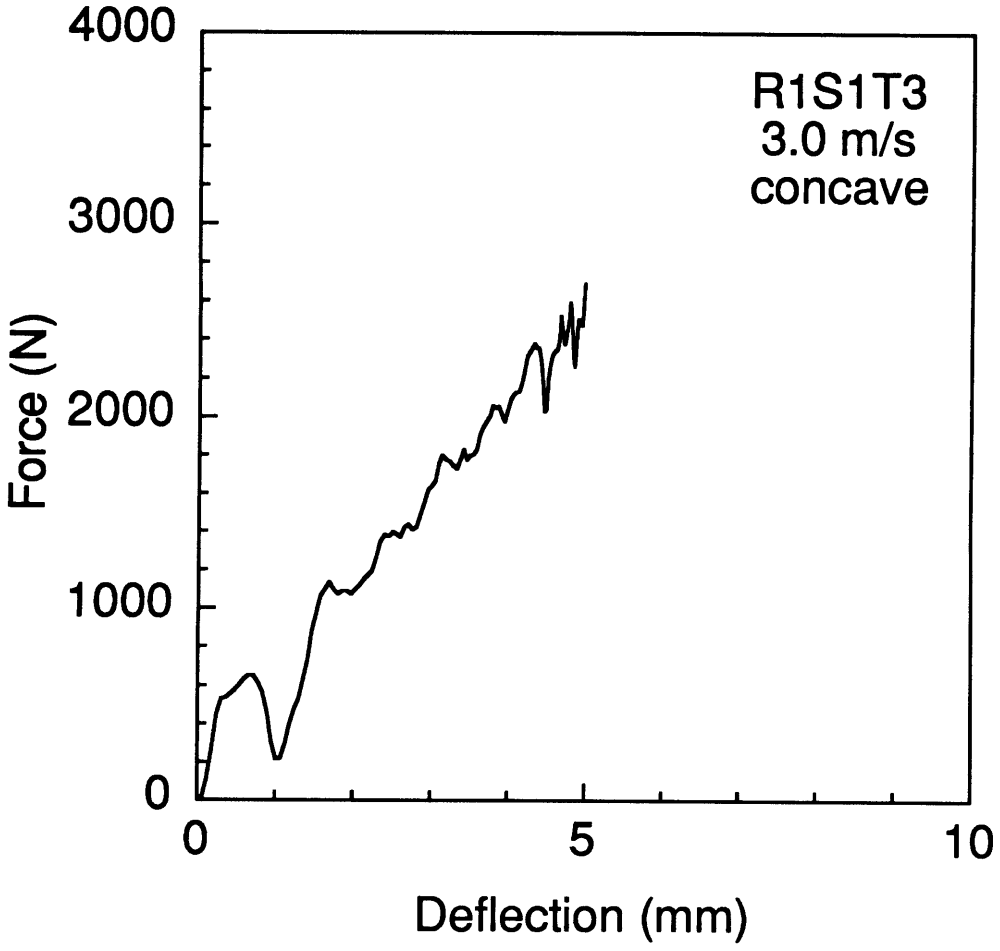

Figure C.11 Force-deflection response of specimen R1S1T3 (concave) impacted at 3.0 m/s.

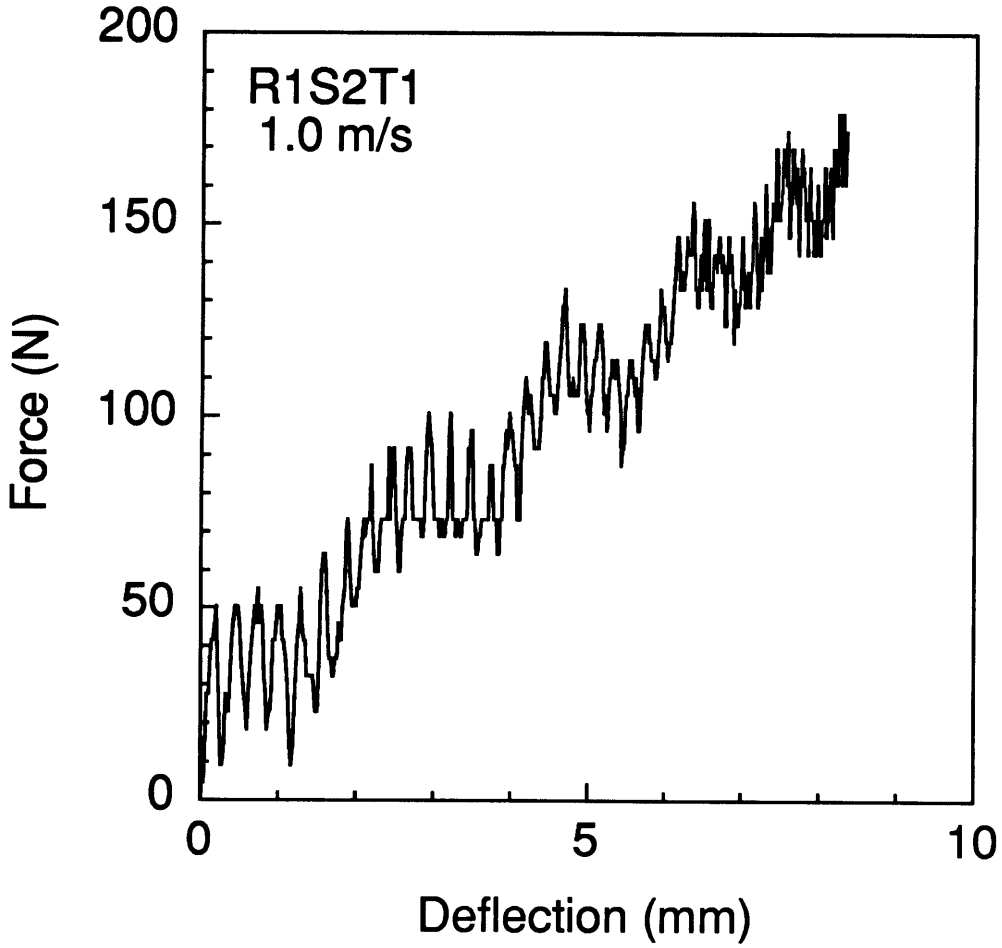

Figure C.12 Force-deflection response of specimen R1S2T1 impacted at 1.0 m/s.

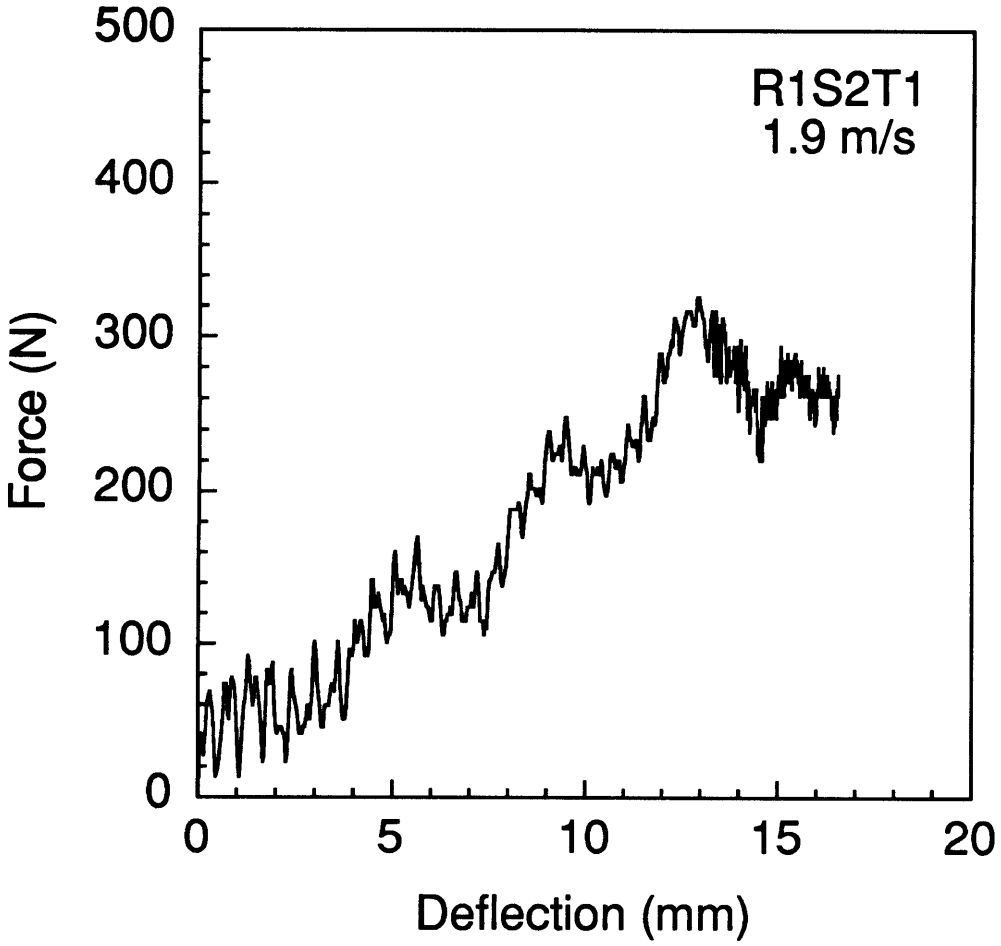

Figure C.13 Force-deflection response of specimen R1S2T1 impacted at 1.9 m/s.

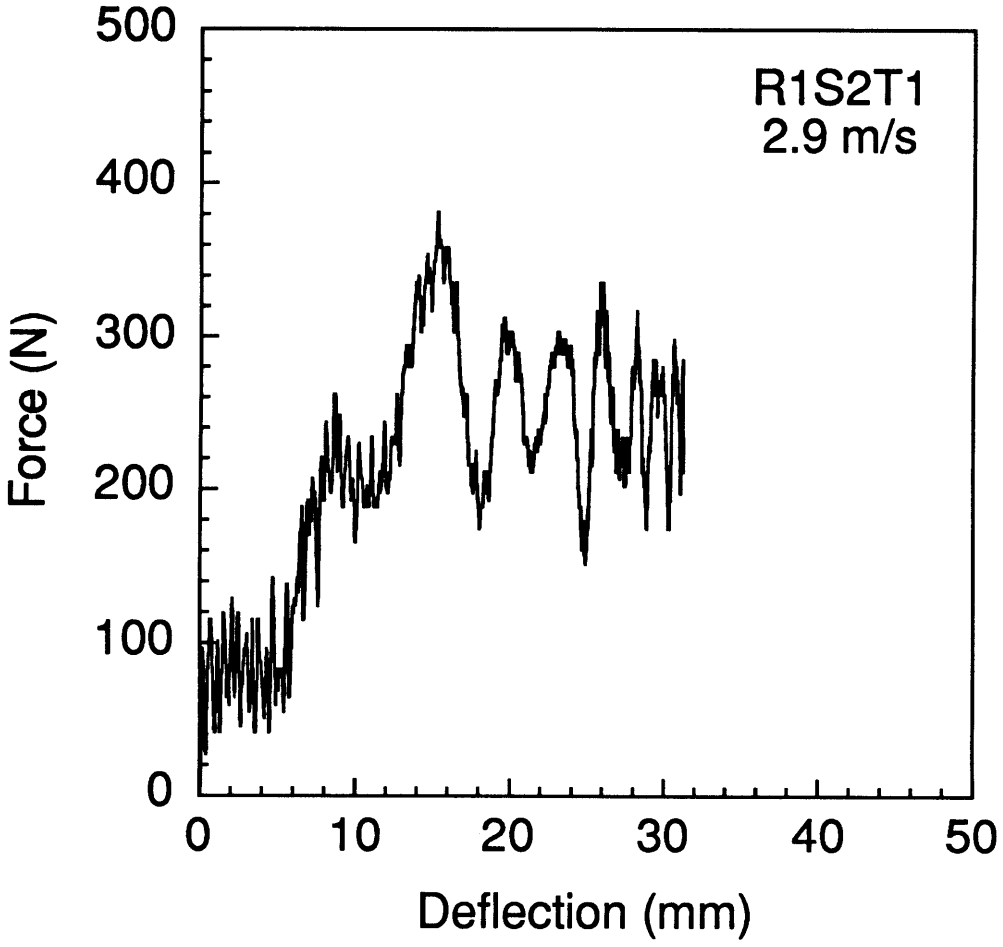

Figure C.14 Force-deflection response of specimen R1S2T1 impacted at 2.9 m/s.

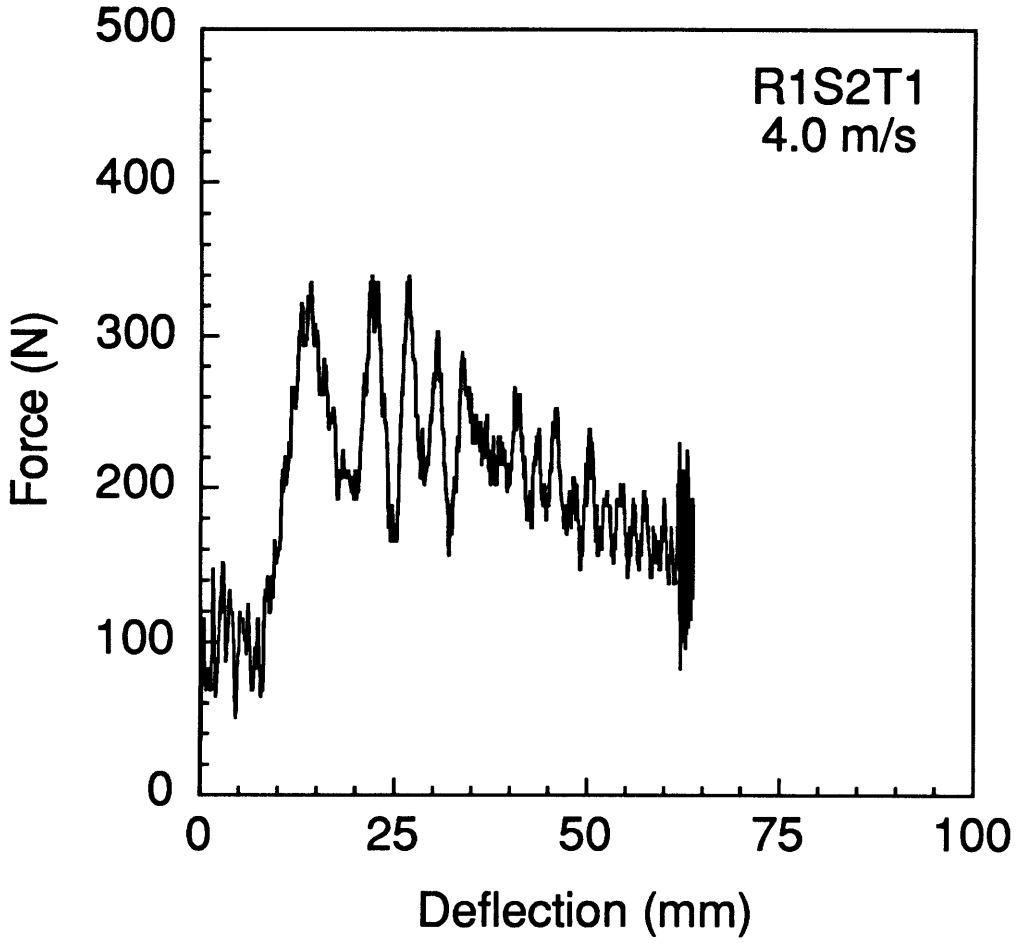

Figure C.15 Force-deflection response of specimen R1S2T1 impacted at 4.0 m/s.

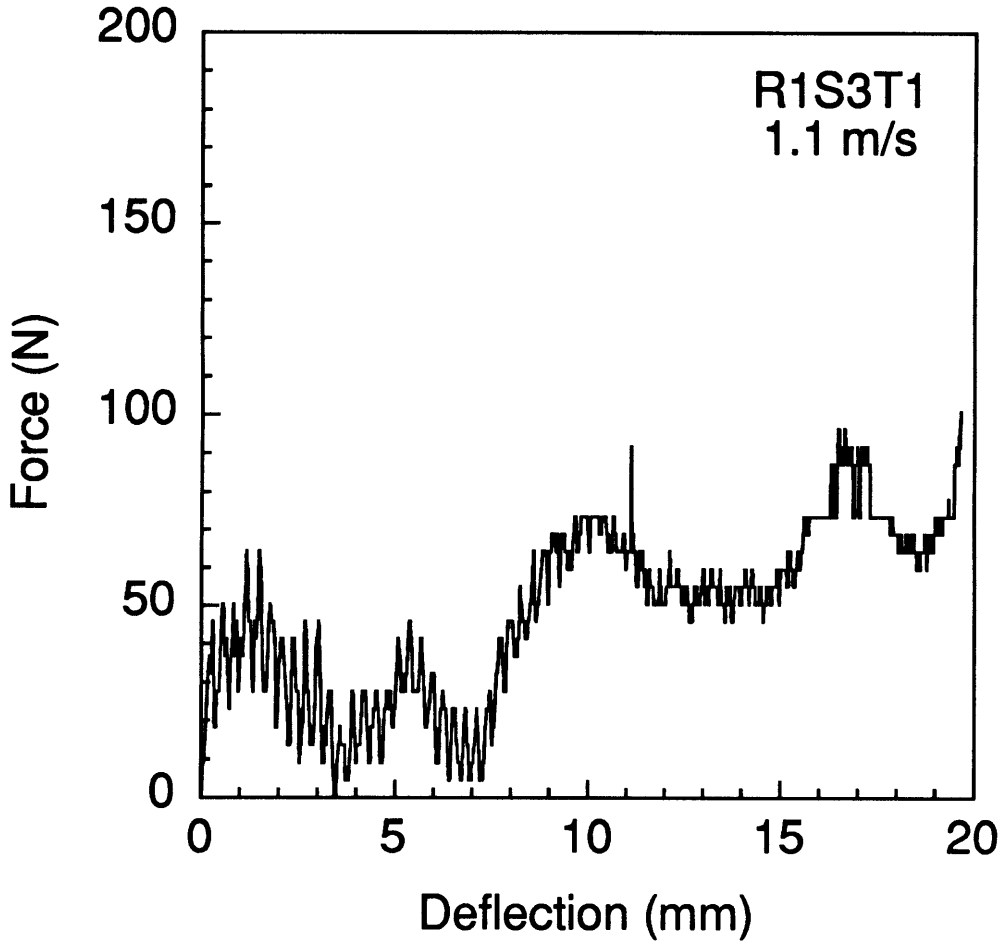

Figure C.16 Force-deflection response of specimen R1S3T1 impacted at 1.1 m/s.

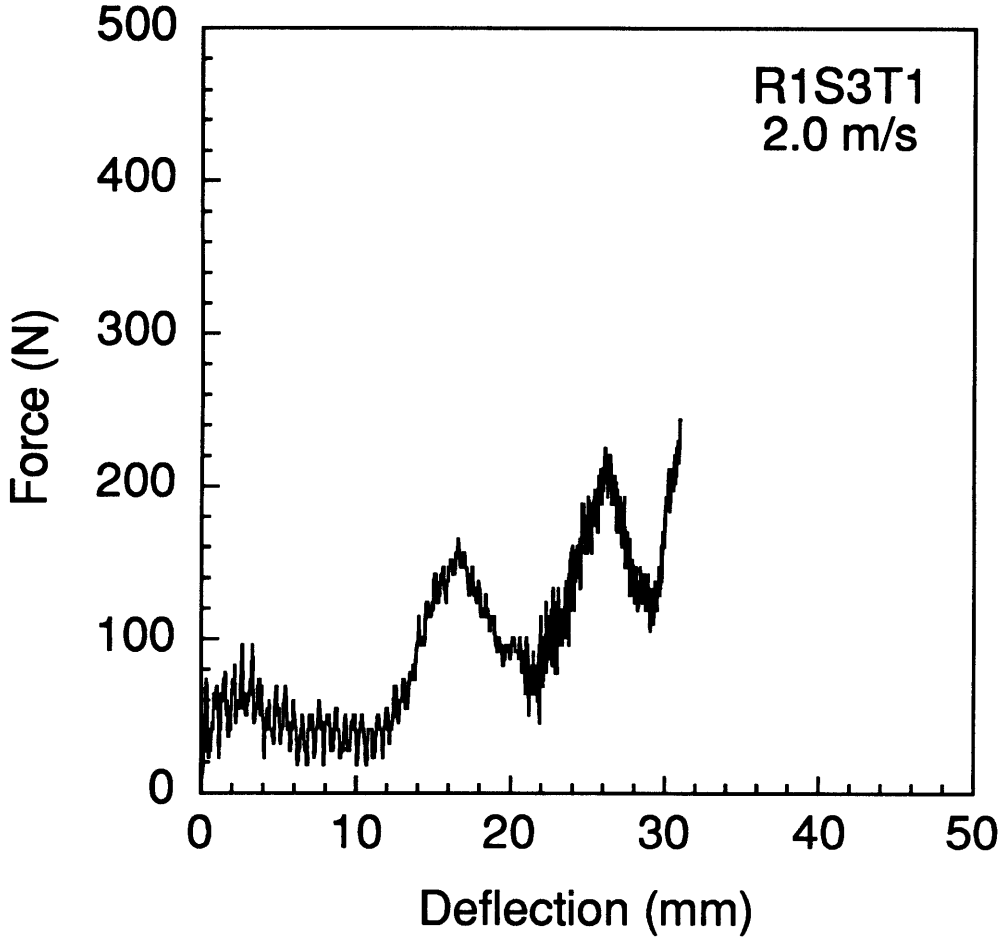

Figure C.17 Force-deflection response of specimen R1S3T1 impacted at 2.0 m/s.

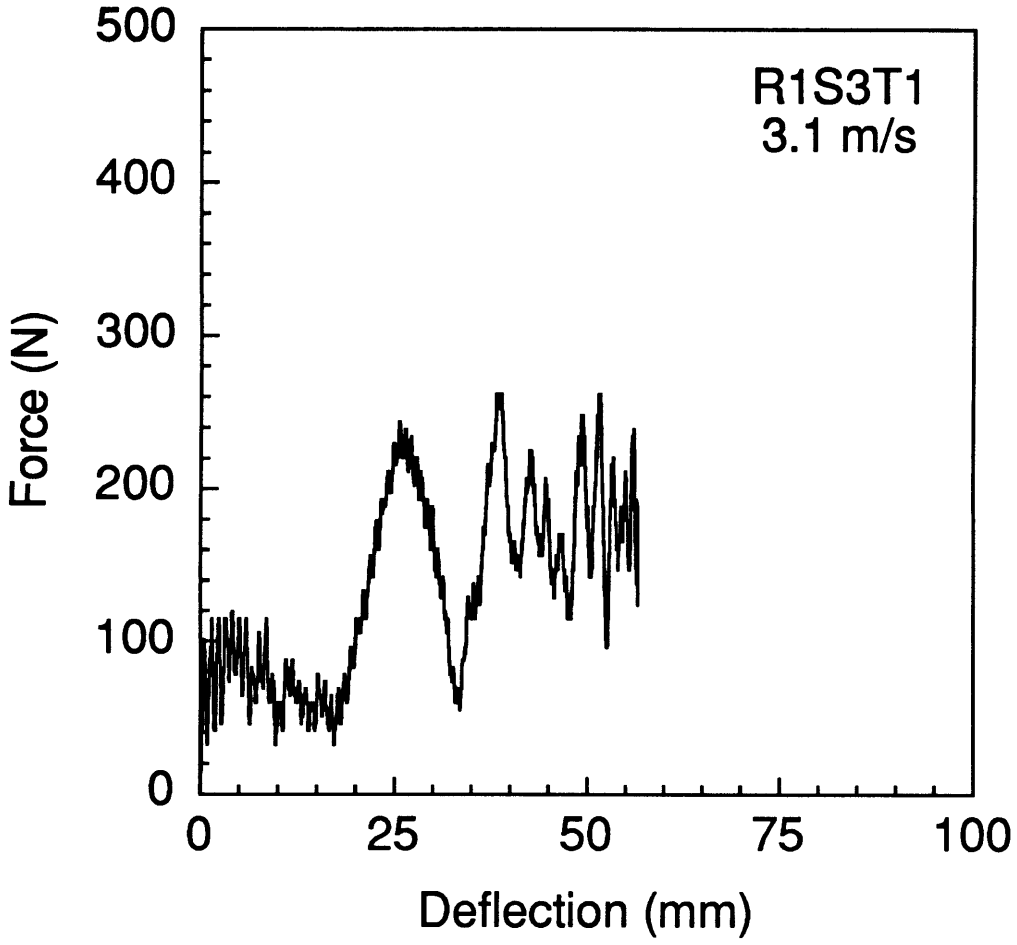

Figure C.18 Force-deflection response of specimen R1S3T1 impacted at 3.1 m/s.

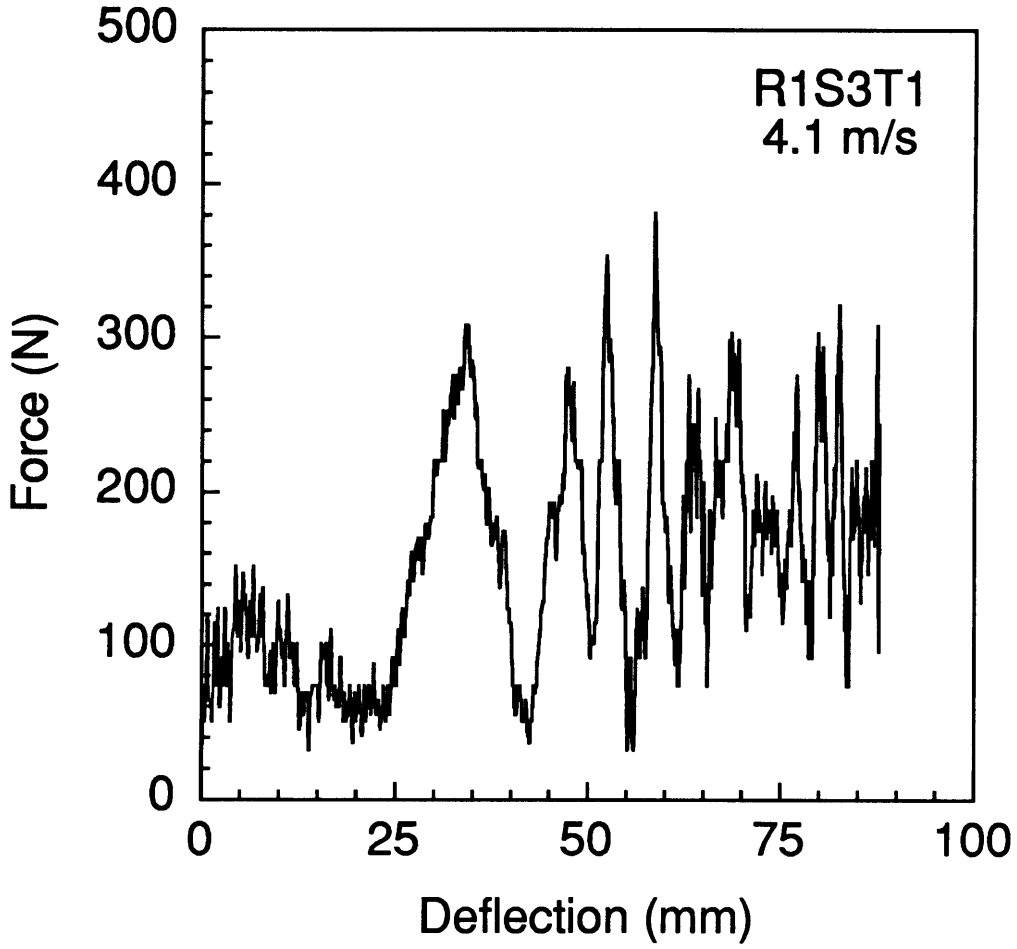

Figure C.19 Force-deflection response of specimen R1S3T1 impacted at 4.1 m/s.

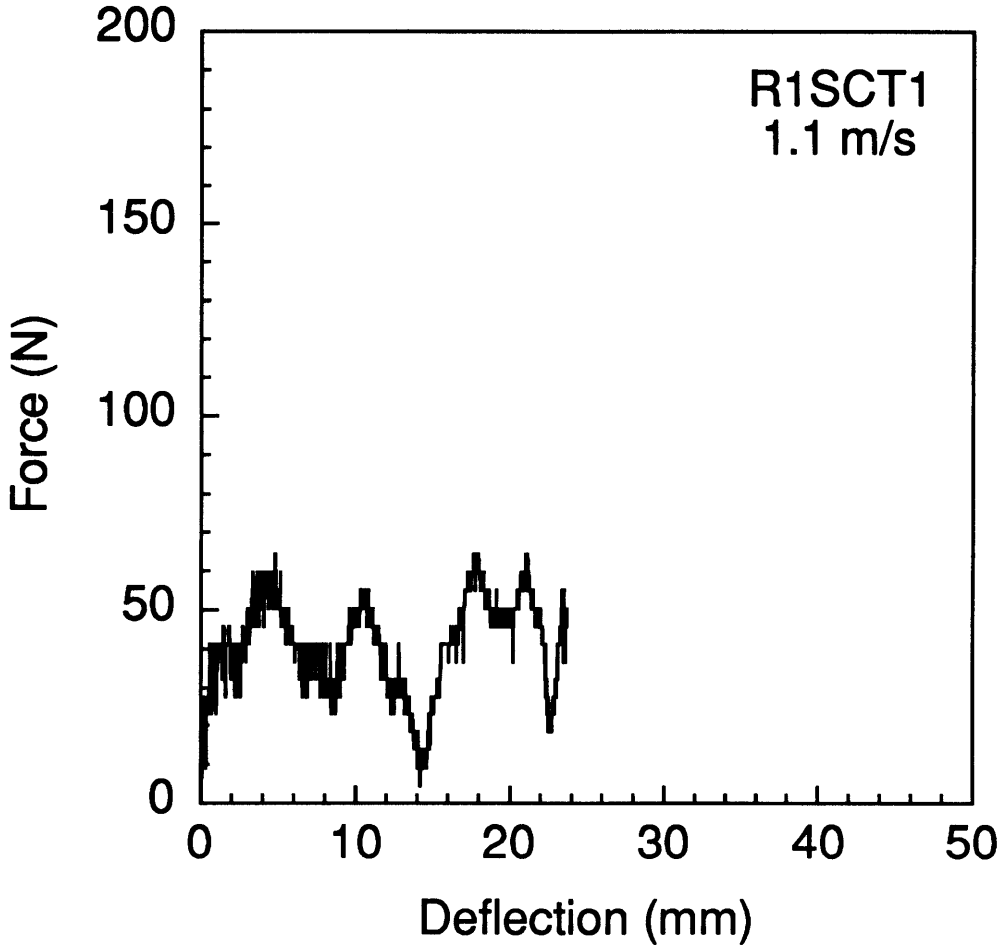

Figure C.20 Force-deflection response of specimen R1SCT1 impacted at 1.1 m/s.

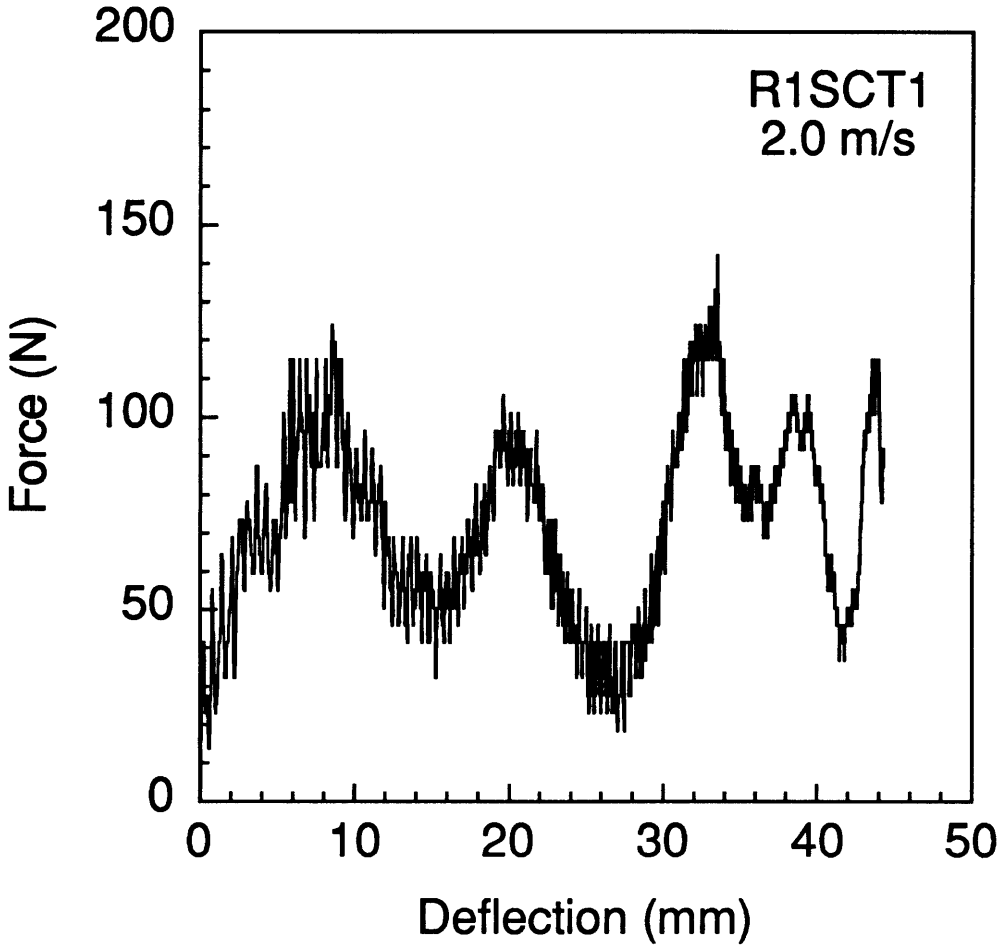

Figure C.21 Force-deflection response of specimen R1SCT1 impacted at 2.0 m/s.

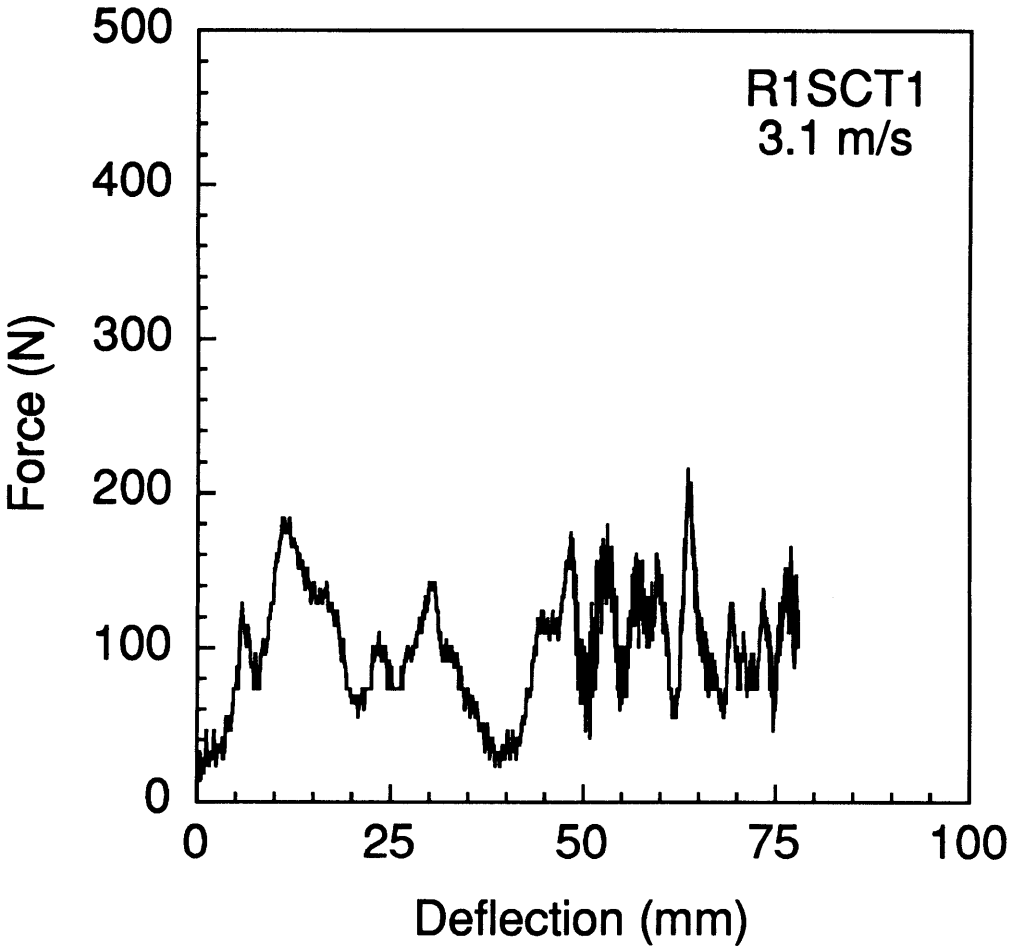

Figure C.22 Force-deflection response of specimen R1SCT1 impacted at 3.1 m/s.

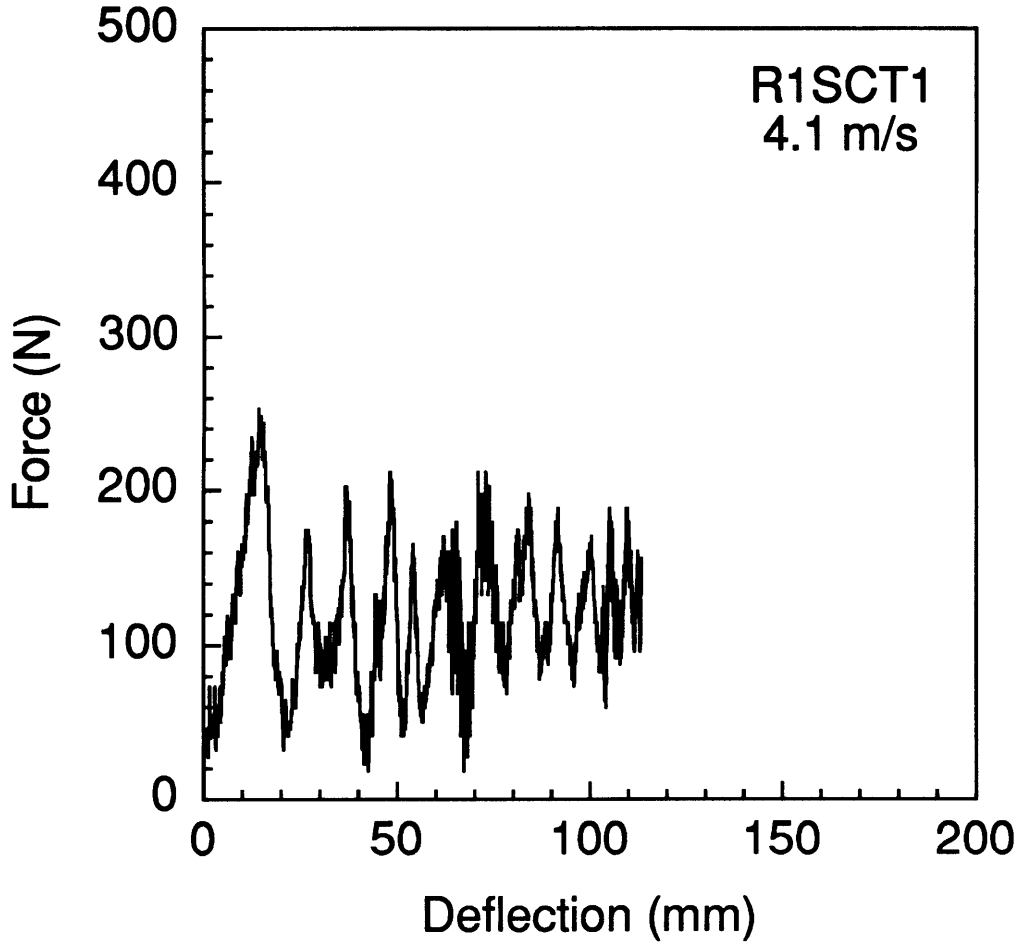

Figure C.23 Force-deflection response of specimen R1SCT1 impacted at 4.1 m/s.

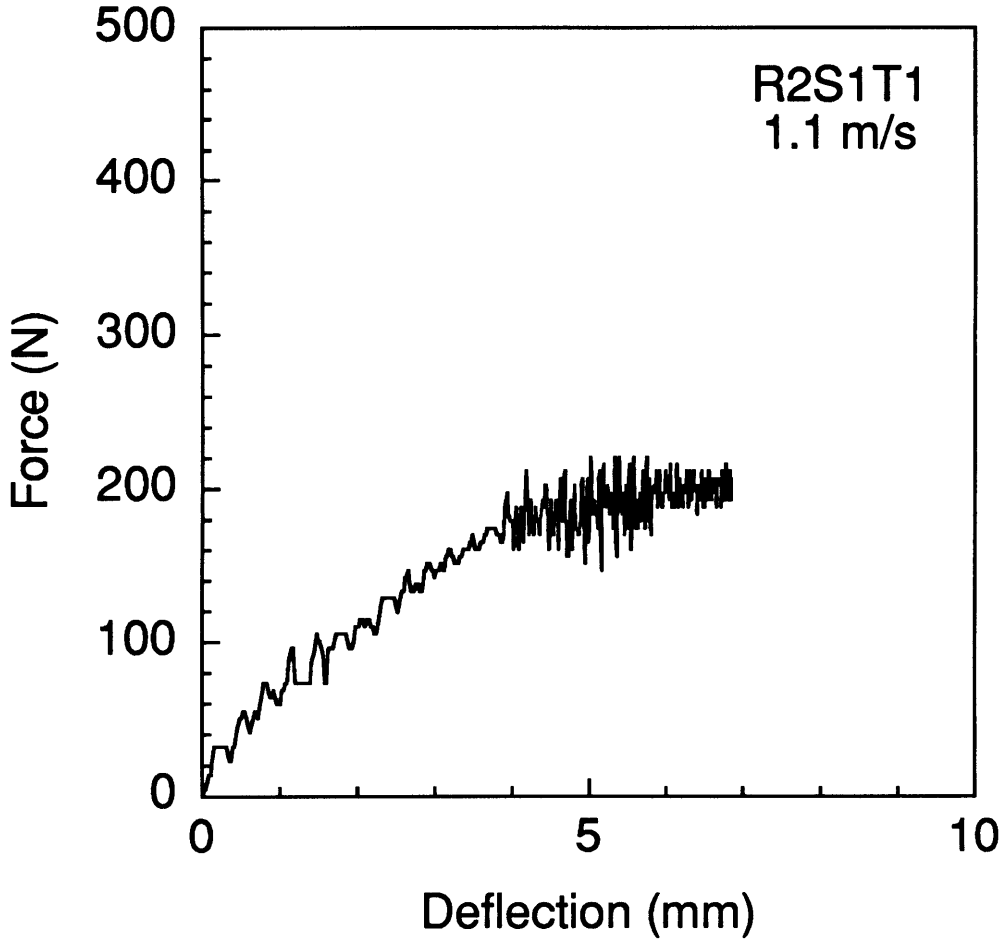

Figure C.24 Force-deflection response of specimen R2S1T1 impacted at 1.1 m/s.

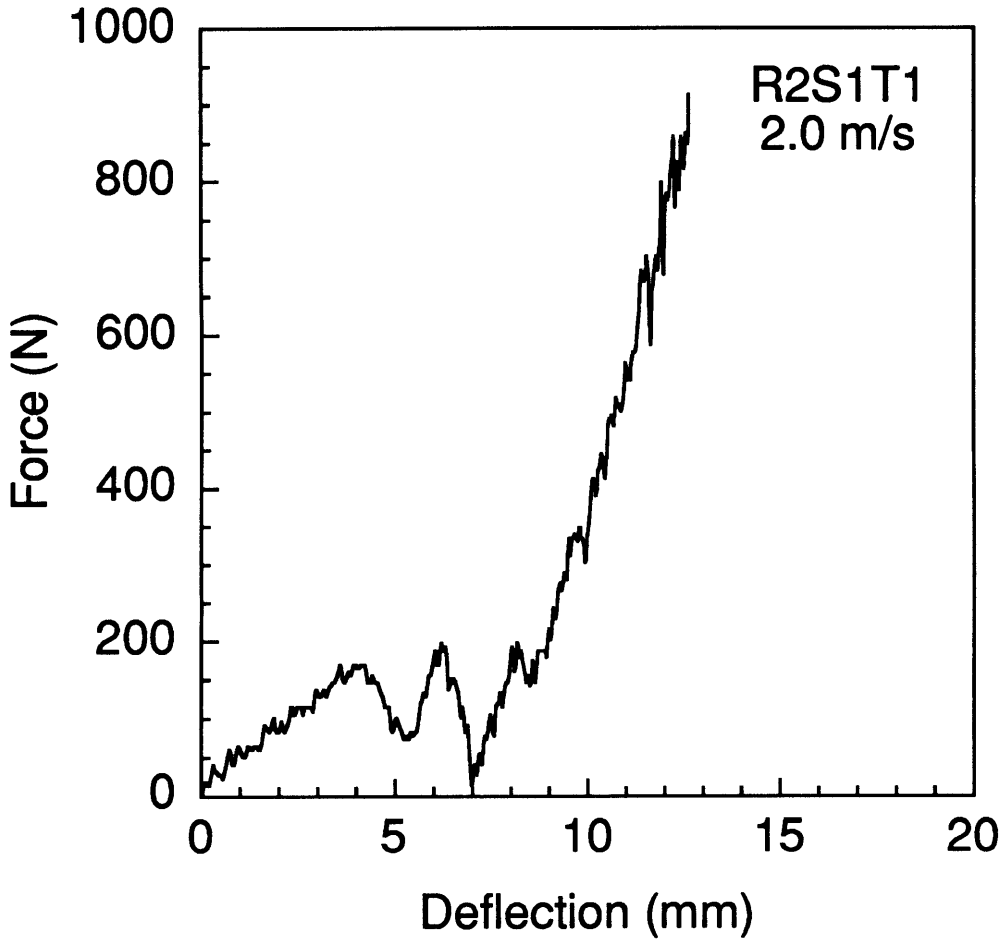

Figure C.25 Force-deflection response of specimen R2S1T1 impacted at 2.0 m/s.

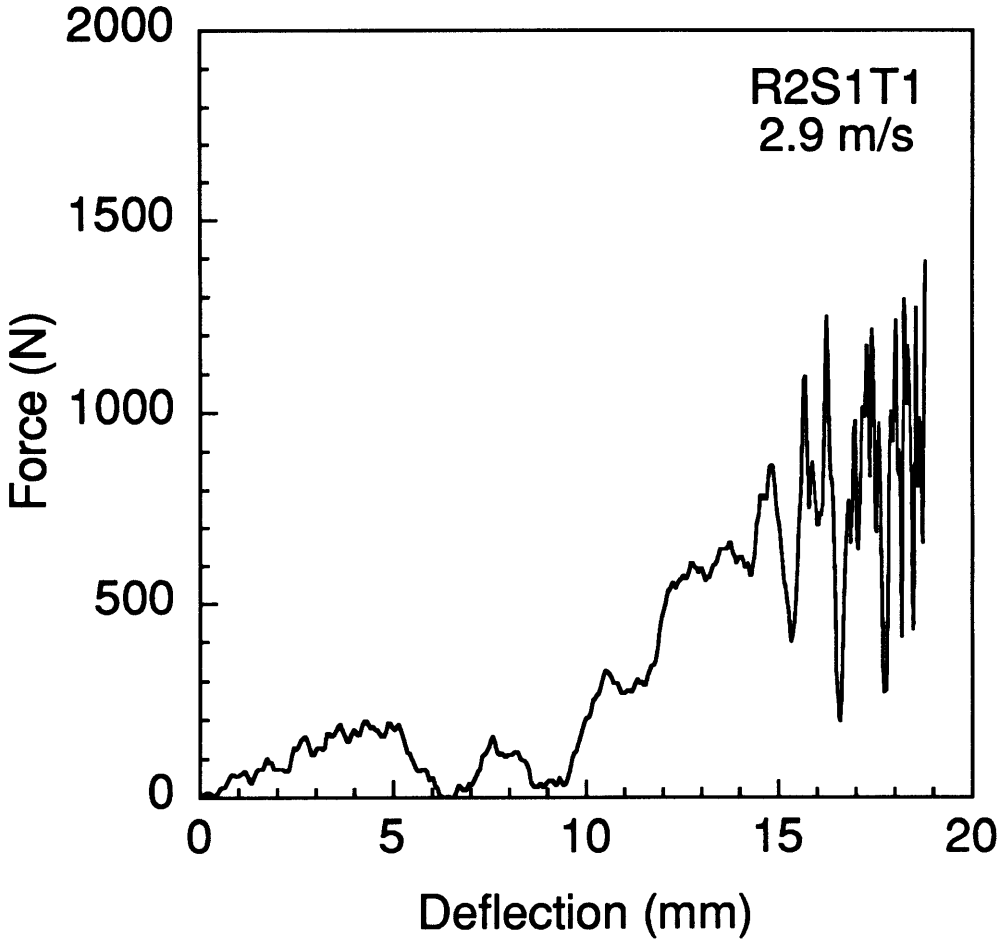

Figure C.26 Force-deflection response of specimen R2S1T1 impacted at 2.9 m/s. This specimen slipped in-plane during testing.

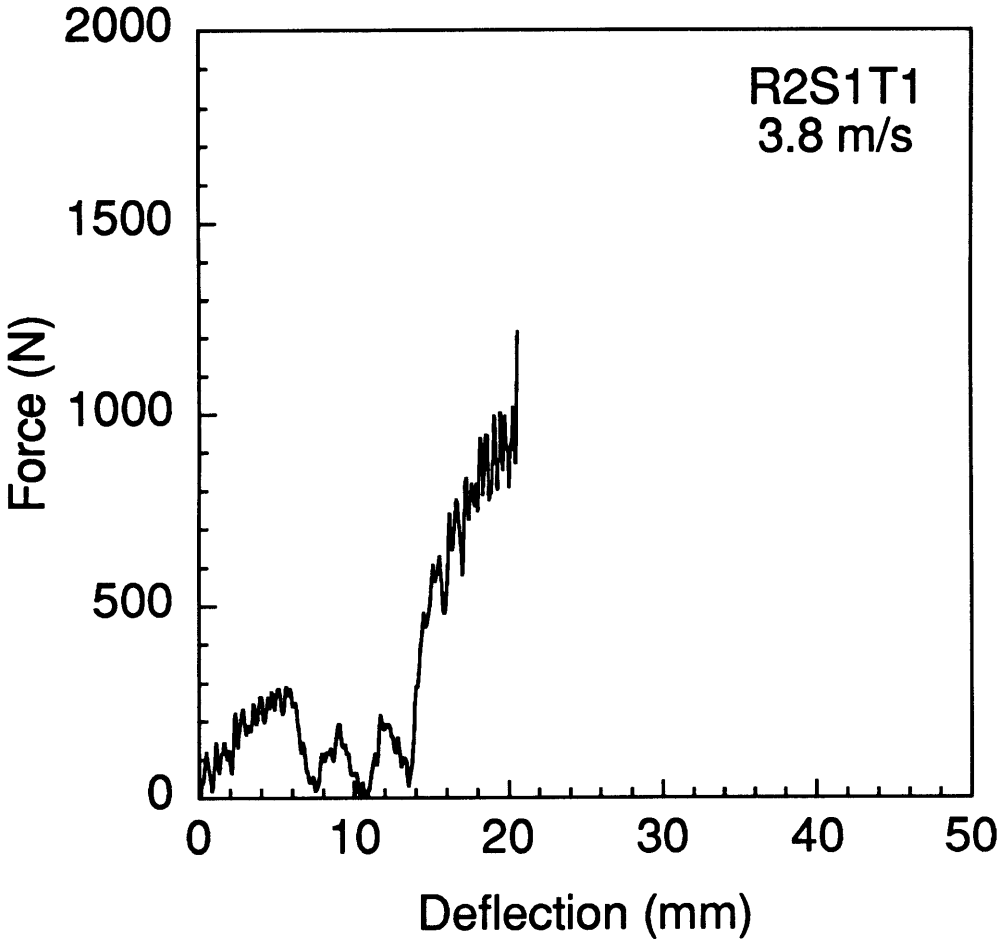

Figure C.27 Force-deflection response of specimen R2S1T1 impacted at 3.8 m/s. This specimen was penetrated during testing.

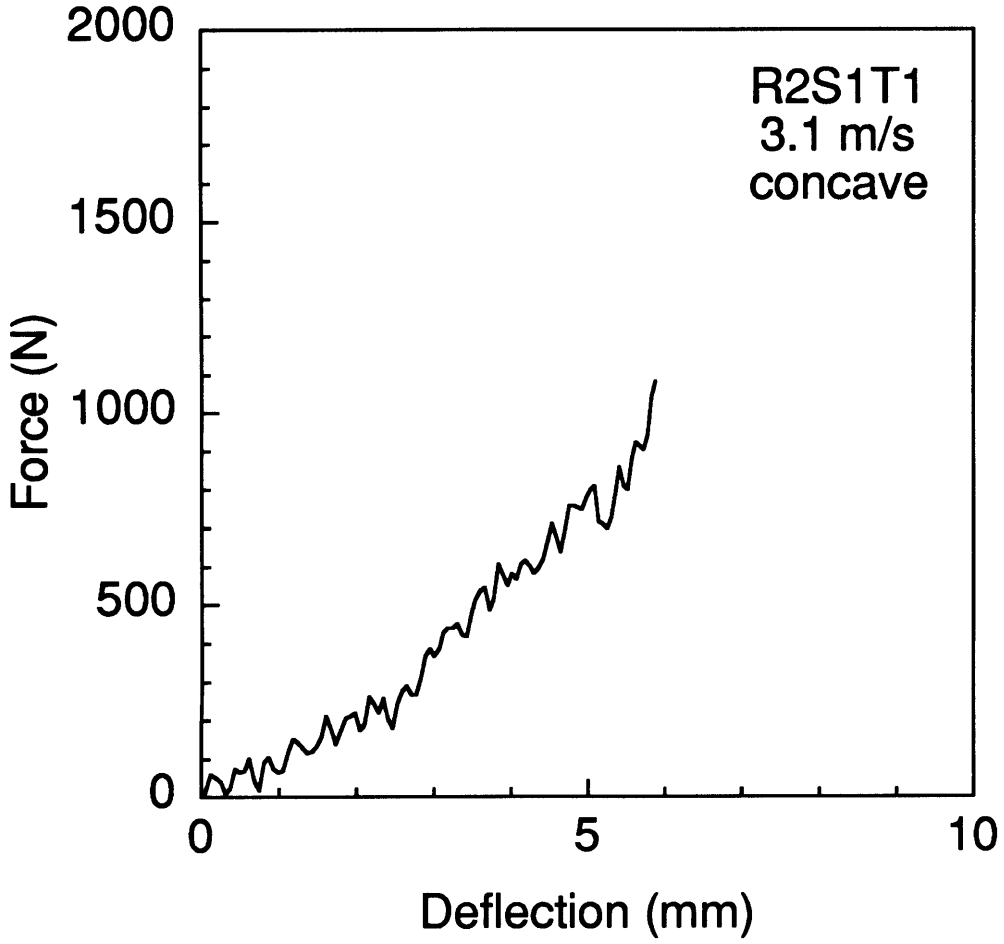

Figure C.28 Force-deflection response of specimen R2S1T1 (concave) impacted at 3.1 m/s. This specimen was penetrated during testing.

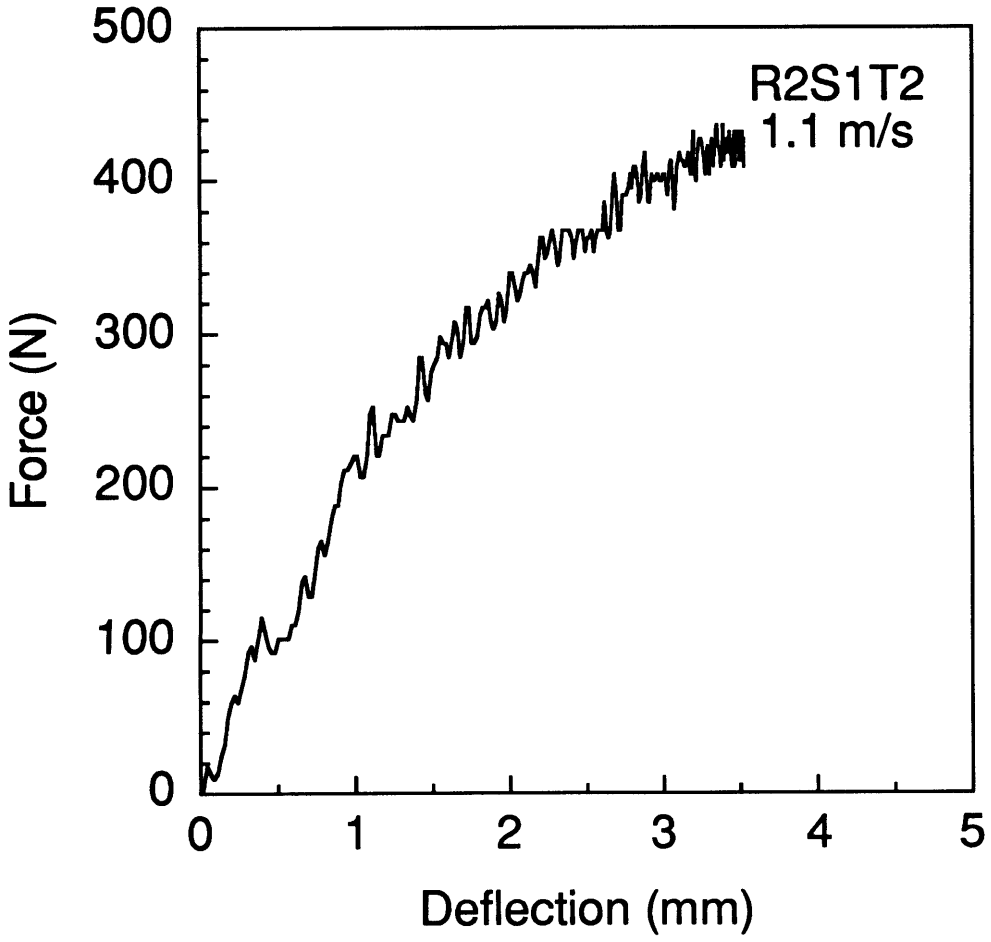

Figure C.29 Force-deflection response of specimen R2S1T2 impacted at 1.1 m/s.

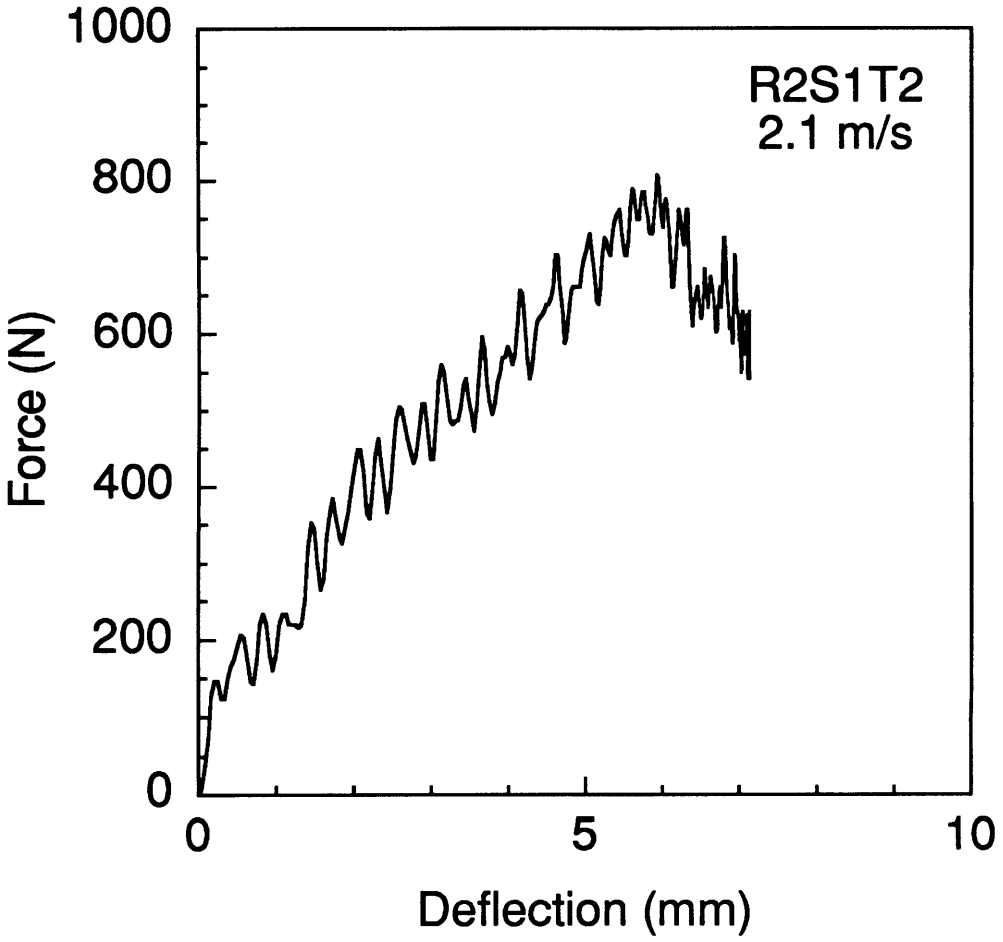

Figure C.30 Force-deflection response of specimen R2S1T2 impacted at 2.1 m/s.

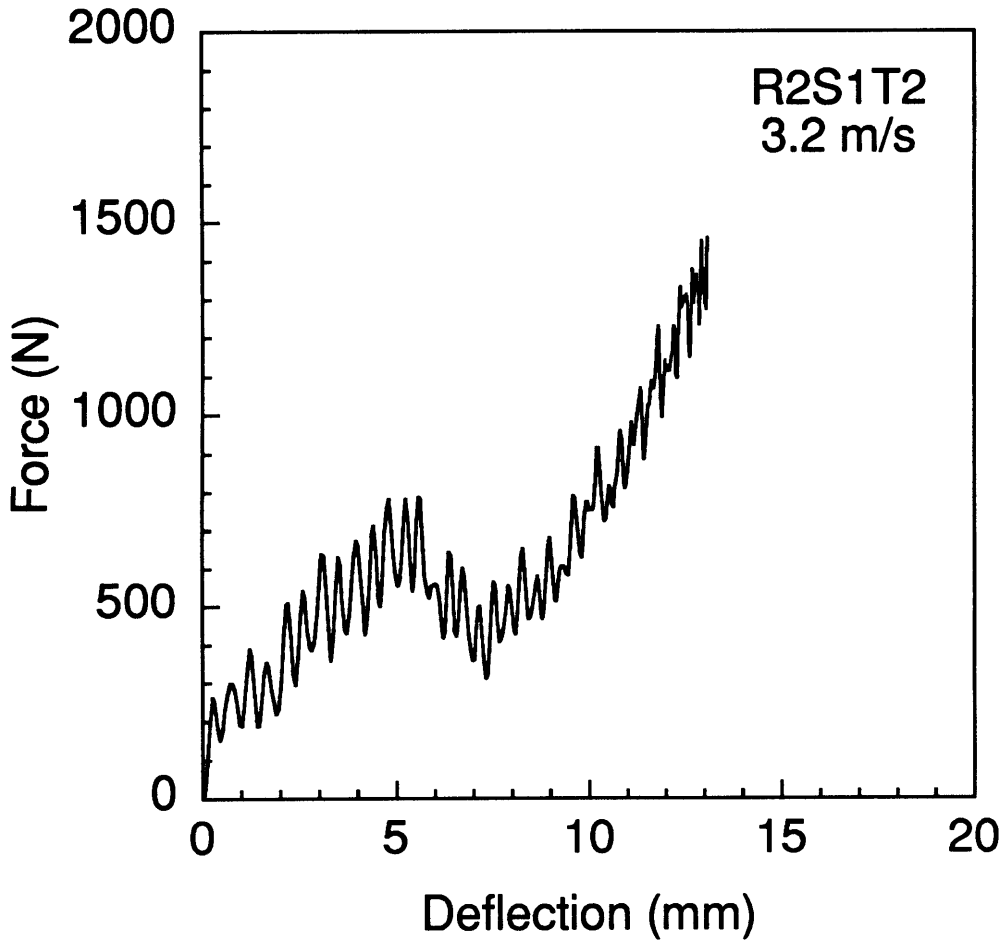

Figure C.31 Force-deflection response of specimen R2S1T2 impacted at 3.2 m/s.

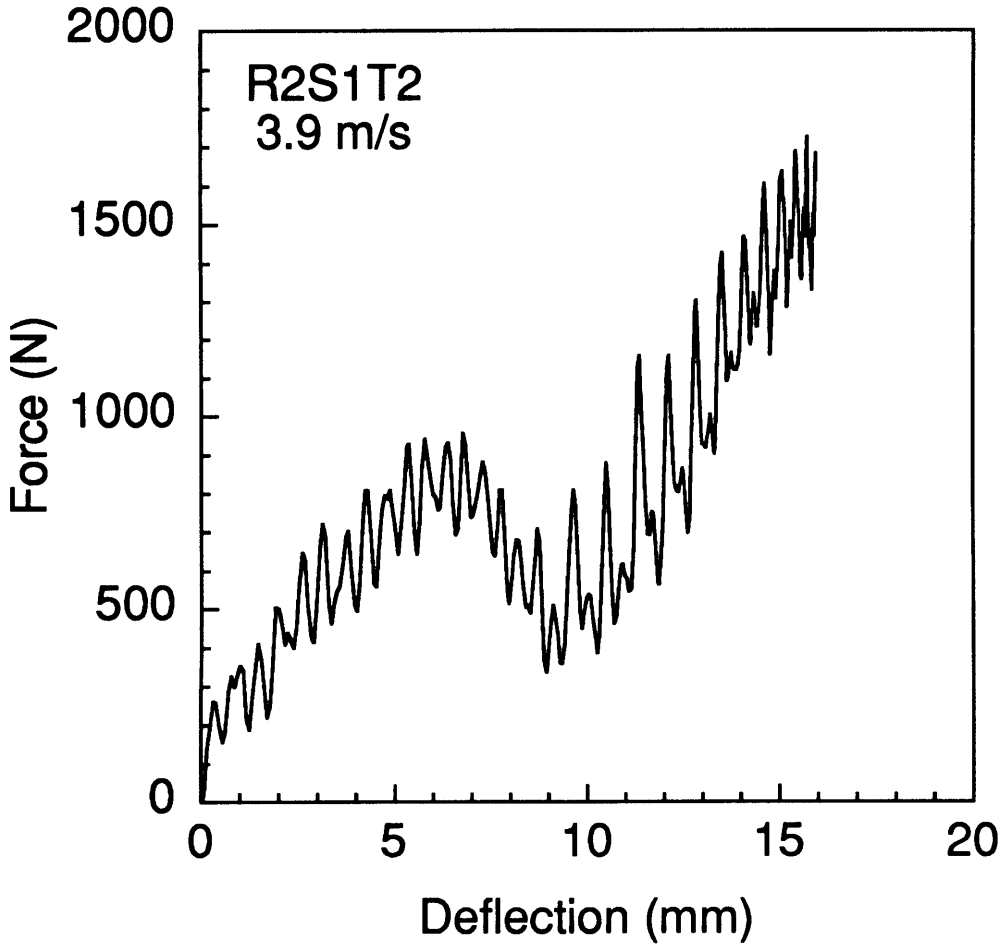

Figure C.32 Force-deflection response of specimen R2S1T2 impacted at 3.9 m/s.

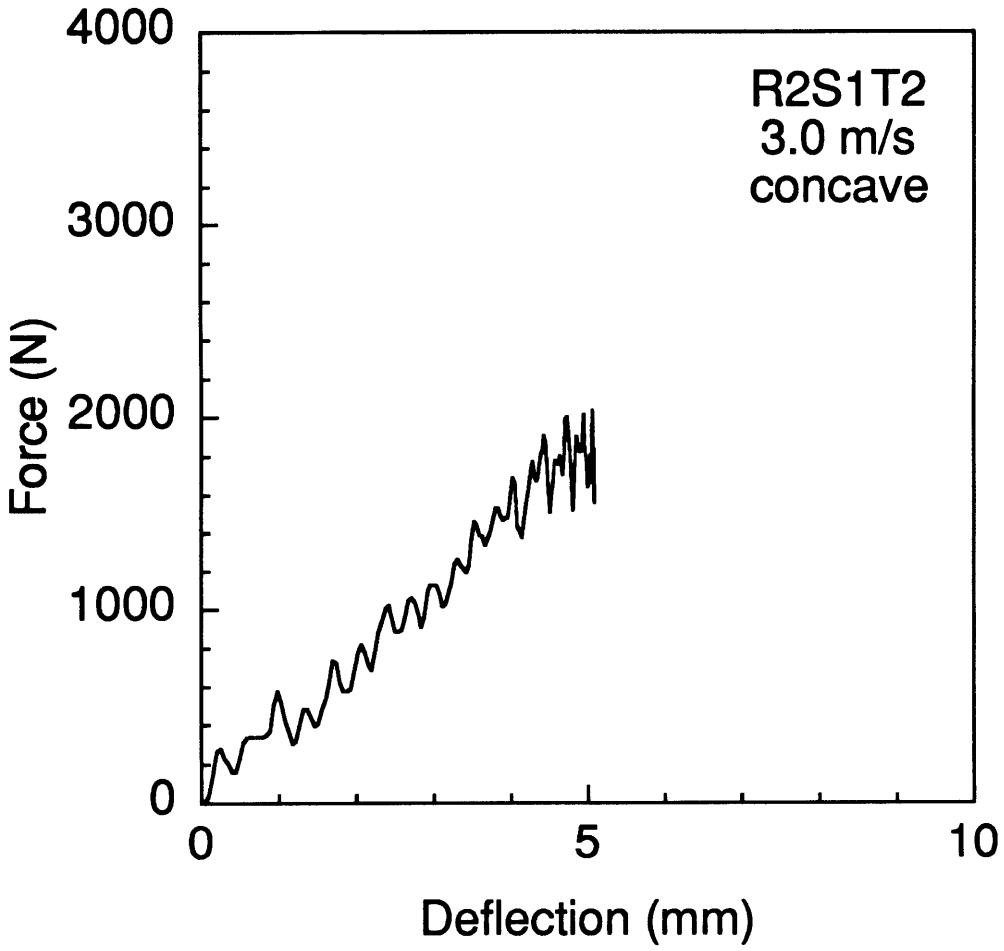

Figure C.33 Force-deflection response of specimen R2S1T2 (concave) impacted at 3.0 m/s.

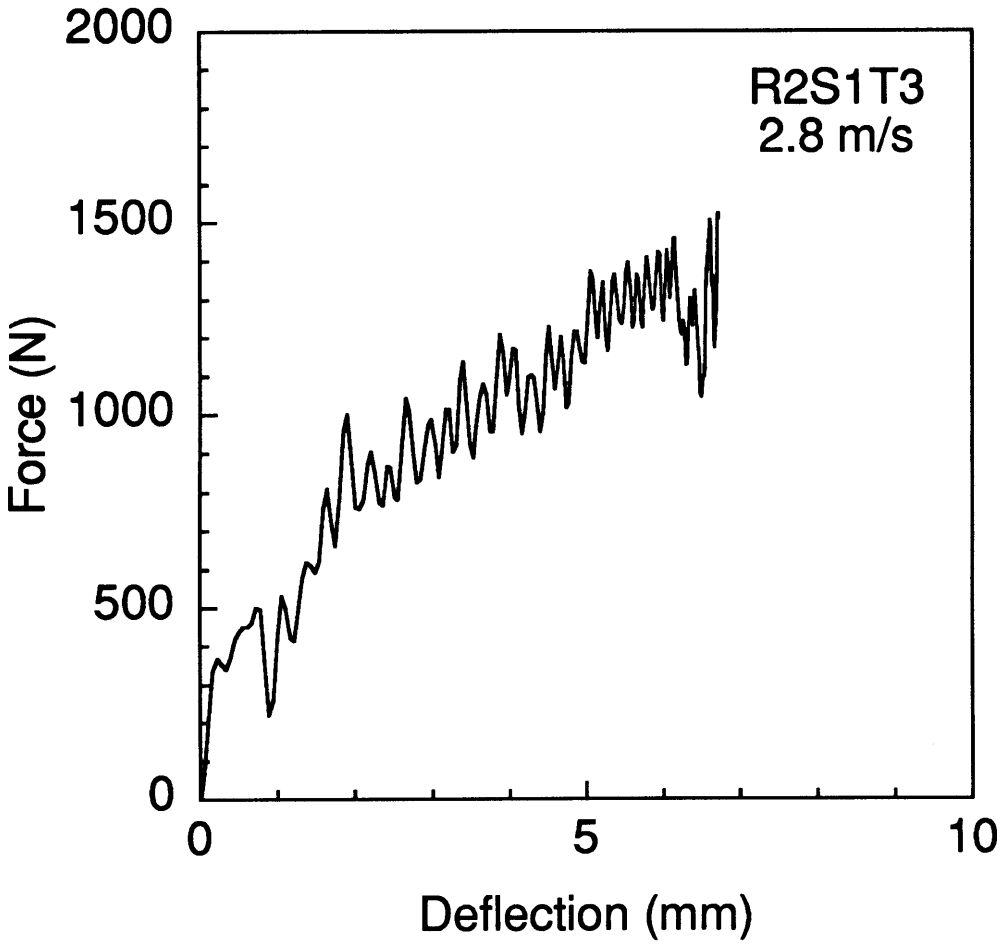

Figure C.34 Force-deflection response of specimen R2S1T3 impacted at 2.8 m/s.

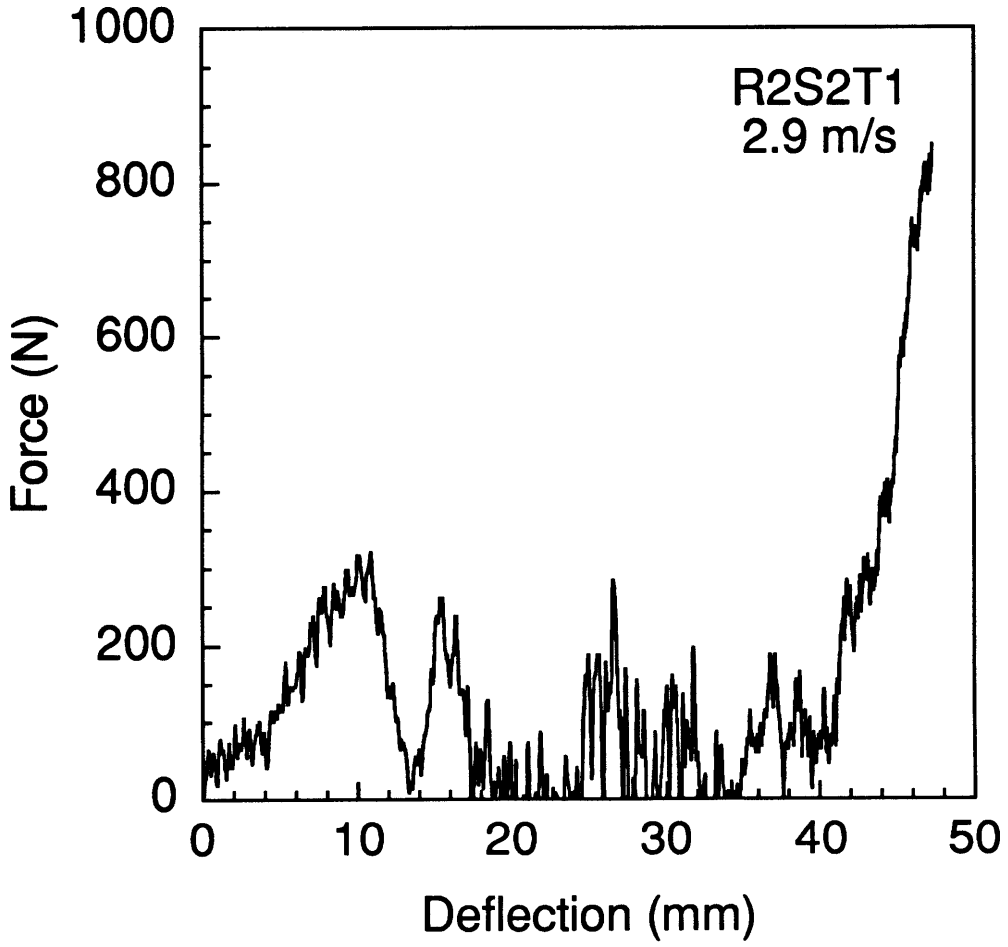

Figure C.35 Force-deflection response of specimen R2S2T1 impacted at 2.9 m/s.

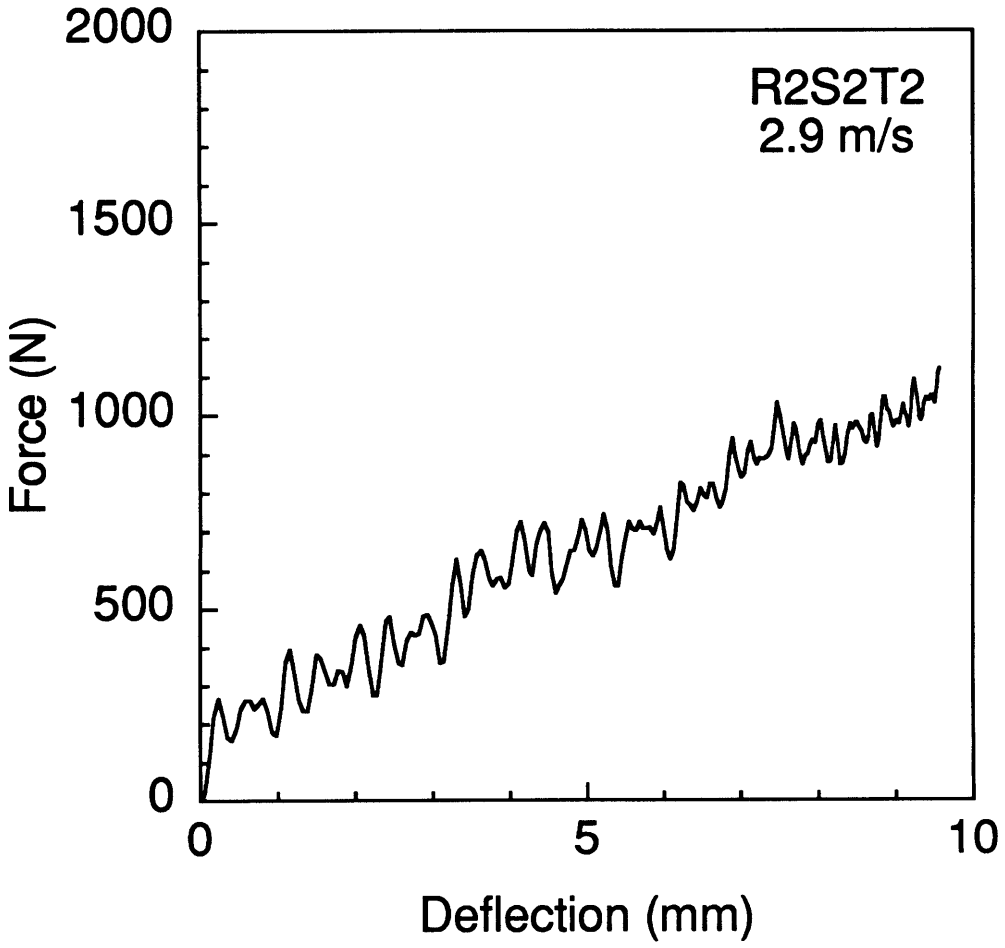

Figure C.36 Force-deflection response of specimen R2S2T2 impacted at 2.9 m/s.

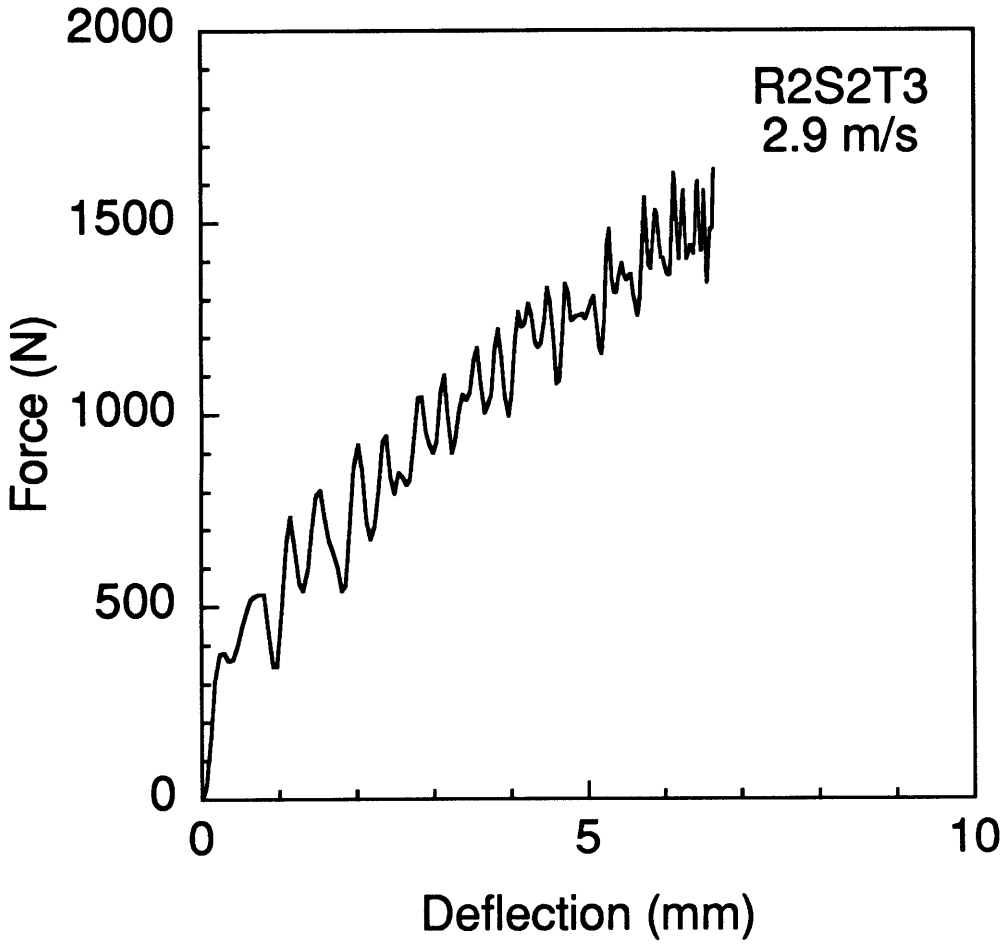

Figure C.37 Force-deflection response of specimen R2S2T3 impacted at 2.9 m/s.

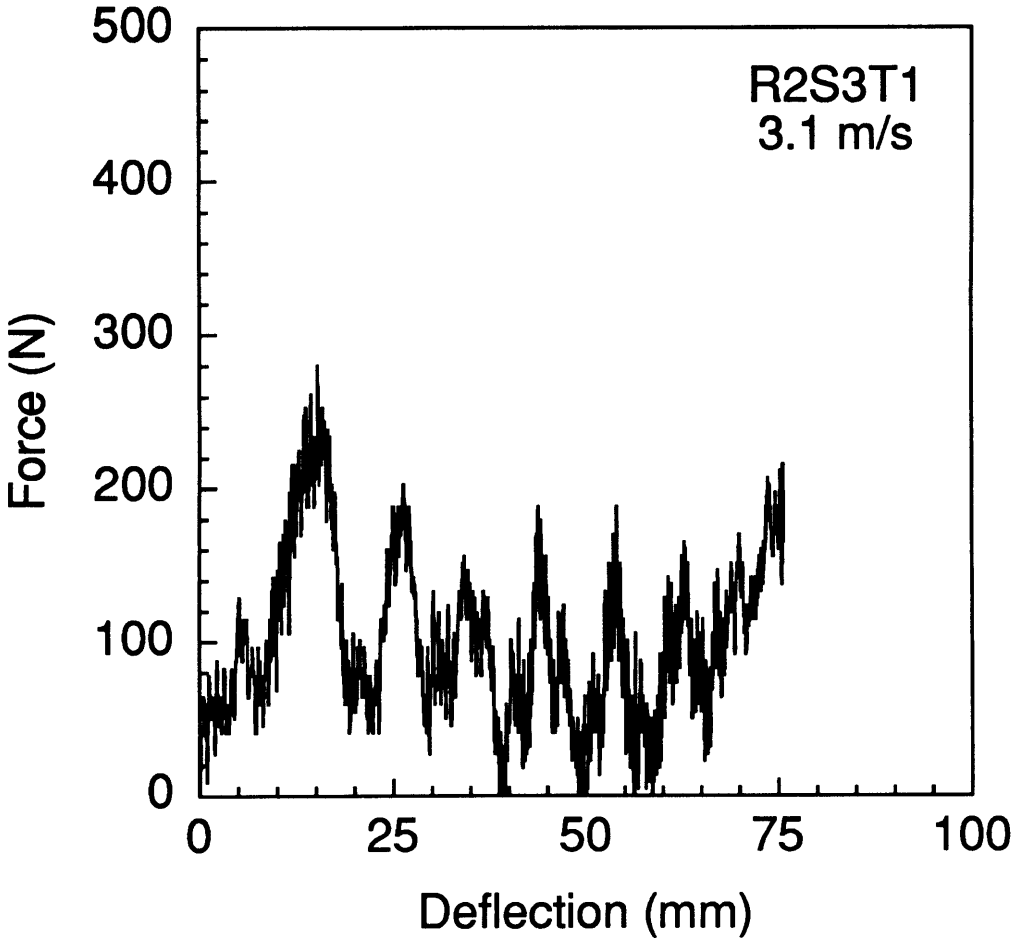

Figure C.38 Force-deflection response of specimen R2S3T1 impacted at 3.1 m/s.

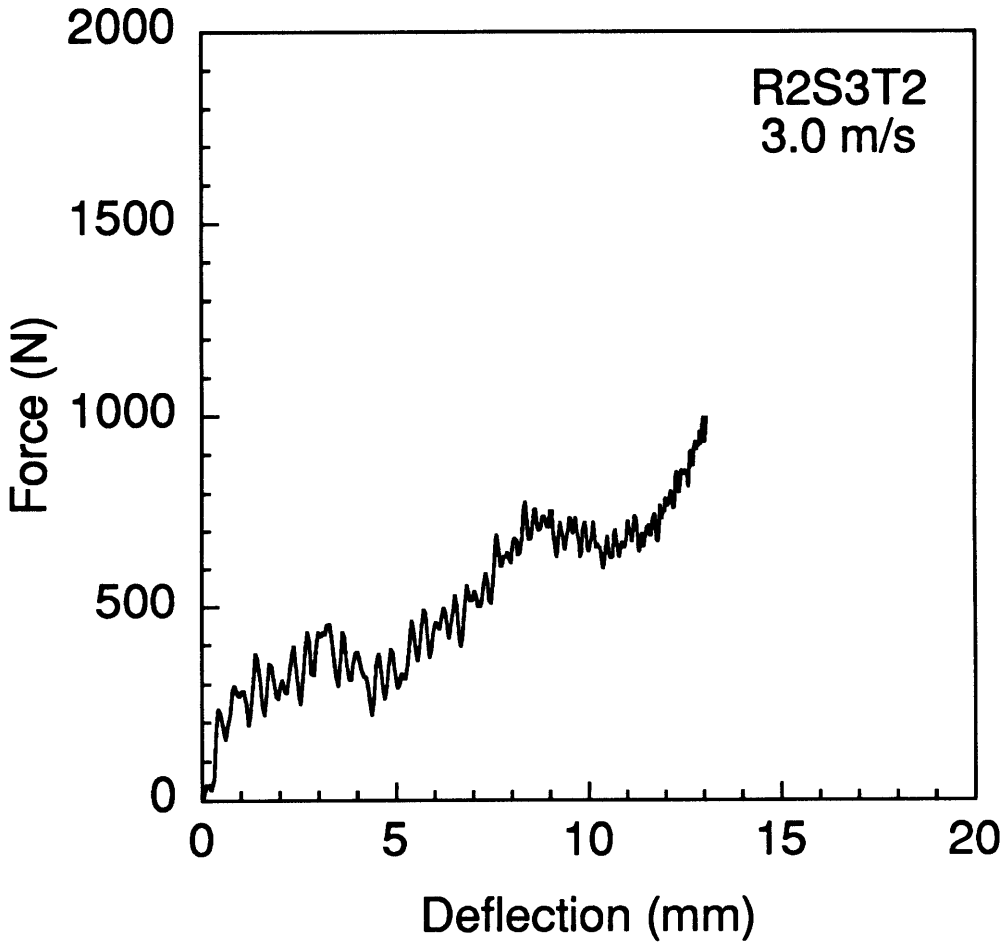

Figure C.39 Force-deflection response of specimen R2S3T2 impacted at 3.0 m/s.

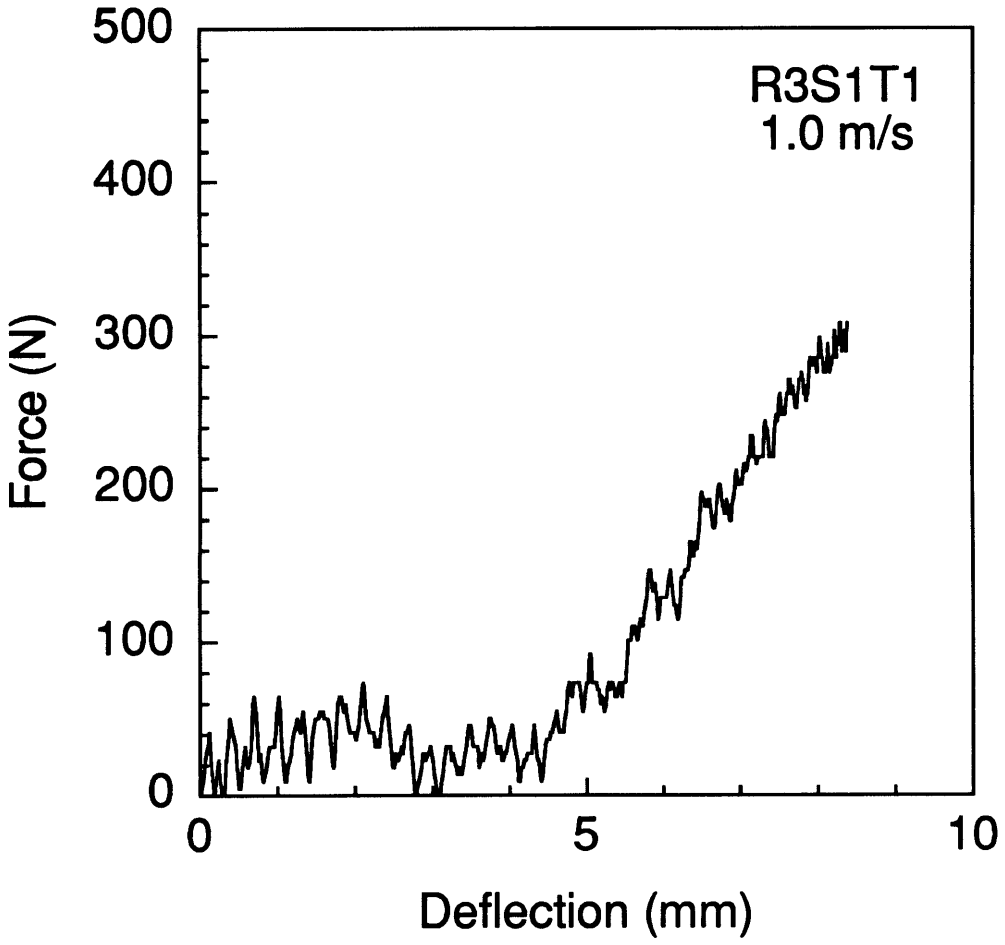

Figure C.40 Force-deflection response of specimen R3S1T1 impacted at 1.0 m/s.

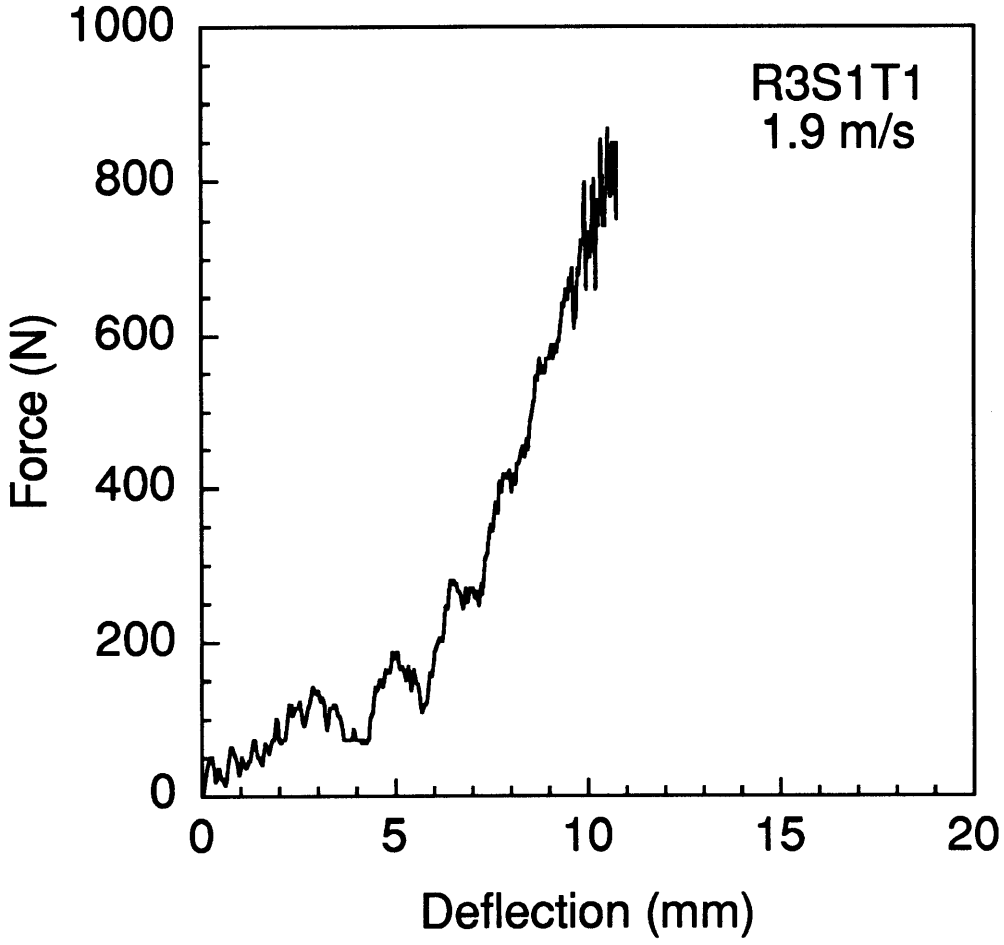

Figure C.41 Force-deflection response of specimen R3S1T1 impacted at 1.9 m/s.

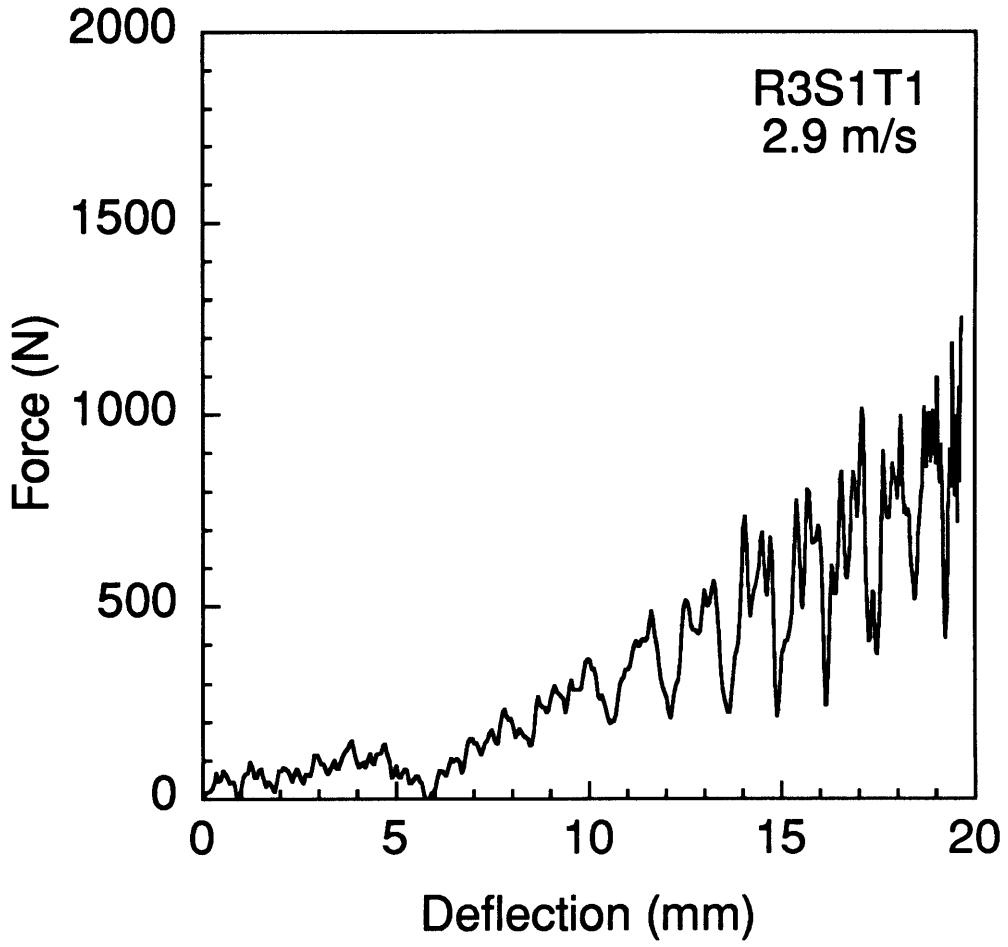

Figure C.42 Force-deflection response of specimen R3S1T1 impacted at 2.9 m/s. This specimen slipped in-plane during testing.

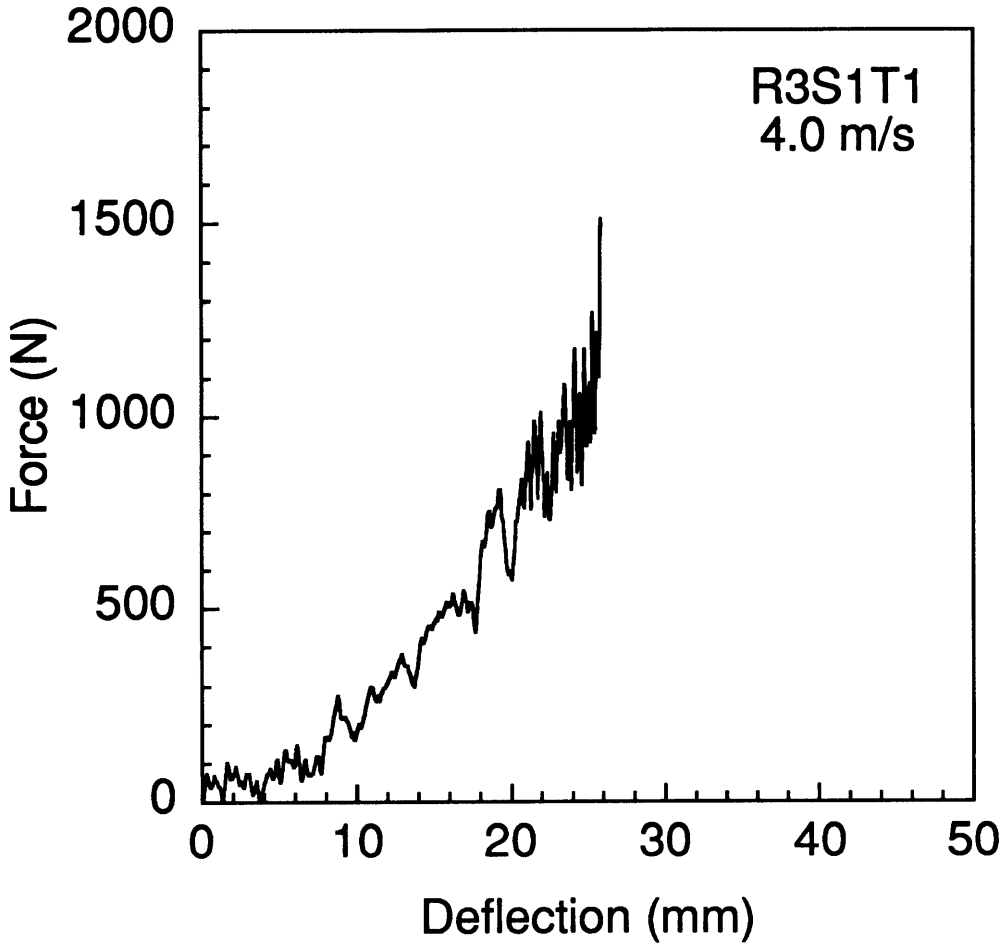

Figure C.43 Force-deflection response of specimen R3S1T1 impacted at 4.0 m/s. This specimen slipped in-plane and was penetrated during testing.

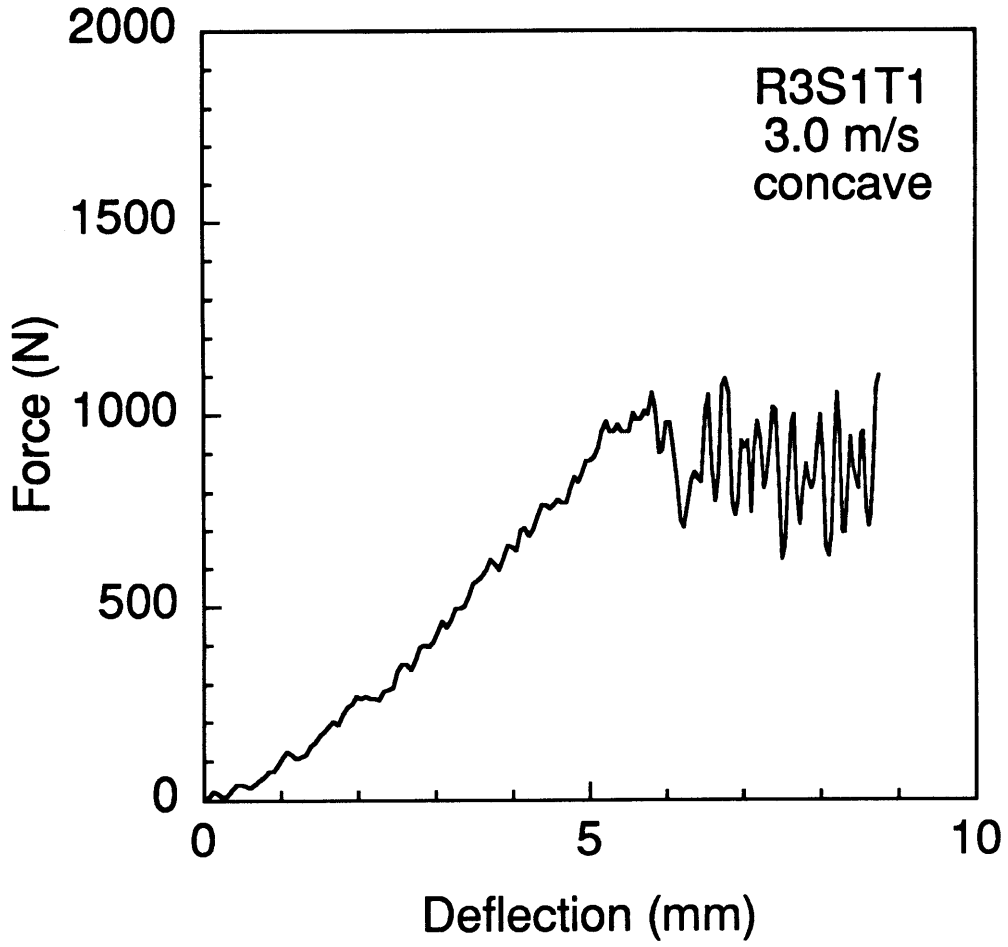

Figure C.44 Force-deflection response of specimen R3S1T1 (concave) impacted at 3.0 m/s. This specimen was penetrated during testing.

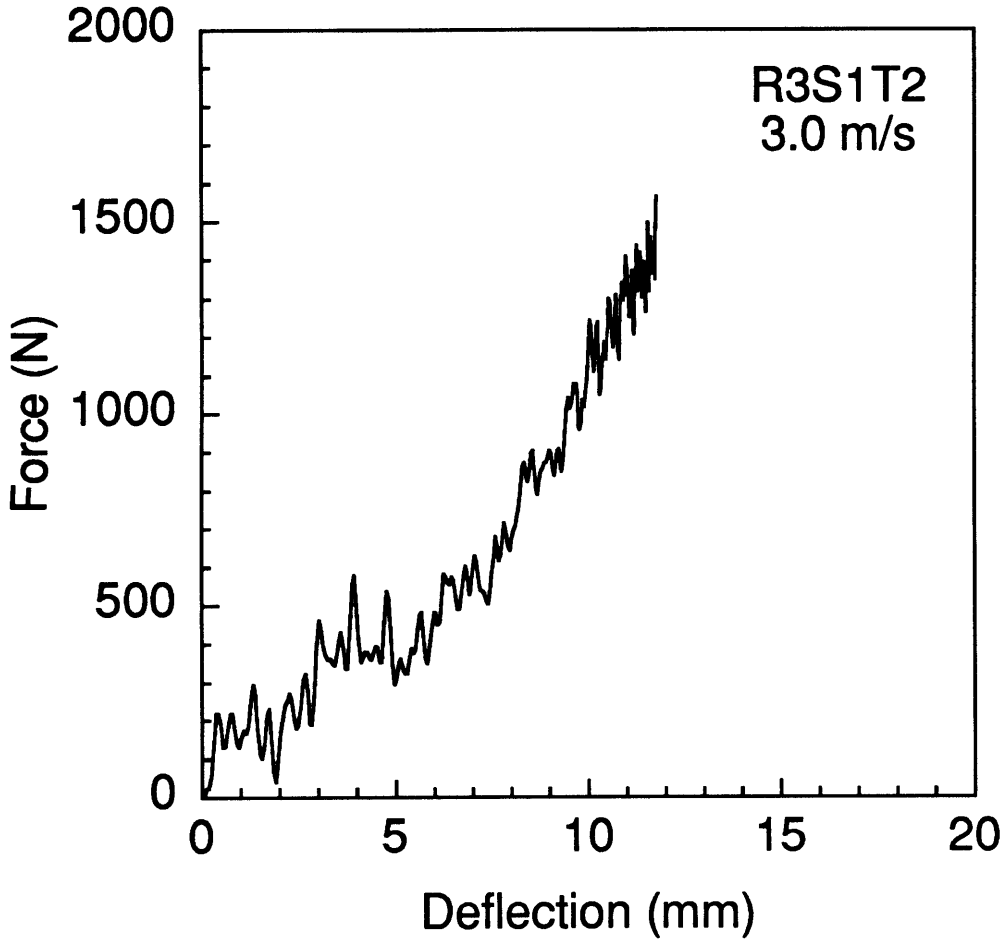

Figure C.45 Force-deflection response of specimen R3S1T2 impacted at 3.0 m/s.

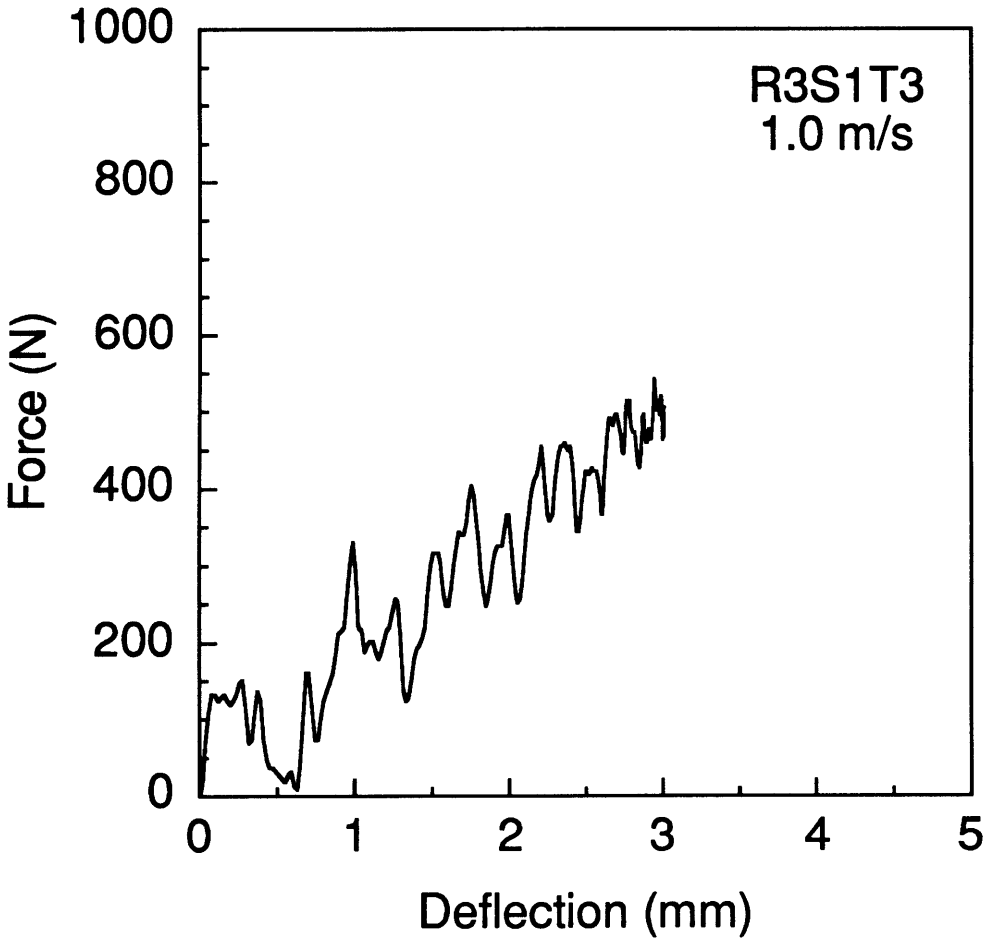

Figure C.46 Force-deflection response of specimen R3S1T3 impacted at 1.0 m/s.

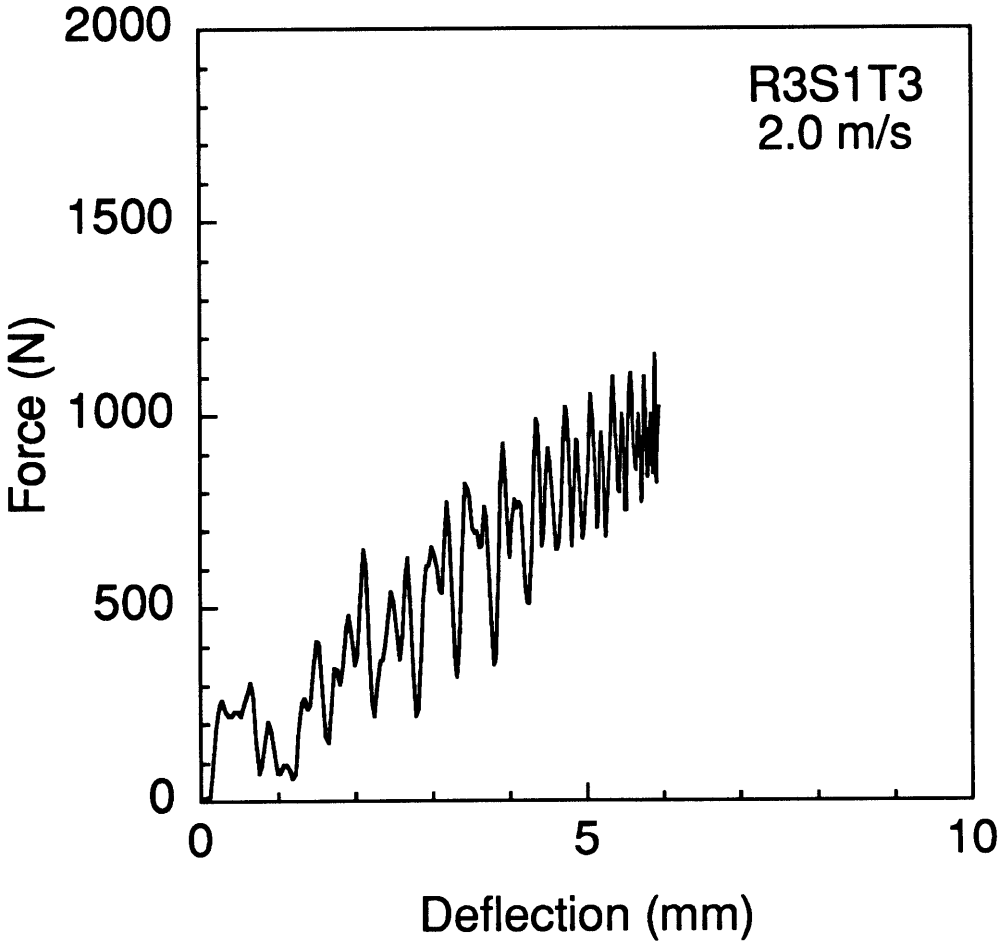

Figure C.47 Force-deflection response of specimen R3S1T3 impacted at 2.0 m/s.

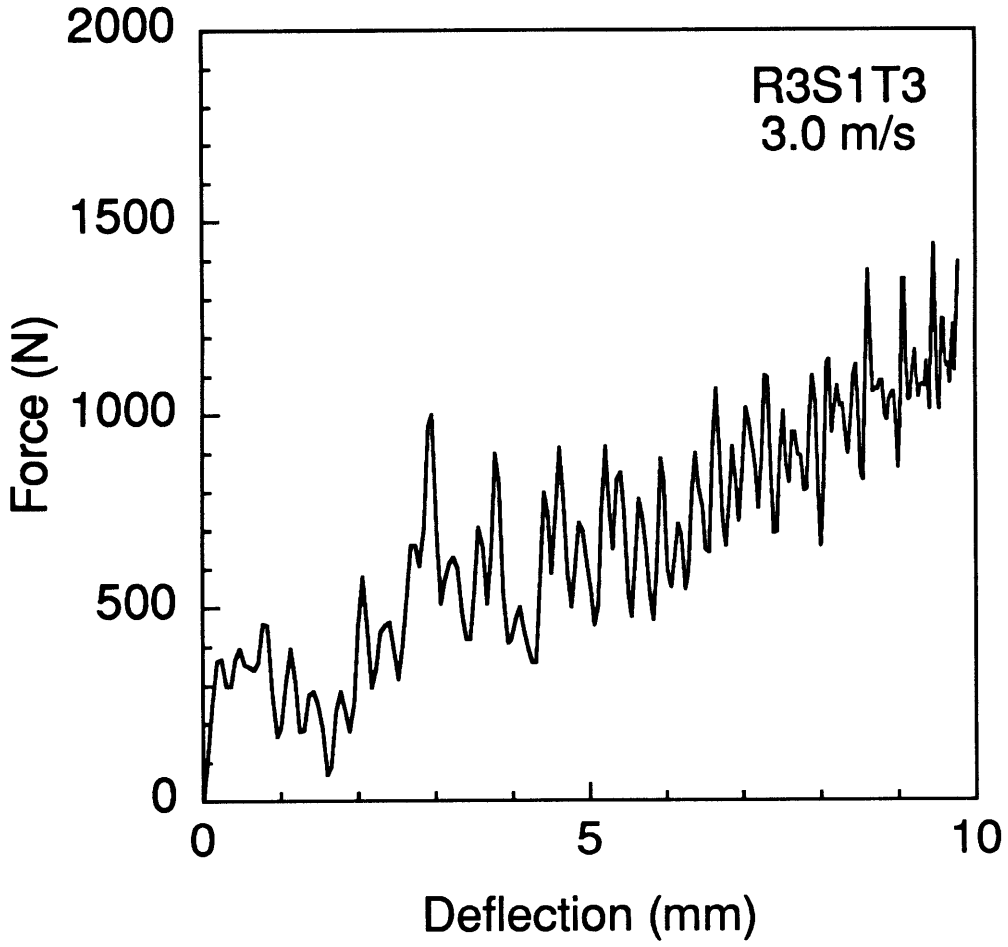

Figure C.48 Force-deflection response of specimen R3S1T3 impacted at 3.0 m/s.

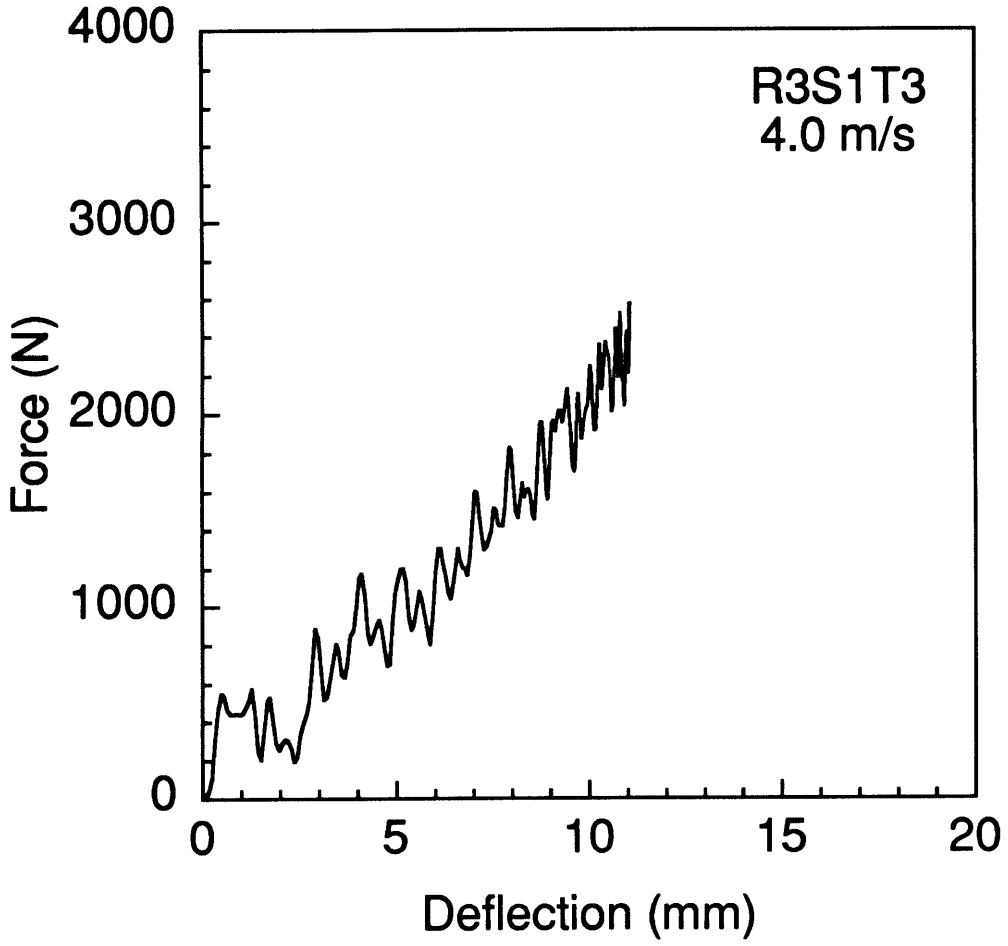

Figure C.49 Force-deflection response of specimen R3S1T3 impacted at 4.0 m/s.

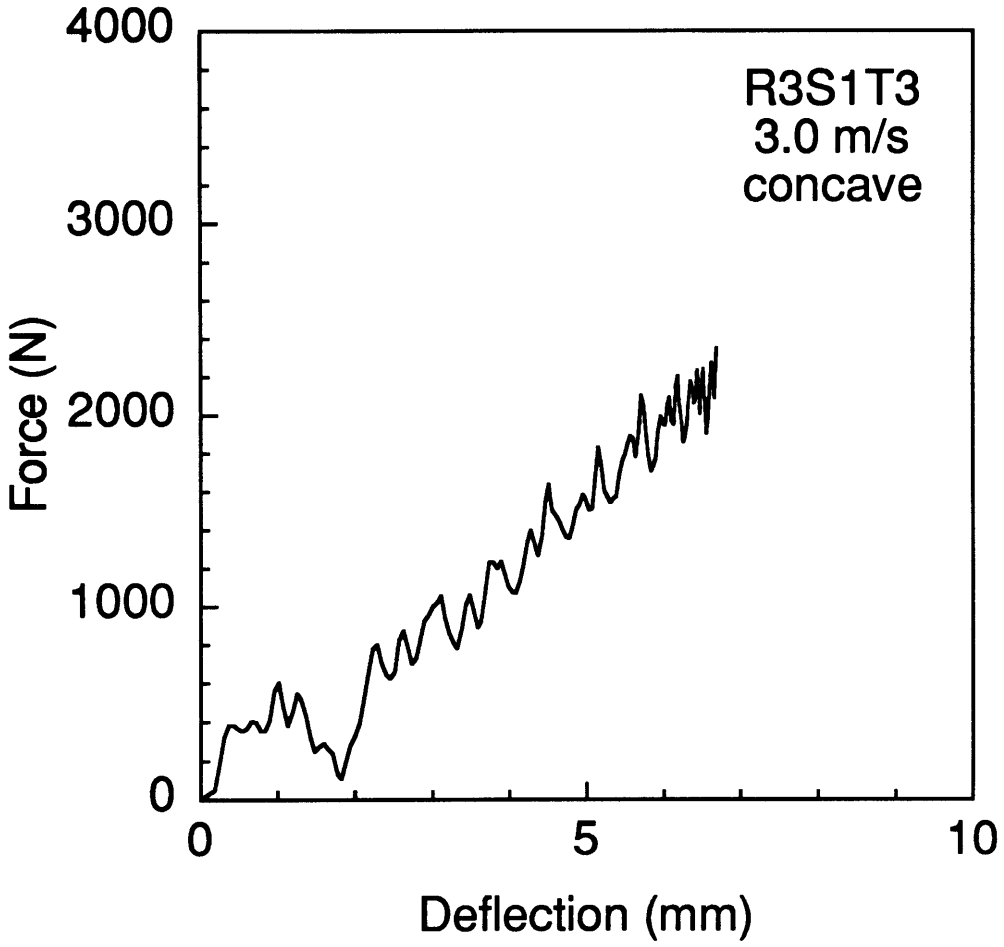

Figure C.50 Force-deflection response of specimen R3S1T3 (concave) impacted at 3.0 m/s.

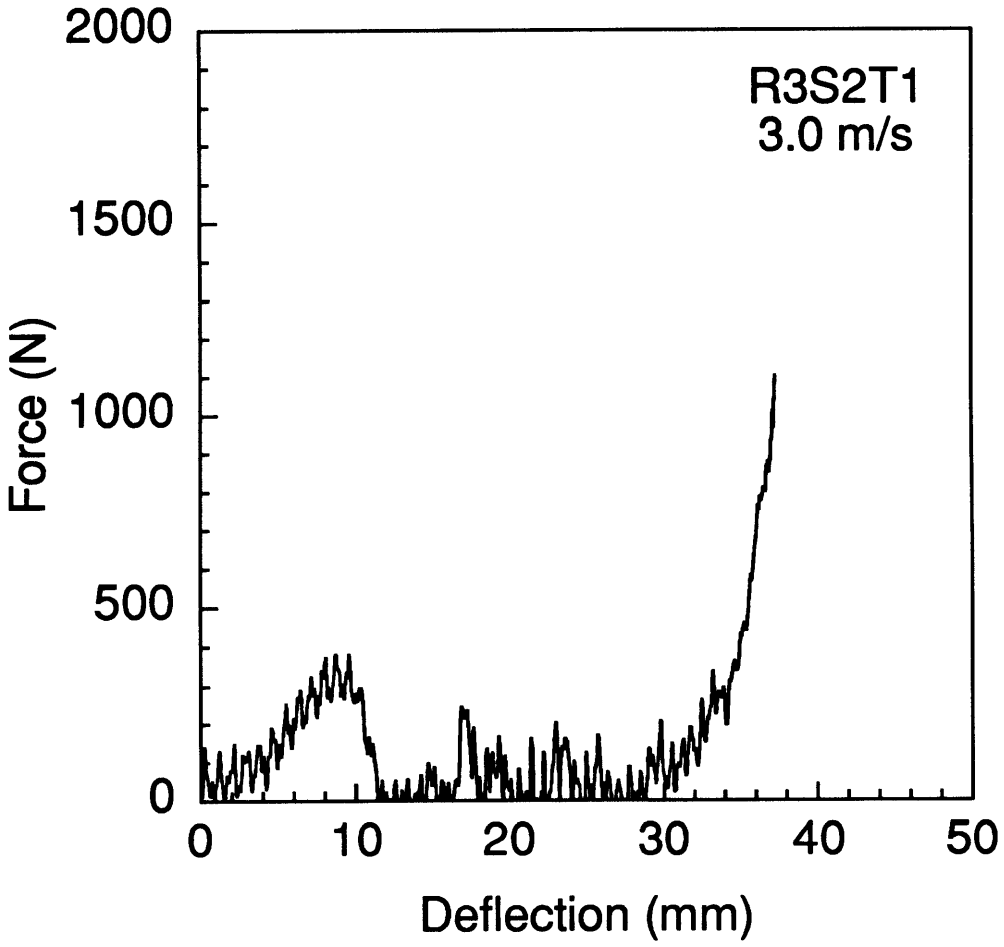

Figure C.51 Force-deflection response of specimen R3S2T1 impacted at 3.0 m/s.

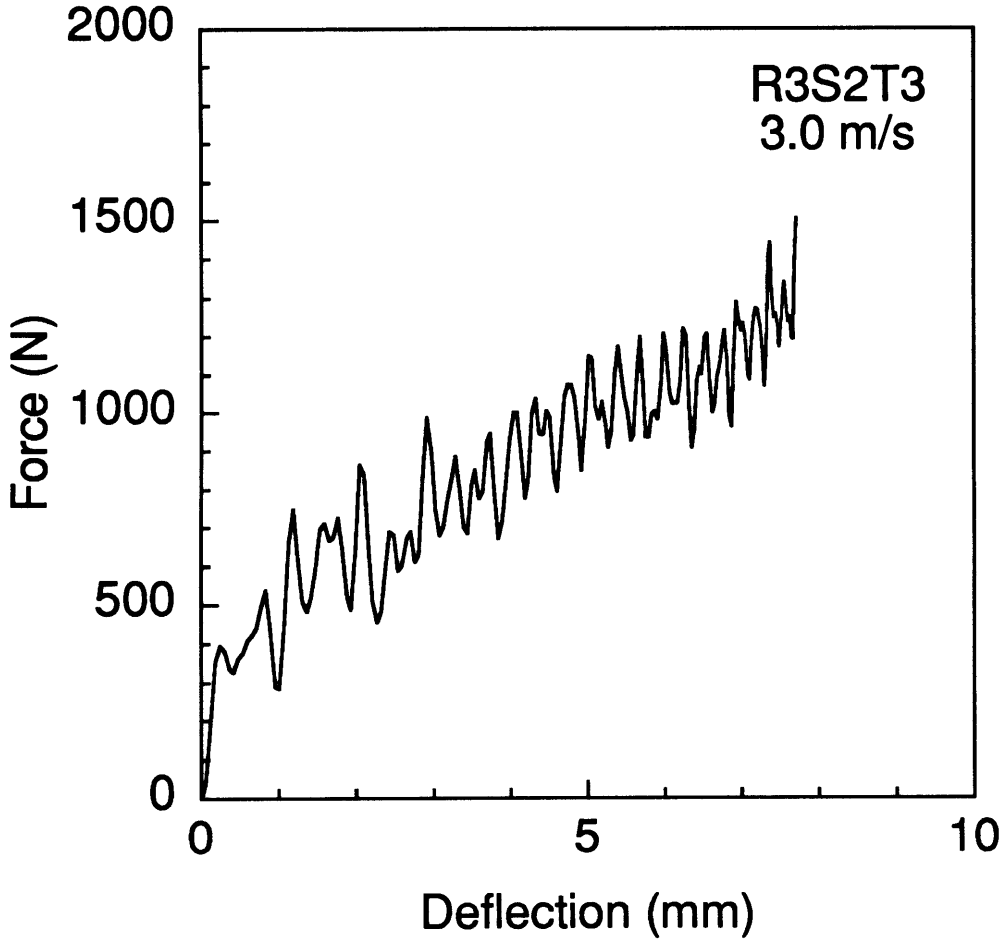

Figure C.52 Force-deflection response of specimen R3S2T3 impacted at 3.0 m/s.

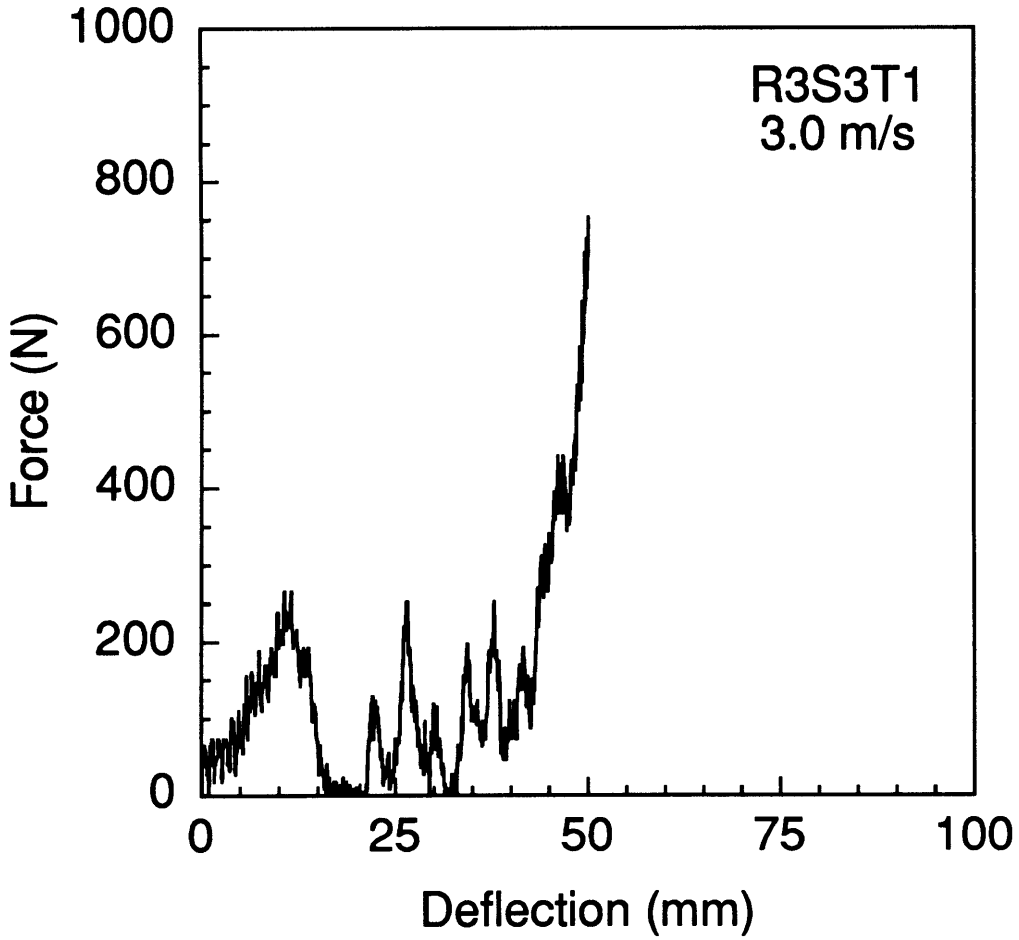

Figure C.53 Force-deflection response of specimen R3S3T1 impacted at 3.0 m/s.

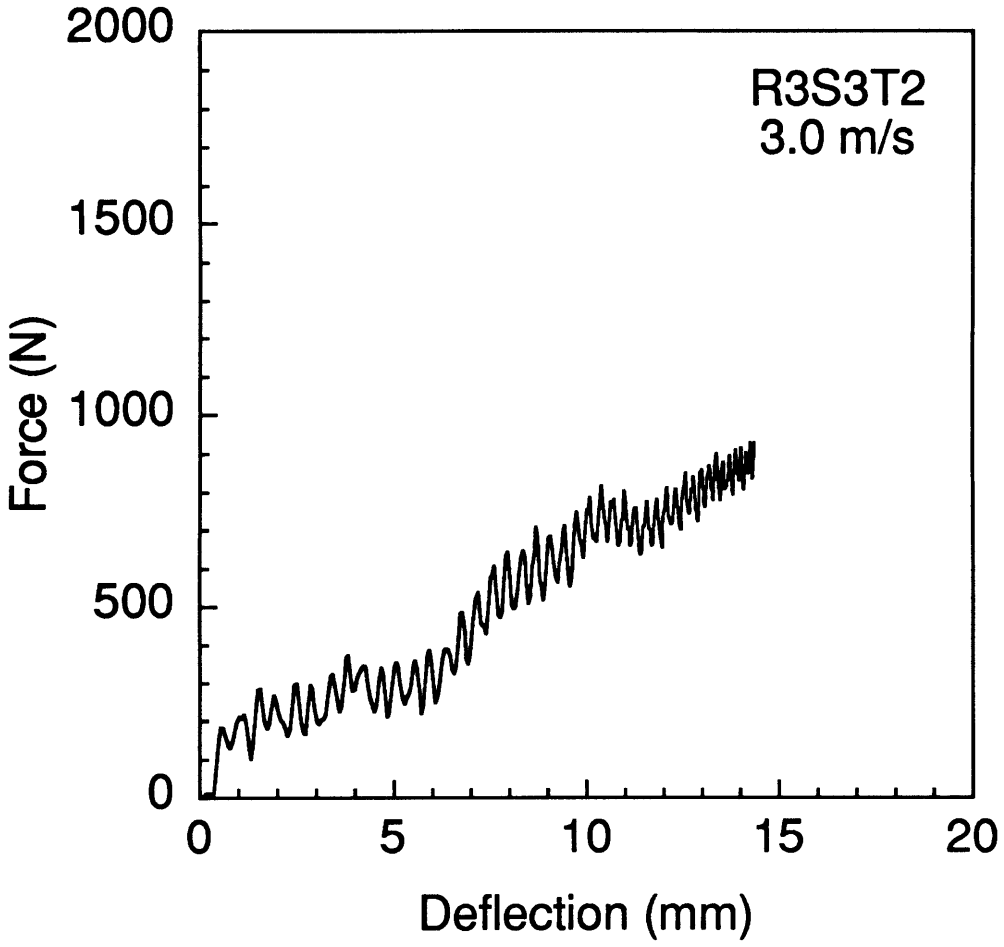

Figure C.54 Force-deflection response of specimen R3S3T2 impacted at 3.0 m/s.

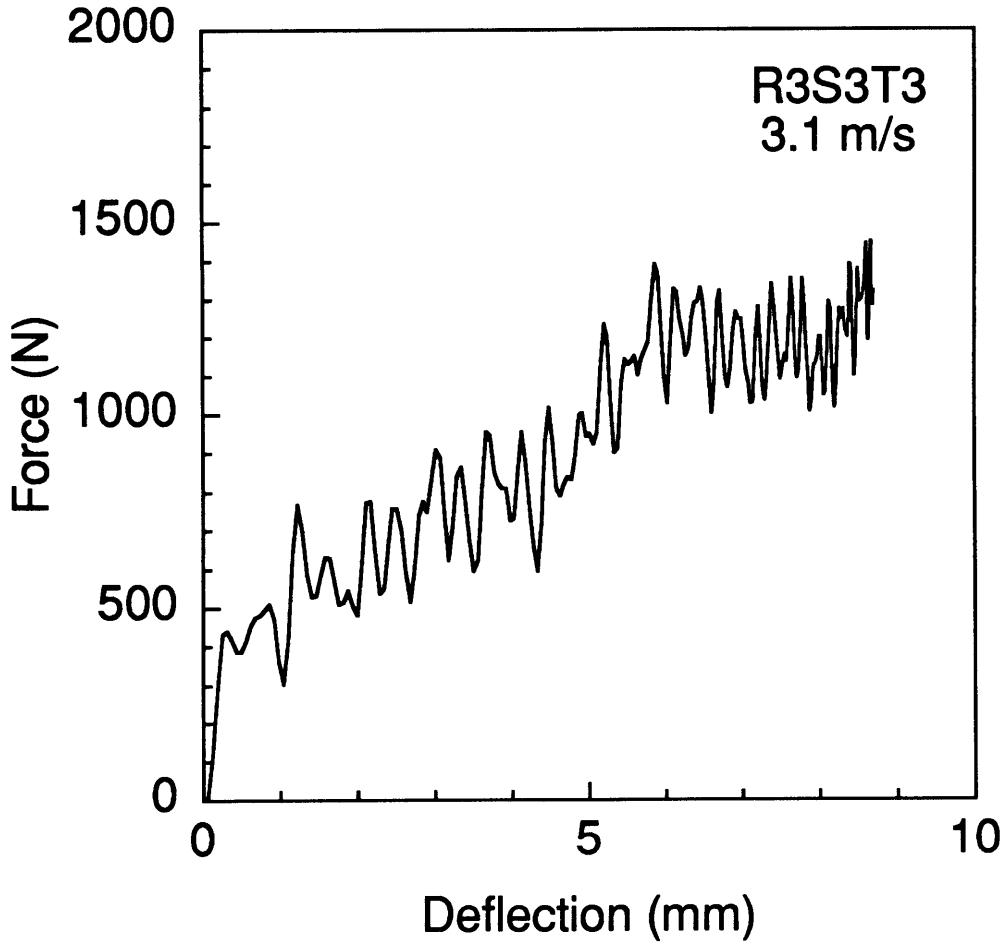

Figure C.55 Force-deflection response of specimen R3S3T3 impacted at 3.1 m/s.

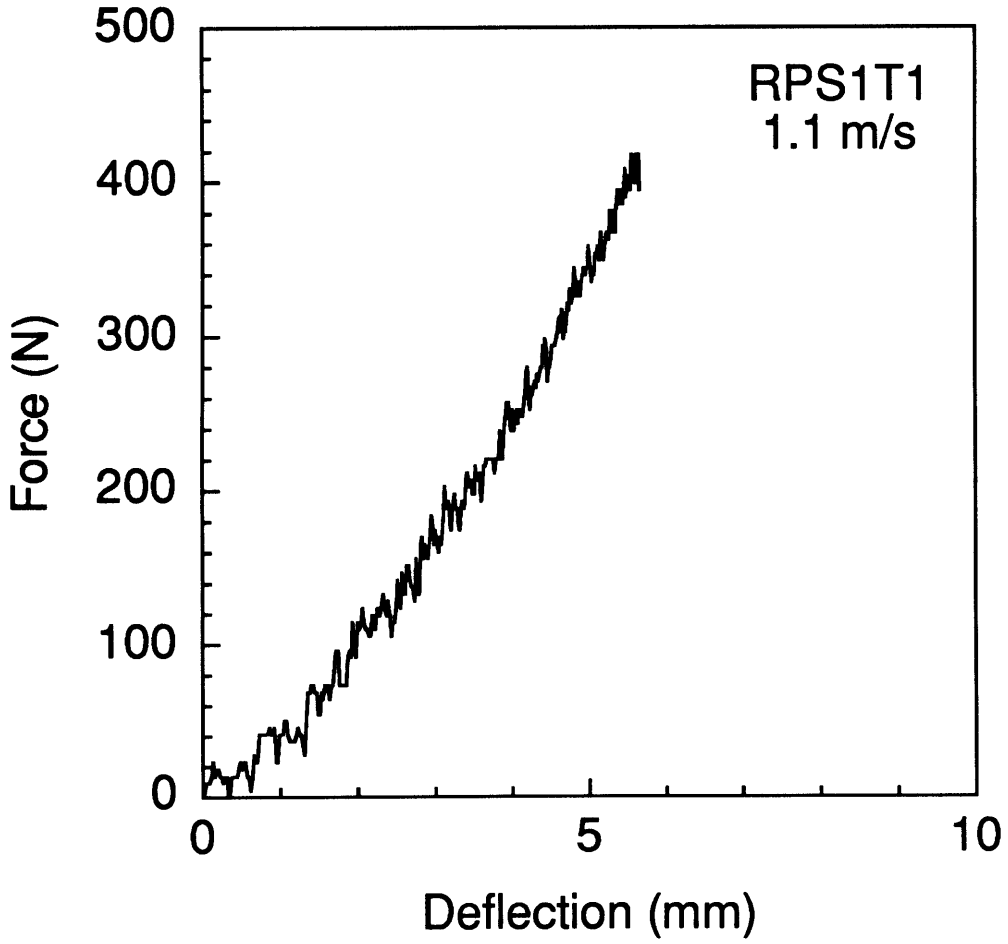

Figure C.56 Force-deflection response of specimen RPS1T1 impacted at 1.1 m/s.

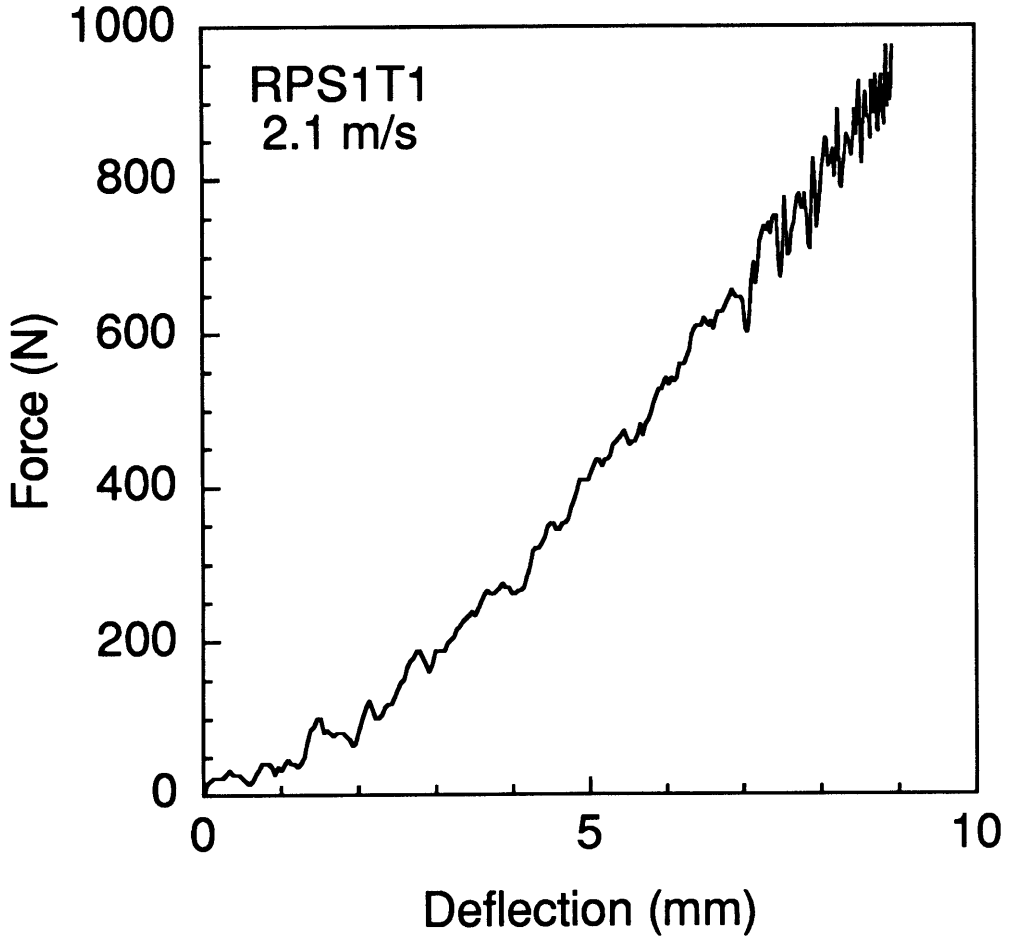

Figure C.57 Force-deflection response of specimen RPS1T1 impacted at 2.1 m/s.

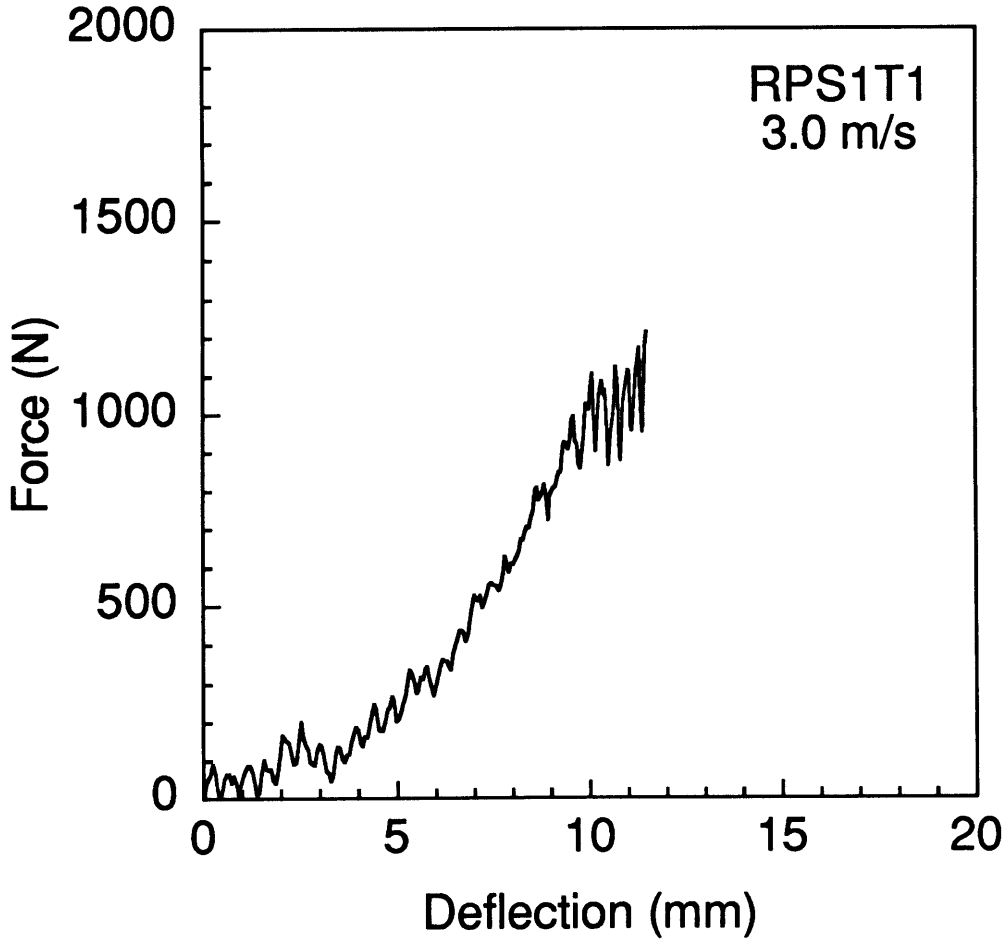

Figure C.58 Force-deflection response of specimen RPS1T1 impacted at 3.0 m/s. This specimen was penetrated during testing.

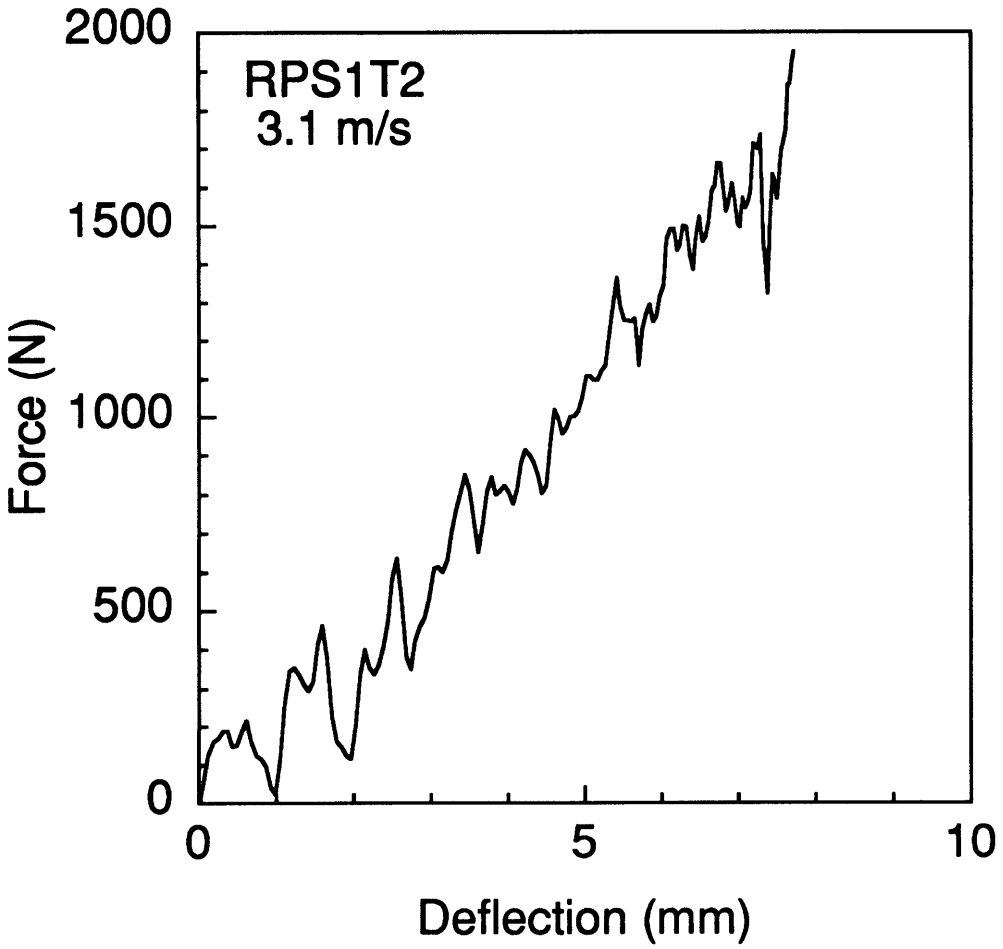

Figure C.59 Force-deflection response of specimen RPS1T2 impacted at 3.1 m/s.

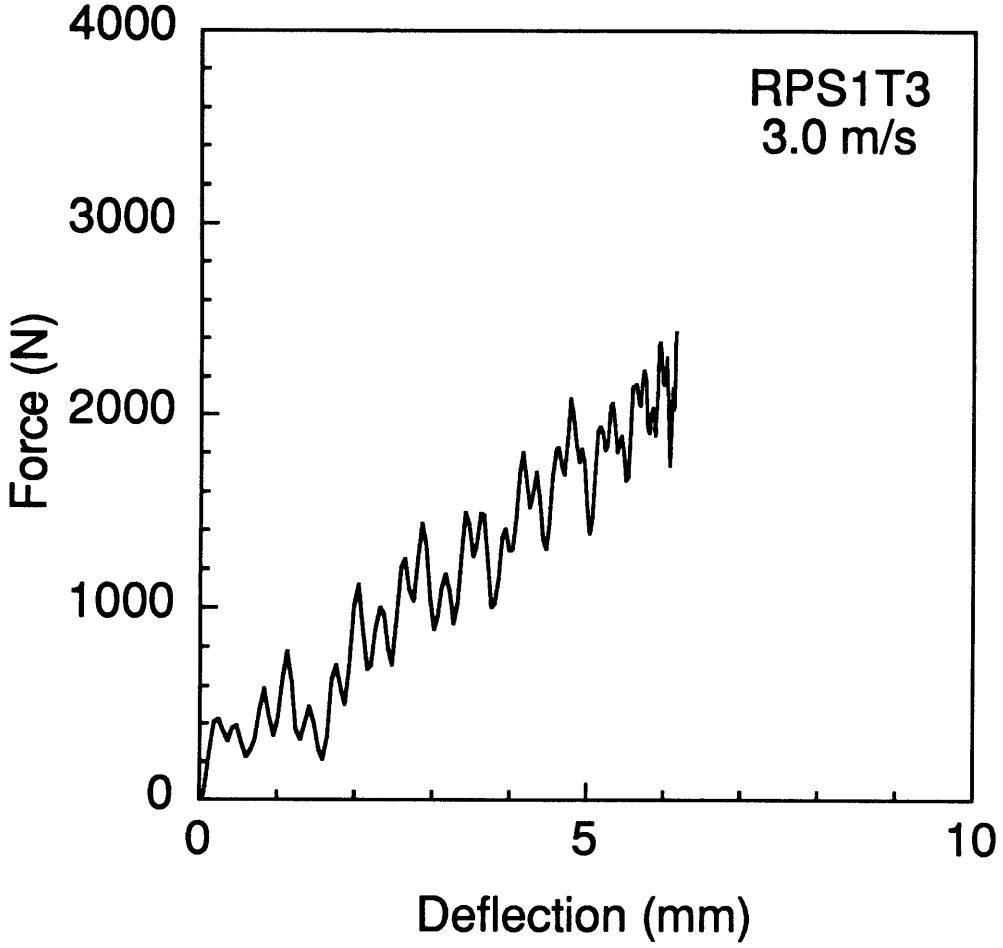

Figure C.60 Force-deflection response of specimen RPS1T3 impacted at 3.0 m/s.

Appendix D

Damage Data for Impact Tests

Data from visual and x-ray photography damage evaluation for impacted specimens is presented in Table D.1. The damage metrics in Table D.1 are explained in chapter 5. Visual damage data is provided for both the front (impact side) and back surface of the specimens. As described in chapter 5, damage lengths in the axial and circumferential shell directions of the elliptical marred region that is observed where the impactor contacted the specimen are used as damage metrics for front-surface damage. An elliptical area based on the damage lengths in the circumferential and axial directions is also calculated for each specimen. Matrix split lengths are used as the metric for the back-surface damage. The length of each observed matrix split is given in Table D.1. Delamination of the back surface is observed for some specimens to occur between matrix splits; this is indicated by enclosing the matrix split lengths in parentheses. X-ray photography damage length data along the 45° and -45° directions is presented for all specimens as well as the average and ratio of the -45° to 45° lengths. As noted in chapter 5, three specimens are known to have slipped in-plane during impact testing. Slipping is indicated by underlining in Table D.1.

Table D.1 Data[a] from Visual and X-ray Photography Damage Evaluation for Impact Tests

		Visual Damage Data							
		Front Surface			Back Surface	X-ray Photography Data			
Specimen[b]	Test Velocity[c]	Axial Length (mm)	Circumferential Length (mm)	Elliptic Area (mm^2)	Matrix Split Lengths (mm)	45° Length (mm)	-45° Length (mm)	Average (mm)	Ratio -45°/45°
R1S1T1	1.0	0	0	0	0	0	0	0	-
R1S1T1	2.1	0	0	0	0	0	0	0	-
R1S1T1	*3.0*	*4*	*5*	*16*	*10*	*21*	*5*	*13*	*0.24*
R1S1T1	***3.9***	***14***	***13***	***143***	***penetration***	-	-	***penetration***	-
R1S1T1c	1.1	0	0	0	0	7	5	6	0.71
R1S1T1c	2.0	8	11	69	50, 50, 50, 50	27	11	19	0.41
R1S1T1c	**3.0**	**12**	**14**	**132**	**penetration**	-	-	**penetration**	-
R1S1T2	2.9	5	5	20	60, 50, 40	70	60	65	0.86
R1S1T2c	2.9	5	4	16	20	26	10	18	0.38
R1S1T3	2.9	6	4	19	80, 20	70	60	65	0.86
R1S1T3c	3.0	4	4	13	30	27	12	20	0.44
R1S2T1	1.0	0	0	0	0	0	0	0	-
R1S2T1	1.9	0	0	0	0	0	0	0	-
R1S2T1	2.9	3	2	5	0	0	0	0	-
R1S2T1	4.0	2	3	5	0	0	0	0	-
R1S3T1	1.1	0	0	0	0	0	0	0	-
R1S3T1	2.0	1	2	2	0	0	0	0	-
R1S3T1	3.1	1	2	2	0	0	0	0	-
R1S3T1	4.1	2	2	3	0	0	0	0	-
R1SCT1	1.1	1	1	1	0	0	0	0	-
R1SCT1	2.0	1	1	1	0	0	0	0	-
R1SCT1	3.1	2	2	3	0	0	0	0	-
R1SCT1	4.1	2	2	3	0	0	0	0	-
R2S1T1	1.1	2	2	3	0	0	0	0	-
R2S1T1	*2.0*	*3*	*2*	*5*	*10*	*14*	*5*	*10*	*0.36*
R2S1T1	*2.9*	*7*	*7*	*39*	*(30, 40)*	*50*	*10*	*30*	*0.20*
R2S1T1	***3.8***	***13***	***15***	***153***	***penetration***	-	-	***penetration***	-

Table D.1 Data[a] from Visual and X-ray Photography Damage Evaluation for Impact Tests (continued-2)

Specimen[b]	Test Velocity[c]	Visual Damage Data: Front Surface: Axial Length (mm)	Front Surface: Circumferential Length (mm)	Front Surface: Elliptic Area (mm^2)	Back Surface: Matrix Split Lengths (mm)	X-ray Photography Data: 45° Length (mm)	-45° Length (mm)	Average (mm)	Ratio -45°/45°
R2S1T1c	**3.1**	**13**	**15**	**153**	**penetration**	-	-	**penetration**	-
R2S1T2	1.1	0	0	0	0	10	5	8	0.50
R2S1T2	2.1	2	2	3	0	11	11	11	1.00
R2S1T2	*3.2*	*3*	*4*	*10*	*40, 30, 20*	*31*	*11*	*21*	*0.35*
R2S1T2	*3.9*	*4*	*4*	*13*	*40*	*37*	*10*	*24*	*0.27*
R2S1T2c	3.0	7	5	28	30, 10	40	13	27	0.33
R2S1T3	2.8	3	3	7	50	55	30	43	0.55
R2S2T1	*2.9*	*2*	*4*	*6*	*10*	*9*	*5*	*7*	*0.56*
R2S2T2	2.9	3	2	5	0	21	9	15	0.43
R2S2T3	2.9	3	2	5	40, 30, 30, 20	70	40	55	0.57
R2S3T1	*3.1*	*2*	*3*	*5*	*0*	*0*	*0*	*0*	-
R2S3T2	3.0	2	2	3	0	16	10	13	0.63
R3S1T1	*1.0*	*0*	*0*	*0*	*0*	*0*	*0*	*0*	-
R3S1T1	*1.9*	*4*	*4*	*13*	*20*	*16*	*4*	*10*	*0.25*
R3S1T1	***2.9***	***3***	***4***	***10***	***20***	***16***	***6***	***11***	***0.38***
R3S1T1	***4.0***	***10***	***11***	***87***	***penetration***	-	-	***penetration***	-
R3S1T1c	**3.0**	**12**	**15**	**141**	**penetration**	-	-	**penetration**	-
R3S1T2	*3.0*	*3*	*3*	*7*	*30*	*38*	*10*	*24*	*0.26*
R3S1T3	1.0	0	0	0	0	0	0	0	-
R3S1T3	2.0	0	0	0	30	15	8	12	0.53
R3S1T3	3.0	0	0	0	40	15	13	14	0.87
R3S1T3	4.0	6	5	24	90, 50	80	17	49	0.21
R3S1T3c	3.0	4	3	10	40	30	20	25	0.67
R3S2T1	*3.0*	*8*	*7*	*44*	*(50, 40) 30, 30, 20, 10*	*57*	*10*	*34*	*0.18*
R3S2T3	3.0	2	4	6	0	25	14	20	0.56
R3S3T1	*3.0*	*2*	*3*	*5*	*20*	*10*	*6*	*8*	*0.60*
R3S3T2	3.0	2	2	3	0	15	10	13	0.67

Table D.1 Data[a] from Visual and X-ray Photography Damage Evaluation for Impact Tests (continued-3)

		Visual Damage Data							
		Front Surface			Back Surface	X-ray Photography Data			
Specimen[b]	Test Velocity[c]	Axial Length (mm)	Circumferential Length (mm)	Elliptic Area (mm^2)	Matrix Split Lengths (mm)	45° Length (mm)	-45° Length (mm)	Average (mm)	Ratio -45°/45°
R3S3T3	3.1	0	0	0	40	23	13	18	0.57
RPS1T1	1.1	0	0	0	0	5	1	3	0.20
RPS1T1	2.1	4	4	13	20	12	4	8	0.33
RPS1T1	**3.0**	**13**	**15**	**153**	**penetration**	-	-	**penetration**	-
RPS1T2	3.1	7	6	33	(70, 40)	44	12	28	0.27
RPS1T3	3.0	5	3	12	50	41	17	29	0.41

[a] *Italics* indicate peak force occurred on the second equilibrium path (instability), underline indicates specimen slipped in-plane after instability, **bold** indicates penetration, and () indicates delamination is clearly visible between the two matrix splits.

[b] "c" after specimen identification indicates concave test.

[c] Impact velocity in m/s.

Appendix E

Quasi-static Response Data

Quasi-static test data for all specimens is presented in this appendix. The response is comprised of force-deflection histories measured during testing (both loading and unloading paths) and scanned x-ray photographs of the resultant damage state. Axis scales for the force-deflection histories were chosen based on a compromise between showing specifics of each specimen response (smallest scale showing entire specimen response) and allowing the response of different specimens to be compared (one scale for all specimens). Five force scales and six deflection scales were found to provide a reasonable compromise (as in appendix C). Specimens that did not evidence damage in the x-ray photographs are indicated by "No Damage" instead of an x-ray photograph. Specimens that were penetrated during loading were not x-rayed and are indicated by "Penetration Damage".

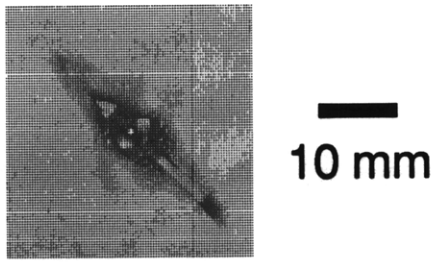

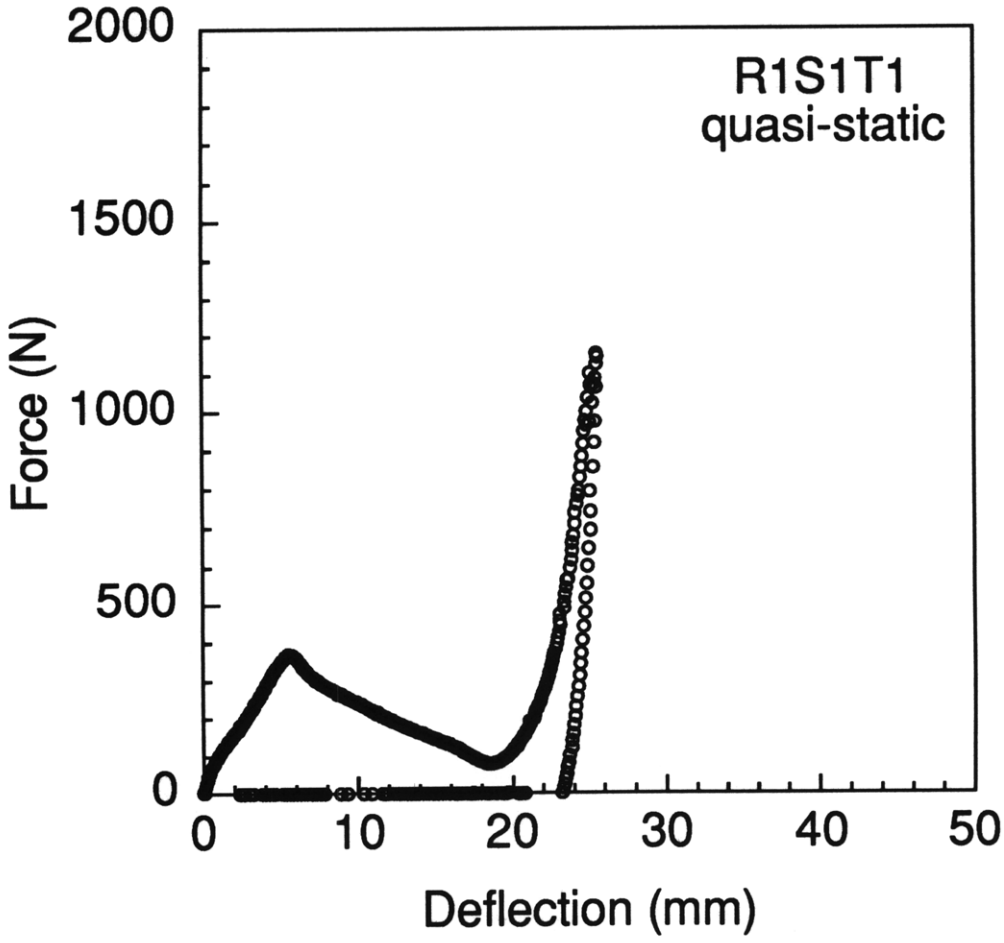

Figure E.1 Results of quasi-static test of specimen R1S1T1: (*top*) x-ray photograph of damage state, and (*bottom*) force-deflection history.

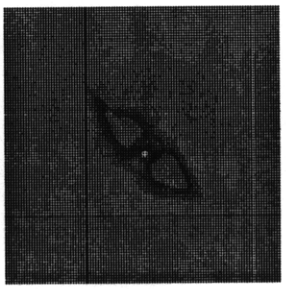

10 mm

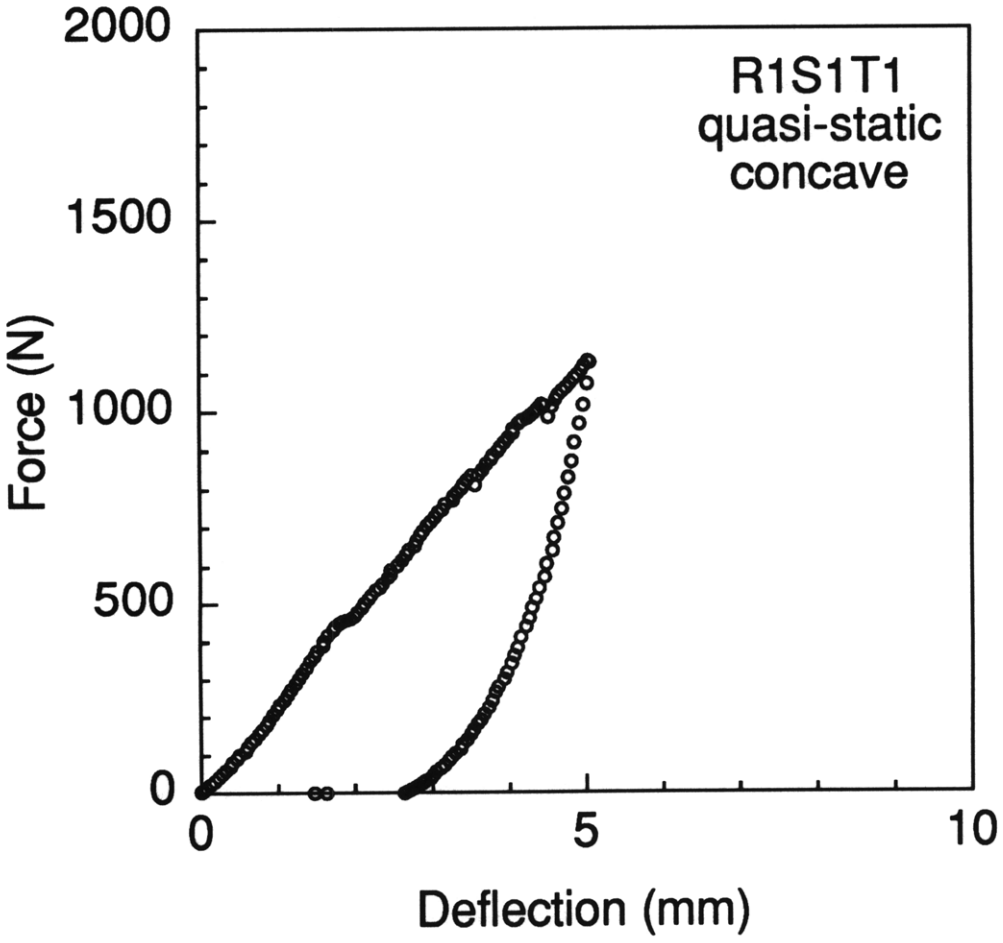

Figure E.2 Results of quasi-static test of specimen R1S1T1 (concave): (*top*) x-ray photograph of damage state, and (*bottom*) force-deflection history.

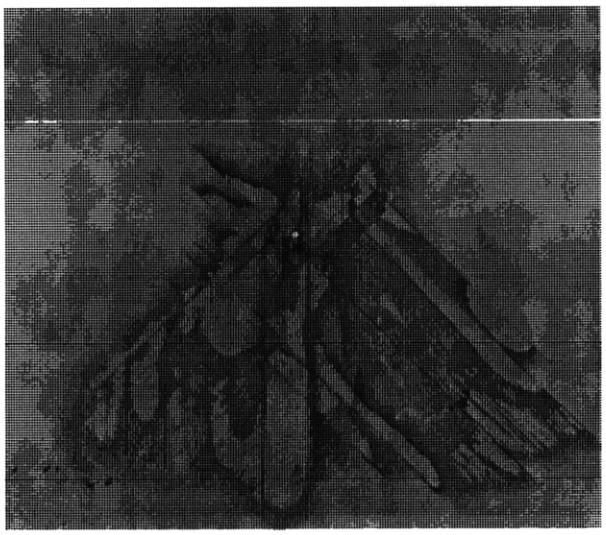

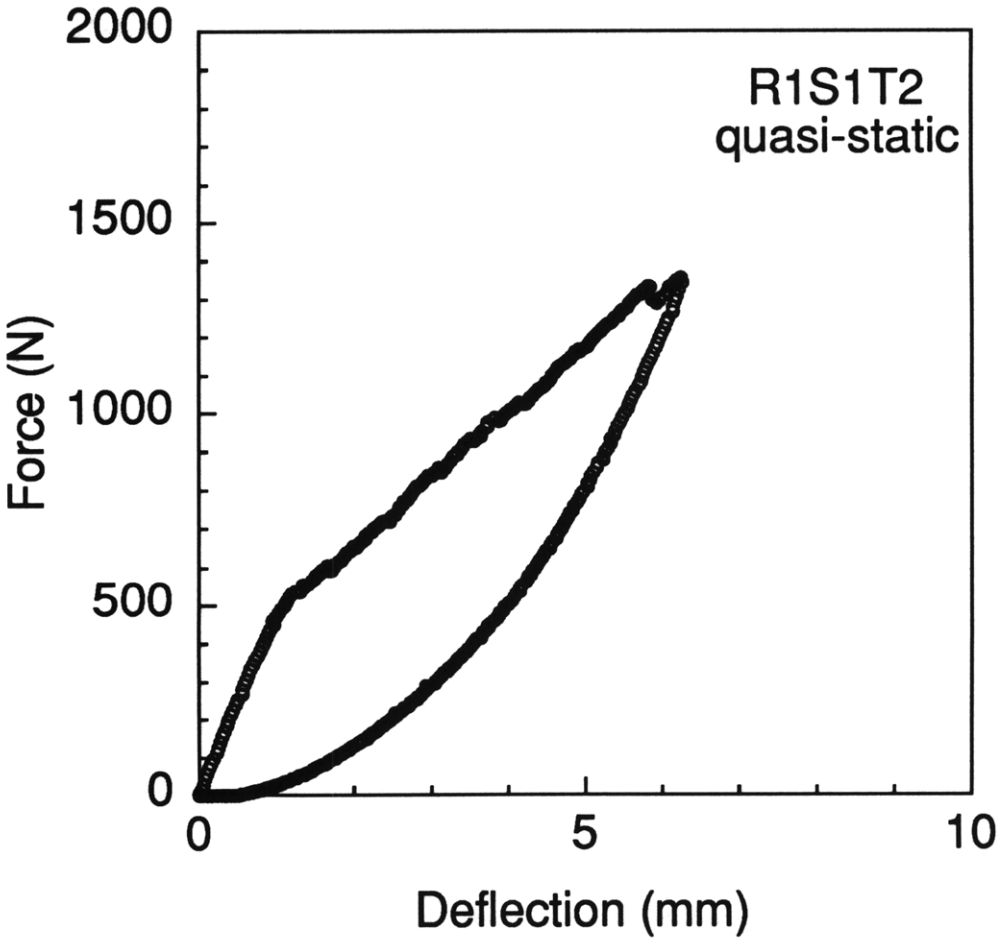

Figure E.3 Results of quasi-static test of specimen R1S1T2: (*top*) x-ray photograph of damage state, and (*bottom*) force-deflection history.

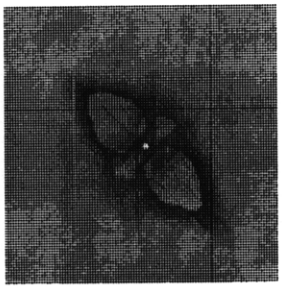

10 mm

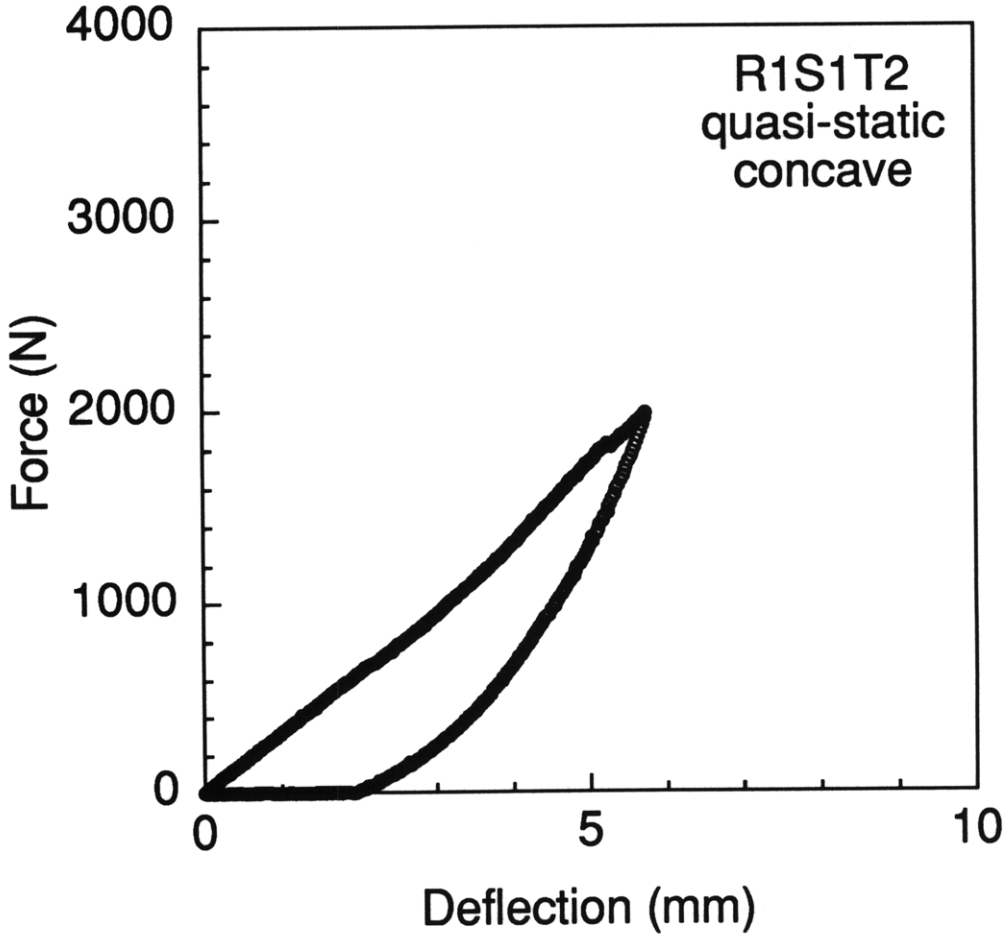

Figure E.4 Results of quasi-static test of specimen R1S1T2 (concave): (*top*) x-ray photograph of damage state, and (*bottom*) force-deflection history.

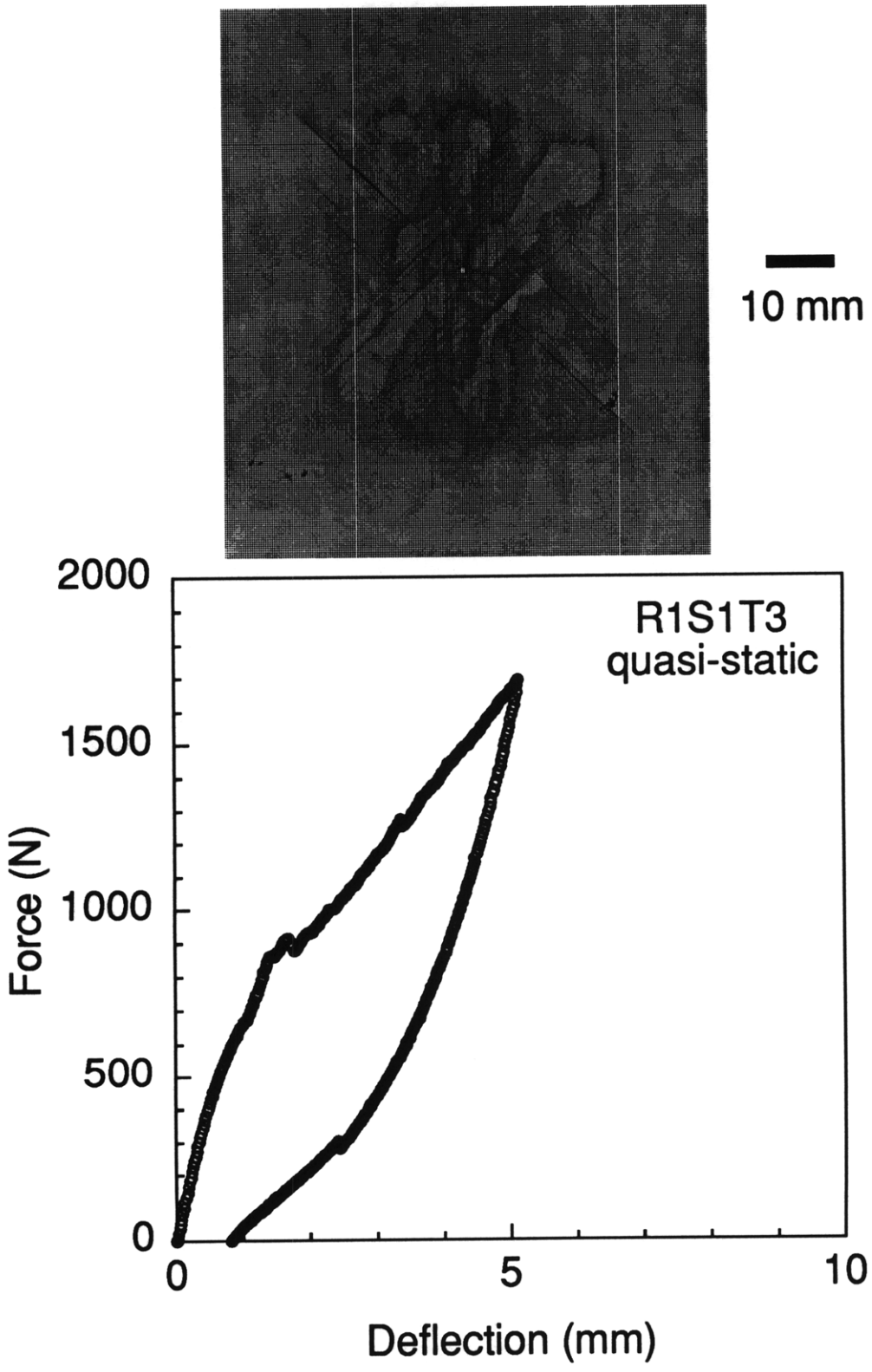

Figure E.5 Results of quasi-static test of specimen R1S1T3: (*top*) x-ray photograph of damage state, and (*bottom*) force-deflection history.

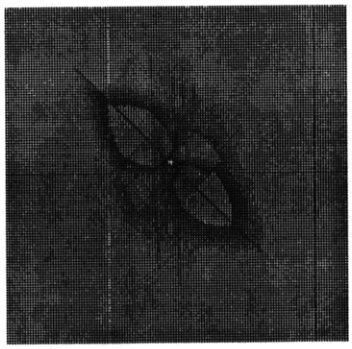

10 mm

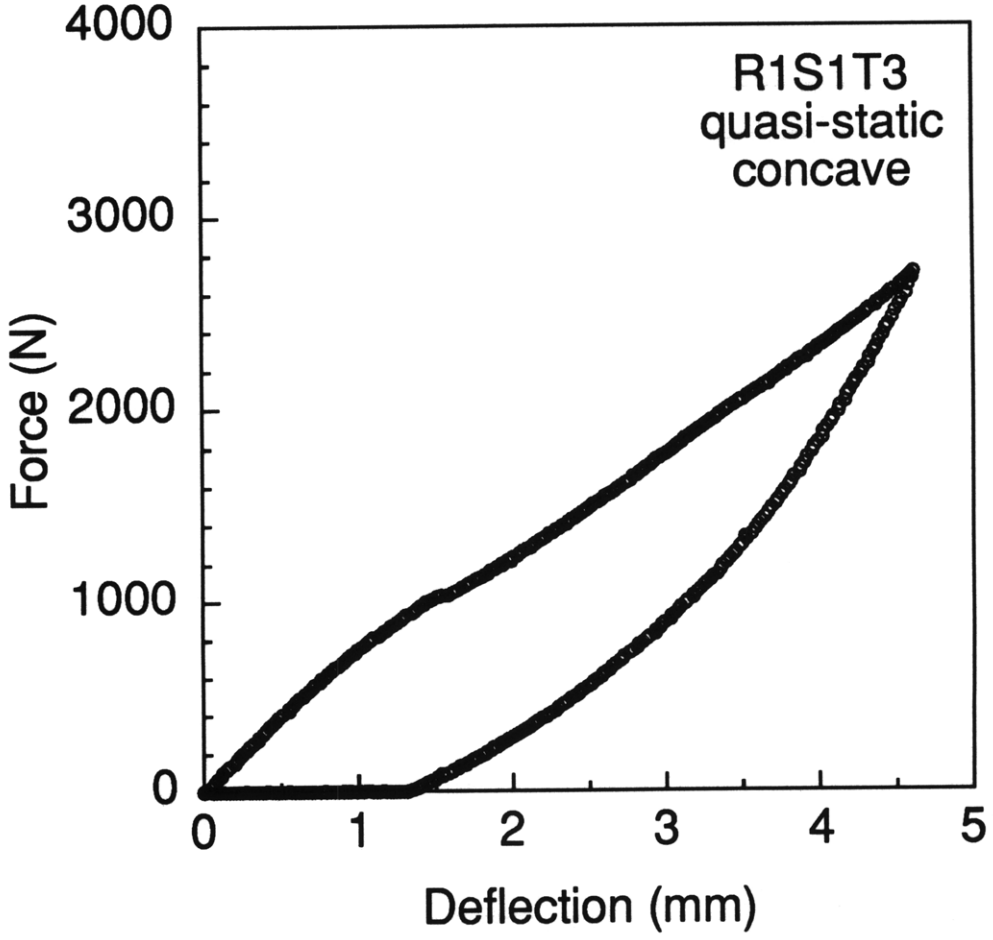

Figure E.6 Results of quasi-static test of specimen R1S1T3 (concave): (*top*) x-ray photograph of damage state, and (*bottom*) force-deflection history.

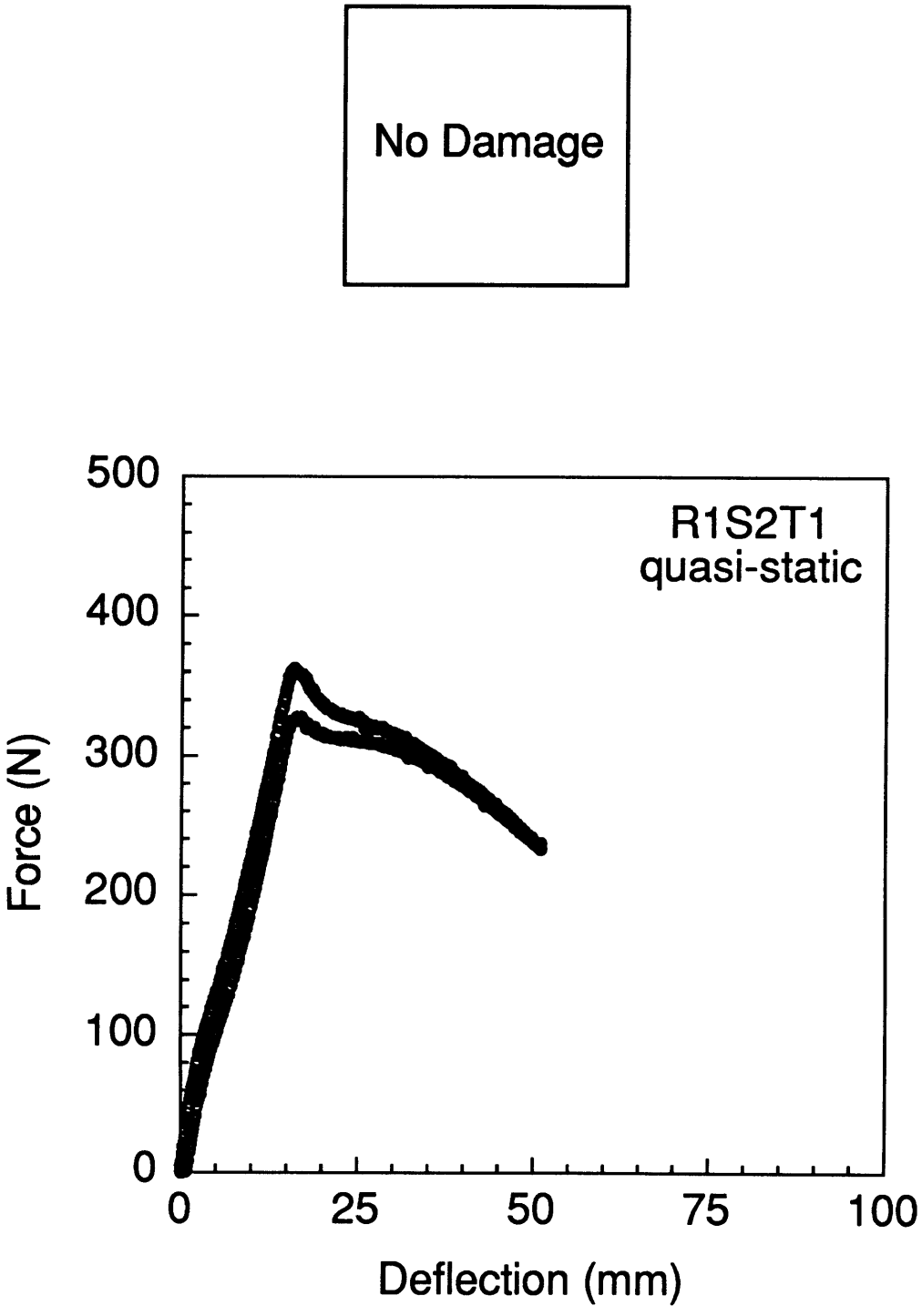

Figure E.7 Results of quasi-static test of specimen R1S2T1: (*top*) no damage is observed in the x-ray photograph, and (*bottom*) force-deflection history.

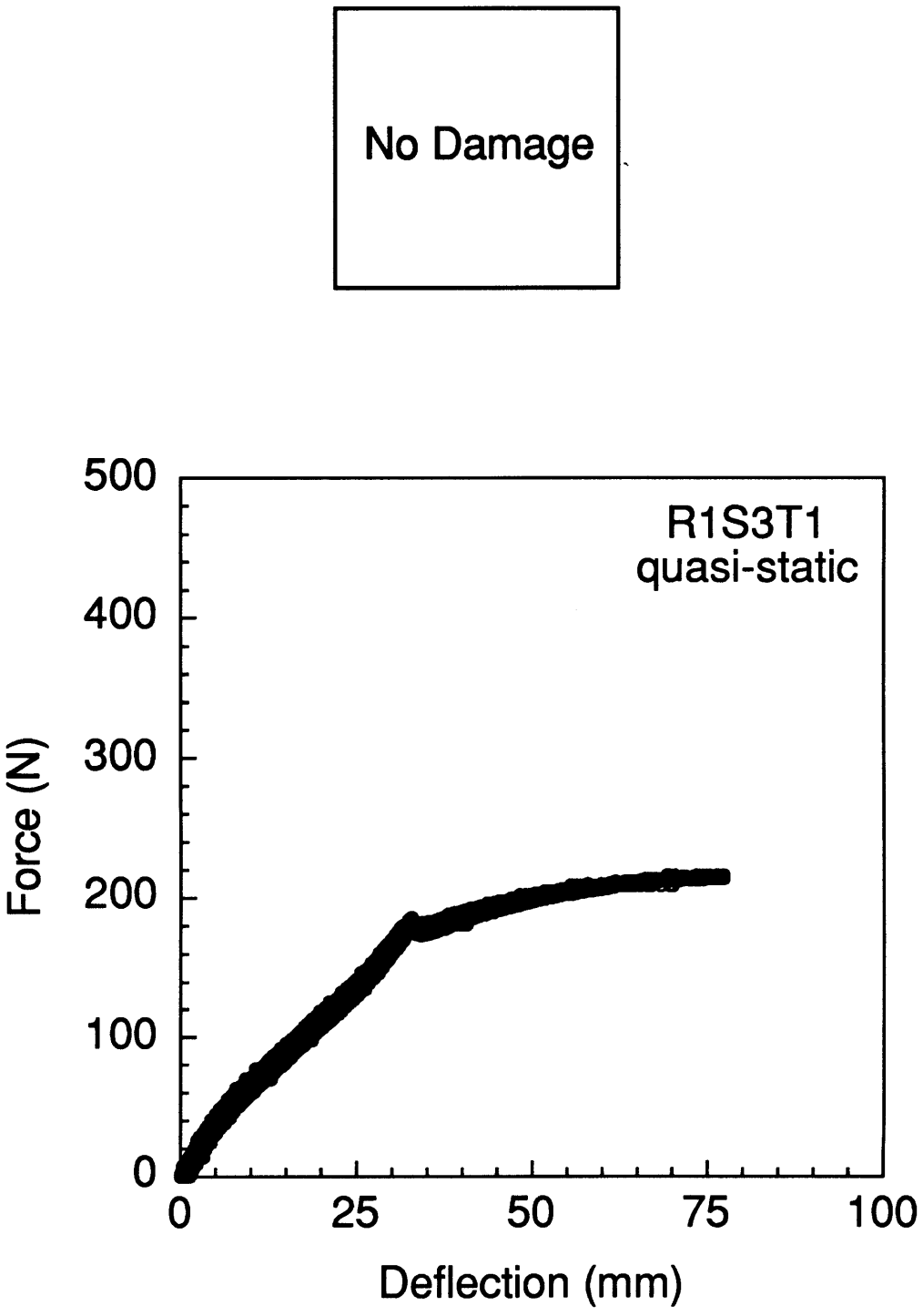

Figure E.8 Results of quasi-static test of specimen R1S3T1: (*top*) no damage is observed in the x-ray photograph, and (*bottom*) force-deflection history.

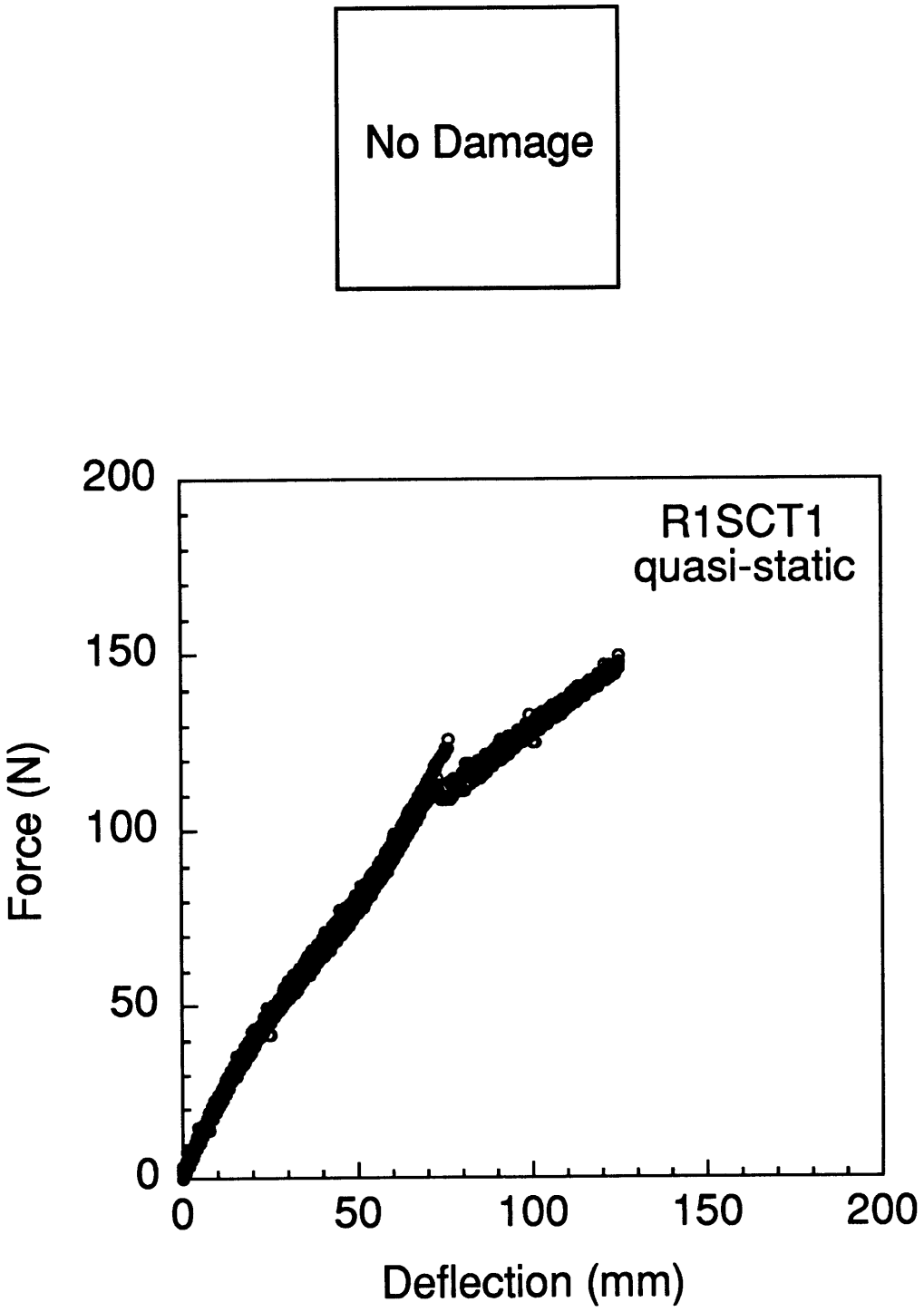

Figure E.9 Results of quasi-static test of specimen R1SCT1: (*top*) no damage is observed in the x-ray photograph, and (*bottom*) force-deflection history.

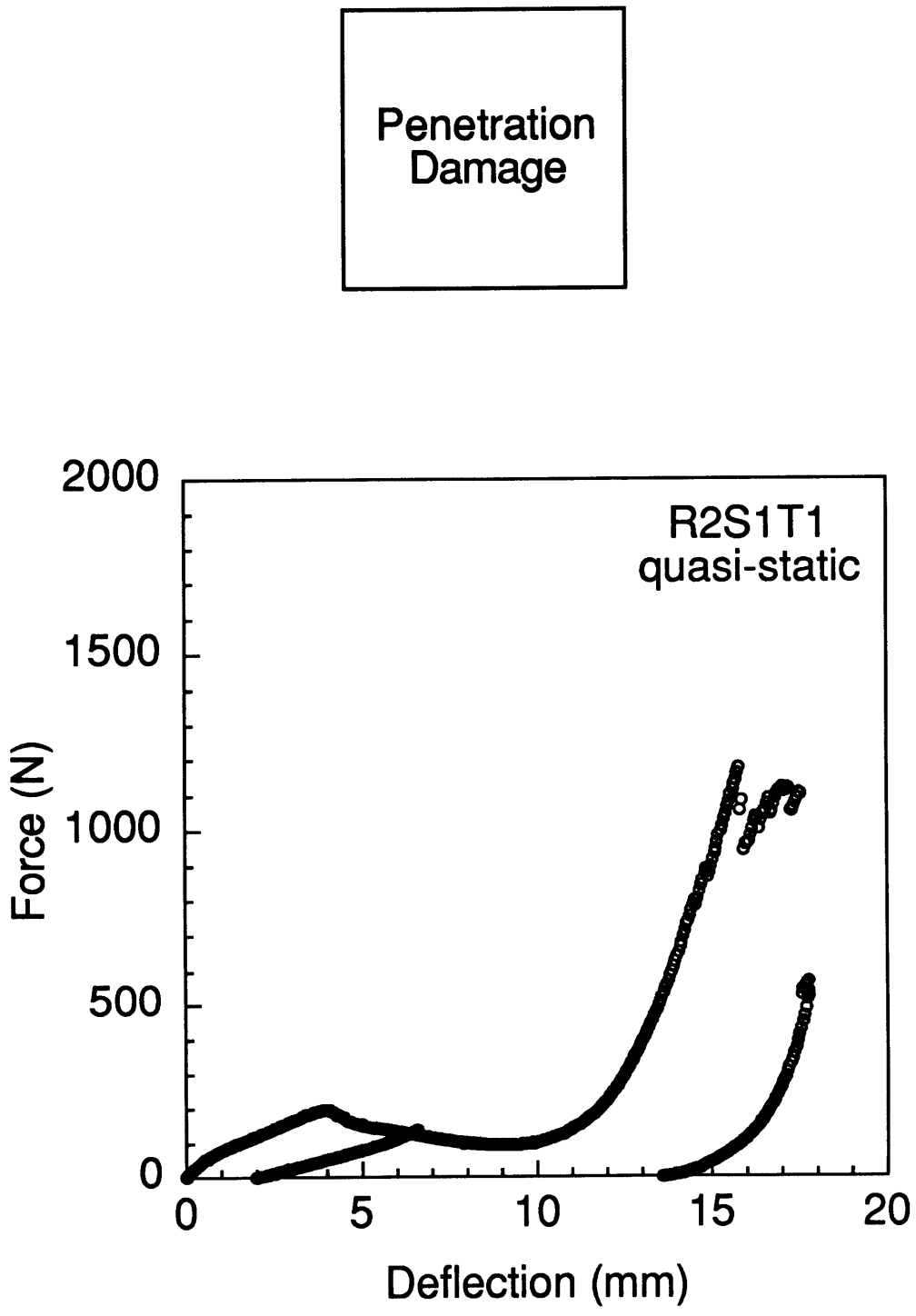

Figure E.10 Results of quasi-static test of specimen R2S1T1: (*top*) penetration damage is observed for this specimen, and (*bottom*) force-deflection history.

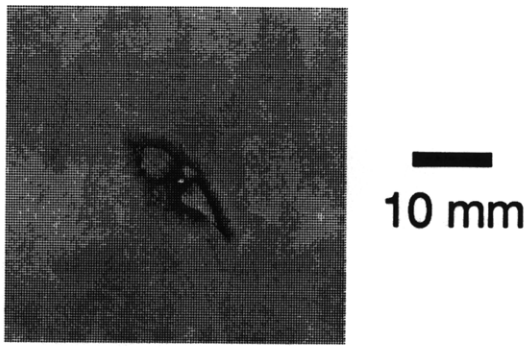

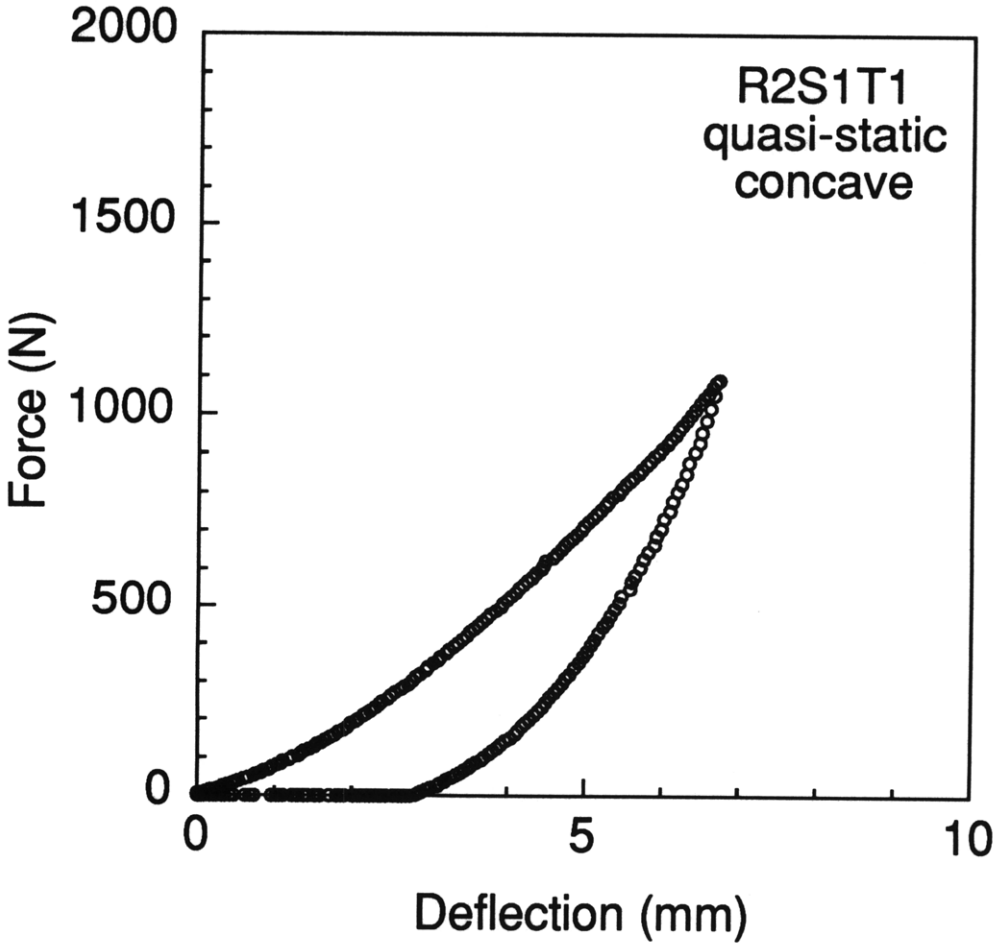

Figure E.11 Results of quasi-static test of specimen R2S1T1 (concave): (*top*) x-ray photograph of damage state, and (*bottom*) force-deflection history.

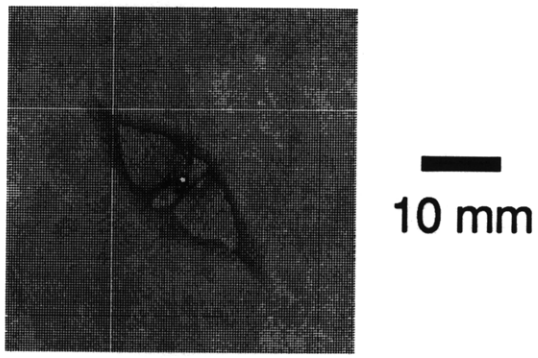

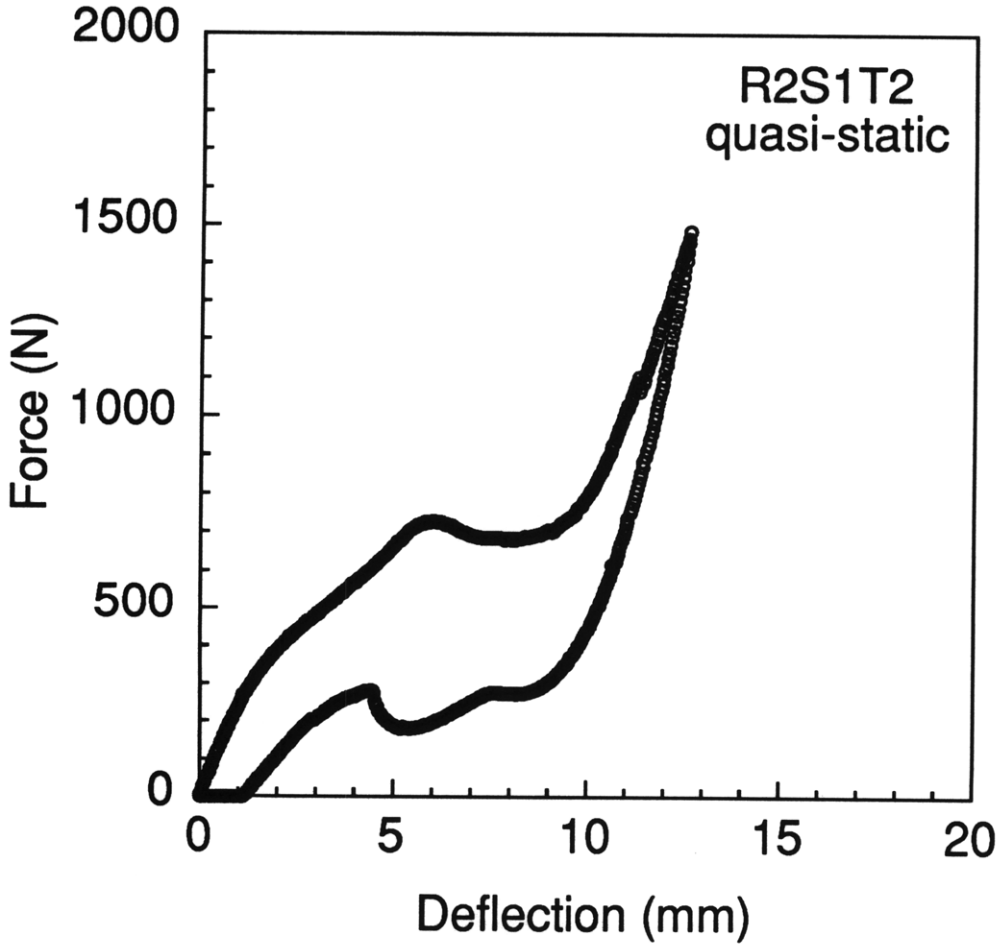

Figure E.12 Results of quasi-static test of specimen R2S1T2: (*top*) x-ray photograph of damage state, and (*bottom*) force-deflection history.

10 mm

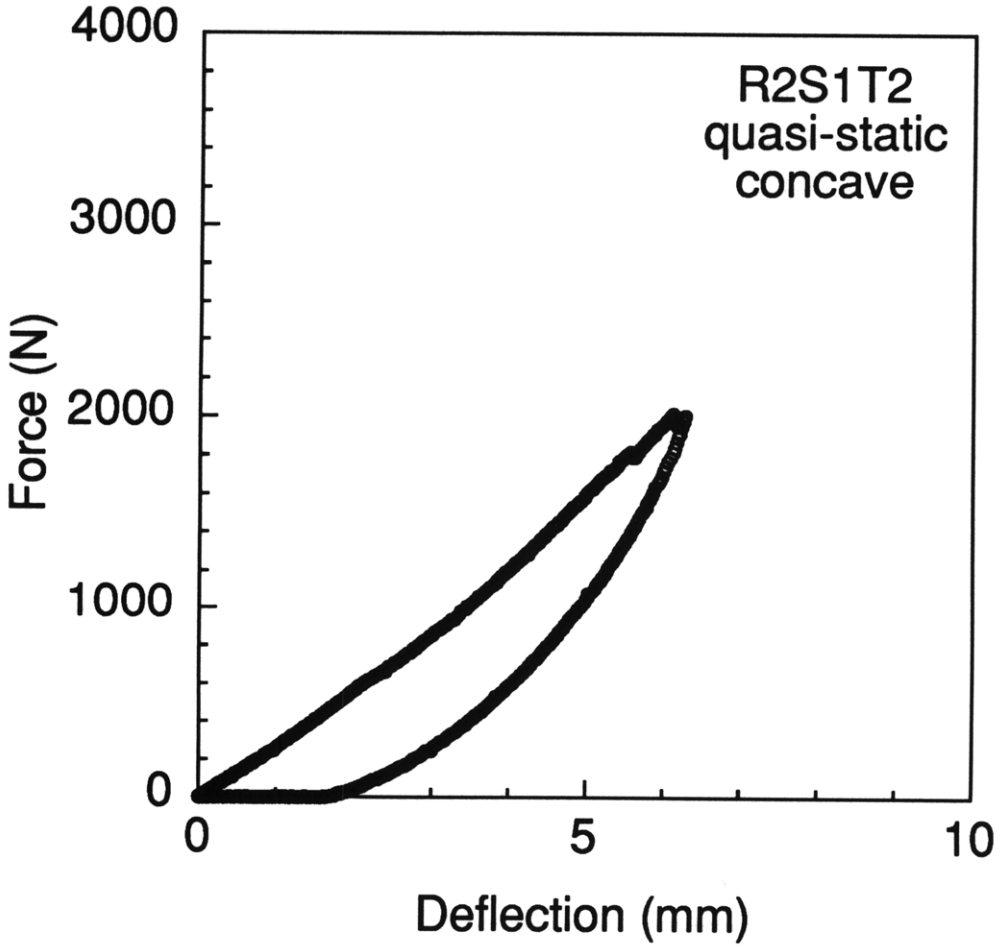

Figure E.13 Results of quasi-static test of specimen R2S1T2 (concave): (*top*) x-ray photograph of damage state, and (*bottom*) force-deflection history.

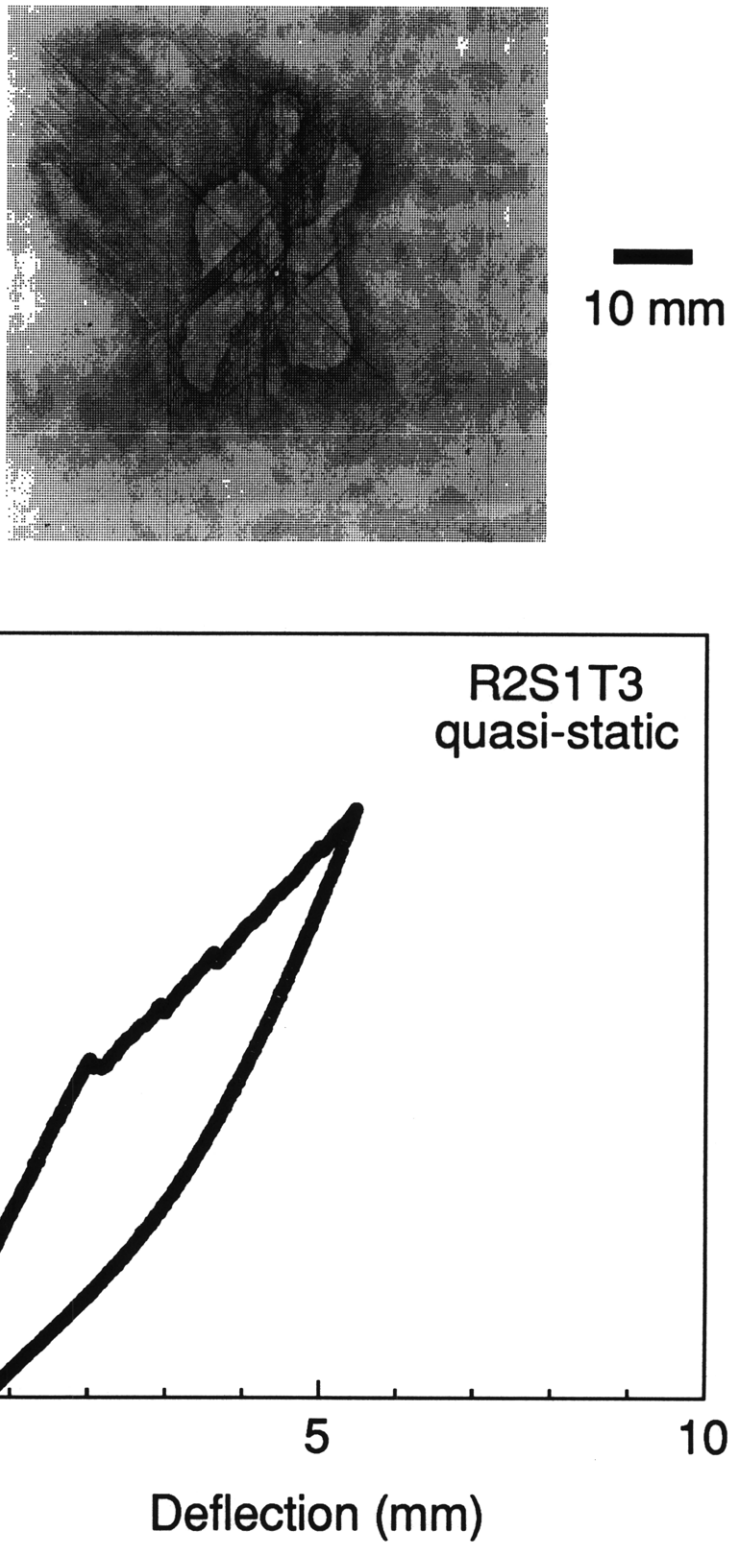

Figure E.14 Results of quasi-static test of specimen R2S1T3: (*top*) x-ray photograph of damage state, and (*bottom*) force-deflection history.

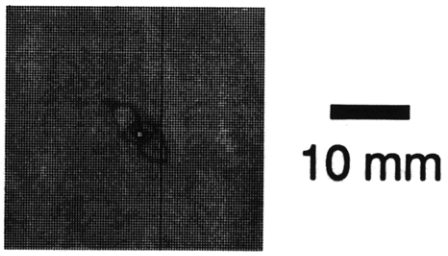

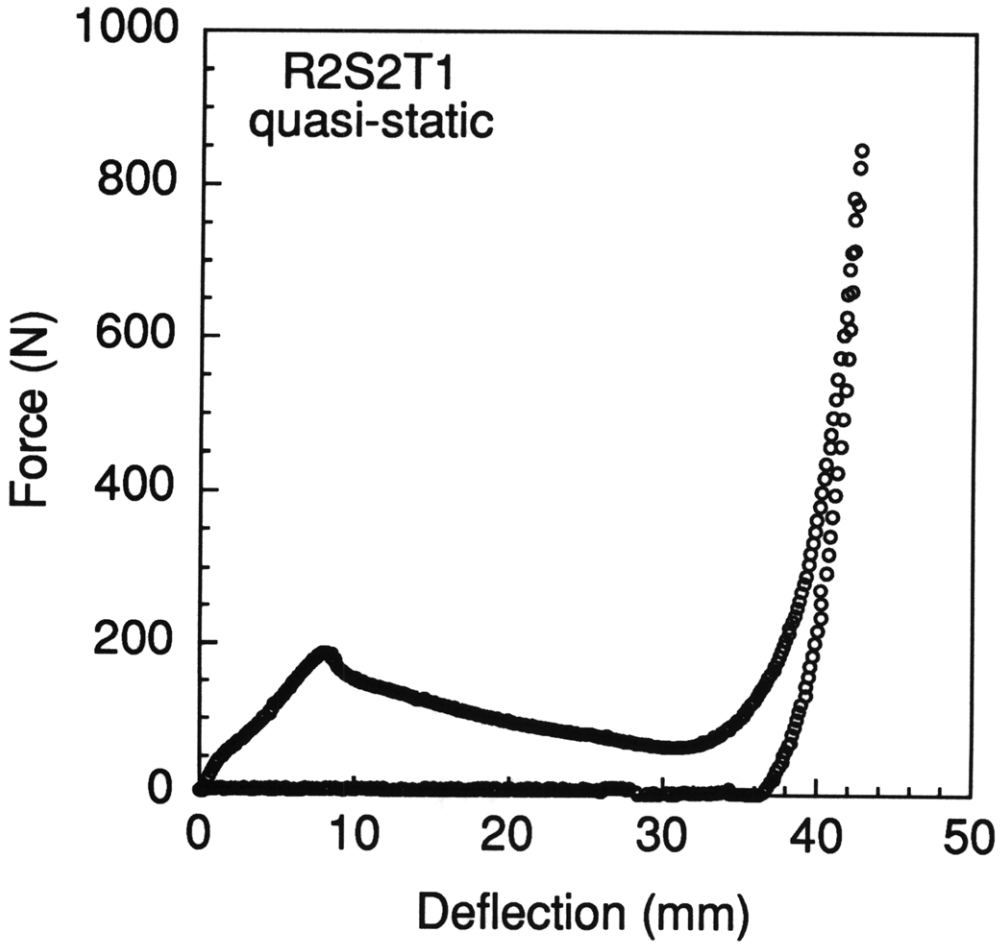

Figure E.15 Results of quasi-static test of specimen R2S2T1: (*top*) x-ray photograph of damage state, and (*bottom*) force-deflection history.

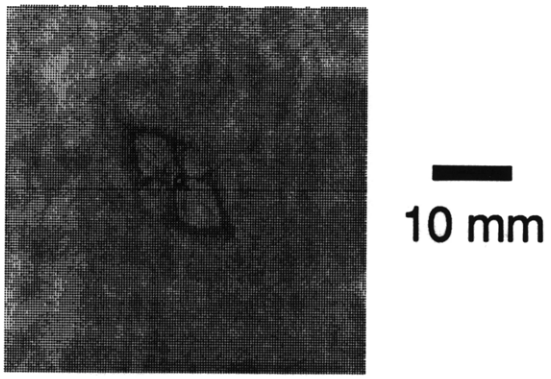

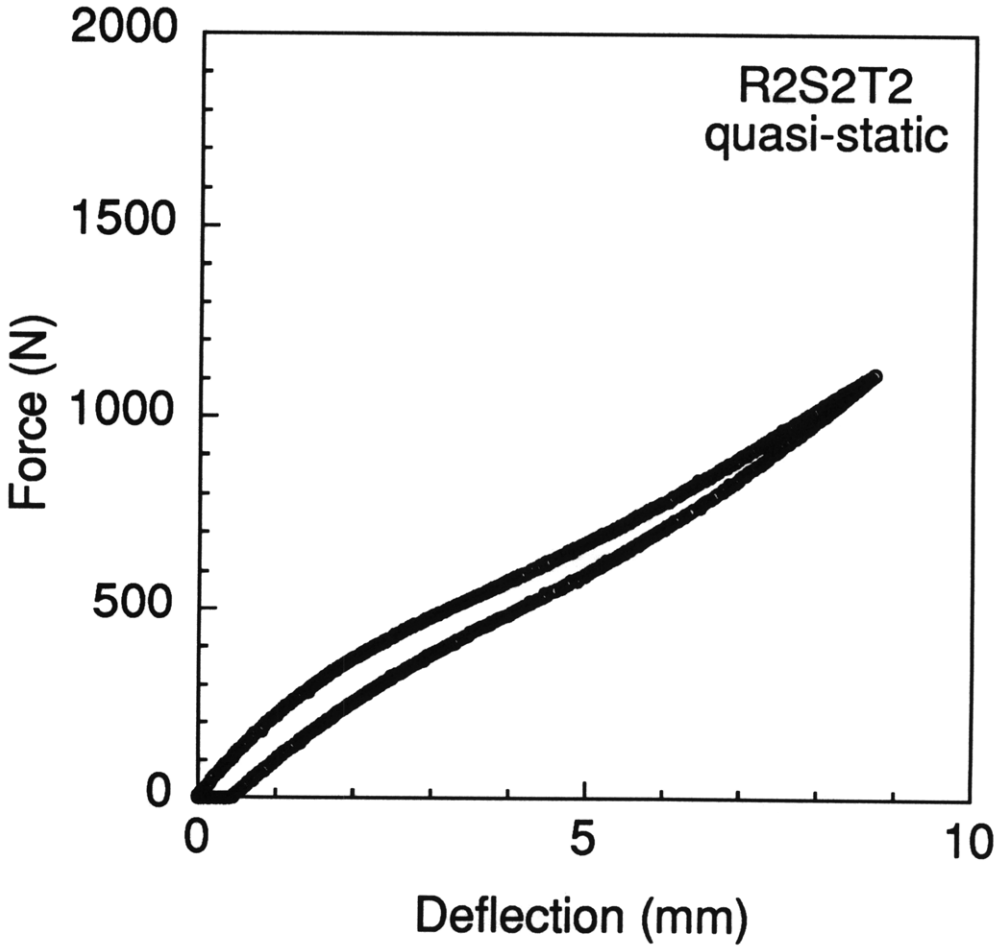

Figure E.16 Results of quasi-static test of specimen R2S2T2: (*top*) x-ray photograph of damage state, and (*bottom*) force-deflection history.

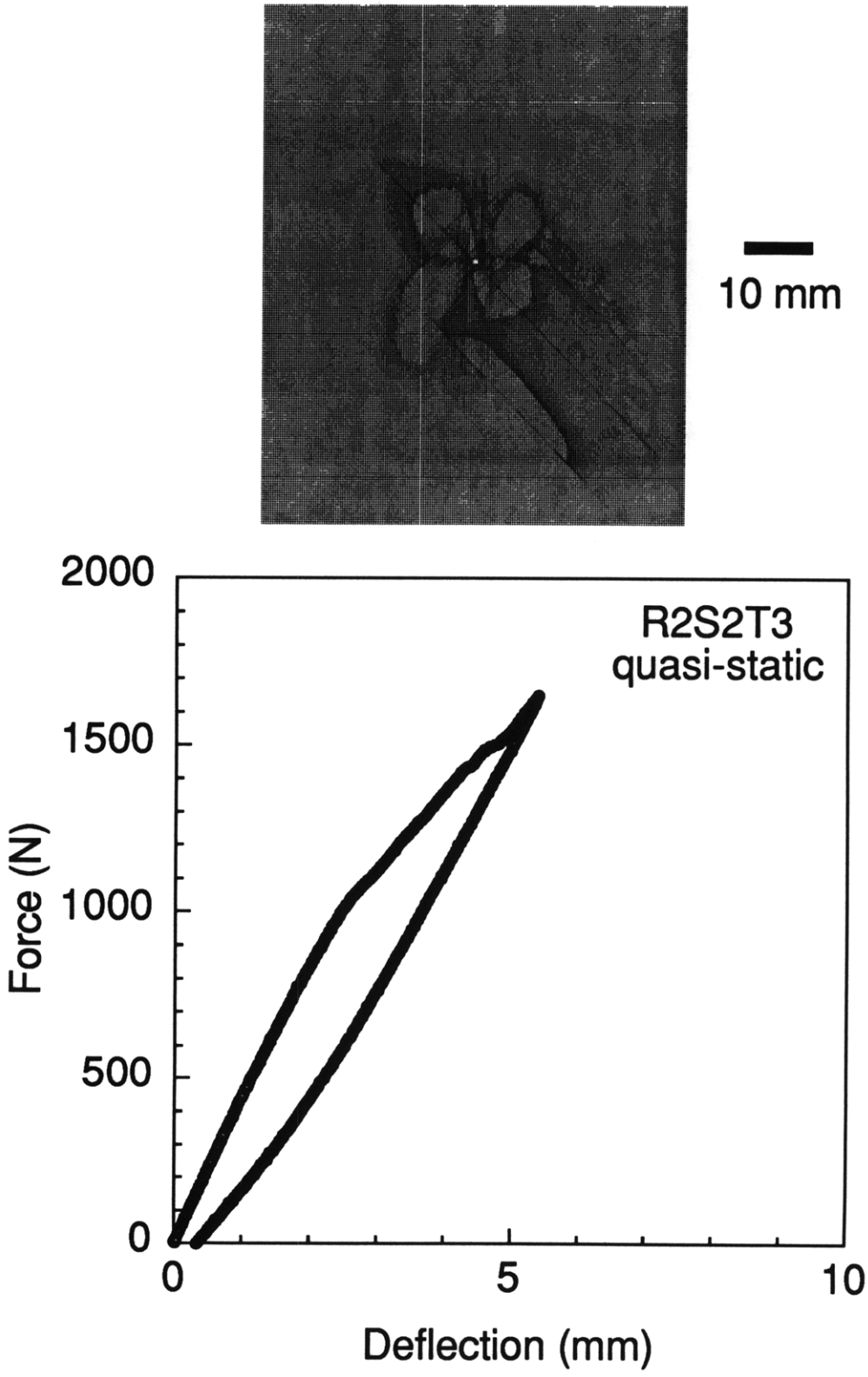

Figure E.17 Results of quasi-static test of specimen R2S2T3: (*top*) x-ray photograph of damage state, and (*bottom*) force-deflection history.

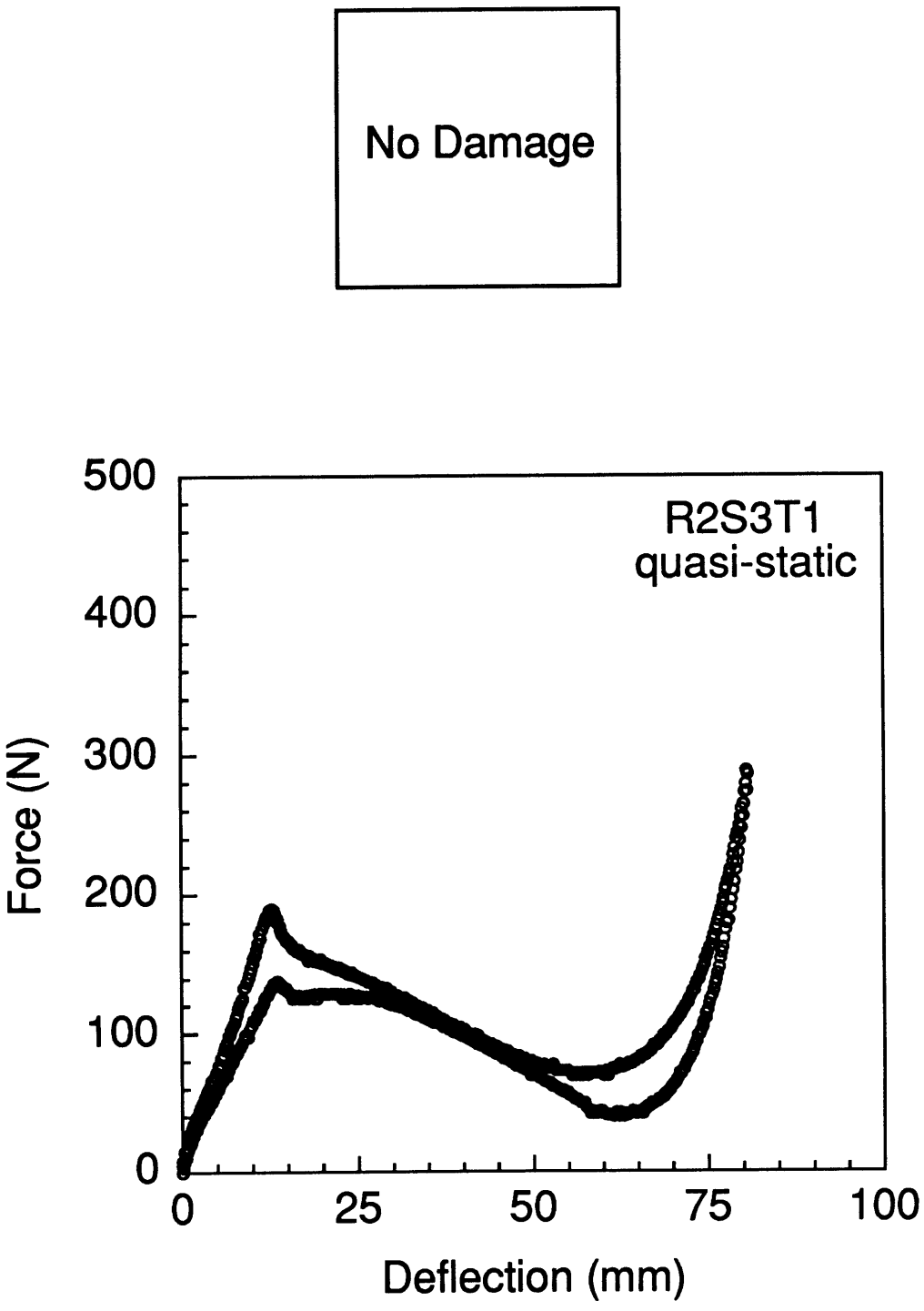

Figure E.18 Results of quasi-static test of specimen R2S3T1: (*top*) no damage is observed in the x-ray photograph, and (*bottom*) force-deflection history.

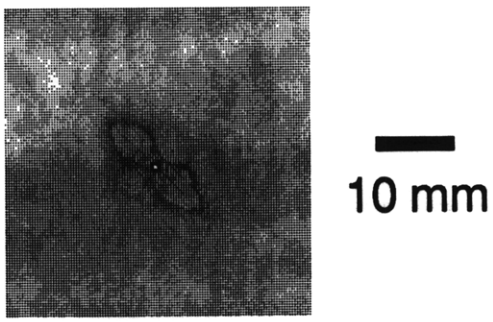

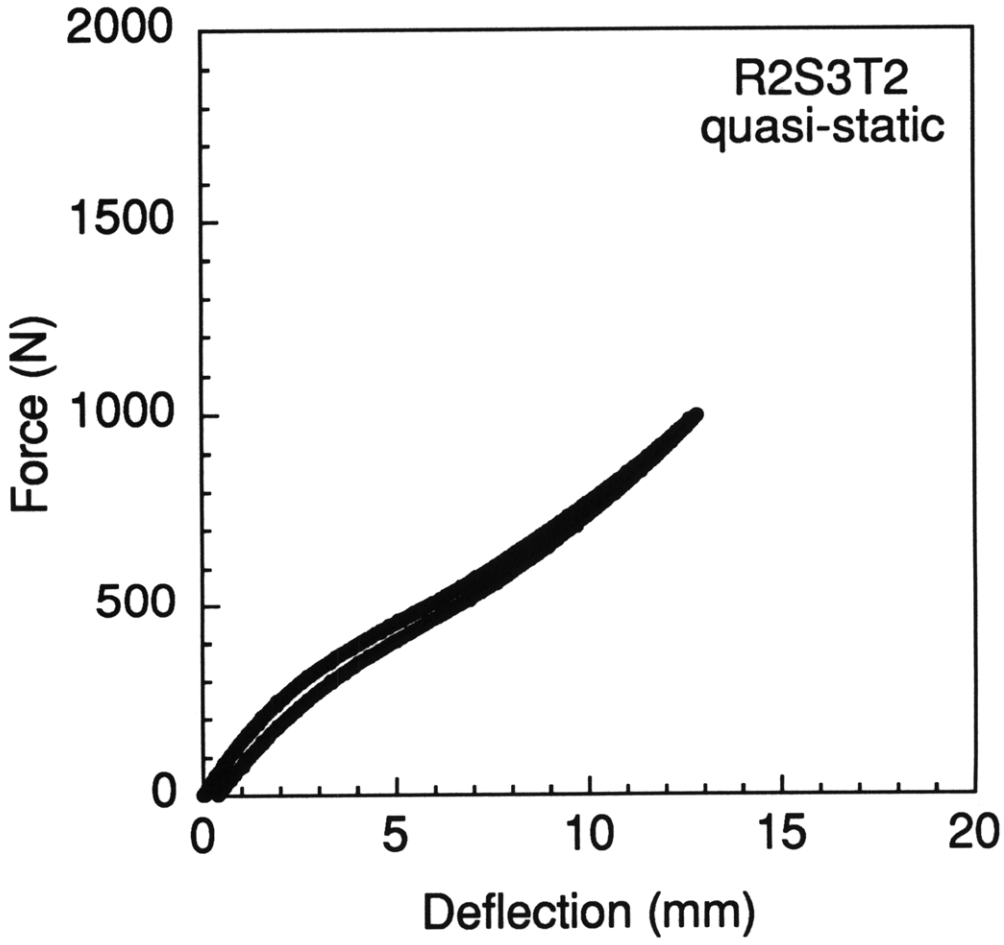

Figure E.19 Results of quasi-static test of specimen R2S3T2: (*top*) x-ray photograph of damage state, and (*bottom*) force-deflection history.

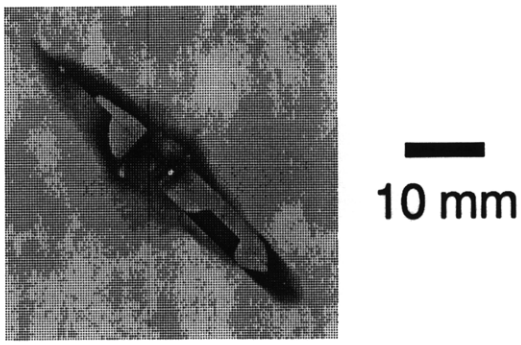

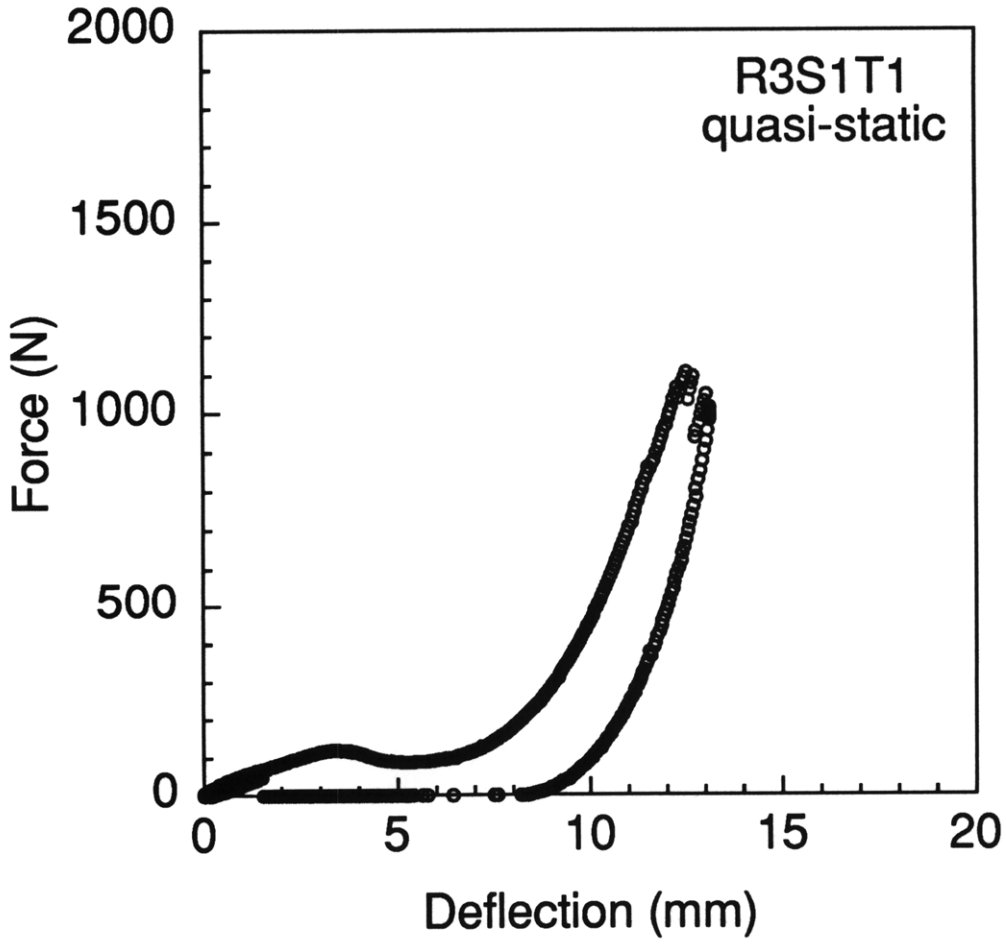

Figure E.20 Results of quasi-static test of specimen R3S1T1: (*top*) x-ray photograph of damage state, and (*bottom*) force-deflection history.

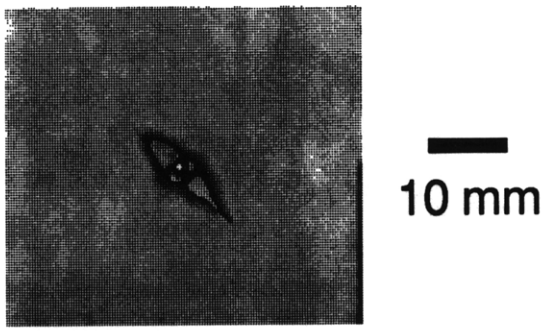

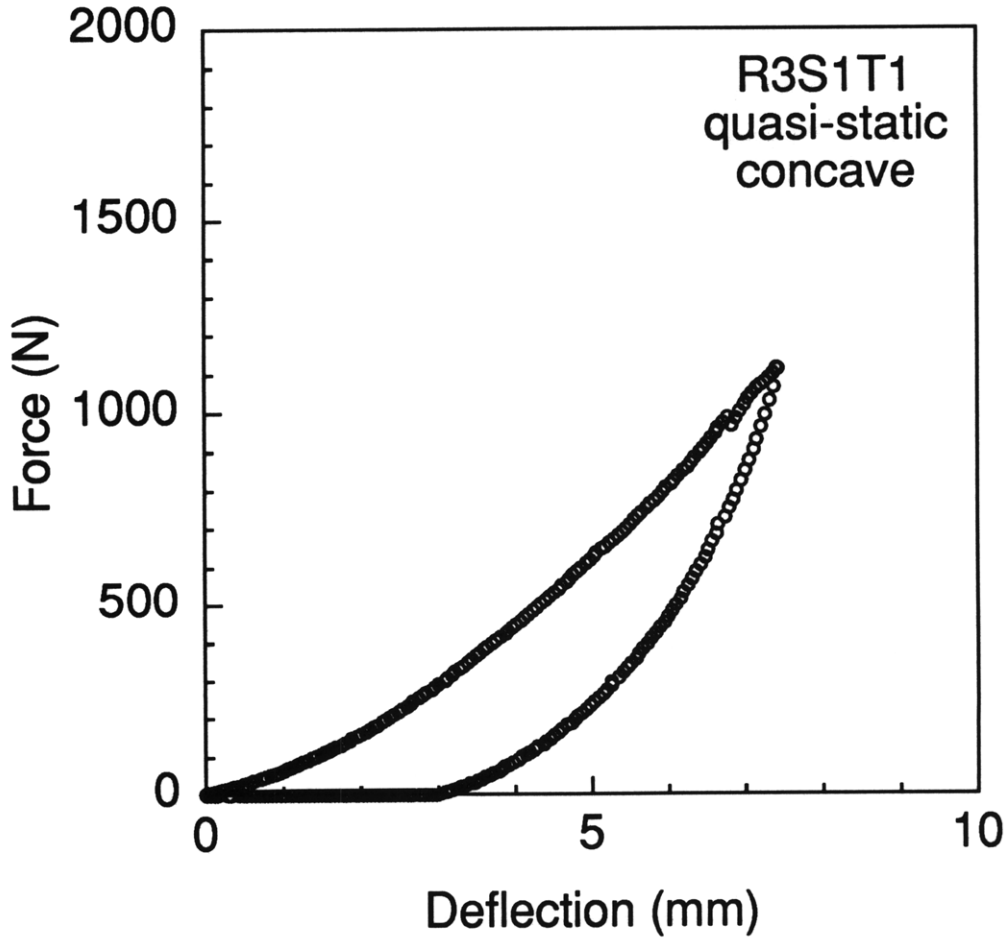

Figure E.21 Results of quasi-static test of specimen R3S1T1 (concave): (*top*) x-ray photograph of damage state, and (*bottom*) force-deflection history.

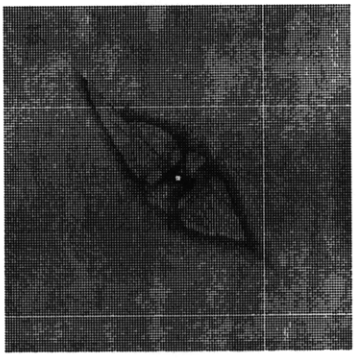

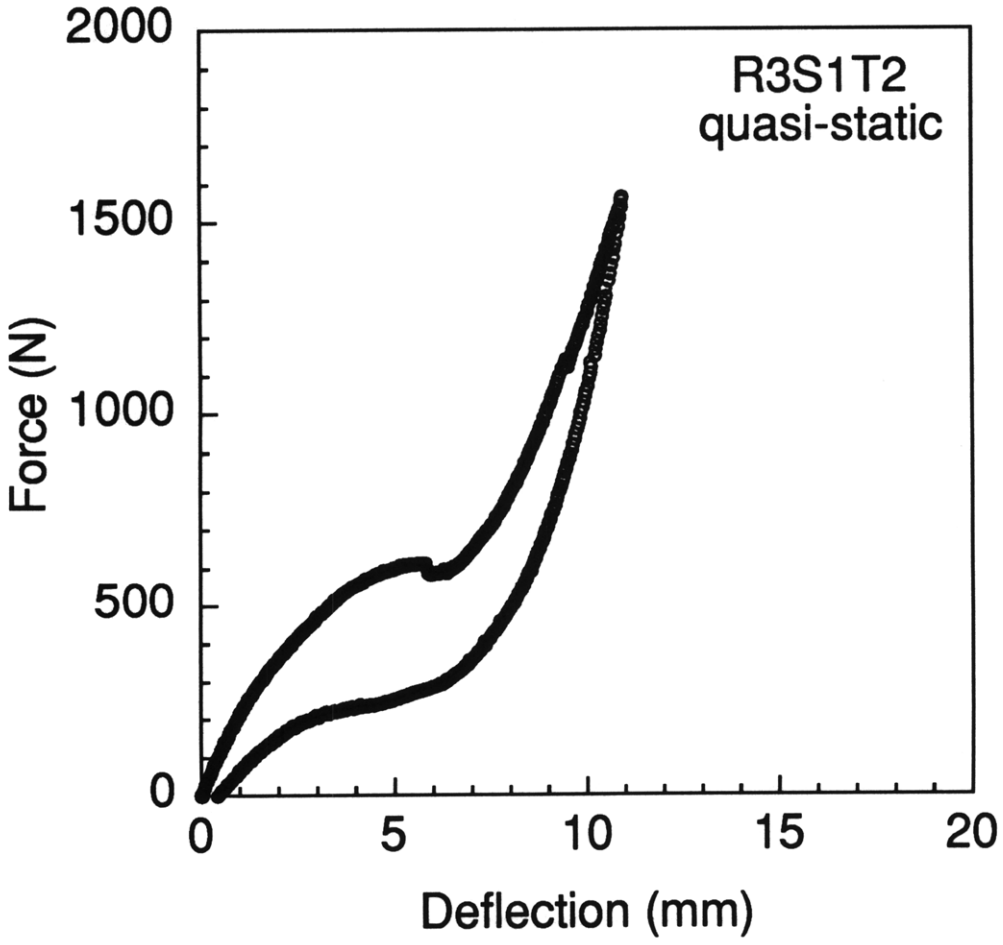

Figure E.22 Results of quasi-static test of specimen R3S1T2: (*top*) x-ray photograph of damage state, and (*bottom*) force-deflection history.

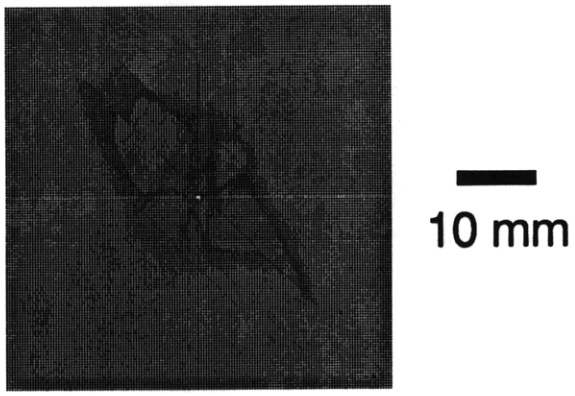

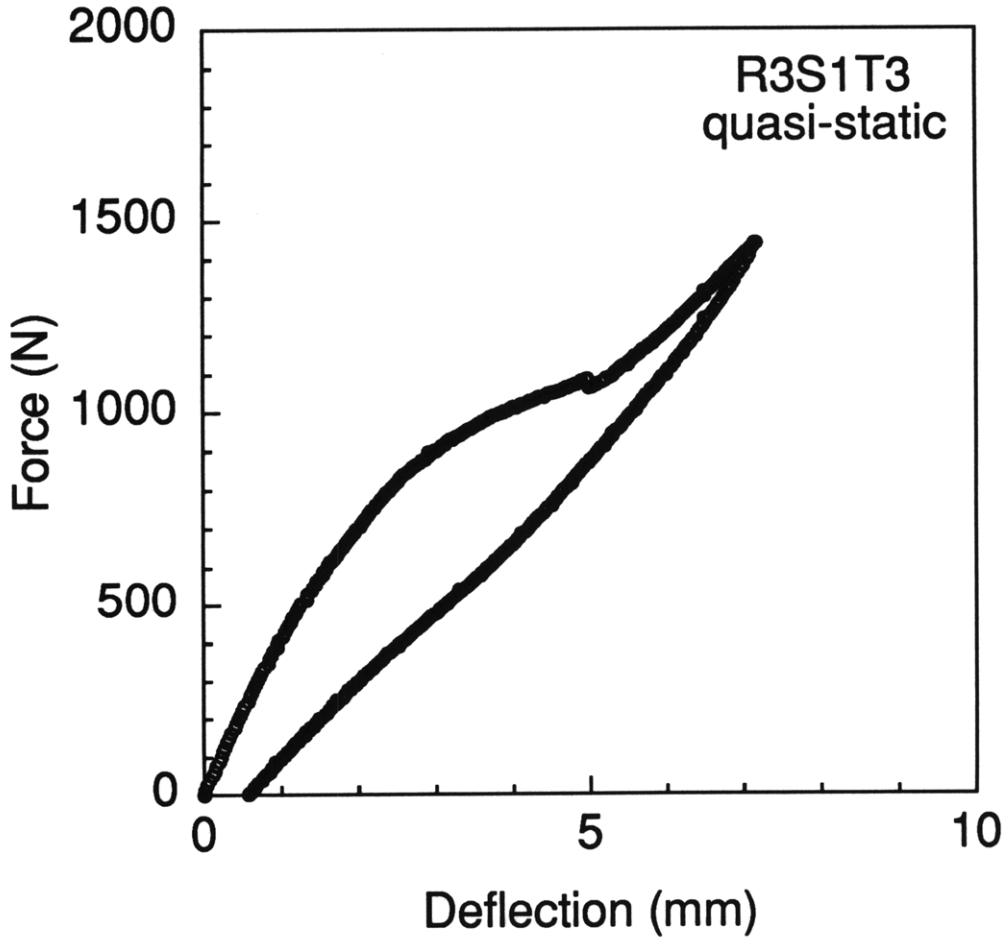

Figure E.23 Results of quasi-static test of specimen R3S1T3: (*top*) x-ray photograph of damage state, and (*bottom*) force-deflection history.

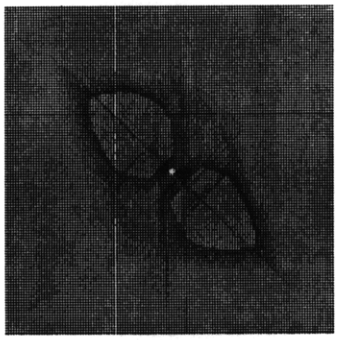

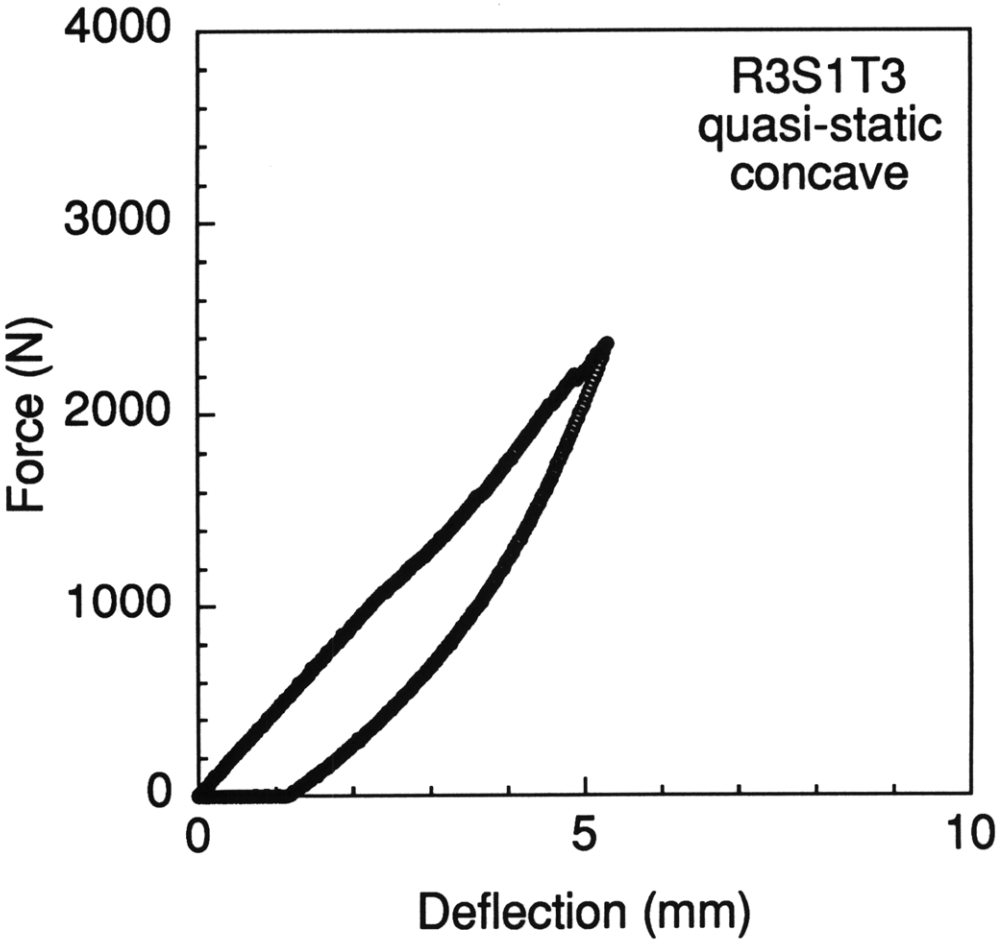

Figure E.24 Results of quasi-static test of specimen R3S1T3 (concave): (*top*) x-ray photograph of damage state, and (*bottom*) force-deflection history.

10 mm

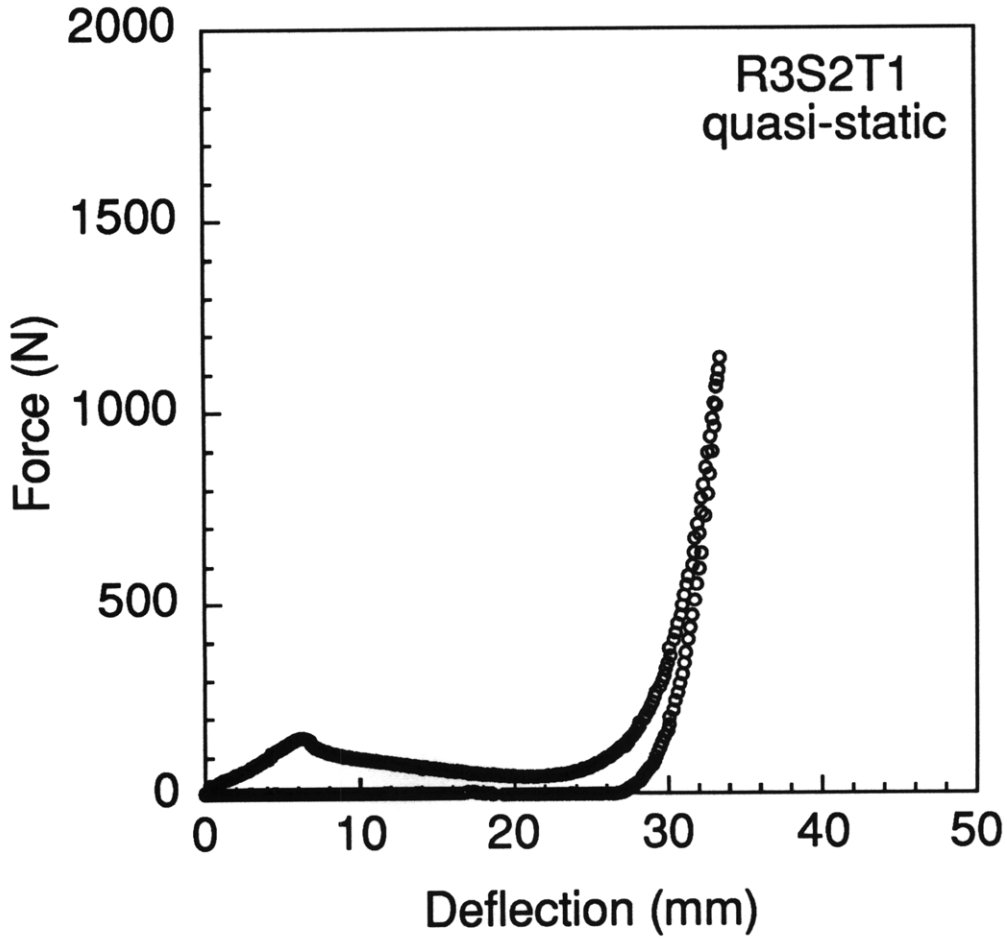

Figure E.25 Results of quasi-static test of specimen R3S2T1: (*top*) x-ray photograph of damage state, and (*bottom*) force-deflection history.

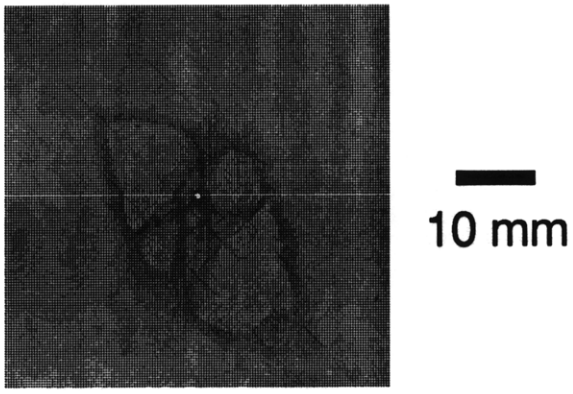

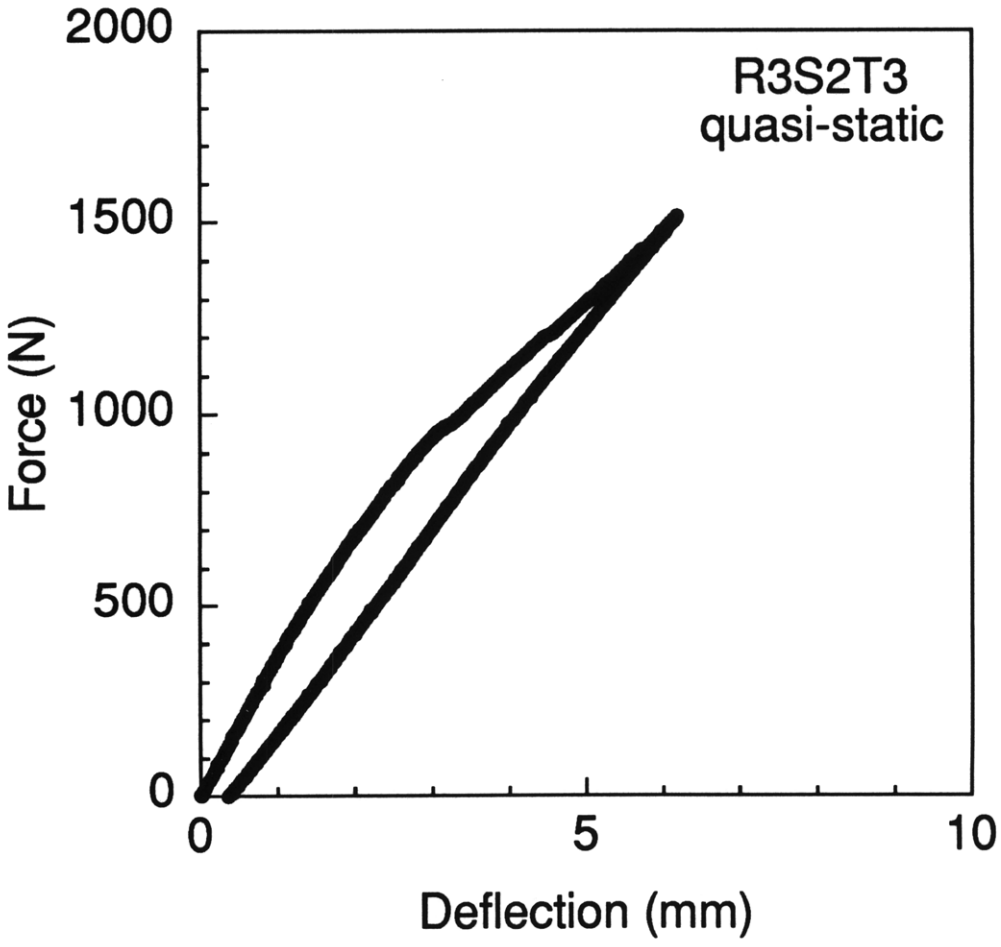

Figure E.26 Results of quasi-static test of specimen R3S2T3: (*top*) x-ray photograph of damage state, and (*bottom*) force-deflection history.

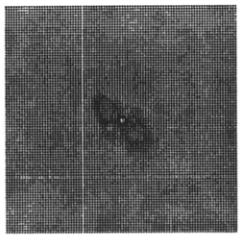

10 mm

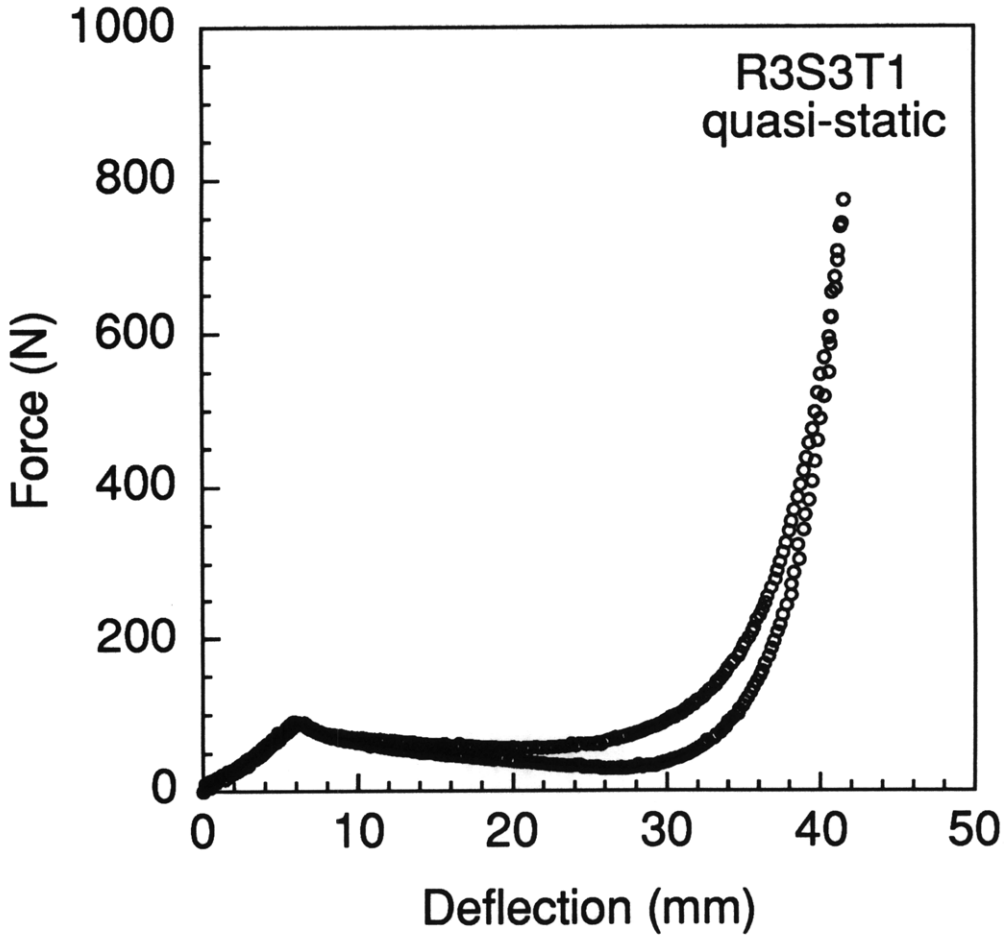

Figure E.27 Results of quasi-static test of specimen R3S3T1: (*top*) x-ray photograph of damage state, and (*bottom*) force-deflection history.

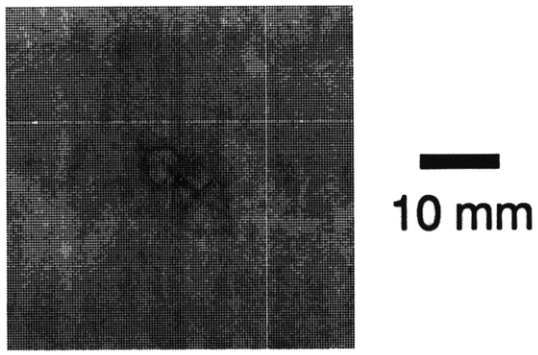

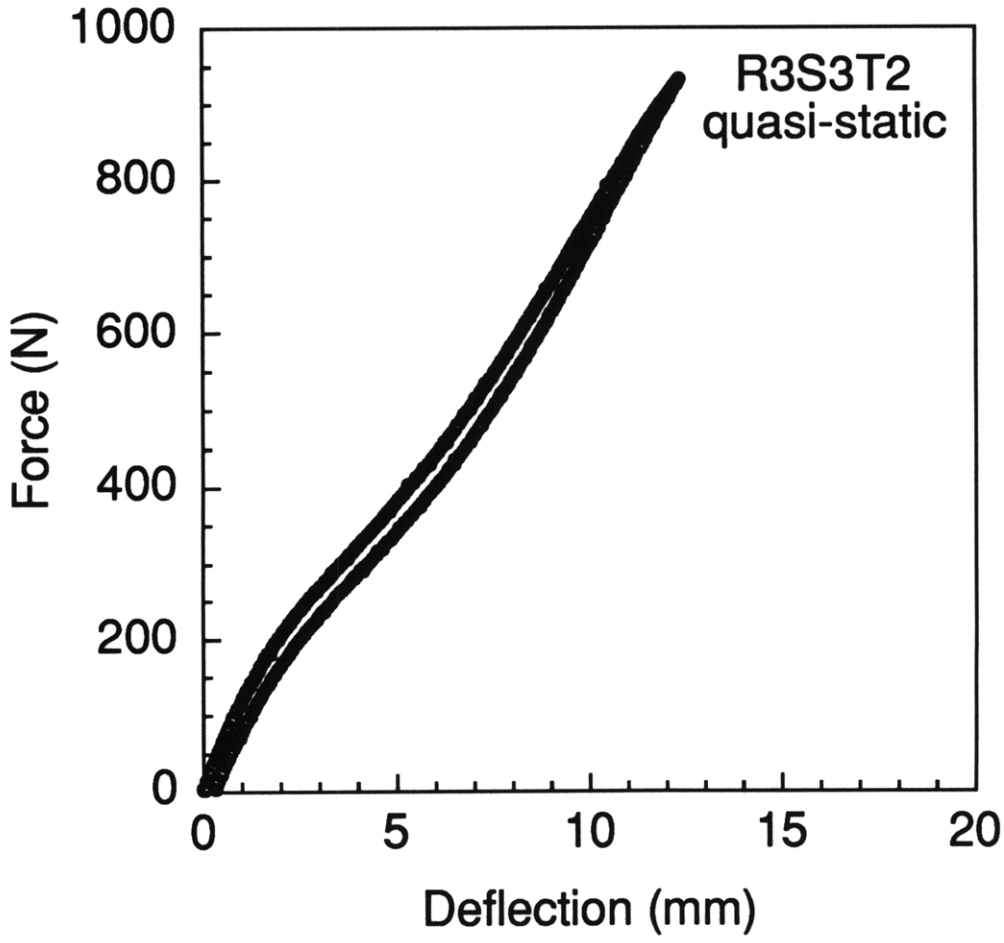

Figure E.28 Results of quasi-static test of specimen R3S3T2: (*top*) x-ray photograph of damage state, and (*bottom*) force-deflection history.

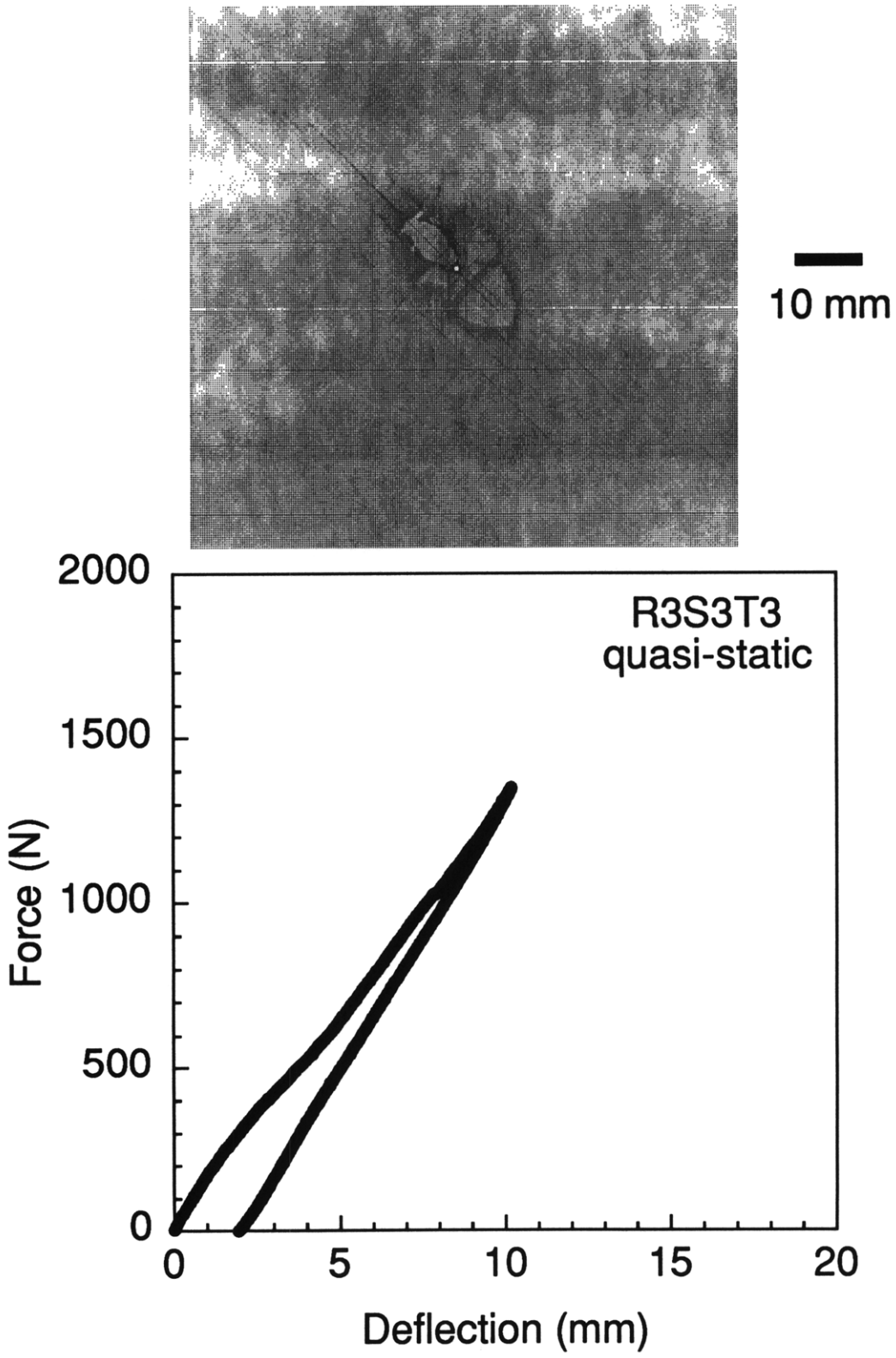

Figure E.29 Results of quasi-static test of specimen R3S3T3: (*top*) x-ray photograph of damage state, and (*bottom*) force-deflection history.

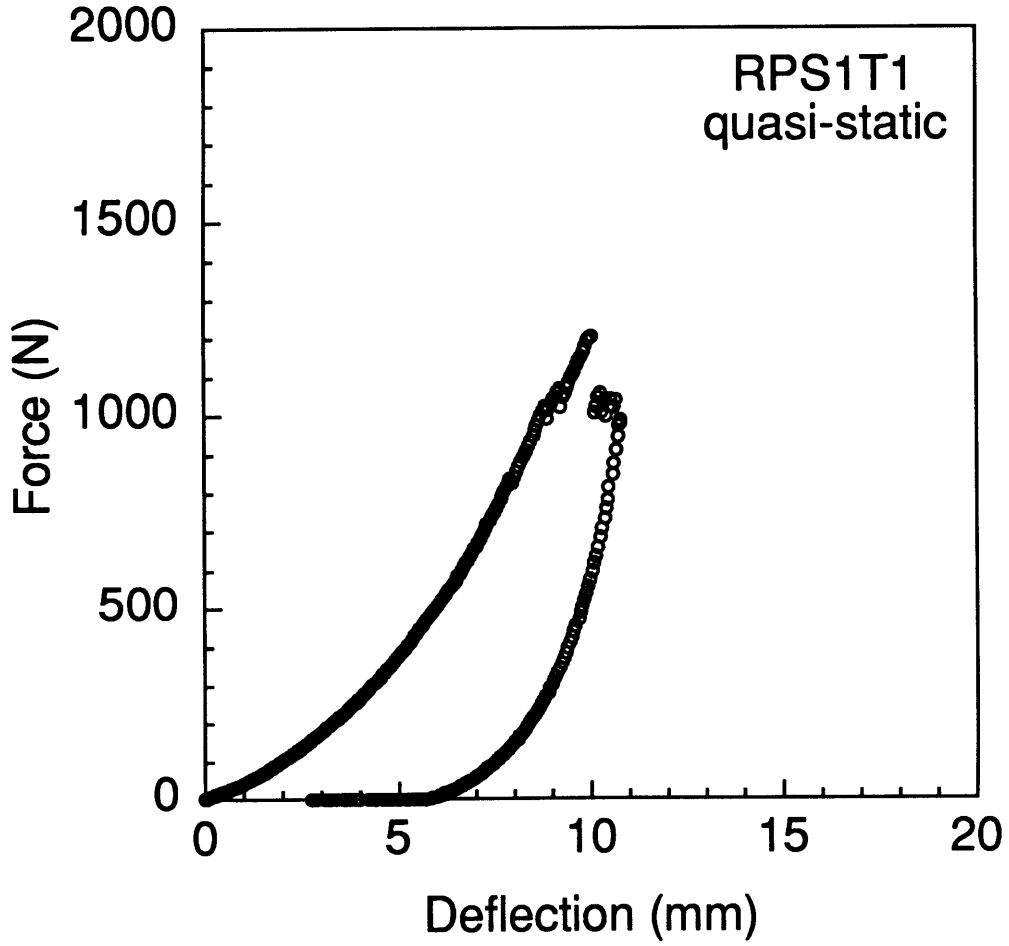

Figure E.30 Results of quasi-static test of specimen RPS1T1: (*top*) penetration damage is observed for this specimen, and (*bottom*) force-deflection history.

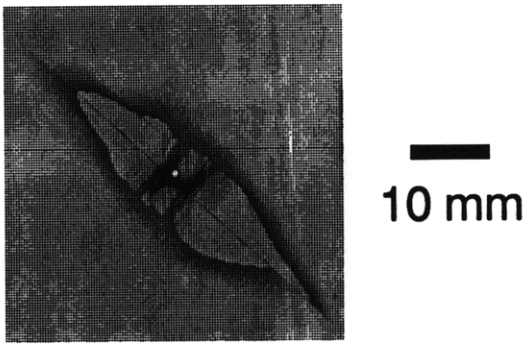

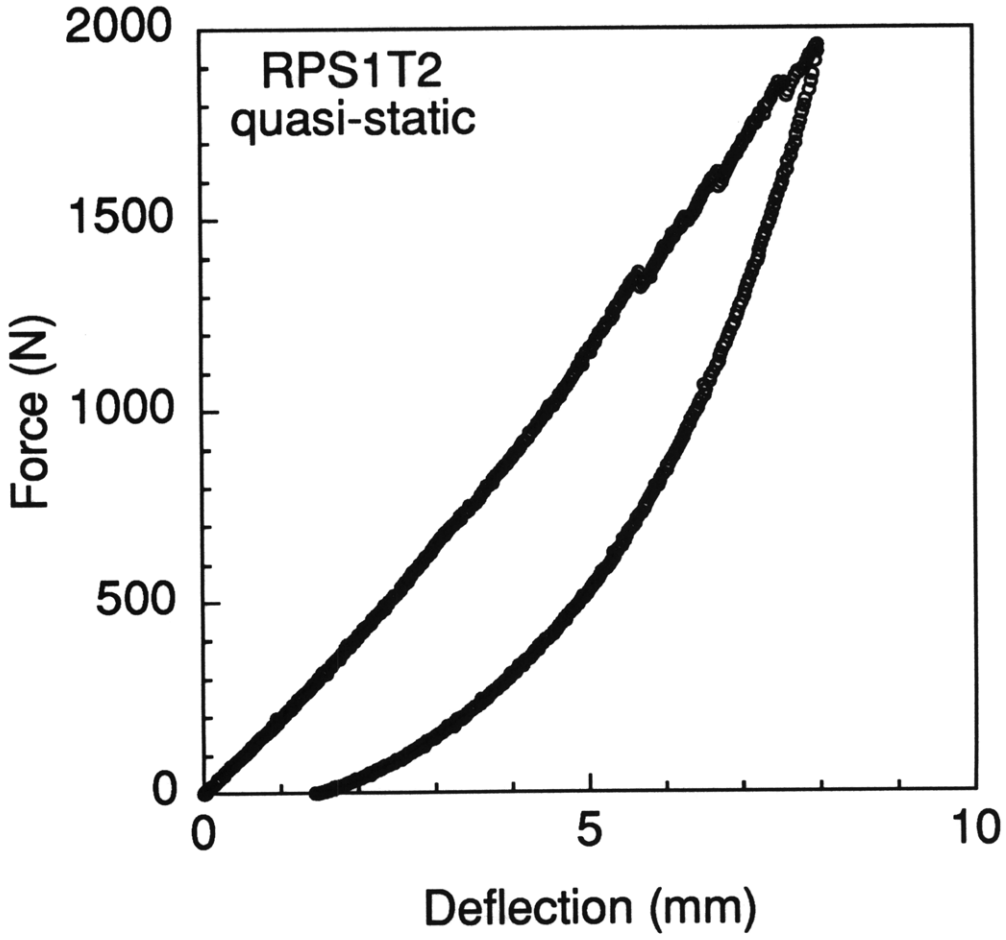

Figure E.31 Results of quasi-static test of specimen RPS1T2: (*top*) x-ray photograph of damage state, and (*bottom*) force-deflection history.

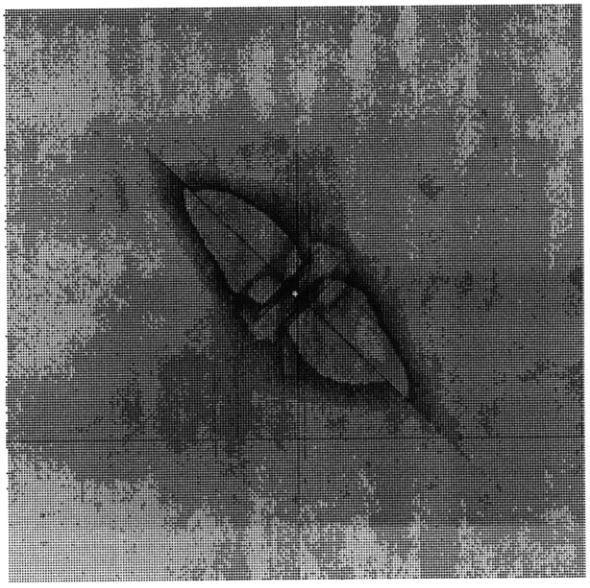

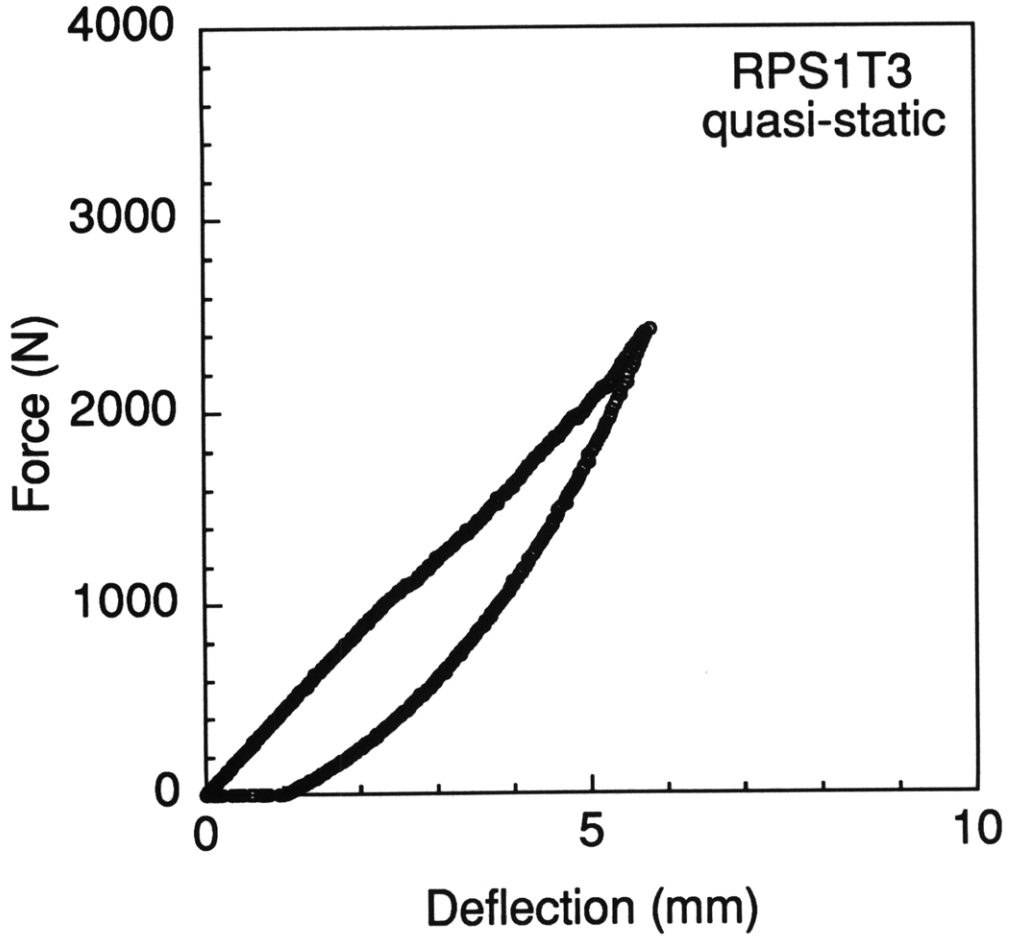

Figure E.32 Results of quasi-static test of specimen RPS1T3: (*top*) x-ray photograph of damage state, and (*bottom*) force-deflection history.

Appendix F

Quasi-static Force-indentation Data

Force-indentation data for all quasi-static tests is presented in this appendix. Calculated values of the contact parameters are given in Table F.1 as well as values of the maximum force, deflection, and indentation used for calculating the curve fits. Pearson's R, described in chapter 5, is provided for both the constrained and unconstrained curve fits. Omissions in Table F.1 indicate that a useful range of data for curve fitting could not be determined. Force-indentation data for all tests is plotted in the figures up to the peak force measured during testing, i.e. unloading data is not plotted. Axis scales for the force-indentation responses were chosen based on a compromise between showing specifics of each specimen response (smallest scale showing entire specimen response) and allowing the response of different specimens to be compared (one scale for all specimens). Five force scales (as in appendix E) and three indentation scales were found to provide a reasonable compromise.

Table F.1 Contact Relation Parameters[a] for Quasi-static Tests

Specimen[b]	Constrained (m=1.5) K[c]	Constrained (m=1.5) R[d]	Unconstrained (m fitted) m	Unconstrained (m fitted) K[c]	Unconstrained (m fitted) R[d]	Maximum Values for Curve Fits Force (N)	Deflection (mm)	Indentation (mm)
R1S1T1	*74.2*	*0.968*	*1.48*	*67.0*	*0.923*	*172*	*2.3*	*0.016*
R1S1T1c	61.9	0.959	1.31	26.4	0.951	180	0.8	0.018
R1S1T2	32.1	0.984	1.90	115	0.983	461	0.9	0.050
R1S1T2c	34.7	0.977	1.65	53.1	0.989	378	1.2	0.046
R1S1T3	-	-	-	-	-	-	-	-
R1S1T3c	50.0	0.991	1.57	58.9	0.988	815	1.1	0.060
R1S2T1	27.3	0.983	1.44	21.5	0.970	82	2.4	0.020
R1S3T1	52.1	0.949	1.46	43.5	0.948	167	29	0.020
R1SCT1	27.7	0.957	1.73	65.5	0.969	117	81	0.024
R2S1T1	***39.1***	***0.965***	***1.58***	***51.6***	***0.965***	***185***	***3.5***	***0.026***
R2S1T1c	54.2	0.925	1.65	80.1	0.974	412	3.4	0.032
R2S1T2	*42.5*	*0.988*	*1.68*	*75.3*	*0.989*	*401*	*2.1*	*0.042*
R2S1T2c	41.1	0.980	1.56	47.0	0.979	415	1.5	0.042
R2S1T3	43.8	0.991	1.50	41.5	0.987	716	1.6	0.062
R2S2T1	-	-	-	-	-	-	-	-
R2S2T2	57.2	0.992	1.44	45.7	0.988	185	0.8	0.020
R2S2T3	40.7	0.992	1.68	64.8	0.992	833	2.0	0.070
R2S3T1	*54.3*	*0.964*	*1.58*	*74.3*	*0.943*	*144*	*9.7*	*0.018*
R2S3T2	39.8	0.986	1.42	28.7	0.963	320	2.8	0.036
R3S1T1	*34.5*	*0.966*	*1.08*	*6.13*	*0.937*	*110*	*2.8*	*0.020*
R3S1T1c	24.8	0.973	1.61	34.0	0.941	158	2.0	0.030
R3S1T2	*39.3*	*0.974*	*1.64*	*57.8*	*0.971*	*416*	*2.5*	*0.042*
R3S1T3	48.1	0.996	1.48	44.2	0.989	614	1.6	0.052
R3S1T3c	46.6	0.986	1.65	69.3	0.990	802	1.8	0.062
R3S2T1	*23.9*	*0.968*	*1.62*	*37.1*	*0.932*	*126*	*5.0*	*0.030*
R3S2T3	33.9	0.978	1.55	35.4	0.991	562	1.6	0.060
R3S3T1	*17.2*	*0.959*	*1.64*	*27.3*	*0.964*	*90*	*6.2*	*0.028*
R3S3T2	43.0	0.985	1.73	97.4	0.988	283	3.2	0.034
R3S3T3	43.1	0.964	1.85	117	0.986	738	5.7	0.060
RPS1T1	**26.3**	**0.969**	**1.41**	**17.3**	**0.947**	**133**	**2.4**	**0.030**
RPS1T2	48.4	0.979	1.44	37.5	0.979	365	1.8	0.038
RPS1T3	42.8	0.995	1.52	44.2	0.991	591	1.3	0.054

[a] *Italics* indicate peak force occurred on the second equilibrium path (instability), **bold** indicates penetration, and "-" indicates that a useful range of data for curve fitting could not be defined.

[b] "c" after specimen identification indicates concave test.

[c] All values in kN/mm^m.

[d] Pearson's R (linear correlation factor).

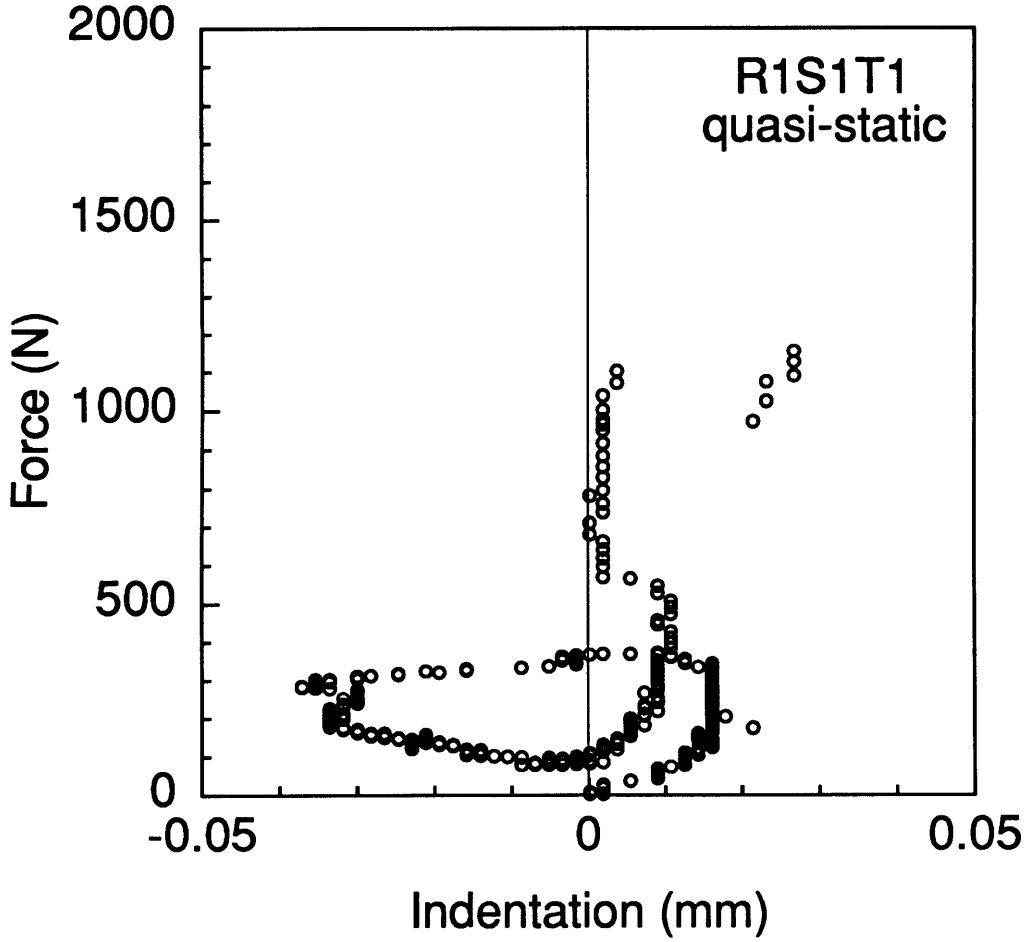

Figure F.1 Force-indentation response for quasi-static loading of specimen R1S1T1.

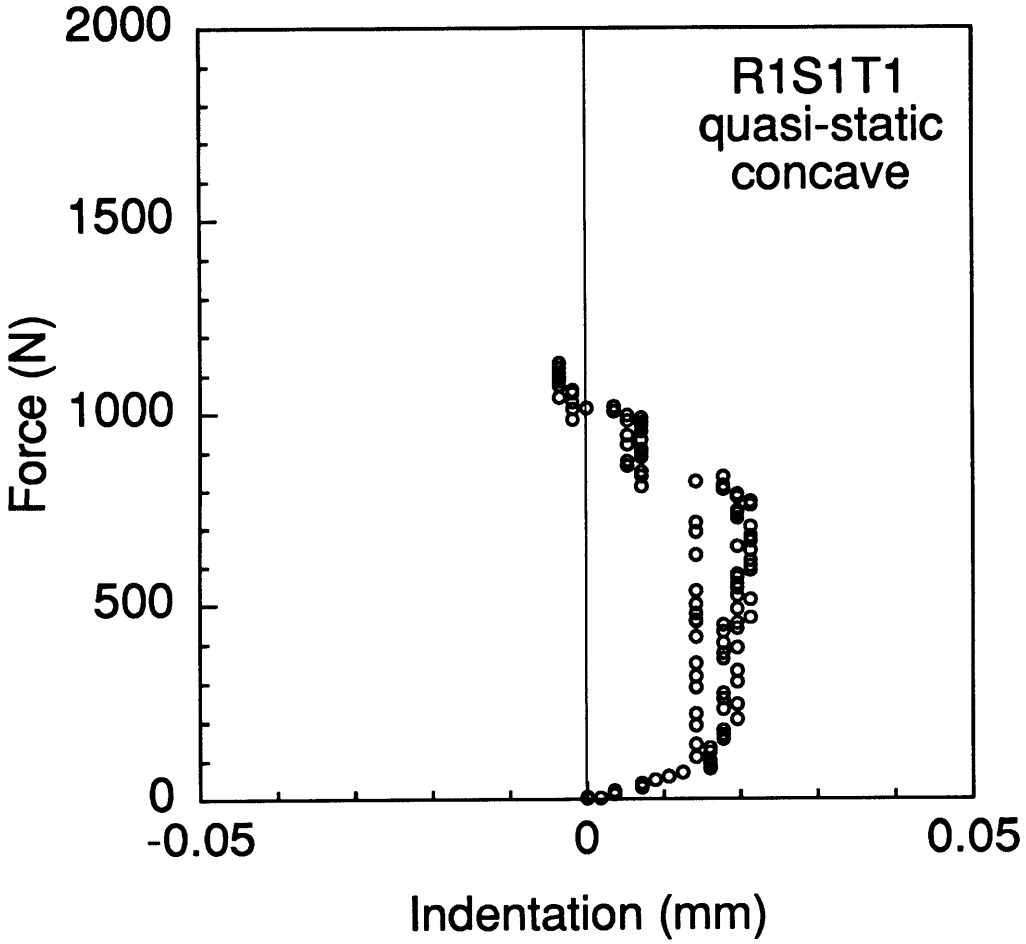

Figure F.2 Force-indentation response for quasi-static loading of specimen R1S1T1 (concave).

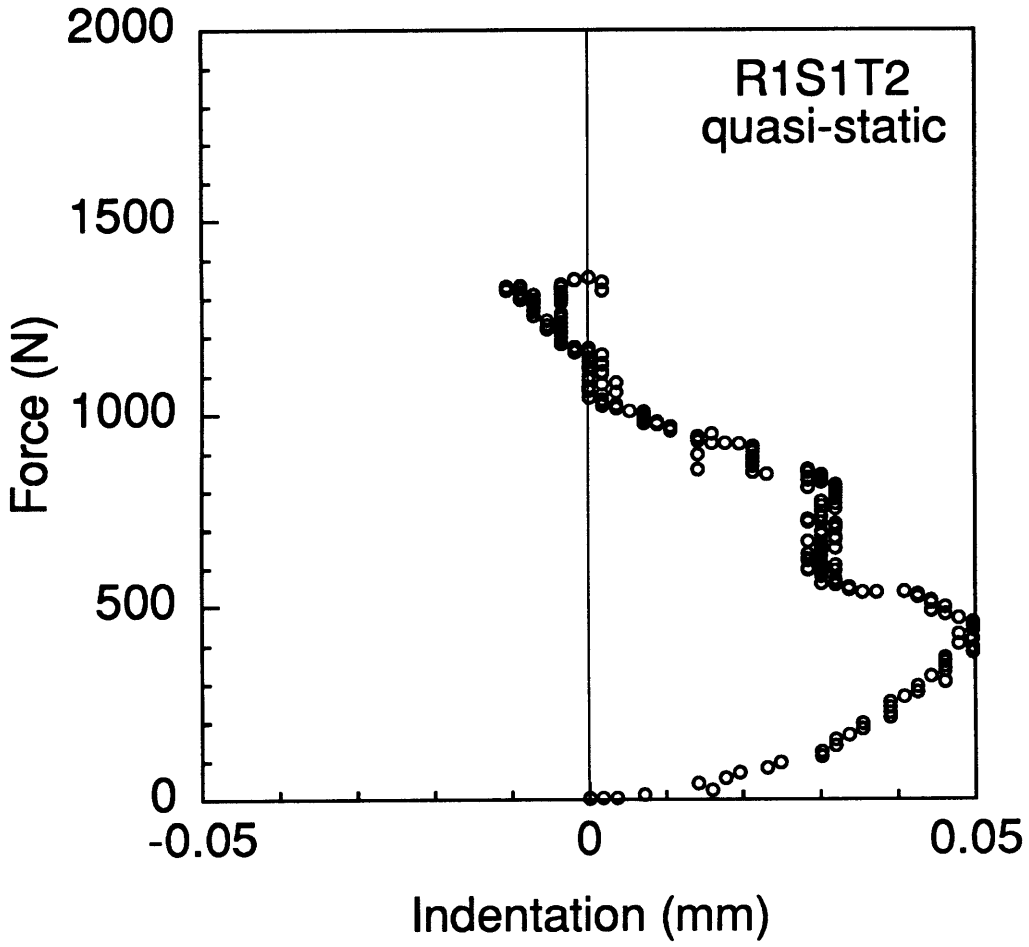

Figure F.3 Force-indentation response for quasi-static loading of specimen R1S1T2.

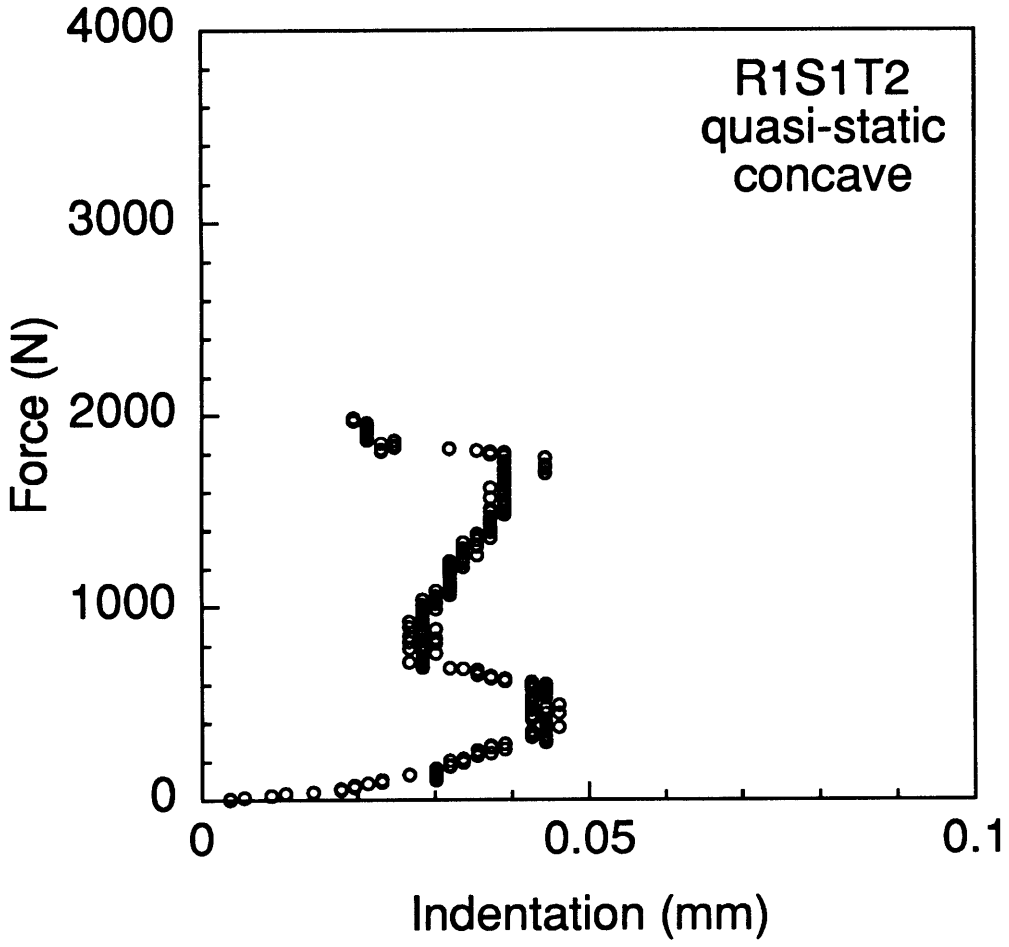

Figure F.4 Force-indentation response for quasi-static loading of specimen R1S1T2 (concave).

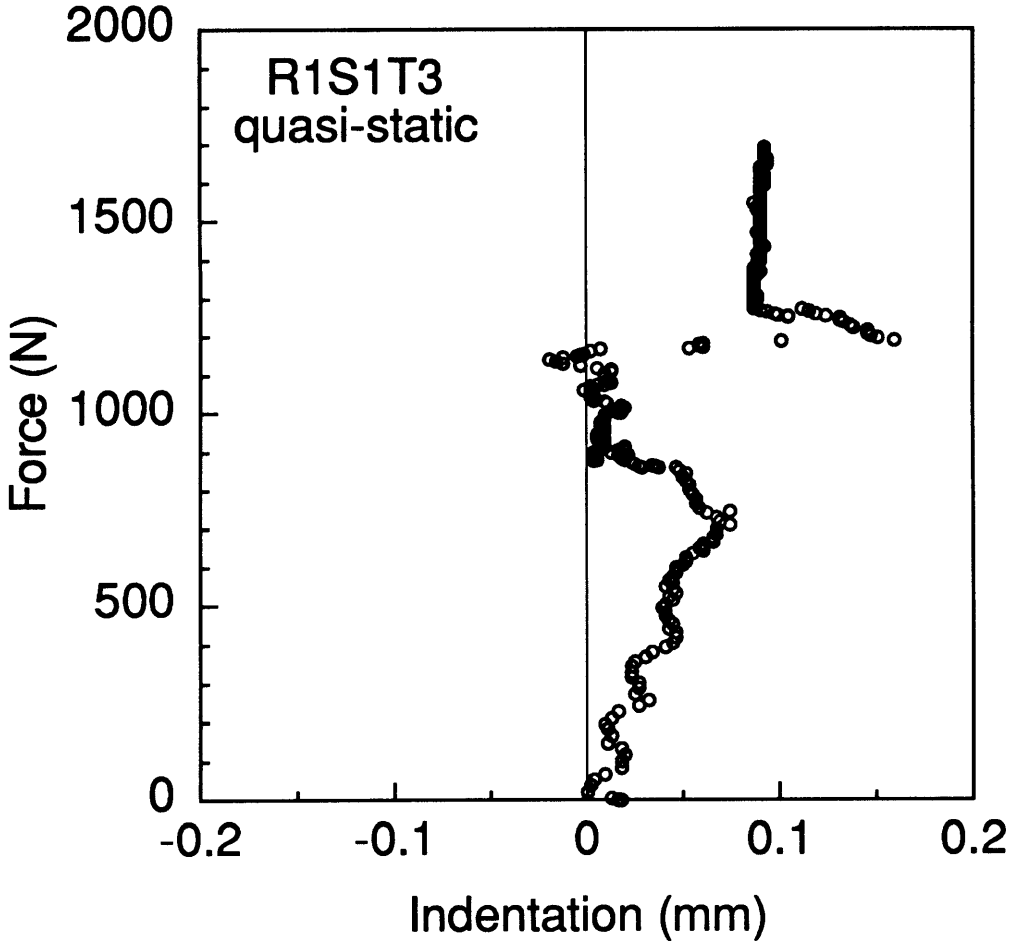

Figure F.5 Force-indentation response for quasi-static loading of specimen R1S1T3.

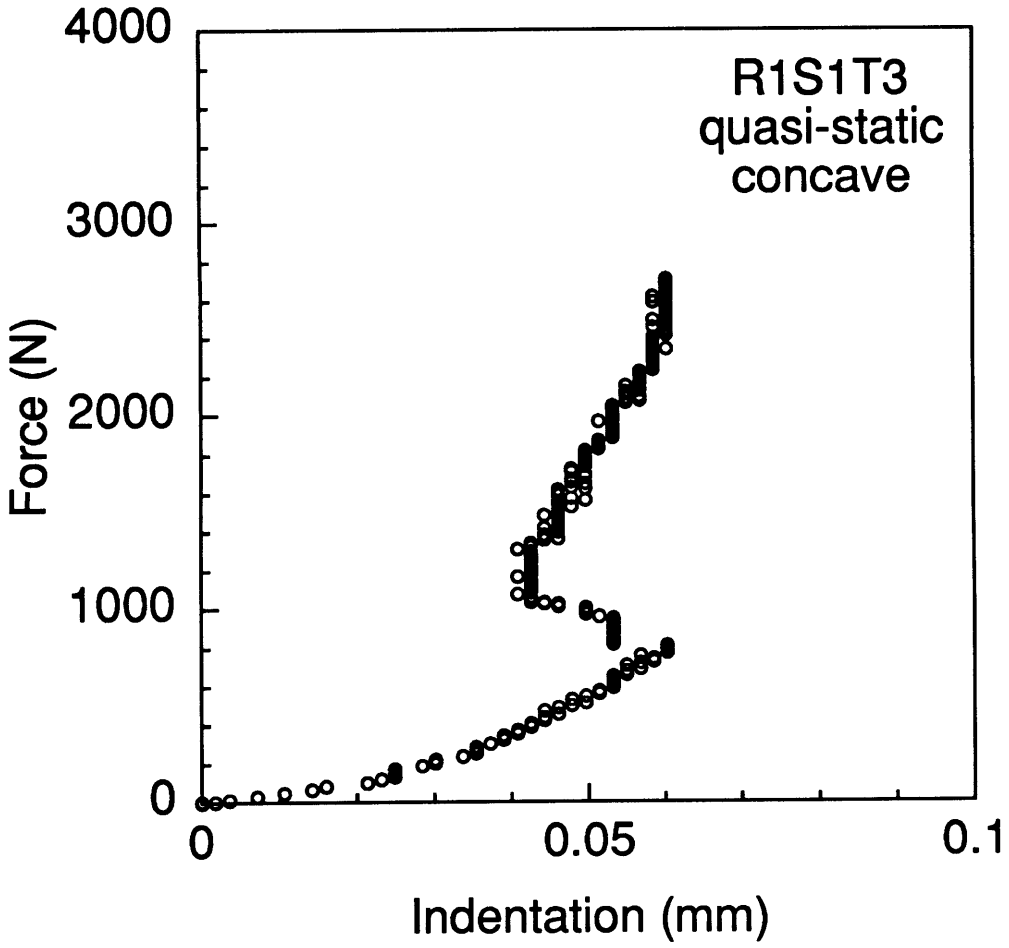

Figure F.6 Force-indentation response for quasi-static loading of specimen R1S1T3 (concave).

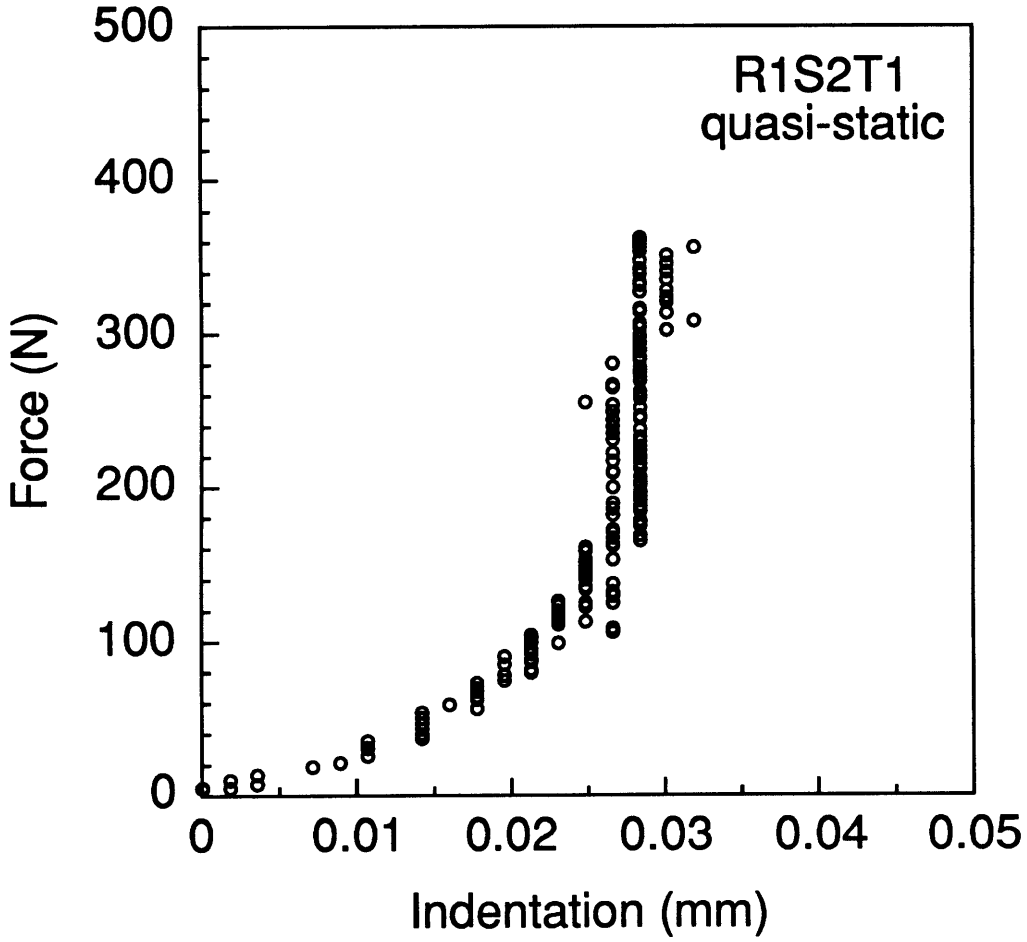

Figure F.7 Force-indentation response for quasi-static loading of specimen R1S2T1.

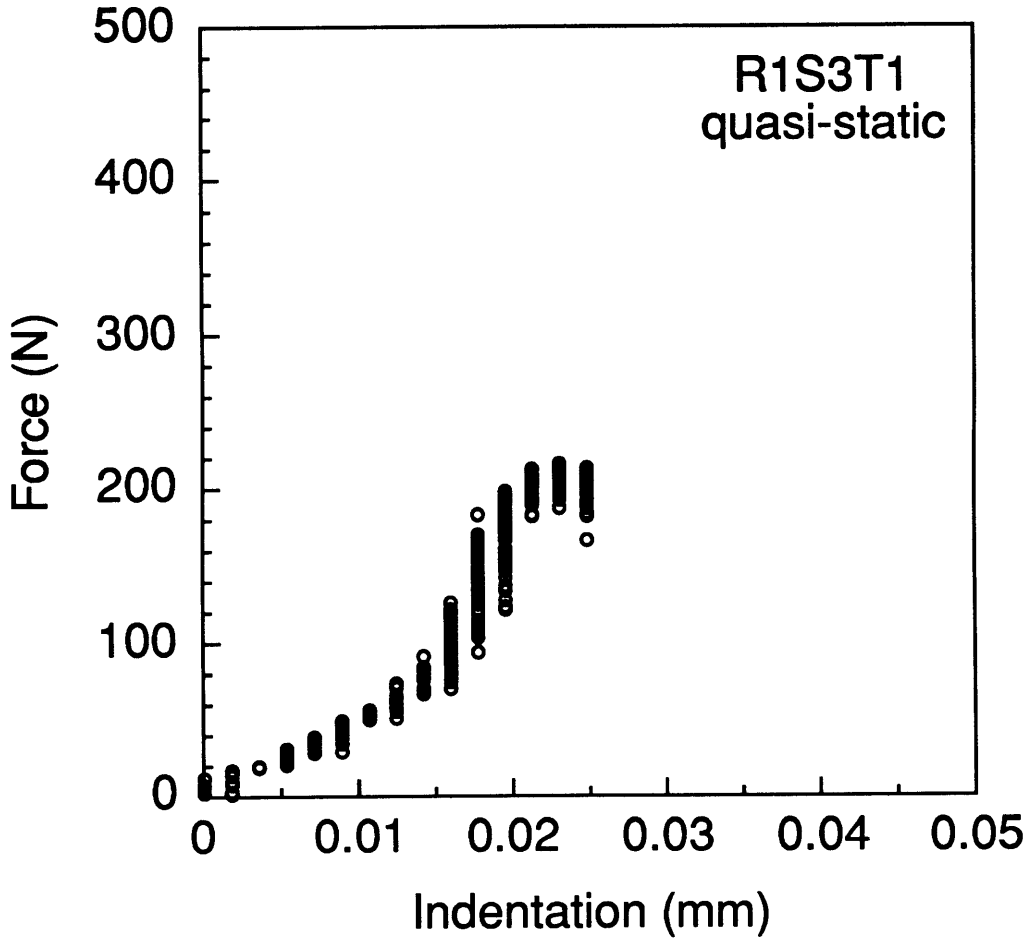

Figure F.8 Force-indentation response for quasi-static loading of specimen R1S3T1.

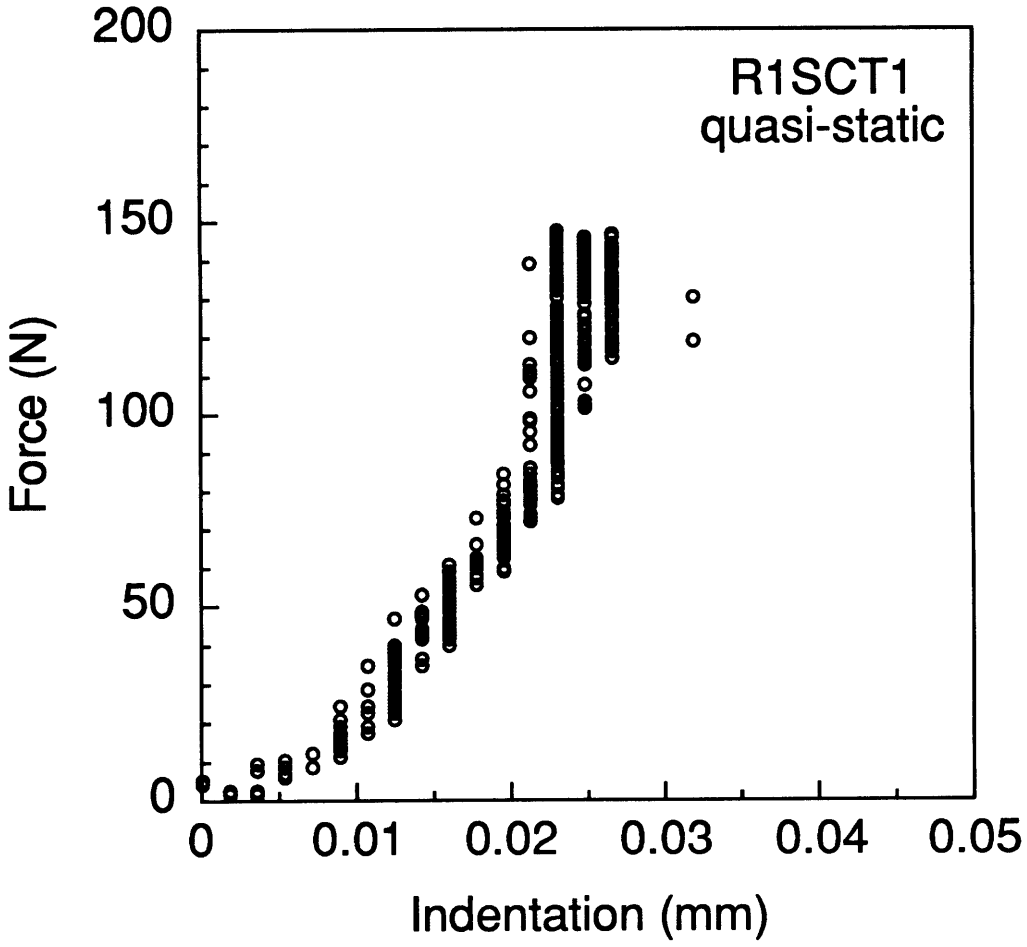

Figure F.9 Force-indentation response for quasi-static loading of specimen R1SCT1.

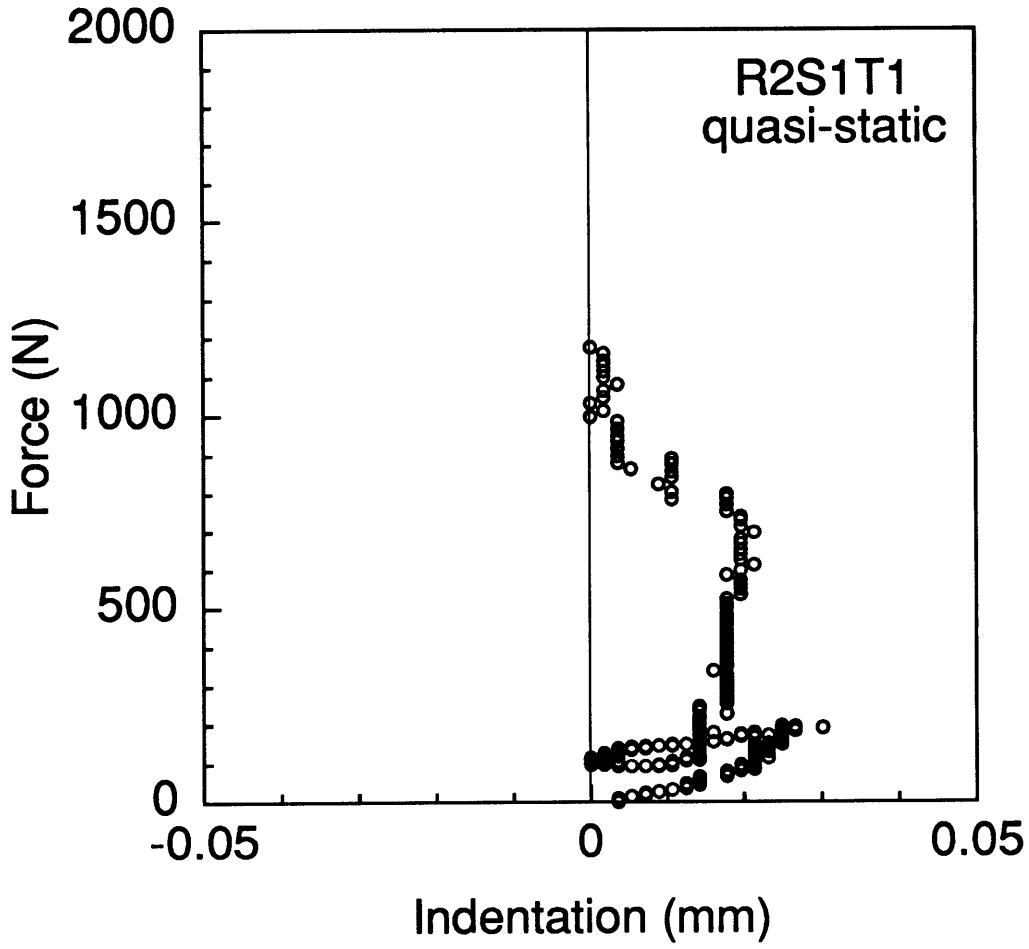

Figure F.10 Force-indentation response for quasi-static loading of specimen R2S1T1.

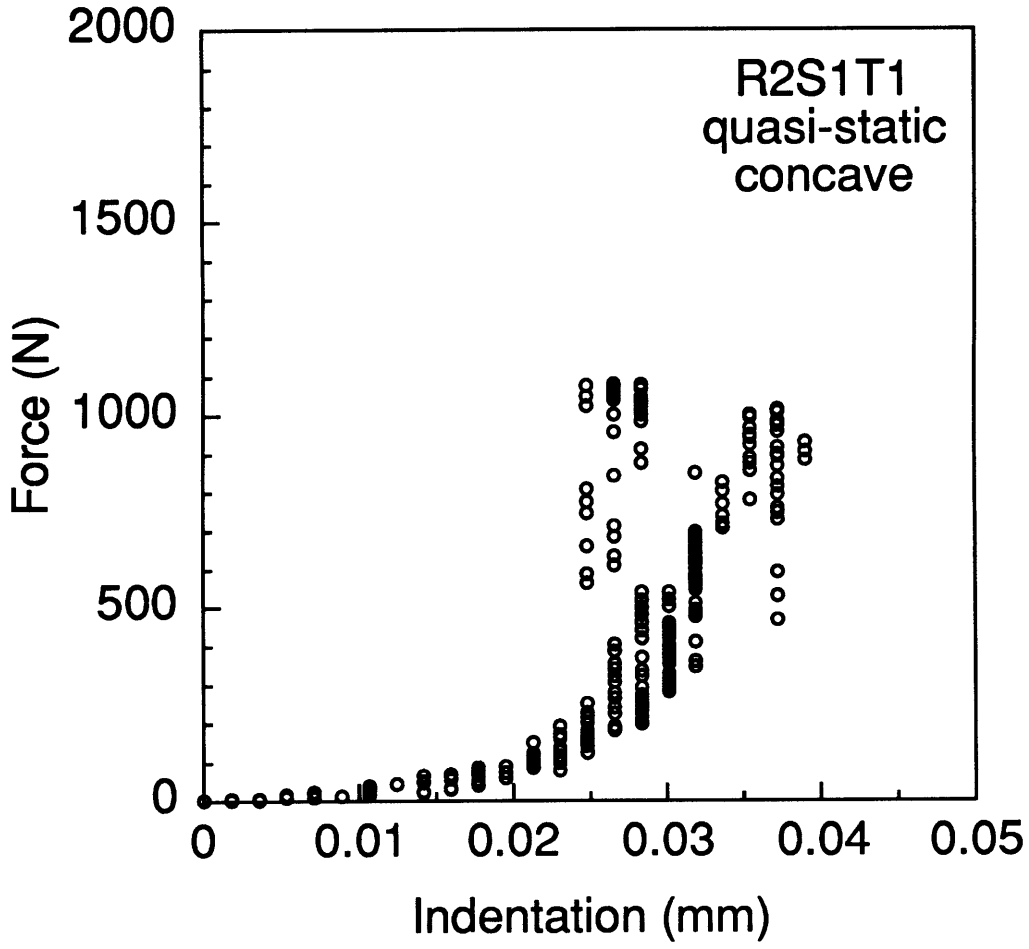

Figure F.11 Force-indentation response for quasi-static loading of specimen R2S1T1 (concave).

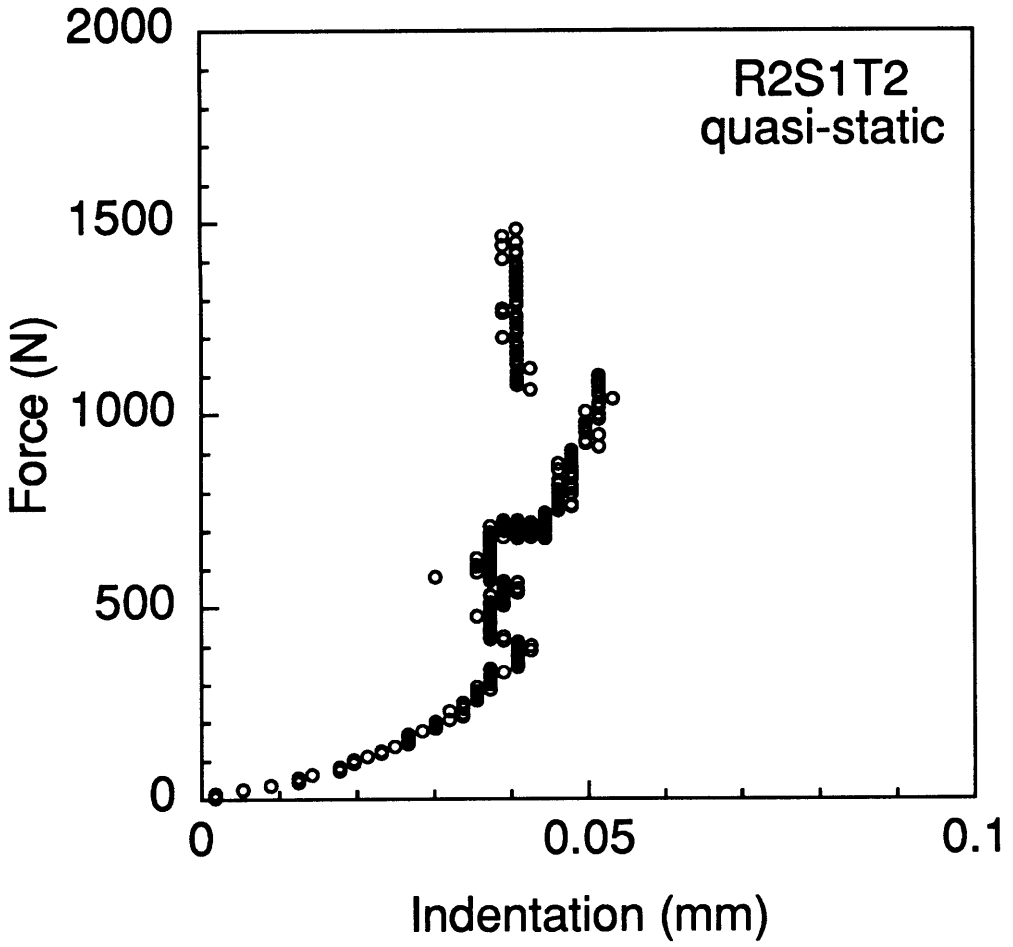

Figure F.12 Force-indentation response for quasi-static loading of specimen R2S1T2.

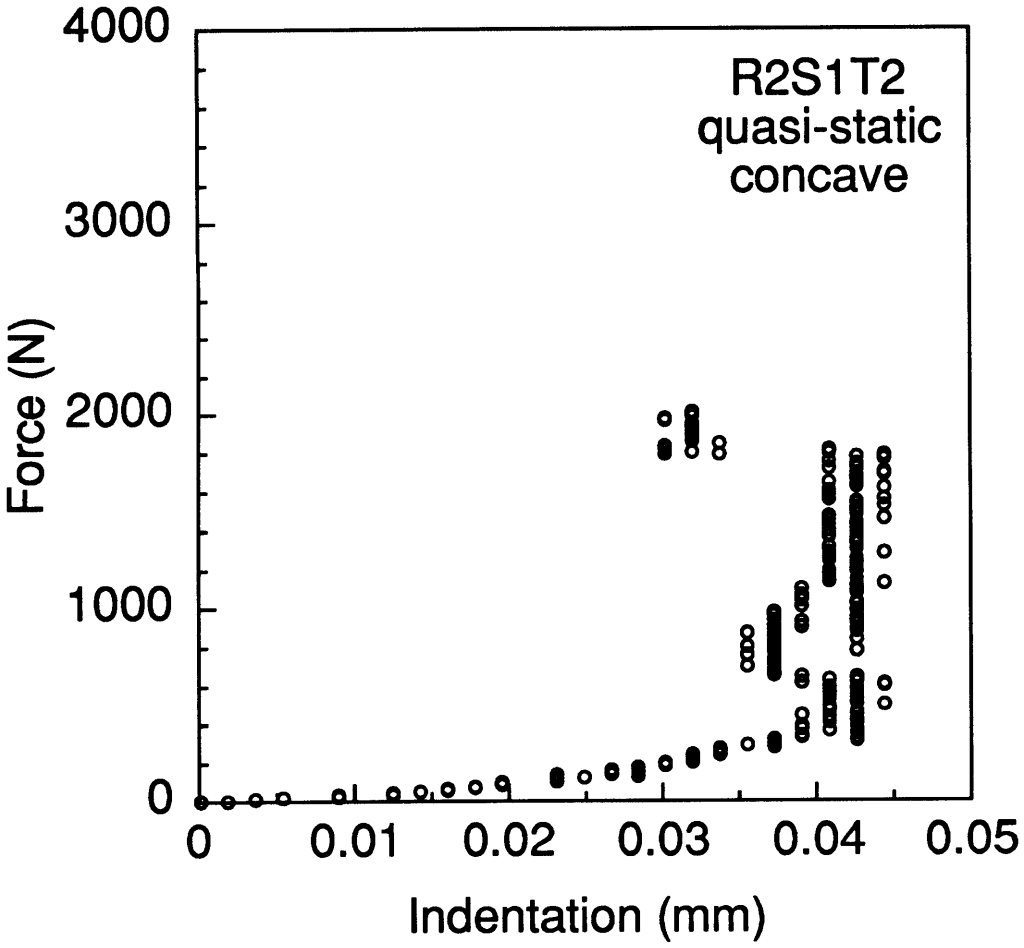

Figure F.13 Force-indentation response for quasi-static loading of specimen R2S1T2 (concave).

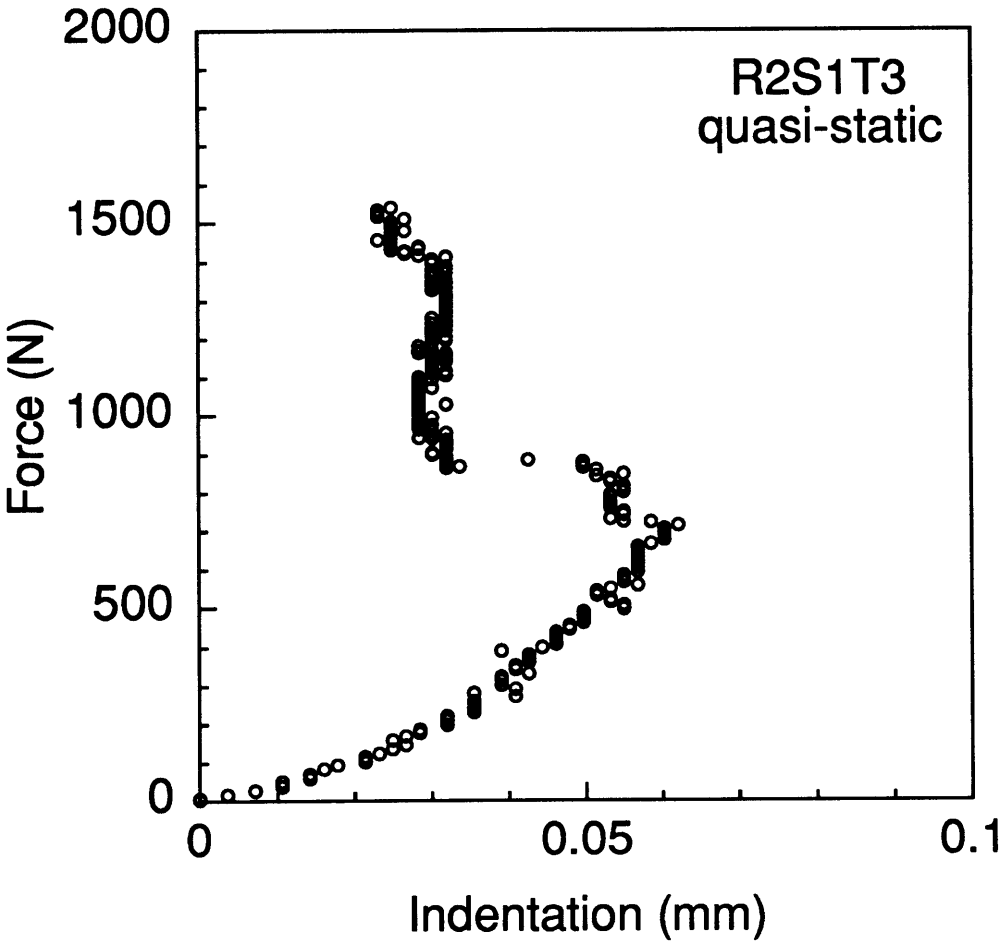

Figure F.14 Force-indentation response for quasi-static loading of specimen R2S1T3.

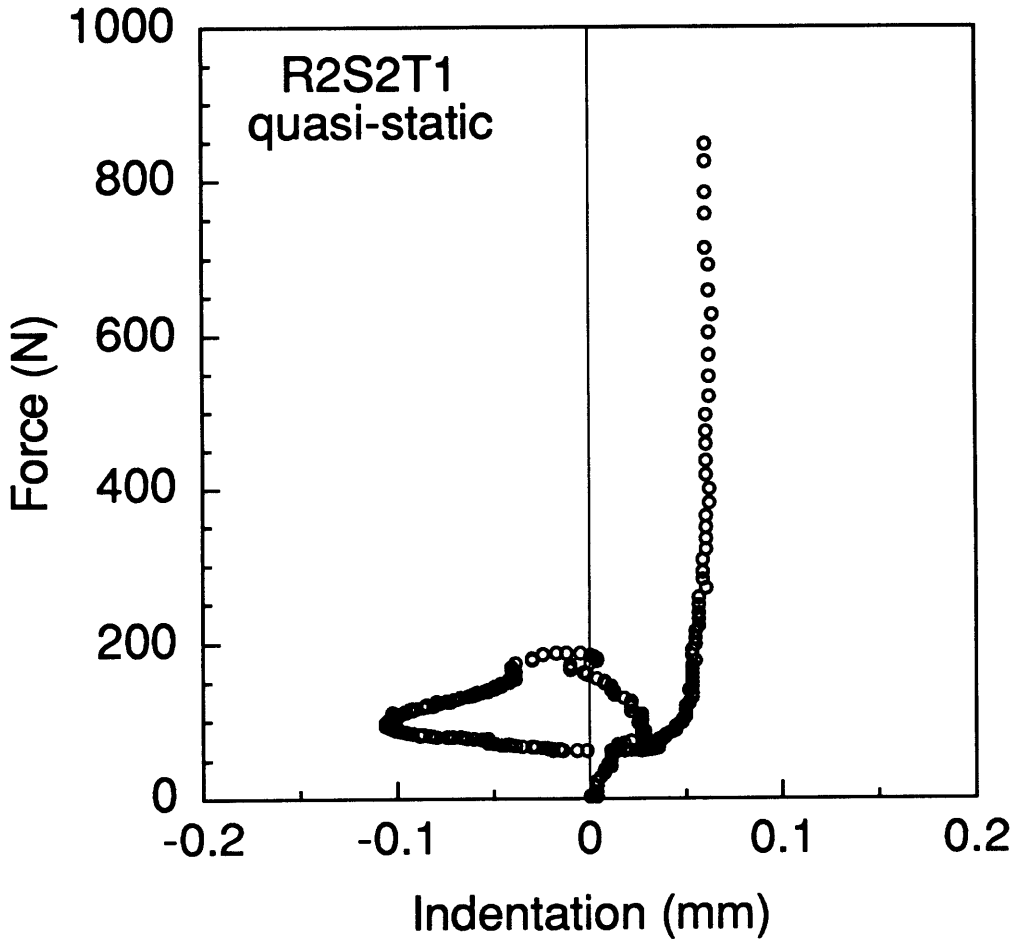

Figure F.15 Force-indentation response for quasi-static loading of specimen R2S2T1.

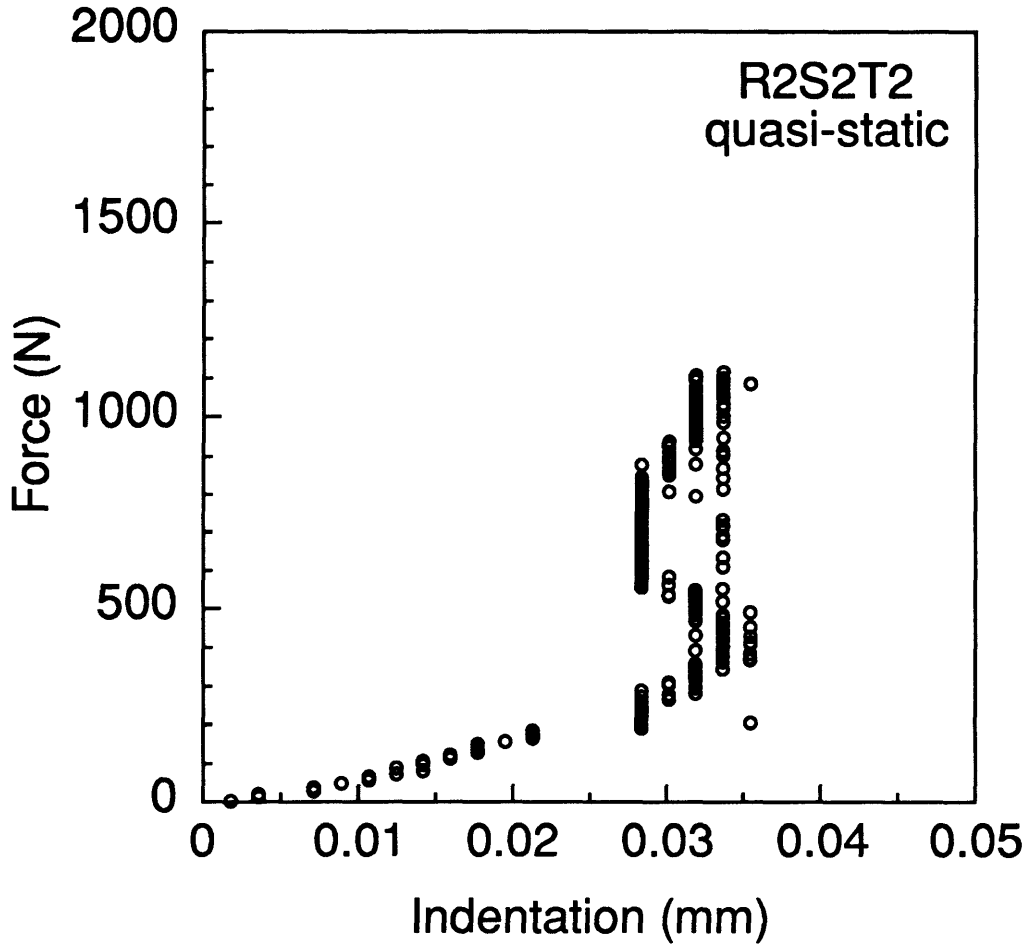

Figure F.16 Force-indentation response for quasi-static loading of specimen R2S2T2.

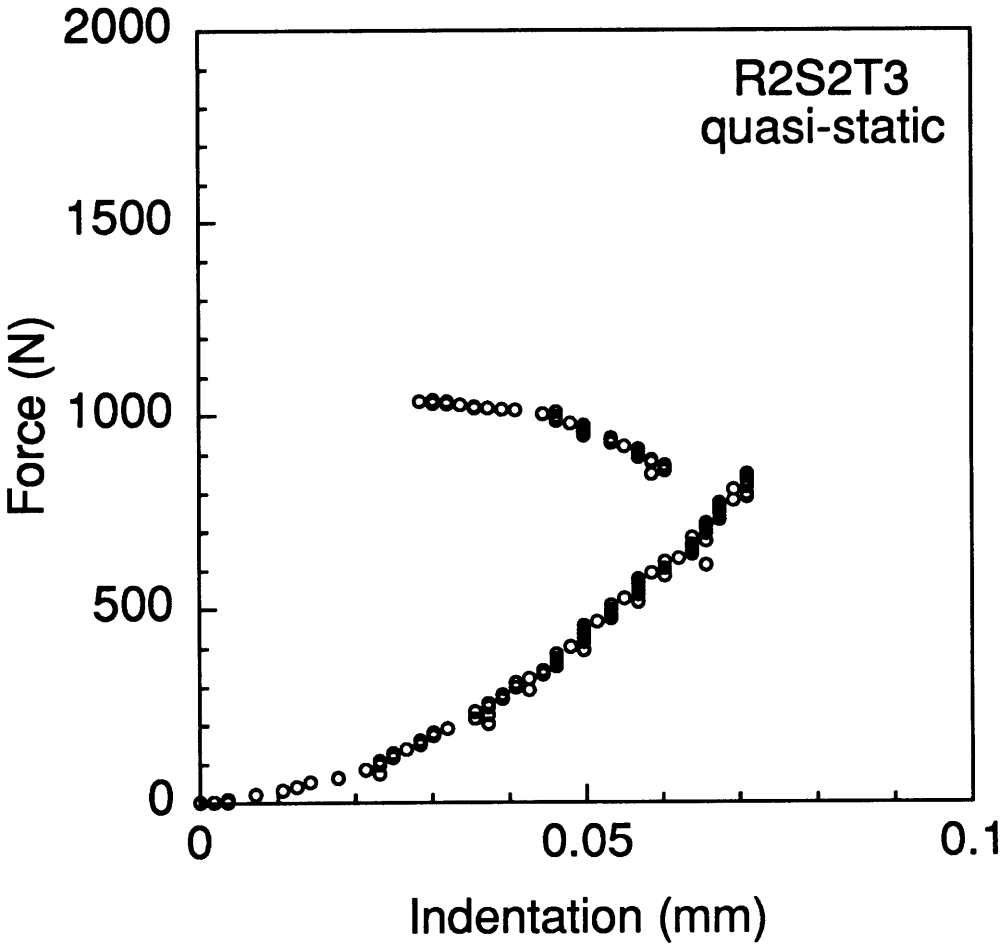

Figure F.17 Force-indentation response for quasi-static loading of specimen R2S2T3.

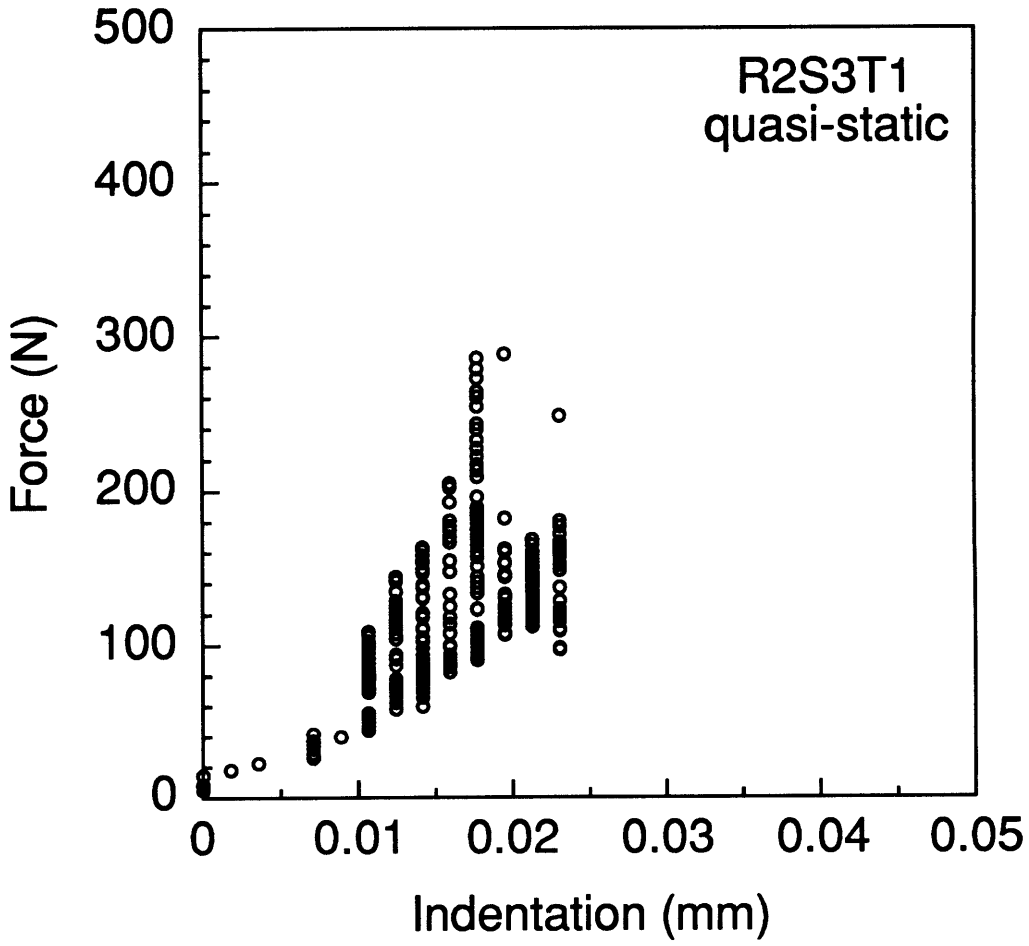

Figure F.18 Force-indentation response for quasi-static loading of specimen R2S3T1.

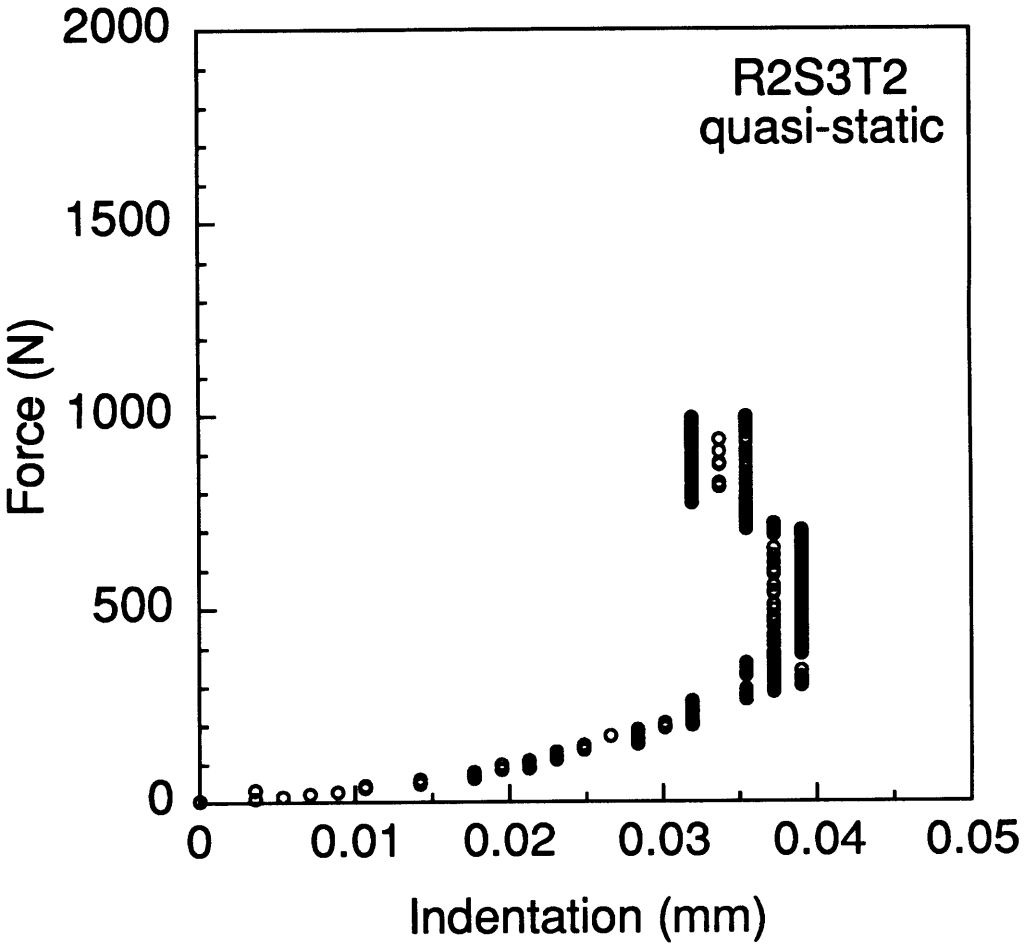

Figure F.19 Force-indentation response for quasi-static loading of specimen R2S3T2.

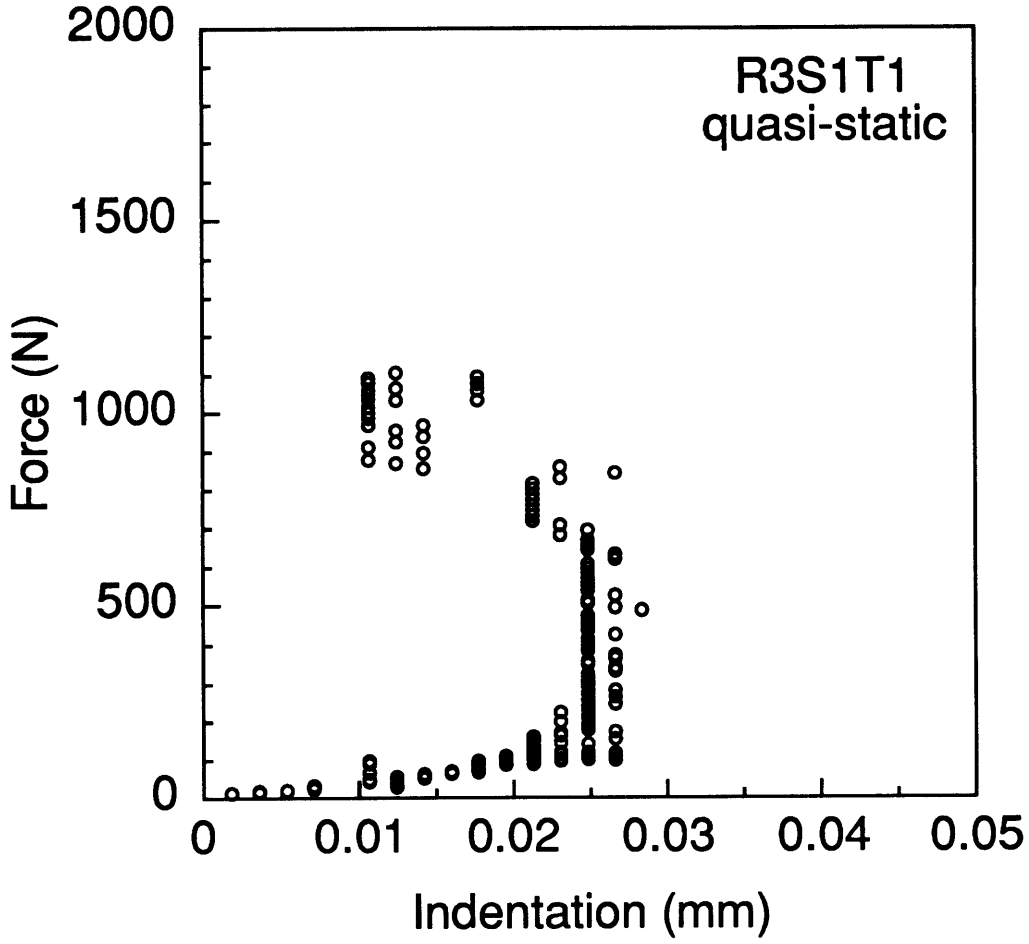

Figure F.20 Force-indentation response for quasi-static loading of specimen R3S1T1.

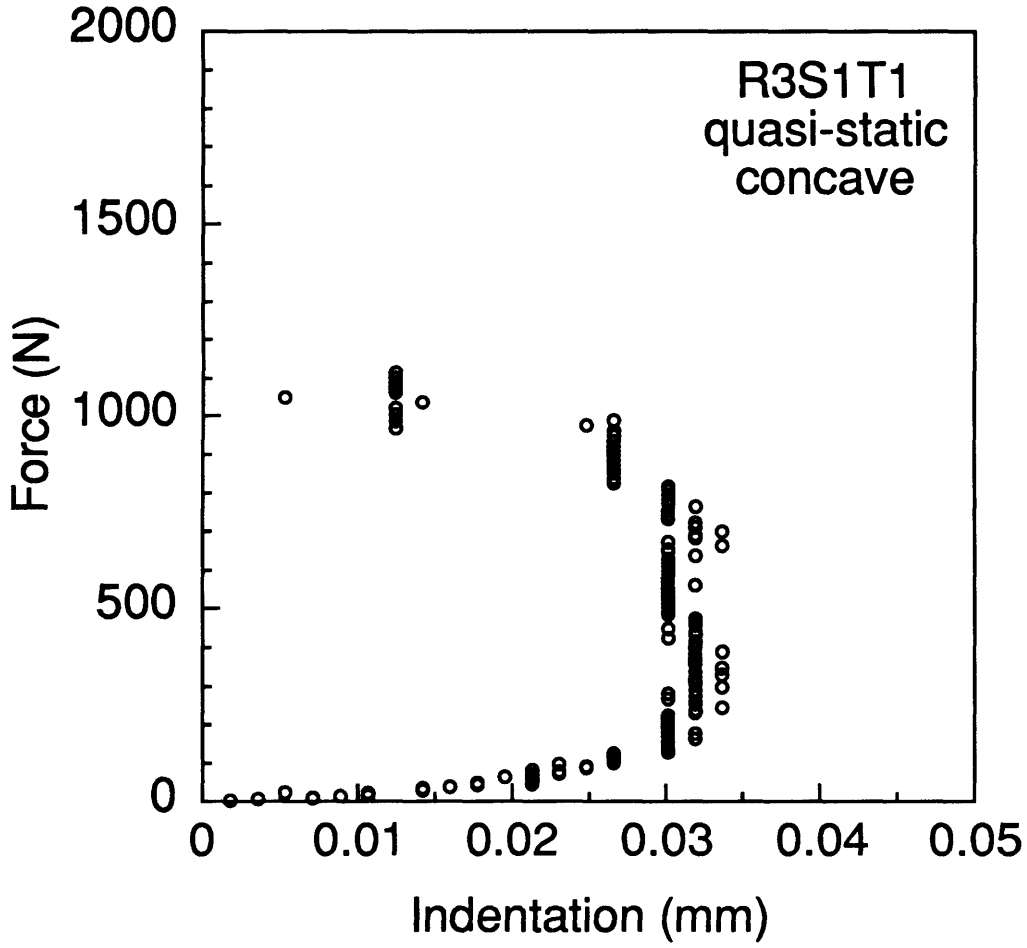

Figure F.21 Force-indentation response for quasi-static loading of specimen R3S1T1 (concave).

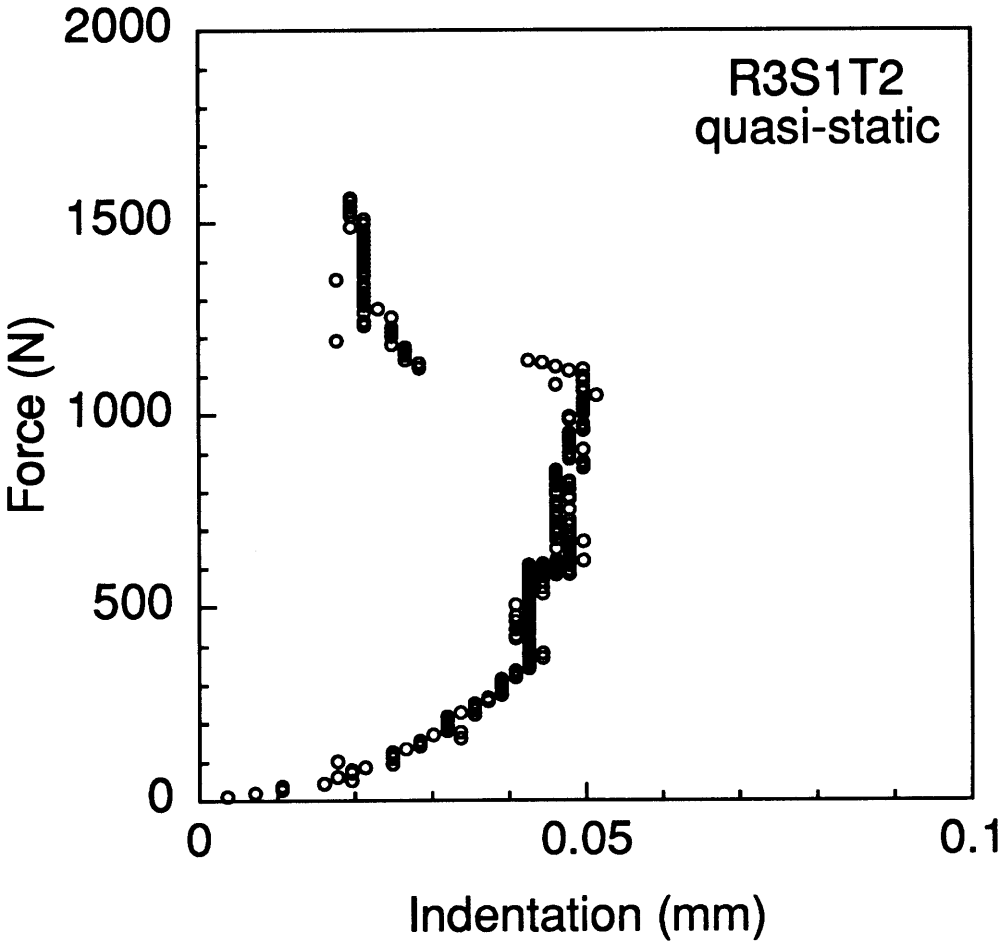

Figure F.22 Force-indentation response for quasi-static loading of specimen R3S1T2.

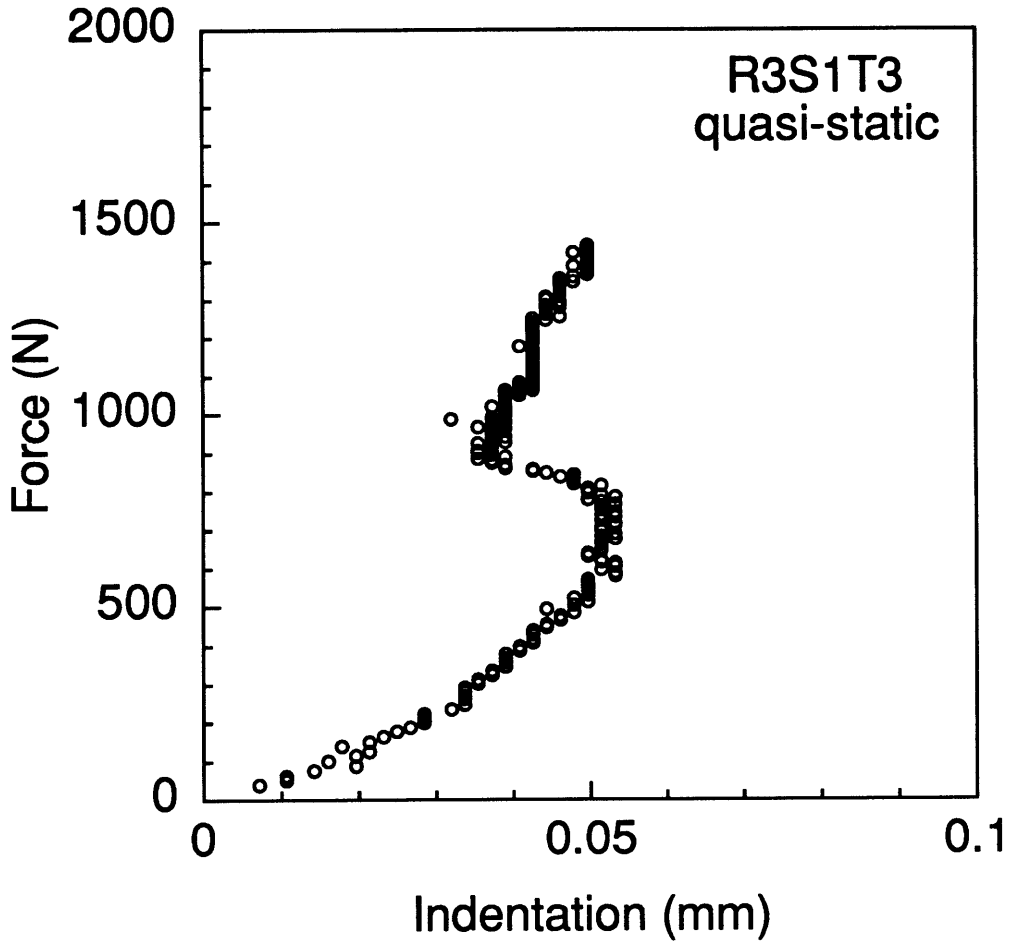

Figure F.23 Force-indentation response for quasi-static loading of specimen R3S1T3.

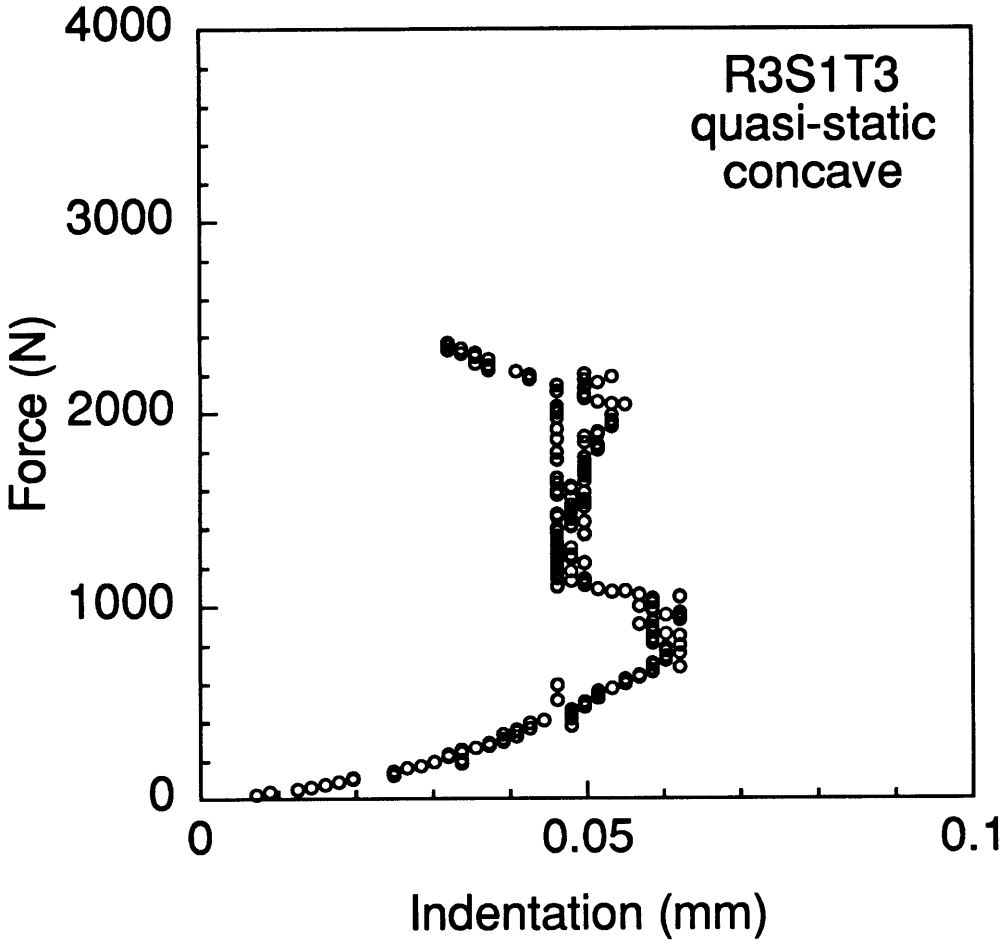

Figure F.24 Force-indentation response for quasi-static loading of specimen R3S1T3 (concave).

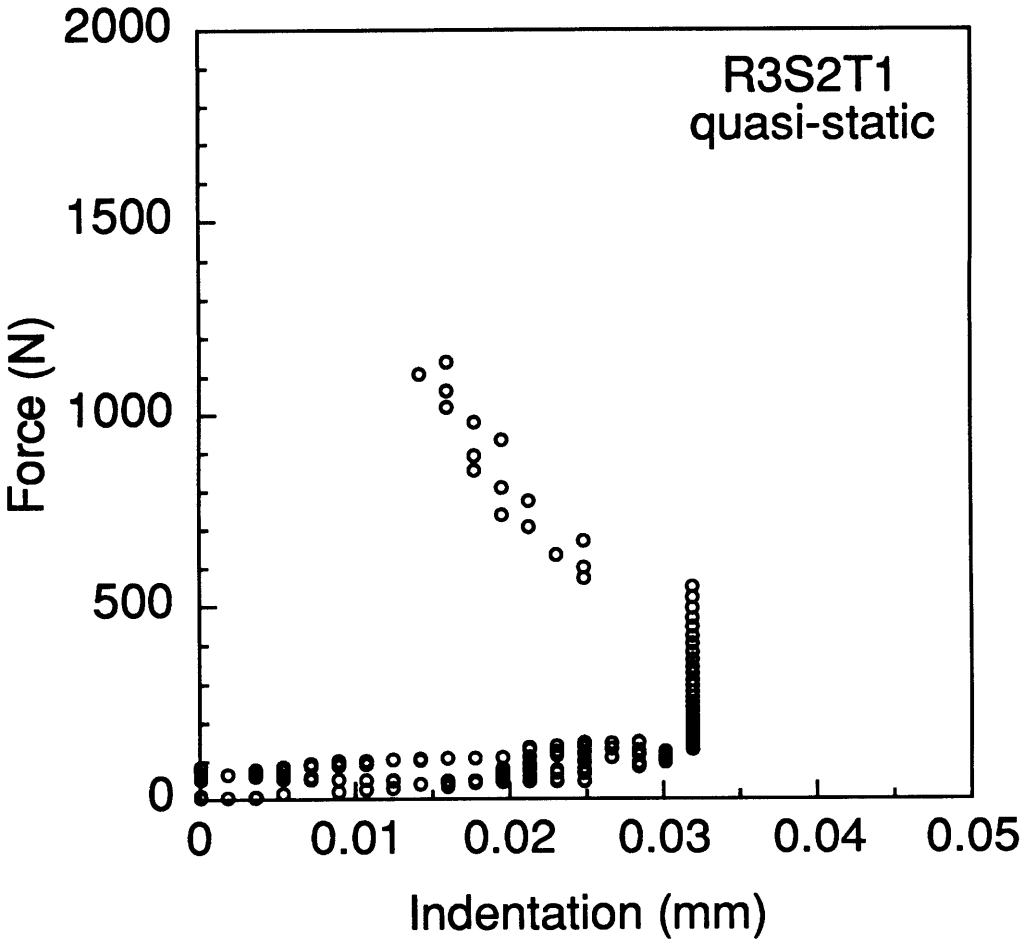

Figure F.25 Force-indentation response for quasi-static loading of specimen R3S2T1.

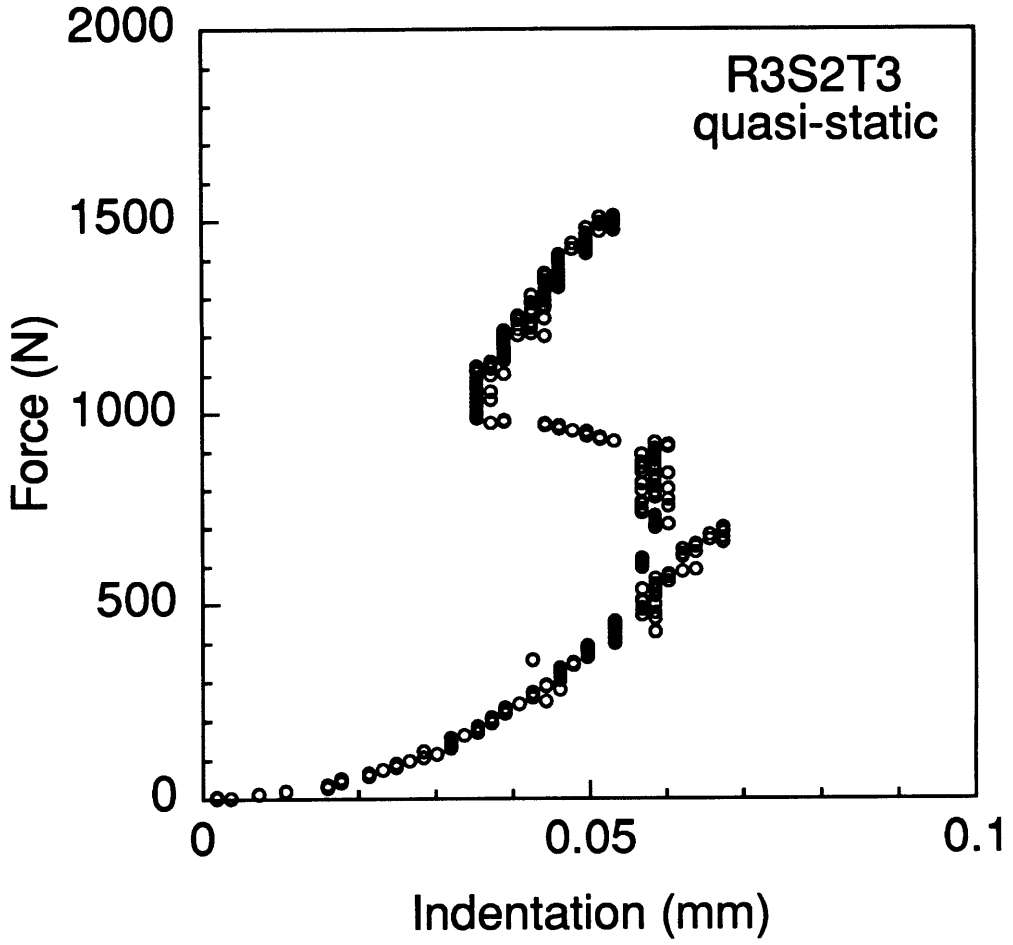

Figure F.26 Force-indentation response for quasi-static loading of specimen R3S2T3.

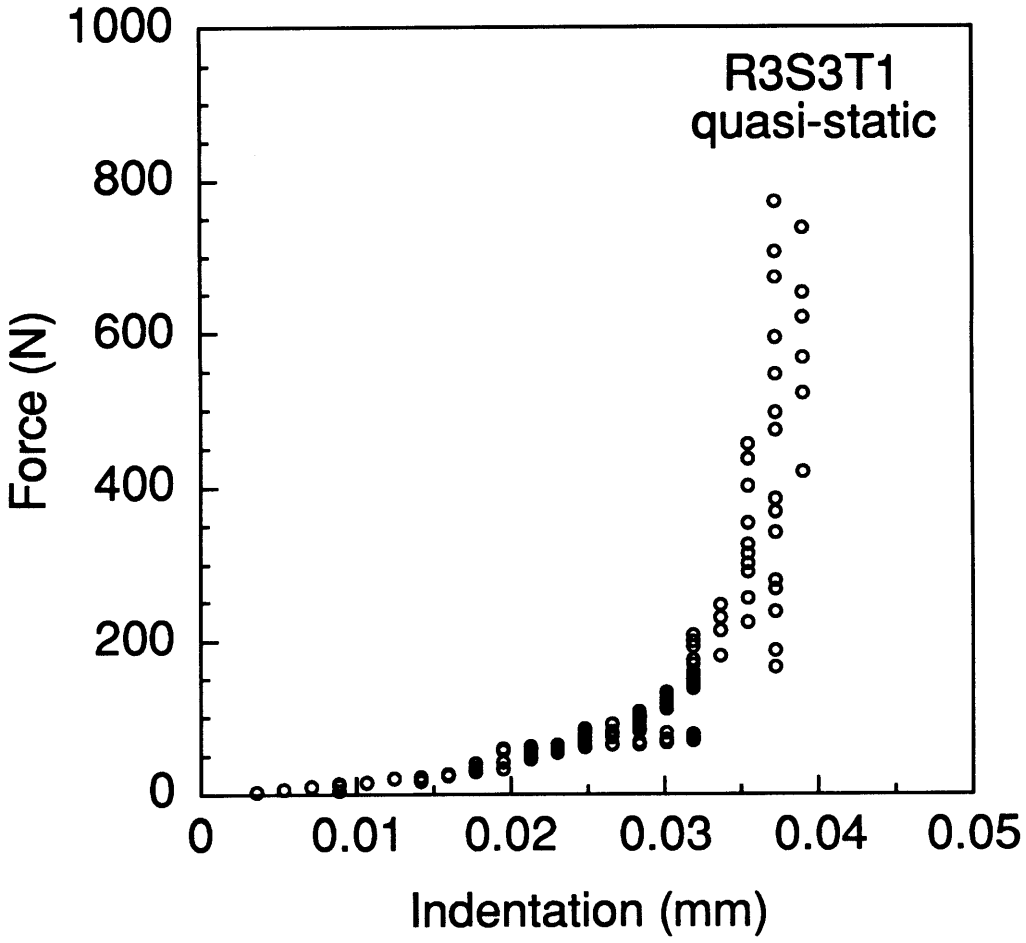

Figure F.27 Force-indentation response for quasi-static loading of specimen R3S3T1.

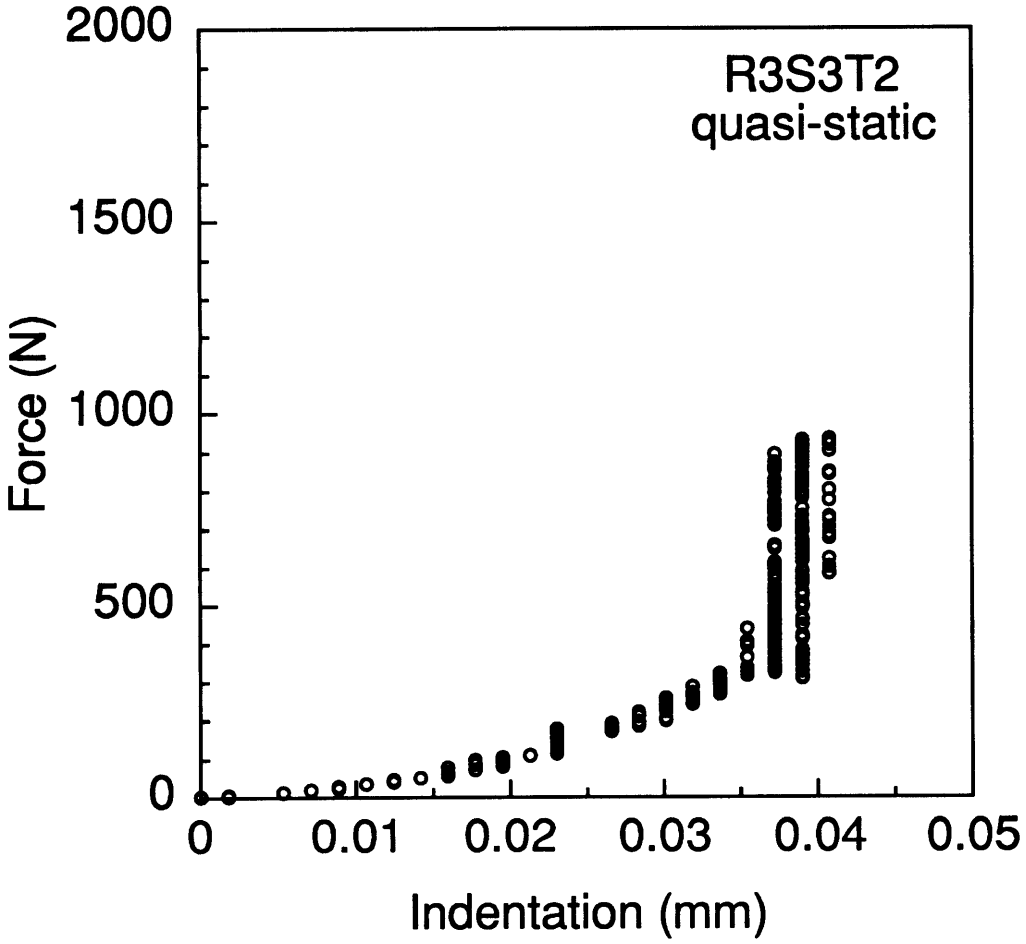

Figure F.28 Force-indentation response for quasi-static loading of specimen R3S3T2.

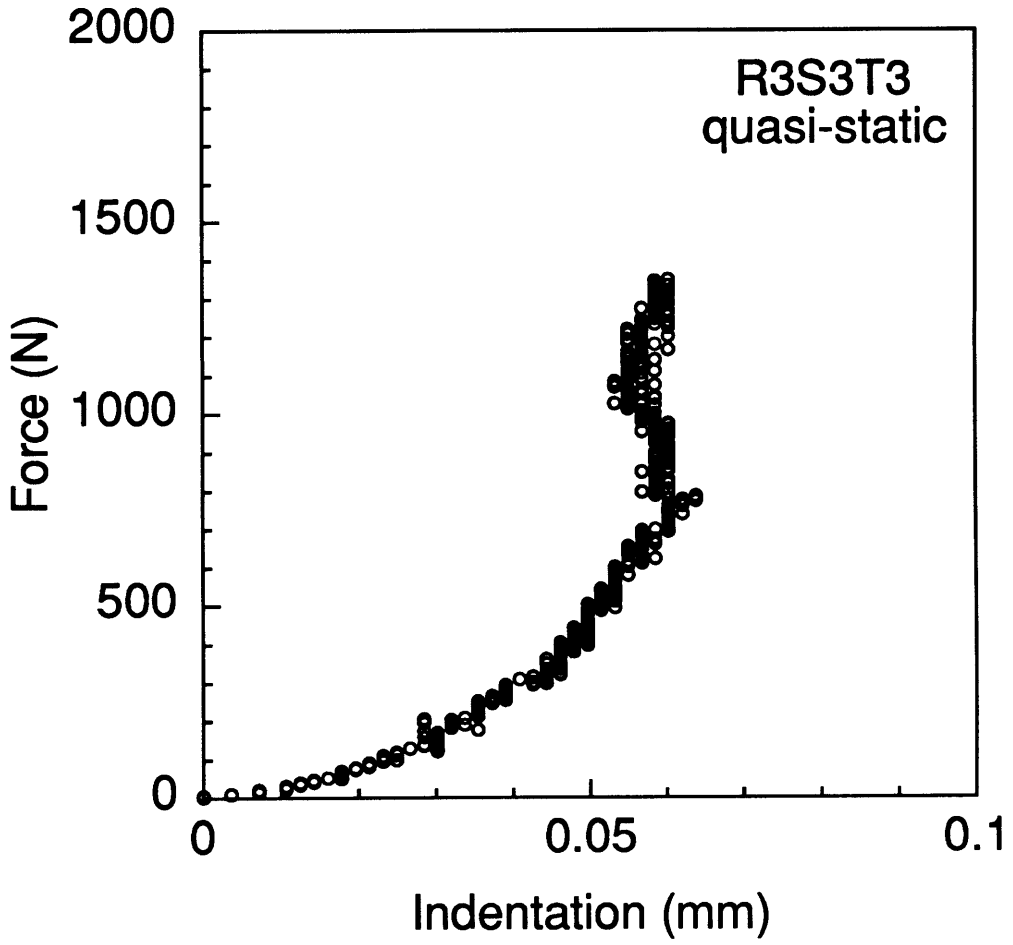

Figure F.29 Force-indentation response for quasi-static loading of specimen R3S3T3.

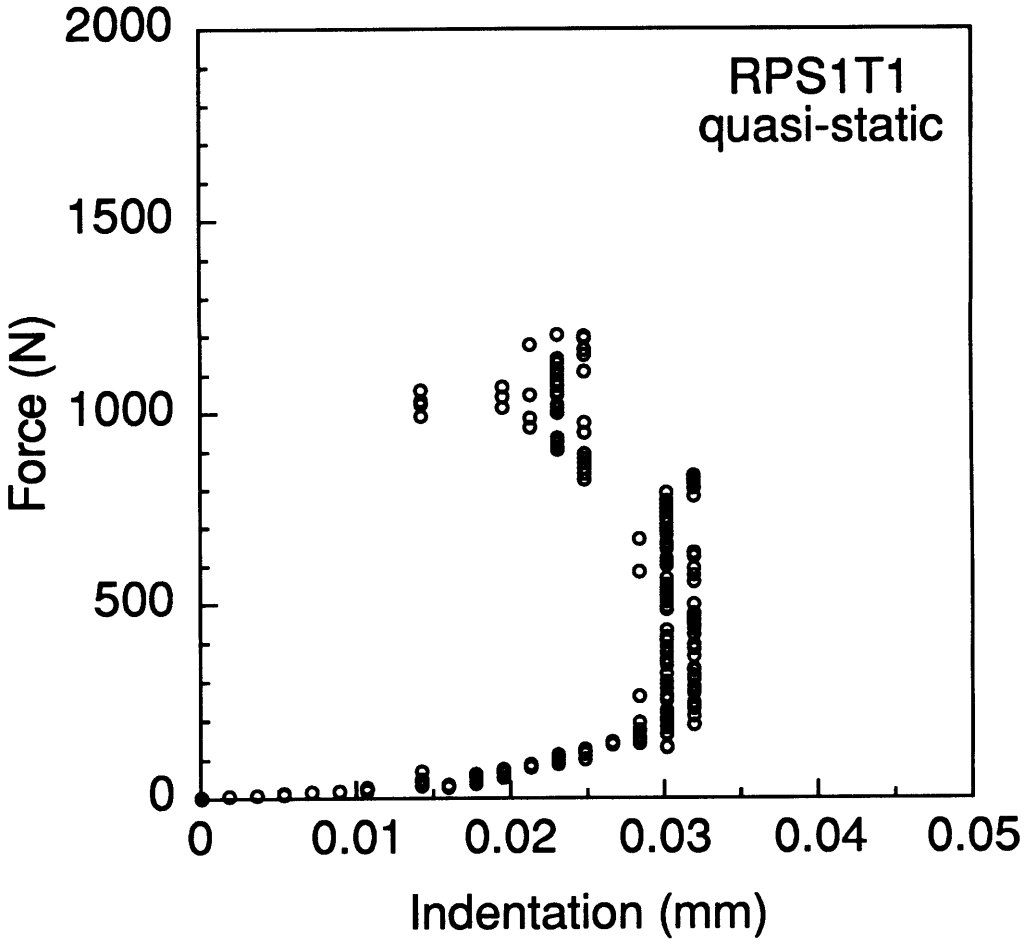

Figure F.30 Force-indentation response for quasi-static loading of specimen RPS1T1.

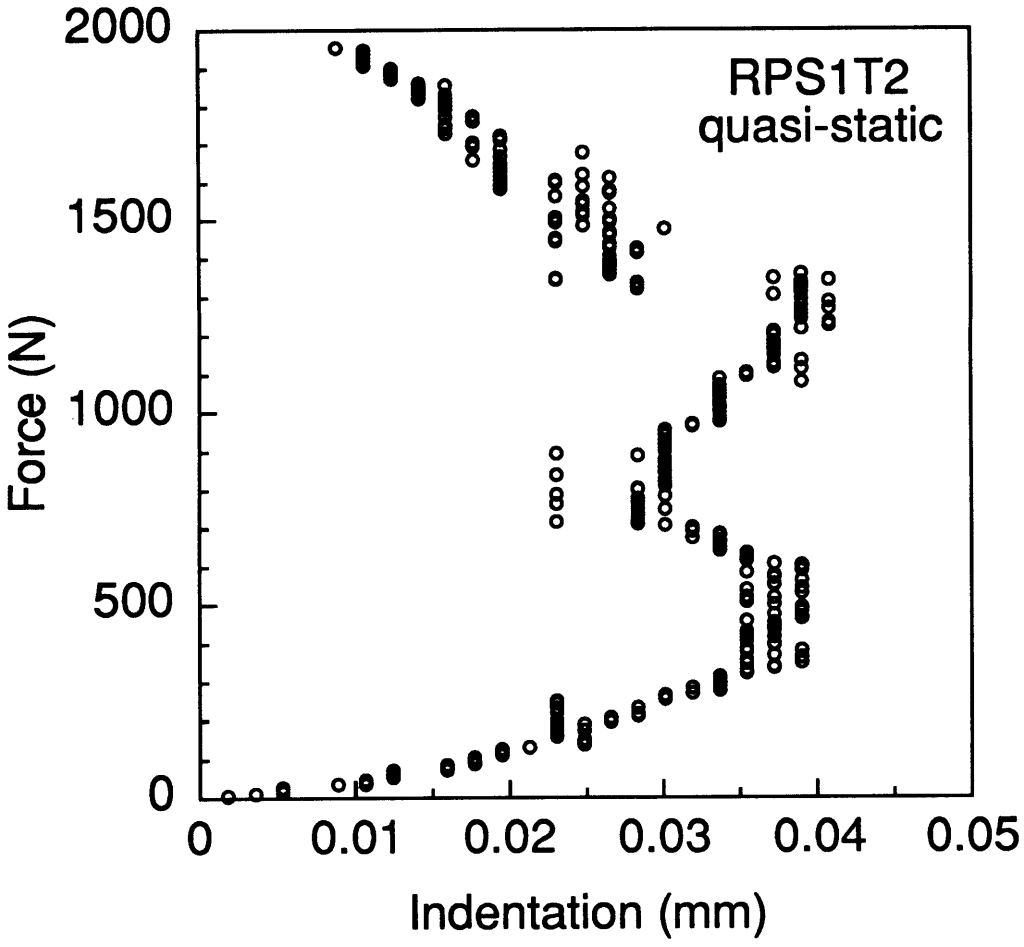

Figure F.31 Force-indentation response for quasi-static loading of specimen RPS1T2.

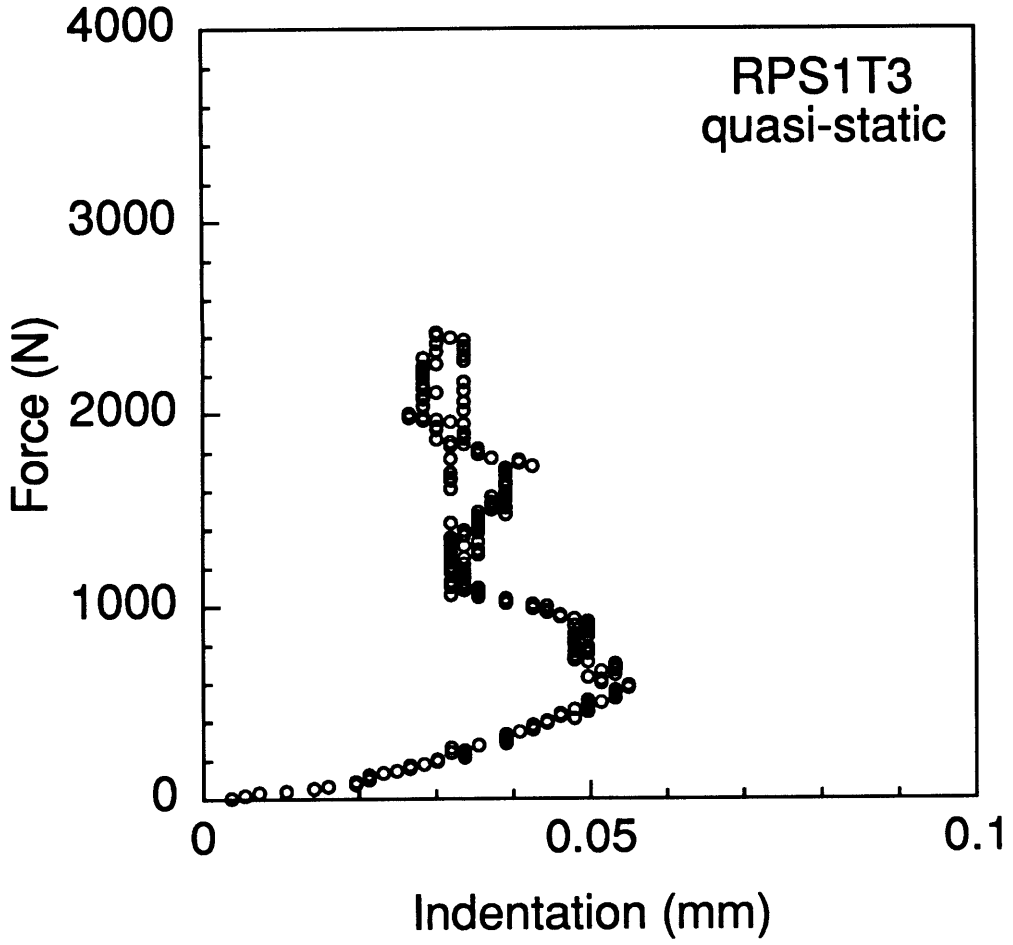

Figure F.32 Force-indentation response for quasi-static loading of specimen RPS1T3.

Appendix G

Damage Data for Quasi-static Tests

Data from visual and x-ray photography damage evaluation for specimens tested quasi-statically is presented in Table G.1. The damage metrics in Table G.1 are explained in chapter 5. Visual damage data is provided for both the front (side contacted) and back surface of the specimens. As described in chapter 5, damage lengths in the axial and circumferential shell directions of the elliptical marred region that is observed where the indentor contacted the specimen are used as damage metrics for front-surface damage. An elliptical area based on the damage lengths in the circumferential and axial directions is also calculated for each specimen. Matrix split lengths are used as the metric for the back-surface damage. The length of each observed matrix split is given in Table G.1. X-ray photography damage length data along the 45° and -45° directions is presented for all specimens as well as the average and ratio of the -45° to 45° lengths.

Table G.1 Data[a] from Visual and X-ray Photography Damage Evaluation for Quasi-static Tests

	Visual Damage Data				X-ray Photography Data			
	Front Surface			Back Surface				
Specimen[b]	Axial Length (mm)	Circumferential Length (mm)	Elliptic Area (mm^2)	Matrix Split Lengths (mm)	45° Length (mm)	-45° Length (mm)	Average (mm)	Ratio -45°/45°
R1S1T1	*6*	*5*	*24*	*20, 10*	*26*	*5*	*16*	*0.19*
R1S1T1c	5	7	28	20	25	6	16	0.24
R1S1T2	5	5	20	40, 30, 30, 20, 20, 10	70	60	65	0.86
R1S1T2c	5	4	16	20	21	11	16	0.52
R1S1T3	5	3	12	70	70	60	65	0.86
R1S1T3c	4	3	10	30	23	13	18	0.57
R1S2T1	2	2	3	0	0	0	0	-
R1S3T1	2	2	3	0	0	0	0	-
R1SCT1	0	0	0	0	0	0	0	-
R2S1T1	***11***	***13***	***112***	***penetration***	-	-	***penetration***	-
R2S1T1c	4	3	10	0	14	7	11	0.50
R2S1T2	*4*	*3*	*10*	*20, 10*	*22*	*9*	*16*	*0.41*
R2S1T2c	5	4	16	30	26	10	18	0.38
R2S1T3	4	2	6	50	65	50	58	0.77
R2S2T1	*3*	*3*	*7*	*0*	*10*	*4*	*7*	*0.40*
R2S2T2	4	3	10	20	17	10	14	0.59
R2S2T3	4	3	10	40, 30, 30	50	30	40	0.60
R2S3T1	*2*	*3*	*5*	*0*	*0*	*0*	*0*	-
R2S3T2	3	2	5	40	16	10	13	0.63
R3S1T1	*7*	*6*	*33*	*40, 30, 20*	*33*	*9*	*21*	*0.27*
R3S1T1c	4	3	10	10	13	4	9	0.31
R3S1T2	*4*	*3*	*10*	*40*	*29*	*9*	*19*	*0.31*
R3S1T3	0	0	0	40, 20	43	17	30	0.40
R3S1T3c	5	3	12	30	29	17	23	0.59
R3S2T1	*4*	*4*	*13*	*10*	*17*	*5*	*11*	*0.29*
R3S2T3	4	2	6	20	40	23	32	0.58

Table G.1 Data[a] from Visual and X-ray Photography Damage Evaluation for Quasi-static Tests (continued-2)

Specimen[b]	Visual Damage Data: Front Surface: Axial Length (mm)	Visual Damage Data: Front Surface: Circumferential Length (mm)	Visual Damage Data: Front Surface: Elliptic Area (mm^2)	Visual Damage Data: Back Surface: Matrix Split Lengths (mm)	X-ray Photography Data: 45° Length (mm)	X-ray Photography Data: -45° Length (mm)	X-ray Photography Data: Average (mm)	X-ray Photography Data: Ratio -45°/45°
R3S3T1	*3*	*3*	*7*	*0*	*8*	*4*	*6*	*0.50*
R3S3T2	3	3	7	0	14	8	11	0.57
R3S3T3	3	2	5	20	24	13	19	0.54
RPS1T1	**9**	**8**	**57**	**penetration**	-	-	**penetration**	-
RPS1T2	6	5	24	40	41	10	26	0.24
RPS1T3	5	4	16	40	40	16	28	0.40

[a] *Italics* indicate peak force occurred on the second equilibrium path (instability), and **bold** indicates penetration.

[b] "c" after specimen identification indicates concave test.